

PRESSURE AND VELOCITY DISTRIBUTION FOR AIR FLOW
THROUGH FRUITS PACKED IN SHIPPING CONTAINERS
USING POROUS MEDIA FLOW ANALYSIS

By

MICHAEL THOMAS TALBOT

A DISSERTATION PRESENTED TO THE GRADUATE SCHOOL OF
THE UNIVERSITY OF FLORIDA
IN PARTIAL FULFILLMENT OF THE REQUIREMENTS FOR THE DEGREE OF
DOCTOR OF PHILOSOPHY

UNIVERSITY OF FLORIDA

1987

UNIVERSITY OF FLORIDA LIBRARIES

ACKNOWLEDGMENT

The author wishes to express his sincere appreciation to Dr. Calvin C. Oliver who served as chairman of his supervisory committee. His guidance, encouragement, and assistance were invaluable throughout the course of this study.

For the leadership, interest, and assistance, they exhibited, appreciation is extended to the other members of his supervisory committee: Mr. J. J. Gaffney, USDA Agricultural Engineer; Dr. H. A. Ingley III, Dr. T. I. Shih, Mechanical Engineering; and Dr. R. F. Matthews, Food Science and Human Nutrition. Special thanks are also expressed for the early contributions of Dr. R. K. Ireby, an original committee member who is presently Chairman of the Mechanical Engineering Department at the University of Toledo, Ohio.

Appreciation is expressed to Dr. R. B. Gaither, Chairman of the Mechanical Engineering Department, and to the faculty members who contributed to his graduate program.

A special word of thanks is necessary for the invaluable assistance of Dean M. M. Lockhart, Dean J. L. Woeste and Dean G. L. Zachariah, as well as the Graduate Council, without which pursuit of this course of study would not have been possible.

He is indebted to the Department of Agricultural Engineering for financial support through full-time employment during the part-time pursuit of this course of study and to Dr. G. W. Isaacs, chairman, for his leadership, encouragement, and untiring willingness to cope with administrative problems involved. Thanks are also due to each of the many staff and faculty members who assisted in numerous ways, especially to Dr. C. D. Baird and Dr. K. V. Chau who actively supported his research as project leaders.

For their cheerful sacrifices and loving patience, the author dedicates this dissertation to his wife, Anita, his son, Michael, and his father, James Vernon (Buck) Talbot, who waited so eagerly and proudly but who could not be here for the completion.

Most of all, the author wishes to acknowledge the source of all knowledge and wisdom--the very God of the universe through His Son the Lord Jesus Christ. To God be the glory, for great things He hath done.

TABLE OF CONTENTS

	Page
ACKNOWLEDGMENT	ii
LIST OF TABLES	vi
LIST OF FIGURES	vii
ABSTRACT	xxvii
INTRODUCTION	1
OBJECTIVES	5
REVIEW OF LITERATURE	6
Background of Research	6
Fluid Flow Through Porous Media	12
PROCEDURE	32
Commercial Finite Element Package.....	43
Verification	44
Two-Dimensional Grain Bin	49
Three-Dimensional Grain Bin	52
Solution for Oranges Packed in Cartons	57
Three-Dimensional Bulk Oranges	60
Three-Dimensional Orange Carton	78
Experimental Temperature Measurement	88
Description of Experimental Facilities	88
Basic Construction of Precooler	88
Refrigeration Components and Controls	89
Air Temperature and Humidity	90
Air Flow	95
Reheat Section	97
Experimental Test Procedures	98
Heat Transfer Model	101
Selection of Model	102
Convective Heat Transfer Coefficient	112
Heat Transfer Model Modifications	116
ANSYS Output Data Reorganization	124
Heat Transfer Program	126
Temperature Response Data Reorganization	128

RESULTS AND DISCUSSION.....	131
Two-Dimensional Grain Bin.....	131
Three-Dimensional Grain Bin.....	139
Three-Dimensional Bulk Oranges.....	154
Three-Dimensional Orange Carton.....	161
Experimental Temperature Measurement.....	165
Heat Transfer Model.....	175
Experimental Error.....	179
Convective Heat Transfer Coefficient.....	181
Variable Porosity.....	182
Approximate Model Thermocouple Location.....	183
Experimental Versus Predicted Temperature Response...	183
SUMMARY.....	197
SUGGESTIONS FOR FUTURE WORK.....	200
APPLICATION OF RESULTS.....	202
CONCLUSIONS.....	204
APPENDIX A METHOD FOR ACCURATELY POSITIONING THERMOCOUPLES IN FRUITS AND VEGETABLES.....	206
APPENDIX B FORTRAN PROGRAMS AND DATA FILES.....	210
APPENDIX C PLOT INFORMATION.....	234
APPENDIX D ADDITIONAL DISCUSSION OF RESULTS FOR TWO- AND THREE-DIMENSIONAL GRAIN BIN MODELS.....	236
APPENDIX E ADDITIONAL EXPERIMENTAL TEMPERATURE RESPONSE GRAPHS.....	290
APPENDIX F ADDITIONAL PREDICTED TEMPERATURE RESPONSE GRAPHS.....	324
APPENDIX G ADDITIONAL PREDICTED VERSUS EXPERIMENTAL TEMPERATURE RESPONSE GRAPHS.....	358
APPENDIX H ADDITIONAL PREDICTED VERSUS EXPERIMENTAL TEMPERATURE REGRESSION GRAPHS.....	425
BIBLIOGRAPHY.....	437
BIOGRAPHICAL SKETCH.....	449

LIST OF TABLES

Table	Page
1. Summary of variable porosity and ANSYS input data.	85
2. Inlet and outlet air vent locations as indicated by the numbers illustrated in Figure 11.....	87
3. Boundary conditions and air flow rates (2 flow rates per venting arrangement) for tests conducted with an experimental orange carton packed with size 100 oranges	87
4. Physical and thermal properties of size 100 Valencia oranges, Gaffney and Baird (1980).....	114
5. Pressure values (inches of water) at specific points for the linear flow problem.....	132
6. Three-dimensional pressure loss data for oranges in bulk and orange carton sides.....	155

LIST OF FIGURES

Figure	Page
1. Region divided into finite element.....	36
2. Various types of finite elements.....	39
3. The node and element grid employed by Segerlind (1982).....	50
4. Boundary conditions used by Segerlind (1982).....	51
5. The node and element locations used in current study.....	53
6. Four different grainbin aeration systems studied by Khompis et al. (1984).....	55
7. Finite element model used by Khompis et al.(1984). 56	
8. The node and element locations used in current study.....	58
9. The experimental setup used by Chau et al. (1983) or measuring air flow resistance in orange.....	64
10. The node and element locations used to model 3-D oranges packed in bulk and in cartons.....	71
11. The experimental orange carton.....	80
12. The node and element locations used to model a 3-D orange carton.....	81
13. Forced-air precooler components and air circulation diagram, Baird et al. (1975).....	91
14. Modification of product bin to accommodate experimental carton.....	92
15. Precooler refrigeration components and controls, Baird et al. (1975).....	93
16. Fruit and thermocouple locations in experimental carton.....	100

17.	Diagram indicating a heat balance on the three types of nodes used in a sphere, Baird and Gaffney (1976).....	104
18.	Flow diagram for the computer program for heat conduction in a sphere with arbitrarily varying air temperature, Baird and Gaffney (1976).....	107
19.	Control volume for heat balance on bed, Baird and Gaffney (1976).....	109
20.	Flow diagram for the computer program to solve deep bed heat transfer equations, Baird and Gaffney (1976).....	113
21.	Typical three-dimensional element showing velocity at centroid and air flow across element faces....	118
22.	Flow diagram for the computer program to solve orange carton heat transfer equations.....	123
23.	Points of comparison for linear airflow calculations.....	132
24.	Plot of experimental isobaric lines from Brooker (1969).....	133
25.	85 percent isobaric contour line from Segerlind (1982).....	134
26.	Isobaric contour lines calculated using ANSYS for a boundary condition of 1 inch of water.....	135
27.	Isobaric contour lines calculated using ANSYS for a boundary condition of 2 inches of water....	136
28.	Isobaric contour lines calculated using ANSYS for a boundary condition of 3 inches of water....	137
29.	Isobaric distribution in percent of total pressure loss on a vertical cutting plane from Khompis (1983).....	141
30.	Isobaric distribution in percent of total pressure loss on horizontal cutting plane at 5 percent of bin height from Khompis (1983).....	142
31.	Isobaric distribution calculated using ANSYS in percent of total pressure loss on the vertical cutting plane.....	143
32.	Isobaric distribution calculated using ANSYS in percent of total pressure loss on the horizontal cutting plane at 5 percent of bin height.....	144

33.	Velocity distribution in meters per minute on a vertical cutting plane from Khompis (1983).....	145
34.	Velocity distribution in meters per minute on a horizontal cutting plane at 5 percent of bin height from Khompis (1983).....	146
35.	Velocity distribution calculated using ANSYS in meters per minute on a vertical cutting plane.....	147
36.	Velocity distribution calculated using ANSYS in meters per minute on a horizontal cutting plane at 5 percent of bin height.....	148
37.	70 percent of total pressure loss isobaric surface from Khompis (1983), view 2.....	149
38.	70 percent of total pressure loss isobaric surface produced by ANSYS, view 2.....	150
39.	Constant velocity surface of 2.4 meters per minute from Khompis (1983), view 2.....	152
40.	Constant velocity surface of 2.8 meters per minute calculated using ANSYS, view 2.....	153
41.	Nodal pressure printout for ANSYS solution.....	162
42.	Element flow rate printout for ANSYS solution....	163
43.	Example of the data printout produced by the data acquisition system for one experimental cooling test.....	166
44.	Experimental center temperature response of oranges in an experimental orange carton for forced-air cooling (Boundary Condition 1-1, thermocouple locations 10, 13, 66, and 69).....	168
45.	Experimental center temperature response of oranges in an experimental orange carton for forced-air cooling (Boundary Condition 1-1, 3rd layer thermocouple locations 31, 35, 36, 44, and 45).....	171
46.	Experimental center temperature response of oranges in an experimental orange carton for forced-air cooling (Boundary Condition 1-1, 2nd layer thermocouple locations 23, 24, 26, 27, and 29).....	172

47.	Experimental center temperature response of oranges in an experimental orange carton for forced-air cooling (Boundary Condition 1-1, 1st layer thermocouple locations 1, 9, 10, 14, and 15).....	173
48.	Graphical representation of three-dimensional color graphics output of cooling response for oranges within an experimental carton.....	174
49.	Predicted center temperature response of oranges in an experimental orange carton for forced-air cooling (Boundary Condition 1-1, 3rd layer thermocouple locations 31, 35, 36, 44, and 45).....	176
50.	Predicted center temperature response of oranges in an experimental orange carton for forced-air cooling (Boundary Condition 1-1, 2nd layer thermocouple locations 23, 24, 26, 27, and 29).....	177
51.	Predicted center temperature response of oranges in an experimental orange carton for forced-air cooling (Boundary Condition 1-1, 1st layer thermocouple locations 1, 9, 10, 14, and 15).....	178
52.	Predicted versus experimental data for Boundary Condition 1-1, 3rd layer thermocouples 31 and 35.....	185
53.	Predicted versus experimental data for Boundary Condition 1-1, 3rd layer thermocouples 44 and 45.....	186
54.	Predicted versus experimental data for Boundary Condition 1-1, 2nd layer thermocouples 23 and 24.....	187
55.	Predicted versus experimental data for Boundary Condition 1-1, 2nd layer thermocouples 26 and 29.....	188
56.	Predicted versus experimental data for Boundary Condition 1-1, 1st layer thermocouples 1 and 9...	189
57.	Predicted versus experimental data for Boundary Condition 1-1, 1st layer thermocouples 14 and 15.....	190

58.	Regression plot of the predicted temperature versus the experimental temperature for Boundary Condition 1-1 and test times of 3, 7, and 11 hours.....	191
A-1.	Thermocouple positioning, part 1.....	208
A-2.	Thermocouple positioning, part 2.....	209
B-1.	Portion of input data file "Dimensions" which lists for each element from left to right, the number, volume, x, y, and z dimensions, and the porosity.....	211
B-2.	Portion of input data file "Data" which lists for each element from left to right, the number, total velocity and x, y, and z component velocities.....	212
B-3.	Fortran program "Data-Reduction" which was used to calculate convective heat transfer coefficient and x, y, and z component mass flow rates at the centroid.....	213
B-4.	Portion of input/output data file "Heat-Mass" which lists for each element, the number, the convective heat transfer coefficient and x, y, and z component mass flow rates at the centroid..	215
B-5.	Fortran program "Flow-Wall" which was used to calculate x, y, and z component mass flow rates across the face of each element.....	216
B-6.	Portion of input/output data file "Mass-Flow" which lists for each element, the number, the x, y, and z component mass flow rates across the face of each element.....	218
B-7.	Fortran program "Temp-ID" which was used to calculate mass flow rates entering each element..	219
B-8.	Portion of input/output data file "Mass-Temp" which lists for each element, the number, the mass flow rates entering the x (left and right), y (bottom and top), and z (back and front) faces of each element along with the corresponding temperature identification label.....	222
B-9.	Fortran program "Heat-Do" which was used to solve the heat transfer model.....	223

B-10.	Input data file "Data-In-1" which lists the product thermal diffusivity, conductivity, and radius, the specific heat of the air and product and product density.....	229
B-11.	Input data file "Data-In-2" which lists number of product nodal points, the initial product temperature, the time increment, total test cooling time, data output print frequency, entering air temperature, and number of elements.	229
B-12.	Portion of input/output data file "Temp-Response" which lists for each element, the number, time (seconds), the air temperature, the product temperature at each of the nodes, and the product mass-average temperature.....	230
B-13.	Fortran program "Plot-Data" which was used to reorganize the temperature response to give 78 thermocouple readings.....	231
D-1.	Numerical pressure pattern for linear air flow through shelled corn from Brooker (1969), for 2 inches of water duct pressure.....	237
D-2.	Numerical pressure pattern for nonlinear air flow through shelled corn from Brooker (1969). The same pattern was obtained for duct pressures of 1, 2, and 3 inches of water.....	238
D-3.	Numerical velocity distribution for nonlinear air flow through shelled corn from Brooker (1969).....	239
D-4.	Plot of experimental isobaric lines from Brooker (1969).....	239
D-5.	85 percent isobaric contour line from Segerlind (1982).....	240
D-6.	Isobaric contour lines calculated using ANSYS for a boundary condition of 1 inch of water.....	242
D-7.	Isobaric contour lines calculated using ANSYS for a boundary condition of 2 inches of water....	243
D-8.	Isobaric contour lines calculated using ANSYS for a boundary condition of 3 inches of water....	244
D-9.	Modified boundary conditions used by Segerlind (1982).....	246
D-10.	85 percent isobaric lines from Segerlind (1982)..	246

D-11. Isobaric pattern for a duct pressure of 3 inches of water from Segerlind (1982).....	247
D-12. Isobaric contour lines calculated using ANSYS with a modified boundary condition of 1 inch of water.....	248
D-13. Isobaric contour lines calculated using ANSYS with a modified boundary condition of 2 inches of water.....	249
D-14. Isobaric contour lines calculated using ANSYS with a modified boundary condition of 3 inches of water.....	250
D-15. Vertical and Horizontal Cuttings Planes used by Khompis (1983).....	252
D-16. Location of the elements on the vertical cutting plane from Khompis (1983).....	253
D-17. Location of the elements on the horizontal cutting plane from Khompis (1983).....	254
D-18. Isobaric distribution in percent of total pressure loss on a vertical cutting plane from Khompis (1983).....	256
D-19. Isobaric distribution in percent of total pressure loss on horizontal cutting plane at 5 percent of bin height from Khompis (1983).....	257
D-20. Isobaric distribution in percent of total pressure loss on a horizontal cutting plane at 50 percent of bin height from Khompis (1983).....	258
D-21. 70 percent of total pressure loss isobaric surface from Khompis (1983).....	260
D-22. 70 percent of total pressure loss isobaric surface from Khompis (1983).....	261
D-23. 70 percent of total pressure loss isobaric surface from Khompis (1983).....	262
D-24. Velocity distribution in meters per minute on a vertical cutting plane from Khompis (1983).....	263
D-25. Velocity distribution in meters per minute on a horizontal cutting plane at 5 percent of bin height from Khompis (1983).....	264

D-26.	Velocity distribution in meters per minute on a vertical cutting plane at 50 percent of bin height from Khompis (1983).....	265
D-27.	Minimum velocity regions for the square duct system from Khompis (1983).....	266
D-28.	Constant velocity surface of 2.4 meters per minute from Khompis (1983).....	267
D-29.	Constant velocity surface of 2.4 meters per minute from Khompis (1983).....	268
D-30.	Constant velocity surface of 2.4 meters per minute from Khompis (1983).....	269
D-31.	Isobaric distribution calculated using ANSYS in percent of total pressure loss on the vertical cutting plane.....	271
D-32.	Isobaric distribution calculated using ANSYS in percent of total pressure loss on the horizontal cutting plane at 5 percent of bin height.....	272
D-33.	Isobaric distribution calculated using ANSYS in percent of total pressure loss on the horizontal cutting plane at 50 percent of bin height.....	273
D-34.	70 percent of total pressure loss isobaric surface produced by ANSYS, view 1.....	276
D-35.	70 percent of total pressure loss isobaric surface produced by ANSYS, view 2.....	277
D-36.	70 percent of total pressure loss isobaric surface produced by ANSYS, view 3.....	278
D-37.	Velocity distribution calculated using ANSYS in meters per minute on a vertical cutting plane.....	281
D-38.	Velocity distribution calculated using ANSYS in meters per minute on a horizontal cutting plane at 5 percent of bin height.....	282
D-39.	Velocity distribution calculated using ANSYS in meters per minute on a horizontal cutting plane at 50 percent of bin height.....	283
D-40.	Constant velocity surface of 2.8 meters per minute calculated using ANSYS, view 1.....	287
D-41.	Constant velocity surface of 2.8 meters per minute calculated using ANSYS, view 2.....	288

D-42.	Constant velocity surface of 2.8 meters per minute calculated using ANSYS, view 3.....	289
E-1.	Experimental center temperature response of oranges in an experimental orange carton for forced-air cooling (Boundary Condition 1-2, 3rd layer thermocouple locations 31, 35, 36, 44, and 45).....	291
E-2.	Experimental center temperature response of oranges in an experimental orange carton for forced-air cooling (Boundary Condition 1-2, 2nd layer thermocouple locations 23, 24, 26, 27, and 29).....	292
E-3.	Experimental center temperature response of oranges in an experimental orange carton for forced-air cooling (Boundary Condition 1-2, 1st layer thermocouple locations 1, 9, 10, 14, and 15).....	293
E-4.	Experimental center temperature response of oranges in an experimental orange carton for forced-air cooling (Boundary Condition 2-1, 3rd layer thermocouple locations 31, 35, 36, 44, and 45).....	294
E-5.	Experimental center temperature response of oranges in an experimental orange carton for forced-air cooling (Boundary Condition 2-1, 2nd layer thermocouple locations 23, 24, 26, 27, and 29).....	295
E-6.	Experimental center temperature response of oranges in an experimental orange carton for forced-air cooling (Boundary Condition 2-1, 1st layer thermocouple locations 1, 9, 10, 14, and 15).....	296
E-7.	Experimental center temperature response of oranges in an experimental orange carton for forced-air cooling (Boundary Condition 2-2, 3rd layer thermocouple locations 31, 35, 36, 44, and 45).....	297
E-8.	Experimental center temperature response of oranges in an experimental orange carton for forced-air cooling (Boundary Condition 2-2, 2nd layer thermocouple locations 23, 24, 26, 27, and 29).....	298

E-9.	Experimental center temperature response of oranges in an experimental orange carton for forced-air cooling (Boundary Condition 2-2, 1st layer thermocouple locations 1, 9, 10, 14, and 15).....	299
E-10.	Experimental center temperature response of oranges in an experimental orange carton for forced-air cooling (Boundary Condition 3-1, 3rd layer thermocouple locations 31, 35, 36, 44, and 45).....	300
E-11.	Experimental center temperature response of oranges in an experimental orange carton for forced-air cooling (Boundary Condition 3-1, 2nd layer thermocouple locations 23, 24, 26, 27, and 29).....	301
E-12.	Experimental center temperature response of oranges in an experimental orange carton for forced-air cooling (Boundary Condition 3-1, 1st layer thermocouple locations 1, 9, 10, 14, and 15).....	302
E-13.	Experimental center temperature response of oranges in an experimental orange carton for forced-air cooling (Boundary Condition 3-2, 3rd layer thermocouple locations 31, 35, 36, 44, and 45).....	303
E-14.	Experimental center temperature response of oranges in an experimental orange carton for forced-air cooling (Boundary Condition 3-2, 2nd layer thermocouple locations 23, 24, 26, 27, and 29).....	304
E-15.	Experimental center temperature response of oranges in an experimental orange carton for forced-air cooling (Boundary Condition 3-2, 1st layer thermocouple locations 1, 9, 10, 14, and 15).....	305
E-16.	Experimental center temperature response of oranges in an experimental orange carton for forced-air cooling (Boundary Condition 4-1, 3rd layer thermocouple locations 31, 35, 36, 44, and 45).....	306
E-17.	Experimental center temperature response of oranges in an experimental orange carton for forced-air cooling (Boundary Condition 4-1, 2nd layer thermocouple locations 23, 24, 26, 27, and 29).....	307

E-18. Experimental center temperature response of oranges in an experimental orange carton for forced-air cooling (Boundary Condition 4-1, 1st layer thermocouple locations 1, 9, 10, 14, and 15).....	308
E-19. Experimental center temperature response of oranges in an experimental orange carton for forced-air cooling (Boundary Condition 4-2, 3rd layer thermocouple locations 31, 35, 36, 44, and 45).....	309
E-20. Experimental center temperature response of oranges in an experimental orange carton for forced-air cooling (Boundary Condition 4-2, 2nd layer thermocouple locations 23, 24, 26, 27, and 29).....	310
E-21. Experimental center temperature response of oranges in an experimental orange carton for forced-air cooling (Boundary Condition 4-2, 1st layer thermocouple locations 1, 9, 10, 14, and 15).....	311
E-22. Experimental center temperature response of oranges in an experimental orange carton for forced-air cooling (Boundary Condition 5-1, 3rd layer thermocouple locations 31, 35, 36, 44, and 45).....	312
E-23. Experimental center temperature response of oranges in an experimental orange carton for forced-air cooling (Boundary Condition 5-1, 2nd layer thermocouple locations 23, 24, 26, 27, and 29).....	313
E-24. Experimental center temperature response of oranges in an experimental orange carton for forced-air cooling (Boundary Condition 5-1, 1st layer thermocouple locations 1, 9, 10, 14, and 15).....	314
E-25. Experimental center temperature response of oranges in an experimental orange carton for forced-air cooling (Boundary Condition 5-2, 3rd layer thermocouple locations 31, 35, 36, 44, and 45).....	315
E-26. Experimental center temperature response of oranges in an experimental orange carton for forced-air cooling (Boundary Condition 5-2, 2nd layer thermocouple locations 23, 24, 26, 27, and 29).....	316

E-27.	Experimental center temperature response of oranges in an experimental orange carton for forced-air cooling (Boundary Condition 5-2, 1st layer thermocouple locations 1, 9, 10, 14, and 15).....	317
E-28.	Experimental center temperature response of oranges in an experimental orange carton for forced-air cooling (Boundary Condition 6-1, 3rd layer thermocouple locations 31, 35, 36, 44, and 45).....	318
E-29.	Experimental center temperature response of oranges in an experimental orange carton for forced-air cooling (Boundary Condition 6-1, 2nd layer thermocouple locations 23, 24, 26, 27, and 29).....	319
E-30.	Experimental center temperature response of oranges in an experimental orange carton for forced-air cooling (Boundary Condition 6-1, 1st layer thermocouple locations 1, 9, 10, 14, and 15).....	320
E-31.	Experimental center temperature response of oranges in an experimental orange carton for forced-air cooling (Boundary Condition 6-2, 3rd layer thermocouple locations 31, 35, 36, 44, and 45).....	321
E-32.	Experimental center temperature response of oranges in an experimental orange carton for forced-air cooling (Boundary Condition 6-2, 2nd layer thermocouple locations 23, 24, 26, 27, and 29).....	322
E-33.	Experimental center temperature response of oranges in an experimental orange carton for forced-air cooling (Boundary Condition 6-2, 1st layer thermocouple locations 1, 9, 10, 14, and 15).....	323
F-1.	Predicted center temperature response of oranges in an experimental orange carton for forced-air cooling (Boundary Condition 1-2, 3rd layer thermocouple locations 31, 35, 36, 44, and 45)...	325
F-2.	Predicted center temperature response of oranges in an experimental orange carton for forced-air cooling (Boundary Condition 1-2, 2nd layer thermocouple locations 23, 24, 26, 27, and 29)...	326

- F-3. Predicted center temperature response of oranges in an experimental orange carton for forced-air cooling (Boundary Condition 1-2, 1st layer thermocouple locations 1, 9, 10, 14, and 15)..... 327
- F-4. Predicted center temperature response of oranges in an experimental orange carton for forced-air cooling (Boundary Condition 2-1, 3rd layer thermocouple locations 31, 35, 36, 44, and 45)... 328
- F-5. Predicted center temperature response of oranges in an experimental orange carton for forced-air cooling (Boundary Condition 2-1, 2nd layer thermocouple locations 23, 24, 26, 27, and 29)... 329
- F-6. Predicted center temperature response of oranges in an experimental orange carton for forced-air cooling (Boundary Condition 2-1, 1st layer thermocouple locations 1, 9, 10, 14, and 15)..... 330
- F-7. Predicted center temperature response of oranges in an experimental orange carton for forced-air cooling (Boundary Condition 2-2, 3rd layer thermocouple locations 31, 35, 36, 44, and 45)... 331
- F-8. Predicted center temperature response of oranges in an experimental orange carton for forced-air cooling (Boundary Condition 2-2, 2nd layer thermocouple locations 23, 24, 26, 27, and 29)... 332
- F-9. Predicted center temperature response of oranges in an experimental orange carton for forced-air cooling (Boundary Condition 2-2, 1st layer thermocouple locations 1, 9, 10, 14, and 15)..... 333
- F-10. Predicted center temperature response of oranges in an experimental orange carton for forced-air cooling (Boundary Condition 3-1, 3rd layer thermocouple locations 31, 35, 36, 44, and 45)... 334
- F-11. Predicted center temperature response of oranges in an experimental orange carton for forced-air cooling (Boundary Condition 3-1, 2nd layer thermocouple locations 23, 24, 26, 27, and 29)... 335
- F-12. Predicted center temperature response of oranges in an experimental orange carton for forced-air cooling (Boundary Condition 3-1, 1st layer thermocouple locations 1, 9, 10, 14, and 15)..... 336
- F-13. Predicted center temperature response of oranges in an experimental orange carton for forced-air cooling (Boundary Condition 3-2, 3rd layer thermocouple locations 31, 35, 36, 44, and 45)... 337

- F-14. Predicted center temperature response of oranges in an experimental orange carton for forced-air cooling (Boundary Condition 3-2, 2nd layer thermocouple locations 23, 24, 26, 27, and 29).. 338
- F-15. Predicted center temperature response of oranges in an experimental orange carton for forced-air cooling (Boundary Condition 3-2, 1st layer thermocouple locations 1, 9, 10, 14, and 15).... 339
- F-16. Predicted center temperature response of oranges in an experimental orange carton for forced-air cooling (Boundary Condition 4-1, 3rd layer thermocouple locations 31, 35, 36, 44, and 45).. 340
- F-17. Predicted center temperature response of oranges in an experimental orange carton for forced-air cooling (Boundary Condition 4-1, 2nd layer thermocouple locations 23, 24, 26, 27, and 29)... 341
- F-18. Predicted center temperature response of oranges in an experimental orange carton for forced-air cooling (Boundary Condition 4-1, 1st layer thermocouple locations 1, 9, 10, 14, and 15)..... 342
- F-19. Predicted center temperature response of oranges in an experimental orange carton for forced-air cooling (Boundary Condition 4-2, 3rd layer thermocouple locations 31, 35, 36, 44, and 45)... 343
- F-20. Predicted center temperature response of oranges in an experimental orange carton for forced-air cooling (Boundary Condition 4-2, 2nd layer thermocouple locations 23, 24, 26, 27, and 29)... 344
- F-21. Predicted center temperature response of oranges in an experimental orange carton for forced-air cooling (Boundary Condition 4-2, 1st layer thermocouple locations 1, 9, 10, 14, and 15)..... 345
- F-22. Predicted center temperature response of oranges in an experimental orange carton for forced-air cooling (Boundary Condition 5-1, 3rd layer thermocouple locations 31, 35, 36, 44, and 45)... 346
- F-23. Predicted center temperature response of oranges in an experimental orange carton for forced-air cooling (Boundary Condition 5-1, 2nd layer thermocouple locations 23, 24, 26, 27, and 29)... 347
- F-24. Predicted center temperature response of oranges in an experimental orange carton for forced-air cooling (Boundary Condition 5-1, 1st layer thermocouple locations 1, 9, 10, 14, and 15)..... 348

- F-25. Predicted center temperature response of oranges in an experimental orange carton for forced-air cooling (Boundary Condition 5-2, 3rd layer thermocouple locations 31, 35, 36, 44, and 45)... 349
- F-26. Predicted center temperature response of oranges in an experimental orange carton for forced-air cooling (Boundary Condition 5-2, 2nd layer thermocouple locations 23, 24, 26, 27, and 29)... 350
- F-27. Predicted center temperature response of oranges in an experimental orange carton for forced-air cooling (Boundary Condition 5-2, 1st layer thermocouple locations 1, 9, 10, 14, and 15)..... 351
- F-28. Predicted center temperature response of oranges in an experimental orange carton for forced-air cooling (Boundary Condition 6-1, 3rd layer thermocouple locations 31, 35, 36, 44, and 45)... 352
- F-29. Predicted center temperature response of oranges in an experimental orange carton for forced-air cooling (Boundary Condition 6-1, 2nd layer thermocouple locations 23, 24, 26, 27, and 29)... 353
- F-30. Predicted center temperature response of oranges in an experimental orange carton for forced-air cooling (Boundary Condition 6-1, 1st layer thermocouple locations 1, 9, 10, 14, and 15)..... 354
- F-31. Predicted center temperature response of oranges in an experimental orange carton for forced-air cooling (Boundary Condition 6-2, 3rd layer thermocouple locations 31, 35, 36, 44, and 45)... 355
- F-32. Predicted center temperature response of oranges in an experimental orange carton for forced-air cooling (Boundary Condition 6-2, 2nd layer thermocouple locations 23, 24, 26, 27, and 29)... 356
- F-33. Predicted center temperature response of oranges in an experimental orange carton for forced-air cooling (Boundary Condition 6-2, 1st layer thermocouple locations 1, 9, 10, 14, and 15)..... 357
- G-1. Predicted versus experimental data for Boundary Condition 1-2, 3rd layer thermocouples 31 and 35. 359
- G-2. Predicted versus experimental data for Boundary Condition 1-2, 3rd layer thermocouples 44 and 45. 360
- G-3. Predicted versus experimental data for Boundary Condition 1-2, 2nd layer thermocouples 23 and 24. 361

- G-4. Predicted versus experimental data for Boundary
Condition 1-2, 2nd layer thermocouples 26 and 29. 362
- G-5. Predicted versus experimental data for Boundary
Condition 1-2, 1st layer thermocouples 1 and 9... 363
- G-6. Predicted versus experimental data for Boundary
Condition 1-2, 1st layer thermocouples 14 and 15. 364
- G-7. Predicted versus experimental data for Boundary
Condition 2-1, 3rd layer thermocouples 31 and 35. 365
- G-8. Predicted versus experimental data for Boundary
Condition 2-1, 3rd layer thermocouples 44 and 45. 366
- G-9. Predicted versus experimental data for Boundary
Condition 2-1, 2nd layer thermocouples 23 and 24. 367
- G-10. Predicted versus experimental data for Boundary
Condition 2-1, 2nd layer thermocouples 26 and 29. 368
- G-11. Predicted versus experimental data for Boundary
Condition 2-1, 1st layer thermocouples 1 and 9... 369
- G-12. Predicted versus experimental data for Boundary
Condition 2-1, 1st layer thermocouples 14 and 15. 370
- G-13. Predicted versus experimental data for Boundary
Condition 2-2, 3rd layer thermocouples 31 and 35. 371
- G-14. Predicted versus experimental data for Boundary
Condition 2-2, 3rd layer thermocouples 44 and 45. 372
- G-15. Predicted versus experimental data for Boundary
Condition 2-2, 2nd layer thermocouples 23 and 24. 373
- G-16. Predicted versus experimental data for Boundary
Condition 2-2, 2nd layer thermocouples 26 and 29. 374
- G-17. Predicted versus experimental data for Boundary
Condition 2-2, 1st layer thermocouples 1 and 9... 375
- G-18. Predicted versus experimental data for Boundary
Condition 2-2, 1st layer thermocouples 14 and 15. 376
- G-19. Predicted versus experimental data for Boundary
Condition 3-1, 3rd layer thermocouples 31 and 35. 377
- G-20. Predicted versus experimental data for Boundary
Condition 3-1, 3rd layer thermocouples 44 and 45. 378
- G-21. Predicted versus experimental data for Boundary
Condition 3-1, 2nd layer thermocouples 23 and 24. 379

- G-22. Predicted versus experimental data for Boundary
Condition 3-1, 2nd layer thermocouples 26 and 29. 380
- G-23. Predicted versus experimental data for Boundary
Condition 3-1, 1st layer thermocouples 1 and 9... 381
- G-24. Predicted versus experimental data for Boundary
Condition 3-1, 1st layer thermocouples 14 and 15. 382
- G-25. Predicted versus experimental data for Boundary
Condition 3-2, 3rd layer thermocouples 31 and 35. 383
- G-26. Predicted versus experimental data for Boundary
Condition 3-2, 3rd layer thermocouples 44 and 45. 384
- G-27. Predicted versus experimental data for Boundary
Condition 3-2, 2nd layer thermocouples 23 and 24. 385
- G-28. Predicted versus experimental data for Boundary
Condition 3-2, 2nd layer thermocouples 26 and 29. 386
- G-29. Predicted versus experimental data for Boundary
Condition 3-2, 1st layer thermocouples 1 and 9... 387
- G-30. Predicted versus experimental data for Boundary
Condition 3-2, 1st layer thermocouples 14 and 15. 388
- G-31. Predicted versus experimental data for Boundary
Condition 4-1, 3rd layer thermocouples 31 and 35. 389
- G-32. Predicted versus experimental data for Boundary
Condition 4-1, 3rd layer thermocouples 44 and 45. 390
- G-33. Predicted versus experimental data for Boundary
Condition 4-1, 2nd layer thermocouples 23 and 24. 391
- G-34. Predicted versus experimental data for Boundary
Condition 4-1, 2nd layer thermocouples 26 and 29. 392
- G-35. Predicted versus experimental data for Boundary
Condition 4-1, 1st layer thermocouples 1 and 9... 393
- G-36. Predicted versus experimental data for Boundary
Condition 4-1, 1st layer thermocouples 14 and 15. 394
- G-37. Predicted versus experimental data for Boundary
Condition 4-2, 3rd layer thermocouples 31 and 35. 395
- G-38. Predicted versus experimental data for Boundary
Condition 4-2, 3rd layer thermocouples 44 and 45. 396
- G-39. Predicted versus experimental data for Boundary
Condition 4-2, 2nd layer thermocouples 23 and 24. 397

- G-40. Predicted versus experimental data for Boundary
Condition 4-2, 2nd layer thermocouples 26 and 29. 398
- G-41. Predicted versus experimental data for Boundary
Condition 4-2, 1st layer thermocouples 1 and 9... 399
- G-42. Predicted versus experimental data for Boundary
Condition 4-2, 1st layer thermocouples 14 and 15. 400
- G-43. Predicted versus experimental data for Boundary
Condition 5-1, 3rd layer thermocouples 31 and 35. 401
- G-44. Predicted versus experimental data for Boundary
Condition 5-1, 3rd layer thermocouples 44 and 45. 402
- G-45. Predicted versus experimental data for Boundary
Condition 5-1, 2nd layer thermocouples 23 and 24. 403
- G-46. Predicted versus experimental data for Boundary
Condition 5-1, 2nd layer thermocouples 26 and 29. 404
- G-47. Predicted versus experimental data for Boundary
Condition 5-1, 1st layer thermocouples 1 and 9... 405
- G-48. Predicted versus experimental data for Boundary
Condition 5-1, 1st layer thermocouples 14 and 15. 406
- G-49. Predicted versus experimental data for Boundary
Condition 5-2, 3rd layer thermocouples 31 and 35. 407
- G-50. Predicted versus experimental data for Boundary
Condition 5-2, 3rd layer thermocouples 44 and 45. 408
- G-51. Predicted versus experimental data for Boundary
Condition 5-2, 2nd layer thermocouples 23 and 24. 409
- G-52. Predicted versus experimental data for Boundary
Condition 5-2, 2nd layer thermocouples 26 and 29. 410
- G-53. Predicted versus experimental data for Boundary
Condition 5-2, 1st layer thermocouples 1 and 9... 411
- G-54. Predicted versus experimental data for Boundary
Condition 5-2, 1st layer thermocouples 14 and 15. 412
- G-55. Predicted versus experimental data for Boundary
Condition 6-1, 3rd layer thermocouples 31 and 35. 413
- G-56. Predicted versus experimental data for Boundary
Condition 6-1, 3rd layer thermocouples 44 and 45. 414
- G-57. Predicted versus experimental data for Boundary
Condition 6-1, 2nd layer thermocouples 23 and 24. 415

G-58.	Predicted versus experimental data for Boundary Condition 6-1, 2nd layer thermocouples 26 and 29.	416
G-59.	Predicted versus experimental data for Boundary Condition 6-1, 1st layer thermocouples 1 and 9...	417
G-60.	Predicted versus experimental data for Boundary Condition 6-1, 1st layer thermocouples 14 and 15.	418
G-61.	Predicted versus experimental data for Boundary Condition 6-2, 3rd layer thermocouples 31 and 35.	419
G-62.	Predicted versus experimental data for Boundary Condition 6-2, 3rd layer thermocouples 44 and 45.	420
G-63.	Predicted versus experimental data for Boundary Condition 6-2, 2nd layer thermocouples 23 and 24.	421
G-64.	Predicted versus experimental data for Boundary Condition 6-2, 2nd layer thermocouples 26 and 29.	422
G-65.	Predicted versus experimental data for Boundary Condition 6-2, 1st layer thermocouples 1 and 9...	423
G-66.	Predicted versus experimental data for Boundary Condition 6-2, 1st layer thermocouples 14 and 15.	424
H-1.	Regression plot of the predicted temperature versus the experimental temperature for Boundary Condition 1-2 and test times of 0.75, 1.75, and 2.75 hours.....	426
H-2.	Regression plot of the predicted temperature versus the experimental temperature for Boundary Condition 2-1 and test times of 2, 5, and 8 hours.....	427
H-3.	Regression plot of the predicted temperature versus the experimental temperature for Boundary Condition 2-2 and test times of 1, 4, and 7 hours.....	428
H-4.	Regression plot of the predicted temperature versus the experimental temperature for Boundary Condition 3-1 and test times of 2, 4, and 6 hours.....	429
H-5.	Regression plot of the predicted temperature versus the experimental temperature for Boundary Condition 3-2 and test times of 0.4, 1.2, and 2.0 hours.....	430

H-6.	Regression plot of the predicted temperature versus the experimental temperature for Boundary Condition 4-1 and test times of 1, 4, and 7 hours.....	431
H-7.	Regression plot of the predicted temperature versus the experimental temperature for Boundary Condition 4-2 and test times of 1, 2.5, and 4 hours.....	432
H-8.	Regression plot of the predicted temperature versus the experimental temperature for Boundary Condition 5-1 and test times of 2, 5, and 8 hours.....	433
H-9.	Regression plot of the predicted temperature versus the experimental temperature for Boundary Condition 5-2 and test times of 1, 2.5, and 4 hours.....	434
H-10.	Regression plot of the predicted temperature versus the experimental temperature for Boundary Condition 6-1 and test times of 2, 6, and 10 hours.....	435
H-11.	Regression plot of the predicted temperature versus the experimental temperature for Boundary Condition 6-2 and test times of 1, 2, and 5 hours.....	436

Abstract of Dissertation Presented to the Graduate School
of the University of Florida in Partial Fulfillment of the
Requirements for the Degree of Doctor of Philosophy

PRESSURE AND VELOCITY DISTRIBUTION FOR AIR FLOW
THROUGH FRUITS PACKED IN SHIPPING CONTAINERS
USING POROUS MEDIA FLOW ANALYSIS

By

Michael Thomas Talbot

August, 1987

Chairman: Dr. C. C. Oliver
Major Department: Mechanical Engineering

Detailed pressure and velocity fields for low air flow rates used for forced cooling of oranges packed in containers cannot be established experimentally. The superficial velocity and overall pressure drop can be determined for oranges packed in bulk and the temperature response during cooling of oranges packed in containers can be measured.

Flow analysis requires the consideration of at least a second order velocity term to account for friction and dynamic effects. The theory of fluid flow through porous media incorporates such an analysis and has been successfully applied to determine the pressure and velocity fields for air flow through semi-infinite bulk agricultural products. The objective of this study was to evaluate the

applicability of porous media flow theory for pressure and velocity flow field predictions for the finite boundary conditions of air flow through oranges packed in shipping containers.

A commercial finite element solution package was adapted to determine the pressure and velocity distribution and was verified by comparison with existing detailed studies of bulk systems. Porous media input parameters and boundary condition specifications for the current study were obtained from studies of pressure loss through oranges in bulk and in simulated orange cartons. An existing heat transfer program was modified to incorporate predicted velocity inputs and calculate temperature response.

Twelve tests were conducted using an experimental orange carton with 88 Valencia oranges (size 100) packed in a face-centered cubic packing arrangement using air flow rates ranging from 1.5×10^{-3} to 2.0×10^{-2} m³/s. The tests involved six different venting arrangements. Temperature responses were measured for 58 orange centers, 10 orange surfaces, and 10 air spaces.

The measured temperature responses for the twelve tests were compared to the predicted temperature responses and provided indirect evaluation of the input flow predictions. Variable porosity to account for edge effects was used to improve initial results.

Although several areas for improvement were noted, the porous media flow analysis was found to provide necessary

flow field information to calculate the thermal response for various flow boundary conditions.

INTRODUCTION

Losses of fresh fruits and vegetables and other horticultural commodities from decay and shriveling as a result of poor temperature management during postharvest handling, transportation, and marketing are substantial in the United States, as well as in other production and consumption areas of the world.

Reduction of such losses is perhaps of more immediate importance than increasing yields through improved production practices. This is especially apparent when one considers that all of the cost and energy inputs for production, harvesting, packing, transportation, etc., are wasted for that portion of the supply for which losses occur near the point of consumption. For most fruits and vegetables, the total cost for harvesting, packing, transportation, storage, selling, etc., greatly exceeds the cost of production. Therefore, the direct costs which can be attributed to losses during marketing are magnified greatly when compared with the alternative of increased production to effect increased supply.

Respiration is the overall process by which stored organic materials (carbohydrates, proteins, fats) are broken into simple end products with a release of energy. Oxygen

(O₂) is used in this process and carbon dioxide (CO₂) is produced by the commodity. The loss of the stored organic materials from the commodity during respiration means hastened senescence as the energy for maintaining the living status of the commodity is exhausted, loss of food value (energy value) for the consumer, reduced flavor quality, especially sweetness, and loss of salable dry weight. The rate of deterioration (perishability) of harvested commodities is generally proportional to their respiration rate. Product temperature is a major determinant of the rate of respiratory activity.

Water loss can be one of the main causes of deterioration since it results in not only direct quantitative losses, but also causes losses in appearance (due to wilting and shriveling), textural quality (softening, flaccidity, limpness, loss of crispness, and juiciness), and nutritional quality. The rate of water loss is controlled by the vapor-pressure difference between the product and its environment, which is governed by the temperature and relative humidity.

Ethylene (C₂H₄) is the simplest organic compound that has an affect on physiological processes of plants. It is a natural product of plant metabolism and is considered the natural aging and ripening hormone. Generally, ethylene production increases with maturity at harvest, physical injuries, disease incidence, increased temperatures up to 30 C (86 F), and water stress. On the other hand, ethylene

production rates of fresh horticultural crops are reduced by storage at the lowest safe temperature of each commodity. Temperature affects both the rate of ethylene production and the sensitivity of products to ethylene.

After harvest, fresh horticultural commodities are susceptible to attack and damage by microbial pathogens. Lower temperature affects the rate of growth and spread of these microorganisms. Physical injuries can result from abuses to fresh commodities at any temperature, but low temperatures reduce the results of injuries.

Temperature is the most important environmental factor that influences the deterioration rate of harvested commodities. It is a well known fact that for each increase of 10 C (18 F) above the optimum temperature, the rate of deterioration increases two- to threefold.

Thus improved cooling of fruits and vegetables before or during shipment, along with proper temperature maintenance throughout the marketing channels, has the potential of greatly reducing these losses.

Nearly all fresh fruits and vegetables are now marketed in corrugated fiberboard shipping containers. These containers provide a barrier to proper air flow and efficient heat transfer required for cooling. Although cooling of fruits and vegetables before packing is much more desirable from a heat transfer standpoint, most products are not cooled until after packing because of other relationships in the overall handling system. Cooling of

fruits and vegetables during transit is a particular problem because of inherent restrictions on the size of the cooling units and on the design of the air circulation system in transit vehicles. Such systems are often inadequate for cooling of fresh produce and problems of overheating, over-ripening, and losses due to decay are common. These problems are further aggravated by increased use of palletized shipping, introduction of new types of produce containers and moves toward maximum utilization of vehicle volume because of increased transportation costs. The need for additional research on air movement as related to cooling of fruits and vegetables in palletized shipments has been widely recognized by industry sources.

During the last thirty years, numerous researchers and commercial shipping companies have conducted research aimed at improved cooling of fruits and vegetables packed in shipping containers. Although substantial improvements have been made, the current level of losses during marketing indicates that much work must be done. Significant further improvements can come only from complete design of the containers, vent arrangements, stacking and loading patterns, air circulation systems and refrigeration controls, based on sound engineering principles. Before this can be accomplished, however, basic research is needed on the mechanisms of heat and mass transfer from the packed product to the surrounding air and on the air flow relationships involved. The objectives of this study follow.

OBJECTIVES

The objectives of this study were to

1. Study the basic principles related to air flow through fruits (and vegetables) packed in fiberboard packing containers.
2. Determine the feasibility of the theory of flow through porous media analysis for this problem.
3. Develop a numerical model to predict air pressure and velocity distribution for air flow through fruits (and vegetables) packed in fiberboard packing containers.
4. Evaluate the experimental cooling response using the mathematical model for flow in conjunction with an existing heat and mass transfer model.

REVIEW OF LITERATURE

Background of Research

A considerable amount of information has been published related to basic theory and experimental research on heat and mass transfer of fruits and vegetables and on various aspects of air cooling produce packed in shipping containers. A number of publications (Anthony 1969, Camp 1979, Chalutz et al. 1974, Harris et al. 1969, Harris and Harvey 1976, Hinds and Robertson 1965, Hinsch et al. 1978, McDonald and Camp 1973, Mitchell et al. 1968, Pentzer et al. 1945, Redit and Hamer 1959, Rij 1977, Winston et al. 1959) provide information on product cooling response during test shipments of fruits and vegetables in refrigerated vehicles as related to loading patterns and air flow arrangement. Such tests give general information on whether a particular system is better than another, but yield little of the basic engineering information needed to design improved transit cooling systems. It is obvious from most of these tests that contact of the cooling air with the product (rather than the capacity of the refrigeration system) was a limited factor in the rate of cooling because of the rather large cooling times in relation to the product heat loads. Biales et al. (1973) and Kindya and Bongers (1979) conducted

shipping tests on cooling of grapefruit with outside ambient air on non-refrigerated ships. They showed that moderate amounts of product cooling can be obtained in this manner in certain regions during times of year when the outside air temperature is relatively low. Such practice has implications relative to cost savings and energy reduction and points out the even greater importance of basic engineering design of the system for optimum performance when the source of refrigeration is limited.

Some researchers (Felsenstein and Zafirir 1975, Hale et al. 1973, Hinsch et al. 1978, McDonald and Camp 1973, McDonald et al. 1979, Olsen et al. 1960, Patchen 1969) have developed new carton designs or have studied the effect of different carton venting arrangements or air flow directions through stacks of cartons as an aid to improved cooling. For the most part, these were all comparative tests and little basic engineering information on air flow rates, air distribution and other important parameters was obtained. Additional studies (Fountain and Hovey 1970, Hale et al. 1969, Hale and Risse 1974, Olsen et al. 1960) have involved packing fruits in shipping containers with pulp or plastic tray packs. However, little information was given to the direct influence of the tray packs on cooling rates other than total cooling times or final temperature at the end of test shipments.

A large amount of experimental research aimed directly at studying cooling response of fruits and vegetables packed

in shipping containers as influenced by different variables, has been conducted by various researchers: Chalutz et al. (1974), Gentry and Nelson (1964), Grierson et al. (1970), Grierson (1975), Guillou (1960), Haas and Felsenstein (1975), Kasmire (1977), Kushman and Ballinger (1962), Leggett and Sutton (1951), Lindsay et al. (1976), Mitchell et al. (1972), Parson et al. (1972), Patchen and Schomer (1971), Pentzer et al. (1945), Perry et al. (1971), Richardson et al. (1955), Sainsbury (1951) and (1961), Sainsbury and Schomer (1967), and Soule et al. (1969). Results of such tests provide data on product temperature response as related to product size, type of container, venting and stacking arrangement and, in most cases, air temperature and air flow rate. Most of these tests were conducted in a valid manner and provide excellent general information on the influence of different variables as they affect cooling rates. Also, they provide some specific engineering data useful in the design of cooling systems but only for the particular product size, the particular containers, stacking arrangements, vent designs, size of product load, air flow rates and temperatures used in the experiments. In most of these tests, the range of variables studied was quite limited. In certain tests, the mass transfer effects on product loss and evaporative cooling, other than the overall product weight loss measurements under the particular conditions of the test, were not obtained.

In order to provide the necessary information for design and analysis of alternate cooling systems, experiments must be conducted in a much more basic manner than those described above. The interaction of the cooling air with the product, the individual containers, and stacks of containers as related to the basics of heat and mass transfer should be evaluated for different product sizes, shapes, and packing configurations. More basic studies of air flow patterns and pressure drops in and around cartons and stacks of cartons are needed. A limited amount of this basic type of research was conducted. Van Beek (1975) studied the effective thermal conductivity of packed spherical products and evaluated the effect of natural convection for different heat flow directions. Meffert and Van Vliet (1971) developed a test system for evaluation of air circulation and product temperature in transit vehicles and validated the results with experiments on model cargo. Wang and Tunpun (1969) conducted basic studies on forced air cooling of tomatoes in cartons. They presented information on temperature response of fruits at 36 positions within two cartons stacked in register at three different air flow rates. They also conducted some basic studies of pressure drop versus air flow relationships for bulk fruit and cartons, packed and empty. Haas et al. (1976) studied pressure drop relationships for oranges, and cartons, packed and empty. They also studied the effect of vent hole size, total area, position, and number on carton pressure

drop. Chau et al. (1983) studied pressure drop, as a function of air flow and packing porosity, for four different sizes of oranges with four different stacking patterns. They also studied the effect the shape and number of carton vent openings had on carton pressure drop. Ramaker (1974) investigated the thermal resistance of corrugated fiber board as used in shipping containers.

Some basic work has been done on analytical methods for evaluating heat transfer in produce packed in cartons. Hicks (1955) and Sainsbury (1961) used basic conduction equations to evaluate theoretical cooling rates as a function of the convective heat transfer coefficient at the container surfaces. Meffert et al. (1971) and Meffert and Van Beek (1975) used analytical solutions for transient heat transfer to predict temperature response in stacks of produce including heat generation from product respiration. However, such solutions are applicable only to certain limited cases. Information given in other publications (Breakiron 1974, Gaffney 1977, Goddard 1972, Ryall and Pentzer 1967, Stewart 1977) has pointed out the need for additional basic research so that cooling systems may be designed based upon sound engineering principles.

Researchers at the University of Florida have extensive background in research related to heat and mass transfer in fruits and vegetables. Most of the experimental work has involved basic studies on cooling of oranges, grapefruits, avocados and bell peppers in bulk loads (Baird and Gaffney

1974a, 1974b, and 1976; Chau et al. 1983, 1984; Gaffney 1977; Gaffney and Baird 1977, 1980). Certain methodologies and techniques for measurement of product temperature, air temperature, flow rates and humidity have been developed and refined during the course of this research (Baird et al. 1975; Gaffney et al. 1980, 1985a, 1985b). In addition to the experimental work, a computer based mathematical model has been developed to analyze heat and mass transfer during cooling of fruits and vegetables in bulk loads (Baird and Gaffney 1974a, 1976; Eshleman et al. 1976; Chau et al. 1984). Currently experimental work in this area involves measurement of thermal and physical properties and transpiration coefficients of oranges and grapefruits and theoretical studies of heat and mass transfer during surface moisture drying of citrus.

This study was a subcomponent of a project concerning heat and mass transfer relationships of fruit and vegetables packed in fiberboard shipping containers. To understand and model the heat transfer during cooling and storage of fresh fruits and vegetables packed in shipping containers, the pressure and velocity field characteristics within the container must be established. Both distributions are difficult to establish experimentally. There are many interrelated variables involved in air cooling of fruits and vegetables. These include thermal properties, physical properties, size, and shape of the product and temperature, flow rate and relative humidity of the cooling air. When

cooling products in containers, additional variables of importance are container size, shape and wall thickness, venting arrangements, stacking arrangements, product packing configurations, and the direction of air flow.

The actual process that occurs between the individual fruits (or vegetables) and the flowing air is complex and not well understood. Previous researchers have studied the cooling, heating and drying of semi-infinite systems of bulk piled agricultural products such as fruits, grains, vegetables, nuts, and root crops using the theory of fluid flow through a porous media to determine the pressure and velocity fields. The validity of porous media flow theory for finite boundary conditions of air flow through fresh fruits and vegetables packed in shipping containers will be evaluated. The theory of porous media flow will be considered before looking at previous work related to other agricultural products.

Fluid Flow Through Porous Media

In addition to the interest received from a purely scientific point of view, the theory of flow through porous media has become important in many fields of scientific and engineering applications.

Such diversified fields as ground water hydrology, petroleum engineering, civil engineering, agricultural engineering, chemical engineering, soil mechanics (physics), water purification, industrial filtration, ceramic

engineering, powder metallurgy, medicine and bioengineering, all rely heavily upon porous media flow theory as fundamental to their individual applications.

Perhaps the most important of these areas of technology that depend on the properties of porous media is hydrology, which relates to water movement in earth and sand structures, like dams, flow to wells from water-bearing formation, intrusion of sea water in coastal areas, filter beds for purification of drinking water and sewage, etc., and petroleum engineering which is primarily concerned with petroleum and natural gas production, exploration, well drilling, and logging, etc. In the introductory chapter of the book by Muskat (1946), R.D. Wyckoff points out that despite the great similarity of the physical systems and the processes in these two fields of technology, each has produced distinct technical literature and terminology. Therefore, it is no surprise that as each branch of science and engineering has addressed specific problems, each has contributed to the vast amount of literature available related to porous media flow theory. Unfortunately, this literature is often difficult to correlate.

Porous media was defined by Collins (1961) as a solid containing pores or voids of sufficient number, either connected or nonconnected, dispersed within it in either a regular or random manner. The interconnected pore space is termed effective pore space. Fluid can flow through a porous material only through the effective pore space.

Muskat (1946) represented an ideal porous media as a body of unconsolidated sand in which all the voids are interconnected, which means total pore space is actually effective pore space.

By the above definition, a system of agricultural products, in bulk piles or in storage structures, which are of non-uniform shape and size, such as fruits, vegetables, grains, beans, peanuts and root crops, can be considered as an ideal porous media. A homogenous fluid, such as air or water, used as a medium for cooling, heating or drying, can flow through an assembly of interconnected channels of varying sizes and shapes in this system of agricultural products.

The actual process that occurs between individual product particles and the flowing fluid is complex and not well understood. For this reason, the only feasible method of analysis is a macroscopic approach, which implies that the values of variables under consideration are averages of indeterminate instantaneous values.

Muskat (1946), Scheidegger (1960), and others indicated that the earliest recorded investigation of the flow through porous media was that of Darcy in 1856. Darcy was interested in the flow characteristics of sand filters. Because of the analytical difficulties in describing this type of flow, Darcy had to resort to an experimental study of the problem. His classic experiments led to the real foundation of the quantitative theory of the flow of homogeneous fluids

through a porous media. He ran experiments in water flowing through a vertical pipe filled with sand. From his investigations, Darcy concluded that the flow rate was proportional to the pressure loss and the cross-sectional area and inversely proportional to the length of the flow path. The famous Darcy's Law is written as follows:

$$(1) \quad Q = k A \Delta h / L$$

Dividing both sides by the cross-sectional area, A, yields

$$(2) \quad \frac{V}{s} = k \Delta h / L$$

where

Q = flow rate in volume per unit time

k = permeability or hydraulic conductivity

A = the cross-sectional area

Δh = pressure loss or head

ΔL = the length of the flow path

$\frac{V}{s}$ = the superficial velocity

The study of the validity of Darcy's Law has been the subject of numerous investigations. These investigations have been of essentially two types: those with the objectives of either verifying Equation 1 or establishing an appropriate modification of this equation and those concerned with the nature of the constant, k, as determined by the properties of the sand or porous media. The bases of

nearly all engineering calculations for porous media flow problems have originated from Darcy's Law and/or purely empirical determinations.

Later investigators found that Darcy's Law is limited in its application only to very low velocity (creep) flow and becomes invalid when inertial forces become effective. Since then, several related theories and approaches have been developed to approximate the flow of fluid through porous media. Scheidegger (1960) recorded six different theories, namely 1. heuristic correlation (curve fitting); 2. dimensional analysis; 3. capillary model; 4. tube bundle theory (sometimes known as Kozeny Theory); 5. drag theory; and 6. statistical theory. Bird et al. (1960) recognized two general theories, namely tube bundle and drag theories. The most acceptable one and the one which has been pursued by other workers is the tube bundle theory. This theory assumes that the packed column is a bundle of tangled tubes of irregular cross-section and that the established principles of flow through a single tube are applicable.

Using the tube bundle approach in introducing the parameter's porosity, hydraulic radius and mean particle diameter into the Hagen-Poiseuille equation, Bird et al. (1960) presented the following equation for laminar flow through porous media:

$$(3) \quad \Delta P / \Delta L = 150 \mu \frac{V}{s} (1-\epsilon)^2 / D_p \epsilon^3$$

where

ϵ = porosity

= void volume/total volume

ρ = fluid viscosity

D = mean diameter of particles of the porous material

ΔP = pressure loss

and the rest of the symbols are as previously defined.

This is the Blake-Kozeny equation (first derived by Kozeny and modified by Blake), which is valid for modified Reynolds number equivalent to $V D \rho / \mu (1 - \epsilon)$ less than 10. This equation is identical to Darcy's equation where the permeability, k , is expressed in terms of the characteristic properties of the material and the fluid.

Similarly, for turbulent flow through a porous media, the relationship is

$$(4) \quad \Delta P / \Delta L = 3.50 \left(\frac{\rho V^2}{s} \right) (1 - \epsilon) / D^3 p$$

where s is the fluid density and the other symbols are as previously defined. The kinetic energy term appears inside the first parenthesis. This implies that the pressure drop is proportional to the loss of kinetic energy which becomes appreciable when the fluid velocity is large. This is the Burke-Plummer equation (first derived by Burke and Plummer), which is valid for modified Reynolds number greater than 1,000.

Based on the theory of Reynolds for resistance to fluid flow, Ergun (1952) illustrated that a pressure drop through a porous media is caused by the simultaneous viscous and kinetic energy losses. Pursuing this, he developed a general equation of fluid flow through porous media, which combines the Blake-Kozeny equation for laminar flow and the Burke-Plummer equation for turbulent flow. This equation (the Ergun equation) is

$$(5) \quad \Delta P / \Delta L = 150 \mu \frac{V^2}{s} \frac{(1-\epsilon)^2}{D^3} + 1.75 \rho \frac{V^3}{s} \frac{(1-\epsilon)}{D^3}$$

The first term on the right side represents the viscous energy loss and the second term on the right side represents the kinetic energy loss.

In terms of dimensionless groups, the Ergun equation can be written as follows:

$$(6) \quad \frac{\Delta P D^3}{\rho V^3} \frac{\epsilon}{L} \frac{1}{s} (1-\epsilon) = 150 \mu (1-\epsilon) / \rho V \frac{D}{s} + 1.75$$

In this form, one can see that if the velocity becomes very large, the first term on the right becomes negligible and the Ergun equation reduces to the Burke-Plummer equation. On the other hand, if the velocity is very small, the second term on the right is negligible compared to the first and the Ergun equation reduces to the Blake-Kozeny equation.

In three-dimensional form, the Ergun equation, Equation (5), may be written as follows:

$$(7a) \quad -\partial P / \partial x = f_1 U + f_2 U^2$$

and

$$(7b) \quad -\partial P / \partial y = f_1 V + f_2 V^2$$

and

$$(7c) \quad -\partial P / \partial z = f_1 W + f_2 W^2$$

where

x, y, z = Rectangular coordinates

$\partial P / \partial x$ = Pressure gradient decreasing along positive x direction

$\partial P / \partial y$ = Pressure gradient decreasing along positive y direction

$\partial P / \partial z$ = Pressure gradient decreasing along positive z direction

$$f_1 = 150\mu(1-\epsilon)^2 / D^3$$

$$f_2 = 1.75\rho(1-\epsilon) / D^3$$

U, V, W = Velocity in $x, y,$ and z directions, respectively.

Bakker-Arkema et al. (1969), after an extensive review of static pressure/air flow relationships in packed beds of

granular biological products, adopted the Ergun equation in their experiments on one-dimensional cooling of cherry pits. They indicated that the Ergun equation was the most general among the available equations.

Stanek and Szekely (1972, 1973) applied the Ergun equation in two-dimensional flow in both isothermal and non-isothermal packed beds. They found that non-uniform bed porosity could cause flow maldistribution.

Lai and Haque (1976) applied the Ergun equation in analyzing the three-dimensional flow of air through non-uniform grain beds by adding a third coordinate axis, z , as indicated in Equation 7. The equations were first written in vector notation as follows:

$$(8) \quad -(\text{grad } P) = \bar{V} \left(f_1 + f_2 |\bar{V}| \right)$$

where

grad = gradient of a scalar function

\bar{V} = Velocity in vector form

$|\bar{V}|$ = Magnitude of the velocity

and the rest of the symbols are as previously defined.

This, together with the continuity equation, was simplified by transforming the equation into dimensionless forms and by using a stream function. The resulting nonlinear partial differential equations were solved numerically by a line by line method. Non-uniform porosity was indicated to cause different velocity and pressure distribution.

Lai (1980) used Ergun's equation to calculate the three-dimensional airflow and pressure distributions through a circular grain bin using the method of lines, coupled with a sophisticated ordinary differential equation integrator. This method is similar to the finite difference method.

Hague et al. (1980) modified Ergun's equation to calculate the pressure and velocity fields for airflow through conical-top grain beds containing corn and fines distributed nonuniformly. A two-dimensional (cylindrical coordinate) finite difference technique was used.

Geertsma (1974) reported it necessary to apply a more general flow law for the prediction or analysis of the production behavior of gas wells. These wells produce high single-phase fluid flow rates through the surrounding reservoir rocks. He indicated the appropriate formula was given in 1901 by Forchheimer and is written as

$$(9) \quad -(\text{grad } P) = \alpha \mu \bar{V} + \beta \rho |\bar{V}| \bar{V}$$

where

α = coefficient of viscous flow resistance

= $1/k$ (approximately)

β = coefficient of inertial flow resistance.

This equation is noted to be of the same form as Equation 8.

Geertsma (1974) and Fircozabadi and Katz (1979) discussed the widely differing views used to describe the mechanisms that consume energy at more than a linear rate

with velocity. The β term has been given various names depending on the users interpretation of the flow mechanism. For example Fircozabadi and Katz (1979) indicated β should be called "velocity coefficient" while Geertsma (1974) defined β as indicated above as the "inertial coefficient." Also noted was the difficulty relating the β term with the porosity, permeability and other measurable porous media characteristics.

Geertsma (1974) reported that the validity of Equation 9 could be checked by plotting the ratio $\rho V/\mu$ as a function of $(\text{grad } P)/\mu V$. He indicated that this plot must yield a straight line. The value of coefficient α will then be determined by the intercept of the straight line plotted and the $(\text{grad } P)/\mu V$ axis while coefficient β is found from the slope of the line with respect to the x-axis. This procedure is applicable for liquids only, since density ρ is nearly independent of the pressure P .

For a gas, Equation 9 cannot be applied directly. However, the equation is applicable for a small distance dx in the flow direction. By introducing the mass flow rate $G = \rho V$ of the gas and using the ideal gas law, $\rho = P/c$ in which

$$c = RT/M$$

where

R = universal gas constant,

T = absolute temperature and

M = molecular weight,

Equation 9 can be rewritten as

$$(10) \quad -\rho \, dP = \alpha \mu G c + \beta G \frac{c^2}{dx}.$$

By performing intergration between $x = L$ and $x = 0$, Equation 10 becomes

$$(11) \quad -\left(\frac{P}{L} - \frac{P}{0}\right) / 2LcGy = \alpha + \beta (G/\mu).$$

Therefore for gases, Geertsma (1974) reported that the validity of Equation 11 could be checked by plotting G/μ as a function of the term on the left side of Equation 11. He indicated that this plot must yield a straight line. The value of coefficient α will then be determined by the intercept of the straight line plotted and the axis of the term on the left side of Equation 11, while coefficient β is found from the slope of the line with respect to the x-axis.

The Agricultural Engineering Department, in addition to other departments of the University of Florida, leases a university version of the ANSYS*** general purpose finite element computer program offered by Swanson Analysis Systems (SASI) (DeSalvo and Swanson 1983).

***The information given herein is supplied with the understanding that no discrimination is intended and no endorsement by the Institute of Food and Agricultural Sciences of the University of Florida is implied. The listing of specific trade names herein does not constitute endorsement of these products in preference to other products which have equivalent capabilities.

During system verification and preparation for student laboratory use, many of the practical structural, thermal and flow engineering analysis techniques were tested. An option exists that allows both 2-D and 3-D isoparametric thermal solid elements to be used to model nonlinear steady-state fluid flow through a porous medium (DeSalvo and Swanson 1983).

The porous media flow problem is formulated in a manner identical to that used for the thermal analysis, requiring only a change of variables to use thermal analysis to obtain a solution. Pressure is the variable rather than temperature. The momentum equation is simplified to

$$(12) \quad -(\text{grad } P) = \text{Reff } \bar{V}$$

where

grad = gradient of a scalar function

P = pressure

\bar{V} = seepage velocity vector

and

$$(13) \quad \text{Reff} = \mu/K + \beta\rho|\bar{V}|$$

where

μ = gas viscosity

K = absolute permeability of porous medias

β = visco-inertial parameter

ρ = density.

The components of Equations 13 are

$$(14) \quad -\partial P / \partial x = \text{Reff } V_x$$

$$(15) \quad -\partial P / \partial y = \text{Reff } V_y$$

$$(16) \quad -\partial P / \partial z = \text{Reff } V_z.$$

The continuity equation is

$$(17) \quad \text{div } (\rho \bar{V}) = 0$$

where div = divergence of a vector field, or

$$(18) \quad \partial(\rho V_x) / \partial x + \partial(\rho V_y) / \partial y + \partial(\rho V_z) / \partial z = 0.$$

Combining Equations 14, 15, 16, and 18 yields

$$(19) \quad \partial(k \partial P / \partial x) / \partial x + \partial(k \partial P / \partial y) / \partial y + \partial(k \partial P / \partial z) / \partial z = 0$$

where $k = \rho / \text{Reff}$. Equation 19 is nonlinear because Reff is a function of velocity. The coefficients of permeability, k , are (k_x, k_y, k_z) internally calculated for each coordinate direction as

$$(20) \quad k = K \rho / (\mu + K \rho \beta |\bar{V}|)$$

To handle the flow of power law fluids, an exponent can be applied to $|\bar{V}|$ as an additional analysis input variable.

Combining Equation 12 and 13 yields

$$(21) \quad -(\text{grad } P) = \mu \bar{V} / K + \beta \rho |\bar{V}| \bar{V},$$

which is the same as Equation 9. In fact, personal inquiry to SASI revealed that the porous media option was based on the work of Geertsma (1974) and Fircozabadi and Katz (1979).

Another modification of Darcy's Law that has received considerable attention is a simplified, semi-empirical approach to account for nonlinear flow patterns of air through porous media. This is accomplished by assuming that the air velocity is proportional to the pressure gradient raised to a power. Shedd (1953) introduced the following equation in the study of air flow through grain storages:

$$(22) \quad V = A(\partial P/\partial n)^B$$

where

- V = interstitial fluid velocity
- $\partial P/\partial n$ = pressure gradient along any direction
- A,B = experimentally determined constants.

Equation 22 is sometimes rearranged in terms of

$$(23) \quad \partial P/\partial n = a V^b,$$

where

a,b = experimentally determined constants

and referred to as the Ramsin Equation.

One major difference between Equation 22 and the Ergun Equation, Equation 6, is the absence of porosity. It is

assumed to be lumped with other characteristic properties of the fluid and porous medium into constants a and b.

Shedd (1953) stated that A and B were not constant over a wide variation in pressure gradients. Equation 22 is a straight line on a log-log plot; however most of the experimental data plots did not produce straight lines.

By generalizing information given by Shedd (1953), Brooker (1961) obtained the two-dimensional velocity component equations

$$(24) \quad V_x = A [(\partial P / \partial x)^2 + (\partial P / \partial y)^2]^{(B-1)/2} \partial P / \partial x$$

and

$$(25) \quad V_y = A [(\partial P / \partial x)^2 + (\partial P / \partial y)^2]^{(B-1)/2} \partial P / \partial y$$

where V_x and V_y are the velocity components and the rest of the symbols are as previously defined.

Brooker (1961) substituted Equations 24 and 25 into the continuity equation, Equation 18 assuming constant density and considering only the x and y directions, to obtain the partial differential equation

$$(26) \quad [(\partial P / \partial x)^2 + (\partial P / \partial y)^2] [\partial^2 P / \partial x^2 + \partial^2 P / \partial y^2] - 2m [(\partial P / \partial x)^2 \partial^2 P / \partial x^2 + 2(\partial P / \partial x)(\partial P / \partial y)(\partial^2 P / \partial x \partial y) + (\partial P / \partial y)^2 \partial^2 P / \partial y^2] = 0$$

where

$$m = (1-B)/2.$$

The finite difference method was used to solve this differential equation. The numerical solution agreed favorably with experimental pressure values measured in a rectangular wheat bin.

Brooker (1969) proposed that the log-log plots of velocity versus pressure gradient be modeled by a series of straight line segments using Equation 22 and reported several values of A and B for a range of pressure gradients. The finite difference method was used to solve Equation 26 with the value of B adjusted at each node corresponding to the value of the gradient $\partial P/\partial n$. Brooker (1969) used this model to calculate pressure and velocity distributions for two-dimensional nonlinear airflow through a rectangular corn bin. The numerical results did not agree well with experimental findings.

Jindal and Thompson (1972) applied Brooker's (1969) model to calculate the two-dimensional pressure distribution for air flow through conical-shaped piles of grain sorghum.

Pierce and Thompson (1974) also applied Brooker's (1969) model by modifying the Jindal and Thompson (1972) model for the prediction of airflow characteristics in conical piles of corn or sorghum.

Marchant (1976a) applied Shedd's equation and used the finite difference method to establish the total airflow through large round hay bales. Three-dimensional airflow

was discussed briefly. Marchant (1976b) also used the finite element method to solve linear airflow problems in two dimensions. The experiments of Brooker (1958) and Borrowman and Boyce (1966) were used in verifying the model.

Segerlind (1982) developed a model for two-dimensional nonlinear airflow and used the finite element technique to solve for the pressure distribution in rectangular grain bins. The model was based on a generalization of Shedd's equation and calculated constant pressure lines through shelled corn similar to the lines measured by Brooker (1969).

Smith (1982) applied the two dimensional finite element method used by Marchant (1976b) to estimate the pressure and velocity distributions in a three-dimensional field of a rectangular heap of grain with an on-floor monoduct system. A comparison was made between experimental values of pressure and velocity of Marchant (1976a) and the calculated results using the finite element method. Smith (1982) found that the pressure could be calculated more accurately than velocity but that both could be calculated with reasonable accuracy in practical problems.

Khompis (1983) applied Shedd's equation and used the finite element method to solve the three-dimensional nonlinear pressure and velocity distribution within cylindrical grain storages. Four types of perforated floor systems were studied using corn as the grain media. Extensive graphics were demonstrated to display the three-dimensional pressure and velocity distributions.

From the above discussion it is evident that the theory of porous media flow has been used extensively in the study of air flow through agricultural commodities. This previous work can be generally classified into three areas of study.

The first area of study is a development of equations for prediction of pressure drop as a result of air flow through bulk fruits and vegetables. In addition to the previous work cited, several workers applied the Shedd or Ergun equation to determine the relationship of pressure drop to velocity of air flow through the various commodities. Patterson et al. (1971) studied cherry pits, shell corn, and navy beans using both the Shedd and Ergun equations. Steele (1974) studied peanuts using Shedd's equation. Akritidis and Siatras (1979) used Shedd's equation in their study of pumpkin seeds. Neale and Messer studied root and bulb vegetables (1976) and leafy vegetables (1978), also using Shedd's equation. Gaffney and Baird (1977) studied bell peppers using Shedd's equation. Wilhelm et al. studied snap beans (1978) and lima beans and southern peas (1981) using Shedd's equation. Abrams and Fish (1978) applied Shedd's equation in their study of sweet potatoes. Rumsey (1981) used the Ergun equation in the study of English walnuts.

The second area of study is the prediction of pressure and velocity field distributions for airflow through bulk agricultural products. These are sufficiently outlined above. It is noted that each of these individual studies

has several common aspects. They all use some modification of Darcy's approach to porous media flow. They all involve a large bulk of porous media (semi-infinite). The air entrance into the porous media was through a line or area source. The air exit from the porous media was through a large exit area. Finally, these various studies used several modeling analysis techniques which were specifically developed for the particular situation being studied. This factor is emphasized as a result of difficulty in using the various models for other than the specific situation for which they were intended.

The third area of study and most limited is the development of equations to predict the pressure drop for airflow through fruits and vegetables packed in shipping containers.

As mentioned above, Wang and Tunpun (1969) studied the pressure drop versus airflow relationships for tomatoes in-bulk and in-cartons. Haas et al. (1976) used a modified Shedd equation to predict equations relating pressure drop to air velocity for oranges in-bulk and in-cartons. Chau et al. (1983) used both the Shedd and Ergun equation to predict the pressure drop as a function of airflow for oranges in-bulk and in-cartons.

No studies exist which predict the pressure and velocity fields for air flow through fruits or vegetables packed in shipping containers.

PROCEDURE

In order to better understand the heat transfer and the product temperature change which occurs when forced air cooling is used to reduce the temperature of fruits and vegetables packed in fiberboard containers, the velocity and pressure fields within the carton must be analyzed.

Intuitively it was anticipated that the velocity characteristic of the air flowing through packed cartons of fruits and vegetables would vary in three dimensions. As mentioned previously, direct measurement of the pressure and velocity within and throughout the packed carton is not feasible with current instrumentation. The measurement of temperature is the only direct method which can be used as an indication of the velocity pattern of the air passing through the carton as the product is cooled.

Extensive temperature response experiments were conducted with oranges packed in an experimental packing container of a size similar to regular packing cartons. The number and location of vent holes could be changed and several flow rates were used. Eighty 36-gage thermocouples were used to measure air temperature entering and leaving the box, air temperature at various locations inside the

box, and surface and interior temperatures of oranges at various locations within the box.

The temperature response data were analyzed graphically and by computer simulation which indicated changes in temperature within the carton through various cutting planes by use of color variation for various temperature ranges.

From this temperature response data, no symmetrical patterns could be identified. This leads to the assumption that the airflow within the orange carton varies in three dimensions.

In order to evaluate the velocity and pressure fields, an analysis technique had to be selected. The two principal numerical solution methods employed by previous researchers are the finite difference and the finite element techniques. Each method has advantages and disadvantages.

The flow of air through a porous media may be described in terms of partial differential equations. In real situations, the geometry of the system to be modeled is usually not simple and these equations cannot be solved by analytical solution. In these cases the use of some numerical solution is necessary. Brooker (1961) and others proposed a finite difference method of solution. In this method the porous medium is divided into a regular grid. The partial differential equations of static pressure at each grid point are approximated by truncated Taylor Series expansion in terms of the static pressure at the surrounding points. In this way algebraic equations can be formed for

each grid point therefore setting up a system of equations to be solved simultaneously. While the finite difference method can give good results, it has several disadvantages:

1. The method is not easily adapted to regions which have boundaries not lying on the grid lines.
2. It is difficult to write a computer program to take account of a general geometric shape.
3. A grid size which gives acceptable accuracy in areas with rapidly varying pressure will be far too small in the areas of slight variation, thus leading to a solution of a large number of superfluous equations.
4. It is difficult to apply the method to media which are not homogeneous and isotropic.
5. For each equation relating air velocity to pressure gradient, a completely different partial differential equation has to be solved thus requiring a new set of equations to be set up in each case.

The finite element method is especially suited for the study of airflow through fruit and vegetable crops because, as well as overcoming the general points 1 to 3, it can also deal easily with 4 and 5 which are very pertinent.

In the past ten years, much work has been done to develop the numerical solution of partial differential equations using the finite element method. The finite element approach has its origins in the field of solid mechanics (elasticity, plasticity, and structural analysis), but its application for use with a much wider range of

problems was soon realized. Finite element methods have replaced finite difference methods in many areas of solid mechanics and are making inroads into fluid mechanics, heat transfer, and other fields. More recently, considerable interest has been shown in its application to nonlinear problems, such as the problem under consideration.

The finite element method is a technique that approximates a continuous quantity, such as a partial differential equation, by a discrete model composed of a set of piecewise continuous functions. This discretization is done on a small but finite portion of the component. As its name suggests, the finite element method consists of dividing the region into a number of smaller elements which can be of any shape (Figure 1). Nodal points are distributed around the boundary of the element and occasionally inside it. These nodes are arbitrarily numbered. The overall model is comprised of a finite number of nodes. At each node the value of the variable (i.e., pressure, flow, temperature, deflections) for a differential equation is either known or unknown. Between the nodes are subdomains called elements. Mathematics converts the partial differential equations into matrix equations that describe each element. The individual elements (in matrix form) are joined together to form an overall model. The results of the finite element simulation output are given in terms of the variable at each nodal point. After the known variables are obtained, internal quantities can be

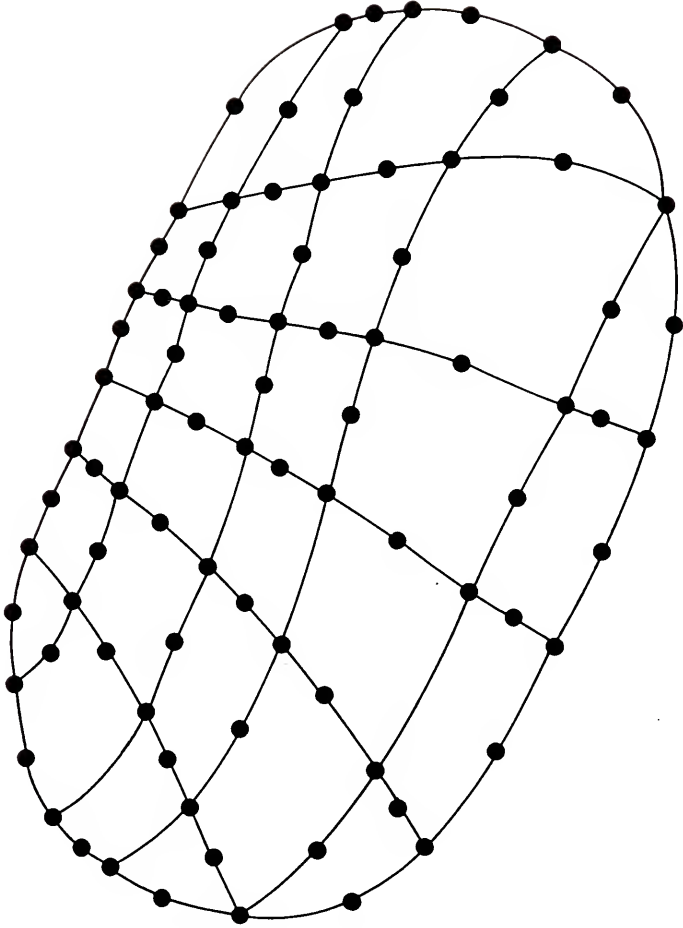


Figure 1. Region divided into finite element.

estimated. An example structural problem would solve for the deflection on a loaded component and then evaluate the stresses inside each element.

With the finite element approach, the partial differential equations describing the desired quantity (such as pressure, flow, temperature, displacement, deflections) in the continuum often are not dealt with directly. Instead, the continuum is divided into a number of finite elements, which are assumed to be joined at a discrete number of points along their boundaries. A functional form is then chosen to represent the variation of desired quantity over each element in terms of the values of this quantity at the discrete boundary points of the element. By using the physical properties of the continuum and the appropriate physical laws (usually involving some sort of minimization principal), a set of simultaneous equations in the unknown quantities at the element boundary points can be obtained. This set of equations is in general quite large, but the matrix is banded.

For those situations where the finite element technology has been developed, there are three primary advantages of the finite element approach over the finite difference methods. These are

1. Irregularly shaped regions can be handled easily, without the special treatment usually required by finite difference methods.

2. The size of the finite element can easily be varied over the region, permitting the use of small elements where strong variations occur and large elements where only slight variations are expected. With finite difference methods, at least in their conventional form, the use of several different mesh sizes can cause bookkeeping difficulty.

3. For comparable accuracy, the finite elements can usually be considerably larger than the mesh elements of a finite difference grid. As a result, when elliptic problems are involved the band matrix referred to earlier is usually small enough to be solved directly without recourse to the iterative methods which are usually necessary in finite difference methods.

The main advantage of the finite element method is that a general computer program can be written to create the overall model matrix. For different applications (e.g., different shape geometry) input is easily changed and a new solution obtained with the same computer program. Other important advantages include the following:

1. Material properties can be different between each element.
2. Irregular shaped geometries can be modeled.
3. The size of elements can be varied.
4. Mixed boundary conditions can be handled (e.g., loads and temperatures).

The number of nodes in an element can vary with the addition of internal nodes that provide a means to curve the element or specify a nonlinear variable. Many types of elements are available (Figure 2).

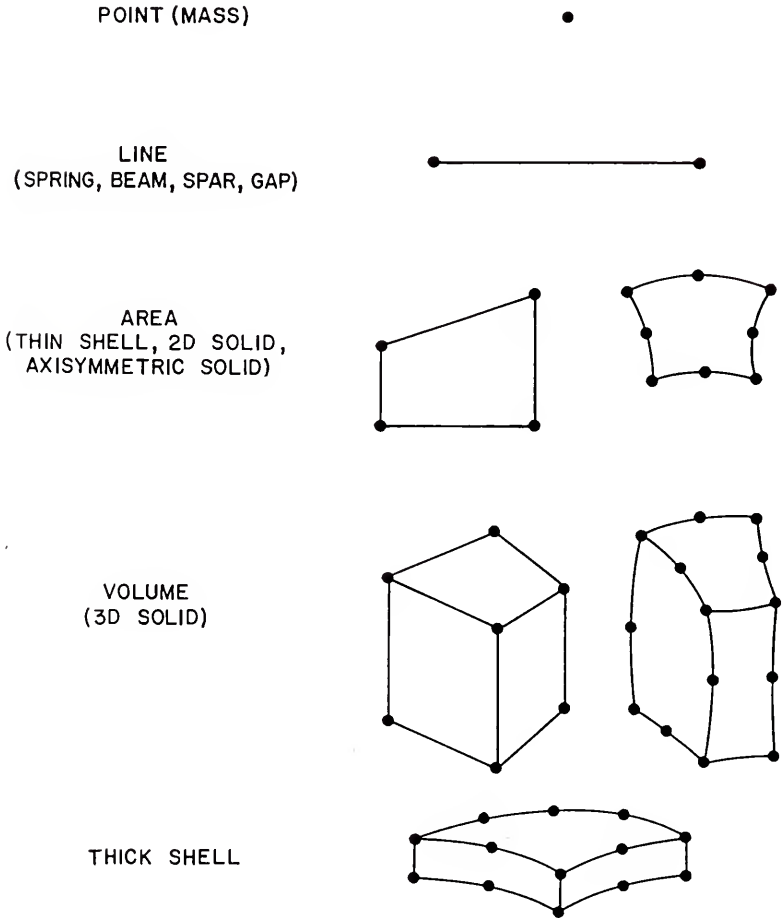


Figure 2. Various types of finite elements.

The two methods (finite element and finite difference) are similar in that an algebraic equation is set up for each nodal point, but the way in which they are set up differs. Compared with finite difference programs, for example, they are easier to use and require fewer computer resources. For modeling nonlinear material properties, finite element programs require less than 20 iterations compared with the 200 or 300 required for finite difference programs. With recently developed finite element software, the calculated distributions can be shown graphically on a computer screen, which makes it relatively easy to see areas of high and low pressure distribution. Working with a geometrical model of a particular size, an engineer can vary the input specifications such as material properties and inlet and outlet locations and see the effect of these variations on the resulting pressure distributions. The program also calculates performance parameters. With this information, the engineer can upgrade the design geometry and change the material requirements and modify the energy losses, and thereby achieve the best design performance with the least amount of material or achieve the optimum cooling. The procedure is quick and relatively inexpensive when compared with conditional procedures such as building and testing prototypes.

After review of the above literature and analysis of the temperature response data, application of a 3-D finite

element nonlinear porous media flow analysis for the problem under consideration was thought feasible.

As mentioned above, previous modeling involved a porous media which was of much larger scale and without the more significant boundary conditions for the situation of air flow through a packing container. Also the finite element models developed by previous workers were developed specifically for the problem which they were addressing. Although the 3-D finite element porous media flow analysis appeared feasible, in the early stages of this study it was not deemed appropriate to devote a considerable amount of time in developing a specific model for this situation before feasibility of the approach was confirmed.

Finite element programs are available and are becoming the most utilized engineering tool for design. These large and powerful tools have been written by engineering graduate students and professors with advanced technical knowledge in their areas of expertise and therefore might pose a problem to the majority of engineers who have little background in finite elements and other dynamic simulation computer programs. This leads the average engineer relying on the program written by others and thus using the analysis techniques as a black box: entering input and receiving output. The degree of success in using a finite element program is related to the assumptions and models developed by the program originator. The user of the finite element program must realize that the actual results from the finite

element model are a function of engineering judgement used to select the element type and size, and a function of the computer program with its associated mathematical assumptions.

Also mentioned above was the discovery that the SASI finite element analysis package, DeSalvo and Swanson (1983), contained an option which allows the modeling of nonlinear steady state fluid flow through a porous medium. This solution technique was studied and appeared to be applicable to the case at hand. A limited review was unable to identify other commercial solution packages which offered the needed analysis option and capabilities.

If the SASI package or a similar general finite element computer program was readily accessible to the workers interested in porous media flow analysis applied to agricultural crops, a tool would be available which would allow for a uniform solution technique and easy comparison of the results of various workers. Therefore, in addition to evaluating the feasibility of the finite element porous media flow analysis, this study is also evaluating the feasibility of applying a commercial general computer program. If it is established that the analysis technique is feasible, as well as, the general computer program, then the industry which provides such software can be encouraged and solicited to provide the needed software for widespread adoption and application.

Commercial Finite Element Package

The ANSYS finite element computer program is based on classical engineering concepts and documented finite element and numerical analysis techniques (DeSalvo and Swanson 1983). This self-contained general purpose program uses efficient solution techniques to solve a large class of engineering problems. It is user oriented, command driven, has extensive graphic capabilities, and is documented, benchmarked, and verified.

A typical analysis consists of three phases: Pre-Processing (Analysis Definition), Solution, and Post-Processing (Interpretation of Results).

The Pre-Processing phase is very important since the accuracy of the solution depends directly upon the degree of accuracy of the problem description. Input data prepared in the analysis definition would include the model description, boundary conditions, and the analysis type and options.

The model description involves creating the desired geometry, selection(s) from the element library, specification of geometric (real) constants describing properties of elements (e.g., area, moment of inertia, and height of a beam), and identification of material properties (e.g., viscosity, conductivity, and density). The user must ensure dimensional homogeneity.

The analysis is performed in the solution phase. For the nonlinear porous media flow case, this involves the solution of the matrix equation

$$(27) \quad [K] \{P\} = \{Q\}$$

where

[K] = the transmissivity matrix, defined by Reff in equation 13.

{P} = pressure vector (unknown)

{Q} = mass flow rate vector

and the calculations of the pressure and mass flow distributions.

The solution results are evaluated in the third phase. The user should determine if the objective of the analysis was met. Tools to use in making this decision include graphics (contour maps, distorted shape plots, and graphs of one variable versus another); scans of results; and combinations of results.

Therefore, the use of ANSYS is straightforward, but careful engineering judgment must be exercised during the analysis definition phase in selecting the geometry and elements, as well as specifying the input parameters and boundary conditions.

Verification

In order to verify the ANSYS calculated solutions, the solutions must be compared with known theoretical solutions, experimental results, and/or with other calculated solutions. The extensive verification problem manual, DeSalvo (1982), provided by SASI does contain a ground water flow verification problem. However, it does not contain a

porous media flow problem of the type under consideration with which to compare the ANSYS output to a theoretical solution. Therefore, before attempting to solve the problem under consideration, ANSYS was used to solve similar porous media flow problems which have been solved by other workers.

ANSYS was used to solve the two-dimensional rectangular grain bin problem solved by Segerlind (1982) and one of the three-dimensional grain bin problems solved by Khompis et al. (1984). As noted above, ANSYS is based on an Ergun Equation analysis while the work of Segerlind (1982) and Khompis et al. (1984) is based on a Shedd Equation analysis. Patterson (1969) determined the coefficients for pressure drops through grain beds using both the Shedd Equation and Ergun Equation. It is assumed that appropriate coefficients can be selected for the Ergun Equation, that correspond to the coefficients used in the Shedd Equation by Segerlind (1982) and Khompis et al. (1984). It is further assumed, that ANSYS provides a satisfactory solution if the calculated results are within reasonable accuracy of the results determined by Segerlind (1982) and Khompis et al. (1984).

The input coefficients needed to use ANSYS are indicated in Equation 13. The gas viscosity and the density are for air and are taken from standard data tables. The absolute permeability of the porous media and the visco-inertial parameter are derived from experimental results.

The work of Patterson (1969) is used to obtain values for these last two parameters.

Patterson (1969) used a modified Ergun Equation

$$(28) \quad \Delta P / \Delta L = K_e \left[150 \frac{\mu V}{s} (1-\epsilon)^2 / D_p^2 + 1.75 \rho V^2 (1-\epsilon) / D_p^3 \right]$$

where

K_e = modified Ergun product constant.

Equation 28 is identical to Equation 5 with the addition of the product multiplication factor, K_e . Comparing Equation 28 and Equations 12 and 13, the absolute permeability of the porous media, K , and the visco-inertial parameter, β , needed for ANSYS input can be equated as follows:

$$(29) \quad 1/K = K_e \left[150 (1-\epsilon)^2 / D_p^2 \epsilon \right]$$

and

$$(30) \quad \beta = K_e \left[1.75 (1-\epsilon) / D_p^3 \epsilon \right].$$

Patterson (1969) reported all the parameters required to solve Equations 29 and 30, for shelled corn and various other biological materials. For shelled corn at a moisture content of 16.01 %, a temperature of 87 F, and a normal fill, Patterson (1969) reported the following values:

$$D_p = 0.032 \text{ feet}; \quad \epsilon = 0.43; \quad \text{and} \quad K_e = 4.5$$

The conditions of the corn are similar to that used in the work of Segerlind (1982) and Khompis et al. (1984). Both studies used coefficients which were reported in the research of Shedd (1953). This research was based on normal fill, shelled yellow dent corn at a moisture content of 12.4 %. However, Shedd (1953) reported only a 1 % variation in the pressure drop for the same corn at a moisture content of 15.8 %.

Solving Equations 29 and 30 using the values given above results in the following:

$$1/K = 2.69 \times 10^6 \text{ ft}^{-2} ; \quad \text{or,} \quad K = 3.71 \times 10^{-7} \text{ ft}^2 ;$$

and $\beta = 1.76 \times 10^3 \text{ ft}^{-1}$. The following viscosity and density for the air were used:

$$\mu = 1.24 \times 10^{-5} \text{ lbm/ft-sec} ; \quad \text{and} \quad \rho = 7.25 \times 10^{-2} \text{ lbm/ft}^3 .$$

The English Engineering system of units was used by Segerlind (1982) and the SI system of units was used by Khompis et al. (1984) and Chau et al. (1983). Conversion factors were used to modify the units of the viscosity and density to insure dimensional homogeneity. When the desired units for the pressure are inches of water and the desired units for the velocity are feet per minute, the unit conversion results in the following values for viscosity and density for input to ANSYS:

$$\frac{\mu}{g} = 1.24 \times 10^{-9} \text{ in. water-min};$$

$$\frac{\rho}{g} = 1.20 \times 10^{-7} \text{ in. water-min}^2 / \text{ft}^2;$$

where the Newton's Law gravitational constant is

$$g = 32.2 \text{ ft-lbm/lbf-sec}^2.$$

When the desired units for the pressure are Pascals and the desired units for the velocity are meters per second, the unit conversion results in the following values:

$$\mu = 1.846 \times 10^{-5} \text{ kg/m-sec}; \text{ and } \rho = 1.1614 \text{ kg/m}^3.$$

After conversion of the units, the other input parameters for ANSYS become

$$1/K = 2.9 \times 10^{-7} \text{ m}^{-2}; \text{ or, } K = 3.45 \times 10^{-8} \text{ m}^2;$$

$$\text{and } \beta = 5.77 \times 10^{-3} \text{ m}^{-1}.$$

Now all the necessary input data to use the ANSYS finite element program are known.

Two-Dimensional Grain Bin

The physical problem selected for solution by Segerlind (1982) was the same rectangular grain bin that was analyzed by Brooker (1961) and (1969). The bin was 121.92 cm wide (48 inches) and 243.8 cm high (96 inches). The duct was 20.32 cm high and 40.64 cm wide (8 inches by 16 inches).

Segerlind (1982) utilized the six node quadratic triangular element in his finite element method solution. The bin was divided into 32 elements with 85 nodes. The horizontal node spacings was 10.16 cm (4 inches) while the vertical spacing was 5.08 cm (2 inches) in the region of the inlet duct. The upper 76.2 cm (30 inches) was modeled with two elements because all of Brooker's (1969) results indicated that a linear pressure gradient existed in this region. The element and node locations used by Segerlind (1982) are shown in Figure 3 and the boundary conditions are shown in Figure 4. Segerlind (1982) noted that the known pressure values at the duct inlet and at the free surface are easily incorporated into all finite element programs. The no-flow or impermeable boundary condition, $\partial P / \partial n = 0$, is automatically enforced on the boundary when the pressure values are not specified. This differs significantly from the finite difference technique used by Brooker (1969) where extra rows of nodes had to be added outside the region to satisfy the no flow boundary condition.

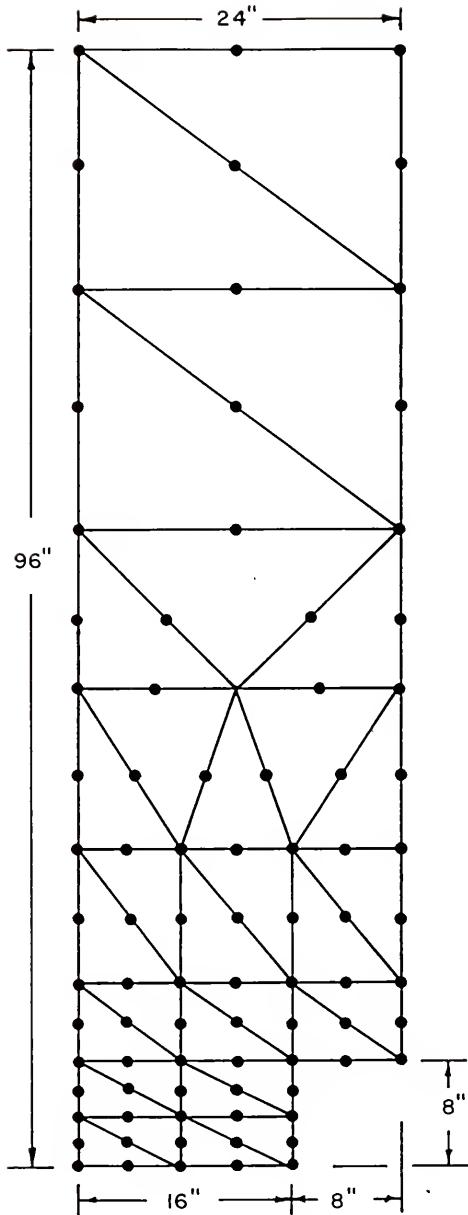


Figure 3. The node and element grid employed by Segerlind (1982).

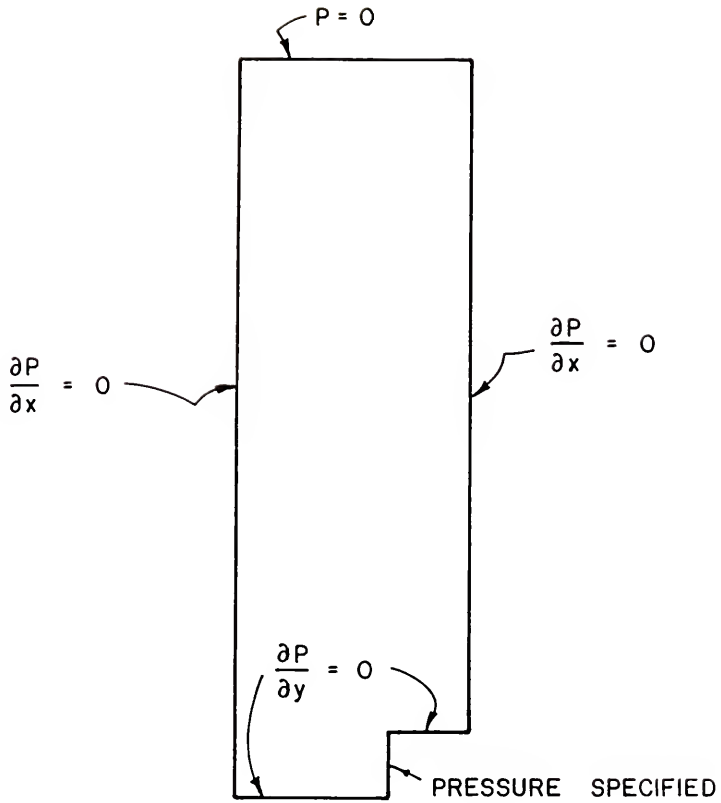


Figure 4. Boundary conditions used by Segerlind (1982).

The ANSYS analysis option to be used did not contain an element type identical to the type used by Segerlind (1982). A four node 2-D isoparametric thermal solid element was used. The element option which allowed modeling of nonlinear steady-state fluid flow through a porous media was used. This element could be formed into a triangular (three node) shape by the duplication of two of the four nodes. The node and element locations used are shown in Figure 5. The model consisted of 85 nodes and 71 elements. All but nine nodes were placed identical to the locations used in Segerlind's (1982) model. Over twice as many elements were required because smaller elements were used which did not contain the midpoint nodes like the elements used by Segerlind (1982). Although this resulted in additional computer solution time, the results were as refined or more refined when compared to Segerlind's (1982) solution. The boundary conditions were specified in a manner similar to Segerlind's (1982) model.

Three-Dimensional Grain Bin

Khompis et al. (1984) extended the procedures of Segerlind (1982) to account for three dimensional pressure and velocity fields in cylindrical grain storages. Four different aeration systems were studied. The four systems were differentiated by the size and shape of the perforated floor. The system to be considered in the present study consisted of the square perforated type floor

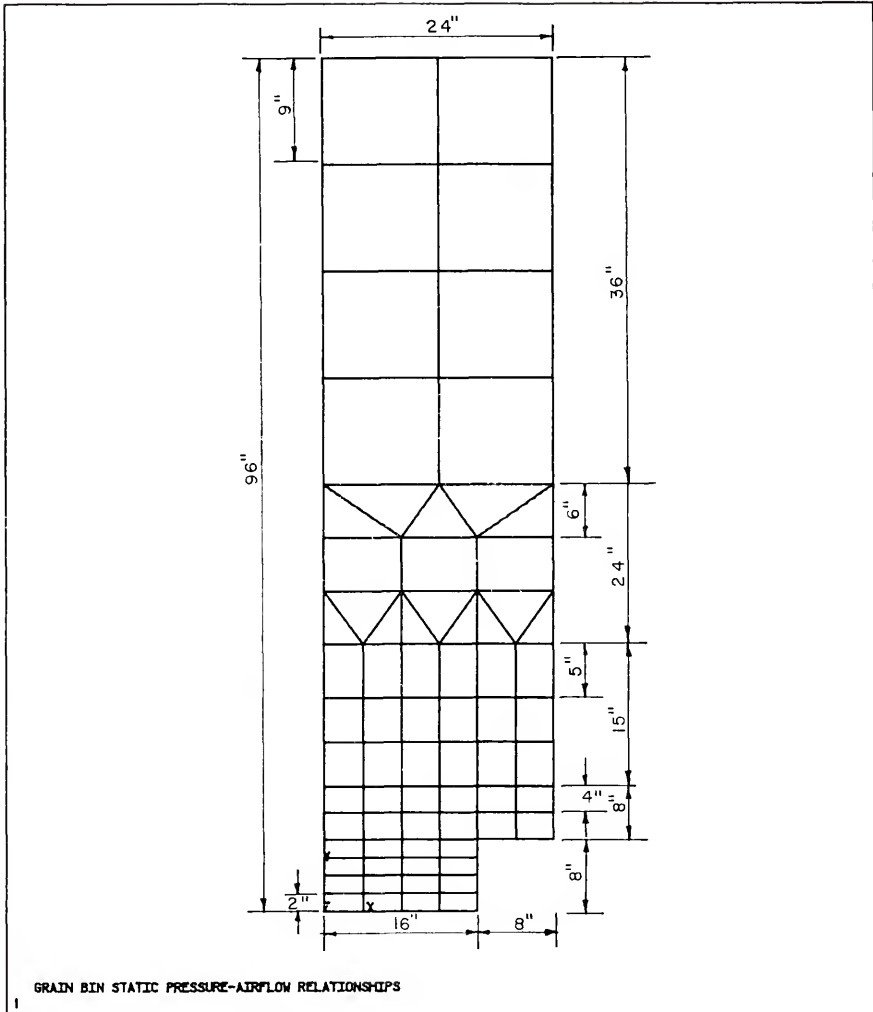


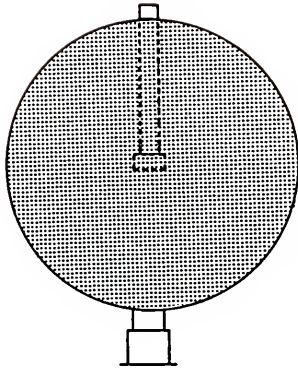
Figure 5. The node and element locations used in current study.

for a bin 12.8 meters high and 18.3 meters in diameter. The perforated floor was 9.15 x 9.15 meters square. Specific details of these sizes and shapes are shown in Figure 6. Flush floor ducts were assumed.

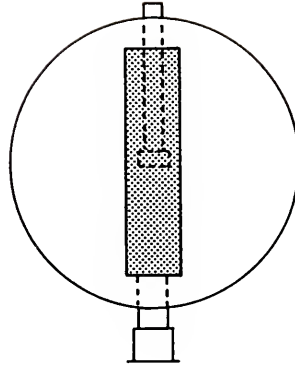
Khompis et al. (1984) used a twenty node, quadratic, three dimensional element for the finite element model. The cylindrical grain storages investigated were symmetrical and the finite element analysis was performed using only half of the grain bin. The limitation of computer central memory and desire for reasonable computing restricted the finite element model to five layers with 12 elements per layer. The 60 elements had 406 nodes. The height of the elements at each layer depended on the distance from the perforated floor and height of the grain storage. The shortest elements were located in the layer in contact with the floor and had a height of about 5 percent of the total grain storage height. The element grid is shown in Figure 7.

The boundary conditions consisted of a pressure of 500 Pascals (2 inches of water) specified at the square perforated floor and atmospheric pressure at the free surface on the top of the grain bin. Again, the no-flow or impermeable boundary condition, $\partial P / \partial n = 0$, is automatically enforced on the boundary when the pressure values are not specified.

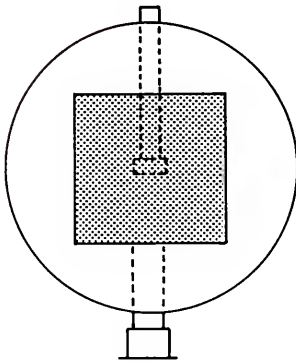
Again, the identical type element which Khompis et al. (1984) used was not available for use with the ANSYS solution package. An eight node 3-D isoparametric thermal solid



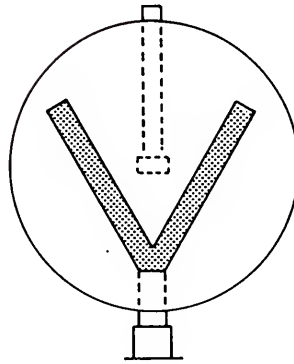
FULL PERFORATED FLOOR



STRAIGHT DUCT

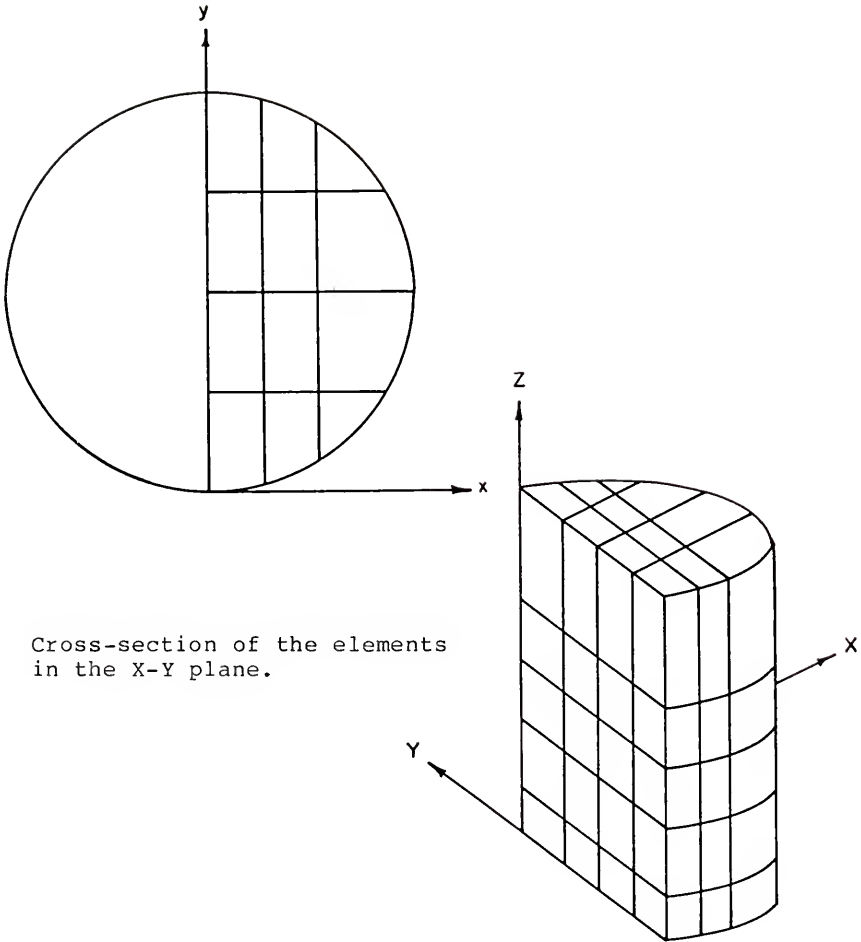


SQUARE DUCT



Y DUCT

Figure 6. Four different grainbin aeration systems studied by Khompis et al. (1984).



Cross-section of the elements
in the X-Y plane.

Division into the elements
of a half cylindrical
grain storage.

Figure 7. Finite element model used by Khompis et al.(1984).

element, which allows modeling of nonlinear steady-state flow through a porous media, was used. This element could be formed into prism or tetrahedron shaped elements by defining duplicate node numbers. Although ANSYS did have twenty node elements like those used by Khompis et al. (1984), these elements did not have the porous media flow option capability. The node and element locations used with ANSYS are shown in Figure 8. The model consisted of 741 nodes and 552 elements.

The comparison of results with those of Segerlind (1982) and Khompis et al. (1984) received detailed coverage in the Results and Discussion section, below. However, the results supported the use of ANSYS to study the problem under consideration. The procedures for this application follow.

Solution for Oranges Packed in Containers

The use of the ANSYS porous media analysis to study the pressure and velocity distributions as air flows through a container of oranges presented several questions that were not significant problems for previous workers. A primary concern was the overall scale of the porous media used in this case. This scale was finite when compared to the semi-infinite cases studied by others. Because of the small dimension of the packing container, boundary (wall) effects could be significant. The wall contact with the fruit or vegetable presented two possible difficulties. The drag

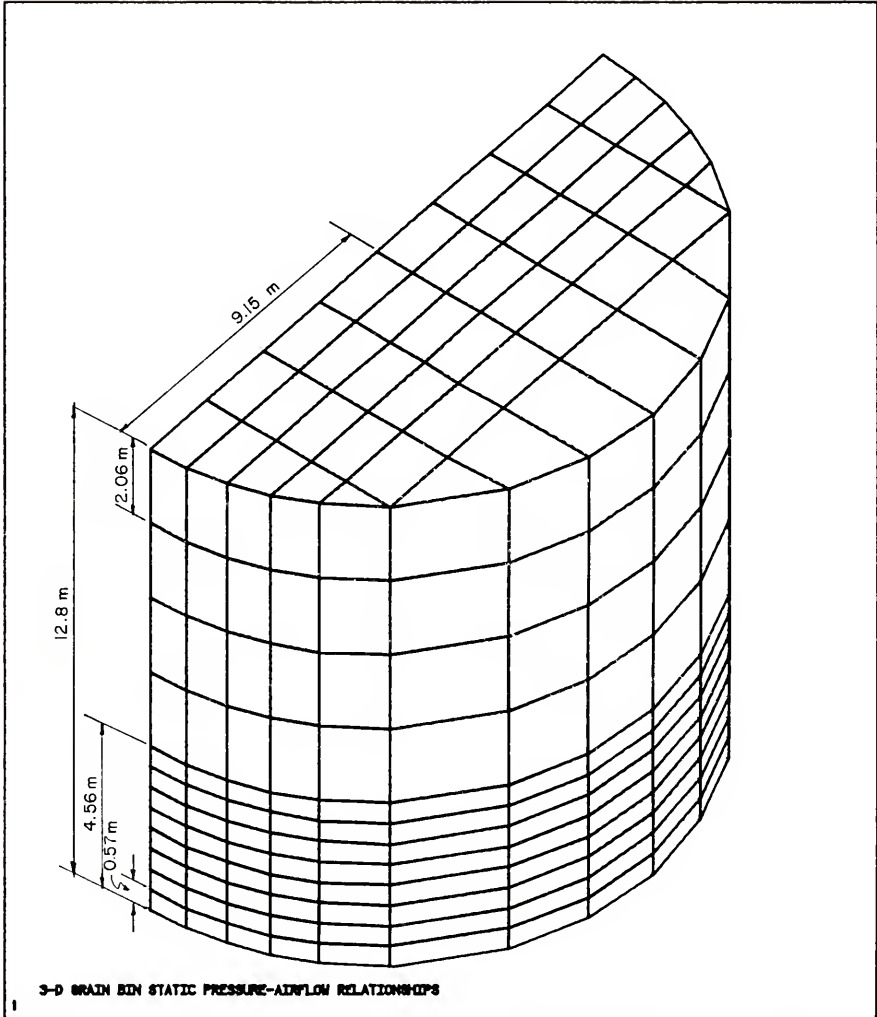


Figure 8. The node and element locations used in current study.

caused as the air passes the wall was one consideration. The second concern, which has been reported by other workers (Pillai 1977, Ridgway and Tarbuck 1968, Stanke and Eckert 1979) relates to the variance of the voidage or porosity adjacent to the walls when compared to the central portion of the porous media.

Other researchers have reported the significant pressure drops produced by the air inlets of packing containers. This point was another possible significant difficulty when comparing the pressure drop of the porous media (fruit or vegetable within the cartons) to that of the pressure drop across the inlet(s) and exit(s).

Another consideration in terms of fruits and vegetables was the compaction possible during packing and subsequent shrinkage with time due to physiological changes and moisture loss. The porosity may change, for example, if the product become more compact due to shrinkage or handling. The porosity next to the inside top of the carton could increase allowing more air to pass through this area.

The impact of some or all of these points of interest is addressed in the Results and Discussion section.

Before verifying the applicability of the ANSYS finite element program modeling air flow through a carton of fruit, the work of Chau et al. (1983) was modeled in order to better understand how the model of a commercial orange carton should be developed.

Three-Dimensional Bulk Citrus

As previously mentioned, Chau et al. (1983) used both the Shedd and Ergun equations to predict pressure drop as a function of air flow for oranges in bulk and packed in cartons. This work involved the determination of pressure drop through empty cartons (for a single carton wall and for both walls of an empty carton) and for oranges packed in the simulated carton. Fruit stacking pattern (bed porosity), fruit size, vent hole shape, vent hole number, and air flow rate were some of the variables studied.

The experimental equipment employed by Chau et al. (1983) is shown in Figure 9. The cross-section of the product bin was 55 cm x 55 cm. The actual cross-section for each test varied slightly depending on fruit size and stacking pattern.

There were 16 tests involving oranges in bulk, which consisted of four orange sizes and four stacking patterns. Since Chau et al. (1983) presented more data for Florida size 80 (8.1 cm) waxed Valencia oranges stacked in a square staggered pattern than other combinations of size and stacking pattern, the present study considered only these data. In the square staggered pattern each layer had a square pattern (every 4 adjacent fruit forming a square) with the next layer offset so each fruit on the subsequent layer rested on 4 fruit from the previous layer. The air flow rate was varied for each test to cover a range of approach velocities from 0.1 to 1.0 meters per second.

Chau et al. (1983) fitted the experimental data using the Ramsin Equation (Equation 22) in terms of pressure change per bed depth of fruit:

$$(31) \quad \Delta P/h = a V^b .$$

For the size 80 oranges stacked in a square staggered pattern, with a bulk depth of 0.33 meters and a porosity of 0.435, the constants in Equation 31 were found to be $a = 278$; and $b = 1.937$.

Chau et al. (1983) presented a variation of Ergun's equations as

$$(32) \quad \Delta P/h = K_1 \mu V (1-\epsilon)^2 / D \epsilon^3 g + K_2 \rho V^2 (1-\epsilon) / D \epsilon^3 g$$

where

$h = \Delta L$ in Equation 5

$K_1 = 150$ in Equation 5

$K_2 = 1.75$ in Equation 5

$g =$ Newton's Law gravitational constant.

This work did not employ a modified Ergun product coefficient, K_e , like that used by Patterson (1969).

Therefore, eliminating K_e and substituting K_1 and K_2 , Equations 29 and 30 can be rewritten

$$(33) \quad 1/K = K_1 \left[(1-\epsilon) / D_p \epsilon^2 \right]^3$$

and

$$(34) \quad \beta = K_2 \left[(1-\epsilon) / D_p \epsilon^3 \right]$$

Chau et al. (1983) determined K_1 and K_2 by fitting the experimental data and reported all the parameters required to solve Equations 33 and 34 for bulk packed oranges. For size 80 oranges arranged in a square staggered stacking pattern, the following values were reported:

$$D_p = 0.081 \text{ meters}; \quad \epsilon = 0.435; \quad K_1 = 890; \quad \text{and} \quad K_2 = 2.73.$$

Solving Equations 33 and 34 using the values given above resulted in the following:

$$1/K = 5.2608 \times 10^5 \text{ m}^{-2}; \quad \text{or,} \quad K = 1.9009 \times 10^{-6} \text{ m}^2;$$

$$\text{and} \quad \beta = 231.3 \text{ m}^{-1}.$$

Since the SI system of units was used by Chau et al. (1983), the desired units for the pressure are Pascals and the desired units for the velocity are meters per second. The inlet air condition used by Chau et al. (1983) are approximately the same as those used by Segerlind (1982) and Khompis et al. (1984). The air viscosity and density

specified above as input for the ANSYS finite element program to solve the problem reported by Khompis et al. (1984) were used again,

$$\mu = 1.846 \times 10^{-5} \text{ kg/m-sec}; \text{ and } \rho = 1.1614 \text{ kg/m}^3.$$

To determine the pressure drop across rectangular and round vent holes, Chau et al. (1983) conducted tests using the experimental set-up shown in Figure 9, for one layer of corrugated fiberboard (simulating one side of a carton) with 4, 6, and 8 vent holes. The tests were repeated with 2 layers of fiberboard separated by 30 centimeters (simulating 2 sides of a carton). Each fiberboard side had 4, 6, or 8 vent holes placed uniformly in the fiberboard cross-section. The cross-sectional area of each vent hole was 12.94 square centimeters. The thickness of the fiberboard used to make the cartons was 3.2 millimeters.

The experimental data were normalized on the basis of actual air velocities through the vent holes (calculated as total flow rate divided by total vent area), and the data points for the tests with 4, 6, and 8 vent holes fitted the same straight line on a log-log plot.

The equations of best fit for the experimental data were presented by Chau et al. (1983) as pressure drop across one side of carton with rectangular vent holes

$$(35) \quad \Delta P = 1.59 \frac{V^2}{i};$$

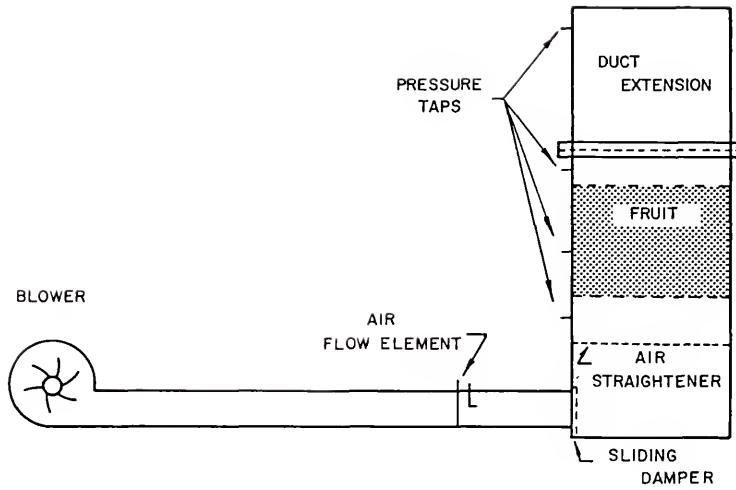


Figure 9. The experimental setup used by Chau et al. (1983) for measuring air flow resistance in orange.

pressure drop across two side of carton with rectangular vent holes

$$(36) \quad \Delta P = 2.78 \frac{V^2}{i};$$

pressure drop across one side of carton with round vent holes

$$(37) \quad \Delta P = 1.76 \frac{V^2}{i}; \text{ and}$$

pressure drop across two side of carton with round vent holes

$$(38) \quad \Delta P = 2.89 \frac{V^2}{i}.$$

Chau et al. (1983) noted that the pressure drop across two sides of the carton was less than twice the pressure drop across one side of the carton alone. The explanation for this difference given by Chau et al. (1983) was that the loss for one carton side is similar to an exit loss. For two sides of the carton, the loss is more like a duct enlargement loss as the air travels between the sides of the carton. The enlargement loss is smaller than an abrupt exit loss.

The explanation for the slightly higher pressure drop for the round vent holes was attributed to roughness of the edges of the holes. The rectangular holes were machine stamped while the round holes were cut using a hole saw.

It is interesting to note that Kaminski (1986a) presented the following equation for static pressure differences:

$$(39) \quad \Delta P_s = C_D \rho \frac{V_m^2}{2g_c}$$

where

ΔP_s = Static pressure difference across a given configuration

C_D = Static pressure coefficient based on highest the highest average velocity for a given configuration

V_m = Highest average velocity

and the other terms are as previously defined.

For turbulent flow, Reynolds Number greater than 10,000, through a square-edged orifice the static pressure coefficient was reported as $C_D = 2.80$.

If Equations 35 and 37 are rearranged into the form of Equation 39, the coefficients of static pressure are respectively, 2.74 and 3.03. Therefore, the pressure loss across a single fiberboard can be approximated by the pressure loss across an orifice or orifice plate.

No such comparison of the pressure loss across two fiberboards, separated by a fixed distance, could be made with the typically presented expansion and contraction configurations reported in various fluid flow text and data books.

Chau et al. (1983) experimentally evaluated the cumulative effect of air flow resistance of the vent holes and the oranges. Measurements were made of the pressure drop across oranges stacked on fiberboard with 4 rectangular vent holes which simulated the fruit with one side of a carton. The pressure drop was also measured across oranges stacked between 2 fiberboards with 4 rectangular vent holes of the same size and location on each fiberboard. All the tests were repeated using 4 different stacking patterns and 4 different orange sizes.

Chau et al. (1983) fitted the experimental data using a modification of Equation 31 which did not normalize the pressure drop to a unit depth of fruit

$$(40) \quad \Delta P = a' V^b$$

This was necessary because the measured pressure drop was a combination of the pressure change across the oranges, which was a function of fruit depth, and the pressure change across the vent holes, which was not a function of fruit depth.

For the size 80 oranges stacked in a square staggered pattern, with a bulk depth of 0.33 meters and a porosity of 0.430, the constants in Equation 40 for oranges with one carton side were found to be

$$a' = 1.85 \times 10^4 \quad \text{and} \quad b = 1.98, \quad \text{while for oranges with two carton sides the constants were found to be}$$

$$a' = 2.46 \times 10^4 \quad \text{and} \quad b = 1.95.$$

Chau et al. (1983) noted that most of the pressure loss was caused by the resistance of the vent holes. The pressure drop across a carton of fruit was always greater than the sum of the pressure drops across each side of the carton plus the pressure drop across the fruit. Wang and Tunpun (1969) reported similar results.

According to Chau et al. (1983), the pressure drop across the sides of the carton was expected to be higher than the sum of the pressure drops across the sides of the carton and the fruit. The fruit disturbed the flow past the vent holes since there was always an amount of obstruction by the fruit. Further, the air flow pattern through the oranges in a carton with vent holes was much different from the uniform flow through bulk loads of oranges even for the same approach velocity. Near the area of the vent holes for flow through oranges in cartons, high localized velocities occurred. Since the pressure loss through the vent holes was proportional to the velocity squared, approximately, the high localized velocities produced a higher overall pressure drop across the vent holes and through the fruit near the vent holes.

All the necessary input data to use the ANSYS finite element program to model the experimental work of Chau et al. (1983) are known.

Extensive modeling using two-dimensional elements, like that employed previously in modeling the work of Segerlind (1982) and Khompis (1983), was carried out but

was not be reported here since the work of Chau et al. (1983) was three-dimensional. The two-dimensional work was very helpful initially in providing necessary direction without the additional computer time required when working with three-dimensions. The two-dimensional modeling results were essentially the same as the three-dimensional modeling, which is discussed in detail below.

Modeling the experimental work of Chau et al. (1983) involved more than one application of the capabilities of the ANSYS finite element solution package. First, the flow through the oranges in bulk was easily modeled as illustrated previously for the grain bin problems of Segerlind (1982) and Khompis (1983). The boundary conditions at the cross-section of the entrance and exit were easily applied for this uniform flow situation. The second application dealt with the reduced boundary conditions as a result of the entrance and exit vents of the oranges packaged in cartons. The third application involved modeling the orifice-type loss through the vents of the carton walls. Finally, the combination of the second and third applications was applied to study the combination losses which were reported by Chau et al. (1983) and Wang and Tunpun (1969).

The physical problem selected for solution was the experimental set-up shown in Figure 9 and described above. An eight node 3-D isoparametric thermal solid element, which allowed modeling of nonlinear steady-state flow

through a porous media, was used to model the pressure loss through oranges in bulk and oranges in cartons, without consideration of the pressure loss through the vent holes. This element could be formed into prism or tetrahedron shaped elements by defining duplicate node numbers. However, only 3-D rectangular elements were needed. The node and element locations are shown in Figure 10. The model consisted of 320 nodes and 196 elements. The nodes were placed every 8.1 cm. The boundary conditions were specified at the inlets and outlets corresponding to data reported by Chau et al. (1983). For the situation with oranges in bulk, the pressure or flow rate across the inlet and outlet cross-sections was specified. For the situation with oranges in cartons, the pressure or flow was specified at nodal locations corresponding to the four inlet and exit vent hole locations of the experimental set-up used by Chau et al. (1983). The inlet and outlet locations were point sources and the velocity and pressure varied in the x-, y-, and z-axis. As noted in previous models, the no-flow or impermeable boundary conditions are automatically enforced on the boundary when no pressure values were specified.

In order to use ANSYS to model the pressure loss through the vent holes in the fiberboard, a new element type was used. The element was the hydraulic conductance element (DeSalvo and Swanson 1983). This uniaxial two node element had the ability to transmit flow between its nodal points.

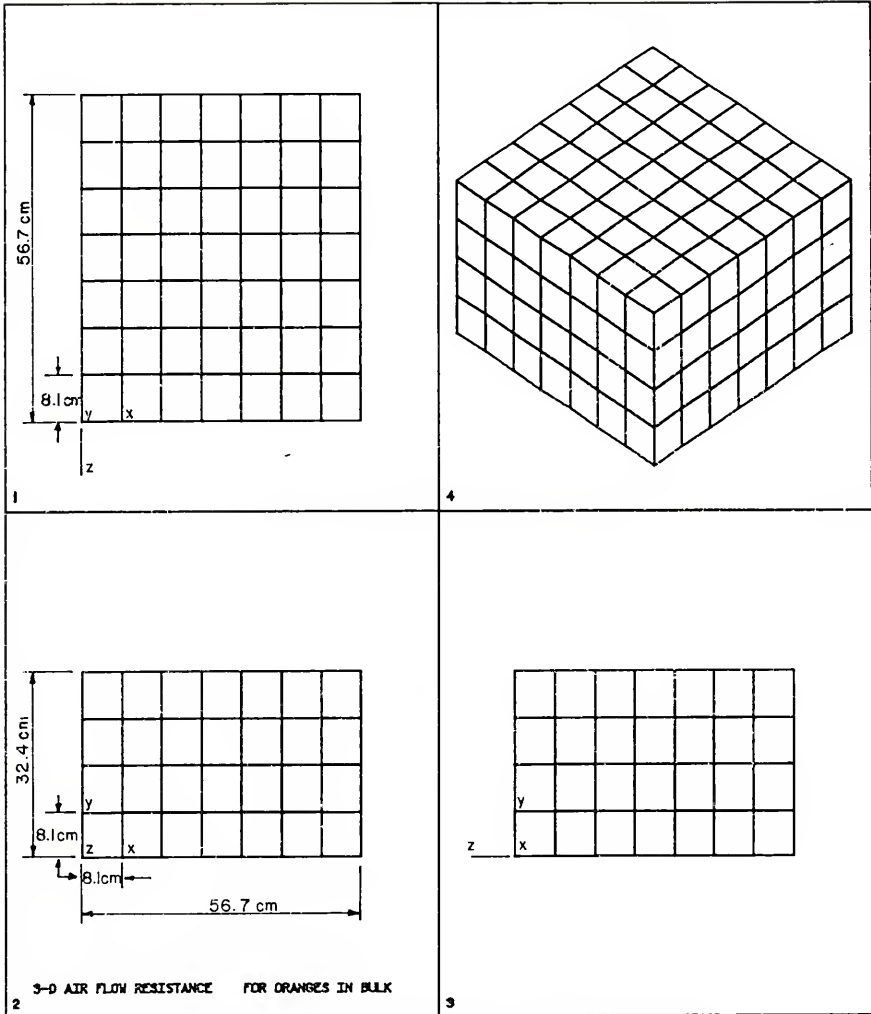


Figure 10. The node and element locations used to model 3-D oranges packed in bulk and in cartons.

The element had a single degree of freedom, pressure, at each node point. The hydraulic conductance element was applicable for two or three dimensional steady-state thermal or fluid flow analysis. The element was defined by two nodal points and a conductance coefficient similar to the coefficients in Equations 35 through 38. The equation solved by this element was

$$(41) \quad \Delta P_s = \frac{\dot{m}^2}{C^2}$$

where

ΔP_s = Static pressure difference across the hydraulic element

C = Conductance coefficient

\dot{m} = Mass flow rate.

The nodal boundary conditions could be specified as a pressure or mass flow rate. For the problem under consideration, the inlet mass flow rate was specified and the outlet pressure was calculated using ANSYS. This hydraulic conductance element could be connected to the porous media element at the vent holes to model the combination pressure loss through the fiberboard vent holes and oranges. For a single carton of oranges, the pressure and air velocity distribution within the carton could be determined without detailed knowledge of the pressure loss that occurs through the vent holes, if the flow rate through

the holes is known. However, when considering multiple cartons of oranges such as a pallet configuration, knowledge of the combination pressure loss through the vent holes becomes very significant.

In order to compare the experimental data reported by Chau et al. (1983) and the results from ANSYS, a range of flow rates was selected which covered the range of the experimental data. The range of flow rates selected (Kg/sec) was from 3.5×10^{-2} to 10.0×10^{-2} in increments of 0.5×10^{-2} . For each flow rate, the velocity was calculated using the air density value mentioned above and the cross-sectional area of the boundary condition considered, either the entire cross-section for oranges in bulk or the cross-sectional area of the vent holes for oranges in cartons. For each velocity, the pressure drop was calculated using the best fit equations for size 80 oranges stacked in a square staggered pattern developed by Chau et al. (1983). Equations 31 and 32 were used to calculate the pressure drop across bulk oranges. Equation 40 was used to calculate the pressure drop across oranges with one and two carton sides. Using input data for size 80 oranges stacked in a square staggered pattern from Equations 33 and 34, the air density and viscosity, and the boundary conditions for oranges in bulk and oranges with one and two carton sides, ANSYS was used to calculate the pressure drop for each flow rate and the results were then

compared with the corresponding results obtained using the best fit equations developed by Chau et al. (1983).

To model the orifice-type pressure through the vents of the carton wall using ANSYS, the conductance coefficient, C , was needed as an input constant for the hydraulic conductance element. The conductance coefficient for one and two carton sides with rectangular vent holes was calculated by equating Equation 41 with Equations 35 and 36, respectively. Since the mass flow rate, \dot{m} , in Equation 41 can be expressed as follows:

$$(42) \quad \dot{m} = \rho V_i A_v$$

where

V_i = Velocity through vent hole

A_v = Area of vent holes

the conductance coefficient for one carton side with rectangular vents holes was

$$(43) \quad C_1 = \rho A_v / (1.59)^{.5}$$

and the conductance coefficient for two carton sides with rectangular vents holes was

$$(44) \quad C_2 = \rho A_v / (2.78)^{.5}$$

For each flow rate, ANSYS was used to calculate the pressure drop for one and two carton sides and the results

were then compared with the corresponding results obtained using Equation 35 and 36, developed by Chau et al. (1983). Because of the derivation of the conductance coefficients, this comparison was expected to reveal identical results. In the case of two carton sides, only one hydraulic conductance element was used to model both sides. An attempt was made to model the two carton sides using two hydraulic conductance elements in series but the apportionment of the conductance coefficient between the first and second element could only be done in an arbitrary manner.

An attempt was made to determine the exact nature of the cumulative effect of air flow resistance across the vent holes and across the oranges. This attempt was made based on the assumption that the major reason for the higher cumulative pressure drop for fruit in cartons when compared to the pressure loss through bulk oranges plus the loss through the carton sides alone was a function of the reduction of the effective vent hole area due primarily to blockage or obstruction by the oranges. Since the area was reduced, the air velocity was increased, producing a greater pressure drop.

The first step in this attempt was the modification of the orifice-type pressure loss. The area, A_v , in Equations 43 and 44 was replaced by an effective vent area, A_e , which was defined as

$$(45) \quad A_e = f \frac{A_v}{r}$$

where f_r = area reduction factor.

Equation 42 was rewritten as follows:

$$(46) \quad \dot{m} = \rho V_i f_r A_v.$$

The conductance coefficient for one carton side with rectangular vents holes was obtained by rewriting Equation 43 as follows:

$$(47) \quad C_1 = \rho f_{r1} A_v / (1.59)^{.5}$$

and the conductance coefficient for two carton sides with rectangular vents holes was obtained by rewriting Equation 44 as follows:

$$(48) \quad C_2 = \rho f_{r2} A_v / (2.78)^{.5}$$

where f_{r1} and f_{r2} are the area reduction factors for one and two carton sides respectively. These reduction factors may also absorb other unexplained causes for the cumulative pressure loss increase.

In order to calculate the area reduction factors the assumption was made that the pressure loss predicted by Equation 40 for oranges with one or two carton sides was equal to the pressure loss calculated by ANSYS for oranges with one or two carton sides plus the orifice-type loss

calculated using Equation 41 which contained the conductance coefficients in terms of the reduction factors for one or two carton sides

$$(49) \quad \Delta P \text{ (Equation 40)} = \Delta P \text{ (ANSYS)} + \Delta P \text{ (Equation 41)}$$

which can be rewritten as

$$(50) \quad \Delta P \text{ (Equation 41)} = \Delta P \text{ (ANSYS)} - \Delta P \text{ (Equation 40)}$$

Substituting Equation 47 for the conductance coefficient in Equation 41 yielded the orifice-type pressure loss for one carton side

$$(51) \quad \Delta P_s = \frac{.2}{r_1} \frac{m^2}{\rho} \frac{f_{r_1}^2}{Av^2} / 1.59$$

Substituting Equation 48 for the conductance coefficient in Equation 41 yielded the orifice-type pressure loss for two carton sides

$$(52) \quad \Delta P_s = \frac{.2}{r_2} \frac{m^2}{\rho} \frac{f_{r_2}^2}{Av^2} / 2.78$$

Substituting Equation 51 into Equation 50 and solving for the reduction factor for oranges with one carton side yielded

$$(53) \quad f_{r_1}^2 = \frac{1.59 \frac{m^2}{\rho} Av^2}{[\Delta P \text{ (ANSYS)} - \Delta P \text{ (Equation 40)}]}$$

Substituting Equation 52 into Equation 50 and solving for the reduction factor for oranges with two carton sides yielded

$$(54) \quad f^2 = \frac{2.78 \text{ m}^2 / \rho A v}{r^2 [\Delta P (\text{ANSYS}) - \Delta P (\text{Equation 40})]}$$

For each flow rate the reduction factor was calculated using the pressure losses calculated using ANSYS and Equation 40 reported by Chau et al. (1983)

Three-Dimensional Orange Carton

The modeling of the experimental work of Chau et al. (1983) was expanded to model an individual carton packed with oranges. The physical problem selected for solution was an experimental box with dimensions similar to a commercial packing container used for oranges. The experimental box, which is shown in Figure 11, was constructed of 3/4 inch (1.85 cm) plywood with a lining of 3/4 inch (1.85 cm) insulation board on the inside of the walls. The interior dimensions of the experimental box, inside the insulation, were 38.1 x 27.94 x 27.94 cm (15 x 11 x 11 inches). The box was used in the evaluation of temperature response during cooling of the oranges, which will be discussed later. The box was constructed to allow 10 possible air inlets or outlets. This allowed analysis of various air flow patterns through the box. The inlet/outlet holes were constructed by drilling holes in the sides of the

box at the desired locations as indicated in Figure 11. Using threaded pipe flanges attached to the outside of the box, 1 inch (2.54 cm) inside diameter (i.d.) threaded pipes were installed so that the ends of the pipes were flush with the interior surface of the insulation. In Florida, commercial citrus cartons usually contain only 2 vent holes on each side of the carton.

Again, extensive modeling using two-dimensional elements, like that employed previously in modeling the work of Segerlind (1982) and Khompis (1983), and Chau et al. (1983), was carried out but was not reported here since the flow through the experimental orange carton was three-dimensional. The two-dimensional work was very helpful initially in providing necessary direction without the additional computer time required when working with three-dimensions. The two-dimensional modeling results were consistent with the three-dimensional modeling, which are discussed in detail below.

An eight node 3-D isoparametric thermal solid element, which allowed modeling of nonlinear steady-state flow through a porous media, was used. This element could be formed into prism or tetrahedron shaped elements by defining duplicate node numbers. However, only 3-D rectangular elements were needed. The node and element locations are shown in Figure 12. The model consisted of 1,815 nodes and 1,400 elements. The nodes adjacent to the walls of the experimental box were placed 1.5 inches (3.81 cm) from the

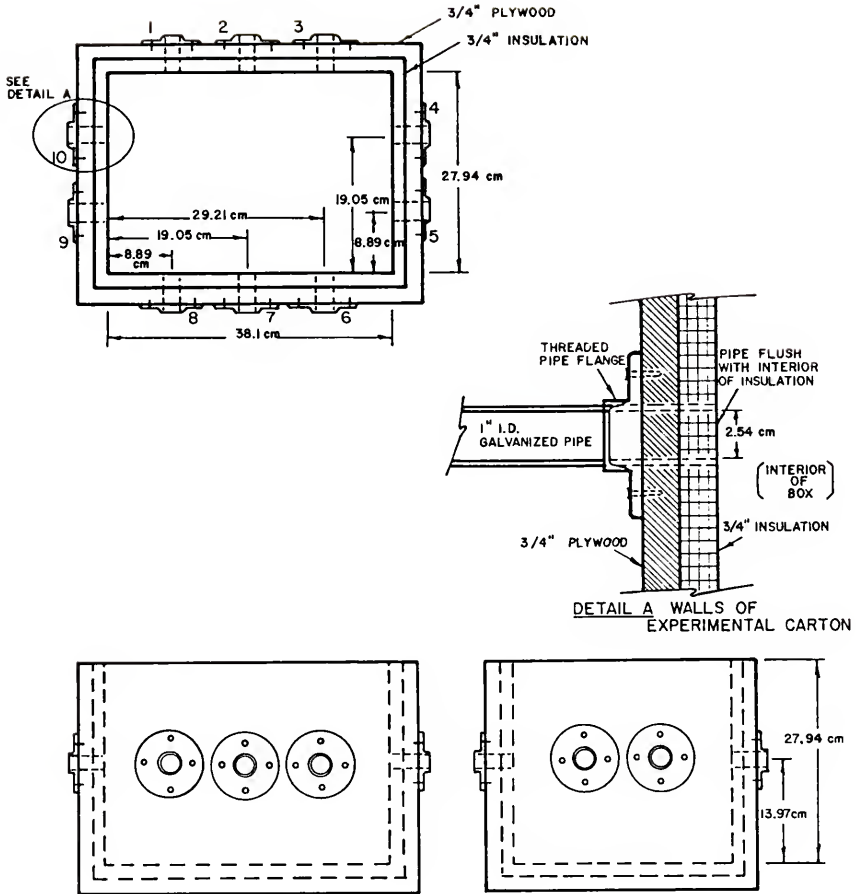


Figure 11. The experimental orange carton.

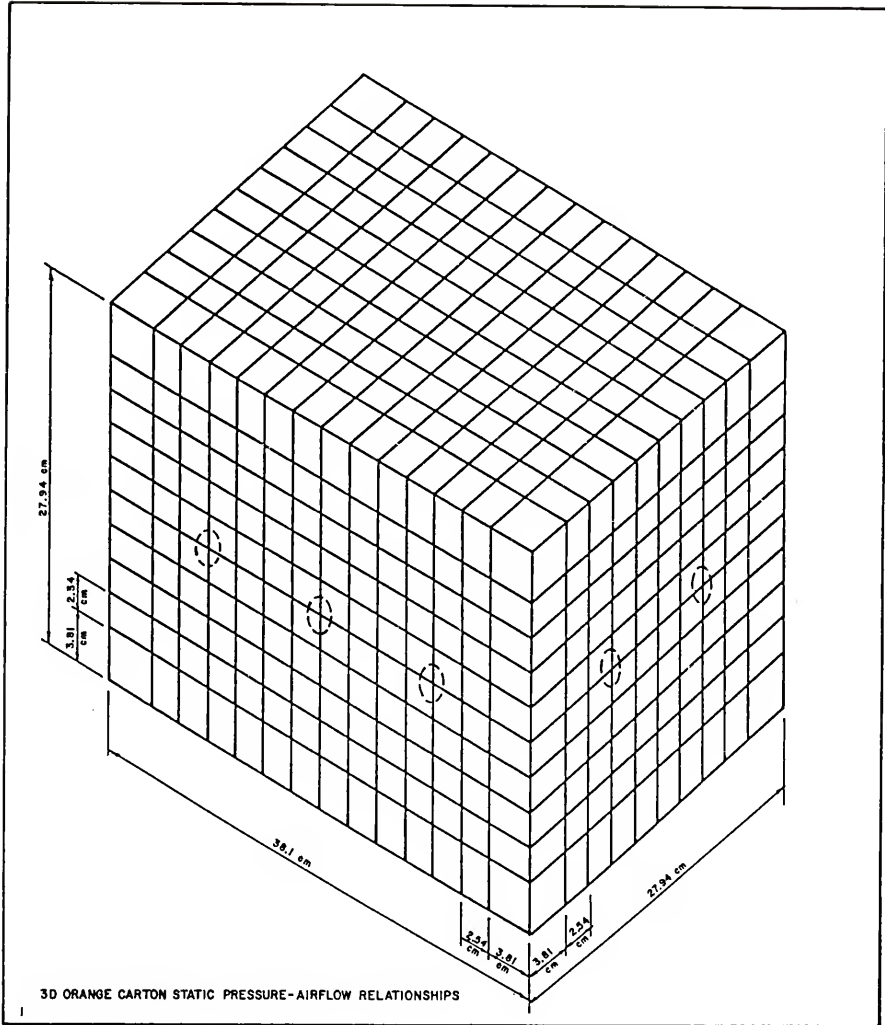


Figure 12. The node and element locations used to model a 3-D orange carton.

walls in order to account for the locations of the vent openings. The remaining interior nodes were placed every 1 inch (2.54 cm) along the axis of the experimental box. The boundary conditions were specified at the nodal locations corresponding to the inlets and outlets vent locations. As noted in previous models, the no-flow or impermeable boundary conditions were automatically enforced on the boundary when no pressure values were specified. The inlet and outlet locations were point sources and the velocity and pressure could vary in the x-, y-, and z-axis.

The necessary input data to use the ANSYS finite element program were obtained from the experimental work of Chau et al. (1983). For size 100 oranges arranged in a square staggered stacking pattern, the following values were reported:

$$D_p = 0.0735 \text{ meters}; \quad \epsilon = 0.405; \quad K_1 = 1566; \quad \text{and} \quad K_2 = 2.22.$$

Solving Equations 33 and 34 using the values given above resulted in the following:

$$1/K = 1.5448 \times 10^{-7} \text{ m}^{-2}; \quad \text{or} \quad K = 6.4731 \times 10^{-7} \text{ m}^2;$$

$$\text{and} \quad \beta = 270.5 \text{ m}^{-1}.$$

A comparison of the temperature response calculated by ANSYS using the constant porosity and derived input parameters specified above with the corresponding

experimental temperature response, produced poor agreement. Temperatures predicted by ANSYS were warmer in regions adjacent to the walls of the container and slightly cooler in the central portion of the container away from the walls. The concern for the variation of the voidage or porosity adjacent to the walls was expressed above and concluded to be the major factor resulting in the poor fit of the experimental temperature response. These preliminary comparisons are not presented in the Results and Discussion Section, rather an attempt was made to adjust the ANSYS program to account for the anticipated variable porosity as described below.

The distance of penetration from the wall of the variable porosity for oranges packed in a three-dimensional orange carton is a subject requiring additional research. Ridgway and Tarbuck (1968) reported that the variation in porosity of large random beds existed to about five sphere diameters from the wall. Pillai (1977) indicated the porosity variation could penetrate up to three particle diameters from the wall for two-dimensional randomly packed beds, but concluded that assuming a constant porosity beyond one particle diameter would result in an error of less than 10%. For the current study, calculation of the porosity adjacent to the walls of the carton was possible using basic geometric relationships. However, the calculations beyond the first set of elements were complex due to the overlapping of the oranges in the three-dimensional stacking

pattern. Therefore, the variable porosity was calculated within the regions occupied by the ANSYS elements adjacent to all six interior walls of the experimental orange carton. Due to the size of the elements adjacent to the wall the variable porosity was calculated in a region one-half the orange diameter from each wall.

The procedure for calculating the porosity adjacent to the walls was accomplished by first assuming the oranges were perfect spheres. The volume of the oranges or portion of an orange lying within the elements adjacent to the walls was calculated. Then the volume of the elements adjacent to the wall was calculated. The porosity was defined in Equation 3 as the ratio of the void volume to total volume. The void volume was calculated by subtracting the volume of the oranges from the volume of the elements. The total volume was the volume of the elements adjacent to the walls.

The elements adjacent to the walls were divided into 4 groups. There were 8 corner elements. There were 112 edge elements located at the intersection of two walls, but not including the corner elements. There were 384 elements located in 4 walls 27.94 x 38.1 cm, not including corner or edge elements. There were 128 elements located in 2 walls 27.94 x 27.94 cm, not including corner or edge elements. The porosity for each of the 4 groups of elements was calculated. The porosity of the remaining 800 elements in the central portion of the carton remained equal to the

constant porosity mentioned above. The porosity for the different element types is shown in Table 1.

ANSYS has the capability of assigning individual material properties (β , K , etc.) to each individual element. Therefore, the Equations 33 and 34 were solved based on the porosity for each of the selected groups of elements considered and using the values of D , K_1 , and K_2 specified above. The results of these calculation for β and K are shown in Table 1.

Table 1. Summary of variable porosity and ANSYS input data.

Element Location (Number of Elements)	Porosity, ϵ	K	β
Center (800)	0.405	6.4731E-7	270.5
Corners (8)	0.476	1.3550E-6	146.7
Edges (112)	0.607	4.9953E-6	53.1
4 Surfaces, 27.94 x 38.1 cm (384)	0.450	1.0392E-6	182.3
2 Surfaces, 27.94 x 27.94 cm (128)	0.465	1.2118E-6	160.7

In addition, the air viscosity and density were assumed not to vary significantly during the cooling process, and the values for these properties were obtained for an average cooling test temperature of 10 C (50 F)

$$\mu = 1.762 \times 10^{-5} \text{ kg/m-sec} ; \text{ and } \rho = 1.24 \text{ kg/m}^3 .$$

The assignment of individual material property values to the different element groups added additional statements to the ANSYS problem formulation file but ANSYS proved to be very flexible and simple to apply this powerful capability. It is possible to provide a set of input parameters based on the porosity for each element if required. However, this study did not include within its scope the necessary time to empirically evaluate the variable porosity inside the orange carton beyond one-half sphere diameter from the wall.

Considering the numbered vent locations shown in Figure 11, the flow patterns presented in Table 2, were evaluated.

The boundary conditions for the air flow rates were obtained from the experimental temperature response study of size 100 square staggered packed oranges and are shown in Table 3. However, the ANSYS model has the capability to analyze a wide range of air flow rates. The air flow rates in Table 3 are the equal flow through each of the inlet vents for a particular boundary condition. Therefore, the total inlet flow rate for Boundary Condition 2 is twice the value reported in Table 3. For use in the ANSYS model the volume flow rates were converted to mass flow rates

using the value of the air density for the inlet air temperature for a particular experimental test, 0 to 1.67 C (32 to 35 F).

Table 2. Inlet and outlet air vent locations as indicated by the numbers illustrated in Figure 11.

Boundary condition number	Inlet vents	Outlet vents
1	2	7
2	1, 3	6, 8
3	1, 2, 3	6, 7, 8
4	2	4, 7, 10
5	2	7, 10
6	1	6

Table 3. Boundary conditions and air flow rates (2 flow rates per venting arrangement) for tests conducted with an experimental orange carton packed with size 100 oranges.

Boundary Condition Number	Balanced air flow rate, m / s ³ per each inlet vent	
	(1)	(2)
	1	1.58 E-3
2	1.56 E-3	4.40 E-3
3	1.21 E-3	6.09 E-3
4	5.31 E-3	2.06 E-2
5	4.72 E-3	1.33 E-2
6	1.53 E-3	5.46 E-3

Before detailing the incorporation of the velocity and pressure distributions calculated with ANSYS into an existing heat transfer model, the procedures for obtaining the experimental temperature data for the size 100 oranges packed in the experimental box are discussed below.

Experimental Temperature Measurement

Description of Experimental Facilities

A forced-air cooler designed specifically for research, Baird et al. (1975), with a capability of controlling all of the important variables relating to cooling biological materials, was used for this study. Air velocity, air temperature, relative humidity, container venting and product stacking arrangement were the variables that could be controlled. Temperature distribution within the individual product and within the product container, static pressure loss across the product container, and product moisture loss were among the parameters that could be measured during a test.

Information obtained from the cooling studies using this facility were compared with the temperature response data predicted by a heat transfer model to be discussed below.

Basic Construction of Precooler

Figure 13 shows the general location of the components and the air circulation diagram for the cooling facility. The overall length of the cooler was 8 m and the outside dimensions of the product chamber section were 2.5 x 2.5 x 3.5 m high. The product chamber was initially designed to accommodate a product load which could have dimensions of up to 1.2 x 1.2 m in cross-section and 2.5 m high. This allowed cooling tests using pallet boxes or pallet loads.

In order to study an individual carton, the product chamber was modified as shown in Figure 14 to accept the experimental orange carton mentioned above. The basic wall construction of the unit was wood studding with 8.5 cm of rigid polyurethane foamed in place between the plywood sheeting. The outside of the cooler was sealed with caulking and epoxy paint to minimize water vapor movement.

Refrigeration Components and Controls

Figure 15 shows each component of the refrigeration system. The condensing unit was water cooled with a two-cylinder 5.6 kW compressor. The compressor was equipped with an automatic cylinder unloader which inactivates one of the cylinders when the suction pressure drops below an adjustable preset value. The refrigeration system was designed to allow continuous operation of the compressor, since intermittent operation would result in poor temperature control. Air temperature control was accomplished through the use of an automatic controller which operates a motorized pressure regulating valve on the suction side of the evaporator.

Since the cooling load sometimes varies over a wide range during a single test while the compressor was operating continuously, it is necessary to have a hot-gas bypass valve in addition to the cylinder unloader to provide for additional capacity reduction. As indicated in Figure 15, this valve recirculates hot gas from the compressor back

through the evaporator when the suction pressure drops below an adjustable, preset level.

The direct expansion evaporator coils shown in Figure 13 are standard models without housing or fan. They have wide-spaced fins (1/2 cm) so that a thin layer of ice collected during a test will not significantly affect the air flow rate. Both evaporators are equipped with defrosting heaters which can be actuated manually. The heaters can also be used to provide additional heat load on the refrigeration system which is sometimes desirable in order to achieve better control. Refrigerant 502 was used in this system since it allows a wide range of operating temperature without changing the thermal expansion valves and other control components.

Air Temperature and Humidity

Since the air was recirculated, the dew point of the cooling air approached the evaporator temperature unless moisture was added. In some cases an undesirable drying effect can be caused by a large water vapor pressure difference between air and the product surface. In order to minimize this effect, the cooler was equipped with a steam humidifier which injected steam into the air after it passes through the evaporator coils. Adding steam to the air in this manner resulted primarily in a latent heat increase, and very little sensible heating occurred. For example, when air at 0 C and 70% RH is saturated by adding 100 C steam, the air

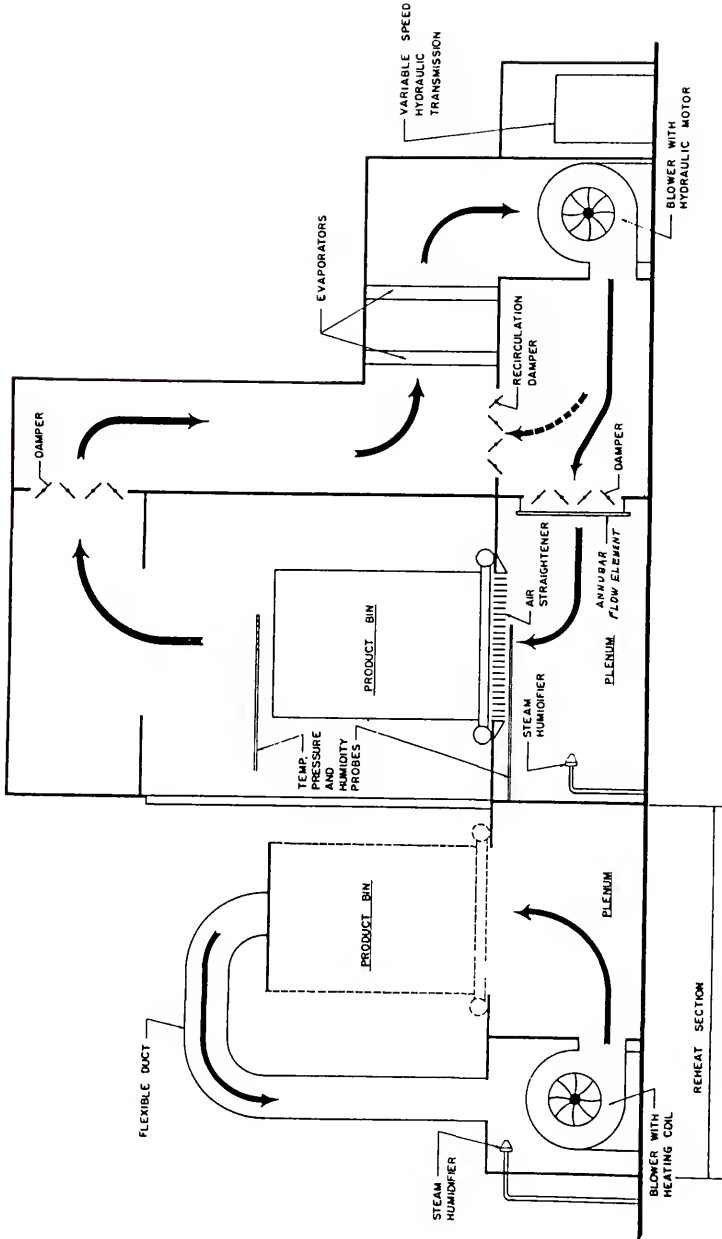
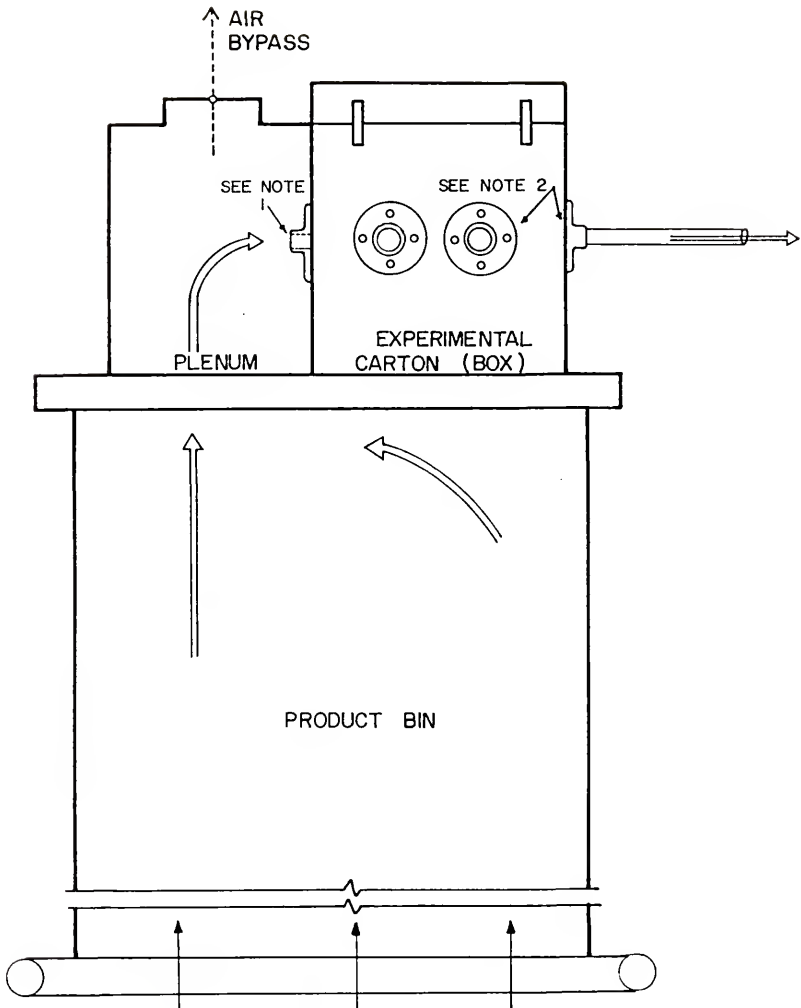


Figure 13. Forced-air precooler components and air circulation diagram, Baird et al. (1975)



NOTE 1: AIR ENTERS THROUGH SOME COMBINATION OF THREE INLET VENTS.

NOTE 2: AIR EXITS THROUGH SOME COMBINATION OF SEVEN OUTLET VENTS.

Figure 14. Modification of product bin to accommodate experimental carton.

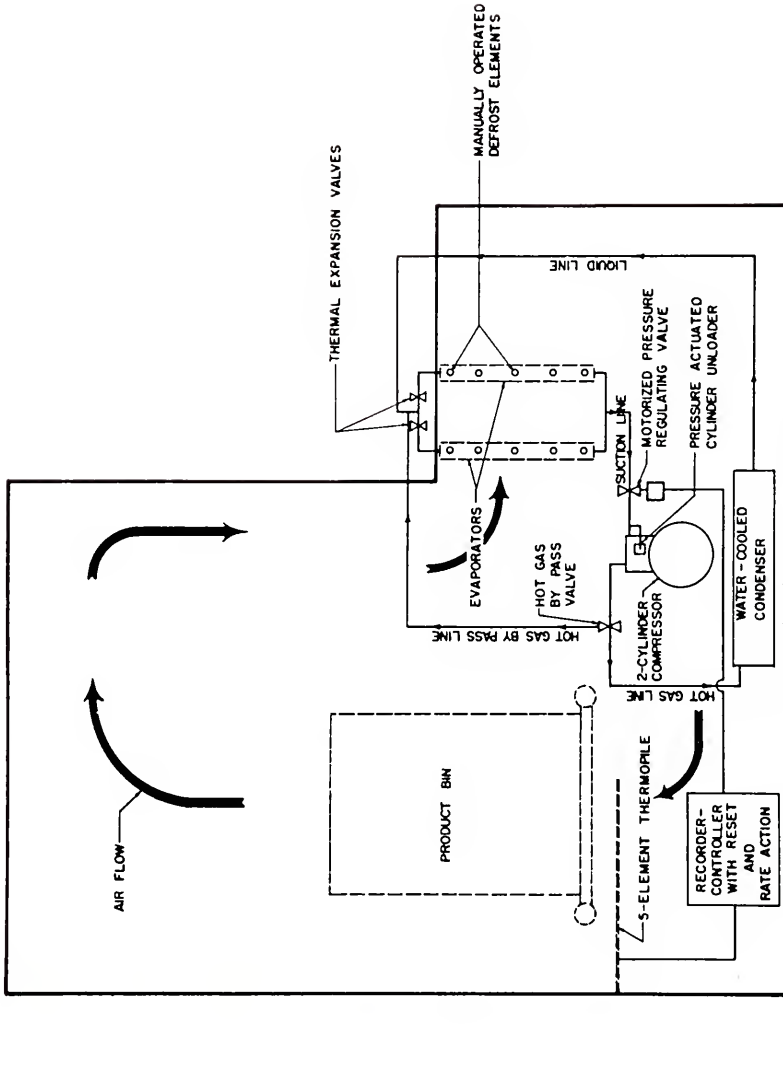


Figure 15. Precooler refrigeration components and controls, Baird et al. (1975).

temperature is increased less than 0.2 C. This procedure presents no problem in controlling the air temperature since the temperature sensor is downstream from the humidifier. The use of large evaporators, thus keeping the temperature difference between the coil and the air small, resulted in higher humidities. However, the humidity was always below 100% if moisture was not added back to the air after passing through the coils. Even when the air entering the product chamber was saturated, there was still a potential for drying in a product bed because the air was heated by the preceding layer of product.

The method to determine the amount of moisture loss during cooling, was to weigh individual product samples from the top of the carton immediately before and after each test.

The automatic control of air temperature entering the product chamber was accomplished by the use of a proportional controller with reset and rate action, which regulated the motorized valve on the evaporator. The primary sensing element for the automatic controller was a thermocouple which was placed in the air stream at the entrance of the product carton. The manipulated variable was the evaporator pressure which was regulated by the motorized valve. For tests conducted during this study, the inlet air temperature was maintained essentially constant.

Air Flow

The location of the air handling unit and air flow patterns are shown in Figure 13. The air was circulated with a backward curved centrifugal blower having a capacity of $7.6 \text{ m}^3/\text{s}$ when operating against 1 kPa static pressure. The backward curved vanes produced a relatively high operating pressure and provided approach velocities of up to 5 m/s entering the product chamber.

The blower was driven by a hydraulic motor controlled by a variable speed hydraulic transmission which allowed the air flow rate to be regulated by the rpm of the blower rather than by dampers. The transmission and electric motor were located outside of the cooler, which minimized the heat produced inside the cooler. The blower was placed downstream from the evaporator coils so that the temperature of the air through the blower would remain constant throughout a test. If the blower were placed upstream from the evaporators, the temperature of air moving through the fan would vary during the test causing a variation in the velocity through the product chamber.

The air enters a large plenum and passes through an air-straightening section beneath the product bin to ensure that the air entering products packed in bulk is uniformly distributed as it enters the product bin. In conjunction with the air-straightening vanes, small patches of screen wire were added to produce resistance in areas which have a high velocity. The velocity profile of the air entering the

product bin did not vary more than 5% when measured with a hot-wire anemometer probe at 15 cm intervals.

In order to simulate the forced air cooling of a carton of fruit, the experimental carton and the entrance plenum for this carton were securely fastened to the top of the product bin. As illustrated in Figure 14, the air entered the plenum of the experimental carton and underwent a ninety degree turn prior to entering some combination of any three 2.54 cm inlet holes. The air passed through the product and exited through some combination of any five 2.54 cm outlet holes. Table 2 presents the inlet and outlet combinations evaluated during this study. The air then continued into the product chamber and through the precooler as illustrated in Figure 13.

The air flow rate leaving the carton was measured to within ± 2 percent (based on manufacturers claims for the accuracy for the two primary components of the air flow rate measuring system) through the use of an "annubar" flow element installed in a 2.54 cm inside diameter pipe connected to the threaded pipe flanges attached to the outlet of the carton. When more than one outlet was used, a hot-wire anemometer was used to measure the relative flow leaving each hole. The flow rate was determined as a function of the difference between velocity pressure and static pressure. The pressure difference was measured with an electronic differential pressure manometer which had a resolution of 0.13 Pa.

The damper in the top of the experimental carton plenum was used to bypass air for test with low air flow rates through the product carton. Also at the start of a test the experimental carton with the exit vents sealed was attached to the plenum. Cold air was circulated through the plenum for a few minutes until the desired entering air temperature was achieved at the entrance to the experimental carton. Then the desired exit vents were opened to start the test.

The venting arrangements were obtained by the use of rubber stoppers which were large enough to seal the pipes at the inlet or exit vent. The vent openings which were not needed for a particular test were plugged.

Reheat Section

The reheat section, as shown in Figure 13, was a self-contained unit placed adjacent to the product chamber so that a container load of product was rolled out and reheated for repeated tests on the same product load. It was used to heat the product to a predetermined uniform temperature before the initial test. The reheat section was equipped with a blower, heater, temperature controller, and humidifier. Since the product was heated outside of the cooling chamber, the cooler could operate prior to the beginning of a test and maintain the desired temperature while the product is being heated. The primary source of heat for the heating section was a hot water-heated coil with secondary electric heaters used for fine control. The

electric heaters were regulated by a proportional automatic controller.

Experimental Test Procedures

Twelve tests were conducted with an experimental orange carton packed with 18 kg of size 100 Valencia oranges using air flow rates ranging from 1.53×10^{-3} to 2.06×10^{-2} m³/s. These tests were conducted on six different venting arrangements with two flow rates for each (Table 3).

Each cooling test was conducted using 88 sized fruit which were weighed and placed into the experimental orange carton in a face-centered cubic packing arrangement, which was the same configuration termed square-staggered by Chau et al. (1983). This stacking pattern resulted in five horizontal layers of fruit, with 18 fruit in the bottom, middle and top layers and 17 fruit in the second and fourth layers. Thermocouples were placed at the center of 58 oranges and at the surface of 10 oranges. Ten thermocouples were also placed in the air spaces adjacent to the surface thermocouples to measure the air temperature within the orange carton. Other temperature measurement included the entering and leaving air temperatures.

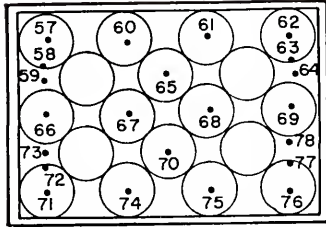
Appendix A depicts the method used for placing the thermocouples in the product. The thermocouples were constructed from 36-gage, insulated copper-constantan wire. The location of the oranges in each layer of the

experimental orange carton and the location of the thermocouples are shown in Figure 16.

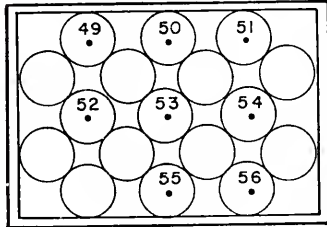
Temperature was recorded on a microprocessor-controlled data acquisition system capable of receiving 80 thermocouple inputs. Each thermocouple and other data inputs were read at 3, 6, 12, or 15 minute intervals throughout the test. The scan interval was controlled by settings on the digital clock of the datalogger and was selected based on the total length of the test run. A longer time interval was used for the lower flow rate tests. The product in the experimental orange carton was brought to a uniform temperature by the reheat section just prior to placement of the carton into the cooling chamber. The condition of the entering cooling air was maintained essentially constant. Problems associated with the last two variables are addressed in the Results and Discussion section.

The digital datalogger was linked to a line printer through a microcomputer which were used to display and record temperatures and other variables in the precooler, in the heating section, and within the product container prior to the start of cooling tests. In addition to the selected scan interval, individual channels were monitored or printed between scans in order to observe the progress of the test. The microcomputer also recorded all data on floppy disk for later processing on the microcomputer or for data transfer to a mini-computer for additional processing.

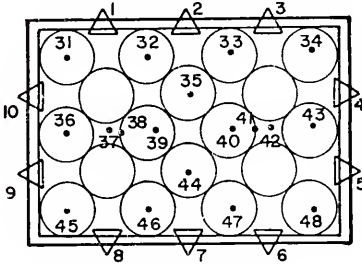
5TH LAYER
(TOP)



4TH LAYER



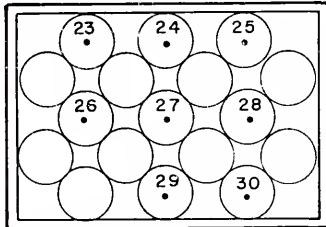
3RD LAYER



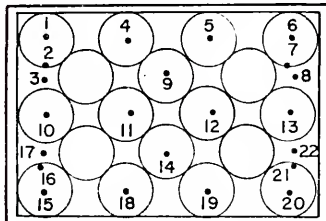
DIRECTION OF
AIR FLOW



2ND LAYER



1ST LAYER
(BOTTOM)



-  INLET/OUTLET VENT
-  FRUIT
-  THERMOCOUPLE

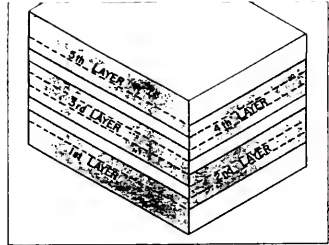


Figure 16. Fruit and thermocouple locations in experimental carton.

The most significant data processing procedure involved graphical plots of the cooling response for various locations within the experimental carton, which are presented in the Results and Discussion section and Appendix C. The analysis of the graphical curves was difficult because of the three-dimensional nature of the data. To obtain a better understanding of the progress of cooling within the experimental carton, a color graphics program was used to display the three-dimensional cooling response. This program projected the five layers of oranges. As the program ran and the data recorded during a test was read, the color of the circles representing the oranges changed according to a defined temperature/color relationship. In addition, the temperature to the nearest degree was displayed at the center of the circle. This method provided a real time observation of the cooling process and is also illustrated in the Results and Discussion section.

Heat Transfer Model

In earlier sections, the ANSYS calculated solutions for flow were verified by modeling experimental flow problems of other researchers and comparing the results. However, no experimental flow results for air flow through fruits packed in containers were available for comparison with the ANSYS calculated solutions. The experimental temperature response for air flow through oranges packed in an experimental carton were determined as described above. In order verify

the ANSYS calculated solution for air flow through fruits packed in the experimental box, the predicted pressure and velocity data were incorporated into an existing heat transfer model. The heat transfer model provided a calculated temperature response which was compared to the experimental temperature response. This indirect method of comparison was necessary because of the difficulty in measuring the pressure and velocity, which was noted previously and because no experimental flow problems of this type were found in the literature.

Again, for the purposes of the current study, it was not deemed appropriate to devote a considerable amount of time in developing a specific heat transfer model before the feasibility of the porous media flow approach was assessed. Further it was considered essential that a validated heat transfer model be applied so as to concentrate the evaluation on the flow model results rather than attempting to simultaneously validate both the porous media flow analysis and a heat transfer analysis.

Selection of a Model

The literature contains many citations of heat and mass transfer models. However, as mentioned in the Review of Literature section, in addition to considerable experimental work, researchers at the University of Florida have developed several computer based mathematical models to analyze the heat and mass transfer during the cooling of fruits and vegetables (Baird and Gaffney 1974a, 1976; Eshleman et al.

1976; Chau et al. 1984). These works included modeling of the temperature response of an individual fruit or vegetable exposed to forced air convection cooling. This individual fruit model was then used in conjunction with a bed model to predict the cooling response of bulk fruits and vegetables subjected to forced air cooling. The approach of this study was to use the individual fruit model and modify the bed model in such a way to treat each of the ANSYS generated elements as a bed. Each three-dimensional element interacted with surrounding elements. The velocity and pressure distributions calculated by the ANSYS porous media flow analysis were input into the modified heat transfer model to provide a temperature response for comparison with the experimental data.

Baird and Gaffney (1976) developed a one-dimensional explicit finite difference numerical model for individual fruits or vegetables using heat transfer equations for a homogeneous sphere without heat sources. The sphere was divided into concentric shells of equal thickness Δr , except for the outermost shell which had a thickness of $\Delta r/2$. The node in each volume element was at the midpoint between the two surfaces of the shell, except for the surface node. For a sphere there were three types of nodes: surface nodes, interior nodes, and center nodes. The partition of a sphere into nodes and volume elements is shown in Figure 17.

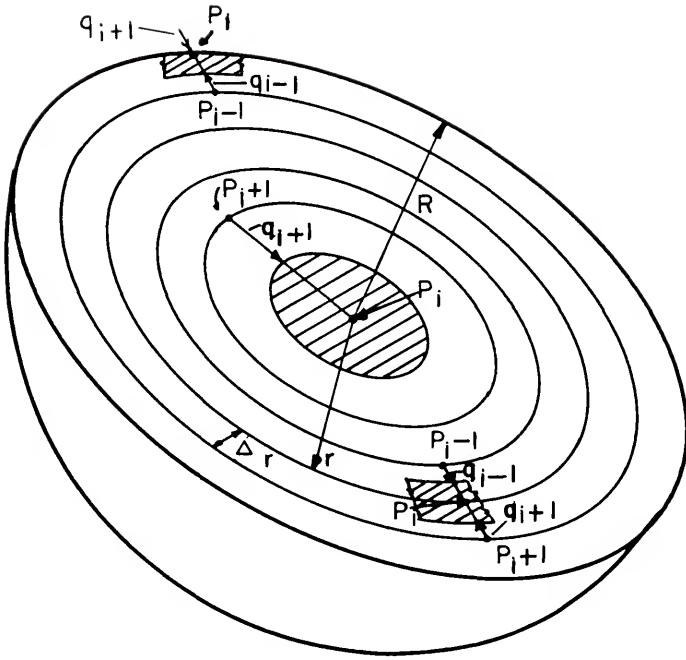


Figure 17. Diagram indicating a heat balance on the three types of nodes used in a sphere, Baird and Gaffney (1976).

By writing an energy balance equation for each node, Baird and Gaffney (1976) obtained the following equations for surface nodes:

$$(55) \quad T_i^{n+1} = (3\alpha_p \Delta t / \Delta r) (R - \Delta r / 2)^2 / [R^3 - (R - \Delta r / 2)^3] T_{i-1}^n + 3R^2 h \alpha_p \Delta t / k [R^3 - (R - \Delta r / 2)^3] T_\infty^n + \{1 - 3\alpha_p \Delta t / [R^3 - (R - \Delta r / 2)^3] [(R - \Delta r / 2)^2 / \Delta r + R^2 h / k]\} T_i^n,$$

interior nodes

$$(56) \quad T_i^{n+1} = \{1 - \alpha_p \Delta t / (\Delta r)^2 [1 - \Delta r / 2r] + (1 + \Delta r / 2r)\} T_i^n + \alpha_p \Delta t / (\Delta r)^2 [(1 - \Delta r / 2r) T_{i-1}^n + (1 + \Delta r / 2r) T_{i+1}^n],$$

and center nodes

$$(57) \quad T_i^{n+1} = [6\alpha_p \Delta t / (\Delta r)^2] T_{i+1}^n + \{1 - 6\alpha_p \Delta t / (\Delta r)^2\} T_i^n,$$

where

T_i^{n+1} = temperature at the i th node at time $n+1$

T_∞^n = surrounding temperature at time n

R = radius of product (sphere)

h = convective heat transfer coefficient

k_p = product thermal conductivity

c_p = product specific heat

ρ_p = product density

α_p = product thermal diffusivity ($k_p / \rho_p c_p$)

r = radial distance from product (sphere) center

Δt = time step.

Baird and Gaffney (1976) indicated that the following conditions must be satisfied to insure convergence:

$$(58) \left\{ 1 - \frac{3\alpha_p \Delta t}{R^3} \left[R^3 - (R - \Delta r/2)^3 \right] \left[\frac{(R - \Delta r/2)^2}{\Delta r} + R \frac{h}{k_p} \right] \right\} \geq 0$$

$$(59) \left\{ 1 - \frac{\alpha_p \Delta t}{(\Delta r)^2} \left[1 - \frac{\Delta r}{2r} \right]^2 + \left(1 + \frac{\Delta r}{2r} \right)^2 \right\} \geq 0$$

$$(60) \left\{ 1 - \frac{6\alpha_p \Delta t}{(\Delta r)^2} \right\} \geq 0.$$

The upper limit for the time increment is the smallest value that satisfies the condition above.

Baird and Gaffney (1976) developed a computer program to evaluate Equations 55, 56, and 57 for temperature, T , as a function of r and t . The arbitrarily varying fluid temperature, T_∞^n , was entered as input data. A flow diagram for the computer program is shown in Figure 18.

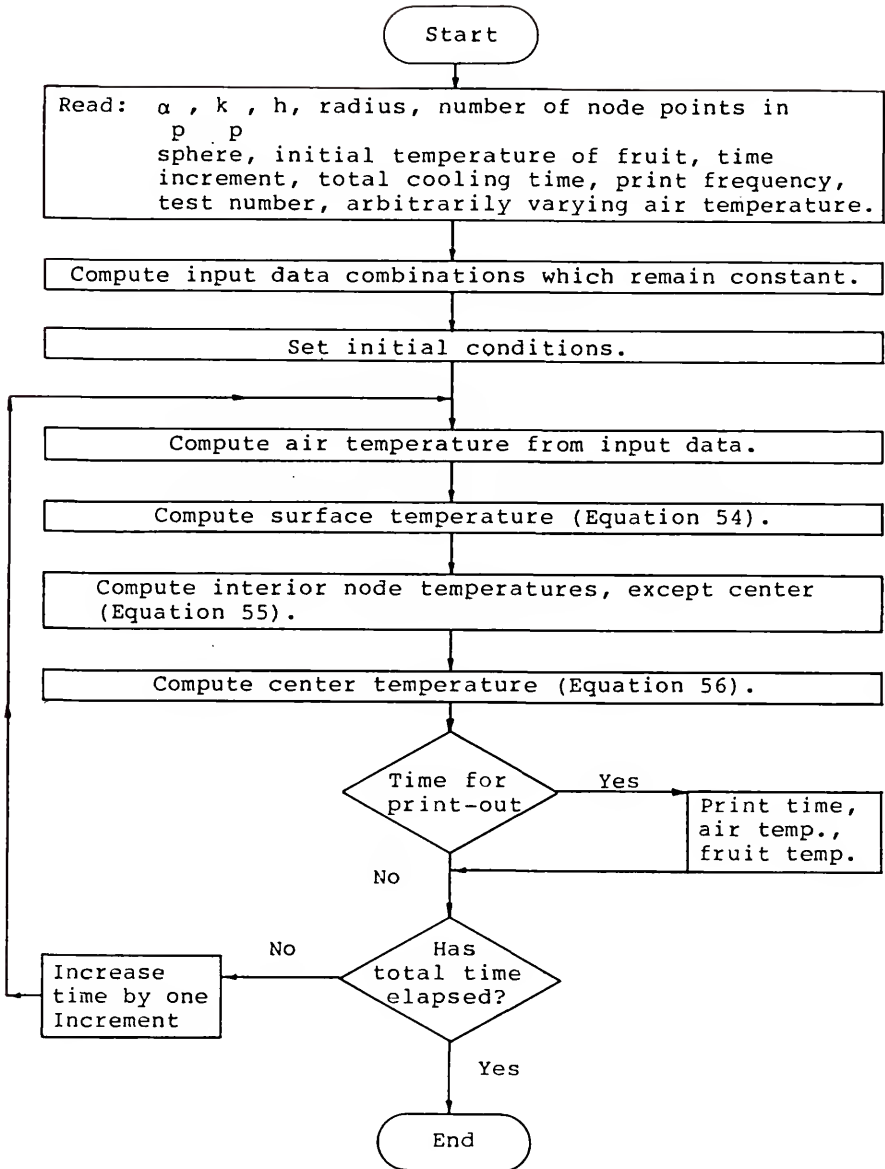


Figure 18. Flow diagram for the computer program for heat conduction in a sphere with arbitrarily varying air temperature, Baird and Gaffney (1976).

The oranges used for the current study were fairly homogeneous and nearly spherical in shape. The above model was used with the assumptions of homogeneous spheres. However, this model was also successfully modified to provide numerical solutions for non-homogeneous products (like grapefruit) and irregular, axi-symmetrical shapes (Eshleman et al. 1976).

The Baird and Gaffney (1976) model neglected the heat of respiration as a heat source in the conduction equation but Chau et al. (1984) modified this model to included heat of respiration as well as evaporative (transpiration) cooling and radiation heat transfer. The model developed by Chau et al. (1984) also modified the node and element locations resulting in a non-capacitance surface node. For the current study the original less complex model was chosen as adequate.

Baird and Gaffney (1976) extended the analysis of the temperature distribution within an individual product to include temperature distribution within a bulk load of products.

To obtain the governing equations describing the product temperature in a bulk load of fruits or vegetables and the temperature of the air as it flows through the load, Baird and Gaffney (1976) wrote a heat balance for a volume $A dx$ as shown in Figure 19. A is the cross-sectional area of the bulk load and dx is the height of the control volume.

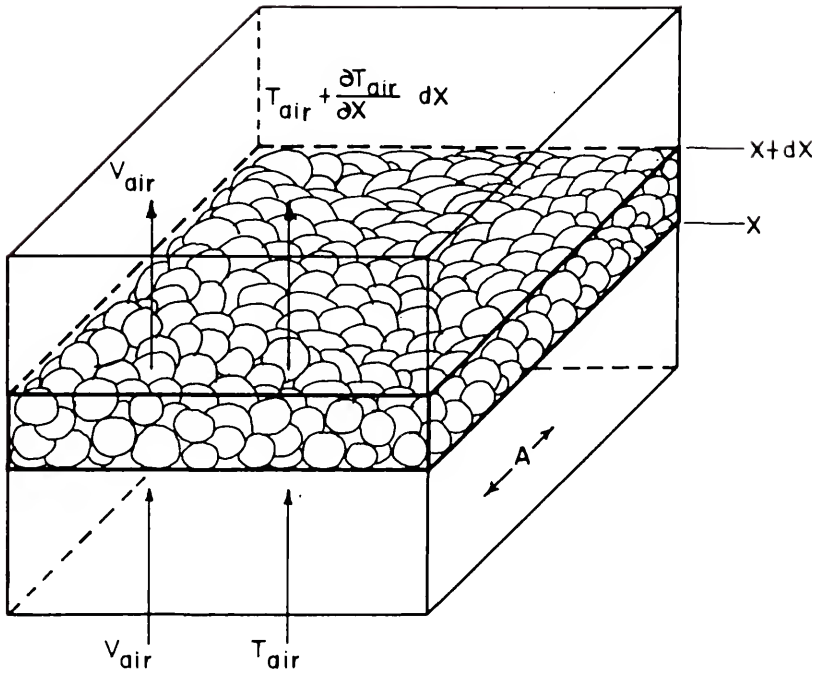


Figure 19. Control volume for heat balance on bed, Baird and Gaffney (1976).

Baird and Gaffney (1976) used the following assumptions in the development of the solution:

1. Air velocity in all interstices of the bulk load was constant.

2. No conduction heat transfer occurred between individual products.

3. Thermal properties of the air and product were constant.

4. No mass transfer occurred between the product and the cooling air.

The following symbols were used by Baird and Gaffney (1976) in the derivation of a control volume heat balance:

T_a = temperature of the air

T_p = temperature of product

A = cross-sectional area of the packed bed

V_a = superficial velocity of air

ρ_p = bulk density of product

ρ_a = density of air

c_a = specific heat of air

c_p = specific heat of product

t = time

x = distance from air inlet.

The change in the energy of the air as it moved through the control volume was equal to the change in the internal energy of the product in the control volume and reported by Baird and Gaffney (1976) to be

$$V_a \rho_a c_a A (\partial T / \partial x) dx dt = - \rho_p c_p (\partial T / \partial t) dt A dx$$

or

$$(61) \quad \frac{\partial T}{\partial x} = - \left[\frac{\rho_p c_p}{V_a \rho_a c_a} \right] \frac{\partial T}{\partial t}.$$

By considering the differential layer of the control volume to be a finite layer, Baird and Gaffney (1976) were able to approximate Equation 61 as

$$(62) \quad \frac{\Delta T}{\Delta x} = - \left[\frac{\rho_p c_p}{V_a \rho_a c_a} \right] \frac{\Delta T}{\Delta t}.$$

The solution of Equation 62 along with Equations 55, 56, and 57, constitute the numerical model for heat transfer in a bulk load of products as reported by Baird and Gaffney (1976). In order to solve this set of equations, Baird and Gaffney (1976) computed the mass-average temperature of the fruit after each time period. Mass-average temperature denotes a single value from the temperature profile of a product that would become the uniform product temperature upon reaching equilibrium under adiabatic conditions.

Baird and Gaffney (1976) reported that the temperature profile in a sphere was not linear during transient cooling and therefore the mass-average temperature was not located

exactly at the point of average mass but shifted according to the shape of the temperature profile. For the solution, Baird and Gaffney (1976) determined the mass-average temperature by computing the mass-average temperature for each spherical shell and then computed a weighted average temperature based on the mass of each spherical shell.

In order to account for the shift in the location of the mass average temperature due to the low heat capacity of the rind (ρc_p), Baird and Gaffney (1976) assigned values for heat capacity and thermal conductivity to the outer and inner shells of the spherical model corresponding to that of the rind and juice vesicles as determined separately (Table 4). The average thickness of the rind for Valencia oranges (Table 4) corresponded to the outer segment of a ten segment sphere.

The flow diagram for the computer program that Baird and Gaffney (1976) used to solve Equations 55, 56, 57, and 62, is shown in Figure 20.

Convective Heat Transfer Coefficient

Baird and Gaffney (1976) emphasized the importance of accuracy and availability of input data for successful application of any model for a specific set of conditions. For the bed model the input data consisted primarily of thermal and physical properties of the product and the cooling fluid and the convective heat transfer coefficient for each set of conditions.

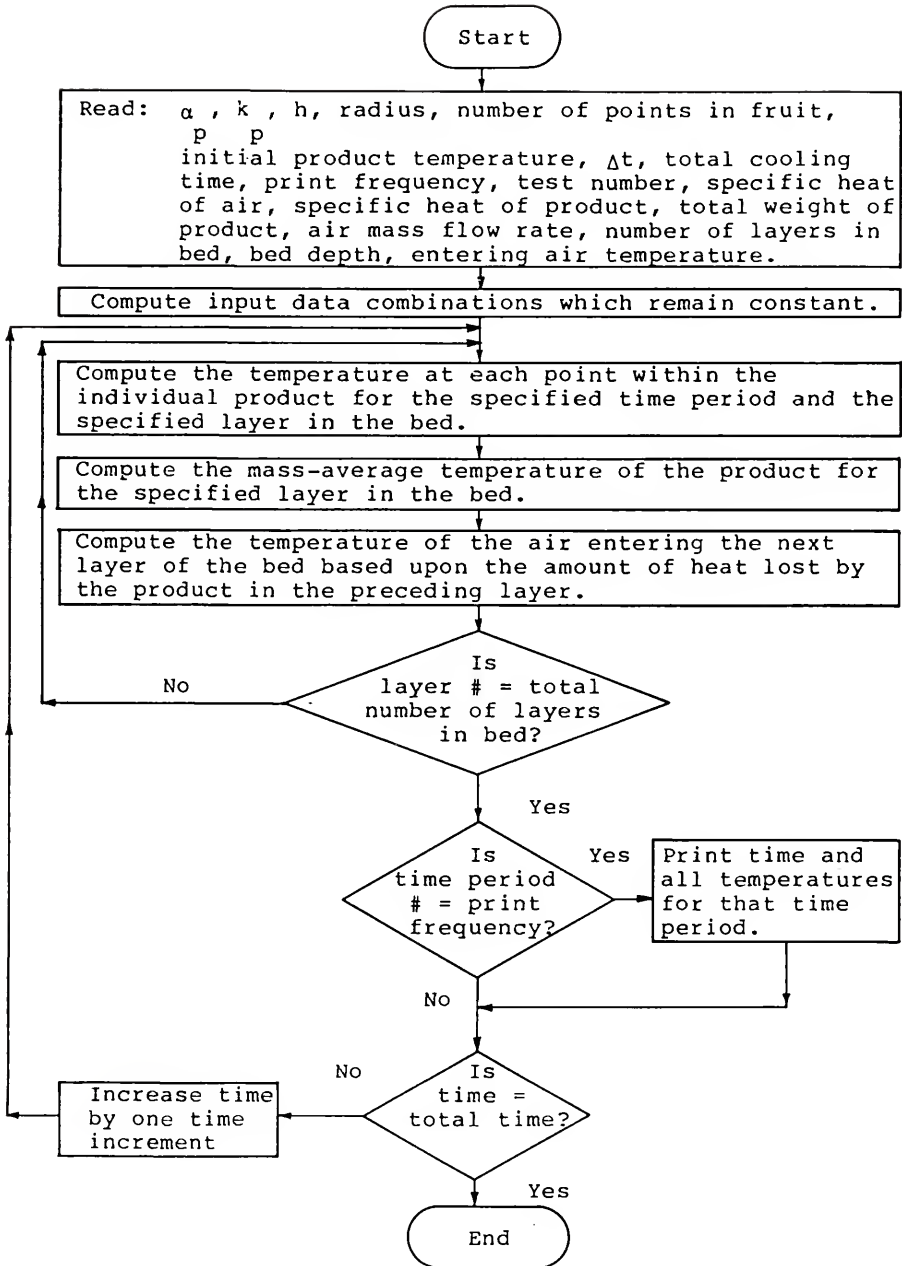


Figure 20. Flow diagram for the computer program to solve deep bed heat transfer equations, Baird and Gaffney (1976).

Table 4. Physical and thermal properties of size 100 Valencia oranges, Gaffney and Baird (1980).

Property	Units	Mean Value
Average diameter	cm	7.26
Whole weight	gm	209.1
Measured surface area	² cm	162.2
Whole volume	³ cm	222.0
Average Rind thickness	cm	0.34
Rind, % Radius	%	9.91
Whole s.g.	-	0.947
Rind s.g.	-	0.795
Flesh s.g.	-	0.998
Whole specific heat	J/kg-K	3830
Rind specific heat	J/kg-K	3550
Flesh specific heat	J/kg-K	3900
Flesh Thermal Diffusivity	² m /s	1.21 E-7
Flesh Thermal Conductivity	W/m-K	0.469

Baird and Gaffney (1976) expressed concern over the lack of consistency frequently found in the considerable published data available on thermal properties for fruits and vegetables. This lack of consistency motivated Gaffney and Baird (1980) to publish various physical and thermal properties needed to numerically calculate rates of transient heat flow for Florida Valencia oranges (Table 4) and Marsh grapefruit.

A similar but worse situation with respect to the inconsistency in the reported values of the convective heat transfer coefficient for fruits and vegetables prompted Baird and Gaffney (1976) to develop a method for determining h . The h value was determined experimentally by selecting a value of h which caused the numerical model results to best fit the experimental data obtained at a particular air flow rate. A comparison of the experimental and theoretical mass average temperature of the entire bed, determined at approximately the half-cooling time, was used as the criterion for determining the best fit to the experimental data. The h value determined by this procedure was considered an "effective heat transfer coefficient" since factors not accounted for in the model, such as deviation from spherical shapes, possible evaporative cooling due to moisture transfer from the fruit surface, and conduction heat transfer between individual products, were possibly included.

The value of h determined by the procedure reported by Baird and Gaffney (1976), for each air flow rate used in the experimental tests, formed a relationship between air flow rate and the h value. This relationship was presented through the use of the dimensionless parameters, Nusselt number, Nu , and Reynolds number, Re ,

$$(63) \quad Nu = 1.17 Re^{0.529}$$

where

$$Nu = \frac{hD}{k_a}$$

and

$$Re = \frac{\rho V D}{\mu_a}$$

Equation 63 can be rearranged in terms of the convective coefficient as follows:

$$(64) \quad h = 1.17 \left(\frac{k}{D} \right) \left[\frac{\rho V D}{\mu_a} \right]^{0.529}$$

Heat Transfer Model Modifications

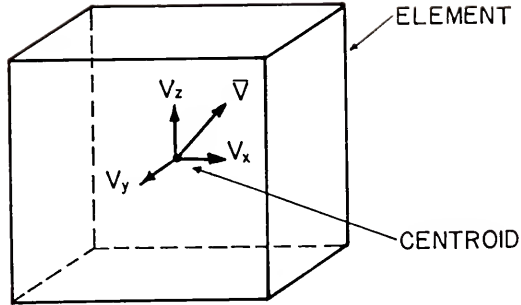
The individual fruit model reported by Baird and Gaffney (1976) and described above was used without major changes for the current study.

The bed model reported by Baird and Gaffney (1976) and also described above required major revision for the current study. Each of the three-dimensional element defined by

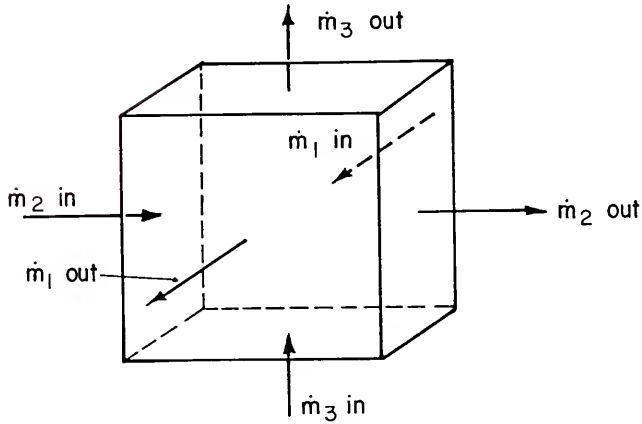
the ANSYS porous media flow analysis was treated like an individual bed similar to the bed model reported by Baird and Gaffney (1976). However, a major difference between these two studies was the nature of the air flow. In the Baird and Gaffney (1976) bed model, the air flow was one-dimensional or plug flow, while in the ANSYS porous media flow analysis the air flow was three-dimensional. The three-dimensional nature of the air flow presented several analysis complications but the velocity and pressure distributions calculated by ANSYS allowed determination of the air flow rate at any location within the defined element model (orange carton).

A typical three-dimensional element is shown in Figure 21. The air flow rate in or out of each face of the element was determined from data provided by the ANSYS model. The method for this procedure is presented in a following section. Depending on the location within the finite element model, each element was one of five types. The first type element occurred at the inlet and outlet boundary conditions. The other four types depended upon the number of exterior walls the element contained, either one, two, or three. No flow occurred through these exterior walls.

In order to determine the temperature of the air entering a particular element from adjacent elements (or inlet boundary condition) the enthalpy entering each face of the element was used. The air entering through each face would mix within the element. Assuming ideal mixing and



VELOCITY VECTOR AND THREE COMPONENTS



AIR FLOW RATE IN AND OUT

Figure 21. Typical three-dimensional element showing velocity at centroid and air flow across element faces.

neglecting variation of the air density and specific heat, the resulting temperature from the mixture was calculated as illustrated below

$$(65) \quad \dot{m}_1 T_1 + \dot{m}_2 T_2 + \dot{m}_3 T_3 = \dot{m}_t T_m$$

where

$\dot{m}_1, \dot{m}_2, \dot{m}_3$ = air flow rates entering element through faces 1, 2, and 3, respectively,

T_1, T_2, T_3 = temperature of air entering element through faces 1, 2, and 3, respectively,

\dot{m}_t = total air flow rate entering element, $\dot{m}_1 + \dot{m}_2 + \dot{m}_3$

T_m = temperature as a result of perfect mixing.

Equation (65) was rearranged in terms of T_m to give

$$(66) \quad T_m = (\dot{m}_1 T_1 + \dot{m}_2 T_2 + \dot{m}_3 T_3) / \dot{m}_t$$

The perfect mixing resulted in T_m which was the entering air temperature used for the individual fruit model.

The next step was to determine the convection heat transfer coefficient, h . The velocity, V_a in Equation 64 was defined as the superficial velocity. The best representative velocity for determining the convective

coefficient was identified as the ANSYS calculated velocity at the centroid of the element. This velocity was defined as the superficial velocity by Ergun (1952) and Geertsma (1974). The magnitude of the centroidal velocity vector, $|\bar{V}|$ was substituted for V_a in Equation 64 and provided the following relationship for determining the convective heat transfer coefficient in terms of the velocity at the centroid of the element:

$$(67) \quad h = 1.17 \left(\frac{k}{D} \right) \left[\rho_a |\bar{V}| \frac{D}{\mu} \right]^{0.529}$$

Using the individual fruit model, the temperature at each point within the individual product for the specified time period and specified element was calculated.

The final step consisted of calculating the temperature of the air leaving the element. This was accomplished by an analysis similar to that used by Baird and Gaffney (1976) in the development of Equation 62. The change in the energy of the air as it moved through the element (control volume) was equal to the change in the internal energy of the product within the element

$$\dot{m} c_a \left(\frac{\partial T}{\partial v} \right) dv dt = - \rho_p c_p \left(\frac{\partial T}{\partial t} \right) dt dv_p$$

The volume of the product is related to the volume of the element by the porosity, ϵ ,

$$(68) \quad v_p = (1-\epsilon)v$$

where

v = volume of the element

v_p = volume of the product.

Inserting Equation 68 for the product volume in the energy balance above and solving for the change in air temperature resulted in the following:

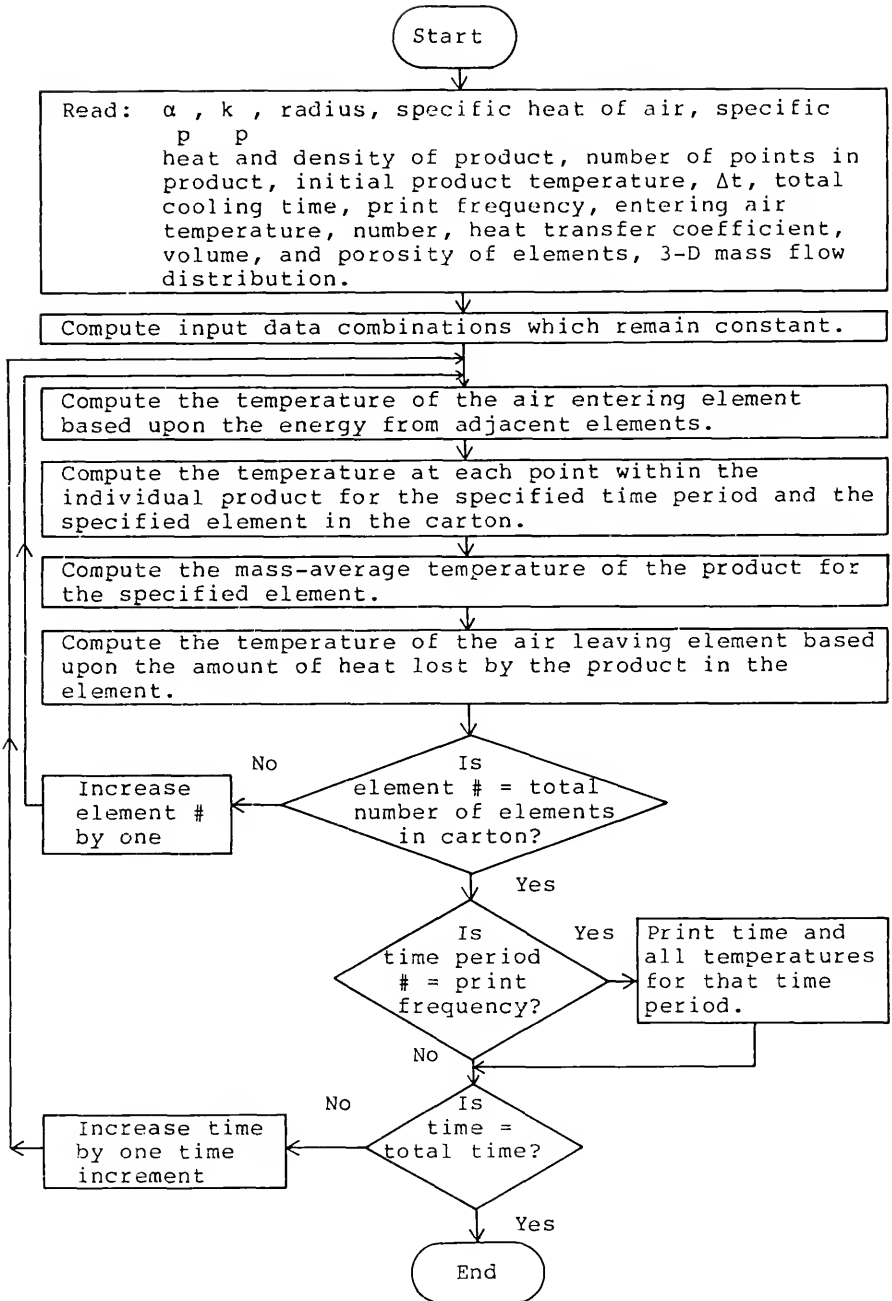
$$(69) \quad \frac{\partial T}{\partial v} = - (1-\epsilon) \left[\rho_p c_p / m_t c_a \right] \frac{\partial T}{\partial t}.$$

By considering the differential control volume (element) to be a finite volume, Equation 69 was approximated by

$$(70) \quad \frac{\Delta T}{\Delta v} = - (1-\epsilon) \left[\rho_p c_p / m_t c_a \right] \frac{\Delta T}{\Delta t}.$$

The temperature leaving each face of an element was determined from the air temperature change calculated using Equation 70 and the value of the air temperature that entered the element calculated using Equation 66. Then the procedure was repeated for the next element. The flow diagram for the computer program used to solve Equations 55, 56, 57, and 70 is shown in Figure 22.

Figure 22. Flow diagram for the computer program to solve orange carton heat transfer equations.



ANSYS Output Data Reorganization

The ANSYS output shown in the Results and Discussion section provided the total velocity (magnitude of the velocity vector) and the three components of the velocity vector at the centroid of the element, in addition to the element volume and pressure gradient. To obtain the necessary data for the heat transfer model, the ANSYS output was reorganized. This was accomplished with three Fortran programs. The logic of these programs was complex because of the three-dimensional elements used and matrices required to handle the large amount of data, which included the element identification, mass flow rate across each element face, the area of each face, the volume of each element, the velocity (vector magnitude and three components) at the centroid of each element, the velocity across each element face, the porosity of each element and the temperatures at various locations and times.

A data file named "Dimensions", was created which contained the element volume calculated by ANSYS and the three component dimensions of each element. The latter were manually input since this information could not be obtained as output from the ANSYS solution. Because of the physical dimensions of the experimental orange carton that was modeled, the elements used in the ANSYS model were of more than one size. This factor also increased the complexity of the data handling. In addition, the porosity of each

element was added to this data file for later use in the heat transfer model.

The first program named "Data-Reduction", read the element volume and three component dimensions from the first data file "Dimensions" and the total velocity (magnitude of the velocity vector) and the three components of the velocity vector at the centroid of the element from a second data file "Data", created from the ANSYS solution. This program calculated the component mass flow rates at the centroid of each element by multiplying the component velocity at the centroid by the density of the air and the area of the face normal to the velocity component. The area was calculated by dividing the element volume by the element dimension in the direction of flow. The heat transfer coefficient was also calculated using the total velocity and Equation 67. The output file was named "Heat-Mass". The air viscosity and density obtained as noted above for an average cooling test temperature of 10 C (50 F) were used for the calculations.

The second program named "Flow-Wall", calculated the mass flow rate across an element face by averaging the values of the mass flow rate at the centroids of the elements sharing the face. The mass flow rates were obtained from data file "Heat-Mass". This was performed for each of the three component axis. For faces that were adjacent to the orange carton walls, the mass flow rate was

of course zero except at inlets or exits. This output data file was named "Mass-Flow".

The third program named "Temp-ID", used the mass flow rates across each face from data file "Mass-Flow", including flows through the inlet and exit vents to calculate the flow rates into each element. A complex logical procedure using the flow direction sign convention and coordinate axes sign convention identified the air flow rates entering each element through each face as specified in Equation 65. Actually the flow could enter from any of the six faces. For example the flow into a particular element could be from both the positive and negative x-axis faces. The program accounted for this possibility. In addition, the program created an identification procedure such that the entering temperatures specified in Equation 65 were logically identified and correlated with the corresponding mass flow rate from the source element. This identification variable was necessary because the temperature leaving each element varied as a function of time. The output file was called "Mass-Temp".

Heat Transfer Program

With the ANSYS results reorganized, a fourth Fortran program named "Heat-Do", was written to solve the heat transfer model outlined by the flow chart procedures presented in Figure 22. The product thermal diffusivity, conductivity, and radius, the specific heat of the air and the product and the product density were read from data file

"Data-In-1". The number of nodal points in the product, initial product temperature, time increment (iterative time step), total test cooling time, data output print frequency, entering air temperature, and number of elements, were read from data file "Data-In-2". The heat transfer coefficients for each element were read from data file "Heat-Mass". The volume and porosity for each element were read from data file "Dimensions". Finally, the mass flow rate into each element and the associated element temperature identification variable were read from data file "Mass-Temp".

For the vent locations used on the experimental carton, the flow calculated by ANSYS was symmetric top and bottom. Therefore, only the bottom 700 elements were used in the heat transfer program in order to reduce the number of calculations required. However, the model has the capability to solve the full set of elements for non-symmetric problems.

The element number do-loop procedure was varied depending on the location and number of inlet and exit vents, in other words the flow boundary conditions. Efforts were made to insure that the do-loop element number sequence proceeded in such a manner that the element calculations followed the same pattern as the air flow. In other words, each new element considered by the program was identified in the same order as the time path of the air flow. The calculations proceeded from the entrance hole element by element, to the left and right until the carton wall or a

symmetric plane between two holes was encountered. Then the calculations proceeded down one row of elements and then to the left and right as before, until the bottom of the carton was encountered. The calculations proceeded away from the entrance hole as vertical layers one after the last until the center plane of the carton was reached.

Calculations proceeded from the center plane from the bottom row of elements, element by element, to the left and right in the same pattern as before and up a row of elements at a time until the top row of elements was encountered (horizontal center plane). The calculations then proceeded to the bottom row of elements in the next vertical layer of elements. Again the calculations proceeded as vertical layers one after the last until the exit hole was reached. The element do-loop was repeated for each time increment.

The "Heat-Do" program produced an output file called "Temp-Response" which contained the element air temperature, product temperature at each of the nodes, and product mass-average temperature for each element for each time printed as specified by the print frequency increment.

Temperature Response Data Reorganization

The temperature response data had to be reorganized in order to compare the numerical temperature response with the experimental temperature response data. As noted above, the temperature response of the air, product surface, and other product interior node locations were known, for each

element region. The reorganization of the temperature response was accomplished by identifying where the thermocouple locations would occur in the model to correspond to the same locations in the experimental carton. Logically the location of the thermocouple in the model should correspond to the physical dimension location of the thermocouple in the experimental test. However, there were problems associated with the identification of thermocouple locations in the model because of the size and multiple sizes of the elements. The elements were smaller than the oranges, 2.54 to 3.91 cm size element dimensions versus 3.675 cm diameter oranges. The physical location of an orange if superimposed on the elements in the corresponding physical location could contain all or a portion of as many as 27 elements. Another factor was related to the variable porosity employed in the numerical solution. This variable porosity was only assigned to the elements adjacent to the interior surface of the orange carton, a distance of 3.81 cm. Therefore an orange could contain two elements which were both near the physical thermocouple location while one element might lie in the variable porosity region and the other in the constant porosity region. These two elements had a measureable difference in temperature response. Therefore selection of one of these elements over the other to represent the thermocouple location would have an affect on the temperature response used to compare the

numerical temperature response to the experiment temperature response.

A program named "Plot-Data" was written to reorganize the ANSYS temperature response from data file "Temp-Response" so that the thermocouple locations in the model corresponded as closely as possible to the experimental thermocouple locations. The 78 thermocouple locations were assigned an air, product surface or center time dependent temperature value for a particular element of the 700 elements available. The element selected was as close to the experimental carton physical location as possible with selection preference to an element in the variable porosity region over an element otherwise as close to the physical location but not in a variable porosity region.

The five undocumented programs and portions of the associated input and output files discussed above are provided in Appendix B for the reader's convenience. Additional information can be obtained from the author at the address listed in the Biographical Sketch.

A discussion of the ANSYS plotting technique and the plotting technique used to plot the temperature response and other data presented by the current study is found in Appendix C.

The results of this investigation and a discussion of these results are presented in the following section.

RESULTS AND DISCUSSION

Two-Dimensional Grain Bin

Equation 23 governs the linear airflow problem solved by Brooker (1961 and 1969) and Segerlind (1982) when a is constant and b is equal to one. Equation 21 also governs the linear airflow problem in the current study when β is equal to zero. Segerlind (1982) solved the linear problem and compared the results with the values reported by Brooker (1961). The values at some of the points near the duct are summarized in Table 5. The location of the points are shown in Figure 23. A duct pressure of 2 inches of water was used.

The ANSYS solution was an iterative process. The first iteration was linear with the value of β equal to zero. After the first iteration, the iterative process continued using the input value of β until the solution attained a specified convergence criteria. Single precision accuracy input variables were used, but ANSYS calculations employed double precision mathematics. The linear results of the previous work and the current study are in good agreement.

Table 5. Pressure values (inches of water) at specific points for the linear flow problem.

Point	Brooker	Segerlind	ANSYS
A	1.818	1.806	1.803
B	1.864	1.855	1.852
C	1.808	1.794	1.791
D	1.854	1.841	1.838
E	1.774	1.760	1.757
F	1.816	1.797	1.796

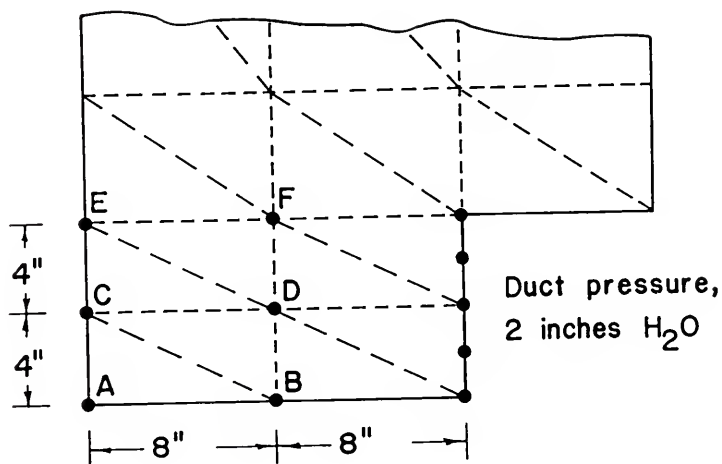


Figure 23. Points of comparison for linear airflow calculations.

Segerlind (1982) used the values for a and b specified by Brooker (1969) and further generalized the work of Shedd (1953) to solve the nonlinear problem using a finite element model and attempted to explain the disagreement between the numerical solution and experimental data reported by Brooker (1969). Segerlind's calculated values were compared with the experimentally determined isobaric lines given by Brooker (1969). The 85 percent of total pressure loss contour line for a duct pressure of 3 inches of water calculated by Segerlind (1982) is shown in Figure 25. Segerlind (1982) concluded that the comparison with Brooker's experimental data was not good, since the 85 percent contour line was located entirely above the duct.

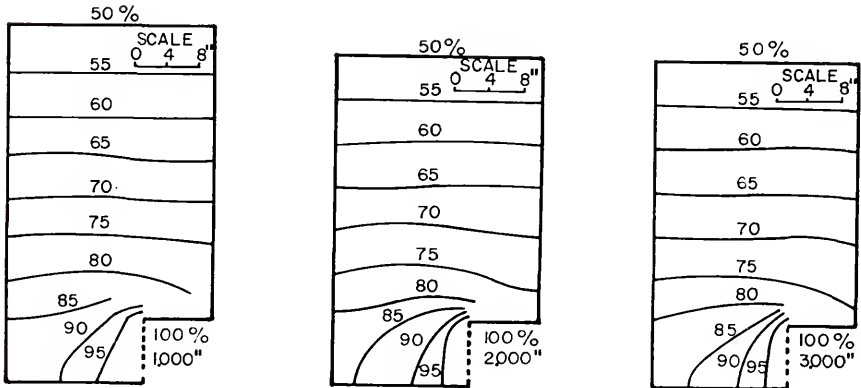


Figure 24. Plot of experimental isobaric lines from Brooker (1969).

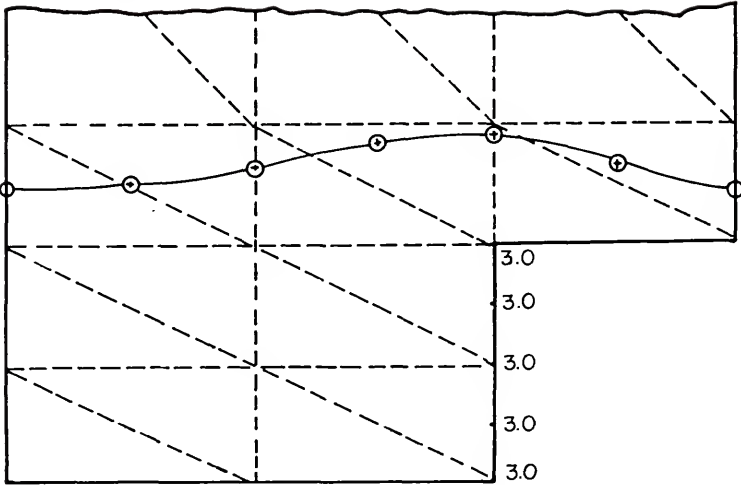


Figure 25. 85 percent isobaric contour line from Segerlind (1982).

The isobaric contour lines calculated using ANSYS for a boundary conditions of 1, 2, and 3 inches of water are shown in Figures 26, 27, and 28. The change in pressure pattern is similar to that exhibited in Brooker's (1969) experimental data in Figure 24.

As noted by Segerlind (1982), the 85 percent isobaric line for a duct pressure of 3 inches of water shown in Figure 24, touches the bottom of the bin and the top of the duct. The 85 percent isobaric line shown in Figure 28 is in better agreement with the experimental data (Figure 24) than Segerlind's numerical solution as shown in Figure 25.

The disagreement between Figures 26, 27, and 28 and the corresponding three pressure patterns illustrated in Figure 24 is evident by comparing the respective 85 percent isobaric lines. The pressure patterns calculated by ANSYS

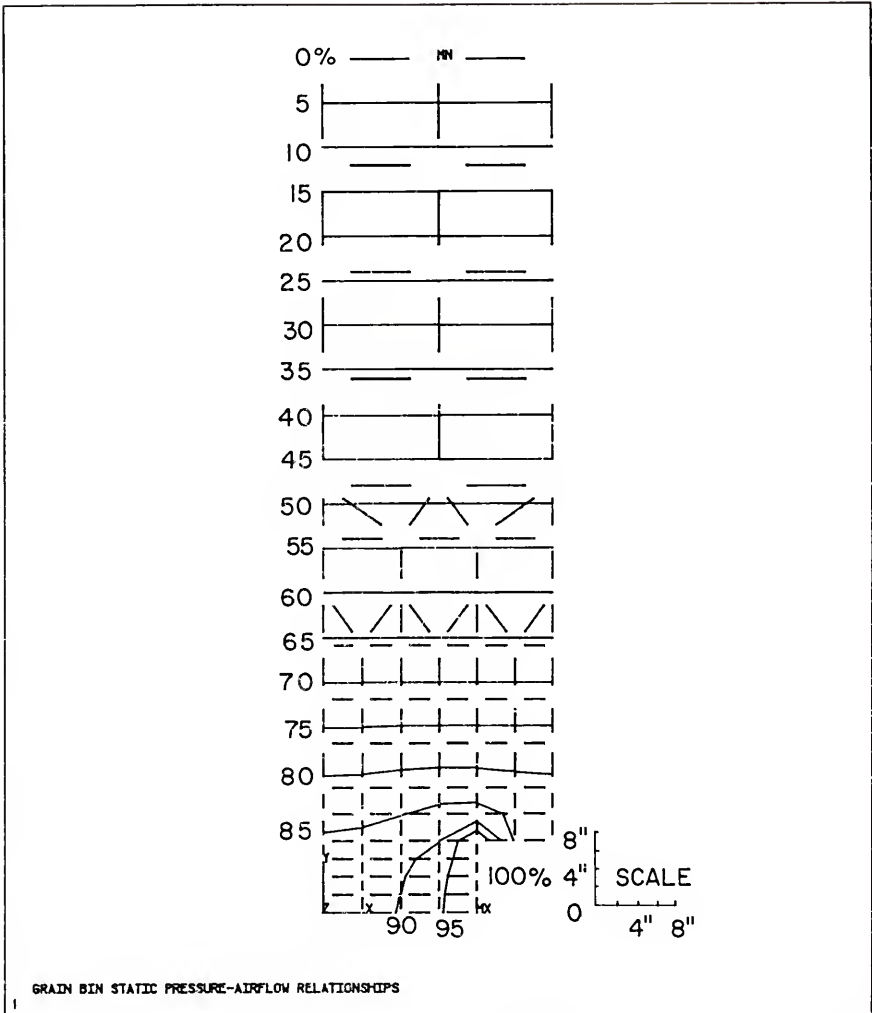


Figure 26. Isobaric contour lines calculated using ANSYS for a boundary condition of 1 inch of water.

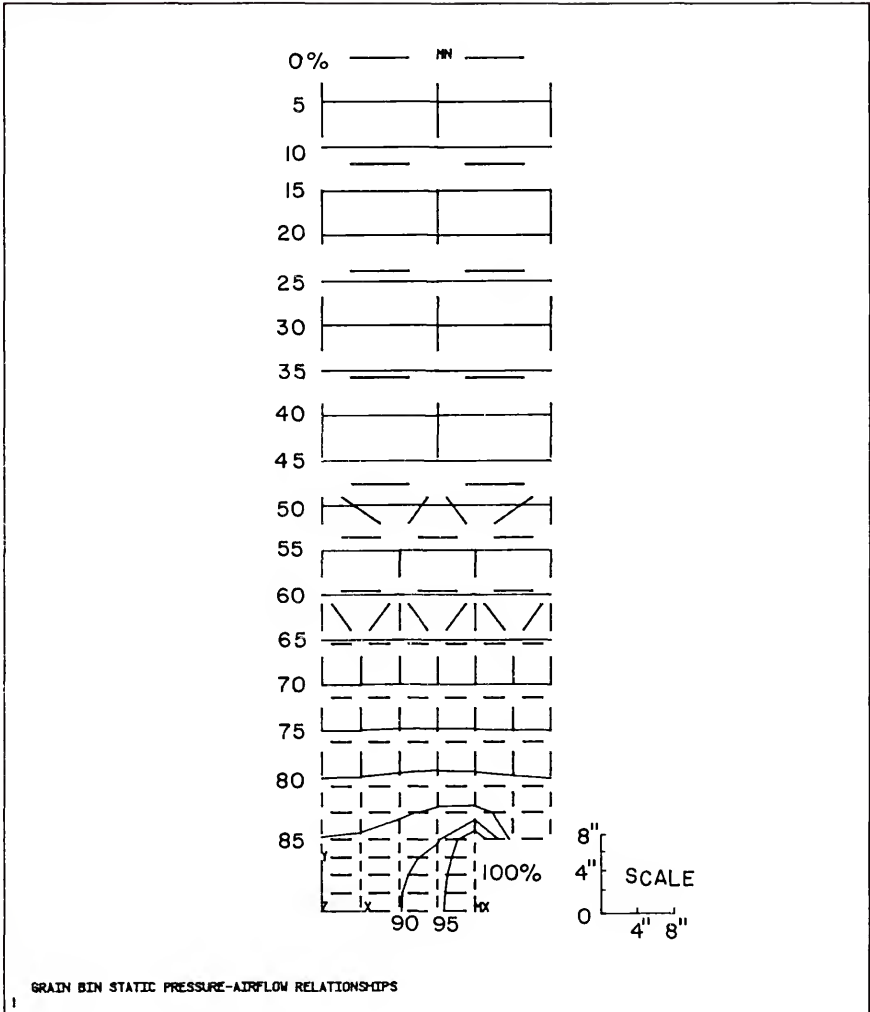


Figure 27. Isobaric contour lines calculated using ANSYS for a boundary condition of 2 inches of water.

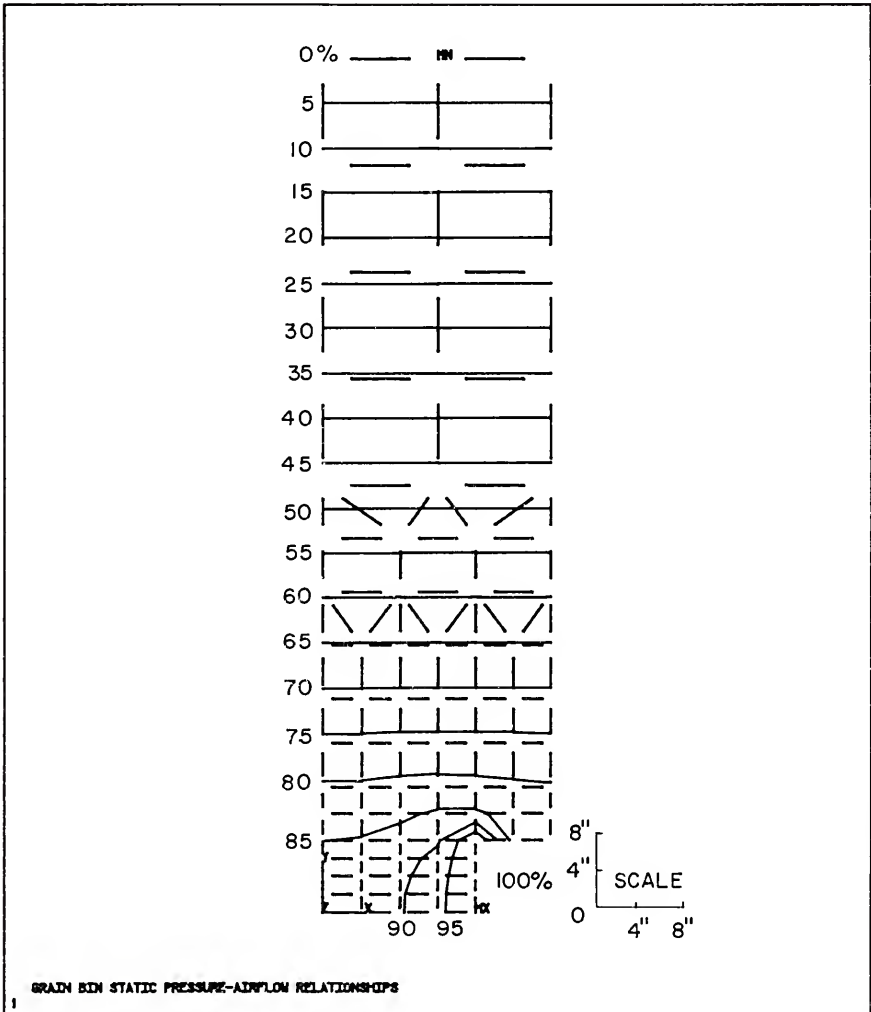


Figure 28. Isobaric contour lines calculated using ANSYS for a boundary condition of 3 inches of water.

in Figures 26, 27, and 28, change in a manner very similar to the experimental data in Figure 24. However, the pressure loss for the experimental data occurred more rapidly near the duct entrance. Additional discussion concerning the results presented above are included in Appendix D.

In an effort to achieve a better agreement with Brooker's experimental data, Segerlind (1982) changed the boundary conditions and solved the problem again using the new boundary conditions. The isobaric pressure lines were also calculated using ANSYS for the modified boundary conditions. A detail comparison of the results of both efforts is presented in Appendix D.

In the attempt to determine if the ANSYS calculated results provide a reasonable solution to the nonlinear problem solved by Brooker (1969) and Segerlind (1982), the decision was not as evident as for the linear problem. In order to methodically compare the ANSYS solution with the solutions presented by Brooker (1969) and Segerlind (1982), several factors must be taken into account. The two finite element models were based on a different governing equations (Shedd versus Ergun). The coefficients necessary to use the governing equations were obtained from different sources. Therefore the porous media from which the coefficients were empirically determined were not necessarily identical. The experimental data presented by Brooker (1969) were not easily extracted. Neither the procedures for obtaining

these data nor the degree of accuracy was presented by Brooker (1969). Segerlind (1982) based his model performance heavily upon these experimental data. It appears that ANSYS does provide a reasonable solution since the results are similar to Segerlind's, as well as, Brooker's results.

Three-Dimensional Grain Bin

In extending the procedures of Segerlind (1982) to account for three-dimensional air flow through cylindrical grain storages, Khompis (1983) used a model that consisted of three components or separate computer programs. Details of the model used by Khompis (1983) are presented in Appendix D.

The results produced by Khompis (1983) were entirely graphical. Two-dimensional pressure and velocity distribution contour lines on the cutting planes were presented. Three-dimensional pressure and velocity surfaces for a quarter section of the square duct perforated floor system were also displayed. The three-dimensional graphics program used by Khompis (1983) allowed the displays to be viewed from any angle, any elevation, and any distance.

Using the appropriate post-processing commands, ANSYS provided the capability to plot the various pressure and velocity distributions reported by Khompis (1983). The constant pressure and velocity lines for any desired two-dimensional section were plotted and viewed from any angle, elevation, and distance. The three-dimensional surfaces

were also plotted using ANSYS, although the surfaces were not as sharp as the perspective transect diagrams produced by the graphics package used by Khompis (1983).

Examples of the graphical results presented by Khompis (1983) and produced by ANSYS are presented in this section. A detailed comparison of these graphical results is presented in Appendix D.

The two-dimensional pressure distribution patterns for the square duct perforated floor reported by Khompis (1983) are shown in Figures 29 and 30. The corresponding results produced by ANSYS are shown in Figures 31 and 32. The isobaric patterns calculated by ANSYS are very similar to those presented by Khompis (1983).

The two-dimensional velocity distributions reported by Khompis (1983) for the square duct system, are represented in Figures 33 and 34. The two-dimensional velocity distributions calculated using ANSYS for the square duct system are shown in Figures 33 and 34. The constant velocity lines calculated using ANSYS and by Khompis (1983) exhibit similar patterns.

One view of the three-dimensional 70 percent isobaric surface presented by Khompis (1983) is illustrated in Figure 37. The corresponding view of the three-dimensional 70 percent of total pressure isobaric surface produced by ANSYS is shown in Figure 38. The shapes of the surfaces are similar, but the surfaces plotted by Khompis (1983) are of a higher graphical quality.

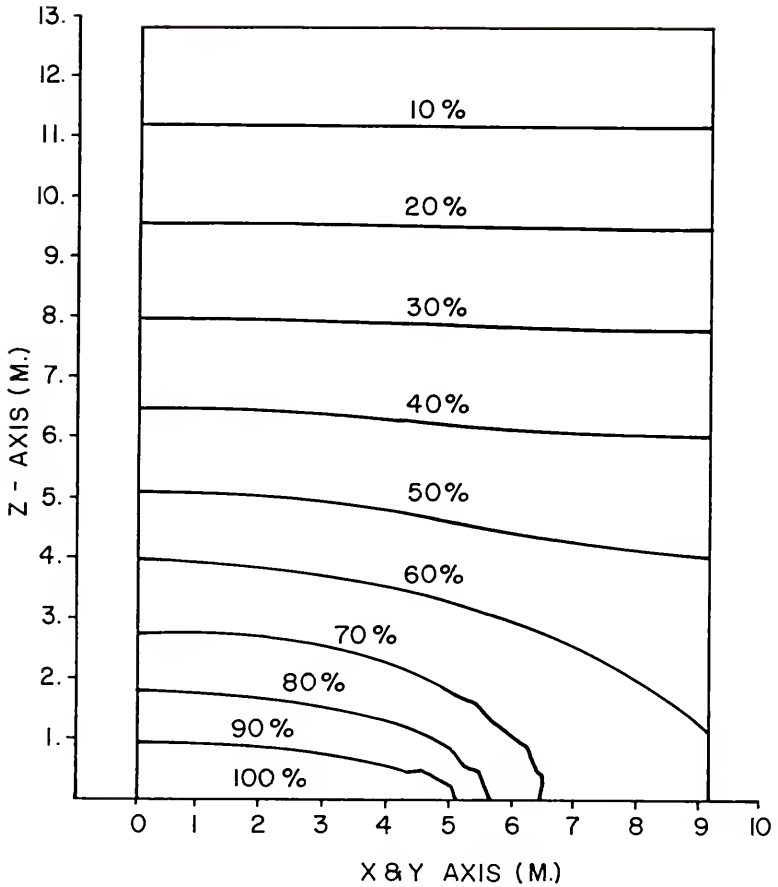
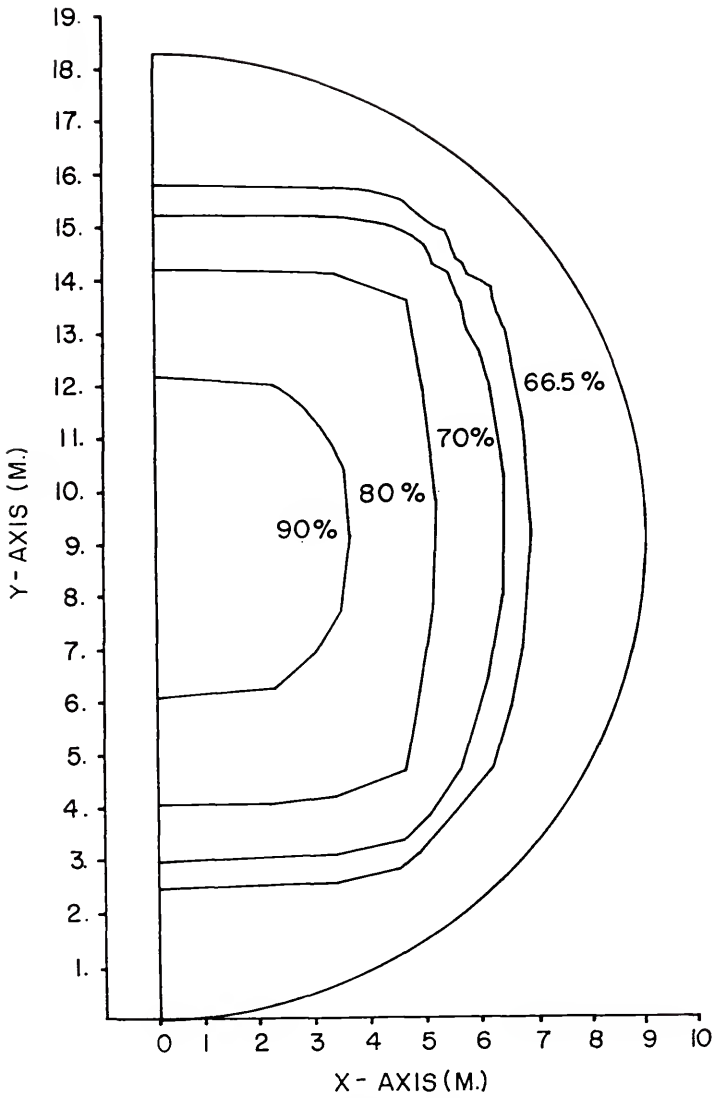


Figure 29. Isobaric distribution in percent of total pressure loss on a vertical cutting plane from Khompis (1983).



ISO - PRESSURE LINES ON CUTTING PLANE

Figure 30. Isobaric distribution in percent of total pressure loss on horizontal cutting plane at 5 percent of bin height from Khompis (1983).

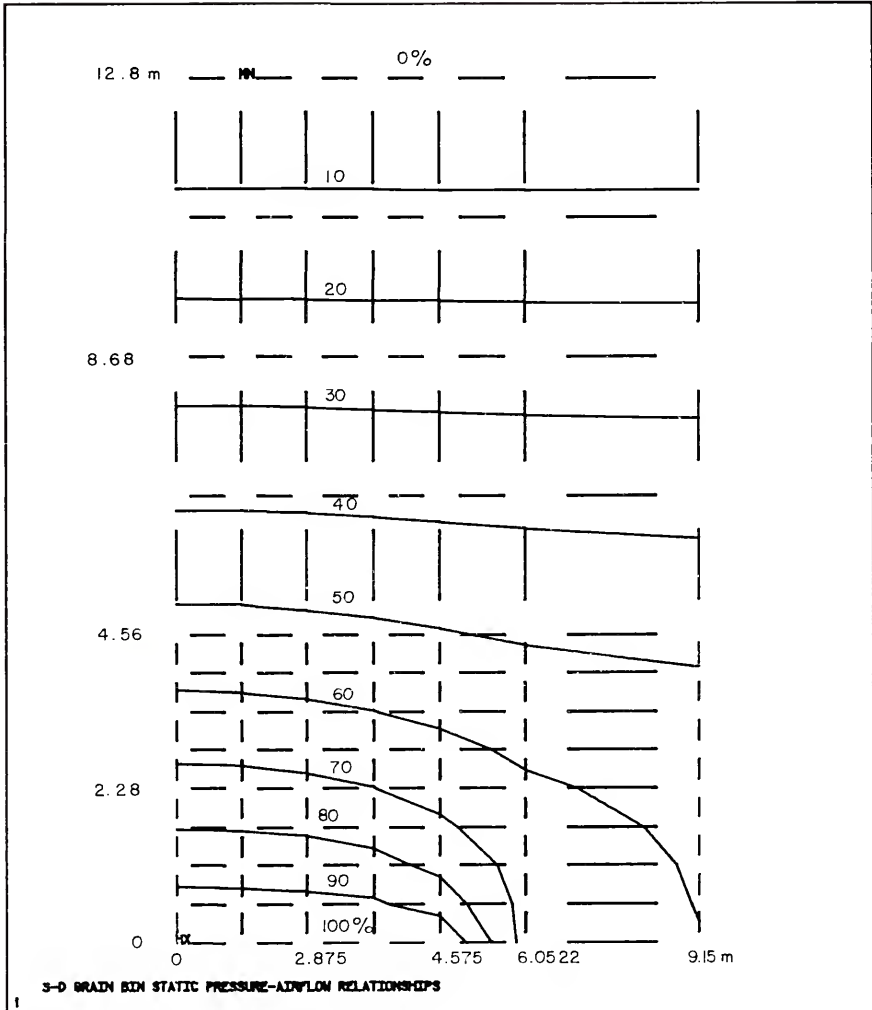


Figure 31. Isobaric distribution calculated using ANSYS in percent of total pressure loss on the vertical cutting plane.

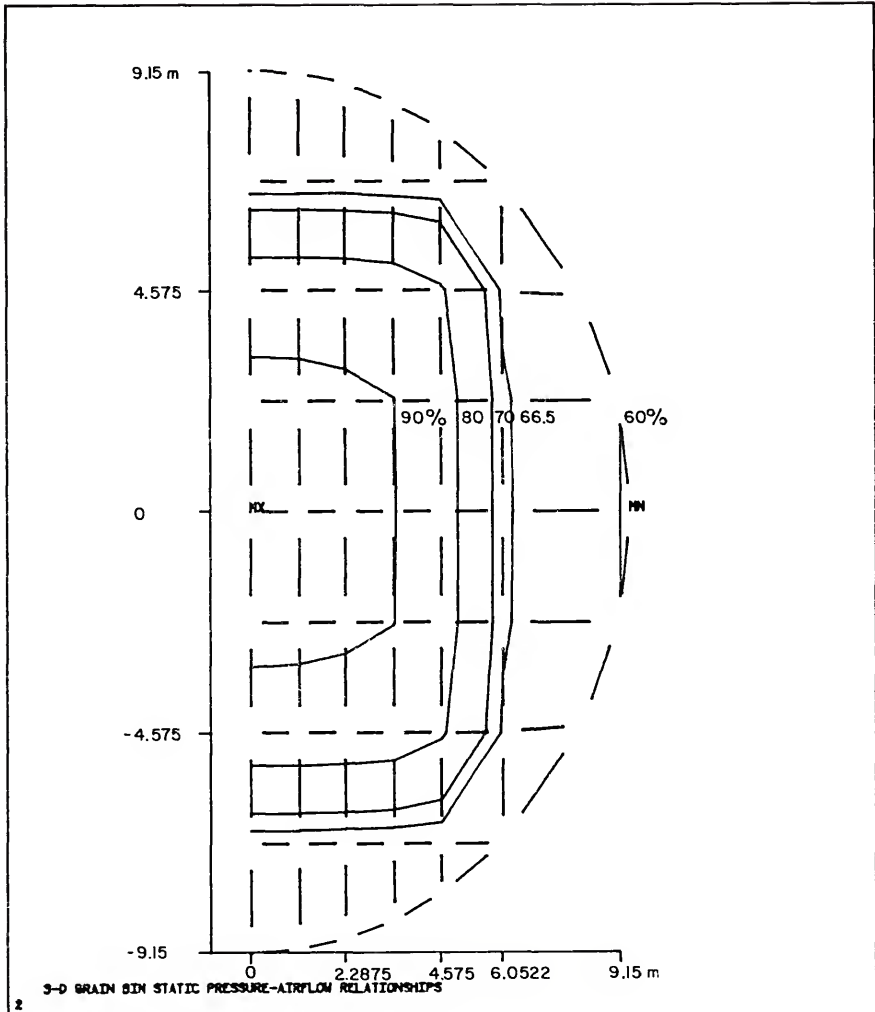


Figure 32. Isobaric distribution calculated using ANSYS in percent of total pressure loss on the horizontal cutting plane at 5 percent of bin height.

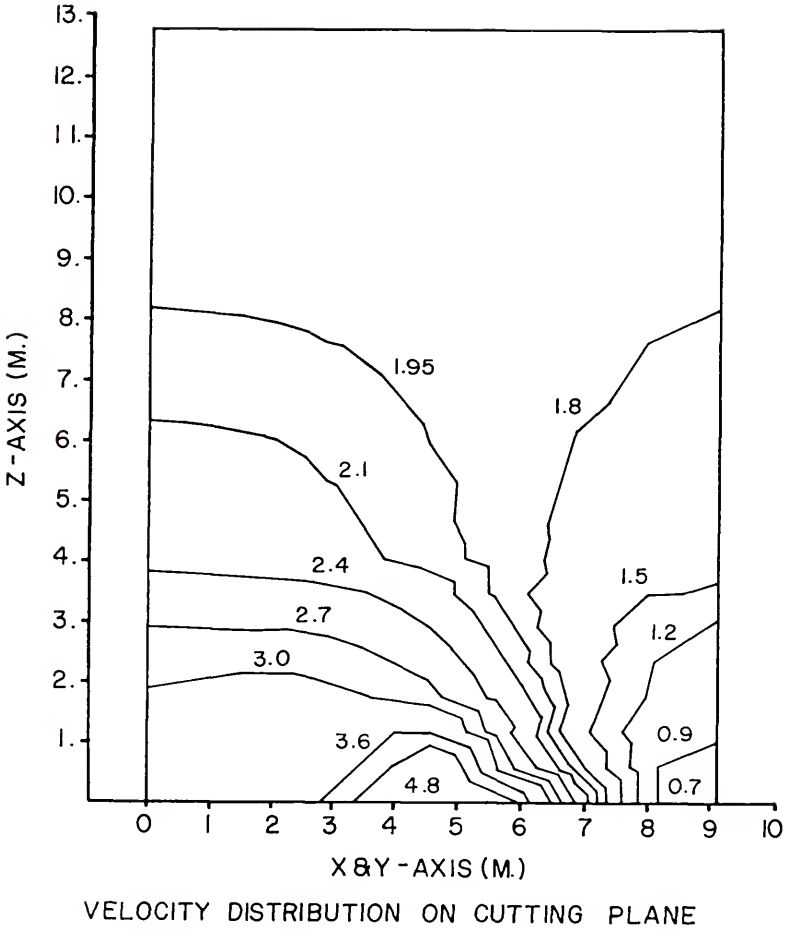


Figure 33. Velocity distribution in meters per minute on a vertical cutting plane from Khompis (1983).

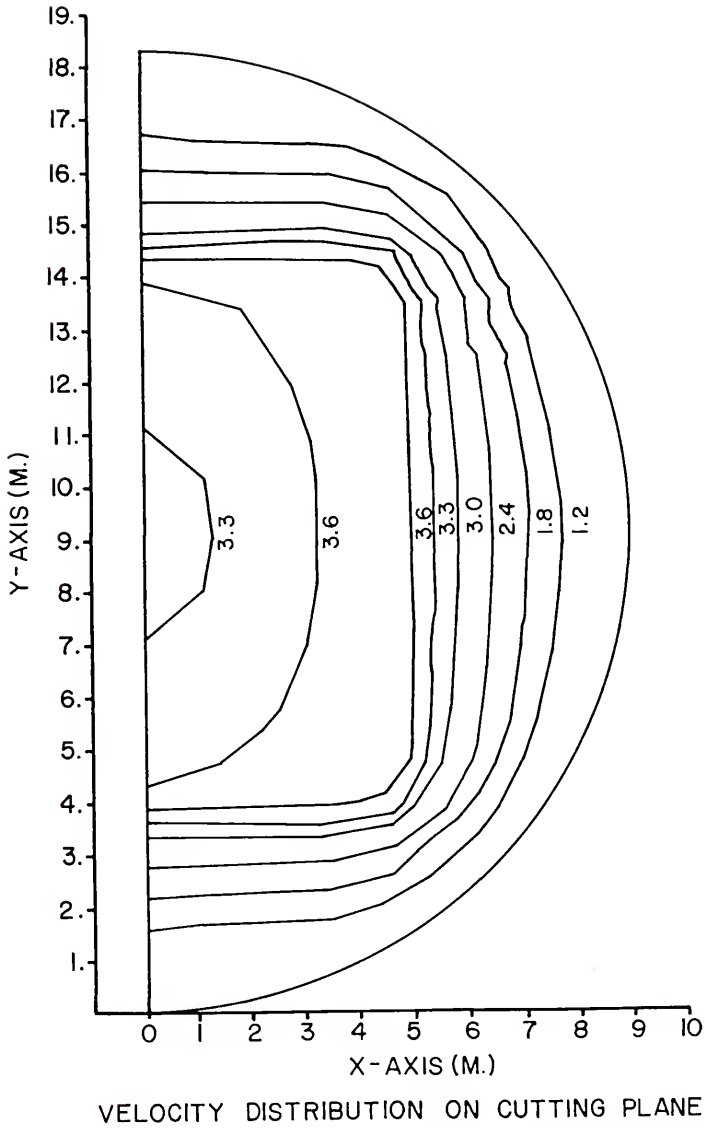


Figure 34. Velocity distribution in meters per minute on a horizontal cutting plane at 5 percent of bin height from Khompis (1983).

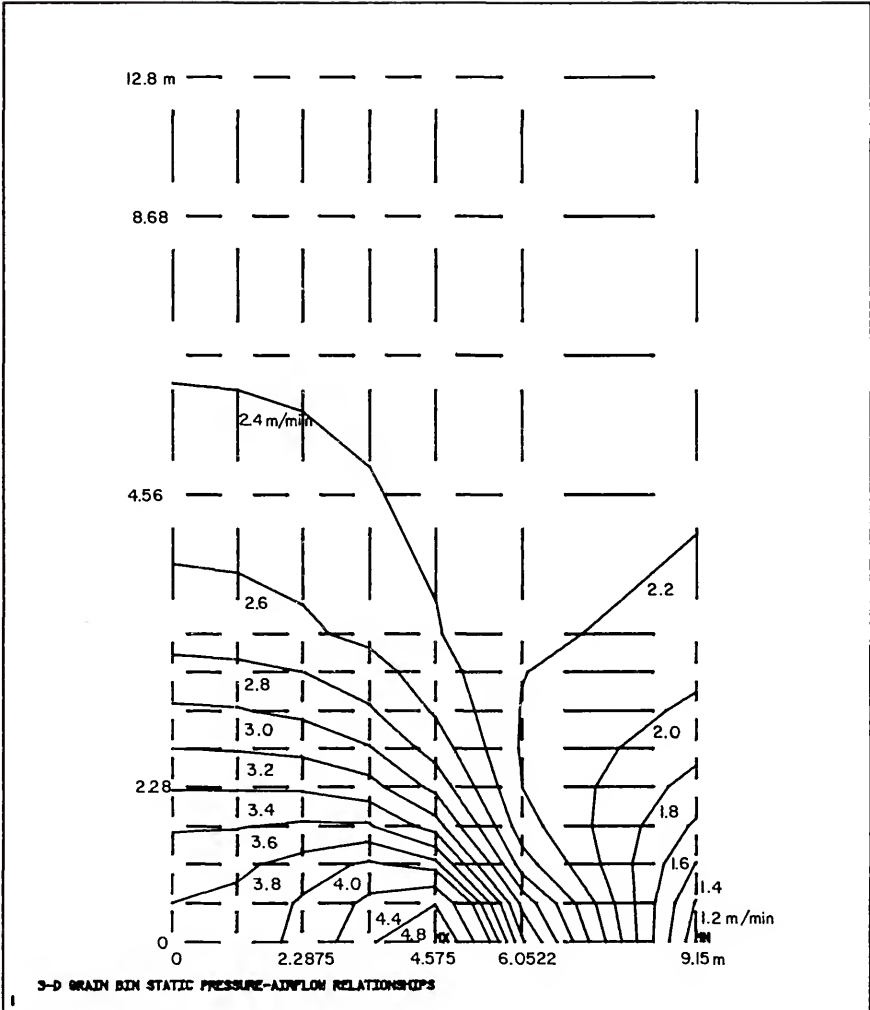


Figure 35. Velocity distribution calculated using ANSYS in meters per minute on a vertical cutting plane.

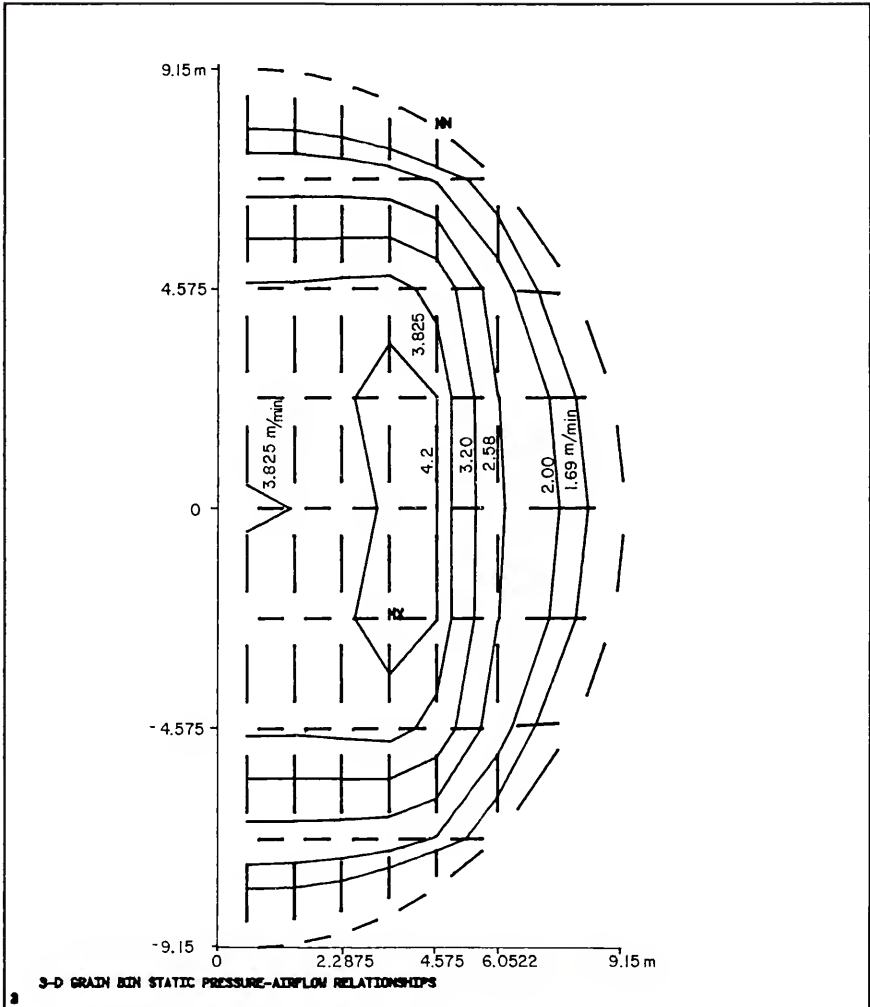


Figure 36. Velocity distribution calculated using ANSYS in meters per minute on a horizontal cutting plane at 5 percent of bin height.

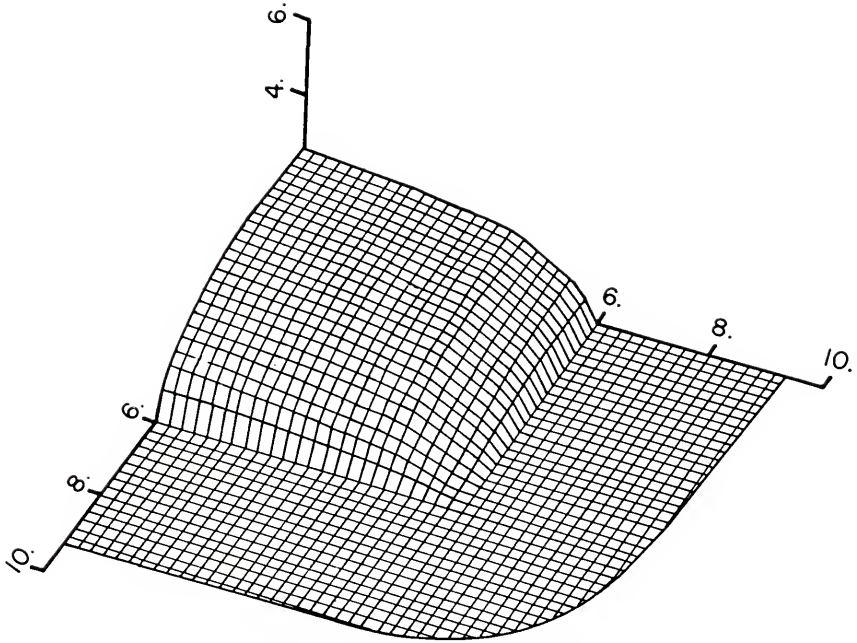


Figure 37. 70 percent of total pressure loss isobaric surface from Khompis (1983), view 2.

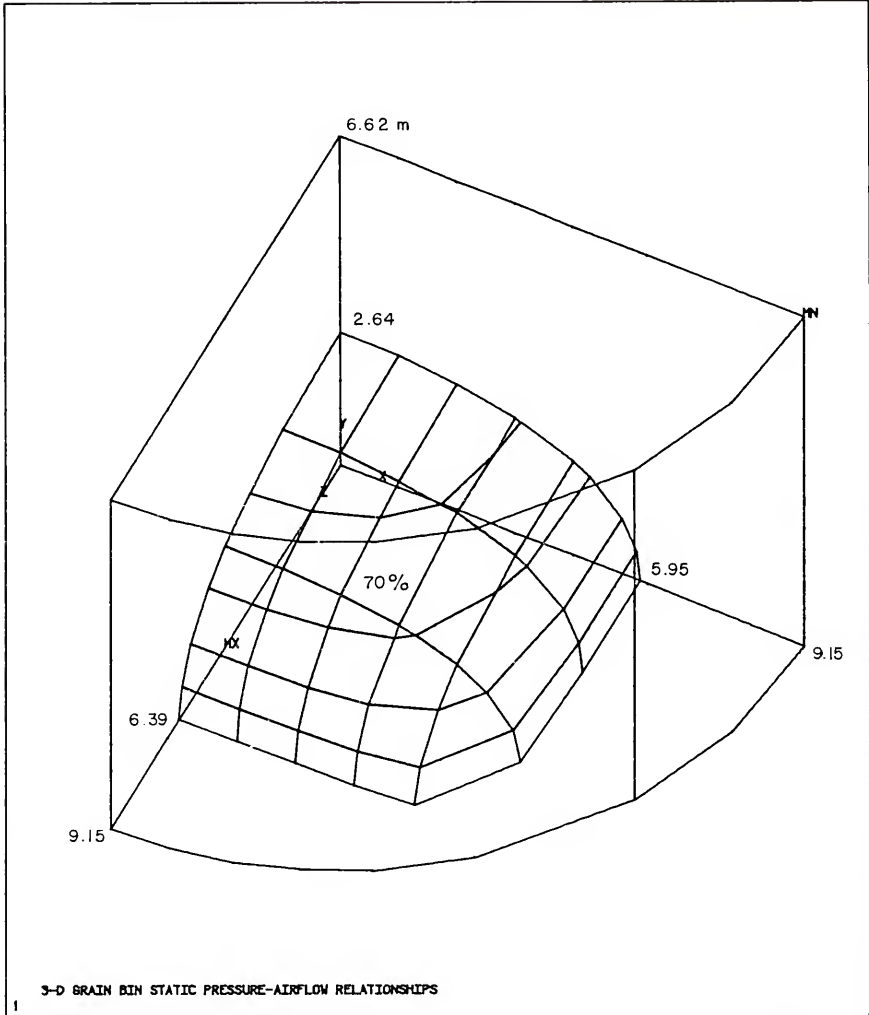


Figure 38. 70 percent of total pressure loss isobaric surface produced by ANSYS, view 2.

One view of the three-dimensional 2.4 meters per minute velocity surface presented by Khompis (1983) is illustrated in Figure 39. The velocity calculated by ANSYS penetrates further up into the grain within the bin than the velocity calculated by Khompis (1983). In order to compare a similar three-dimensional velocity surface, the constant velocity of 2.8 meters per meter was selected. One view of the three-dimensional 2.8 meters per minute velocity surface calculated using ANSYS is illustrated in Figure 40.

In the attempt to determine if the ANSYS calculated results provide a good solution to the nonlinear three-dimensional problem solved by Khompis (1983), the decision is much more evident than the comparison of the two-dimensional problem considered above. However, several factors must also be taken into account. The finite element models used by Khompis (1983) and with ANSYS were based on a different velocity-pressure relationship equations (Shedd versus Ergun). The coefficients necessary to use the equations were obtained from different sources. Therefore the porous media from which the coefficients were empirically determined were not necessarily identical. Khompis (1983) used three separate computer programs to obtain the three-dimensional results. The first program consisted of a coarse finite element grid. The two subsequent programs used finer finite element grids. The finite element grid used with ANSYS was the same throughout the solution procedure and corresponded to the grid in

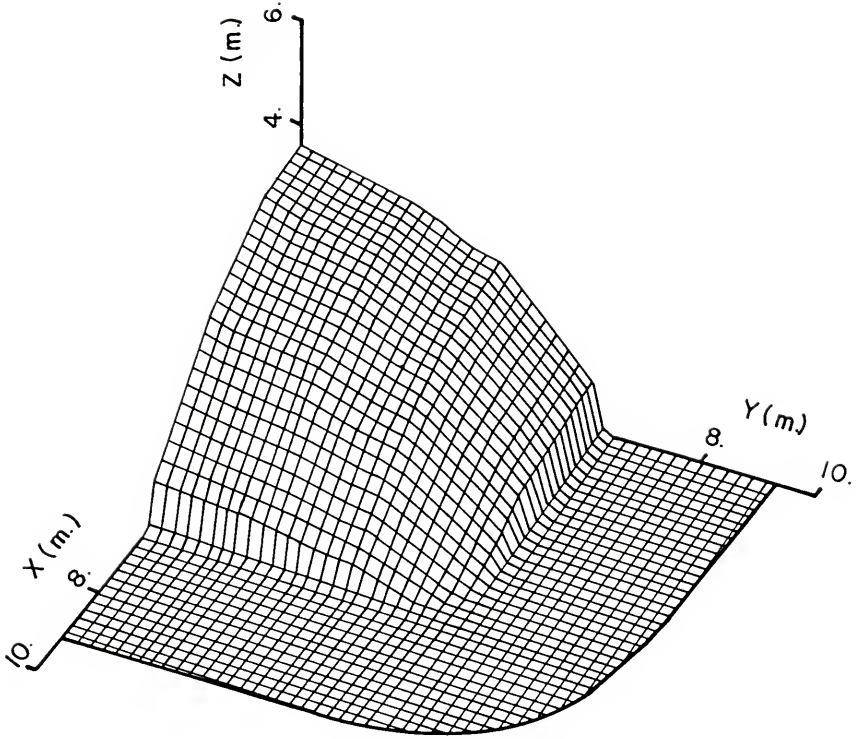


Figure 39. Constant velocity surface of 2.4 meters per minute from Khompis (1983). view 2.

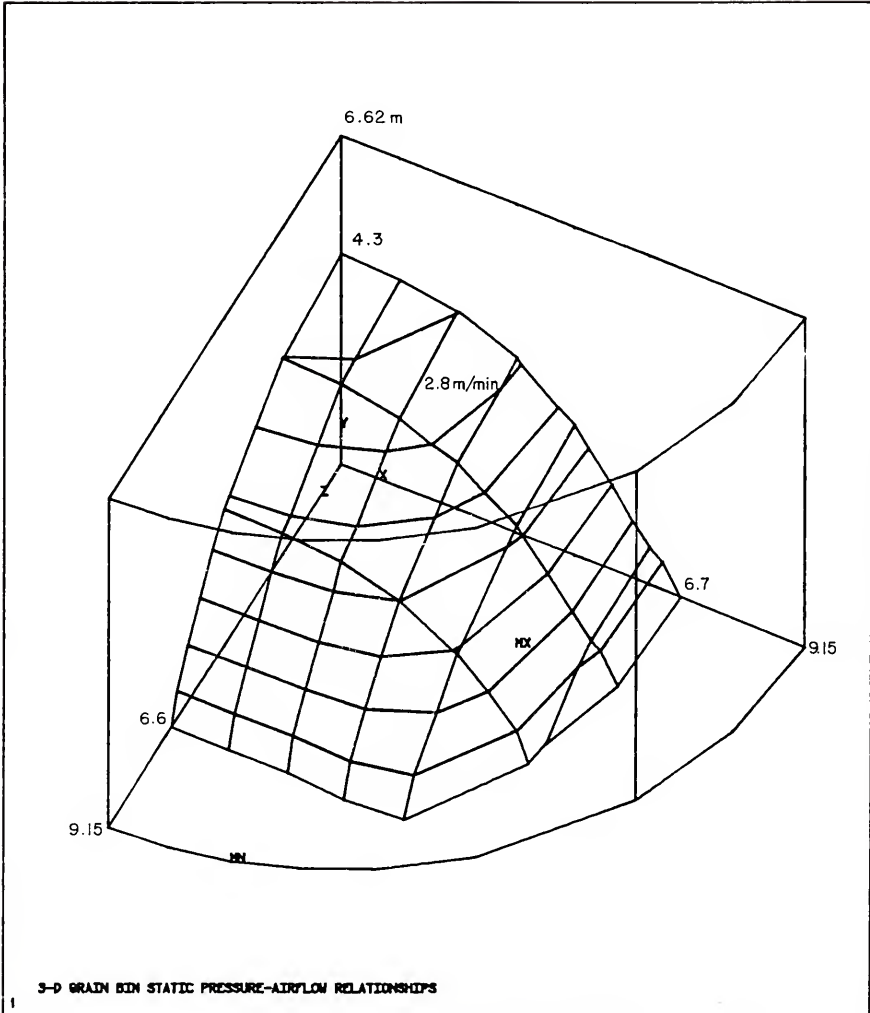


Figure 40. Constant velocity surface of 2.8 meters per minute calculated using ANSYS, view 2.

the first program used by Khompis (1983). The location of nodes and element size and shape effected the contours which were plotted. The pressure and velocity are calculated for particular positions within the element--at the centroid, at nodes, etc. For example ANSYS calculates the pressure at each node and the velocity at the centroid of the element. When constant velocity or isobaric contour lines or surfaces are requested, numerical interpolation or extrapolation type computations are used to provide the required data. This could produce slight distortions of the true line or surface location. In the comparison of various contour locations as discussed above, graphical interpolation was used. However, due to the difficulty associated with the graphical interpolation, the accuracy was limited. It appears that ANSYS does provide a satisfactory solution since the results are very consistent with the results obtained by Khompis (1983) despite the factors mentioned above. A detailed comparison of these results is presented in Appendix D.

Three-Dimensional Bulk Oranges

Table 6 contains the results of the modeling of the pressure drop study reported by Chau et al. (1983). The first column lists the 14 flow rates used in the comparison. Columns 2 through 4 contain the calculations of the pressure drop across oranges packed in bulk. As indicated, the second and third columns are calculations using the best fit equations reported by Chau et al. (1983), while the fourth

Table 6. Three-dimensional pressure loss data for oranges in bulk and orange carton sides.

1 FLOW RATE	2 ORANGES IN BULK			3 ORANGES WITH ONE CARTON SIDES			4 ORANGES WITH TWO CARTON SIDES		
	ΔP EQ 31 (Pa)	ΔP EQ 32 (Pa)	ΔP ANSYS (Pa)	ΔP EQ 40 (Pa)	ΔP ANSYS (Pa)	f	ΔP EQ 40 (Pa)	ΔP ANSYS (Pa)	f
E+2 (kg/sec)						r1 EQ 53			r2 EQ 54
3.5	0.94	1.08	1.06	170.4	8.61	0.58	243.3	16.13	0.64
4.0	1.21	1.36	1.34	222.0	11.09	0.58	315.7	20.81	0.65
4.5	1.52	1.67	1.64	280.0	13.88	0.58	397.2	26.09	0.65
5.0	1.87	2.02	1.98	345.4	16.99	0.58	487.8	31.95	0.65
5.5	2.25	2.34	2.35	417.1	20.40	0.58	587.4	38.42	0.65
6.0	2.66	2.80	2.75	495.5	24.14	0.58	696.0	45.47	0.65
6.5	3.10	3.24	3.19	580.6	28.18	0.58	813.6	53.12	0.65
7.0	3.58	3.72	3.65	672.4	32.54	0.58	940.1	61.36	0.65
7.5	4.01	4.22	4.14	770.8	37.21	0.58	1075.5	70.20	0.66
8.0	4.64	4.76	4.67	875.9	42.19	0.58	1219.8	79.63	0.66
8.5	5.22	5.32	5.23	987.6	47.49	0.58	1372.8	89.65	0.66
9.0	5.83	5.92	5.82	1105.9	53.09	0.58	1534.7	100.27	0.66
9.5	6.47	6.56	6.44	1230.9	59.02	0.58	1705.3	111.48	0.66
10.0	7.15	7.22	7.09	1362.4	65.25	0.58	1884.7	123.28	0.66

column represents the results calculated using ANSYS. As expected, the ANSYS calculations are essentially the same as the results based on the two best-fit equations. Equation 32 and the element used in the ANSYS analysis were based on the Ergun equation and the input data were the same. Equation 31 was based on the Shedd equation. Both Equations 31 and 32 contain experimental error which accounts for the slight disagreement between the results of these two equations as well as in comparison with the ANSYS results.

Equations 31 and 32 are repeated here for the convenience of the reader,

$$(31) \quad \Delta P/h = a V^b$$

and

$$(32) \quad \Delta P/h = K_1 \mu V^2 (1-\epsilon)^2 / D_p \epsilon^3 g_c + K_2 \rho V^2 (1-\epsilon) / D_p \epsilon^3 g_c$$

where

$$a = 278$$

$$b = 1.937$$

$$K_1 = 150$$

$$K_2 = 1.75$$

$$g_c = \text{Newton's Law gravitational constant.}$$

Columns 5 and 6 contain the results, for oranges with one carton side, calculated with the best-fit equation

reported by Chau et al. (1983) and by ANSYS, respectively. Columns 8 and 9 contain the results for oranges with two carton sides.

The values of the pressure loss in columns 5 and 8 illustrate the significant increase caused by the vent holes. In column 6 and 9 the ANSYS results do not show as great an increase as columns 5 and 8. ANSYS did show an increased pressure loss due to the reduced area but did not include the loss through the opening as was the case for the values reported in columns 5 and 8.

The pressure loss calculated using Equation 40 in columns 5 and 8 indicated a very large increase when compared to the bulk oranges in columns 2 or 3. The pressure loss through oranges with two carton sides is about 1.4 times the pressure loss through oranges with one carton side. The pressure loss through oranges in bulk represented less than 2 % of the total pressure loss through oranges with one sides and through oranges with two sides.

Equation 40 is repeated here for the convenience of the reader,

$$(40) \quad \Delta P = a' V^b$$

where $a' = 1.85 \times 10^4$ and $b = 1.98$ for oranges with one carton side, while $a' = 2.46 \times 10^4$ and $b = 1.95$ for oranges with two carton sides.

The ANSYS calculated pressure loss in columns 6 and 9 show a marked increase over the bulk pressure loss in

column 4. The values in column 6 are over eight times larger than column 3 while the values in column 9 are over sixteen times the values in column 3. The pressure loss for oranges with one and two sides reflected the loss as a result of the reduced entrance and exit area but did not include the loss that was produced by the inlet or exit holes.

As reported by Chau et al. (1983), the pressure loss for oranges with two carton sides (column 8) was less than twice the pressure loss for oranges with one carton side (column 5). The ANSYS calculated pressure loss for oranges with two carton sides (column 9) was nearly twice the pressure loss for oranges with one carton side (column 6).

Columns 7 and 10 contain the calculated area reduction factors for oranges with one (Equation 53) and two carton sides (Equation 54), respectively. The reduction factor in column 7 remained essentially constant with a value of 58 % for the entire range of flow rates studied. The reduction factor in column 10 exhibited a slight increase with increased flow rate with an average value of about 65 %.

Equations 53 and 54 are repeated here for the convenience of the reader,

$$(53) \quad f_{r1} = \frac{1.59 \cdot 10^{-2} \text{ m} / \rho A v}{[\Delta P (\text{ANSYS}) - \Delta P (\text{Equation } 40)]}$$

and

$$(54) \quad f_r^2 = \frac{2.78 \text{ m}^2 / \rho A v}{[\Delta P (\text{ANSYS}) - \Delta P (\text{Equation 40})]} .$$

The assumptions used to calculate the reduction factors appear to be feasible based on the results. An approximate measurement of the apparent reduction of the vent area by the oranges was made using slides of the experimental test conducted by Chau et al. (1983). A projection of the close-up slide of the vent openings was used to determine the ratio of the area of the portion of oranges observed through the vent to the area of the vent. This ratio was in the range of 40 to 60 %. This was not an exact method of measurement since the vent area was a plane cross-sectional area while the area of the portion of oranges observed in the vent was a projected area. However, the measurements indicate that the calculated values of the reduction factors were well within reason.

As mentioned previously, for the current study the pressure loss through the vent holes was not critical. ANSYS was used to determine the pressure and air velocity distribution within the carton based upon the knowledge of the flow rate through the vent holes (boundary condition). The loss through the holes has many important implications concerning future expansion of the current work. For example detailed knowledge of the pressure loss through the vent holes could be very important in the analysis of forced air energy cost, the optimum design of vent hole size and location, and for pressure and velocity distribution studies

with several cartons in series or parallel arrangements such as would be the case for pallet loads.

ANSYS was capable of modeling the pressure loss within the carton of oranges (porous media) accurately. The pressure loss through the vent holes was a significant factor. The data reported above indicates that ANSYS can be used to model the carton inlet and outlet pressure loss through the use of the hydraulic conductance element. However, additional work must be accomplished to identify the required input information, including the conductance coefficient and the reduction factor. The relationship of the pressure loss for oranges with one carton side and with two carton sides must also be better understood.

Based on the results produced by ANSYS in modeling the work of Segerlind (1982), Khompis (1983), and Chau et al. (1983), it was concluded that ANSYS was an excellent analysis technique for investigating the pressure and velocity distributions in orange cartons. The empirical input parameters needed to use ANSYS were identified and available. The physical geometry and boundary conditions were easily developed. The output data was appropriate for use in the heat transfer model to determine the temperature response. Therefore, the current work continued with confidence that ANSYS would provide the necessary data to accurately evaluate the feasibility of porous media flow theory for the finite boundary conditions of air flow through fruits or vegetables packed in shipping containers.

Three-Dimensional Orange Carton

ANSYS was used to solve the twelve orange carton air flow boundary conditions presented in Tables 2 and 3 above. The output from the ANSYS solution was available in tabular report type printout, user specified output selection, and various graphical plots. A portion of the nodal pressure printout for one of the problems (Boundary Condition 6-1) solved is shown in Figure 41. Each node was listed along with the corresponding pressure in units of Pascal.

The pressure was labeled "TEMP" since the element used was a three-dimensional solid heat transfer element but the problem was solved using an available nonlinear porous media flow option. With this option, the thermal parameters were interpreted as analogous fluid flow parameters. Therefore, the temperature degree of freedom became equivalent to a pressure degree of freedom. In Figure 42, the "ELEMENT HEAT FLOW RATES" title is interpreted as element mass flow rates. The "3-D SOLID 70" label indicated the ANSYS element type and number.

Figure 42 provides a portion of the element printout for the problem presented in Figure 41. For each element the printout provided the following: the element number; the nodes connecting the element; the material type (which was significant since more than one type porous media was used); the element volume; the pressure gradient (total and x-, y-, and z-components); the mass flux; and the fluid (air) velocity (total and x-, y, and z- components).

3D ORANGE CARTON STATIC PRESSURE-AIRFLOW RELATIONSHIPS BC61
 17.5191 MAY 22,1987 CP= 138.358
 **** TEMPERATURE SOLUTION **** TIME = 0.00000 LOAD STEP= 1 ITERATION= 100 CUH, ITER.= 29
 NODE TEMP NODE TEMP NODE TEMP NODE TEMP

1	6.0965	2	6.0938	3	6.0922	4	6.0881	5	6.0823
6	6.0746	7	6.0659	8	6.0568	9	6.0479	10	6.0399
11	6.0328	12	6.0269	13	6.0222	14	6.0204	15	6.0168
16	6.0915	17	6.0920	18	6.0911	19	6.0871	20	6.0811
21	6.0735	22	6.0648	23	6.0558	24	6.0471	25	6.0390
26	6.0320	27	6.0261	28	6.0214	29	6.0169	30	6.0134
31	6.0890	32	6.0884	33	6.0854	34	6.0813	35	6.0755
36	6.0681	37	6.0599	38	6.0512	39	6.0427	40	6.0349
41	6.0279	42	6.0220	43	6.0170	44	6.0125	45	6.0117
46	6.0831	47	6.0825	48	6.0793	49	6.0750	50	6.0692
51	6.0621	52	6.0541	53	6.0457	54	6.0375	55	6.0298
56	6.0230	57	6.0171	58	6.0122	59	6.0081	60	6.0074
61	6.0765	62	6.0758	63	6.0724	64	6.0680	65	6.0622
66	6.0553	67	6.0476	68	6.0395	69	6.0315	70	6.0239
71	6.0172	72	6.0114	73	6.0066	74	6.0028	75	6.0021
76	6.0699	77	6.0692	78	6.0656	79	6.0610	80	6.0552
81	6.0485	82	6.0409	83	6.0329	84	6.0250	85	6.0174
86	6.0106	87	6.0049	88	6.0003	89	5.9967	90	5.9960
91	6.0638	92	6.0631	93	6.0593	94	6.0545	95	6.0487
96	6.0419	97	6.0344	98	6.0263	99	6.0182	100	6.0105
101	6.0036	102	5.9979	103	5.9935	104	5.9900	105	5.9894
106	6.0585	107	6.0577	108	6.0537	109	6.0488	110	6.0429
111	6.0360	112	6.0284	113	6.0201	114	6.0118	115	6.0038
116	5.9967	117	5.9909	118	5.9866	119	5.9834	120	5.9828
121	6.0542	122	6.0534	123	6.0489	124	6.0438	125	6.0379
126	6.0310	127	6.0232	128	6.0147	129	6.0060	130	5.9977
131	5.9904	132	5.9846	133	5.9805	134	5.9775	135	5.9769
136	6.0525	137	6.0490	138	6.0445	139	6.0397	140	6.0338
141	6.0268	142	6.0188	143	6.0101	144	6.0010	145	5.9923
146	5.9848	147	5.9788	148	5.9748	149	5.9739	150	5.9743
151	6.0491	152	6.0455	153	6.0437	154	6.0399	155	6.0330

Figure 41. Nodal pressure printout for ANSYS solution.

```

**** ELEMENT HEAT FLOW RATES ***** TIME = 0.000000 LOAD STEP= 1 ITER.= 100 CUM. J1ER.= 29

EL= 1 NODES= 1 2 17 16 166 167 182 181 MAT= 4 VOL= 0.5531E-04 3-D SOLID 70
PRESSURE GRADIENT (TOTAL,X,Y,Z)= 0.20222 -0.54563E-01 0.16103 -0.10948
MASS FLUX= 0.16289E-01 FLUID VELOCITY (TOTAL,X,Y,Z)= 0.13137E-01 0.35446E-02 -0.10461E-01 0.71119E-02

EL= 2 NODES= 2 3 18 17 167 168 183 182 MAT= 5 VOL= 0.3687E-04 3-D SOLID 70
PRESSURE GRADIENT (TOTAL,X,Y,Z)= 0.14928 -0.98949E-01 0.10158 -0.46622E-01
MASS FLUX= 0.34529E-01 FLUID VELOCITY (TOTAL,X,Y,Z)= 0.27846E-01 0.18458E-01 0.18949E-01 0.86968E-02

EL= 3 NODES= 3 4 19 18 168 169 184 183 MAT= 5 VOL= 0.3687E-04 3-D SOLID 70
PRESSURE GRADIENT (TOTAL,X,Y,Z)= 0.17407 -0.15673 0.70420E-01 -0.27846E-01
MASS FLUX= 0.38673E-01 FLUID VELOCITY (TOTAL,X,Y,Z)= 0.31190E-01 0.28084E-01 0.12618E-01 0.49895E-02

EL= 4 NODES= 4 5 20 19 169 170 185 184 MAT= 5 VOL= 0.3687E-04 3-D SOLID 70
PRESSURE GRADIENT (TOTAL,X,Y,Z)= 0.24781 -0.23357 0.71284E-01 -0.28890E-01
MASS FLUX= 0.49793E-01 FLUID VELOCITY (TOTAL,X,Y,Z)= 0.40155E-01 0.38172E-01 -0.11551E-01 0.46813E-02

EL= 5 NODES= 5 6 21 20 170 171 186 185 MAT= 5 VOL= 0.3687E-04 3-D SOLID 70
PRESSURE GRADIENT (TOTAL,X,Y,Z)= 0.31754 -0.30993 0.62300E-01 -0.29939E-01
MASS FLUX= 0.59082E-01 FLUID VELOCITY (TOTAL,X,Y,Z)= 0.47646E-01 0.46504E-01 -0.93479E-02 0.44924E-02

EL= 6 NODES= 6 7 22 21 171 172 187 186 MAT= 5 VOL= 0.3687E-04 3-D SOLID 70
PRESSURE GRADIENT (TOTAL,X,Y,Z)= 0.36157 -0.35752 0.45005E-01 -0.29820E-01
MASS FLUX= 0.64493E-01 FLUID VELOCITY (TOTAL,X,Y,Z)= 0.52011E-01 0.51428E-01 -0.64738E-02 0.42895E-02

EL= 7 NODES= 7 8 23 22 172 173 188 187 MAT= 5 VOL= 0.3687E-04 3-D SOLID 70
PRESSURE GRADIENT (TOTAL,X,Y,Z)= 0.37221 -0.37015 0.26867E-01 -0.28445E-01
MASS FLUX= 0.65756E-01 FLUID VELOCITY (TOTAL,X,Y,Z)= 0.53029E-01 0.52735E-01 -0.38278E-02 0.40526E-02

EL= 8 NODES= 8 9 24 23 173 174 189 188 MAT= 5 VOL= 0.3687E-04 3-D SOLID 70
PRESSURE GRADIENT (TOTAL,X,Y,Z)= 0.35555 -0.35429 0.13127E-01 -0.26878E-01
MASS FLUX= 0.63771E-01 FLUID VELOCITY (TOTAL,X,Y,Z)= 0.51428E-01 0.51246E-01 -0.18987E-02 0.38877E-02

```

Figure 42. Element flow rate printout for ANSYS solution.

Various plots of the isobaric and constant velocity lines were used in the course of post-processing of the results but are not reported since similar plots were illustrated in the three-dimensional grain bin analysis.

The ANSYS Post-Processor was used to select, sort, and perform several mathematical operations on the element output information in order to provide the necessary data input to the heat transfer model. The total velocity listed in Figure 42 provided the magnitude of the centroidal velocity vector which was used to determine the convective heat transfer coefficient. The velocity components listed in Figure 42 were used to calculate the mass flow rate across each face of the element. The element volume was used in the heat transfer program in the evaluation of Equation 71 and for other calculations related to volume of the oranges within each element.

An example of the ANSYS output data (input files "Data" and "Dimensions") reorganized for use in the heat transfer model is presented in Appendix B.

Before considering the temperature response calculated using the ANSYS data, the experimental temperature results are presented in the following section.

Experimental Temperature Measurement

The primary means of data storage was on floppy disk but a hardcopy backup was printed. Figure 43 provides a portion of the raw data printout produced by the data acquisition system for one experimental test. The printout provided the time-temperature readings for the various thermocouples located within the experimental orange carton. The test number, air flow rate and other significant items of data not recorded on the printout were recorded during the each test on the floppy disk for subsequent data retrieval operations.

The data illustrated in Figure 43 was from Boundary Condition Number 6-1 (1.53 E-3 m³/s flow rate). The flow rate was low and therefore a 15 minute scan interval was used. The oranges and experimental carton were initially at a temperature of approximately 90 F (32.2 C) while the entering air temperature was maintained at approximately 35 F (1.7 C) during the test. The first number in Figure 43 indicates the data channel and the second number indicates the corresponding data reading. Channels 1-59 and 140-158 were for thermocouples located at the orange center or surface or in the air spaces adjacent to surface thermocouples (Figure 16). The first scan shown in Figure 43 was recorded at 1 hour and 15 minutes after the start of the test and the second scan was recorded at six hours after the start of the test. Data channel 5

indicated a malfunctioning thermocouple. Because of the time and effort involved in preparing the load of oranges in the experimental carton, the test was not stopped to correct for one thermocouple problem. None of the tests considered for this study contained more than two bad thermocouples.

For each boundary condition it is possible to produce a graph of the temperature at any thermocouple location as a function of time. It should be noted that only a small portion of the output can be indicated on any one figure or the graph will not remain legible. In order to present the appropriate amount of data in the most efficient manner, the number of graphical plots was restricted to the minimum necessary to convey the relevant findings of this study.

Considering the thermocouple locations indicated in Figure 16 (insert provided), Figure 44 presents the temperature response (Boundary Condition 1-1) for two thermocouples in the fifth (top) layer and two thermocouples in the bottom (1st) layer of the experimental orange carton. These four thermocouples represent a set of symmetric pairs for the top and bottom layers and for the left and right sides of each of these layers of oranges. The difference in temperature response of thermocouples 10 and 66, as well as, 13 and 69, illustrate a general trend exhibited by all 12 experimental tests. The top layer of oranges cooled faster than the bottom layer of oranges in the experimental carton. The temperature difference between the top and bottom layer for a particular thermocouple location and time was

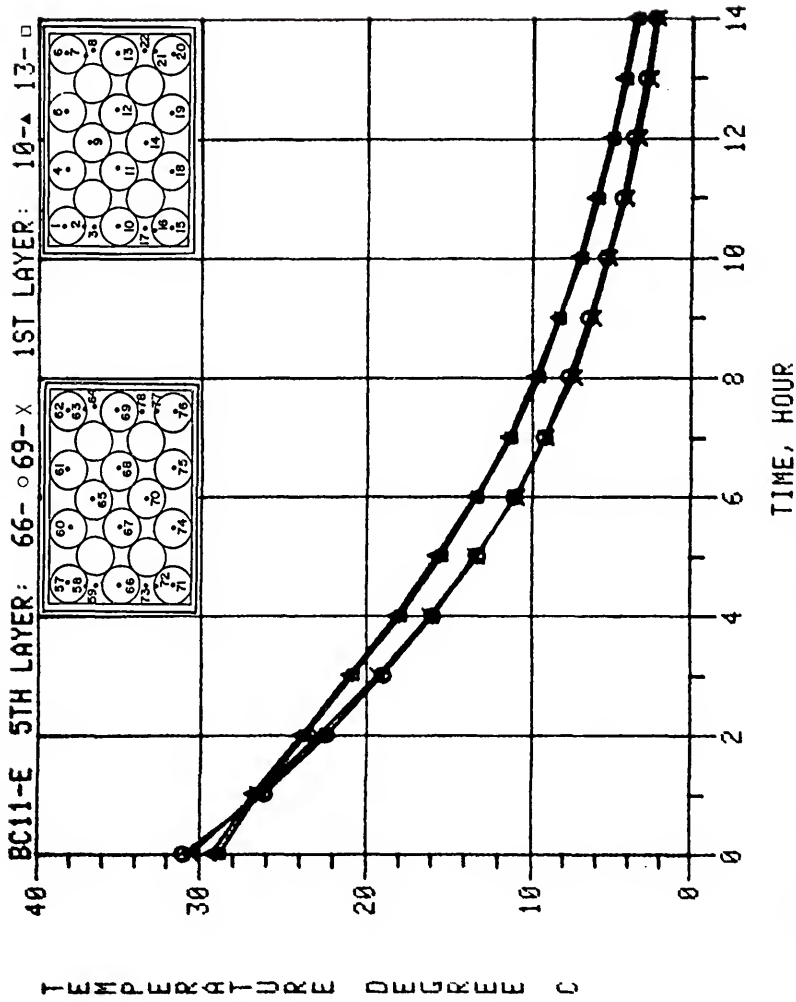


Figure 44. Experimental center temperature response of oranges in an experimental orange carton for forced-air cooling (Boundary Condition 1-1, thermocouple locations 10, 13, 66, and 69).

generally less than 6 F (3 C). Study of this trend indicated that the cause of the difference was due to increased void area adjacent to the inside surface of the top wall of the experimental orange carton. Compaction of the oranges from movement of the orange carton into and out of the cooling chamber and physiological shrinkage, in addition to other factors addressed below in the discussion of experimental error, was apparently the primary reason for the increased void space (porosity) above the top layer of oranges.

A comparison of the temperature response of thermocouples 10 and 13, as well as, 66 and 69 indicates that oranges symmetrically located on either side of the inlet air vent cooled at the same rate. This was the general trend for the first four boundary conditions with symmetric vent locations. Boundary Condition 6 was diagonally symmetric while Boundary Condition 5 was nonsymmetric and a comparison of geometrical symmetric thermocouple pairs was not applicable.

In the discussion of the heat transfer program, for the vent locations on the experimental carton, the flow calculated by ANSYS was symmetric top and bottom. Therefore the temperature response calculated from the ANSYS flow data was also symmetric top and bottom. For the first four symmetric boundary conditions, the ANSYS temperature response on either side of the air inlet vent was also symmetric.

The reason for the discussion of the model results at this particular time is related to the decision above concerning the efficient presentation of results in graphical form. Considering the above factors the decision was further developed to present the temperature response for thermocouples located in the bottom three layers of the orange carton. Further, this decision included only the thermocouple locations on the left side of each of the three bottom layers (as viewed in Figure 16). For the first four boundary conditions the later portion of the decision was practical. Since Boundary Condition 5 contained the nonsymmetric outlet vent on the left side, significant information was gained by considering only this side. Boundary Condition 6 was diagonally symmetric and the inlet air vent was on the left side. Finally, only the thermocouples located at the center of oranges were considered.

Figures 45 through 47 show the graphical output data for the left side of the three bottom layers of Boundary Condition 1-1.

The graphical results shown in this section are only examples from the complete range of tests. Additional graphs of the temperature response for the other boundary conditions are presented in Appendix E.

Figure 48 is an example of the interactive color graphics program output which was used to visualize the three-dimensional cooling response of the oranges within the

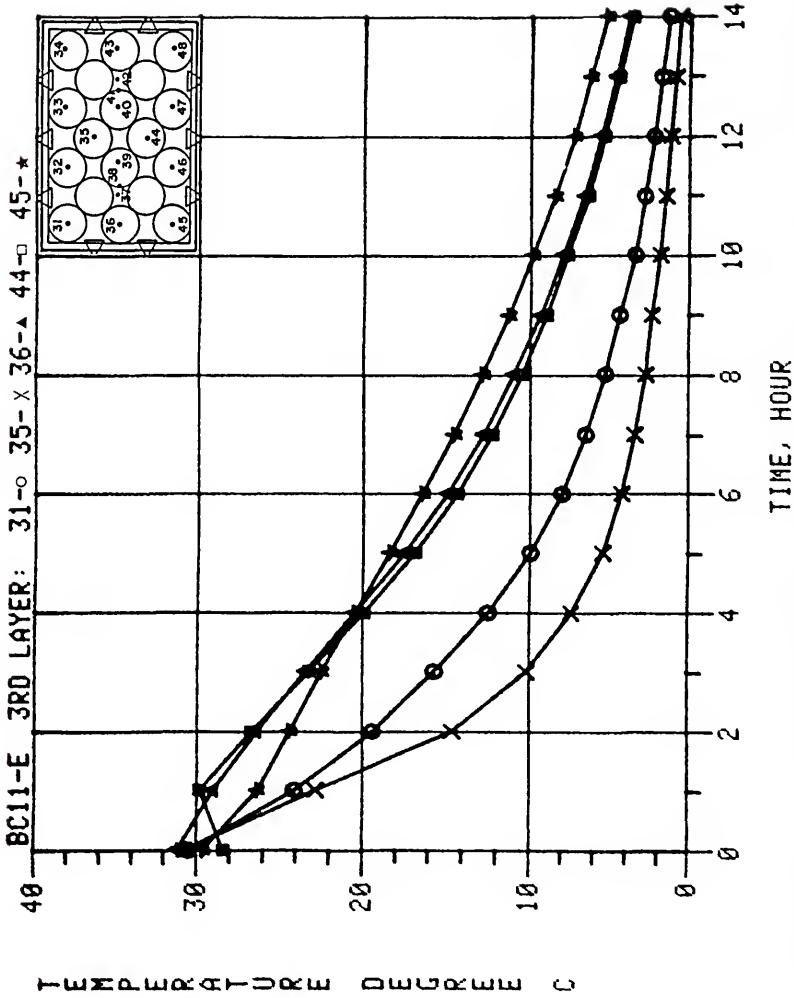


Figure 45. Experimental center temperature response of oranges in an experimental orange carton for forced-air cooling (Boundary Condition 1-1, 3rd layer thermocouple locations 31, 35, 36, 44, and 45).

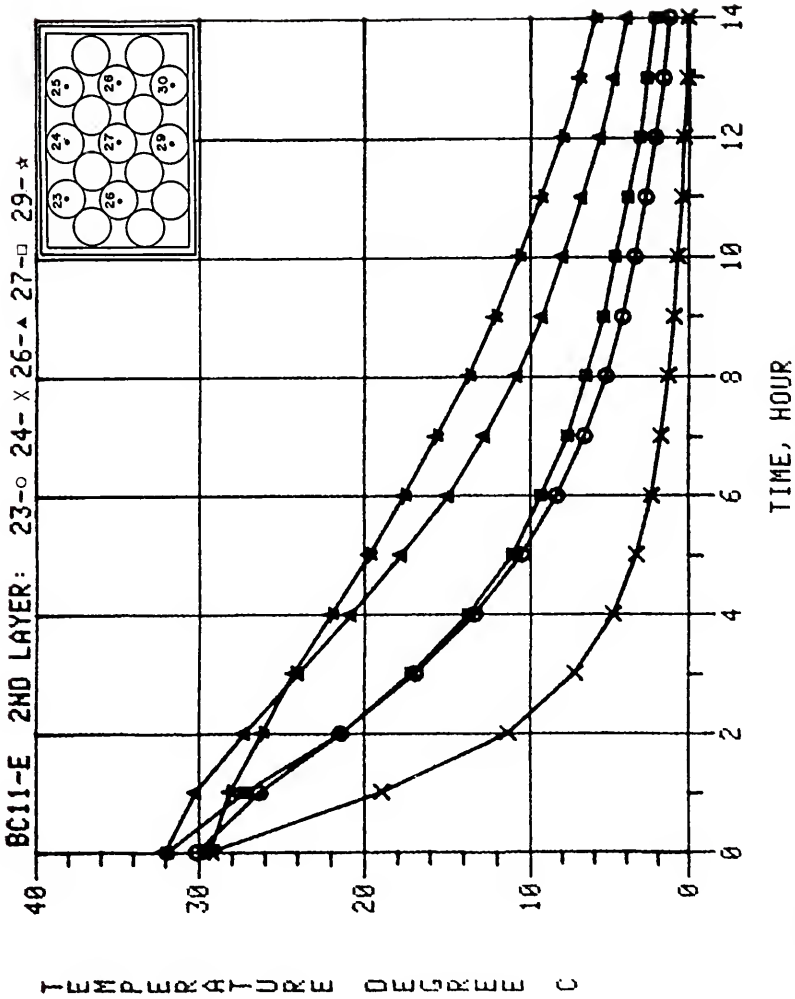


Figure 46. Experimental center temperature response of oranges in an experimental orange carton for forced-air cooling (Boundary Condition 1-1, 2nd layer thermocouple locations 23, 24, 26, 27, and 29).

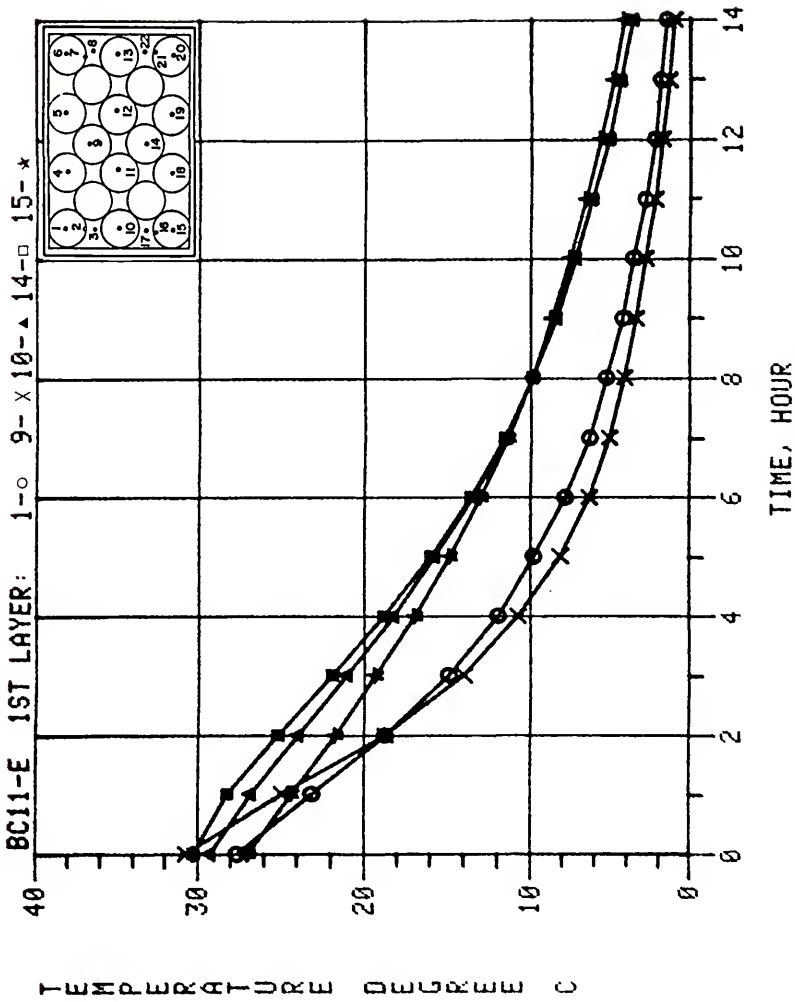
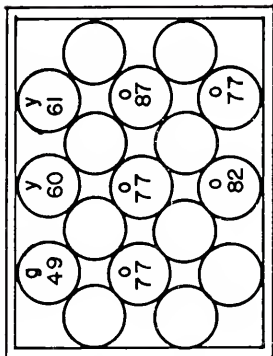


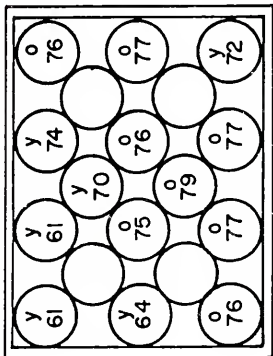
Figure 47. Experimental center temperature response of oranges in an experimental orange carton for forced-air cooling (Boundary Condition 1-1, 1st layer thermocouple locations 1, 9, 10, 14, and 15).

TEST 6188401
 CFM 21.1
 TOTAL TIME 5.0
 AVG. TRATIO 0.75
 TIME 0.70

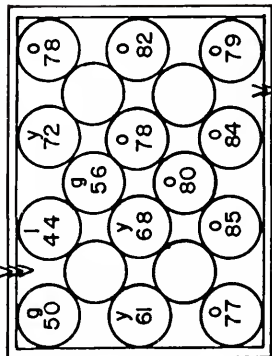
FOURTH LAYER



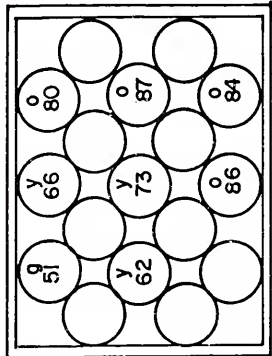
TOP LAYER



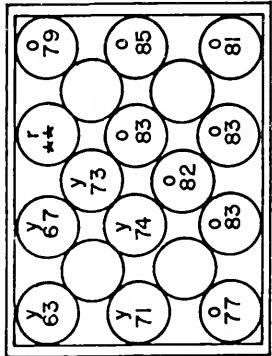
MIDDLE LAYER



SECOND LAYER



BOTTOM LAYER



r - Red (Above 90)

y - Yellow (61 - 74)

o - Orange (75 - 90)

g - Green (45 - 60)

Color Key: l - Light Blue (30 - 44)

Figure 48. Graphical representation of three-dimensional color graphics output of cooling response for oranges within an experimental carton.

experimental carton. As discussed in the Procedure section, the program projected the five layers of oranges in the arrangement which each layer occupied in the experimental carton. The program read the experimental data file for a particular test and displayed the temperature ratio of the orange at a particular time according to a defined temperature-color relationship. The program also displayed the temperature ratio in per cent at the center of the circles representing the oranges. The program was capable of continuous display for a real time observation of the cooling process and also allowed the display of specific time frames.

Heat Transfer Model

Printouts of the heat transfer program and associated input and output files are provided in Appendix B. In addition the program used to reorganize the temperature response calculated by the heat transfer program is also presented in Appendix B, along with portions of the input and output files.

The time-temperature calculation produced by the heat transfer model for the approximated thermocouple locations for the left side of the three bottom layers of Boundary Condition 1-1 are illustrated in Figures 49 to 51. These graphs correspond to the temperature response plots of the experimental data shown in Figures 45 to 47 above. The plots of the heat transfer model results which correspond to each graph shown in Appendix E are presented in Appendix F.

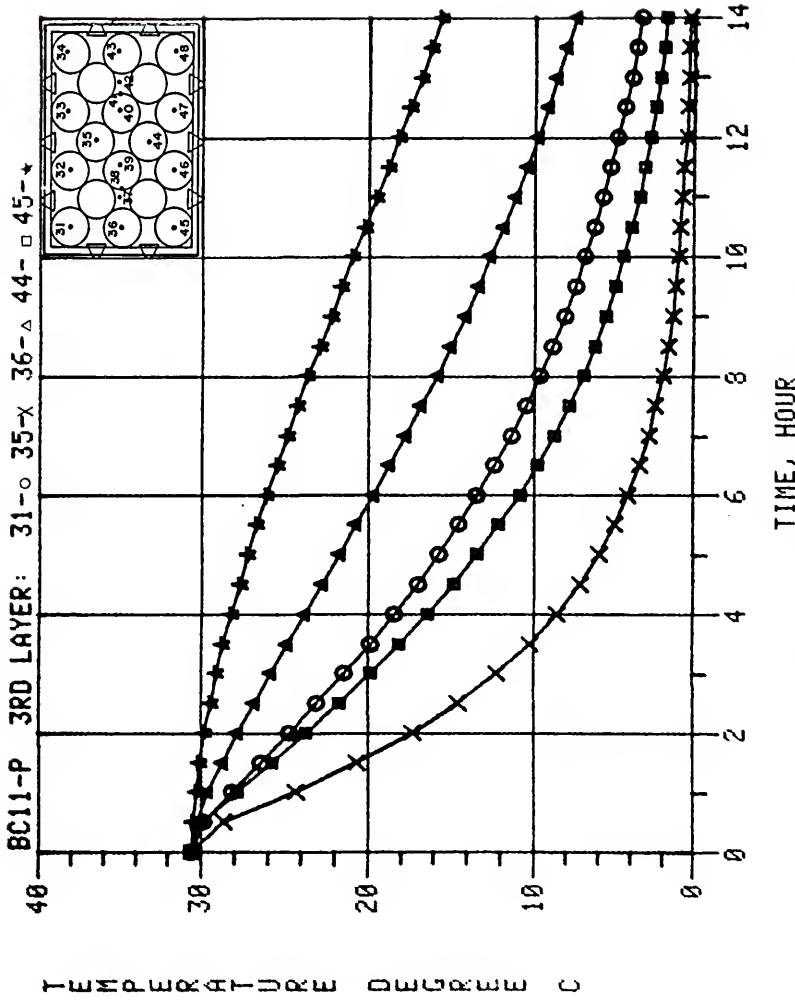


Figure 49. Predicted center temperature response of oranges in an experimental orange carton for forced-air cooling (Boundary Condition 1-1, 3rd layer thermocouple locations 31, 35, 36, 44, and 45).

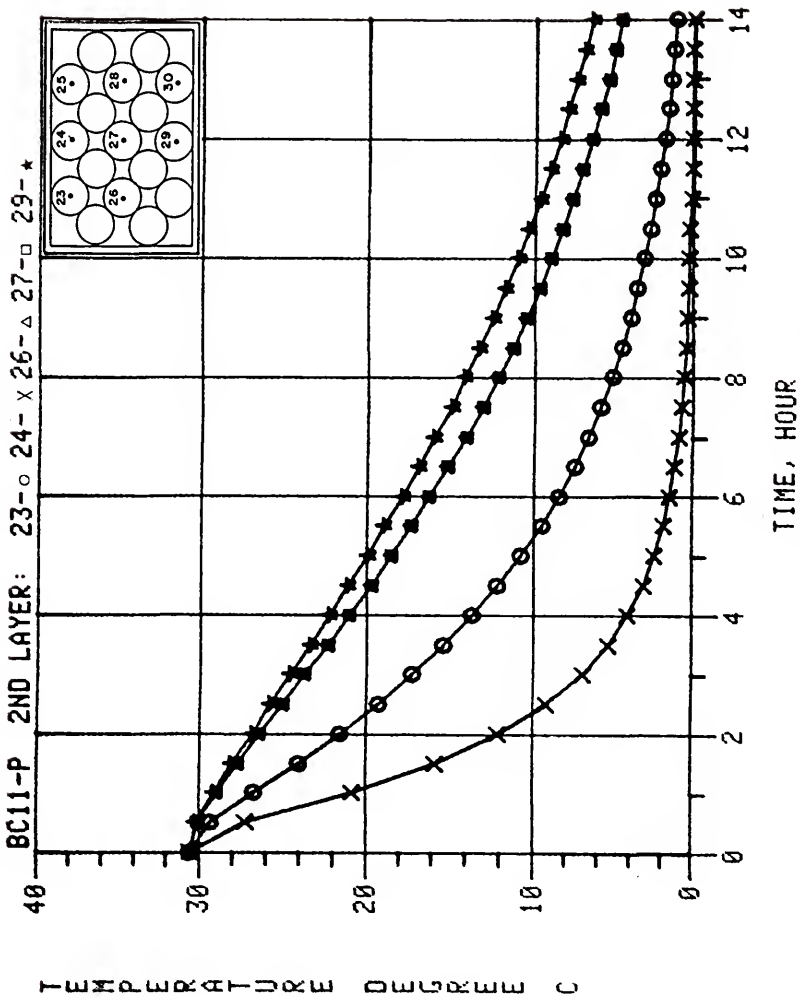


Figure 50. Predicted center temperature response of oranges in an experimental orange carton for forced-air cooling (Boundary Condition 1-1, 2nd layer thermocouple locations 23, 24, 26, 27, and 29).

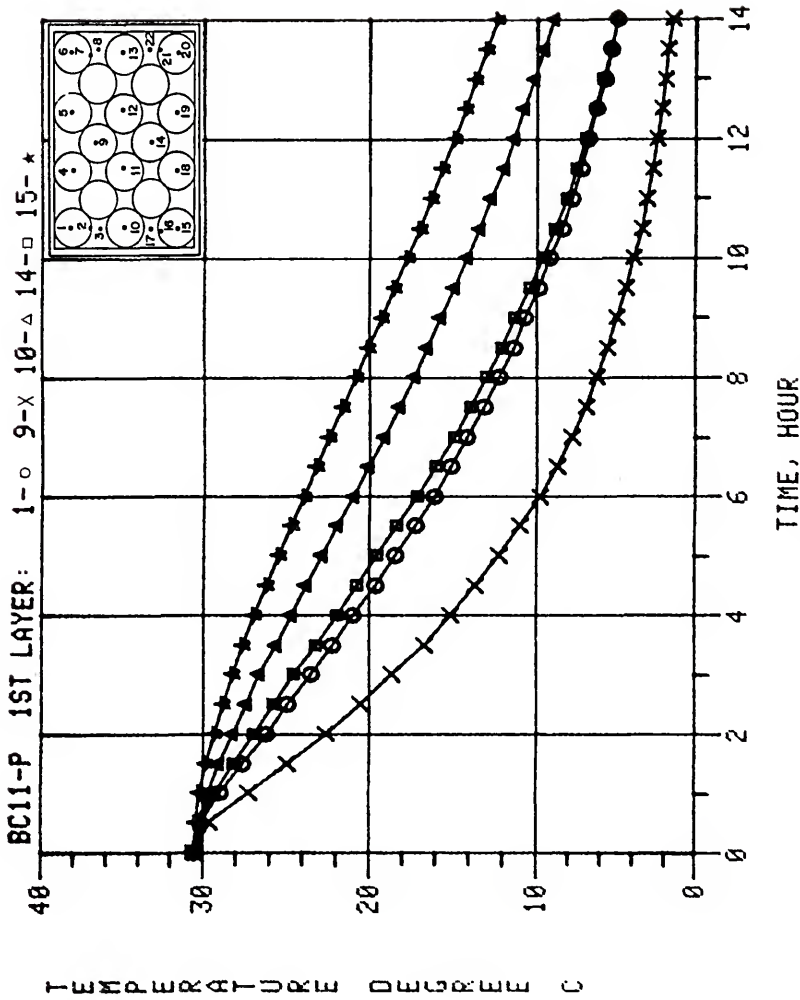


Figure 51. Predicted center temperature response of oranges in an experimental orange carton for forced-air cooling (Boundary Condition 1-1, 1st layer thermocouple locations 1, 9, 10, 14, and 15).

Before presenting a direct comparison of experimental and calculated temperature response data, the experimental error, convective heat transfer coefficient, variable porosity, and approximate model thermocouple locations will be discussed below.

Experimental Error

In order to better understand the relationships when comparing experimental and numerical temperature response data an understanding of the extent of experimental inaccuracy is important.

Although the equipment and procedures used to measure the experimental temperature response have been developed and perfected over the last ten years, there are a number of factors which directly effect the final temperature measurement. The instrumentation accuracy, the control of the air flow rate, the control of the inlet air temperature, the precise location of the thermocouples, the size and shape of the oranges, and the uniformity of packing the oranges, are but a few of the many variables which have a direct bearing on the final temperature readings. Considering these and other factors, the temperature readings are considered to be accurate to no less than 1.1 C (2 F).

In the Procedure section, the initial product temperature and inlet air temperature were described as controlled with little variation. In actual experimental

situations the control of these two important variables sometimes presented problems.

The initial temperature was obtained as described in the Procedures section by reheating the carton of oranges as packed with thermocouples in place. Although it was possible to apply heat until the oranges were at almost the same steady state temperature, the amount of time required to accomplish this was excessive in terms of productivity as well as physiological maintenance of the oranges. Deteriorated oranges required the entire orange carton to be emptied and filled with a new load of oranges which had been prepared with thermocouples. The model required an initial product temperature. The actual initial temperature at each thermocouple location could have been applied to the heat transfer model but this was not practical from a realistic standpoint. Therefore the average initial experimental temperature was used in the heat transfer model. The standard deviation was such that the experimental and model thermocouple initial temperatures could be slightly different up to 3.3 C (6 F). This of course altered the cooling curve of the model and produced a poorer comparison of experimental to model data.

Over the several hours required for a complete test run, during periods of occasional unsupervised or nonmonitored periods, the air temperature control had a tendency to drift if not manually corrected periodically. The model air

temperature was of course constant and did not allow for variations during the test.

Because of a desire for increased accuracy 36-gauge thermocouple wire was used. However, this wire was very fine and easily damaged. Thermocouples were calibrated using an ice bath but at high temperatures slight variations between thermocouples were evident. Also the sheer number of thermocouple leads presented a requirement for diligent attention to detail.

Convective Heat Transfer Coefficient

The convective heat transfer coefficient reported by Baird and Gaffney (1976) for cooling of oranges in beds was used in this study. This coefficient appeared to be satisfactory for the accomplishment of the current project objectives. For the thermocouples nearest the air inlet(s) for all boundary conditions, the slope of the cooling response curves for the experimental and predicted data were nearly the same. The value of the convective coefficient was concluded to be a reasonable approximation of the actual convective coefficient. More work on developing a heat transfer coefficient for air flow through cartons is needed.

In order to investigate the sensitivity of the model, one test was evaluated with the convective heat transfer coefficient halved and another with the coefficient doubled. The model was very sensitive to this forced change. Therefore if an improved value for the convective heat

transfer coefficient were developed the model would provide a better fit of the experimental data.

A tendency in modeling research is to force the model to fit the experimental data. For this study a similar approach was not appropriate since the development and verification of a heat transfer model was not the objective. Future work will involve the development of a much improved heat transfer model which compliments the porous media flow technique and finite element method. The major emphasis was the evaluation of the porous media technique for this type problem.

Variable Porosity

As mentioned in the Procedures section, preliminary evaluation of the model did not apply variable porosity. The fit of the experimental data was very poor. The method for determining and applying the variable porosity was also discussed above. Additional experimental work is needed in order to provide the necessary variable porosity data for various size and shape cartons, with various product packing arrangements. The indication observed was that with an increased porosity in the region of from one to three diameters from each interior carton surface, that more air would flow through these regions and less air would flow though the center core region. This would improve the fit of the predicted temperature response to that of the experimental temperature response.

Approximate Model Thermocouple Location

Future efforts should be made to design the element size and grid location to allow the physical location of the thermocouples to coincide with the center of a single element. This would provide a more reliable method for comparing experimental and numerical temperature response.

Use of the average of the eight elements surrounding the physical location of the thermocouple was practical from a standpoint of uniform calculation procedure, but this tended to lessen the effect of the variable porosity in the row of elements adjacent to the carton walls.

A detailed comparison of element temperature response in the same physical region as the thermocouple revealed that one or two elements could have been selected which would have provided a very close fit of the experimental temperature response. This extra effort would have provided a better fit of the experimental data but was not deemed practical since the analysis required tedious and time consuming manual review.

Experimental Versus Predicted Temperature Response

From the temperature response plots for Boundary Condition 1-1 for the experimental and predicted data presented in Figures 45 to 47 and 49 to 51 above, four thermocouples were selected from each of the three layers for direct comparison of the temperature response curves of predicted versus experimental data. For the left side of

the third layer, thermocouples 31 and 35 were selected and plotted in Figure 52, while thermocouples 44 and 45 were plotted in Figure 53. For the left side of the second layer, thermocouples 23 and 24 were selected and plotted in Figure 54, while thermocouples 26 and 29 were plotted in Figure 55. For the left side of the bottom layer, thermocouples 1 and 9 were selected and plotted in Figure 56, while thermocouples 14 and 15 were plotted in Figure 57.

The same temperature response curves comparing each of the experimental plots in Appendix E to the corresponding calculated plots in Appendix F are presented in Appendix G.

In order to consolidate the large amount of data for each test into a more compact presentation, a regression plot of the predicted temperature versus the experimental temperature was formed for each thermocouple location for three specific times. The time periods were selected to consider the early, middle, and late stages of each test. The only temperatures not plotted were for the locations for which the thermocouple malfunctioned. For Boundary Condition 1-1 and test times of 3, 7, and 11 hours, the regression plot is presented in Figure 58. Regression plots for the other 11 test are presented in Appendix H.

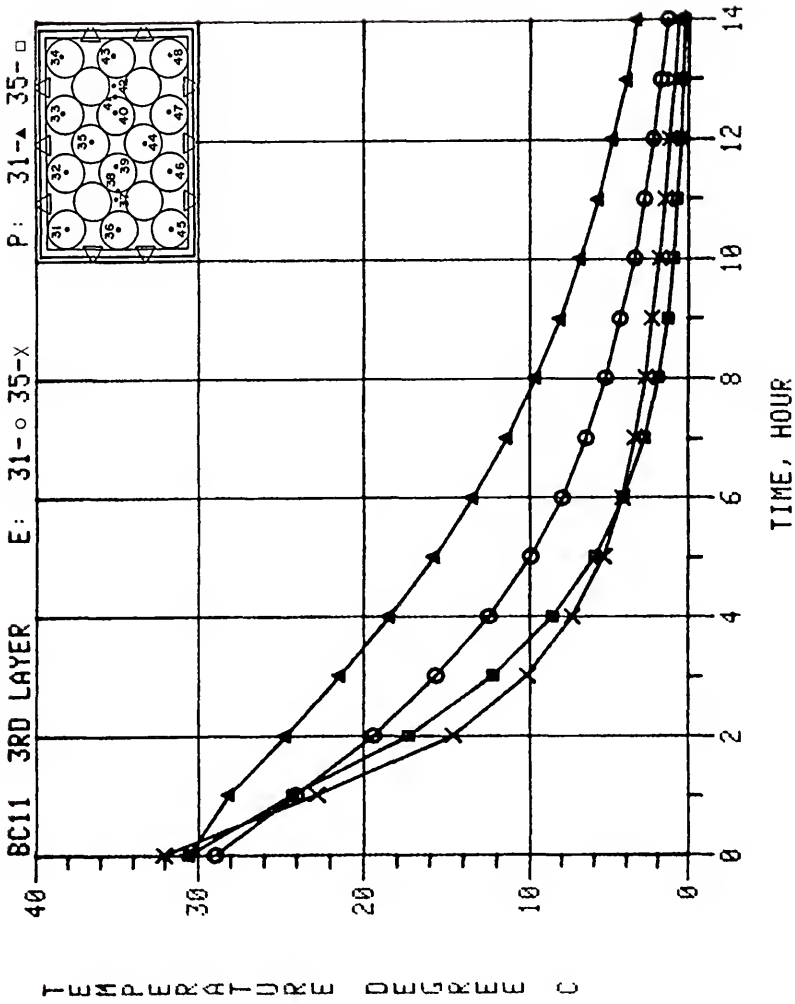


Figure 52. Predicted versus experimental data for Boundary Condition 1-1, 3rd layer thermocouples 31 and 35.

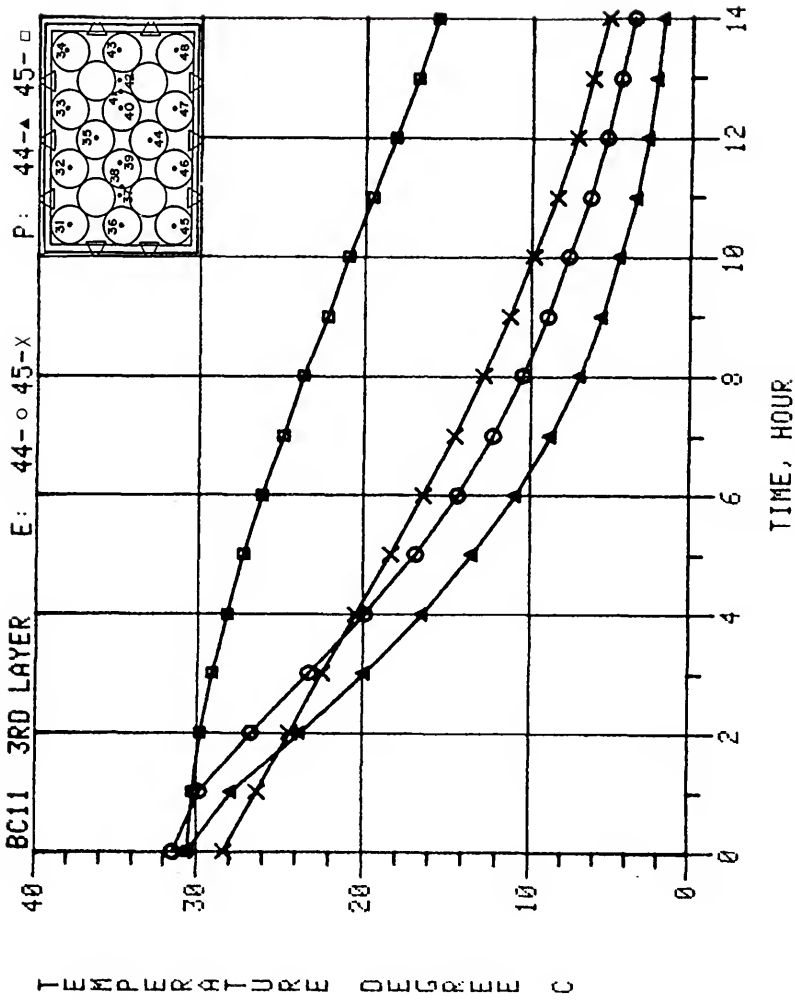


Figure 53. Predicted versus experimental data for Boundary Condition 1-1, 3rd layer thermocouples 44 and 45.

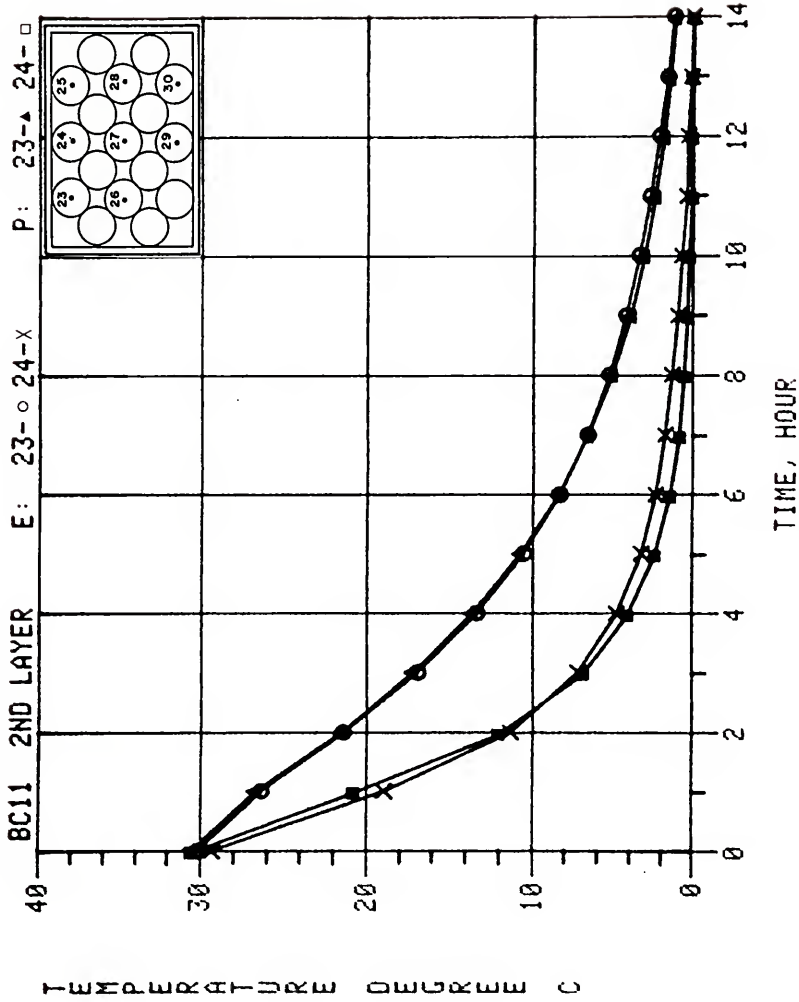


Figure 54. Predicted versus experimental data for Boundary Condition 1-1, 2nd layer thermocouples 23 and 24.

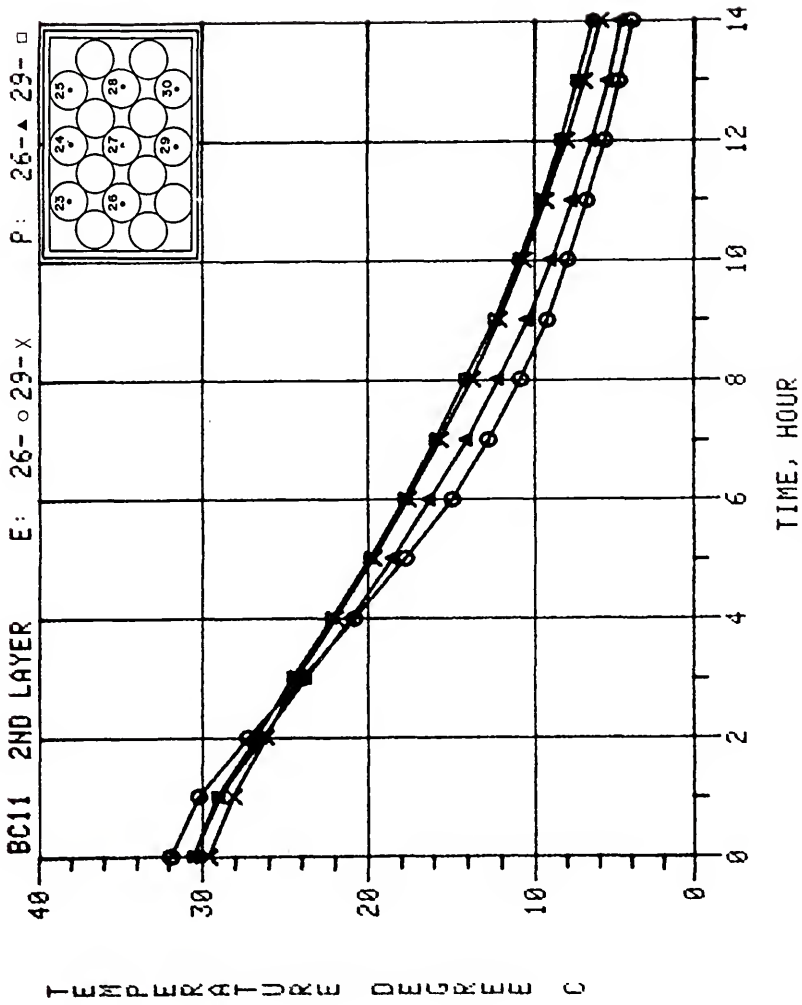


Figure 55. Predicted versus experimental data for Boundary Condition 1-1, 2nd layer thermocouples 26 and 29.

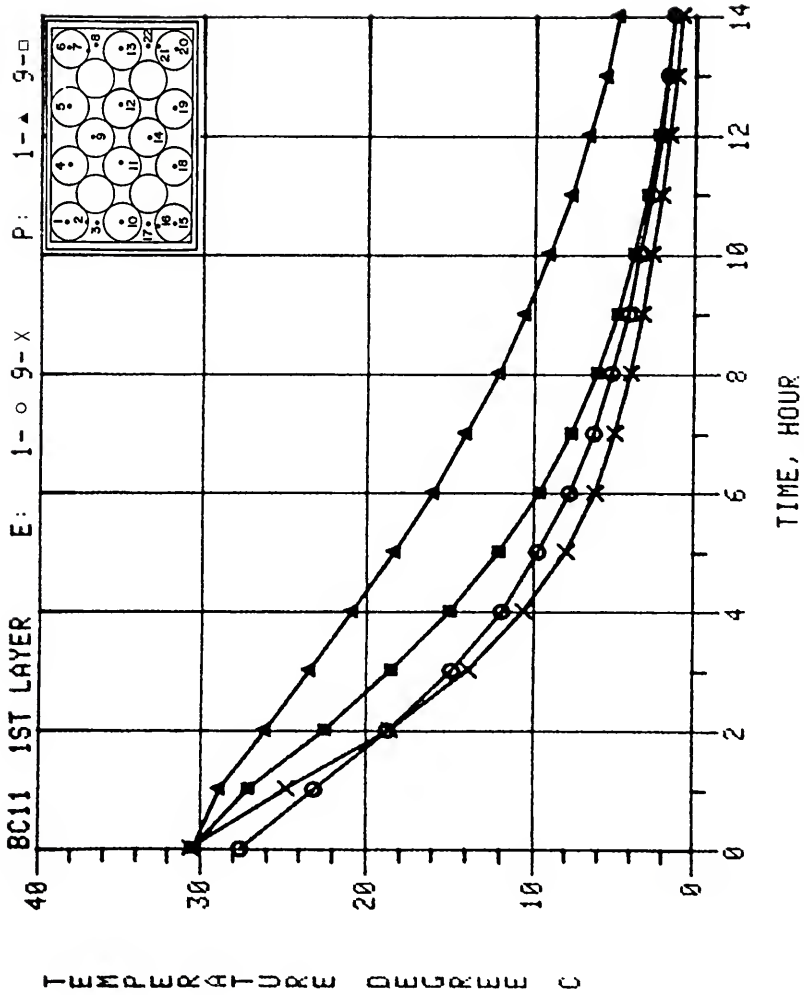


Figure 56. Predicted versus experimental data for Boundary Condition 1-1, 1st layer thermocouples 1 and 9.

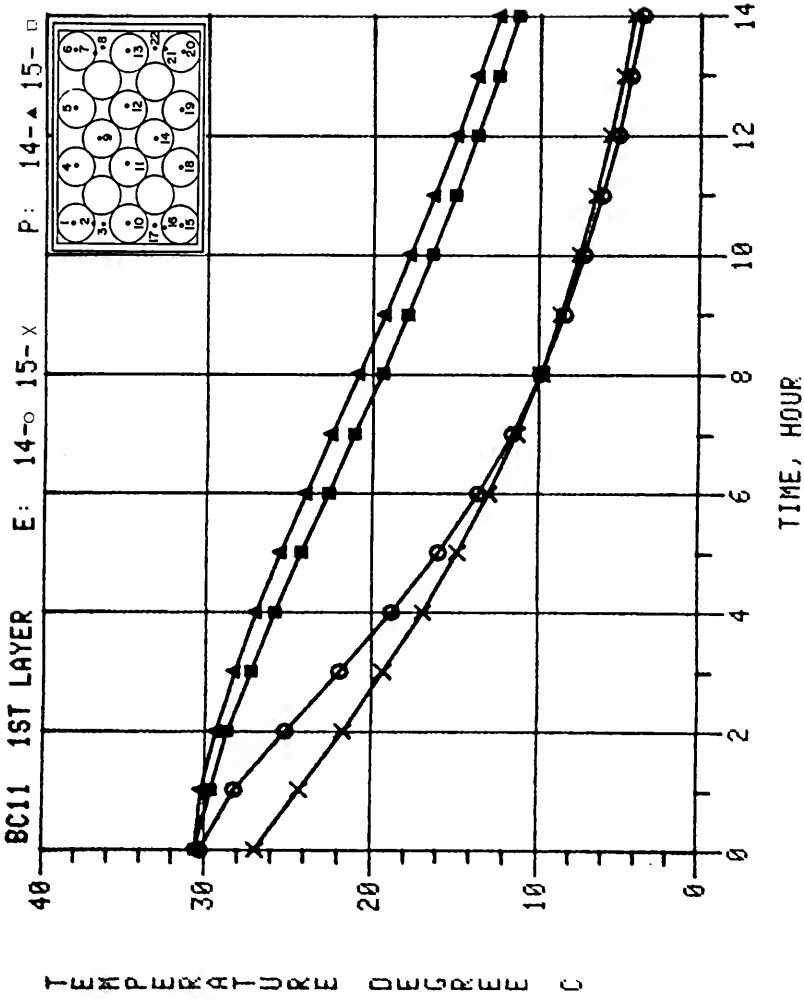


Figure 57. Predicted versus experimental data for Boundary Condition 1-1, 1st layer thermocouples 14 and 15.

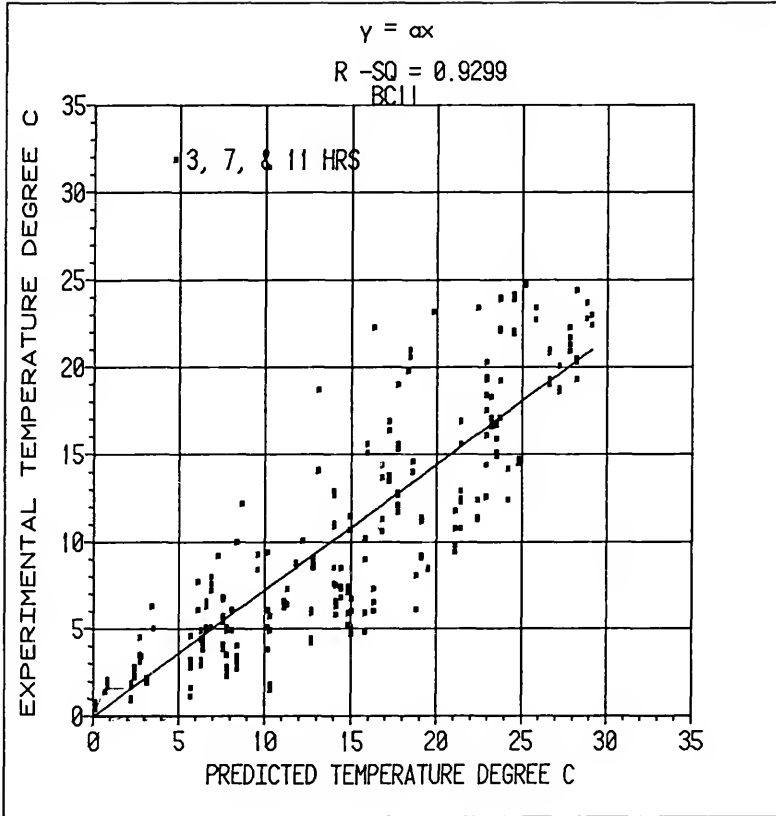


Figure 58. Regression plot of the predicted temperature versus the experimental temperature for Boundary Condition 1-1 and test times of 3, 7, and 11 hours.

Several trends exhibited by all twelve boundary conditions are evident in Figures 52 through Figure 58. The first trend indicated that the experimental and predicted cooling responses fit better for oranges in the center or core of the orange carton than for oranges near the walls of the orange carton. The oranges in the corners exhibited the worse fit. In Figure 52, for the corner thermocouple 31 the in the left half of the third layer of oranges, the experimental data indicated more cooling than the predicted data while the experimental and predicted temperature responses for thermocouple 35 were in better agreement. Although not presented, the experimental and predicted cooling responses of thermocouple 32, which was near the inlet on the third layer adjacent to the inlet wall, were almost the same.

In Figure 53, the predicted cooling response for thermocouple 44, which was in the core of the orange carton, indicates more rapid cooling for the predicted cooling response than for the experimental cooling response. Thermocouple 45 located in the corner on the third layer of oranges exhibits a much slower predicted cooling response than the experimental cooling response. This follows the first general trend but also illustrates a second general trend. The predicted cooling response for oranges adjacent to the carton walls illustrated a increasingly poorer fit to the experimental temperature response as the distance from the air inlet increased. For example, the difference

between predicted and experimental temperature responses in the third layer for thermocouple 45 was much worse than the poor fit of thermocouple 31.

In Figure 54, the predicted versus experimental data for thermocouples 23 and 24, which were in the second layer of oranges adjacent to the inlet carton, was nearly identical. This was also a general trend. In Figure 55, the predicted versus experimental data for second layer thermocouples 26 and 29 also exhibited close agreement. Thermocouple 26 was in the core of the orange carton near but not adjacent to the carton wall while thermocouple 29 was adjacent to the outlet carton wall just below the outlet vent.

In Figure 56, thermocouples 1 and 9 are adjacent to the bottom of the orange carton. As expected, the agreement between predicted and experimental temperature responses is not close. The predicted and experimental temperature responses of thermocouple 9 are in closer agreement than those of the corner thermocouple 1.

In Figure 57, the agreement between the predicted and experimental temperature responses for thermocouples 14 and 15 is poorer than for thermocouples 1 and 9. Thermocouples 14 and 15 are also adjacent to the bottom of the orange carton but the distance from the air inlet is greater. Thermocouple 15 is further away from the air inlet than any other thermocouple considered.

In Figure 58, the regression plot of the predicted temperature versus the experimental temperature illustrates that the predicted data underestimated the cooling response of the oranges in the experimental carton. If the predicted and experimental data were identical, the data fitting line would have a slope of 1.0, while the actual data exhibited a slope of 0.75. However, as indicated above, one data trend was a better fit for oranges in the core region of the carton. A review of Figure 16 reveals that the thermocouples located in the oranges adjacent to the orange carton walls far exceed the number of thermocouples located in oranges in the core region of the orange carton.

Another general trend that was observed concerned the high and low flow rates for each of the six boundary conditions. The higher flow rates produced improved agreement between the predicted and experimental temperature responses.

The more extreme boundary conditions of Boundary Conditions 1, 4, 5, and 6 (single air inlet) produced poorer agreement between experimental and predicted temperature responses than the more uniform Boundary Conditions 2 and 3 (two and three air inlets, respectively). Future improvements will allow for better evaluation of even the most extreme boundary conditions. However, the majority of orange cartons currently used contain at least two vent holes on each side of the carton.

The predicted temperature response within the orange carton compared well with the experimental temperature response in some regions while in other regions the comparison ranged from good to poor. One distinction that should be reiterated is that the experimental data was obtained for oranges packed in an experimental carton while the flow data calculated by ANSYS was from finite elements representing a porous media. Also the heat transfer procedures were adapted from the study of bed cooling of oranges and this conservative heat transfer analysis underestimated the cooling of the oranges.

Several factors were discussed above which no doubt effected the degree of fit of predicted to experimental temperature response. The factors discussed in the Experimental Error section were no doubt important. The difference in experimental and predicted initial temperatures can be seen in Figures 56 and 57 for thermocouples 1 and 15, respectively. The convective heat transfer coefficient was also obtained from the study of bed cooling of oranges and probably produced some variation between the predicted and experimental temperature response. However, the most significant factors were the variable porosity and the approximate location of the thermocouples to represent the temperature of the model. Better knowledge of the variable porosity within the orange carton and improvements in the element size and location along with development of an improved heat transfer program,

incorporating an appropriate convective heat transfer coefficient, will substantially increase the accuracy of the technique used.

SUMMARY

This study involved the application of several existing procedures in a unique way. A commercial finite element solution package was used to determine the pressure and velocity distribution for air flow through a porous media. This procedure was first verified by comparing the results from the porous media analysis with the results of research related to the pressure and velocity distributions for air flow through two- and three-dimensional grain bins. Based upon favorable results the porous media technique was used to model research concerning the pressure loss through oranges in bulk and oranges packed in simulated orange cartons. Again favorable results led to the evaluation of the pressure and velocity distributions of air flow through a three-dimensional orange carton using the finite element porous media flow analysis. However, the air flow field for the orange carton was not known and not readily measurable using current instrumentation. In order to verify the porous media analysis for this problem an indirect method of comparison was developed. The experimental temperature was measured for twelve different test conditions for oranges packed in an experimental orange carton and cooled using an experimental cooling facility. The flow and boundary conditions used for the twelve tests

were used as input data for the porous media flow model to calculate the pressure and velocity distributions for the oranges packed in the experimental orange carton. The absolute permeability and the visco-inertial input parameters were calculated using experimentally determined modified Ergun product coefficients, orange diameter, and variable porosity. An existing heat transfer program was modified to incorporate the calculated velocity distribution and provided a predicted temperature response. Considerable work was involved after obtaining the calculated velocity distribution in order to determine the predicted temperature response. The experimental and predicted temperature responses for the twelve tests were compared and this comparison was used to indirectly evaluate the flow information calculated by the porous media flow analysis. Although several areas for improvement were noted, the porous media flow analysis was found to provide adequate information if variable porosity within the orange carton was considered. The objective of this study was not to develop a comprehensive model to evaluate the many variables related to forced air cooling and to predict the cooling response of produce packed in containers. However, the porous media flow model and heat transfer model have the capability to solve the pressure and velocity distributions and temperature response for any size and shape carton, any size, number and location of vent holes, any packing arrangement, any size (close to spherical) fruit or

vegetable, for any air flow rate and cooling temperature typically encountered in the field. Suggested improvements will produce a very valuable tool for designing systems for cooling fruits and vegetables in cartons.

SUGGESTIONS FOR FUTURE WORK

The pressure loss through the vent holes of the carton was not critical for the current study. Further development is necessary in order to expand the current analysis to multiple carton configurations. A method was discussed for determining an orifice type pressure loss through the vent openings and should be further evaluated.

The selection of element size and location can be improved to provide smaller elements in regions of high pressure gradients and flow rates. The size and location of the elements should also be selected such that the approximate location of the experimental thermocouples is near the center of the element in order to enhance the comparison of the experimental and predicted temperature response data.

Additional evaluation of the variable porosity for various packing configurations and container sizes is required in order to have the necessary input data for the porous media flow model. This research will require use of methodology for determining porosity available in the literature. Not only should this type research provide the variable porosity near the walls and constant porosity in the center of the containers for various size and shaped fruits and vegetables, but the increased porosity due to

compaction near the top of the container should be addressed.

A heat transfer model should be developed which is more adapted to the finite element package and porous media flow model in order to better apply the pressure and velocity data fields to calculate more accurate temperature response data. This could involve the design of a custom system for extending the heat transfer analysis or could involve coordination with commercial software developers in an effort to increase the capability of the available porous media flow models by incorporation of a heat transfer analysis. More advanced software could model the pressure-velocity and heat-mass transfer simultaneously. For either approach, additional research is needed to establish the representative convective heat transfer coefficient.

APPLICATION OF RESULTS

The method presented for determining an orifice type pressure loss through the vent openings provides an approach for modeling the total pressure drop across individual or multiple configurations of fruits or vegetables packed in shipping containers. An understanding of the total pressure drop is required to expand the procedures of the current study.

The procedures outlined for using porous media flow analysis to determine the velocity and pressure distributions for forced air cooling of fruits and vegetables packed in shipping containers have been presented in sufficient detail that others interested in this subject can apply the procedures without the requirement to perform the extensive background work necessary to validate the current study.

The heat transfer program was developed as a means of predicting the temperature response to indirectly evaluate the flow calculations of the porous media model by comparing the predicted temperature response to the experimental temperature response. The porous media flow model and heat transfer model require further development as noted above. However, the two models have the capability to predict the pressure and velocity distributions and temperature response

for a wide range of variables for forced air cooling fruits and vegetables packed in shipping containers. As a comparative tool, the models can be used to evaluate the design of containers (size and shape), vent arrangements, vent size and number, air flow rates, cooling temperature, packing arrangements, and other variables. The time required for cooling, the pressure drop through the orange carton, and the energy requirements for air movement and cooling are but a few of the important parameters which could be obtained. These evaluations can be accomplished without the requirement for extensive experimental verifications.

After suggested improvements to the porous media flow model and the heat transfer model have been accomplished, then the industry which provides the general commercial computer programs should be encouraged and solicited to provide the needed software for widespread adoption and application.

The experimental data used to verify the porous media flow model contains valuable information that can be used in other aspects beyond the scope of the current work for extended analysis of the various cooling variables. One important use of this data would be for further development of the heat transfer model.

CONCLUSIONS

The pressure drops produced by the air inlets of packing containers are significant and must be included in the study of the pressure and velocity distribution for air flow through multiple configurations of fruits and vegetables packed in containers.

Because of the small overall dimensions of the packing containers, the variance of the porosity or voidage adjacent to the container walls must be included in the porous media flow analysis of air flow through fruits or vegetables packed in containers.

The increased porosity or voidage adjacent to the inside surface of container due to compaction of the fruit or vegetable must also be considered in the porous media flow analysis of air flow through fruits and vegetables packaged in containers.

Commercial finite element solution software packages present promise for studying porous media flow problems such as forced air cooling of fruits and vegetables and air flow through grain storage structures. These software packages provide workers interested in porous media flow analysis applied to agricultural crops with a tool that allows a uniform solution technique and easy comparison of results.

The porous media flow analysis procedure is feasible for the study of forced air cooling of fruits and vegetables packed in shipping containers. The finite boundary conditions of the shipping containers require the use of variable porosity. This technique provides a valuable tool for establishing the pressure and velocity distributions which are needed to model the heat transfer during cooling and storage of fresh fruits and vegetables packed in shipping containers.

APPENDIX A
METHOD FOR ACCURATELY POSITIONING THERMOCOUPLES
IN FRUITS AND VEGETABLES

Materials

1. 36 gage thermocouples with teflon insulation.
2. 16 gage intravenous catheter with hypodermic needle.

Procedures

1. Insert needle with hollow teflon catheter through fruit (Figure A-1).
2. Remove needle, leaving catheter in place.
3. Thread thermocouple wire through catheter from opposite end (Figure A-1).
4. Remove catheter from fruit, leaving thermocouple wire in place (Figure A-1).
5. Mark thermocouple wire at desired penetration depth with "whiteout" (Figure A-1).
6. Cut piece of catheter to a length of 1.6 mm (1/16 inch) shorter than the desired penetration depth for thermocouple.
7. Slide short piece of catheter over needle and position needle in fruit with end of needle at desired location of thermocouple junction (Figure A-1).
8. Slide short piece of catheter on needle into fruit (Figure A-2).
9. Remove needle from fruit.
10. Slide thermocouple wire into catheter until "whiteout" mark is at surface of fruit. Junction will now extend 1.6 mm (1/16 inch) beyond end of catheter (Figure A-2).

11. Pull on other end of thermocouple wire to remove loop. (Figure A-2).
12. Seal wound at surface with vinyl cement.

Comments

1. The above method allows precise placement of the thermocouple junction, prevents the thermocouple from moving, and provides a reverse temperature gradient in the thermocouple wire to minimize conduction errors.
2. For surface thermocouple, complete steps 1 through 4 to run thermocouple wire through edge of fruit near surface. Then use hypodermic needle to make a hole along surface, thread thermocouple into hole until it comes out other side and then pull back on wire until junction is right at surface (Figure A-2).

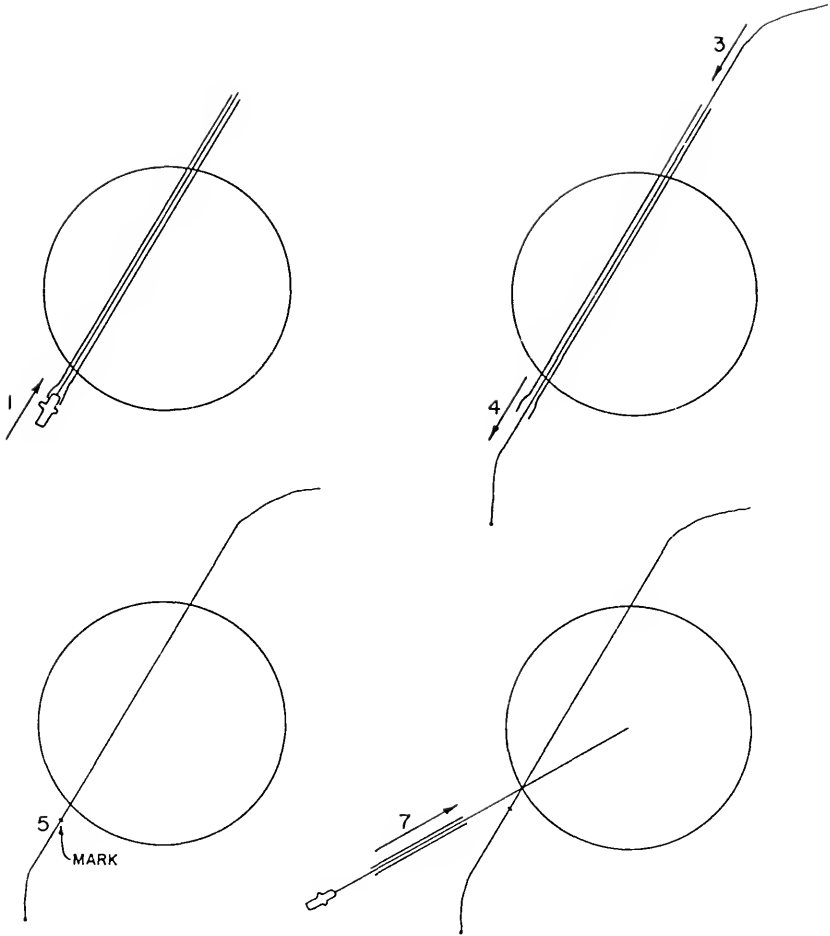


Figure A-1. Thermocouple positioning, part 1.

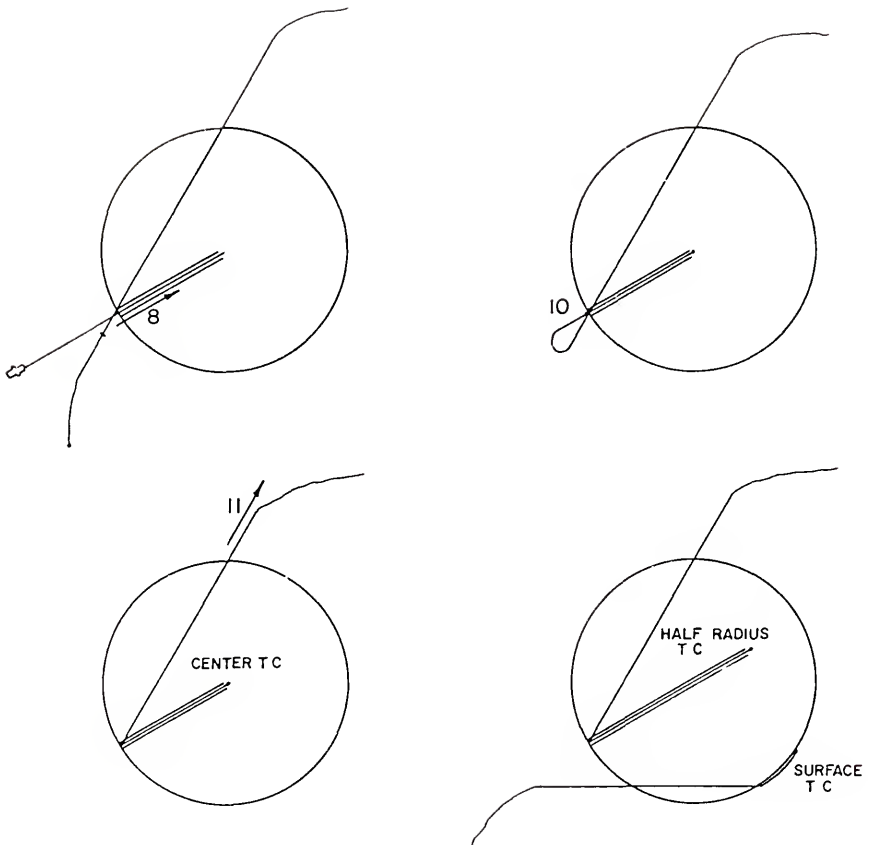


Figure A-2. Thermocouple positioning, part 2.

APPENDIX B
FORTRAN PROGRAMS AND DATA FILES

Examples of the fortran programs and portions of the input and output data files used to calculate the predicted temperature response from the ANSYS calculated flow field data are shown on the following pages.

The programs and data files varied depending upon the boundary condition under consideration. For example the "Heat-Do" program for Boundary Condition 3 was much more complex than one of the single inlet boundary conditions. Boundary Condition 3 required 12 do-loops compared to 4 do-loops for Boundary Condition 1, in order to insure the element calculations proceeded in the same pattern as the air flow within the experimental carton of oranges.

This information is provided to illustrate the work required to transform the ANSYS flow output data into the predicted temperature response.

1	0.55306341E-04	0.381E-01	0.381E-01	0.381E-01	0.476
2	0.36870894E-04	0.254E-01	0.381E-01	0.381E-01	0.607
3	0.36870894E-04	0.254E-01	0.381E-01	0.381E-01	0.607
4	0.36870894E-04	0.254E-01	0.381E-01	0.381E-01	0.607
5	0.36870894E-04	0.254E-01	0.381E-01	0.381E-01	0.607
6	0.36870894E-04	0.254E-01	0.381E-01	0.381E-01	0.607
7	0.36870894E-04	0.254E-01	0.381E-01	0.381E-01	0.607
8	0.36870894E-04	0.254E-01	0.381E-01	0.381E-01	0.607
9	0.36870894E-04	0.254E-01	0.381E-01	0.381E-01	0.607
10	0.36870894E-04	0.254E-01	0.381E-01	0.381E-01	0.607
11	0.36870894E-04	0.254E-01	0.381E-01	0.381E-01	0.607
12	0.36870894E-04	0.254E-01	0.381E-01	0.381E-01	0.607
13	0.36870894E-04	0.254E-01	0.381E-01	0.381E-01	0.607
14	0.55306341E-04	0.381E-01	0.381E-01	0.381E-01	0.476
15	0.36870894E-04	0.381E-01	0.381E-01	0.254E-01	0.607
16	0.24580596E-04	0.254E-01	0.381E-01	0.254E-01	0.450
17	0.24580596E-04	0.254E-01	0.381E-01	0.254E-01	0.450
18	0.24580596E-04	0.254E-01	0.381E-01	0.254E-01	0.450
19	0.24580596E-04	0.254E-01	0.381E-01	0.254E-01	0.450
20	0.24580596E-04	0.254E-01	0.381E-01	0.254E-01	0.450
21	0.24580596E-04	0.254E-01	0.381E-01	0.254E-01	0.450
22	0.24580596E-04	0.254E-01	0.381E-01	0.254E-01	0.450
23	0.24580596E-04	0.254E-01	0.381E-01	0.254E-01	0.450
24	0.24580596E-04	0.254E-01	0.381E-01	0.254E-01	0.450
25	0.24580596E-04	0.254E-01	0.381E-01	0.254E-01	0.450
26	0.24580596E-04	0.254E-01	0.381E-01	0.254E-01	0.450
27	0.24580596E-04	0.254E-01	0.381E-01	0.254E-01	0.450
28	0.36870894E-04	0.381E-01	0.381E-01	0.254E-01	0.607
29	0.36870894E-04	0.381E-01	0.381E-01	0.254E-01	0.607
30	0.24580596E-04	0.254E-01	0.381E-01	0.254E-01	0.450
31	0.24580596E-04	0.254E-01	0.381E-01	0.254E-01	0.450
32	0.24580596E-04	0.254E-01	0.381E-01	0.254E-01	0.450
33	0.24580596E-04	0.254E-01	0.381E-01	0.254E-01	0.450
34	0.24580596E-04	0.254E-01	0.381E-01	0.254E-01	0.450
35	0.24580596E-04	0.254E-01	0.381E-01	0.254E-01	0.450
36	0.24580596E-04	0.254E-01	0.381E-01	0.254E-01	0.450
37	0.24580596E-04	0.254E-01	0.381E-01	0.254E-01	0.450
38	0.24580596E-04	0.254E-01	0.381E-01	0.254E-01	0.450
39	0.24580596E-04	0.254E-01	0.381E-01	0.254E-01	0.450
40	0.24580596E-04	0.254E-01	0.381E-01	0.254E-01	0.450
41	0.24580596E-04	0.254E-01	0.381E-01	0.254E-01	0.450
42	0.36870894E-04	0.381E-01	0.381E-01	0.254E-01	0.607
43	0.36870894E-04	0.381E-01	0.381E-01	0.254E-01	0.607
44	0.24580596E-04	0.254E-01	0.381E-01	0.254E-01	0.450
45	0.24580596E-04	0.254E-01	0.381E-01	0.254E-01	0.450
46	0.24580596E-04	0.254E-01	0.381E-01	0.254E-01	0.450
47	0.24580596E-04	0.254E-01	0.381E-01	0.254E-01	0.450
48	0.24580596E-04	0.254E-01	0.381E-01	0.254E-01	0.450

Figure B-1. Portion of input data file "Dimensions" which lists for each element from left to right, the number, volume, x, y, and z dimensions, and the porosity.

1	0.13136630E-01	0.35446030E-02	-0.10460746E-01	0.71119369E-02
2	0.27845898E-01	0.18457967E-01	-0.18748981E-01	0.86967595E-02
3	0.31189748E-01	0.28083696E-01	-0.12617884E-01	0.49895299E-02
4	0.40155323E-01	0.38172135E-01	-0.11550922E-01	0.46812707E-02
5	0.47646405E-01	0.46503919E-01	-0.93479493E-02	0.44923531E-02
6	0.52010678E-01	0.51427632E-01	-0.64737679E-02	0.42894714E-02
7	0.53029239E-01	0.52735418E-01	-0.38278263E-02	0.40526060E-02
8	0.51427839E-01	0.51245522E-01	-0.18986817E-02	0.38876944E-02
9	0.48117065E-01	0.47961938E-01	-0.68986619E-03	0.37984957E-02
10	0.43766038E-01	0.43600884E-01	0.21097834E-04	0.37984879E-02
11	0.38729853E-01	0.38530682E-01	0.45844885E-03	0.38958733E-02
12	0.33116470E-01	0.32831803E-01	0.83461974E-03	0.42516732E-02
13	0.27667418E-01	0.26018282E-01	0.28779293E-02	0.89583804E-02
14	0.70412564E-02	0.50845045E-02	0.27946560E-03	0.48630242E-02
15	0.36179769E-01	0.16919507E-02	-0.15814228E-01	0.32496510E-01
16	0.11771360E-01	0.40565005E-02	-0.42493161E-02	0.10200639E-01
17	0.13720002E-01	0.78561604E-02	-0.41453962E-02	0.10456332E-01
18	0.15879730E-01	0.11495278E-01	-0.39942775E-02	0.10201478E-01
19	0.17869211E-01	0.14588486E-01	-0.33426077E-02	0.97627736E-02
20	0.19005972E-01	0.16490341E-01	-0.23654524E-02	0.91487845E-02
21	0.19123691E-01	0.17046247E-01	-0.14124400E-02	0.85525440E-02
22	0.18392745E-01	0.16499676E-01	-0.69054700E-03	0.80979576E-02
23	0.17139615E-01	0.15236218E-01	-0.22707853E-03	0.78468143E-02
24	0.15624232E-01	0.13548048E-01	0.49351569E-04	0.77823249E-02
25	0.14056519E-01	0.11637091E-01	0.20531178E-03	0.78817309E-02
26	0.12738163E-01	0.97175116E-02	0.28335661E-03	0.82310674E-02
27	0.12128366E-01	0.87276299E-02	0.11647981E-03	0.84209369E-02
28	0.26289937E-01	0.91179813E-02	-0.19507544E-02	0.24580842E-01
29	0.40326126E-01	0.17919548E-02	-0.60290752E-02	0.39832594E-01
30	0.14028327E-01	0.48712143E-02	-0.28921387E-02	0.12833580E-01
31	0.15838895E-01	0.78844664E-02	-0.37330317E-02	0.13220071E-01
32	0.17540803E-01	0.11149251E-01	-0.36112103E-02	0.13051173E-01
33	0.18875924E-01	0.13894897E-01	-0.30432026E-02	0.12408515E-01
34	0.19583484E-01	0.15660938E-01	-0.22182048E-02	0.11546750E-01
35	0.19529893E-01	0.16273578E-01	-0.13953744E-02	0.10707021E-01
36	0.18846206E-01	0.15904048E-01	-0.74963400E-03	0.10033590E-01
37	0.17732058E-01	0.14823433E-01	-0.30652044E-03	0.97261382E-02
38	0.16379990E-01	0.13280337E-01	-0.28594254E-04	0.95883223E-02
39	0.14967670E-01	0.11491257E-01	0.12420285E-03	0.95099289E-02
40	0.13654654E-01	0.97255559E-02	0.13922741E-03	0.95835148E-02
41	0.12372167E-01	0.82344992E-02	-0.66512795E-04	0.92335861E-02
42	0.31212037E-01	0.41622473E-02	-0.37025766E-03	0.30931050E-01
43	0.42772152E-01	0.23618740E-02	-0.34212288E-02	0.42569634E-01
44	0.15010850E-01	0.56571666E-02	-0.16418023E-02	0.13806758E-01
45	0.16500589E-01	0.82048869E-02	-0.21919155E-02	0.14147253E-01
46	0.17903370E-01	0.10906360E-01	-0.21639520E-02	0.14032080E-01
47	0.19016739E-01	0.13256693E-01	-0.18530477E-02	0.13507874E-01
48	0.19625337E-01	0.14842868E-01	-0.13772628E-02	0.12765041E-01
49	0.19670165E-01	0.15515254E-01	-0.87848573E-03	0.12059044E-01
50	0.19197603E-01	0.15322065E-01	-0.44679567E-03	0.11557796E-01

Figure B-2. Portion of input data file "Data" which lists for each element from left to right, the number, total velocity and x, y, and z component velocities.

```

OPEN(UNIT=5,FILE='DIMENSIONS',STATUS='OLD')
OPEN(UNIT=6,FILE='DATA-61C',STATUS='OLD')
OPEN(UNIT=7,FILE='HEAT-MASS-61C',STATUS='NEW')
C   OPEN(UNIT=8,FILE='CHECK-AREA-DC',STATUS='NEW')
C*** CONSTANT PHYSICAL AND THERMAL PROPERTIES ***
C*** AIR PROPERTIES SET FOR 50 F ON 27 APR 87
C*** AIR DENSITY, KG/M**3
      DENSITY = 1.24
C*** AIR VISCOSITY, KG/M-S
      VISCOSITY = 1.762E-5
C*** AIR THERMAL CONDUCTIVITY, W/M C
      CONDTY = 2.50E-2
C*** NUSSELT-REYNOLDS COEFFICIENT CONSTANT, A
      CA = 1.17
C*** NUSSELT-REYNOLDS EXPONENT CONSTANT, B
      CB = 0.529
C*** DIAMETER OF ORANGES, M
      DIA = 0.0735
C*** APR 14, 1987: MADE POROSITY EQUAL TO ONE TO REMOVE FROM HTC EQN.
C*** POROSITY OF PACKING PATTERN, DECIMAL PERCENT
C   POROSITY = 0.435
C   POROSITY = 1.000
C*** ELEMENT NUMBER COUNTER
      I = 0
C
1   CONTINUE
C***INPUT ELEMENT PHYSICAL DIMENSIONS AND VELOCITY DATA ***
      READ(5,77,END=999)VOL,X,Y,Z
      READ(6,78,END=999)VT,VX,VY,VZ
C
C*** CALCULATE CROSS-SECTIONAL AREA PERBENDICULAR FLOW DIRECTION, M**2
      AX = VOL/X
      AY = VOL/Y
      AZ = VOL/Z
C
C*** CALCULATE THE COMPONENT MASS FLOW RATE (AT CENTROID), KG/S
      FLOWX = DENSITY*AX*VX
      FLOWY = DENSITY*AY*VY
      FLOWZ = DENSITY*AZ*VZ
C

```

Figure B-3. Fortran program "Data-Reduction" which was used to calculate convective heat transfer coefficient and x, y, and z component mass flow rates at the centroid.

```
C*** CALCULATE THE CONVECTIVE HEAT TRANSFER COEFFICIENT, W/M**2-S-C
      HTC = CA*CONDY/DIA*(DENSITY*POROSITY*VT*DIA/VISCOSITY)**CB
      I = I + 1
C
      WRITE(7,79)I,HTC,FLOWX,FLOWY,FLOWZ,X,Y,Z
C
      WRITE(8,80)I,AX,AY,AZ
77     FORMAT(10X,E14.8,3(2X,E9.3))
78     FORMAT(8X,4(1X,E15.8))
79     FORMAT(2X,I4,2X,1PE15.4,2X,1PE15.4,2X,1PE15.4,2X,1PE15.4,2X,
*1PE15.4,2X,1PE15.4,2X,1PE15.4)
80     FORMAT(I4,3E11.3)
      GO TO 1
999   CONTINUE
C*** NOTE: CHECK FORMAT OF INPUT VELOCITY FIELD
      CLOSE(5)
      CLOSE(6)
      CLOSE(7)
C
      CLOSE(8)
      STOP
      END
```

1	3.7074E+00	6.3803E-06	-1.8829E-05	1.2801E-05
2	5.5165E+00	3.3224E-05	-2.2739E-05	1.0436E-05
3	5.8576E+00	5.0551E-05	-1.5141E-05	5.9874E-06
4	6.6953E+00	6.8710E-05	-1.3861E-05	5.6175E-06
5	7.3293E+00	8.3707E-05	-1.1218E-05	5.3908E-06
6	7.6772E+00	9.2570E-05	-7.7685E-06	5.1474E-06
7	7.7563E+00	9.4924E-05	-4.5934E-06	4.8631E-06
8	7.6315E+00	9.2242E-05	-2.2784E-06	4.6652E-06
9	7.3676E+00	8.6331E-05	-8.2784E-07	4.5582E-06
10	7.0073E+00	7.8481E-05	2.5317E-08	4.5582E-06
11	6.5685E+00	6.9355E-05	5.5014E-07	4.6750E-06
12	6.0463E+00	5.9097E-05	1.0015E-06	5.1020E-06
13	5.4978E+00	4.6833E-05	3.4535E-06	1.0750E-05
14	2.6656E+00	9.1521E-06	5.0304E-07	8.7534E-06
15	6.3360E+00	2.0303E-06	-1.8977E-05	5.8494E-05
16	3.4983E+00	4.8678E-06	-3.3994E-06	1.2241E-05
17	3.7936E+00	9.4274E-06	-3.3163E-06	1.2548E-05
18	4.0986E+00	1.3794E-05	-3.1954E-06	1.2242E-05
19	4.3627E+00	1.7506E-05	-2.6741E-06	1.1715E-05
20	4.5073E+00	1.9788E-05	-1.8924E-06	1.0979E-05
21	4.5221E+00	2.0455E-05	-1.1299E-06	1.0263E-05
22	4.4298E+00	1.9800E-05	-5.5244E-07	9.7175E-06
23	4.2675E+00	1.8283E-05	-1.8166E-07	9.4162E-06
24	4.0636E+00	1.6258E-05	3.9481E-08	9.3388E-06
25	3.8425E+00	1.3964E-05	1.6425E-07	9.4581E-06
26	3.6474E+00	1.1661E-05	2.2668E-07	9.8773E-06
27	3.5540E+00	1.0473E-05	9.3184E-08	1.0105E-05
28	5.3513E+00	1.0942E-05	-2.3409E-06	4.4245E-05
29	6.7103E+00	2.1503E-06	-7.2349E-06	7.1698E-05
30	3.8384E+00	5.8454E-06	-2.3137E-06	1.5400E-05
31	4.0930E+00	9.4613E-06	-2.9864E-06	1.5864E-05
32	4.3201E+00	1.3379E-05	-2.8890E-06	1.5661E-05
33	4.4910E+00	1.6674E-05	-2.4346E-06	1.4890E-05
34	4.5793E+00	1.8793E-05	-1.7746E-06	1.3856E-05
35	4.5726E+00	1.9528E-05	-1.1163E-06	1.2848E-05
36	4.4873E+00	1.9085E-05	-5.9971E-07	1.2100E-05
37	4.3449E+00	1.7788E-05	-2.4522E-07	1.1671E-05
38	4.1664E+00	1.5936E-05	-2.2875E-08	1.1506E-05
39	3.9723E+00	1.3789E-05	9.9362E-08	1.1508E-05
40	3.7840E+00	1.1671E-05	1.1138E-07	1.1500E-05
41	3.5916E+00	9.8814E-06	-5.3210E-08	1.1080E-05
42	5.8598E+00	4.9947E-06	-4.4431E-07	5.5676E-05
43	6.9226E+00	2.8342E-06	-4.1055E-06	7.6625E-05
44	3.9784E+00	6.7886E-06	-1.3134E-06	1.6568E-05
45	4.1826E+00	9.8458E-06	-1.7535E-06	1.6977E-05
46	4.3671E+00	1.3088E-05	-1.7312E-06	1.6838E-05
47	4.5087E+00	1.5908E-05	-1.4824E-06	1.6209E-05
48	4.5845E+00	1.7811E-05	-1.1018E-06	1.5318E-05
49	4.5900E+00	1.8618E-05	-7.0279E-07	1.4471E-05

Figure B-4. Portion of input/output data file "Heat-Mass" which lists for each element, the number, the convective heat transfer coefficient and x, y, and z component mass flow rates at the centroid.

```

      DIMENSION FLOWX(1400),FLOWY(1400),FLOWZ(1400),FLOWX1(1400),
      *FLOWX2(1400),FLOWY1(1400),FLOWY2(1400),FLOWZ1(1400),FLOWZ2(1400),
      *X(1400),Y(1400),Z(1400)
      OPEN(UNIT=5,FILE='HEAT-MASS-61C',STATUS='OLD')
      OPEN(UNIT=6,FILE='MASSFLOW-61C',STATUS='NEW')
C      OPEN(UNIT=7,FILE='CHECK-IT-61C',STATUS='NEW')
      OPEN(UNIT=8,FILE='DIMENSIONS',STATUS='OLD')
C***INPUT FLOW DATA
      DO 9 I=1,700,1
        READ(5,5) FLOWX(I), FLOWY(I), FLOWZ(I)
        5 FORMAT(27X,3E17,6)
        READ(8,6) X(I), Y(I), Z(I)
        6 FORMAT(24X,3E11.3)
        9 Continue
C***CHECK INPUT FLOW DATA
C      DO 11 I=1,14,1
C      WRITE(7,8) I, FLOWX(I), FLOWY(I), FLOWZ(I), X(I),Y(I),Z(I)
        8 FORMAT(2X,I4,3E17.6,3E11.3)
        11 Continue
C***FLOW ACROSS ELEMENT FACE IN X-DIRECTION
C (Note: This includes false values for walls and BC values)
      DO 19 II=1,699,1
        A=X(II)/(X(II+1)+X(II))
        FLOWX2(II)=(1-A)*FLOWX(II) + A*FLOWX(II+1)
        FLOWX1(II+1)=FLOWX2(II)
        19 CONTINUE
C***FLOW ACROSS FACE IS ZERO EXCEPT FOR BC VALUES
      DO 29 III=1,687,14
        FLOWX1(III)=0.0
        29 CONTINUE
      DO 39 IIII=14,700,14
        FLOWX2(IIII)=0.0
        39 CONTINUE
C*** BC VALUES
C***FLOW ACROSS ELEMENT FACE IN Y-DIRECTION
C (Note: This includes false values for walls)
      DO 49 J=1,560,1
        B=Y(J)/(Y(J+140)+Y(J))
        FLOWY2(J)=(1-B)*FLOWY(J) + B*FLOWY(J+140)
        FLOWY1(J+140)=FLOWY2(J)
        49 CONTINUE
C***FLOW ACROSS FACE IS ZERO
      DO 59 JJ=1,140,1
        FLOWY1(JJ)=0.0
        59 CONTINUE

```

Figure B-5. Fortran program "Flow-Wall" which was used to calculate x, y, and z component mass flow rates across the face of each element.

```

C***FLOW ACROSS ELEMENT FACE IN Z-DIRECTION
C (Note: This includes false values for walls and BC values)
  DO 79 K=1,686,1
    C=Z(K)/(Z(K+14) + Z(K))
    FLOWZ2(K)=(1-C)*FLOWZ(K) + C*FLOWZ(K+14)
    FLOWZ1(K+14)=FLOWZ2(K)
  79 CONTINUE
C***FLOW ACROSS FACE IS ZERO EXCEPT FOR BC VALUES
  DO 109 KK=1,5,1
    DO 89 KKK=(1+((KK-1)*140)),(14+((KK-1)*140)),1
      FLOWZ1(KKK)=0.0
    89 CONTINUE
    DO 99 KKKK=(127+((KK-1)*140)),(140+((KK-1)*140)),1
      FLOWZ2(KKKK)=0.0
    99 CONTINUE
  109 CONTINUE
C
C*** BC VALUES
C
C***NODE 829 FOR BC #6-1C CORRECTED 8, 26 MAY 87
C BC829=0.00000000
C FLOWZ1(571)=0.382670E-3 OLD
  FLOWZ1(564)=0.492492E-3
C FLOWZ1(572)=0.382330E-3 OLD
  FLOWZ1(563)=0.492508E-3
C FLOWZ1(711)=BC837
C FLOWZ1(712)=BC837
C***NODE 987 FOR BC #6-1C
C BC979=0.000000
  FLOWZ2(697)=FLOWZ2(564)
  FLOWZ2(698)=FLOWZ2(563)
C FLOWZ2(829)=BC979
C FLOWZ2(830)=BC979
C
  DO 129 N=1,700
    WRITE(6,120) N, FLOWX1(N), FLOWX2(N), FLOWY1(N), FLOWY2(N), FLOWZ1(N),
      *FLOWZ2(N)
  120 FORMAT(2X, I4, 6E17.6)
  129 CONTINUE
C** NOTE CHANGE TO BC INPUT FOR BC STUDIED
  CLOSE(5)
  CLOSE(6)
C  CLOSE(7)
  CLOSE(8)
  STOP
  END

```

Figure B-5--continued

1	0.000000E+00	0.224865E-04	0.000000E+00	-0.600208E-04	0.000000E+00	0.402168E-04
2	0.224865E-04	0.418875E-04	0.000000E+00	-0.256724E-04	0.000000E+00	0.115190E-04
3	0.418875E-04	0.596305E-04	0.000000E+00	-0.261150E-04	0.000000E+00	0.992376E-05
4	0.596305E-04	0.762085E-04	0.000000E+00	-0.252562E-04	0.000000E+00	0.959220E-05
5	0.762085E-04	0.881385E-04	0.000000E+00	-0.204148E-04	0.000000E+00	0.918532E-05
6	0.881385E-04	0.937470E-04	0.000000E+00	-0.137058E-04	0.000000E+00	0.864636E-05
7	0.937470E-04	0.935830E-04	0.000000E+00	-0.779428E-05	0.000000E+00	0.810304E-05
8	0.935830E-04	0.892865E-04	0.000000E+00	-0.380894E-05	0.000000E+00	0.769658E-05
9	0.892865E-04	0.824060E-04	0.000000E+00	-0.150090E-05	0.000000E+00	0.747300E-05
10	0.824060E-04	0.739189E-04	0.000000E+00	-0.191947E-06	0.000000E+00	0.742656E-05
11	0.739189E-04	0.642260E-04	0.000000E+00	0.580044E-06	0.000000E+00	0.754486E-05
12	0.642260E-04	0.529650E-04	0.000000E+00	0.115654E-05	0.000000E+00	0.796718E-05
13	0.529650E-04	0.317606E-04	0.000000E+00	0.244082E-05	0.000000E+00	0.103630E-04
14	0.317606E-04	0.000000E+00	0.000000E+00	0.150298E-05	0.000000E+00	0.300484E-04
15	0.000000E+00	0.373280E-05	0.000000E+00	-0.197822E-04	0.000000E+00	0.650960E-04
16	0.373280E-05	0.171470E-05	0.000000E+00	-0.810556E-05	0.115190E-04	0.138205E-04
17	0.171470E-05	0.116107E-04	0.000000E+00	-0.916732E-05	0.992376E-05	0.142060E-04
18	0.116107E-04	0.156500E-04	0.000000E+00	-0.905416E-05	0.959220E-05	0.139515E-04
19	0.156500E-04	0.186470E-04	0.000000E+00	-0.733724E-05	0.918532E-05	0.133025E-04
20	0.186470E-04	0.201215E-04	0.000000E+00	-0.492060E-05	0.864636E-05	0.124175E-04
21	0.201215E-04	0.201275E-04	0.000000E+00	-0.276466E-05	0.810304E-05	0.115555E-04
22	0.201275E-04	0.190415E-04	0.000000E+00	-0.132924E-05	0.769658E-05	0.109087E-04
23	0.190415E-04	0.172705E-04	0.000000E+00	-0.468016E-06	0.747300E-05	0.105436E-04
24	0.172705E-04	0.151110E-04	0.000000E+00	0.194304E-07	0.742656E-05	0.104224E-04
25	0.151110E-04	0.128125E-04	0.000000E+00	0.288810E-06	0.754486E-05	0.104830E-04
26	0.128125E-04	0.110670E-04	0.000000E+00	0.412332E-06	0.796718E-05	0.106986E-04
27	0.110670E-04	0.106606E-04	0.000000E+00	0.169346E-06	0.103630E-04	0.105926E-04
28	0.106606E-04	0.000000E+00	0.000000E+00	-0.154608E-05	0.300484E-04	0.499605E-04
29	0.000000E+00	0.436736E-05	0.000000E+00	-0.112664E-04	0.650960E-04	0.746163E-04
30	0.436736E-05	0.765335E-05	0.000000E+00	-0.514078E-05	0.138205E-04	0.159940E-04
31	0.765335E-05	0.114202E-04	0.000000E+00	-0.586746E-05	0.142060E-04	0.164205E-04
32	0.114202E-04	0.150265E-04	0.000000E+00	-0.578142E-05	0.139515E-04	0.162495E-04
33	0.150265E-04	0.177335E-04	0.000000E+00	-0.483148E-05	0.133025E-04	0.155495E-04
34	0.177335E-04	0.191605E-04	0.000000E+00	-0.340654E-05	0.124175E-04	0.145870E-04
35	0.191605E-04	0.193605E-04	0.000000E+00	-0.209172E-05	0.115555E-04	0.136595E-04
36	0.193605E-04	0.184365E-04	0.000000E+00	-0.110412E-05	0.109087E-04	0.129845E-04
37	0.184365E-04	0.168420E-04	0.000000E+00	-0.455268E-06	0.105436E-04	0.126170E-04
38	0.168420E-04	0.148425E-04	0.000000E+00	-0.619524E-07	0.104224E-04	0.124915E-04
39	0.148425E-04	0.127300E-04	0.000000E+00	0.149155E-06	0.104830E-04	0.124880E-04
40	0.127300E-04	0.107762E-04	0.000000E+00	0.186674E-06	0.106886E-04	0.124330E-04
41	0.107762E-04	0.792672E-05	0.000000E+00	-0.618986E-07	0.105926E-04	0.120780E-04
42	0.792672E-05	0.000000E+00	0.000000E+00	-0.385054E-06	0.499605E-04	0.601245E-04
43	0.000000E+00	0.520684E-05	0.000000E+00	-0.651648E-05	0.746163E-04	0.762820E-04
44	0.520684E-05	0.831720E-05	0.000000E+00	-0.280074E-05	0.159840E-04	0.163810E-04
45	0.831720E-05	0.114669E-04	0.000000E+00	-0.320034E-05	0.164205E-04	0.167470E-04
46	0.114669E-04	0.144980E-04	0.000000E+00	-0.314792E-05	0.162495E-04	0.166500E-04
47	0.144980E-04	0.168595E-04	0.000000E+00	-0.267484E-05	0.155495E-04	0.161435E-04
48	0.168595E-04	0.182145E-04	0.000000E+00	-0.198470E-05	0.145870E-04	0.154345E-04
49	0.182145E-04	0.185020E-04	0.000000E+00	-0.125528E-05	0.136595E-04	0.147855E-04
50	0.185020E-04	0.178440E-04	0.000000E+00	-0.631946E-06	0.129845E-04	0.143720E-04
51	0.178440E-04	0.164450E-04	0.000000E+00	-0.167248E-06	0.126170E-04	0.142285E-04
52	0.164450E-04	0.145380E-04	0.000000E+00	0.142786E-06	0.124915E-04	0.142645E-04
53	0.145380E-04	0.123640E-04	0.000000E+00	0.312314E-06	0.124880E-04	0.143300E-04
54	0.123640E-04	0.101352E-04	0.000000E+00	0.335474E-06	0.124330E-04	0.142610E-04
55	0.101352E-04	0.715288E-05	0.000000E+00	0.151143E-06	0.120780E-04	0.139850E-04
56	0.715288E-05	0.000000E+00	0.000000E+00	0.406702E-06	0.601245E-04	0.680430E-04
57	0.000000E+00	0.595526E-05	0.000000E+00	-0.345808E-05	0.762820E-04	0.737260E-04
58	0.595526E-05	0.895735E-05	0.000000E+00	-0.138672E-05	0.163810E-04	0.155440E-04
59	0.895735E-05	0.115555E-04	0.000000E+00	-0.159416E-05	0.167470E-04	0.158365E-04

Figure B-6. Portion of input/output data file "Mass-Flow" which lists for each element, the number, the x, y, and z component mass flow rates across the face of each element.

```

      DIMENSION FLOWXINL(700),FLOWXINR(700),FLOWYINU(700),FLOWYINO(700),
      *FLOWZINB(700),FLOWZINF(700),FLOWX1(700),FLOWX2(700),FLOWY1(700),
      *FLOWY2(700),FLOWZ1(700),FLOWZ2(700),ITXINL(700),ITXINR(700),
      *ITYINU(700),ITYINO(700),ITZINB(700),ITZINF(700)
      OPEN(UNIT=5,FILE='MASSFLOW-61C',STATUS='OLD')
      OPEN(UNIT=6,FILE='MASS-TEMP-61C',STATUS='NEW')
C     OPEN(UNIT=7,FILE='CHECK-IT-61C',STATUS='NEW')
C***INPUT FLOW DATA
      DO 9 I=1,700,1
      READ(5,5) FLOWX1(I),FLOWX2(I),FLOWY1(I),FLOWY2(I),FLOWZ1(I),
      *FLOWZ2(I)
      5 FORMAT(6X,6E17.6)
      9 Continue
C***CHECK INPUT FLOW DATA
C     DO 11 I=1,14,1
C     WRITE(7,8) I,FLOWX1(I),FLOWX2(I),FLOWY1(I),FLOWY2(I),FLOWZ1(I),
C     *FLOWZ2(I)
C     8 FORMAT(2X,I4,6E17.6)
      11 Continue
C***FLOW INTO ELEMENT IN X-DIRECTION
C     (Note: This includes flow from right and/or left or none.)
      DO 19 II=1,700,1
      IF((FLOWX1(II).LE. 0.0).AND.(FLOWX2(II).LT. 0.0)) THEN
      FLOWXINR(II)=ABS(FLOWX2(II))
      ITXINR(II)=II+1
      FLOWXINL(II)=0.0
      ITXINL(II)=II
      ELSE IF((FLOWX1(II).GT. 0.0).AND.(FLOWX2(II).GE. 0.0)) THEN
      FLOWXINL(II)=ABS(FLOWX1(II))
      ITXINL(II)=II-1
      FLOWXINR(II)=0.0
      ITXINR(II)=II
      ELSE IF((FLOWX1(II).GT. 0.0).AND.(FLOWX2(II).LT. 0.0)) THEN
      FLOWXINL(II)=ABS(FLOWX1(II))
      ITXINL(II)=II-1
      FLOWXINR(II)=ABS(FLOWX2(II))
      ITXINR(II)=II+1
      ELSE IF((FLOWX1(II).LE. 0.0).AND.(FLOWX2(II).GE. 0.0)) THEN
      FLOWXINL(II)=0.0
      ITXINL(II)=II
      FLOWXINR(II)=0.0
      ITXINR(II)=II
      END IF
      19 CONTINUE

```

Figure B-7. Fortran program "Temp-ID" which was used to calculate mass flow rates entering each element.

```

C***FLOW INTO ELEMENT IN Y-DIRECTION
C (Note: This includes flow from above and/or below or none)
  DO 49 J=1,700,1
    IF((FLOWY1(J),LE, 0.0).AND.(FLOWY2(J),LT, 0.0)) THEN
      FLOWYINO(J)=ABS(FLOWY2(J))
      ITYINO(J)=J+140
      FLOWYINU(J)=0.0
      ITYINU(J)=J
    ELSE IF((FLOWY1(J),GT, 0.0).AND.(FLOWY2(J),GE, 0.0)) THEN
      FLOWYINO(J)=ABS(FLOWY1(J))
      ITYINU(J)=J-140
      FLOWYINO(J)=0.0
      ITYINO(J)=J
    ELSE IF((FLOWY1(J),GT, 0.0).AND.(FLOWY2(J),LT, 0.0)) THEN
      FLOWYINU(J)=ABS(FLOWY1(J))
      ITYINU(J)=J-140
      FLOWYINO(J)=ABS(FLOWY2(J))
      ITYINO(J)=J+140
    ELSE IF((FLOWY1(J),LE, 0.0).AND.(FLOWY2(J),GE, 0.0)) THEN
      FLOWYINU(J)=0.0
      ITYINU(J)=J
      FLOWYINO(J)=0.0
      ITYINO(J)=J
    END IF
  49 CONTINUE
C***FLOW INTO ELEMENT IN Z-DIRECTION
C (Note: This includes flow from front and/or back or none)
  DO 79 K=1,700,1
    IF((FLOWZ1(K),LE, 0.0).AND.(FLOWZ2(K),LT, 0.0)) THEN
      FLOWZINF(K)=ABS(FLOWZ2(K))
      ITZINF(K)=K+14
      FLOWZINB(K)=0.0
      ITZINB(K)=K
    ELSE IF((FLOWZ1(K),GT, 0.0).AND.(FLOWZ2(K),GE, 0.0)) THEN
      FLOWZINB(K)=ABS(FLOWZ1(K))
      ITZINB(K)=K-14
      FLOWZINF(K)=0.0
      ITZINF(K)=K
    ELSE IF((FLOWZ1(K),GT, 0.0).AND.(FLOWZ2(K),LT, 0.0)) THEN
      FLOWZINB(K)=ABS(FLOWZ1(K))
      ITZINB(K)=K-14
      FLOWZINF(K)=ABS(FLOWZ2(K))
      ITZINF(K)=K+14
    ELSE IF((FLOWZ1(K),LE, 0.0).AND.(FLOWZ2(K),GE, 0.0)) THEN
      FLOWZINB(K)=0.0
      ITZINB(K)=K
      FLOWZINF(K)=0.0
      ITZINF(K)=K
    END IF
  79 CONTINUE

```

Figure B-7--continued

```

C*** DEFINE TEMPERATURE IDENTIFIER FOR BC ELEMENTS
C*** FOR BC-1-1 BC-1-2 BC-3-1 BC-3-2 BC-4-1 BC-4-2 BC-5-1 BC-5-2
C   ITZINB(567)=0
C   ITZINB(568)=0
C*** FOR BC-2-1 BC-2-2 BC-3-1 BC-3-2
C   ITZINB(563)=0
C   ITZINB(564)=0
C   ITZINB(571)=0
C   ITZINB(572)=0
C*** FOR BC-6-1
C   ITZINB(571)=0
C   ITZINB(572)=0
C*** FOR BC-6-2
C   ITZINB(563)=0
C   ITZINB(564)=0
C
C   DO 129 N=1,700
C     WRITE(6,120) N, FLOWXINL(N), FLOWXINR(N), FLOWYINU(N), FLOWYIND(N),
C       *FLOWZINB(N), FLOWZINF(N), ITXINL(N), ITXINR(N), ITYINU(N), ITYIND(N),
C       *ITZINB(N), ITZINF(N)
C   120 FORMAT(2X, I4, 6E17.6, 6I5)
C   129 CONTINUE
C*** NOTE CHANGE IT*IN*() VALUES FOR BC STUDIED
C   CLOSE(5)
C   CLOSE(6)
C   STOP
C   END

```

2	0.224865E-04	0.000000E+00	0.000000E+00	0.256724E-04	0.000000E+00	0.000000E+00	1	2	2	142
3	0.418875E-04	0.000000E+00	0.000000E+00	0.261150E-04	0.000000E+00	0.000000E+00	2	3	3	143
4	0.596305E-04	0.000000E+00	0.000000E+00	0.252562E-04	0.000000E+00	0.000000E+00	3	4	4	144
5	0.762685E-04	0.000000E+00	0.000000E+00	0.204148E-04	0.000000E+00	0.000000E+00	4	5	5	145
6	0.881385E-04	0.000000E+00	0.000000E+00	0.137058E-04	0.000000E+00	0.000000E+00	5	6	6	146
7	0.937470E-04	0.000000E+00	0.000000E+00	0.779428E-05	0.000000E+00	0.000000E+00	6	7	7	147
8	0.938330E-04	0.000000E+00	0.000000E+00	0.380894E-05	0.000000E+00	0.000000E+00	7	8	8	148
9	0.892865E-04	0.000000E+00	0.000000E+00	0.150099E-05	0.000000E+00	0.000000E+00	8	9	9	149
10	0.824660E-04	0.000000E+00	0.000000E+00	0.191947E-06	0.000000E+00	0.000000E+00	9	10	10	150
11	0.739180E-04	0.000000E+00	0.000000E+00	0.000000E+00	0.000000E+00	0.000000E+00	10	11	11	1
12	0.642260E-04	0.000000E+00	0.000000E+00	0.000000E+00	0.000000E+00	0.000000E+00	11	12	12	1
13	0.529650E-04	0.000000E+00	0.000000E+00	0.000000E+00	0.000000E+00	0.000000E+00	12	13	13	1
14	0.317660E-04	0.000000E+00	0.000000E+00	0.000000E+00	0.000000E+00	0.000000E+00	13	14	14	1
15	0.000000E+00	0.000000E+00	0.000000E+00	0.197822E-04	0.000000E+00	0.000000E+00	15	15	15	155
16	0.373280E-05	0.000000E+00	0.000000E+00	0.810556E-05	0.115190E-04	0.000000E+00	15	16	16	156
17	0.714760E-05	0.000000E+00	0.000000E+00	0.916732E-05	0.992376E-05	0.000000E+00	16	17	17	157
18	0.116107E-04	0.000000E+00	0.000000E+00	0.905416E-05	0.959220E-05	0.000000E+00	17	18	18	158
19	0.156500E-04	0.000000E+00	0.000000E+00	0.733724E-05	0.918532E-05	0.000000E+00	18	19	19	159
20	0.186470E-04	0.000000E+00	0.000000E+00	0.492060E-05	0.364536E-05	0.000000E+00	19	20	20	160
21	0.201215E-04	0.000000E+00	0.000000E+00	0.276466E-05	0.810304E-05	0.000000E+00	20	21	21	161
22	0.201275E-04	0.000000E+00	0.000000E+00	0.132924E-05	0.769658E-05	0.000000E+00	21	22	22	162
23	0.190415E-04	0.000000E+00	0.000000E+00	0.468016E-06	0.747300E-05	0.000000E+00	22	23	23	163
24	0.172705E-04	0.000000E+00	0.000000E+00	0.000000E+00	0.742456E-05	0.000000E+00	23	24	24	1
25	0.151110E-04	0.000000E+00	0.000000E+00	0.000000E+00	0.754486E-05	0.000000E+00	24	25	25	1
26	0.128125E-04	0.000000E+00	0.000000E+00	0.000000E+00	0.796718E-05	0.000000E+00	25	26	26	1
27	0.110670E-04	0.000000E+00	0.000000E+00	0.000000E+00	0.103630E-04	0.000000E+00	26	27	27	1
28	0.106660E-04	0.000000E+00	0.000000E+00	0.156608E-05	0.300484E-04	0.000000E+00	27	28	28	168
29	0.000000E+00	0.000000E+00	0.000000E+00	0.112644E-04	0.650960E-04	0.000000E+00	29	29	29	169
30	0.436736E-05	0.000000E+00	0.000000E+00	0.514078E-05	0.138205E-04	0.000000E+00	30	30	30	170
31	0.765335E-05	0.000000E+00	0.000000E+00	0.586946E-05	0.142064E-04	0.000000E+00	30	31	31	171
32	0.114202E-04	0.000000E+00	0.000000E+00	0.578142E-05	0.139515E-04	0.000000E+00	31	32	32	172
33	0.150265E-04	0.000000E+00	0.000000E+00	0.483148E-05	0.133025E-04	0.000000E+00	32	33	33	173
34	0.177335E-04	0.000000E+00	0.000000E+00	0.346354E-05	0.124175E-04	0.000000E+00	33	34	34	174
35	0.191605E-04	0.000000E+00	0.000000E+00	0.209172E-05	0.115555E-04	0.000000E+00	34	35	35	175
36	0.193065E-04	0.000000E+00	0.000000E+00	0.110412E-05	0.109087E-04	0.000000E+00	35	36	36	176
37	0.184345E-04	0.000000E+00	0.000000E+00	0.455268E-06	0.105436E-04	0.000000E+00	36	37	37	177
38	0.168420E-04	0.000000E+00	0.000000E+00	0.619524E-07	0.104224E-04	0.000000E+00	37	38	38	178
39	0.148625E-04	0.000000E+00	0.000000E+00	0.000000E+00	0.104830E-04	0.000000E+00	38	39	39	35
40	0.127300E-04	0.000000E+00	0.000000E+00	0.000000E+00	0.106886E-04	0.000000E+00	39	40	40	2
41	0.107762E-04	0.000000E+00	0.000000E+00	0.618986E-07	0.105925E-04	0.000000E+00	40	41	41	181
42	0.792672E-05	0.000000E+00	0.000000E+00	0.385054E-06	0.499305E-04	0.000000E+00	41	42	42	182
43	0.000000E+00	0.000000E+00	0.000000E+00	0.651648E-05	0.741615E-04	0.000000E+00	43	43	43	183
44	0.526684E-05	0.000000E+00	0.000000E+00	0.280074E-05	0.159840E-04	0.000000E+00	43	44	44	184
45	0.831720E-05	0.000000E+00	0.000000E+00	0.320034E-05	0.164205E-04	0.000000E+00	44	45	45	185
46	0.116689E-04	0.000000E+00	0.000000E+00	0.314792E-05	0.162495E-04	0.000000E+00	45	46	46	186
47	0.144980E-04	0.000000E+00	0.000000E+00	0.267484E-05	0.155495E-04	0.000000E+00	46	47	47	187
48	0.168595E-04	0.000000E+00	0.000000E+00	0.198470E-05	0.145870E-04	0.000000E+00	47	48	48	188
49	0.182145E-04	0.000000E+00	0.000000E+00	0.125528E-05	0.136595E-04	0.000000E+00	48	49	49	189
50	0.185020E-04	0.000000E+00	0.000000E+00	0.631946E-06	0.129845E-04	0.000000E+00	49	50	50	190
51	0.178440E-04	0.000000E+00	0.000000E+00	0.167248E-06	0.126170E-04	0.000000E+00	50	51	51	191
52	0.164450E-04	0.000000E+00	0.000000E+00	0.000000E+00	0.124915E-04	0.000000E+00	51	52	52	3
53	0.145380E-04	0.000000E+00	0.000000E+00	0.000000E+00	0.124880E-04	0.000000E+00	52	53	53	3
54	0.123440E-04	0.000000E+00	0.000000E+00	0.000000E+00	0.124330E-04	0.000000E+00	53	54	54	4
55	0.101352E-04	0.000000E+00	0.000000E+00	0.000000E+00	0.120780E-04	0.000000E+00	54	55	55	4
56	0.715288E-05	0.000000E+00	0.000000E+00	0.000000E+00	0.601245E-04	0.000000E+00	55	56	56	4
57	0.000000E+00	0.000000E+00	0.000000E+00	0.345808E-05	0.762820E-04	0.000000E+00	57	57	57	197
58	0.595526E-05	0.000000E+00	0.000000E+00	0.138692E-05	0.163810E-04	0.000000E+00	57	58	58	198
59	0.895735E-05	0.000000E+00	0.000000E+00	0.159416E-05	0.167470E-04	0.000000E+00	58	59	59	199
60	0.116555E-04	0.000000E+00	0.000000E+00	0.155995E-05	0.166500E-04	0.000000E+00	59	60	60	200
61	0.142440E-04	0.000000E+00	0.000000E+00	0.133744E-05	0.161435E-04	0.000000E+00	60	61	61	201
62	0.163235E-04	0.000000E+00	0.000000E+00	0.965680E-06	0.154345E-04	0.000000E+00	61	62	62	202
63	0.176250E-04	0.000000E+00	0.000000E+00	0.524176E-06	0.147855E-04	0.000000E+00	62	63	63	203
64	0.180215E-04	0.000000E+00	0.000000E+00	0.968484E-07	0.143720E-04	0.000000E+00	63	64	64	204
65	0.175170E-04	0.000000E+00	0.000000E+00	0.000000E+00	0.142285E-04	0.000000E+00	64	65	65	5
66	0.162120E-04	0.000000E+00	0.000000E+00	0.000000E+00	0.142665E-04	0.000000E+00	65	66	66	5

Figure B-8. Portion of input/output data file "Mass-Temp" which lists for each element, the number, the mass flow rates entering the x (left and right), y (bottom and top), and z (back and front) faces of each element along with the corresponding temperature identification label.

C*** THIS IS A HEAT TRANSFER PROGRAM TO CALCULATE THE COOLING RESPONSE
 C*** OF ORANGES PACKED IN CARTONS USING POROUS MEDIA FLOW DATA GENERATED
 C*** BY ANSYS.

C

```

    DIMENSION PRSNT(11,700),PREC(11,700),VOL(11),TPSECA(11),TFLSUB(11)
    *,PRSPAV(700),PREPAV(700),HTC(700),T(0:700),FLXINL(700),FLXINR(700)
    *,FLYINU(700),FLYINO(700),FLZINB(700),FLZINF(700),ITXINL(700),
    *ITXINR(700),ITYINU(700),ITYINO(700),ITZINB(700),ITZINF(700),
    *VOLE(700),POROTY(700)
    INTEGER TIMINC
  
```

C

```

C***NOTE: ADJUST DATA-IN-1 AND DATA-IN-2*****
    OPEN(UNIT=5,FILE='DATA-IN-1',STATUS='OLD')
    OPEN(UNIT=6,FILE='DATA-IN-2',STATUS='OLD')
    OPEN(UNIT=7,FILE='HEAT-MASS-61C',STATUS='OLD')
    OPEN(UNIT=8,FILE='DIMENSIONS',STATUS='OLD')
    OPEN(UNIT=9,FILE='MASS-TEMP-61C',STATUS='OLD')
    OPEN(UNIT=10,FILE='CHECK-ERROR-DO-61C',STATUS='NEW')
    OPEN(UNIT=11,FILE='TEMP-RESP-61C',STATUS='NEW')
  
```

C

```

    INPUT DATA
    READ(5,1) ALPHA,CONDY,RADIUS,SHA,SHP,DENP
    1 FORMAT(2X,E9,3,2X,F5,3,2X,E10,4,2X,E10,4,2X,E8,2,2X,E9,3)
    READ(6,2) NPOINT,TPINIT,TIMINC,THETA,INC,ATEMP,NUMEL
    2 FORMAT(2X,I2,2X,F5,2,2X,I2,2X,E9,3,2X,I3,2X,F7,5,2X,I3)
    DO 403 I=1,NUMEL
    READ(7,400) HTC(I)
    400 FORMAT(8X,1PE15,5)
    READ(8,401) VOLE(I),POROTY(I)
    401 FORMAT(10X,E14,8,35X,E4,3)
    READ(9,402) FLXINL(I),FLXINR(I),FLYINU(I),FLYINO(I),FLZINB(I),
    *FLZINF(I),ITXINL(I),ITXINR(I),ITYINU(I),ITYINO(I),ITZINB(I),
    *ITZINF(I)
    402 FORMAT(6X,6E17,6,6I5)
    403 CONTINUE
  
```

C

```

    COMPUTE COMBINATIONS OF INPUT DATA WHICH REMAIN CONSTANT
    352 SEGMENT=NPOINT-1
    RINC=RADIUS/SEGMENT
  
```

C***

```

    CONSTANTS FOR INDIVIDUAL FRUIT MODEL
    B=3.0*ALPHA*TIMINC*(RADIUS-RINC/2.0)**2/RINC/(RADIUS**3-
    *(RADIUS-RINC/2.0)**3)
    H=6.0*ALPHA*TIMINC/RINC**2
    P=1.0-H
  
```

C

```

    NSEG=NPOINT-1
    DO 31 J=1,NSEG
    A=J
    SEG=NSEG
  
```

C***

```

    VOLUME OF SEGMENTS OF SPHERE
    31 VOL(J)=(1.0-(A-1.0)/SEG)**3-(1.0-A/SEG)**3
  
```

Figure B-9. Fortran program "Heat-Do" which was used to solve the heat transfer model.

```

C*** VOLUME OF RIND WHICH CONSISTS OF ONE OUTER SEGMENT OF SPHERE
C   THE CONSTANT IS THE HEAT CAPACITY OF THE RIND (J/KG-K)
260 VOL0=VOL(1)*0.282225E+05
    VOLI=0.0
    DO 261 L=2,NSEG
C*** VOLUME OF FLESH WHICH CONSISTS OF THE INNER SEGMENTS OF SPHERE
C   THE CONSTANT IS THE HEAT CAPACITY OF THE FLESH (J/KG-K)
261 VOLI=VOLI+VOL(L)*0.38922E+05
    TVOL=VOL0+VOLI
    VOL(1)=VOL(1)*(0.282225E+05/TVOL)
    DO 262 L=2,NSEG
262 VOL(L)=VOL(L)*(0.38922E+05/TVOL)
C*** SET INITIAL CONDITIONS
270 TIME=0.0
    N=0
C*** INLET AIR TEMPERATURE AT BOUNDARY CONDITION ELEMENT(S),
    T(0)=ATEMP
    DO 3 J=1,NPOINT
    DO 3 K=1,NUMEL
      3 PRSNT(J,K)=TPINIT
C*** SET INITIAL PRODUCT TEMPERATURE IN ALL ELEMENTS
C*** INITIAL AIR TEMPERATURE IN ALL ELEMENTS EQUAL TO PRODUCT TEMPERATURE
    DO 37 K=1,NUMEL
      PREPAV(K)=TPINIT
37 T(K)=TPINIT
42 NUM=0
41 TIME=TIME+TIMINC
    NUM=NUM+1
C*** START OF DO LOOP FOR BC-6-2
C*** CALCULATIONS PROCEED FROM ENTRANCE HOLE ELEMENT BY ELEMENT, FROM
C   LEFT TO RIGHT (X DIRECTION), THEN DOWN (-Y DIRECTION), PROCEEDING IN
C   THE Z DIRECTION AS VERTICAL LAYERS ONE AFTER THE LAST UNTIL THE EXIT
C   HOLE IS REACHED.
C*** NEW DO LOOP FOR FIRST HALF OF MODEL IN Z DIRECTION (Y DIRECTION FLOW
C   DOWN AND X DIRECTION FLOW TOWARD WALLS)
C
C*** CALCULATIONS PROCEED FROM ENTRANCE HOLE ELEMENT BY ELEMENT,
C   BOTH LEFT AND RIGHT (X DIRECTION), THEN DOWN (-Y DIRECTION),
C   PROCEEDING IN THE Z DIRECTION AS VERTICAL LAYERS ONE AFTER THE LAST
C   UNTIL THE CENTER PLANE (Z DIRECTION) IS REACHED,
    DO 900 LL=561,630,14
    DO 900 MM=LL,(LL-560),-140
    DO 700 K=MM+2,MM,-1
C*** TEMPERATURE OF AIR ENTERING ELEMENT BASED UPON THE ENERGY FROM
C   ADJACENT ELEMENTS, ASSUMING IDEAL MIXING.
    FLTOT=FLXINL(K)+FLXINR(K)+FLYINU(K)+FLYINO(K)+
      *   FLZINB(K)+FLZINF(K)
    TMIX=(FLXINL(K)*T(ITXINL(K))+FLXINR(K)*T(ITXINR(K))+
      *   FLYINU(K)*T(ITYINU(K))+FLYINO(K)*T(ITYINO(K))+
      *   FLZINB(K)*T(ITZINB(K))+FLZINF(K)*T(ITZINF(K)))/FLTOT

```

```

C*** VARIABLE CONSTANTS FOR INDIVIDUAL FRUIT MODEL
  D=1.0-3.0*ALPHA*TIMINC*((RADIUS-RINC/2.0)**2/RINC+RADIUS**2
  * *HTC(K)/CONDTY)/(RADIUS**3-(RADIUS-RINC/2.0)**3)
  IF (D .LT. 0.0) GO TO 100
  C=3.0*RADIUS**2*HTC(K)*ALPHA*TIMINC/CONDTY/(RADIUS**3-
  * (RADIUS-RINC/2.0)**3)
  DO 151 J=1,NPOINT
151 PREC(J,K)=PRSNT(J,K)
  PRSNT(1,K)=B*PREC(2,K)+C*TMIX+D*PREC(1,K)
  M=NPOINT-1
  DO 71 J=2,M
  R=RADIUS-RINC*(J-1)
  E=1.0-ALPHA*TIMINC*(2.0+((RINC/R)**2/2.0))/RINC**2
  IF (E .LT. 0.0) GO TO 101
  F=ALPHA*TIMINC*(1.0-RINC/2.0/R)**2/RINC**2
  G=ALPHA*TIMINC*(1.0+RINC/2.0/R)**2/RINC**2
  71 PRSNT(J,K)=E*PREC(J,K)+F*PREC(J+1,K)+G*PREC(J-1,K)
  J=NPOINT
  PRSNT(J,K)=H*PREC(J-1,K)+P*PREC(J,K)
  DO 301 J=1,NSEG
C*** MASS AVERAGE TEMPERATURE FOR NONLINEAR TEMPERATURE GRADIENT
  301 TPSECA(J)=(PRSNT(J+1,K)-PRSNT(J,K))*0.2063+PRSNT(J,K)
  IO 321 J=1,NSEG
  321 TPLSUB(J)=TPSECA(J)*VOL(J)
  PRSPAV(K)=0.0
  DO 331 J=1,NSEG
  331 PRSPAV(K)=PRSPAV(K)+TPLSUB(J)
  DTMIX=VOLE(K)*(POROTY(K)-1.0)*DENP*SHF*(PRSPAV(K)-PREPAV(K))/
  * (FLTOT*TIMINC*SHA)
  T(K)=TMIX+DTMIX
  700 CONTINUE
  DO 800 K=MM+3,MM+13,1
C*** TEMPERATURE OF AIR ENTERING ELEMENT BASED UPON THE ENERGY FROM
C ADJACENT ELEMENTS, ASSUMING IDEAL MIXING.
  FLTOT=FLXINL(K)+FLXINR(K)+FLYINU(K)+FLYINO(K)+
  * FLZINB(K)+FLZINF(K)
  TMIX=(FLXINL(K)*T(ITXINL(K))+FLXINR(K)*T(ITXINR(K)))+
  * FLYINU(K)*T(ITYINU(K))+FLYINO(K)*T(ITYIND(K))+
  * FLZINB(K)*T(ITZINB(K))+FLZINF(K)*T(ITZINF(K)))/FLTOT
C*** VARIABLE CONSTANTS FOR INDIVIDUAL FRUIT MODEL
  D=1.0-3.0*ALPHA*TIMINC*((RADIUS-RINC/2.0)**2/RINC+RADIUS**2
  * *HTC(K)/CONDTY)/(RADIUS**3-(RADIUS-RINC/2.0)**3)
  IF (D .LT. 0.0) GO TO 100
  C=3.0*RADIUS**2*HTC(K)*ALPHA*TIMINC/CONDTY/(RADIUS**3-
  * (RADIUS-RINC/2.0)**3)
  DO 152 J=1,NPOINT
152 PREC(J,K)=PRSNT(J,K)
  PRSNT(1,K)=B*PREC(2,K)+C*TMIX+D*PREC(1,K)
  M=NPOINT-1
  DO 72 J=2,M
  R=RADIUS-RINC*(J-1)
  E=1.0-ALPHA*TIMINC*(2.0+((RINC/R)**2/2.0))/RINC**2
  IF (E .LT. 0.0) GO TO 101

```

Figure B-9--continued

```

F=ALPHA*TIMINC*(1.0-RINC/2.0/R)**2/RINC**2
G=ALPHA*TIMINC*(1.0+RINC/2.0/R)**2/RINC**2
72 PRSNT(J,K)=E*PREC(J,K)+F*PREC(J+1,K)+G*PREC(J-1,K)
J=NPOINT
PRSNT(J,K)=H*PREC(J-1,K)+P*PREC(J,K)
DO 302 J=1,NSEG
C*** MASS AVERAGE TEMPERATURE FOR NONLINEAR TEMPERATURE GRADIENT
302 TPSECA(J)=(PRSNT(J+1,K)-PRSNT(J,K))*0.2063+PRSNT(J,K)
DO 322 J=1,NSEG
322 TPLSUB(J)=TPSECA(J)*VOL(J)
PRSPAV(K)=0.0
DO 332 J=1,NSEG
332 PRSPAV(K)=PRSPAV(K)+TPLSUB(J)
DTMIX=VQLE(K)*(POROTY(K)-1.0)*DENP*SHP*(PRSPAV(K)-PREPAV(K))/
* (FLTOT*TIMINC*SHA)
T(K)=TMIX+DTMIX
800 CONTINUE
900 CONTINUE
C*** NEW DO LOOP FOR SECOND HALF OF MODEL IN Z DIRECTION (Y DIRECTION
C FLOW UP AND X DIRECTION FLOW TOWARD CENTER OF CARTON)
C
C*** CALCULATIONS PROCEED FROM CENTER PLANE (Z DIRECTION) ELEMENT BY
C ELEMENT, BOTH LEFT AND RIGHT (X DIRECTION), THEN UP (+Y
C (+Y DIRECTION) PROCEEDING IN THE Z DIRECTION AS VERTICAL LAYERS
C ONE AFTER THE LAST UNTIL THE EXIT HOLE IS REACHED.
DO 990 LLL=631,700,14
DO 990 MMM=(LLL-560),LLL,140
DO 790 K=MMM+2,MMM,-1
C*** TEMPERATURE OF AIR ENTERING ELEMENT BASED UPON THE ENERGY FROM
C ADJACENT ELEMENTS, ASSUMING IDEAL MIXING.
FLTOT=FLXINL(K)+FLXINR(K)+FLYINU(K)+FLYIND(K)+
* FLZINB(K)+FLZINF(K)
TMIX=(FLXINL(K)*T(ITXINL(K))+FLXINR(K)*T(ITXINR(K))+
* FLYINU(K)*T(ITYINU(K))+FLYIND(K)*T(ITYIND(K))+
* FLZINR(K)*T(ITZINB(K))+FLZINF(K)*T(ITZINF(K)))/FLTOT
C*** VARIABLE CONSTANTS FOR INDIVIDUAL FRUIT MODEL
D=1.0-3.0*ALPHA*TIMINC*((RADIUS-RINC/2.0)**2/RINC+RADIUS**2
* *HTC(K)/CONDTY)/(RADIUS**3-(RADIUS-RINC/2.0)**3)
IF (D .LT. 0.0) GO TO 100
C=3.0*RADIUS**2*HTC(K)*ALPHA*TIMINC/CONDTY/(RADIUS**3-
* (RADIUS-RINC/2.0)**3)
DO 153 J=1,NPOINT
153 PREC(J,K)=PRSNT(J,K)
PRSNT(1,K)=B*PREC(2,K)+C*TMIX+D*PREC(1,K)
M=NPOINT-1
DO 73 J=2,M
R=RADIUS-RINC*(J-1)
E=1.0-ALPHA*TIMINC*(2.0+((RINC/R)**2/2.0))/RINC**2
IF (E .LT. 0.0) GO TO 101
F=ALPHA*TIMINC*(1.0-RINC/2.0/R)**2/RINC**2
G=ALPHA*TIMINC*(1.0+RINC/2.0/R)**2/RINC**2
73 PRSNT(J,K)=E*PREC(J,K)+F*PREC(J+1,K)+G*PREC(J-1,K)

```

Figure B-9--continued

```

      J=NPOINT
      PRSNT(J,K)=H*PREC(J-1,K)+P*PREC(J,K)
      DO 303 J=1,NSEG
C*** MASS AVERAGE TEMPERATURE FOR NONLINEAR TEMPERATURE GRADIENT
      303 TPSECA(J)=(PRSNT(J+1,K)-PRSNT(J,K))*0.2063+PRSNT(J,K)
      DO 323 J=1,NSEG
      323 TPLSUB(J)=TPSECA(J)*VOL(J)
      PRSPAV(K)=0.0
      DO 333 J=1,NSEG
      333 PRSPAV(K)=PRSPAV(K)+TPLSUB(J)
      DTMIX=VOLE(K)*(POROTY(K)-1.0)*DENP*SHP*(PRSPAV(K)-PREPAV(K))/
      * (FLTOT*TIMINC*SHA)
      T(K)=TMIX+DTMIX
      790 CONTINUE
      DO 890 K=MMM+3,MMM+13,1
C*** TEMPERATURE OF AIR ENTERING ELEMENT BASED UPON THE ENERGY FROM
C ADJACENT ELEMENTS, ASSUMING IDEAL MIXING.
      FLTOT=FLXINL(K)+FLXINR(K)+FLYINU(K)+FLYIND(K)+
      * FLZINB(K)+FLZINF(K)
      TMIX=(FLXINL(K)*T(ITXINL(K))+FLXINR(K)*T(ITXINR(K))+
      * FLYINU(K)*T(ITYINU(K))+FLYIND(K)*T(ITYIND(K))+
      * FLZINB(K)*T(ITZINB(K))+FLZINF(K)*T(ITZINF(K)))/FLTOT
C*** VARIABLE CONSTANTS FOR INDIVIDUAL FRUIT MODEL
      D=1.0-3.0*ALPHA*TIMINC*((RADIUS-RINC/2.0)**2/RINC+RADIUS**2
      * *HTC(K)/CONDY)/(RADIUS**3-(RADIUS-RINC/2.0)**3)
      IF (D .LT. 0.0) GO TO 100
      C=3.0*RADIUS**2*HTC(K)*ALPHA*TIMINC/CONDY/(RADIUS**3-
      * (RADIUS-RINC/2.0)**3)
      DO 154 J=1,NPOINT
      154 PREC(J,K)=PRSNT(J,K)
      PRSNT(1,K)=B*PREC(2,K)+C*TMIX+D*PREC(1,K)
      M=NPOINT-1
      DO 74 J=2,M
      R=RADIUS-RINC*(J-1)
      E=1.0-ALPHA*TIMINC*(2.0+((RINC/R)**2/2.0))/RINC**2
      IF (E .LT. 0.0) GO TO 101
      F=ALPHA*TIMINC*(1.0-RINC/2.0/R)**2/RINC**2
      G=ALPHA*TIMINC*(1.0+RINC/2.0/R)**2/RINC**2
      74 PRSNT(J,K)=E*PREC(J,K)+F*PREC(J+1,K)+G*PREC(J-1,K)
      J=NPOINT
      PRSNT(J,K)=H*PREC(J-1,K)+P*PREC(J,K)
      DO 304 J=1,NSEG
C*** MASS AVERAGE TEMPERATURE FOR NONLINEAR TEMPERATURE GRADIENT
      304 TPSECA(J)=(PRSNT(J+1,K)-PRSNT(J,K))*0.2063+PRSNT(J,K)

```

```

      DO 324 J=1,NSEG
324  TPLSUB(J)=TPSECA(J)*VOL(J)
      PRSPAV(K)=0,0
      DO 334 J=1,NSEG
334  PRSPAV(K)=PRSPAV(K)+TPLSUB(J)
      DTMIX=VOLE(K)*(FOROTY(K)-1,0)*DENP*SHP*(PRSPAV(K)-PREPAV(K))/
      * (FLTOT*TIMINC*SHA)
      T(K)=TMIX+DTMIX
890  CONTINUE
990  CONTINUE
CC*** END OF DO LOOPS
C*** CHECK IF TIME TO WRITE TO OUTPUT FILE
      IF (NUM-INC) 90,20,998
      DO 22 K=1,NUMEL
      WRITE(11,21) K,TIME,T(K),(PRCNT(J,K),J=1,NPOINT),PRSPAV(K)
      21  FORMAT(8X,I5,F7,0,2X,F5,1,2X,11F6,2,3X,F6,2)
      22  CONTINUE
      NUM=0
      N=N+1
C*** CHECK FOR EXCESSIVE WRITING TO OUTPUT FILE
      IF (N .GT. (1+THETA/(INC*TIMINC))) GO TO 1000
C*** CHECK IF TOTAL TEST TIME COMPLETED
      90  IF (TIME .GT. THETA) GO TO 99
      38  DO 39 K=1,NUMEL
      39  PREPAV(K)=PRSPAV(K)
      GO TO 41
      100 WRITE(10,50)
      50  FORMAT (1H1,'D IS LESS THAN ZERO')
      GO TO 1002
      101 WRITE(10,60)
      60  FORMAT (1H1,'E IS LESS THAN ZERO')
      GO TO 1002
      99  WRITE(10,40)
      40  FORMAT(1H1,'TOTAL TEST TIME REACHED')
      GO TO 1002
      998 WRITE(10,999)
      999 FORMAT(1H1,'NUM EXCEEDED INC')
      GO TO 1002
      1000 WRITE(10,1001)
      1001 FORMAT(1H1,'TOO MANY WRITINGS TO OUTPUT FILE')
      1002 CONTINUE
      CLOSE(5)
      CLOSE(6)
      CLOSE(7)
      CLOSE(8)
C***NOTE: ADJUST DATA-IN-1 AND DATA-IN-2
      CLOSE(9)
      CLOSE(10)
      CLOSE(11)
      STOP
      END

```

0.121E-06 0.469 0.3675E-01 0.1007E+04 0.39E+04 0.998E+03 0.405

Figure B-10. Input data file "Data-In-1" which lists the product thermal diffusivity, conductivity, and radius, the specific heat of the air and product and product density.

11 32.22 18 0.108E+05 80 1.66667 700

Figure B-11. Input data file "Data-In-2" which lists number of product nodal points, the initial product temperature, the time increment, total test cooling time, data output print frequency, entering air temperature, and number of elements.

1	1800.	20.9	29.27	29.46	29.63	29.77	29.89	29.99	30.06	30.12	30.16	30.19	30.19	29.64
2	1800.	18.0	27.73	28.14	28.49	28.79	29.05	29.27	29.44	29.57	29.66	29.71	29.73	28.53
3	1800.	16.3	27.18	27.66	28.08	28.44	28.75	29.00	29.21	29.37	29.47	29.54	29.56	28.12
4	1800.	14.5	26.63	27.18	27.66	28.08	28.44	28.74	28.98	29.16	29.28	29.36	29.38	27.72
5	1800.	12.7	26.24	26.83	27.36	27.82	28.21	28.54	28.80	29.01	29.14	29.22	29.25	27.42
6	1800.	10.9	26.11	26.72	27.26	27.73	28.14	28.47	28.74	28.95	29.09	29.18	29.20	27.32
7	1800.	9.4	26.05	26.66	27.21	27.69	28.10	28.44	28.71	28.92	29.07	29.15	29.18	27.28
8	1800.	9.4	26.05	26.66	27.21	27.69	28.10	28.44	28.71	28.92	29.07	29.15	29.18	27.28
9	1800.	10.9	26.11	26.72	27.26	27.73	28.14	28.47	28.74	28.95	29.09	29.18	29.20	27.32
10	1800.	12.7	26.24	26.83	27.36	27.82	28.21	28.54	28.80	29.01	29.14	29.22	29.25	27.42
11	1800.	14.5	26.63	27.18	27.66	28.08	28.44	28.74	28.98	29.16	29.28	29.36	29.38	27.72
12	1800.	16.3	27.18	27.66	28.08	28.44	28.75	29.00	29.21	29.37	29.47	29.54	29.56	28.12
13	1800.	18.0	27.73	28.14	28.49	28.79	29.05	29.27	29.44	29.57	29.66	29.71	29.73	28.53
14	1800.	20.9	29.27	29.46	29.63	29.77	29.89	29.99	30.06	30.12	30.16	30.19	30.19	29.64
15	1800.	22.3	28.59	28.88	29.13	29.34	29.52	29.67	29.79	29.88	29.94	29.98	29.99	29.15
16	1800.	20.8	28.90	29.14	29.36	29.54	29.69	29.82	29.92	29.99	30.05	30.08	30.09	29.38
17	1800.	19.6	28.59	28.88	29.13	29.34	29.52	29.67	29.79	29.88	29.94	29.98	29.99	29.15
18	1800.	17.8	28.22	28.56	28.85	29.10	29.32	29.50	29.64	29.75	29.82	29.86	29.88	28.88
19	1800.	15.9	27.83	28.22	28.56	28.85	29.10	29.31	29.48	29.60	29.69	29.74	29.76	28.60
20	1800.	14.1	27.48	27.91	28.29	28.62	28.90	29.14	29.33	29.47	29.57	29.62	29.64	28.33
21	1800.	12.6	27.16	27.63	28.05	28.41	28.72	28.98	29.19	29.35	29.45	29.52	29.54	28.10
22	1800.	12.6	27.16	27.63	28.05	28.41	28.72	28.98	29.19	29.35	29.45	29.52	29.54	28.10
23	1800.	14.1	27.48	27.91	28.29	28.62	28.90	29.14	29.33	29.47	29.57	29.62	29.64	28.33
24	1800.	15.9	27.83	28.22	28.56	28.85	29.10	29.31	29.48	29.60	29.69	29.74	29.76	28.60
25	1800.	17.8	28.22	28.56	28.85	29.10	29.32	29.50	29.64	29.75	29.82	29.86	29.88	28.88
26	1800.	19.6	28.59	28.88	29.13	29.34	29.52	29.67	29.79	29.88	29.94	29.98	29.99	29.15
27	1800.	20.8	28.90	29.14	29.36	29.54	29.69	29.82	29.92	29.99	30.05	30.08	30.09	29.38
28	1800.	22.3	28.59	28.88	29.13	29.34	29.52	29.67	29.79	29.88	29.94	29.98	29.99	29.15
29	1800.	23.3	28.77	29.03	29.26	29.45	29.62	29.76	29.86	29.95	30.00	30.04	30.05	29.28
30	1800.	23.0	29.26	29.45	29.62	29.76	29.88	29.98	30.06	30.12	30.16	30.18	30.19	29.64
31	1800.	21.7	28.95	29.18	29.39	29.57	29.72	29.84	29.94	30.01	30.06	30.09	30.10	29.41
32	1800.	20.1	28.56	28.85	29.10	29.32	29.51	29.66	29.78	29.87	29.93	29.97	29.98	29.13
33	1800.	18.4	28.13	28.48	28.78	29.05	29.27	29.46	29.60	29.71	29.79	29.84	29.85	28.82
34	1800.	16.8	27.71	28.11	28.47	28.77	29.04	29.25	29.43	29.56	29.65	29.70	29.72	28.51
35	1800.	15.5	27.34	27.79	28.19	28.54	28.83	29.07	29.27	29.42	29.52	29.58	29.60	28.24
36	1800.	15.5	27.34	27.79	28.19	28.54	28.83	29.07	29.27	29.42	29.52	29.58	29.60	28.24
37	1800.	16.8	27.71	28.11	28.47	28.77	29.04	29.25	29.43	29.56	29.65	29.70	29.72	28.51
38	1800.	18.4	28.13	28.48	28.78	29.05	29.27	29.46	29.60	29.71	29.79	29.84	29.85	28.82
39	1800.	20.1	28.56	28.85	29.10	29.32	29.51	29.66	29.78	29.87	29.93	29.97	29.98	29.13
40	1800.	21.7	28.95	29.18	29.39	29.57	29.72	29.84	29.94	30.01	30.06	30.09	30.10	29.41
41	1800.	23.0	29.26	29.45	29.62	29.76	29.88	29.98	30.06	30.12	30.16	30.18	30.19	29.64
42	1800.	23.3	28.77	29.03	29.26	29.45	29.62	29.76	29.86	29.95	30.00	30.04	30.05	29.28
43	1800.	24.1	28.91	29.15	29.36	29.55	29.70	29.82	29.92	30.00	30.05	30.08	30.09	29.38
44	1800.	24.6	29.51	29.67	29.81	29.92	30.02	30.10	30.16	30.21	30.24	30.26	30.27	29.82
45	1800.	23.5	29.23	29.43	29.60	29.75	29.87	29.97	30.05	30.11	30.15	30.18	30.18	29.62
46	1800.	22.0	28.88	29.12	29.34	29.52	29.68	29.81	29.91	29.99	30.04	30.07	30.08	29.36
47	1800.	20.5	28.49	28.79	29.05	29.27	29.47	29.62	29.75	29.84	29.91	29.95	29.96	29.07
48	1800.	19.2	28.10	28.45	28.76	29.03	29.25	29.44	29.59	29.70	29.78	29.83	29.84	28.79
49	1800.	18.1	27.79	28.18	28.53	28.83	29.08	29.29	29.46	29.59	29.68	29.73	29.75	28.57

Figure B-12. Portion of input/output data file "Temp-Response" which lists for each element, the number, time (seconds), the air temperature, the product temperature at each of the nodes, and the product mass-average temperature.

```

C*** THIS IS A DATA REFORMAT PROGRAM TO TRANSFORM THE COOLING RESPONSE
C*** OF ORANGES PACKED IN CARTONS DATA DETERMINED USING POROUS MEDIA FLOW
C*** DATA GENERATED BY ANSYS INTO DATA PLOT FIELDS SIMILIAR TO THE
C*** EXPERIMENTAL DATA FOR USE IN PLOTTING USING VERSA3.
C
      DIMENSION TC(700,0:11),TF(0:28,80),HOUR(28)
C
      OPEN(UNIT=5,FILE='TEMP-RESP-61C',STATUS='OLD')
      OPEN(UNIT=6,FILE='PLOT-61C',STATUS='NEW')
C      OPEN(UNIT=7,FILE='CHECK-IN',STATUS='NEW')
C
C*** DEFINE INITIAL TEMPERATURE A TIME ZERO
      TPINIT=90.0
      HOUR(0)=0.0
C*** OUTPUT PLOT DATA FIELDS FOR TIME ZERO
      DO 5 I=1,80
        TF(0,I)=TPINIT
      5 CONTINUE
      WRITE(6,110) (TF(0,I),I=1,80),HOUR(0)
C*** DEFINE CONSTANTS FOR CONVERSION FROM DEGREES C TO DEGREES F
      A=9.0/5.0
      B=32.0
C  INPUT DATA
C      NOTE: M IS NUMBER OF TIMES DATA IS MEASURED (I.E. TIME INTERVAL
C            OF 1800 SEC, 28 TIMES FOR 14 HOURS) ADJUST AS REQUIRED.
      DO 120 M=1,28
C      NOTE: K IS THE NUMBER OF ELEMENTS, ADJUST AS REQUIRED.
      DO 90 K=1,700
        READ(5,1) K,TIME,(TC(K,I),I=0,11)
      1 FORMAT(8X,I5,F7.0,2X,F5.1,2X,11F6.2)
C      WRITE(7,* ) K,TIME,(TC(K,I),I=0,11)
C
C*** DEFINE DATA FIELDS
      TF(M,1)=TC(157,11)*A+B
      TF(M,57)=TF(M,1)
      TF(M,2)=TC(157,1)*A+B
      TF(M,58)=TF(M,2)
      TF(M,3)=TC(157,0)*A+B
      TF(M,59)=TF(M,3)
      TF(M,4)=TC(160,11)*A+B
      TF(M,60)=TF(M,4)
      TF(M,5)=TC(163,11)*A+B
      TF(M,61)=TF(M,5)
      TF(M,6)=TC(166,11)*A+B
      TF(M,62)=TF(M,6)
      TF(M,7)=TC(166,1)*A+B
      TF(M,63)=TF(M,7)
      TF(M,8)=TC(166,0)*A+B
      TF(M,64)=TF(M,8)

```

Figure B-13. Fortran program "Plot-Data" which was used to reorganize the temperature response to give 78 thermocouple readings.

TF(M,9)=TC(175,11)*A+B
TF(M,65)=TF(M,9)
TF(M,10)=TC(199,11)*A+B
TF(M,66)=TF(M,10)
TF(M,11)=TC(202,11)*A+B
TF(M,67)=TF(M,11)
TF(M,12)=TC(205,11)*A+B
TF(M,68)=TF(M,12)
TF(M,13)=TC(208,11)*A+B
TF(M,69)=TF(M,13)
TF(M,14)=TC(217,11)*A+B
TF(M,70)=TF(M,14)
TF(M,15)=TC(241,11)*A+B
TF(M,71)=TF(M,15)
TF(M,16)=TC(241,1)*A+B
TF(M,72)=TF(M,16)
TF(M,17)=TC(241,0)*A+B
TF(M,73)=TF(M,17)
TF(M,18)=TC(398,11)*A+B
TF(M,74)=TF(M,18)
TF(M,19)=TC(401,11)*A+B
TF(M,75)=TF(M,19)
TF(M,20)=TC(250,11)*A+B
TF(M,76)=TF(M,20)
TF(M,21)=TC(250,1)*A+B
TF(M,77)=TF(M,21)
TF(M,22)=TC(250,0)*A+B
TF(M,78)=TF(M,22)
TF(M,23)=TC(438,11)*A+B
TF(M,49)=TF(M,23)
TF(M,24)=TC(441,11)*A+B
TF(M,50)=TF(M,24)
TF(M,25)=TC(445,11)*A+B
TF(M,51)=TF(M,25)
TF(M,26)=TC(480,11)*A+B
TF(M,52)=TF(M,26)
TF(M,27)=TC(483,11)*A+B
TF(M,53)=TF(M,27)
TF(M,28)=TC(487,11)*A+B
TF(M,54)=TF(M,28)
TF(M,29)=TC(539,11)*A+B
TF(M,55)=TF(M,29)
TF(M,30)=TC(543,11)*A+B
TF(M,56)=TF(M,30)

```

TF(M,31)=TC(576,11)*A+B
TF(M,32)=TC(579,11)*A+B
TF(M,33)=TC(584,11)*A+B
TF(M,34)=TC(587,11)*A+B
TF(M,35)=TC(595,11)*A+B
TF(M,36)=TC(619,11)*A+B
TF(M,37)=TC(620,0)*A+B
TF(M,38)=TC(620,1)*A+B
TF(M,39)=TC(620,11)*A+B
TF(M,40)=TC(627,11)*A+B
TF(M,41)=TC(627,1)*A+B
TF(M,42)=TC(627,0)*A+B
TF(M,43)=TC(628,11)*A+B
TF(M,44)=TC(525,11)*A+B
TF(M,45)=TC(675,11)*A+B
TF(M,46)=TC(678,11)*A+B
TF(M,47)=TC(681,11)*A+B
TF(M,48)=TC(684,11)*A+B
90 CONTINUE
C*** CHANGE TIME TO FRACTIONAL HOURS (FROM SECONDS)
    HOUR(M)=TIME/3600.
C*** AVERAGE TEMPERATURE OF AIR ENTERING
    TF(M,79)=35.0
C***
    TF(M,80)=0.0
C
C*** OUTPUT PLOT DATA FIELDS
    WRITE(6,110) (TF(M,I),I=1,80),HOUR(M)
    110 FORMAT(80(F4.1,1X),1(F6.2,1X))
    120 CONTINUE
C*** NOTE CHANGE TPINIT, TAIR AND M AS APPROPRIATE
    CLOSE(5)
    CLOSE(6)
C
    CLOSE(7)
    STOP
    END

```

APPENDIX C PLOT INFORMATION

Plotting using ANSYS is discussed in Appendix P of the ANSYS Users Manual (DeSalvo and Swanson 1983). Various Tektronix graphic devices were used to produce the ANSYS generated figures in this study. The following model Tektronix terminals were used 4006-1, 4025, 4025A, and 4027A. All these terminals provided on screen interactive plotting of ANSYS data. The 4006-1 terminal was linked to a Tektronix Model 4631 Hard Copy Unit which could provide a copy of the current screen data if the copy key were pressed. The 4631 copies were adequate for analysis but not as suitable for publication. Therefore a Tektronix Model 4662 interactive digital pen plotter was used for most of the ANSYS produced graphics presented in this study.

In order to use the 4662 plotter, ANSYS required certain procedures to construct a proper plot file. In each ANSYS phase interactive graphics is available. A plot file can be created by command. The first step in obtaining a 4662 plot was to use the ANSYS external interactive plotting program PLOT21. This program could display plots directly to the graphic terminal devices (or for 4631 hard copy) or it could write a plot file on command to be used by another ANSYS external plotting program. The file created by PLOT21 was

used by PLT33I. PLT33I is also an interactive plotting program that displays plots directly to graphic terminal devices or when the terminal is properly connected to the 4662 plotter. Wet ink pens were used to prepare the pressure and velocity plots.

The reason for presenting the above information is to explain the process that was required to produce the desired graphical figures generated by ANSYS. Depending on the complexity of the figure, the process from ANSYS to PLOT21 to PLT33I and eventually to the 4662 plotter could take a few minutes to over an hour.

The temperature response figures were produced using the same Tektronix equipment. Locally programmed PLOT 10 Interactive Graphics programs were used to produce the desired results. The temperature response plots were produced using a local program called "Versa3" while the regression plots of predicted versus experimental temperature were produced with a second local program called "Myplot". Both of these programs required manipulation of the temperature data files and several short fortran programs were written to create the necessary format fields.

APPENDIX D
ADDITIONAL DISCUSSION OF RESULTS FOR TWO- AND THREE-
DIMENSIONAL GRAIN BIN MODELS

Two-Dimensional Grain Bin

Brooker (1969) calculated the pressure patterns and velocity distribution for the grain bin using a finite difference model. The linear pressure pattern is shown in Figure D-1, which is a reproduction of Brooker's Figure 3. Brooker (1969) noted that the pressure patterns are the same for the three boundary conditions when the isobaric lines are plotted as a percentage of the duct pressure. The nonlinear pressure pattern presented by Brooker (1969) is illustrated in Figure D-2, a reproduction of Brooker's Figure 2. The nonlinear velocity distribution determined numerically by Brooker (1969) is presented in Figure D-3, a reproduction of Brooker's Figure 4. Brooker (1969) also presented experimentally measured pressure patterns for a bin filled with corn and the same geometry as Segerlind modeled, for duct pressures of 1, 2, and 3 inches of water. Figure 5 from Brooker's paper is reproduced here as Figure D-4. Brooker's only explanation for the disagreement between the experimental data and the calculated results was that the pressure drop through the wire mesh duct opening was not considered in the iteration procedure.

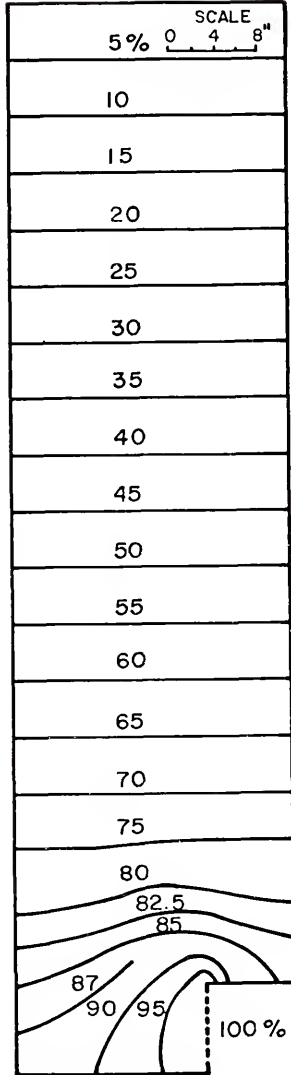


Figure D-1. Numerical pressure pattern for linear air flow through shelled corn from Brooker (1969), for 2 inches of water duct pressure.

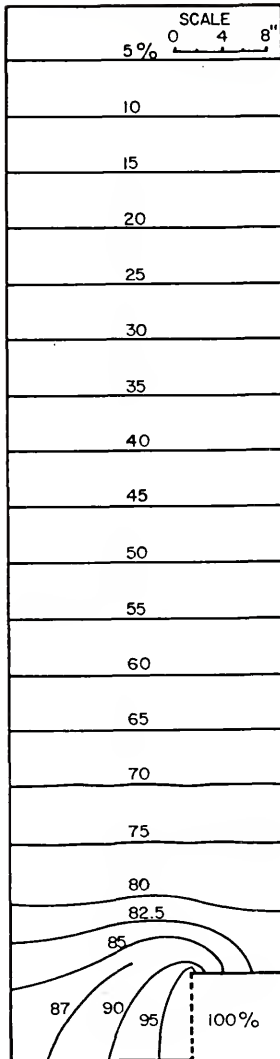


Figure D-2. Numerical pressure pattern for nonlinear air flow through shelled corn from Brooker (1969). The same pattern was obtained for duct pressures of 1, 2, and 3 inches of water.

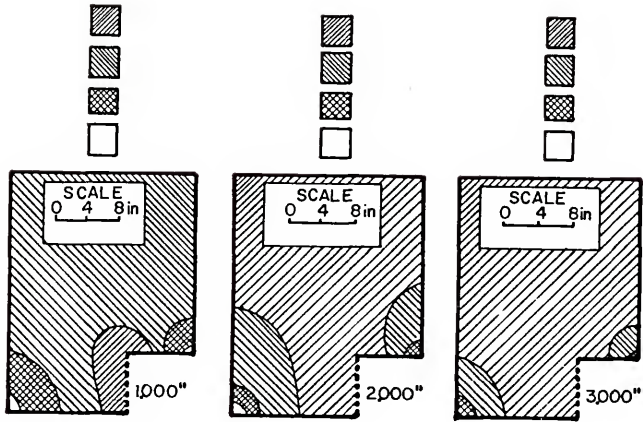


Figure D-3. Numerical velocity distribution for nonlinear air flow through shelled corn from Brooker (1969).

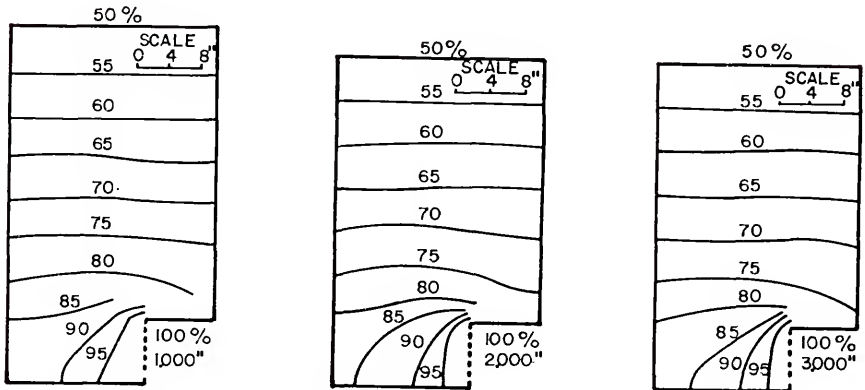


Figure D-4. Plot of experimental isobaric lines from Brooker (1969).

Segerlind (1982) used the values for a and b specified by Brooker (1969) and further generalized the work of Shedd (1953) to solve the nonlinear problem using a finite element model and attempted to explain the disagreement between the numerical solution and experimental data reported by Brooker (1969). Segerlind's calculated values were compared with the experimentally determined isobaric lines given by Brooker (1969). The 85 percent of total pressure loss contour line for a duct pressure of 3 inches of water was calculated by Segerlind (1982) and Segerlind's Figure 5 is reproduced here as Figure D-5. Segerlind (1982) concluded that the comparison with Brooker's experimental data was not good, since the 85 percent contour line was located entirely above the duct.

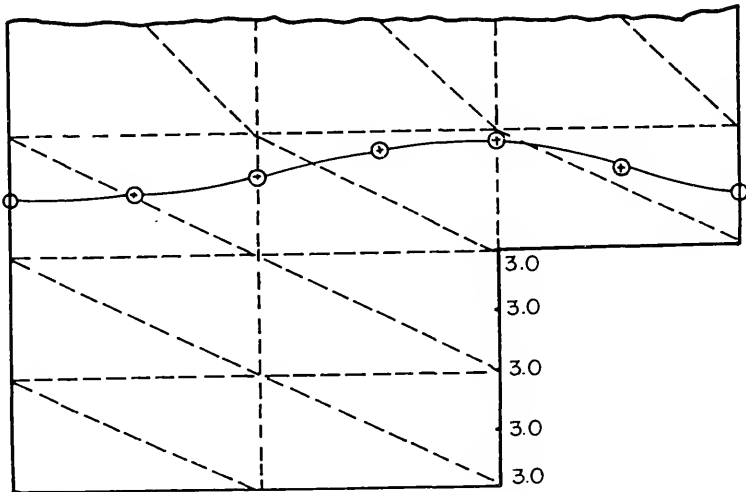


Figure D-5. 85 percent isobaric contour line from Segerlind (1982).

The isobaric contour lines calculated using ANSYS for a boundary conditions of 1, 2, and 3 inches of water are shown in Figures D-6, D-7, and D-8. Unlike the data reported by Brooker (1969) in Figure D-2, the pressure patterns in these three figures changed with a change in the duct pressure. The change in pattern is similar to that exhibited in Brooker's experimental data in Figure D-4. However, this change in the pressure pattern (Figures D-6, D-7, and D-8) was minor and the ANSYS solution was similar to Brooker's numerical solution (Figure D-2). As noted by Segerlind (1982), the 85 percent isobaric line for a duct pressure of 3 inches of water shown in Figure D-4, touched the bottom of the bin and the top of the duct. The 85 percent isobaric line shown in Figure D-8 is in better agreement with the experimental data (Figure D-4) than Segerlind's numerical solution as shown in Figure D-5. The disagreement between Figures D-6, D-7, and D-8 and the corresponding three pressure patterns illustrated in Figure D-4 is evident by comparing the respective 85 percent isobaric lines. The pressure patterns calculated by ANSYS in Figures D-6, D-7, and D-8, changed in a manner very similar to the experimental data in Figure D-4. However, the pressure loss for the experimental data occurred more rapidly near the duct entrance.

Brooker (1969) reported the velocity was uniform in the upper portions of the grain bins as illustrated in Figure D-3. For the respective flows from left to right the

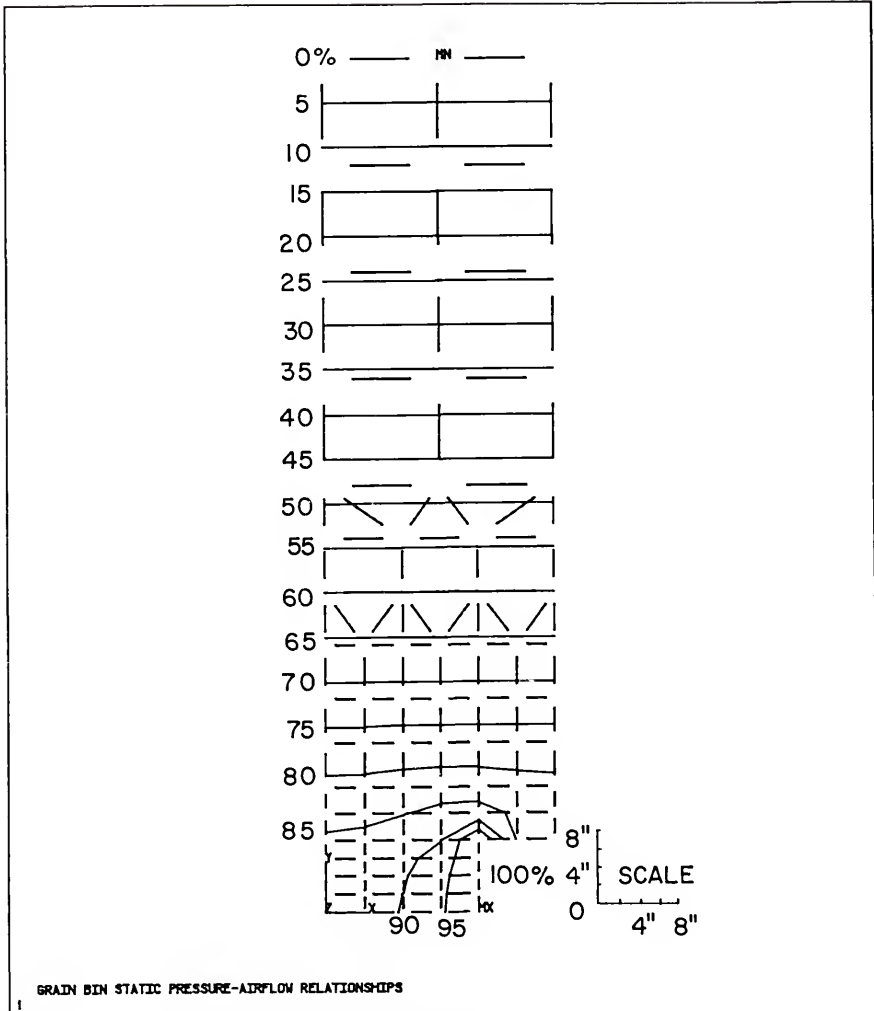


Figure D-6. Isobaric contour lines calculated using ANSYS for a boundary condition of 1 inch of water.

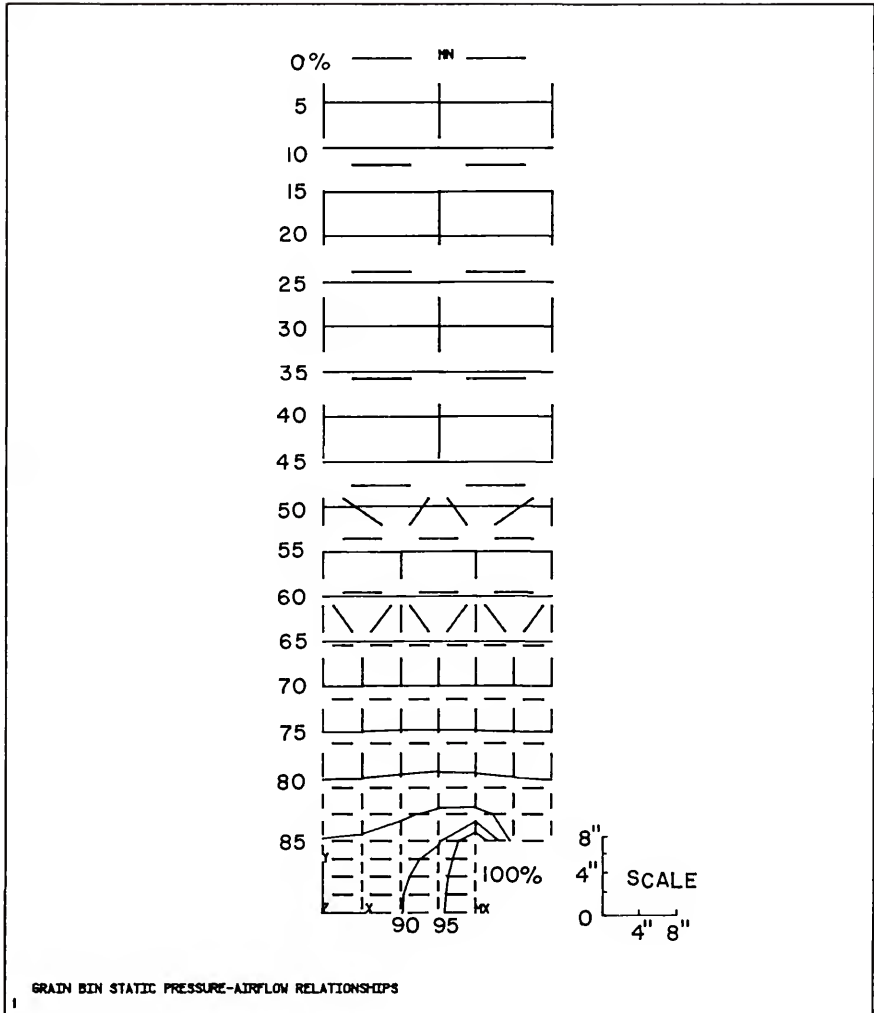


Figure D-7. Isobaric contour lines calculated using ANSYS for a boundary condition of 2 inches of water.

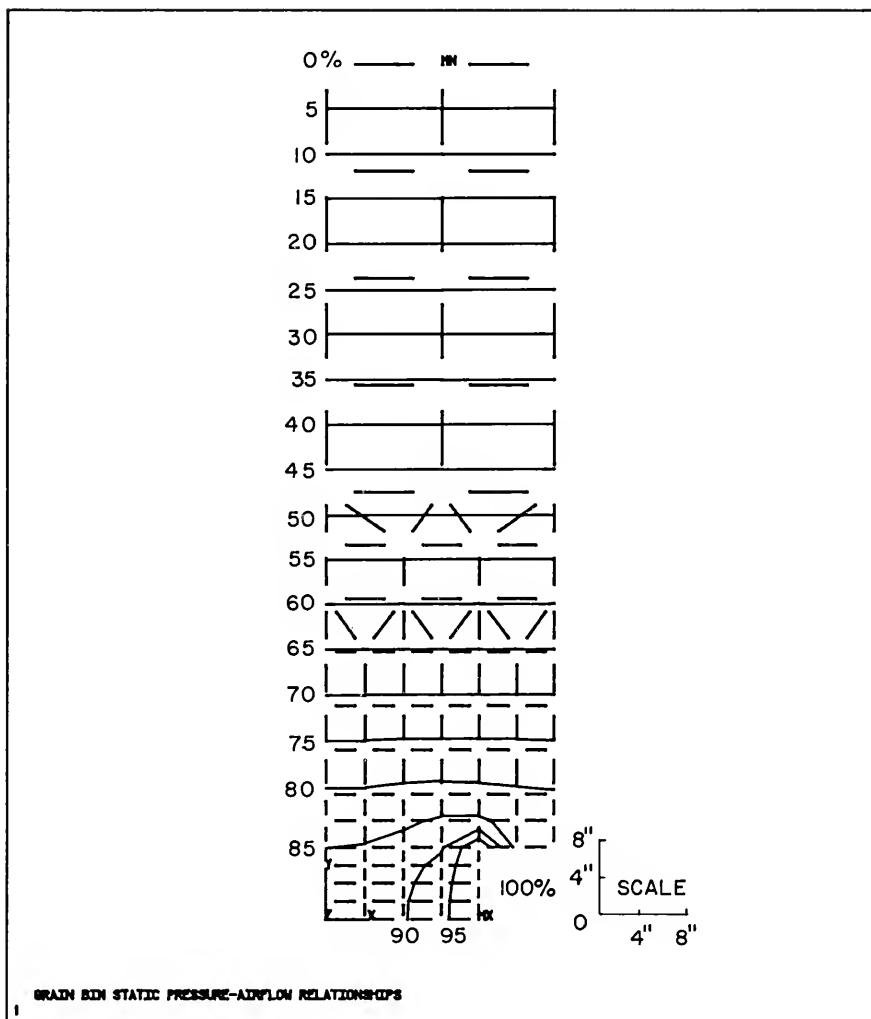


Figure D-8. Isobaric contour lines calculated using ANSYS for a boundary condition of 3 inches of water.

uniform velocity was calculated to be 14.7, 23.7, and 30.7 feet per uniform minute (fpm). ANSYS had the capability to provide detailed velocity information and plots similar to Figure D-3. Since Segerlind (1982) did not report this type data, the velocity plots were not required for data comparison and were not presented. The uniform velocity calculated by ANSYS corresponding to the data presented by Brooker (1969) was higher at 16.9, 26.0, and 33.0 fpm.

In an effort to achieve a better agreement with Brooker's experimental data, Segerlind (1982) changed the boundary conditions by specifying the duct pressure at only the interior nodes of the duct entrance as shown in Figure D-9. The top and bottom nodes were taken to be part of the impermeable boundary. Segerlind (1982) resolved the problem using the new boundary conditions. Figure D-10 illustrates the 85 percent isobaric contour lines for 1, 2, and 3 inches of water duct pressure, presented by Segerlind (1969). Segerlind (1982) concluded that these lines looked similar to Brooker's (1969), noting the 1 inch of water line ended at the left wall while the other two lines intersected the bottom of the bin.

Figure D-11 illustrates a group of isobaric lines for a duct pressure of 3 inches of water, presented by Segerlind (1982). Segerlind stated that these lines also looked similar to Brooker's (1969) experimental results and concluded that the lines intersect the bin wall and bottom at the same locations as Brooker's experimental lines.

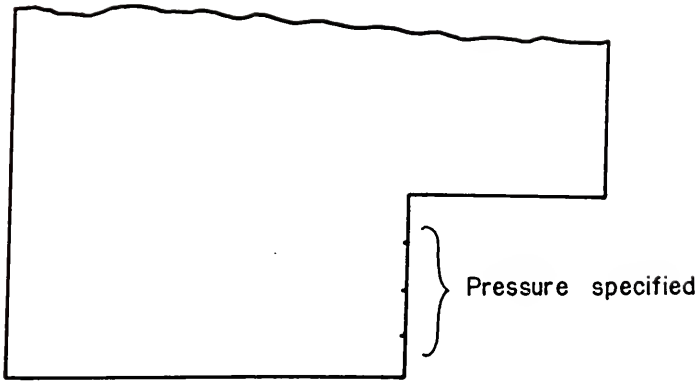


Figure D-9. Modified boundary conditions used by Segerlind (1982).

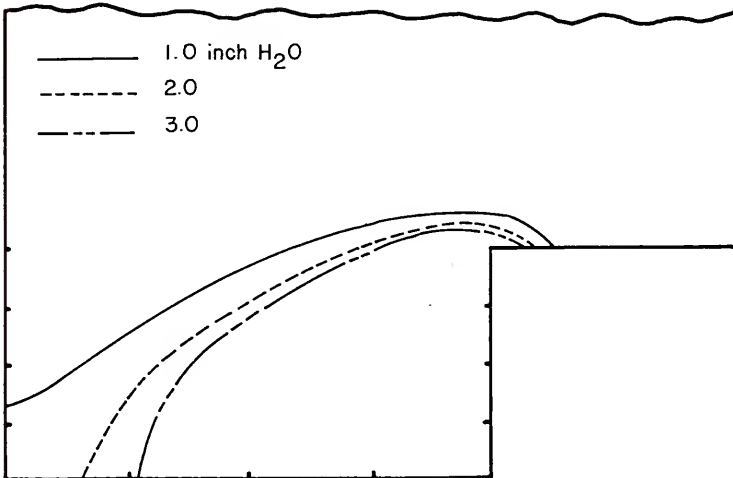


Figure D-10. 85 percent isobaric lines from Segerlind (1982).

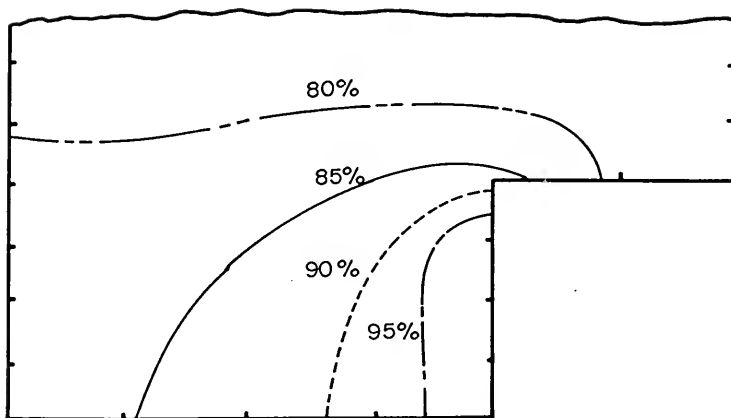


Figure D-11. Isobaric pattern for a duct pressure of 3 inches of water from Segerlind (1982).

The isobaric pressure lines were also calculated using ANSYS for the modified boundary conditions of 1, 2, and 3 inches of water and the results are shown in Figures D-12, D-13, and D-14. The modification in the boundary conditions produced a drastic change in the pressure pattern. The pressure drop was calculated to occur more rapidly closer to the duct entrance (Figures D-12, D-13, and D-14) than indicated by Brooker's experimental data (Figure D-2) or Segerlind's numerical solution with modified boundary conditions (Figures D-11 and D-12). The modified boundary condition did not appear to accurately reflect the physical process. Since the velocity stream lines cross the isobaric lines at right angles, the location of the 90 and 95 percent

isobaric lines in Figure D-11 appears to indicate no air flow from right to left through the duct in this region. Actually, the highest velocity occurred in this region as indicated by Figure D-3 and the ANSYS calculated results.

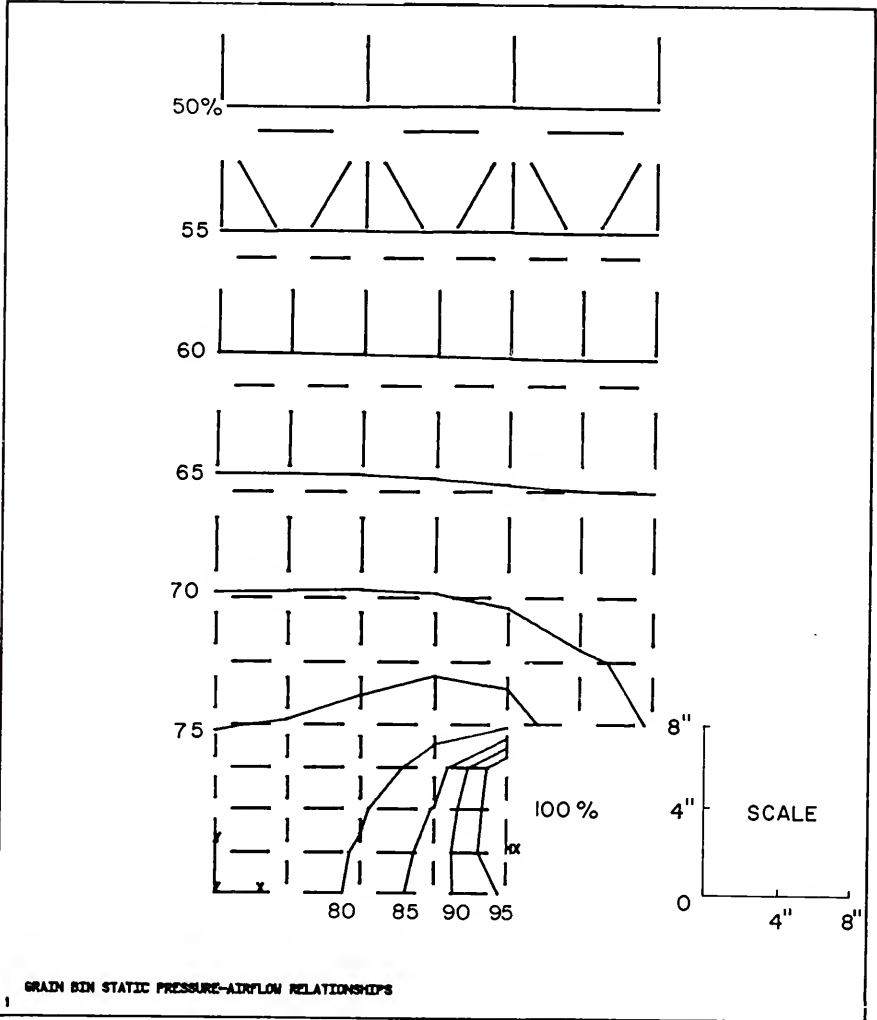


Figure D-12. Isobaric contour lines calculated using ANSYS with a modified boundary condition of 1 inch of water.

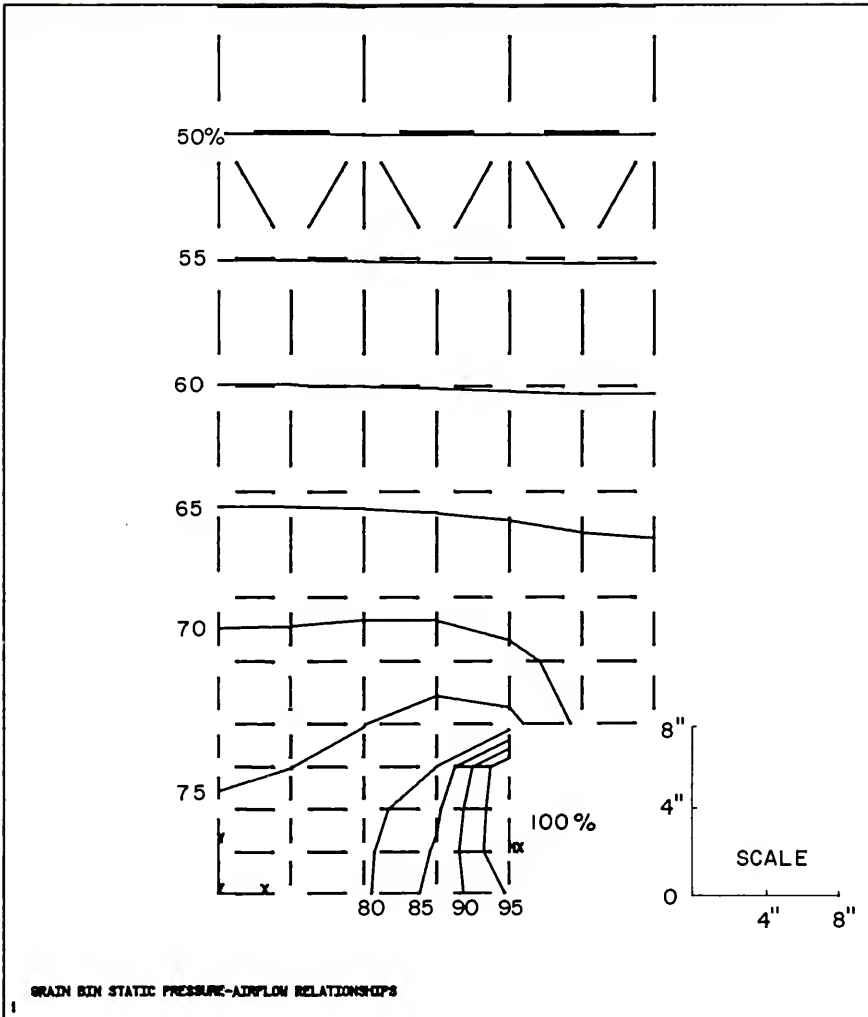


Figure D-13. Isobaric contour lines calculated using ANSYS with a modified boundary condition of 2 inches of water.

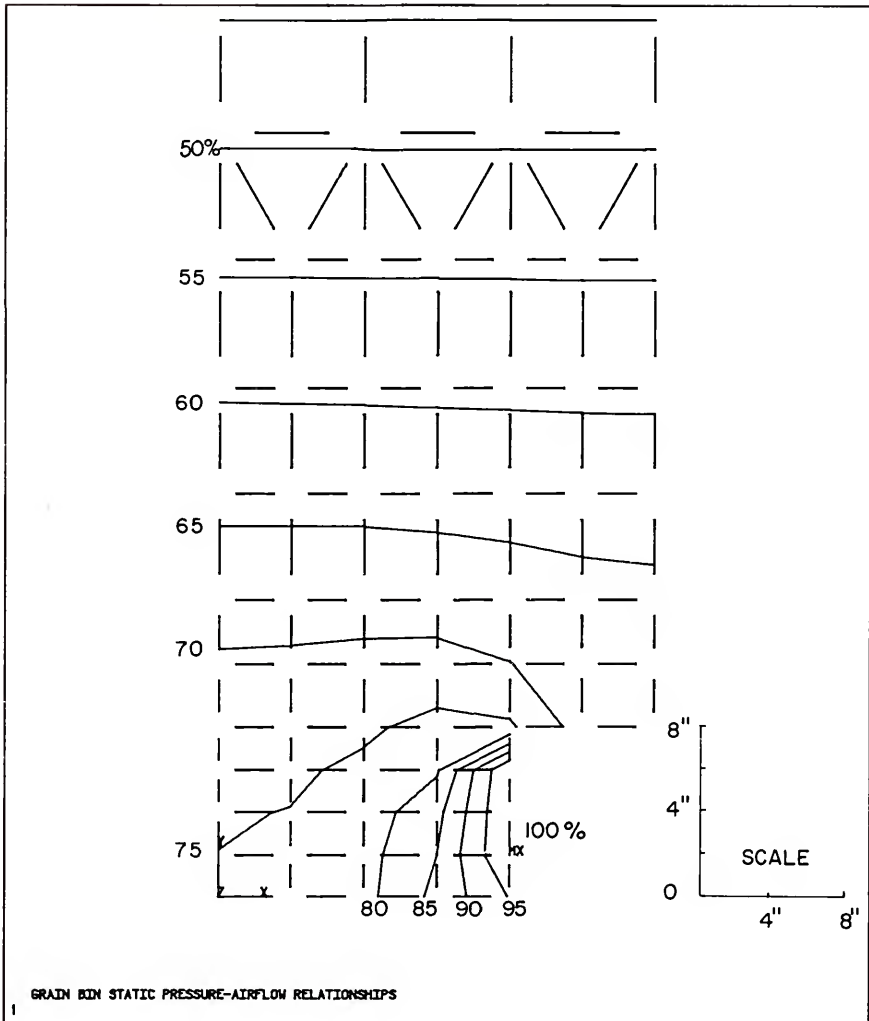


Figure D-14. Isobaric contour lines calculated using ANSYS with a modified boundary condition of 3 inches of water.

Three-Dimensional Grain Bin

In extending the procedures of Segerlind (1982) to account for three dimensional air flow through cylindrical grain storages, Khompis (1983) used a model that consisted of three components or separate computer programs. The first program calculated the three-dimensional nodal pressure values for the element grid shown in Figure 7. As noted in the Procedures Section computer restrictions required the limitation of the number of elements used.

The second computer program generated a two-dimensional finite element grid for specified vertical and horizontal cutting planes. The cutting planes are illustrated in Figure D-15. The element grids on the vertical and horizontal cutting planes are shown in Figures D-16 and D-17. It is noted that these two-dimensional finite element grids contain many more elements than the three-dimensional model employed in the first computer program. The nodal pressures from the first program were used as input for the second program. The second program then was used to generated nodal pressures for all the additional nodes on the cutting planes not present in the three-dimensional finite element program. The nodal velocity values were then calculated using the nodal pressures for the cutting planes. The second program was also used to draw the pressure and velocity distribution contour lines on the cutting planes.

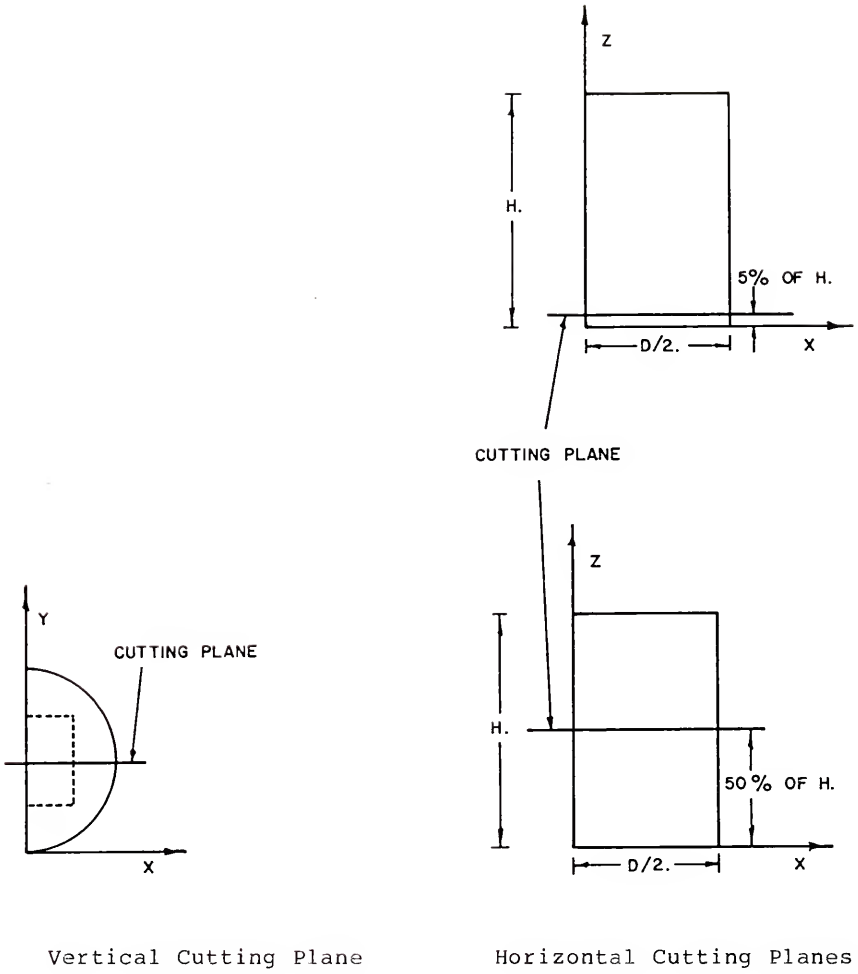


Figure D-15. Vertical and Horizontal Cuttings Planes used by Khompis (1983).

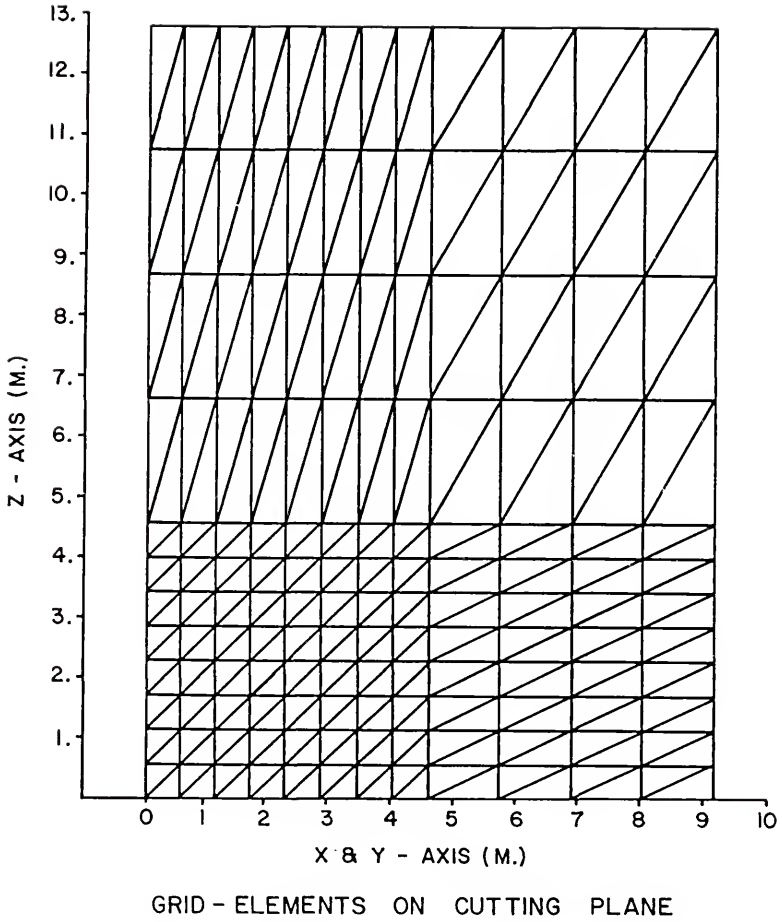


Figure D-16. Location of the elements on the vertical cutting plane from Khompis (1983).

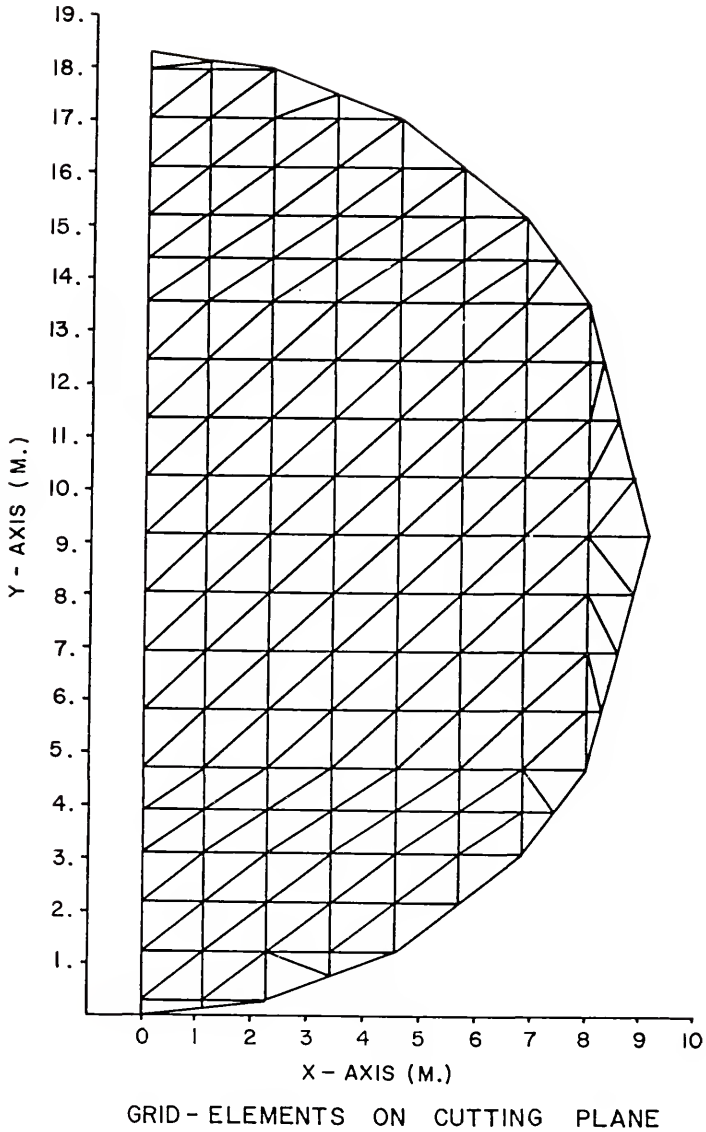


Figure D-17. Location of the elements on the horizontal cutting plane from Khompis (1983).

The third computer program was used to display the three-dimensional pressure and velocity distributions, obtained with the second computer program. The data points from eight cutting planes were used to generate three-dimensional pressure and velocity surfaces for a quarter section of the square duct perforated floor system. The three-dimensional graphics program allowed the display to be viewed from any angle, any elevation, and any distance.

Using the appropriate post-processing commands, ANSYS provided the capability to plot the various pressure and velocity distributions reported by Khompis (1983). The constant pressure and velocity lines for any desired two-dimensional section could be plotted and viewed from any angle, elevation, and distance. The three-dimensional surfaces could also be plotted using ANSYS, although the surfaces were not as sharp as the perspective transect diagrams produced by the graphics package used by Khompis (1983).

The two-dimensional pressure distribution patterns for the square duct perforated floor reported by Khompis (1983) are shown in Figures D-18, D-19, and D-20. Khompis (1983) noted that the pressure changed in a relatively uniform manner with respect to the vertical axis and that over 50 percent of the pressure loss occurred in the lower 50 percent of the total height. Khompis (1983) also pointed out that the pressure at the intersection of the bin wall and floor was 63 percent of the perforated floor pressure.

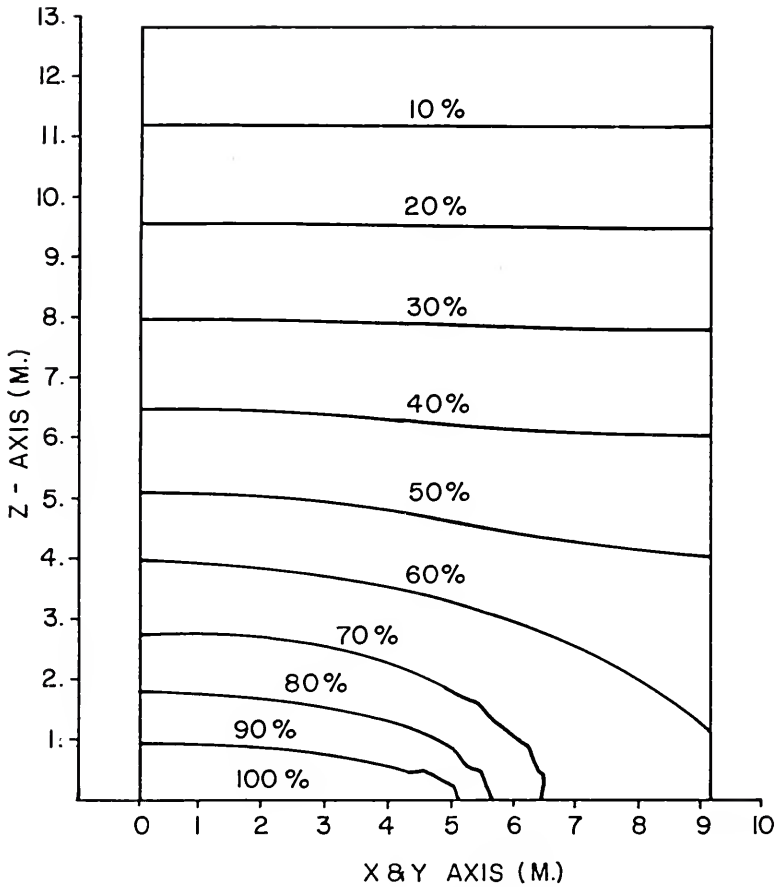
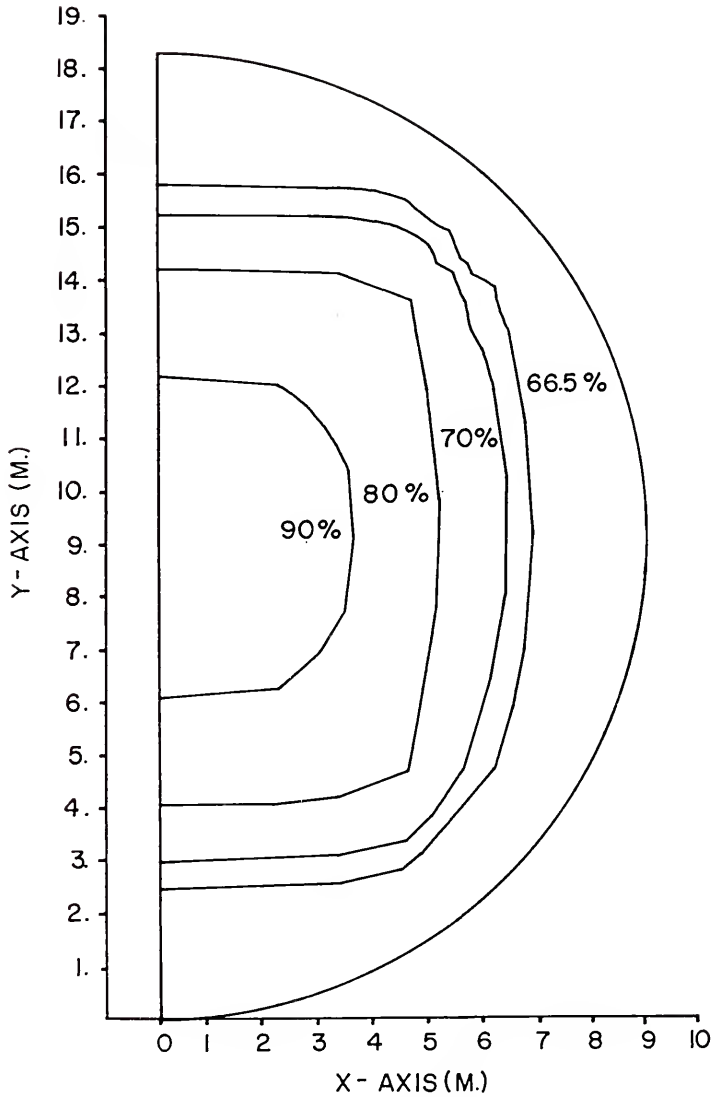
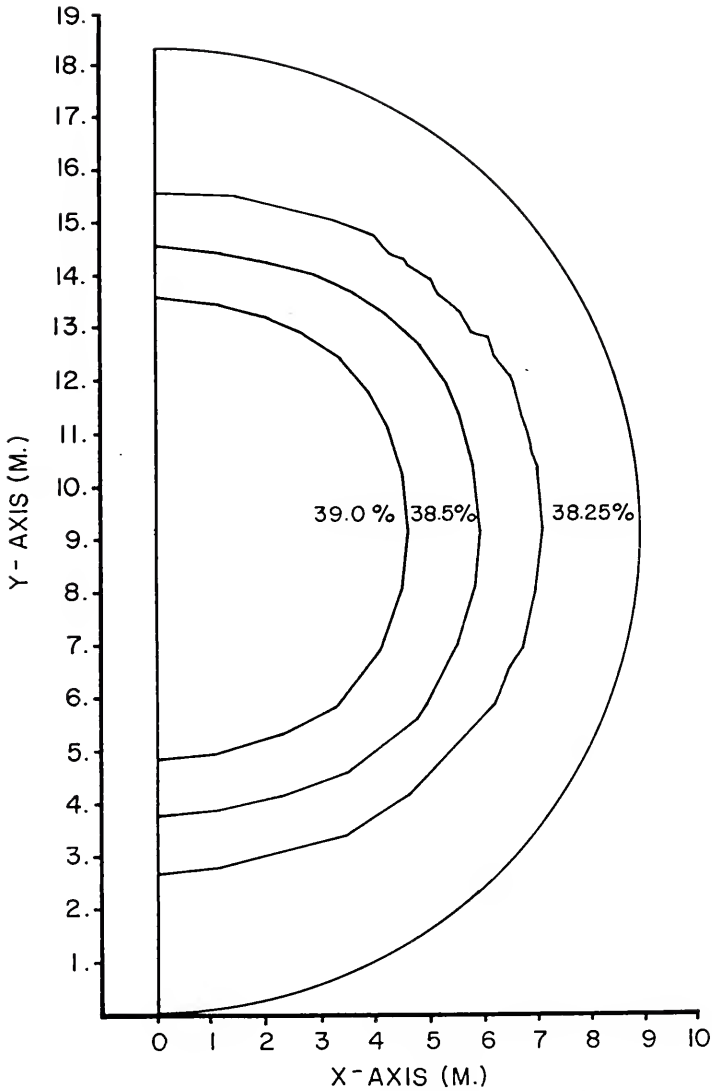


Figure D-18. Isobaric distribution in percent of total pressure loss on a vertical cutting plane from Khompis (1983).



ISO- PRESSURE LINES ON CUTTING PLANE

Figure D-19. Isobaric distribution in percent of total pressure loss on horizontal cutting plane at 5 percent of bin height from Khompis (1983).



ISO- PRESSURE LINES ON CUTTING PLANE

Figure D-20. Isobaric distribution in percent of total pressure loss on a horizontal cutting plane at 50 percent of bin height from Khompis (1983).

The three-dimensional 70 percent isobaric surface presented by Khompis is illustrated in Figures D-21, D-22, and D-23. Khompis (1983) noted that the square shaped surface intersected the bin floor 6 meters from the center of the bin.

The two dimensional velocity distributions reported by Khompis (1983) for the square duct system, are represented in Figures D-24, D-25, and D-26. Khompis (1983) reported the maximum velocity of approximately 5.3 meters per minute occurred near the outer edge of the perforated floor. Further, the velocity decreased rapidly the first 15 percent of the height and above a height of 64 percent (incorrectly reported as 50 percent) the velocity was relatively uniform range between 1.80 and 1.95 meters per minute. The lowest velocity values of approximately 0.7 meters per minute occurred between the bin wall and the floor on a perpendicular line through the mid of each of the sides of the square duct. These regions determined by Khompis (1983) are shown in Figure D-27.

The three-dimensional 2.4 meters per minute velocity surface presented by Khompis (1983) is illustrated in Figures D-28, D-29, and D-30.

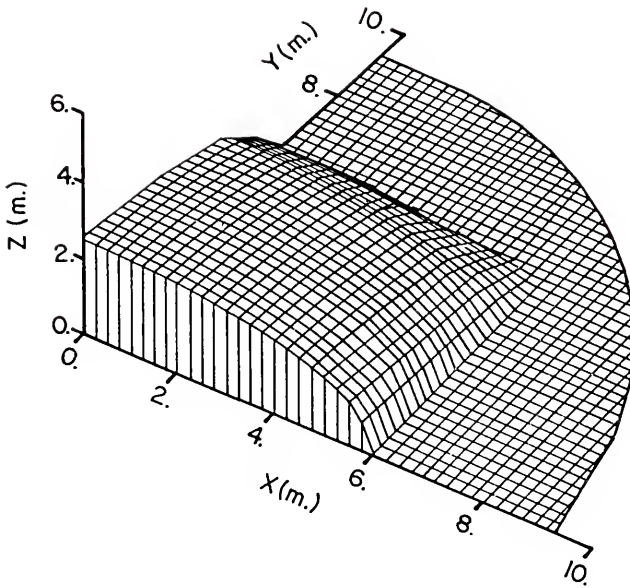


Figure D-21. 70 percent of total pressure loss isobaric surface from Khompis (1983).

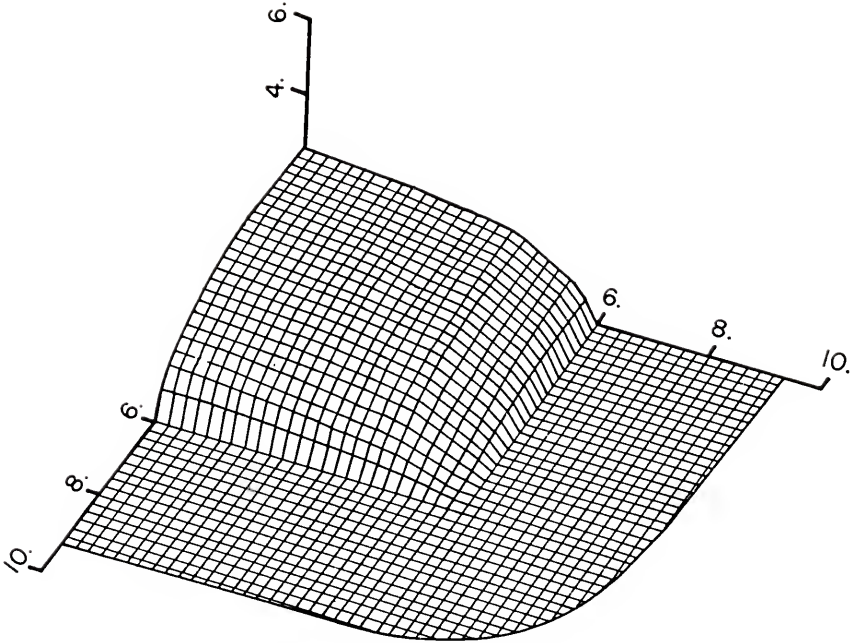


Figure D-22. 70 percent of total pressure loss isobaric surface from Khompis (1983).

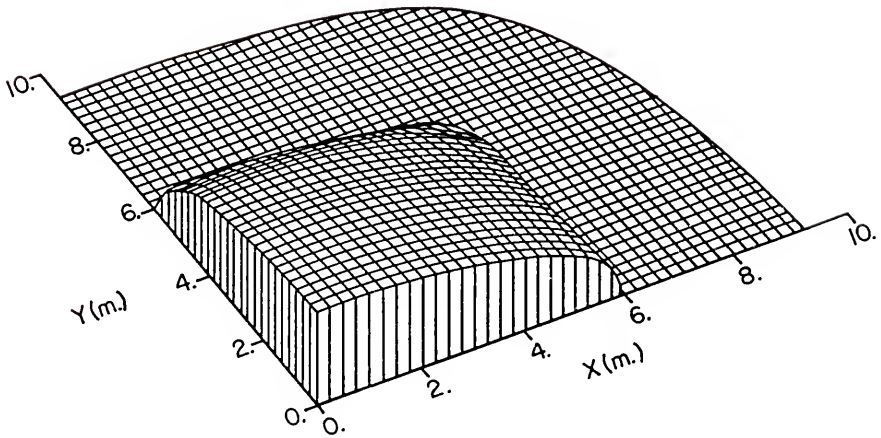


Figure D-23. 70 percent of total pressure loss isobaric surface from Khompis (1983).

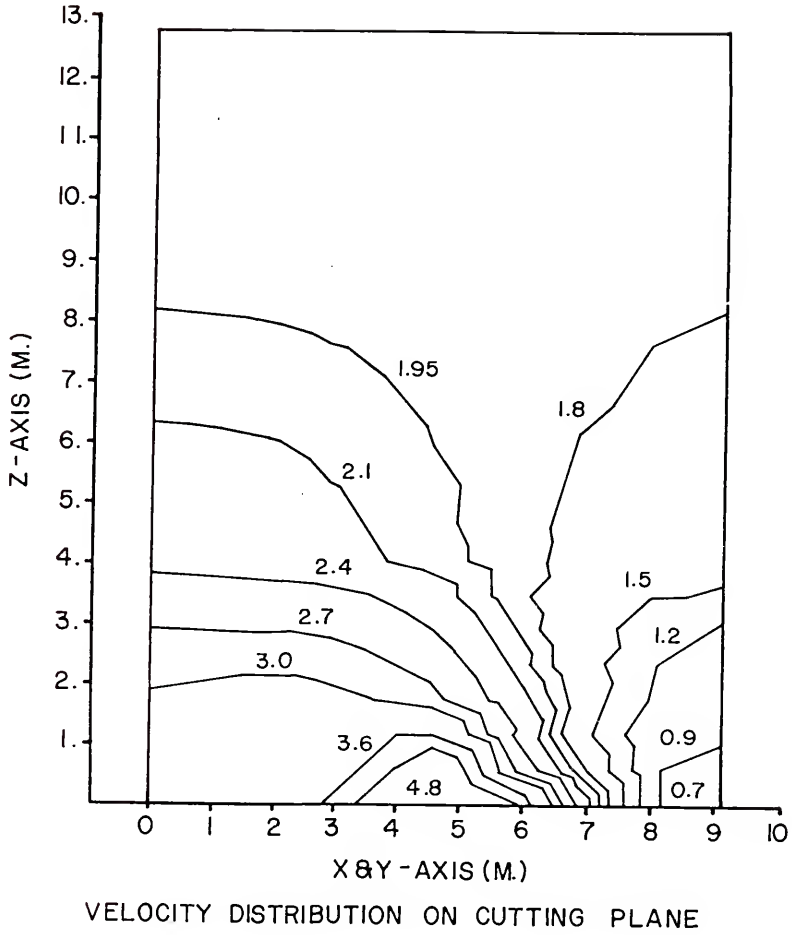


Figure D-24. Velocity distribution in meters per minute on a vertical cutting plane from Khompis (1983).

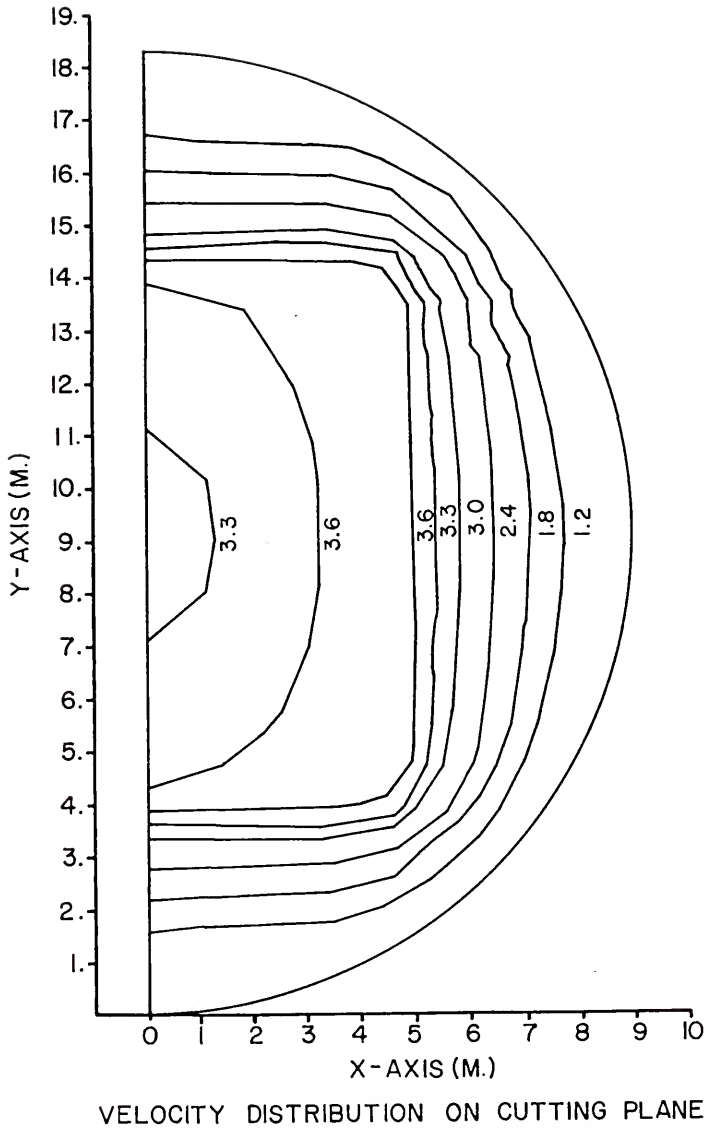
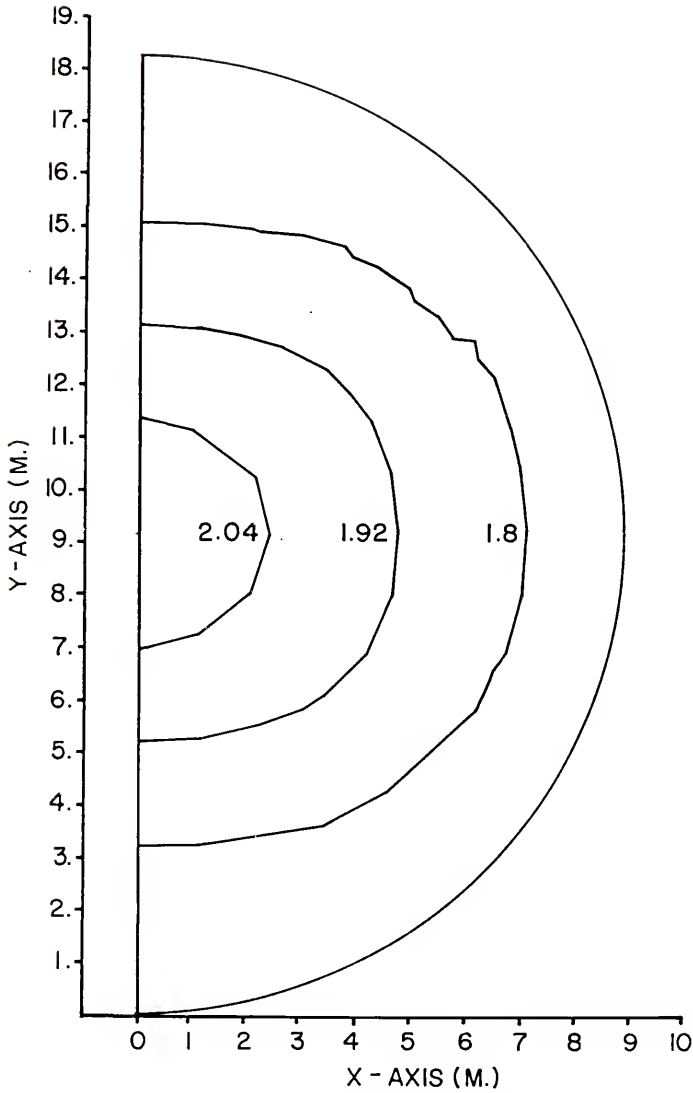


Figure D-25. Velocity distribution in meters per minute on a horizontal cutting plane at 5 percent of bin height from Khompis (1983).



VELOCITY DISTRIBUTION ON CUTTING PLANE

Figure D-26. Velocity distribution in meters per minute on a vertical cutting plane at 50 percent of bin height from Khompis (1983).

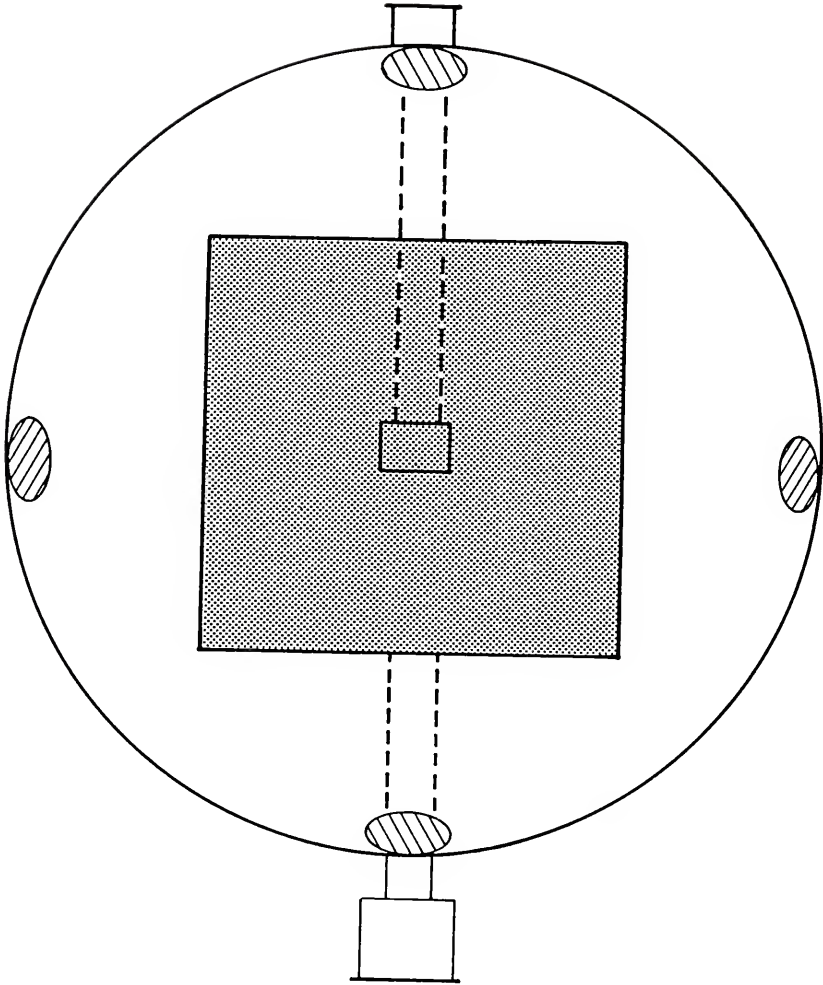


Figure D-27. Minimum velocity regions for the square duct system from Khompis (1983).

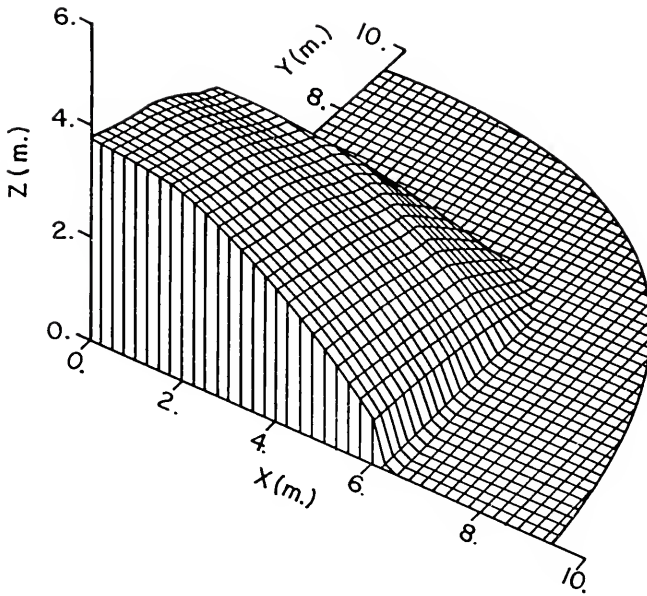


Figure D-28. Constant velocity surface of 2.4 meters per minute from Khompis (1983).

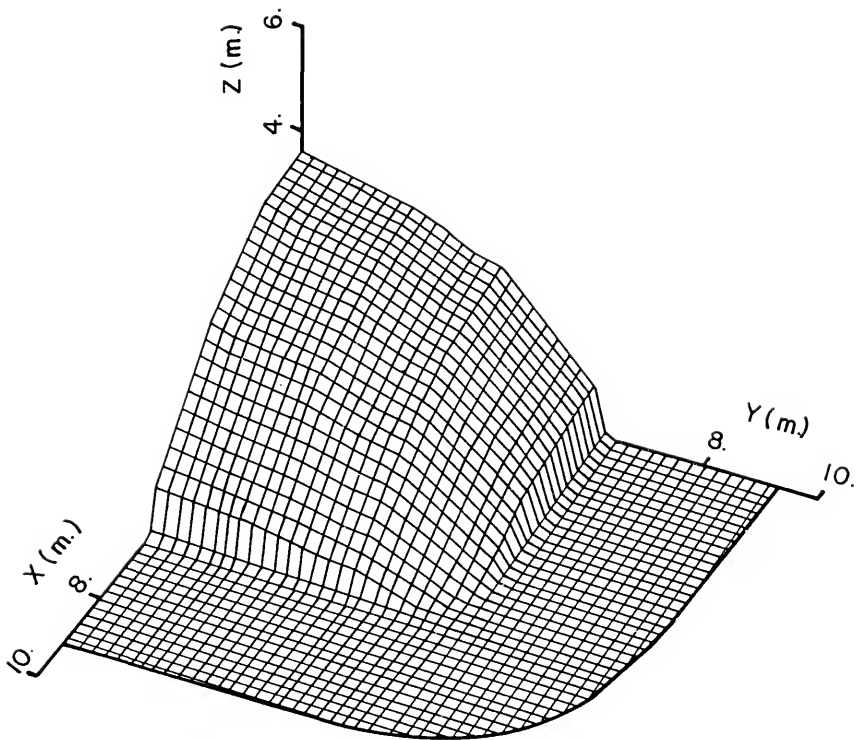


Figure D-29. Constant velocity surface of 2.4 meters per minute from Khompis (1983).

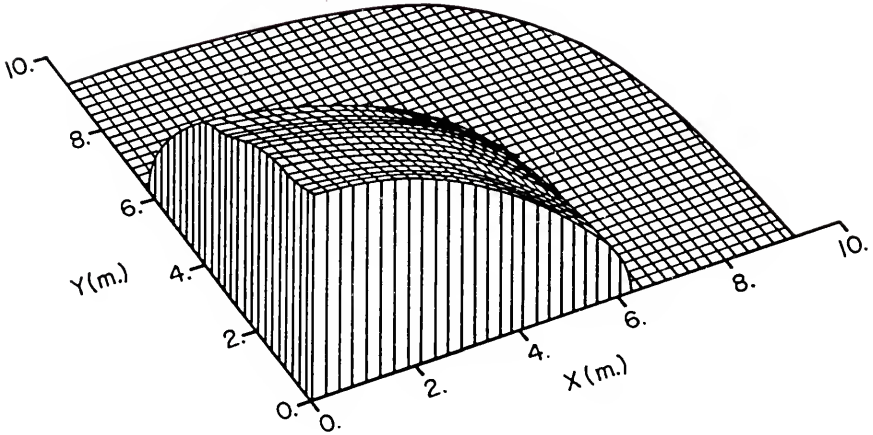


Figure D-30. Constant velocity surface of 2.4 meters per minute from Khompis (1983).

ANSYS was used to solve the problem reported by Khompis (1983) and every effort was made to duplicate this previous solution and presentation of the results. The same iterative convergence criteria of 0.25 Pascals was used for the solution. The same cutting planes that Khompis (1983) used were applied.

The two-dimensional pressure distribution patterns for the square duct perforated floor system calculated by ANSYS are shown in Figures D-31, D-32, and D-33.

The isobaric pattern shown in Figure D-31 was very similar to that presented by Khompis (1983) in Figure D-18. However, the isobaric pattern calculated using ANSYS produced a slightly increased pressure loss. The isobar that intersects the bin wall at the bin floor was determined to be 60.4 percent using ANSYS, while Khompis (1983) calculated 63 percent. The contours calculated by the two methods differ in both the vertical and horizontal directions. The average difference in terms of bin measurements for the intersection of the contours and the vertical and horizontal axis were 1.64 and 0.86 meters, respectively. The horizontal comparison between the ANSYS and Khompis (1983) solutions are better than the vertical comparison. The largest difference occurred for the 60 percent isobar. The value predicted by Khompis (1983) intersects the left vertical axis at a height of 3.93 meters and the right vertical axis at 1.20 meters. The same isobar calculated using ANSYS intersected the left and right vertical axis at

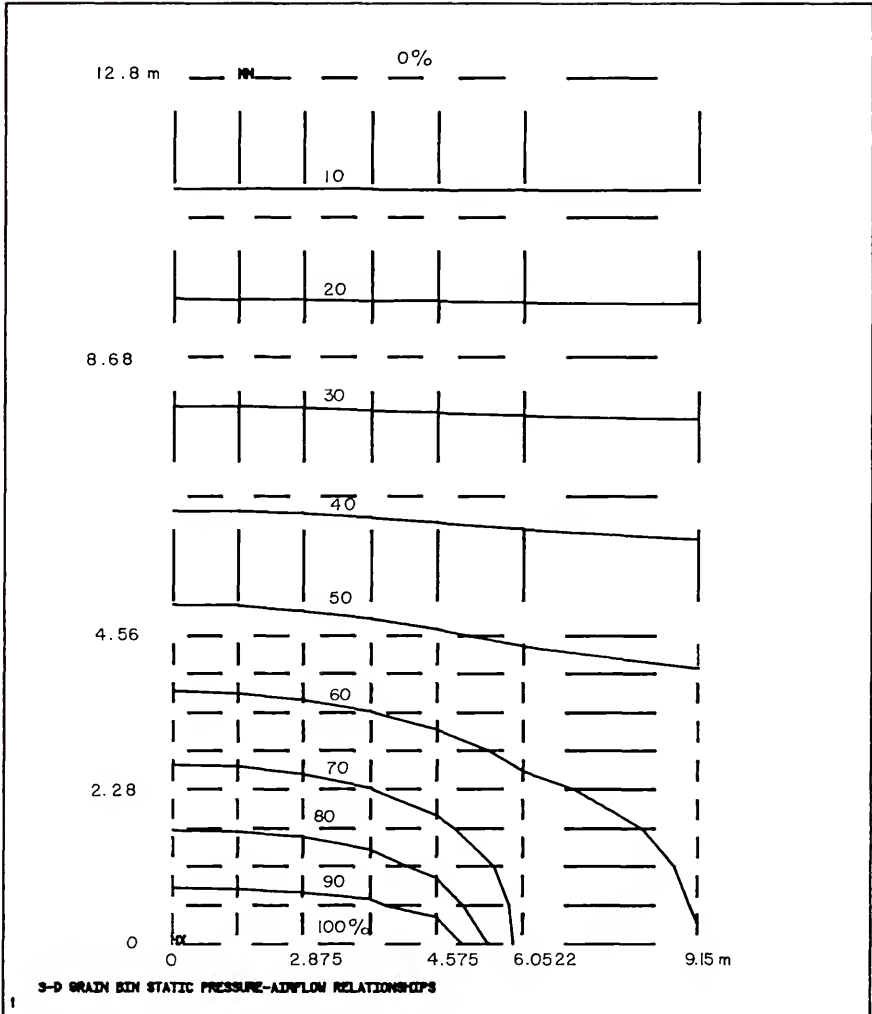


Figure D-31. Isobaric distribution calculated using ANSYS in percent of total pressure loss on the vertical cutting plane.

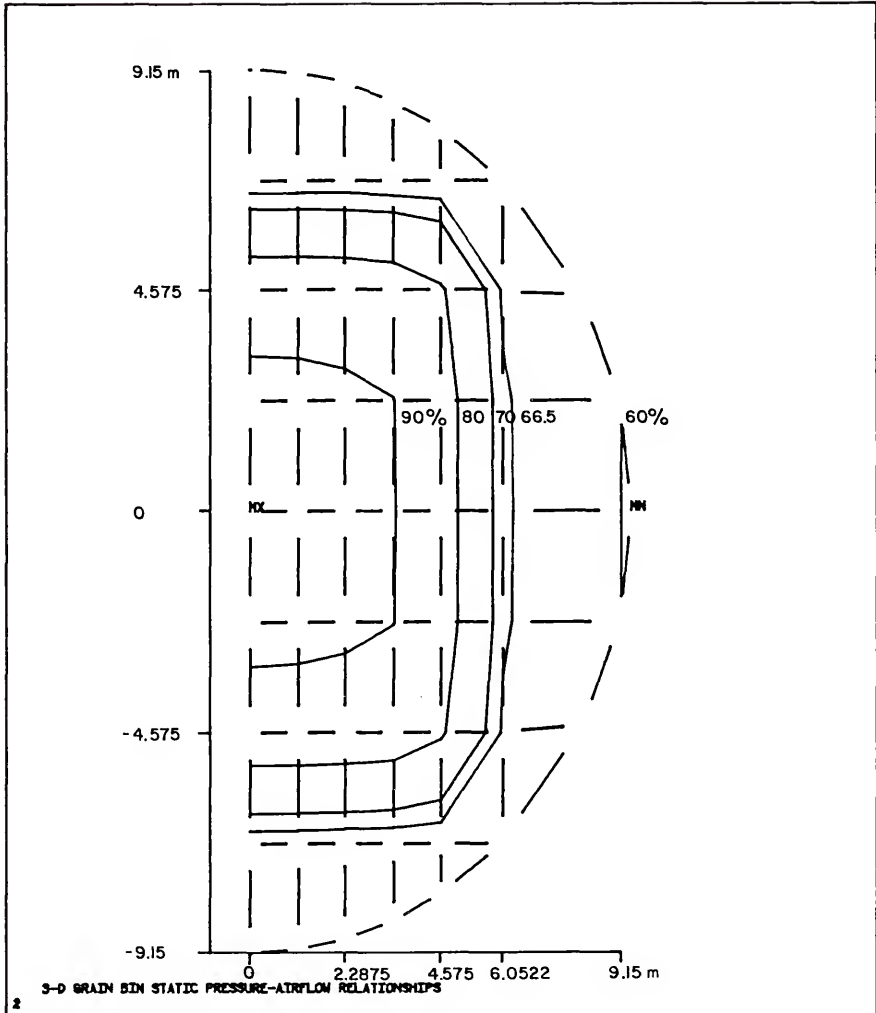


Figure D-32. Isobaric distribution calculated using ANSYS in percent of total pressure loss on the horizontal cutting plane at 5 percent of bin height.

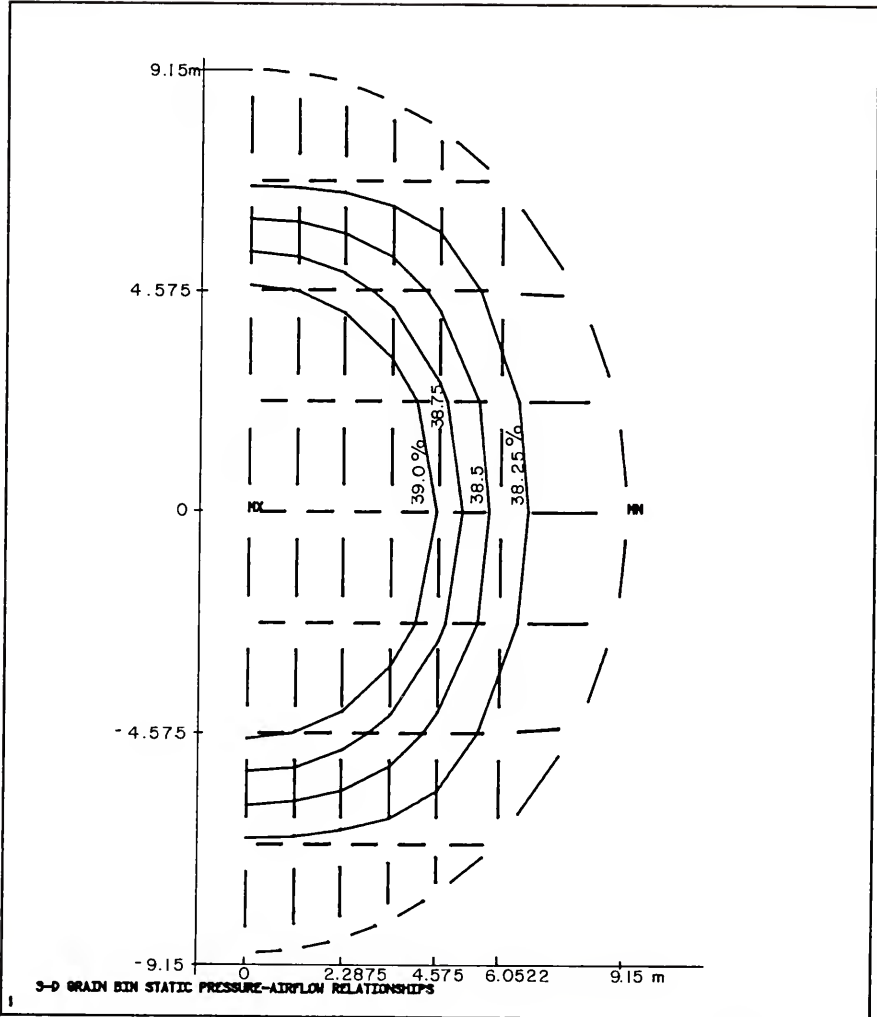


Figure D-33. Isobaric distribution calculated using ANSYS in percent of total pressure loss on the horizontal cutting plane at 50 percent of bin height.

3.70 and 0.25 meters, respectively. All the other contours were in better agreement, but all the ANSYS isobars occurred closer to the duct entrance than the same isobar reported by Khompis (1983).

The isobaric pattern at 5 percent of the bin height shown in Figure D-32 was again very similar to the results reported by Khompis (1983) in Figure D-19. The contours in Figure D-32 have a more blunt shape at the outer face of the semicircular shaped isobar. As noted in the comparison of vertical pressure distribution, the pressure loss calculated by ANSYS along the centerline of the semicircular bin section, occurred more rapidly than the values predicted by Khompis (1983). However, the pressures at the intersection of the left vertical axis (cutting plane of the circular bin) indicated that the pressure loss predicted by Khompis (1983) was slightly greater than that calculated by ANSYS. The 70 percent isobar predicted by Khompis (1983) intersected the axis along centerline of the semicircular bin at a distance of 6.35 meters from the cutting plane of the circular bin and intersects the cutting plane at a distance of 6.10 meters from the centerline. The same isobar calculated by ANSYS intersected the two axis at 5.85 and 6.28 meters, respectively.

The isobaric pattern at 50 percent of the bin height shown in Figure D-33 was again very similar to the results reported by Khompis (1983) in Figure D-20. As noted in the comparison of vertical and 5 percent horizontal pressure

distribution, the pressure loss calculated by ANSYS along the centerline of the semicircular bin section occurred more rapidly than the values predicted by Khompis (1983). As noted for the pressure distribution on the 5 percent horizontal plane, the pressures at the intersection of the left vertical axis indicated that the pressure loss predicted by Khompis (1983) was slightly greater than that calculated by ANSYS. The 38.5 percent isobar predicted by Khompis (1983) intersected the axis along centerline of the bin at a distance of 4.57 meters from the cutting plane of the circular bin and intersected the cutting plane at a distance of 4.275 meters from the centerline. The same isobar calculated by ANSYS intersected the two axis at 4.54 and 4.79 meters, respectively.

The three-dimensional 70 percent of total pressure isobaric surface produced by ANSYS with three perspectives is shown in Figures D-34, D-35, and D-36. Khompis (1983) noted the difficulty in displaying pressure and velocity patterns in three dimensional plots. The three figures plotted using ANSYS were an attempt to duplicated Figures D-21, D-22, and D-23, respectively. The quality of the plots presented by Khompis (1983) are more refined but the capability of ANSYS to provide this graphical data analysis without need for an external plotting package is significant. For the problem under consideration there is not a critical need for three dimensional surface plots.

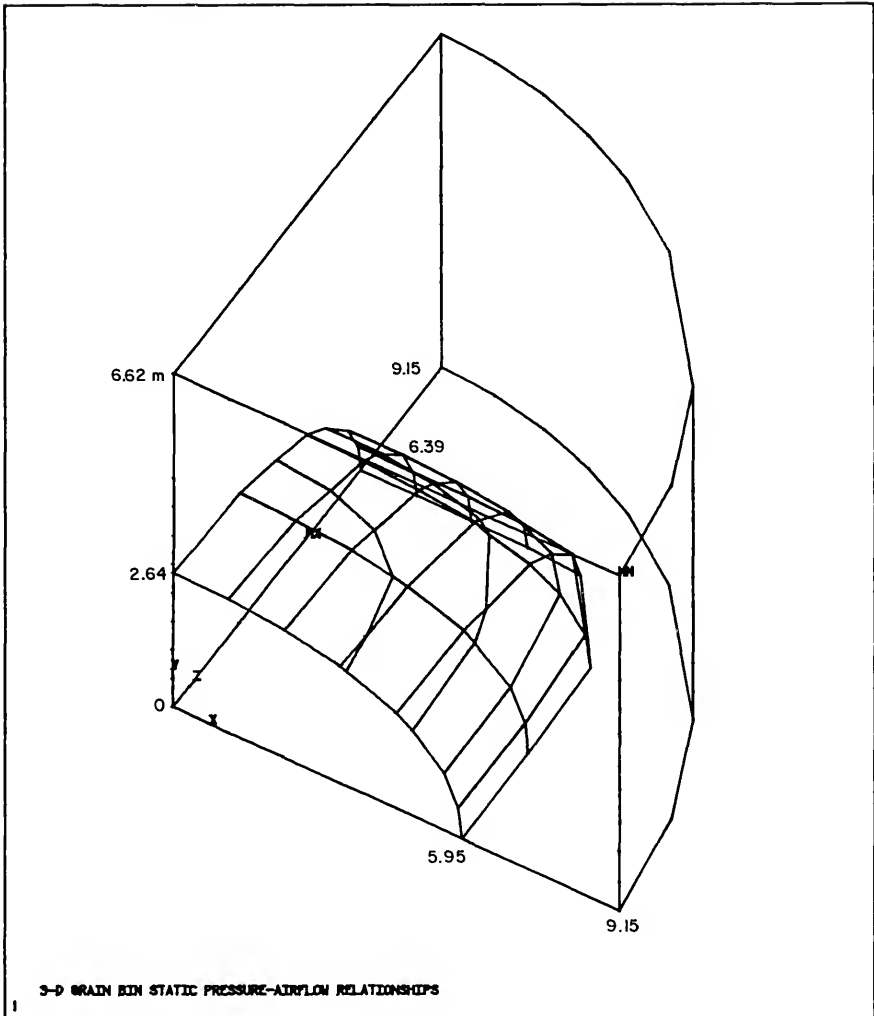


Figure D-34. 70 percent of total pressure loss isobaric surface produced by ANSYS, view 1.

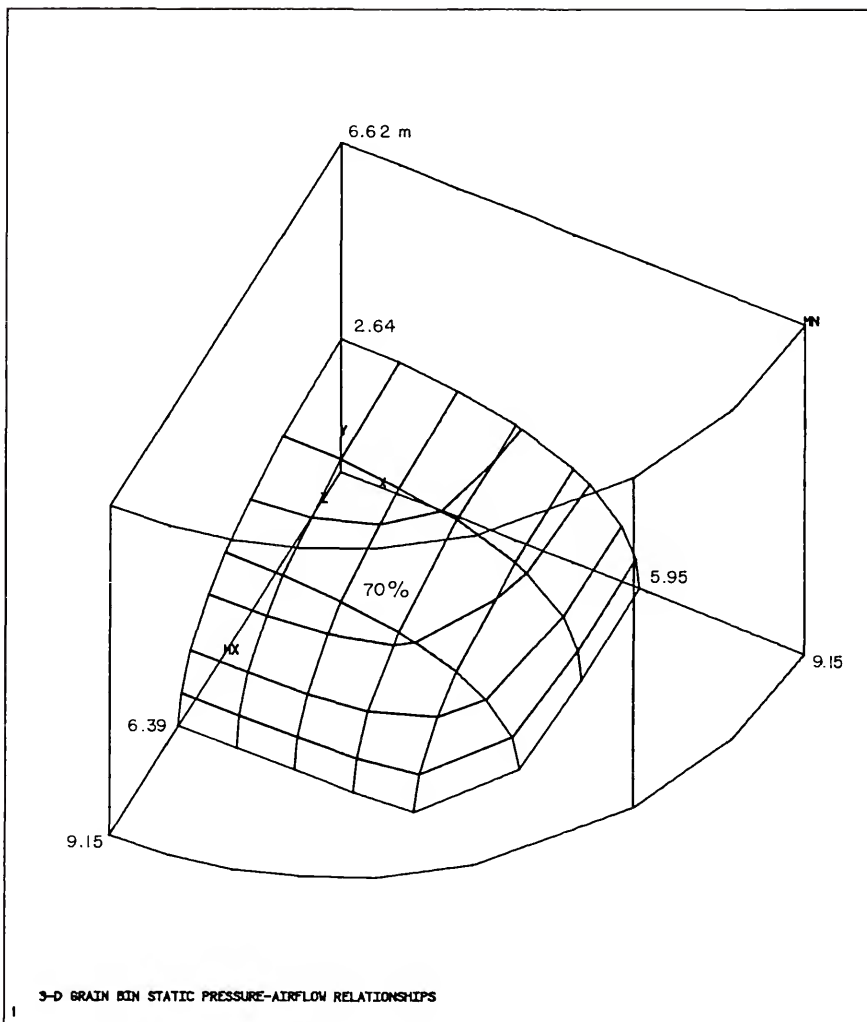


Figure D-35. 70 percent of total pressure loss isobaric surface produced by ANSYS, view 2.

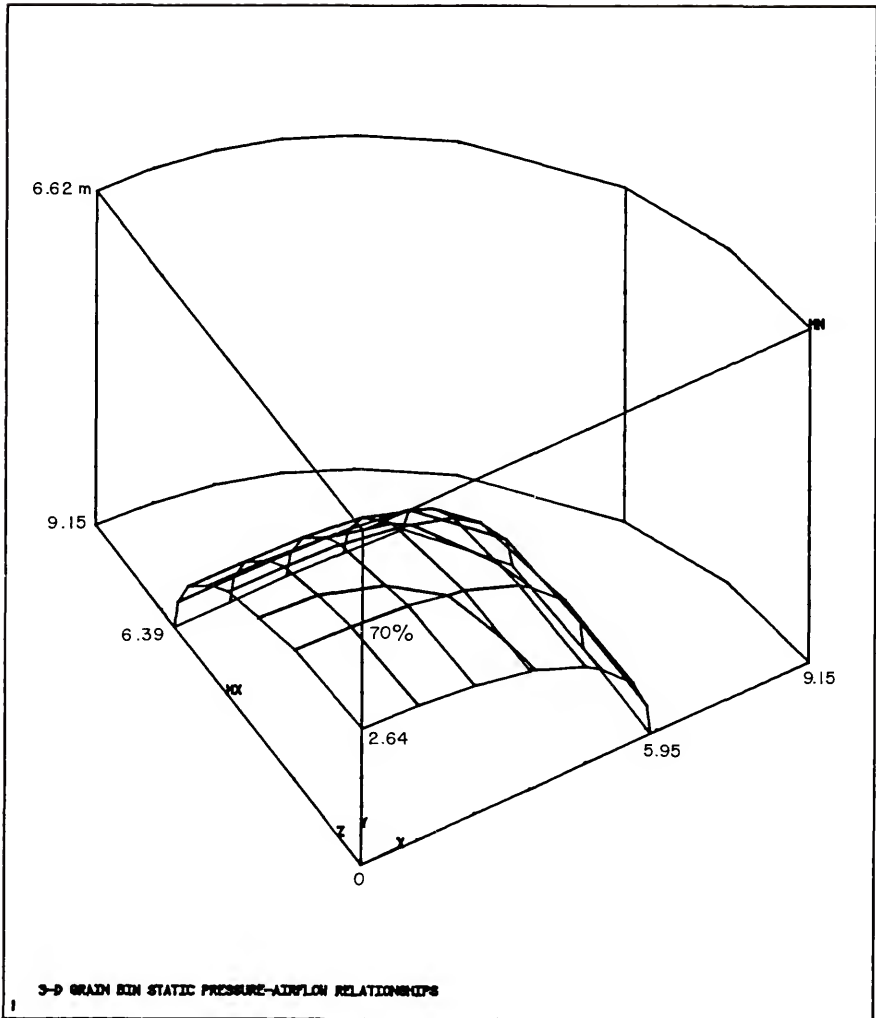


Figure D-36. 70 percent of total pressure loss isobaric surface produced by ANSYS, view 3.

The shape of the 70 percent isobaric surface obtained by Khompis (1983) and with ANSYS were similar. As noted above, the 70 percent isobaric surface that Khompis (1983) determined, intersected the floor 6.00 meters from the center of the bin. In addition this surface intersected the vertical axis at a bin height of 2.46 meters.

Interestingly, when comparing Figure D-18 with Figures D-21, D-22, and D-23, the 70 percent isobar in Figure D-18 intersected the floor and vertical axis at 6.4 and 2.74 meters, respectively. The use of three separate models to produce the two-dimensional and three-dimensional plots by Khompis (1983) resulted in a difference in location of the 70 percent isobar on the two plots. The three-dimensional plot indicated a greater pressure loss occurred closer to the duct entrance.

The 70 percent isobaric surface determined using ANSYS intersected the floor on the cutting plane of the circular bin at 6.39 meters from the center of the bin and intersected the floor on the centerline of the semicircular bin section at 5.95 meters from the center of the bin. The surface also intersected the vertical axis at a bin height of 2.64 meters. The difference in the intersection points at the floor followed a similar pattern exhibited on the 5 and 50 percent horizontal sections shown in Figures D-32, and D-33, respectively. In comparing Figure D-31 with Figures D-34, D-35, and D-36, the 70 percent isobar intersected the bin floor on the centerline of the

semicircular bin at 5.95 meters from the center of the bin and intersected the vertical axis at a bin height of 2.57 meters. As expected, the two- and three-dimensional plots were in good agreement, since the same data was used by ANSYS for all the plots.

Comparing the 70 percent surfaces predicted by Khompis (1983) and determined using ANSYS, it was noted that the pressure loss was very similar. The 70 percent surface predicted by ANSYS occurred slightly further from the entrance duct than the same surface predicted by Khompis (1983). Following the reasoning used above, this would indicate that the pressure loss in the vicinity of the 70 percent isobaric surface predicted by Khompis (1983) was higher than the pressure loss determined using ANSYS.

The two-dimensional velocity distributions calculated using ANSYS for the square duct system are shown in Figures D-37, D-38, and D-39. The constant velocity lines calculated using ANSYS and by Khompis (1983) exhibited similar patterns. The ANSYS solution predicted a penetration of higher velocity flow further up into the grain which was in the bin. This was consistent with the higher pressure loss predicted by ANSYS.

The constant velocity pattern shown in Figure D-37 was very similar to that presented by Khompis (1983) in Figure D-24. The maximum velocity predicted by ANSYS was 5.35 meters per minute which occurred near the outer edge of the perforated square duct. As reported by Khompis (1983), the

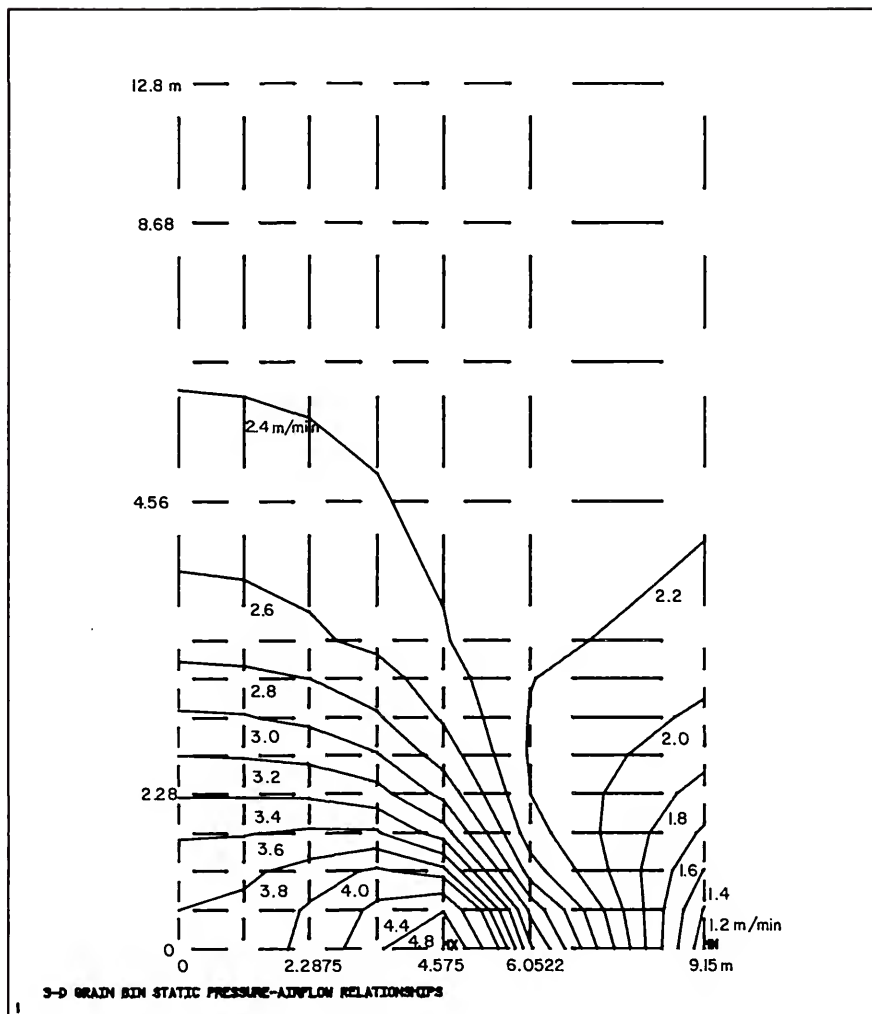


Figure D-37. Velocity distribution calculated using ANSYS in meters per minute on a vertical cutting plane.

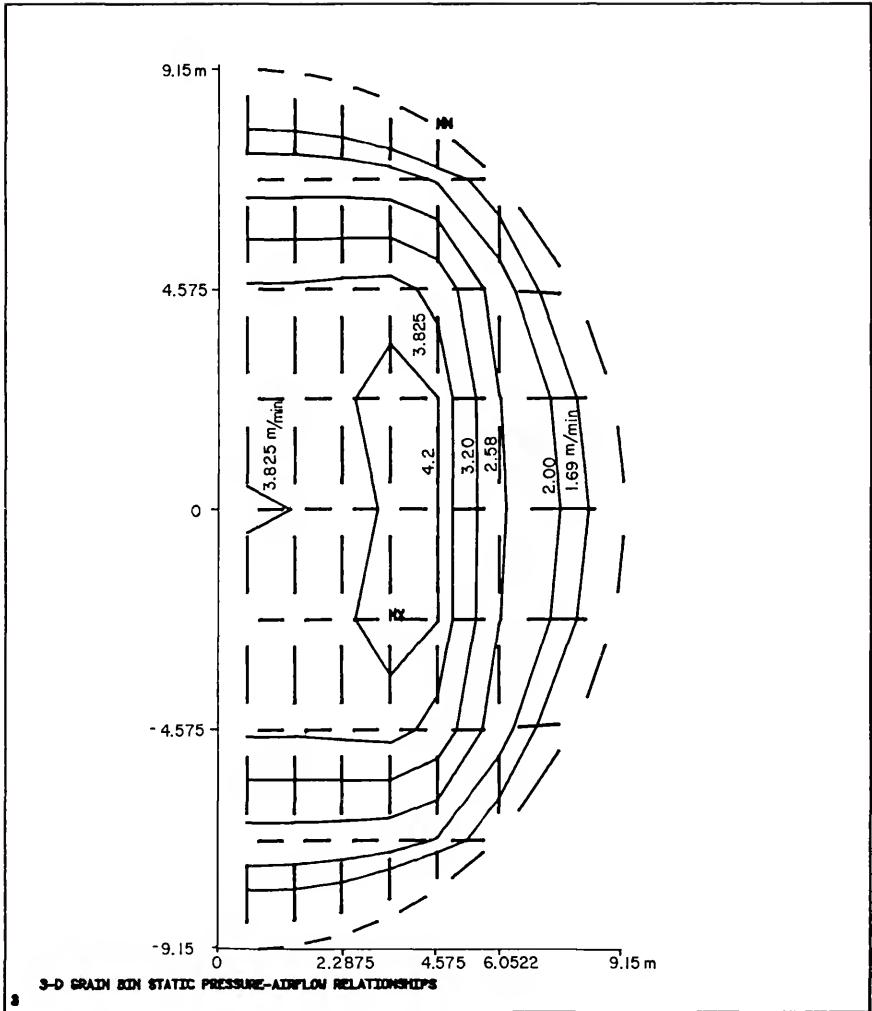


Figure D-38. Velocity distribution calculated using ANSYS in meters per minute on a horizontal cutting plane at 5 percent of bin height.

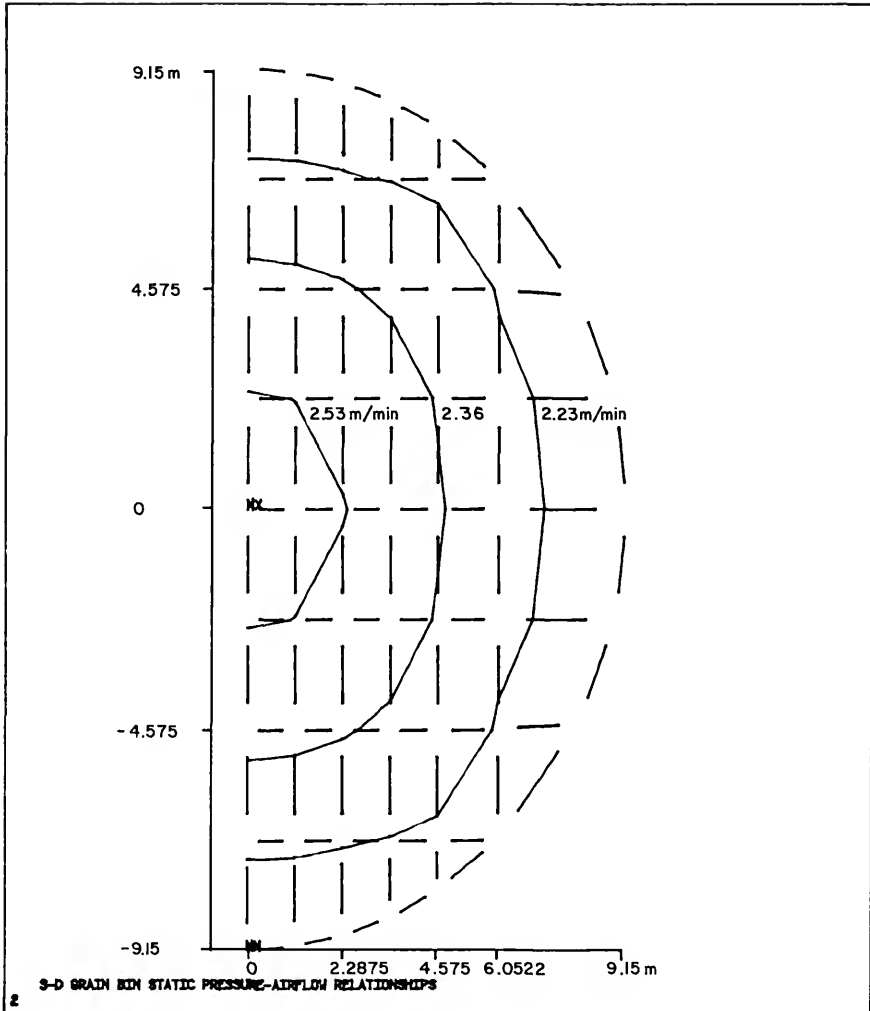


Figure D-39. Velocity distribution calculated using ANSYS in meters per minute on a horizontal cutting plane at 50 percent of bin height.

constant velocity plot from ANSYS demonstrated a rapid velocity decrease during the first 15 percent of the bin height. Above 64 percent of the height, the velocity calculated by ANSYS was relatively uniform in the range between 2.27 to 2.41 meters per minute. The lowest velocity value calculated by ANSYS of 1.07 meters per minute occurred at the same locations described by Khompis (1983) in Figure D-27.

A comparison of the location of the constant velocity lines in relation to the coordinate system of the grain bin, revealed that the values predicted by ANSYS at a particular location in the bin are 0.3 to 0.5 meters per minute higher than the values calculated by Khompis (1983). This was consistent with the difference in predicted pressure loss values determined by the two methods. To illustrate this point, the 2.4 meters per minute velocity contour in Figure D-24 intersected the bin floor 6.80 meters from the center of the bin and intersects the vertical axis at a bin height of 3.79 meters. The 2.8 meters per minute velocity contour in Figure D-37 intersected the two axes nearest the points of intersection of 2.4 meters per minute in Figure D-24, at 6.86 and 4.20 meters, respectively.

The constant velocity pattern at 5 percent of the bin height shown in Figure D-38 was also similar to the results reported by Khompis (1983) in Figure D-25. The constant velocity lines in Figure D-38 were selected to correspond as close as possible with the bin location of the constant

velocity lines presented in Figure D-25. As previously noted, the velocity predicted by ANSYS at a particular location was higher than the velocity predicted by Khompis (1983). Khompis (1983) did not present contours for velocities above 3.6 meters per minute. If Khompis (1983) had plotted the higher velocities, closed velocity contours would have been presented. This was illustrated in Figure D-38 by the 4.2 meters per minute velocity contour.

The constant velocity pattern at 50 percent of the bin height shown in Figure D-39 was again similar to the results reported by Khompis (1983) in Figure D-26. As noted in the comparison of vertical and 5 percent horizontal velocity distributions, the velocity calculated by ANSYS was higher than the velocity calculated by Khompis (1983). The minimum velocity on the 50 percent horizontal plane calculated by ANSYS was 2.17 meters per minute, while the maximum was 2.59 meters per minute.

Like the velocity distribution in Figure D-38, the constant velocity lines in Figure D-39 were selected to correspond as close as possible with the bin location of the constant velocity lines presented in Figure D-26. The 2.53 meters per minute velocity shown in Figure D-39 was not as smooth as the 2.04 meters per minute velocity line in Figure D-26.

As noted above, the velocity calculated by ANSYS penetrated further up into the grain which was in the bin than calculated by Khompis (1983). In order to compare

three similar three-dimensional figures plotted by ANSYS to Figures D-28, D-29, and D-30, the constant velocity of 2.8 meters per meter was selected. The three-dimensional 2.8 meters per minute velocity surface calculated using ANSYS is illustrated in Figures D-40, D-41, and D-42.

The shape of the 2.4 meters per minute constant velocity surface obtained by Khompis (1983) and the 2.8 meters per minute constant velocity surface obtained by ANSYS are similar. The 2.4 meters per minute velocity surface in Figures D-28, D-29, and D-30, intersected the vertical axis and floor of the bin at approximately the same locations as the 2.4 constant velocity line in Figure D-24. The 2.8 meters per minutes velocity surface in Figures D-40, D-41, and D-42, also intersected the vertical axis and bin floor at approximately the same locations as the 2.8 constant velocity line in Figure D-37, as expected. The better agreement between velocities when compared to the agreement of the pressures can be attributed to the fact that in the procedures used by Khompis (1983), the velocity was not calculated in the first model. After the pressures were determined in the second model used by Khompis (1983), then the velocity was calculated. Therefore the velocity data Khompis (1983) used was the same for the two- and three-dimensional velocity plots. This is of course the same case for ANSYS, as noted concerning the pressure loss plots above.

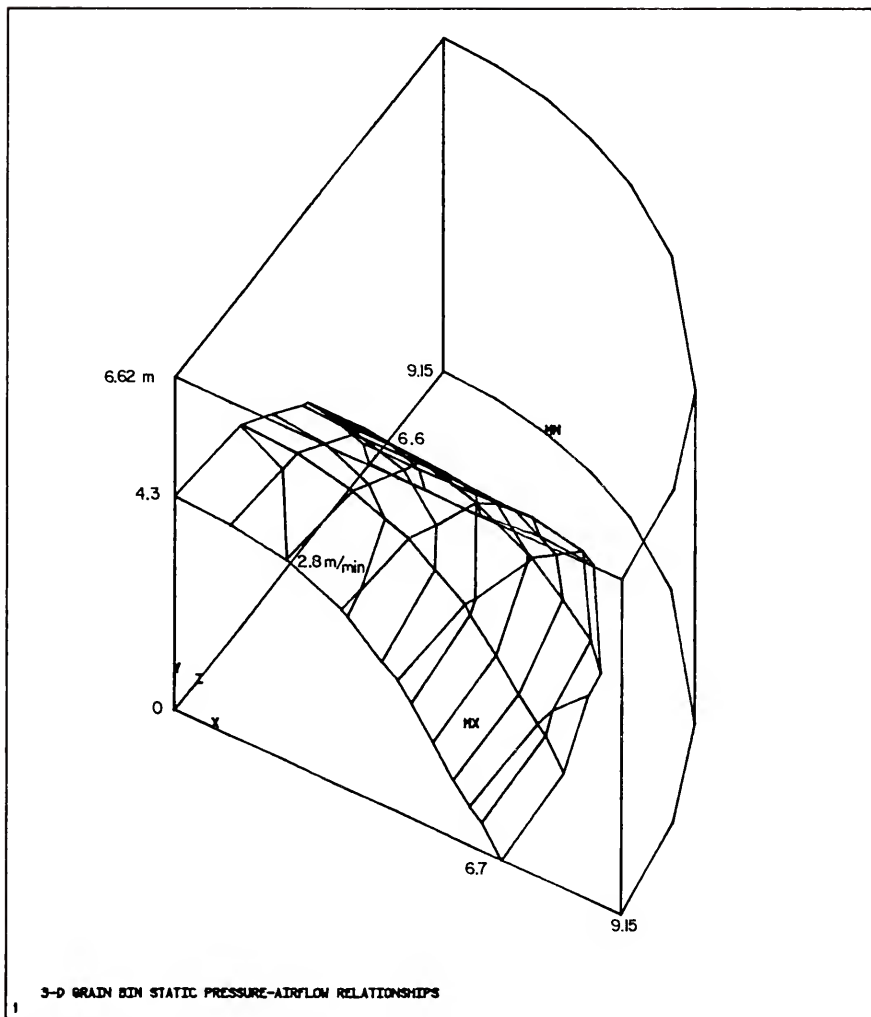


Figure D-40. Constant velocity surface of 2.8 meters per minute calculated using ANSYS, view 1.

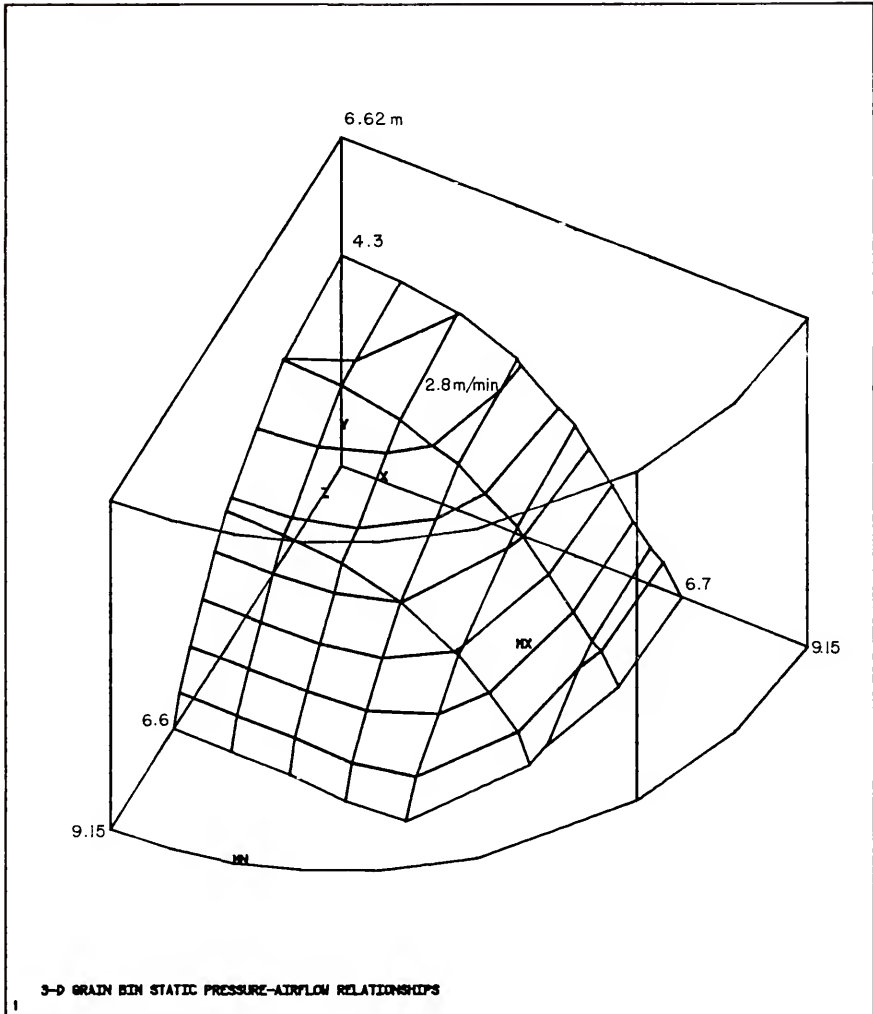


Figure D-41. Constant velocity surface of 2.8 meters per minute calculated using ANSYS, view 2.

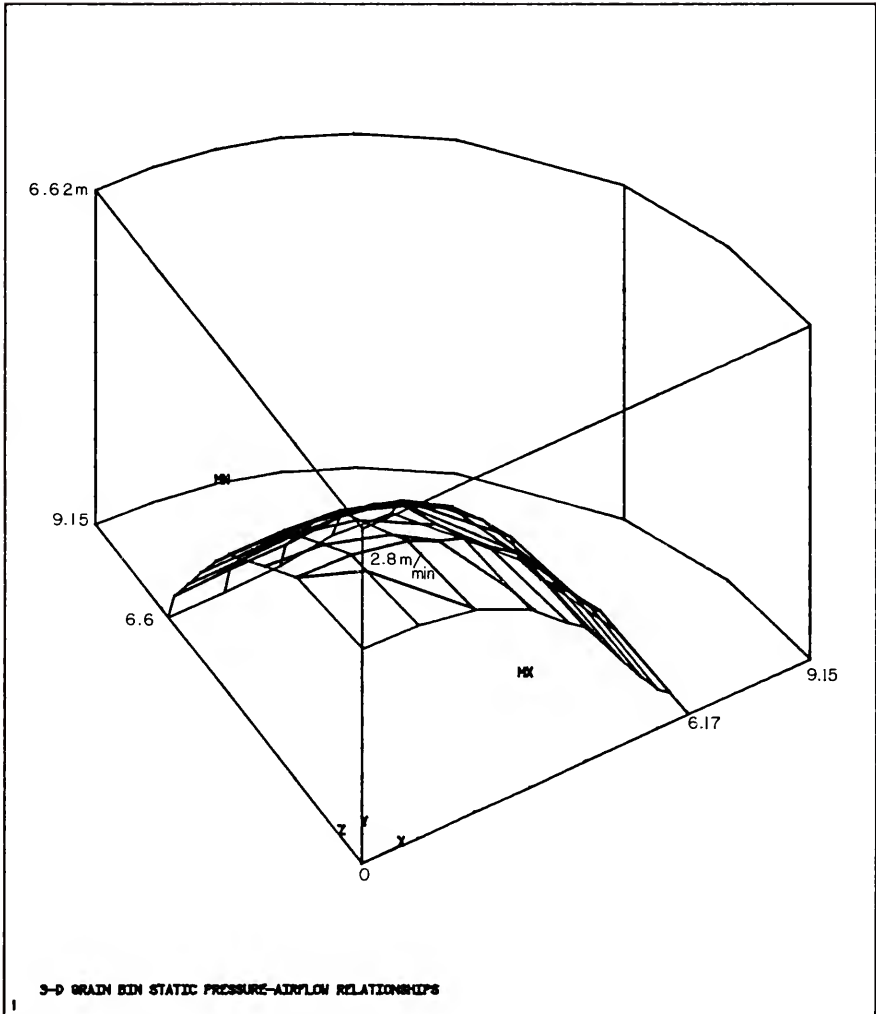


Figure D-42. Constant velocity surface of 2.8 meters per minute calculated using ANSYS, view 3.

APPENDIX E
ADDITIONAL EXPERIMENTAL TEMPERATURE RESPONSE

The experimental temperature response plots for the eleven boundary conditions not presented in the main text are included on the following pages. For each boundary condition, the temperature responses are presented in the same manner as Figures 45, 46, and 47, for Boundary Condition 1-1.

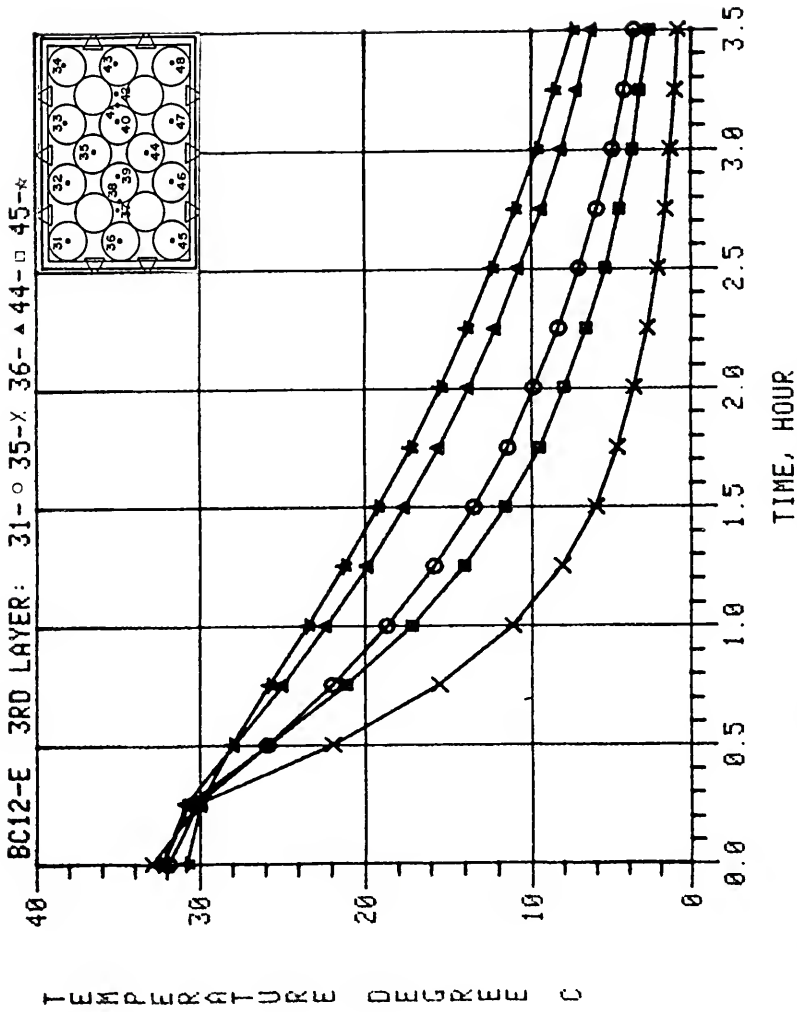


Figure E-1. Experimental center temperature response of oranges in an experimental orange carton for forced-air cooling (Boundary Condition 1-2, 3rd layer thermocouple locations 31, 35, 36, 44, and 45).

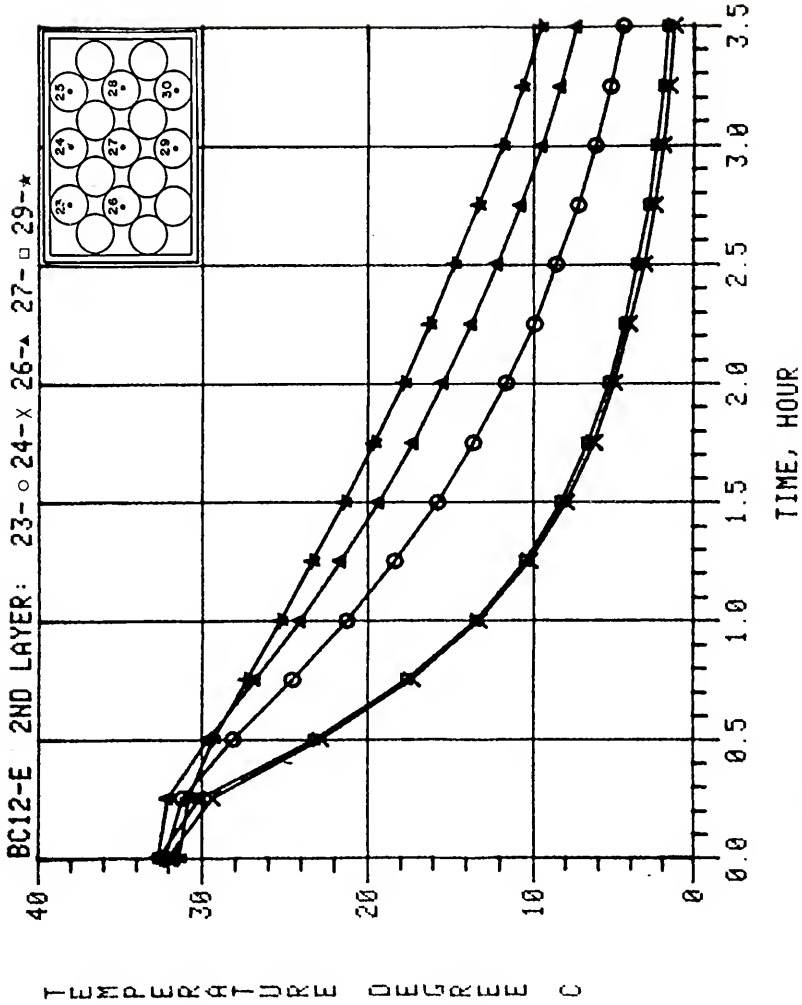


Figure E-2. Experimental center temperature response of oranges in an experimental orange carton for forced-air cooling (Boundary Condition 1-2, 2nd layer thermocouple locations 23, 24, 26, 27, and 29).

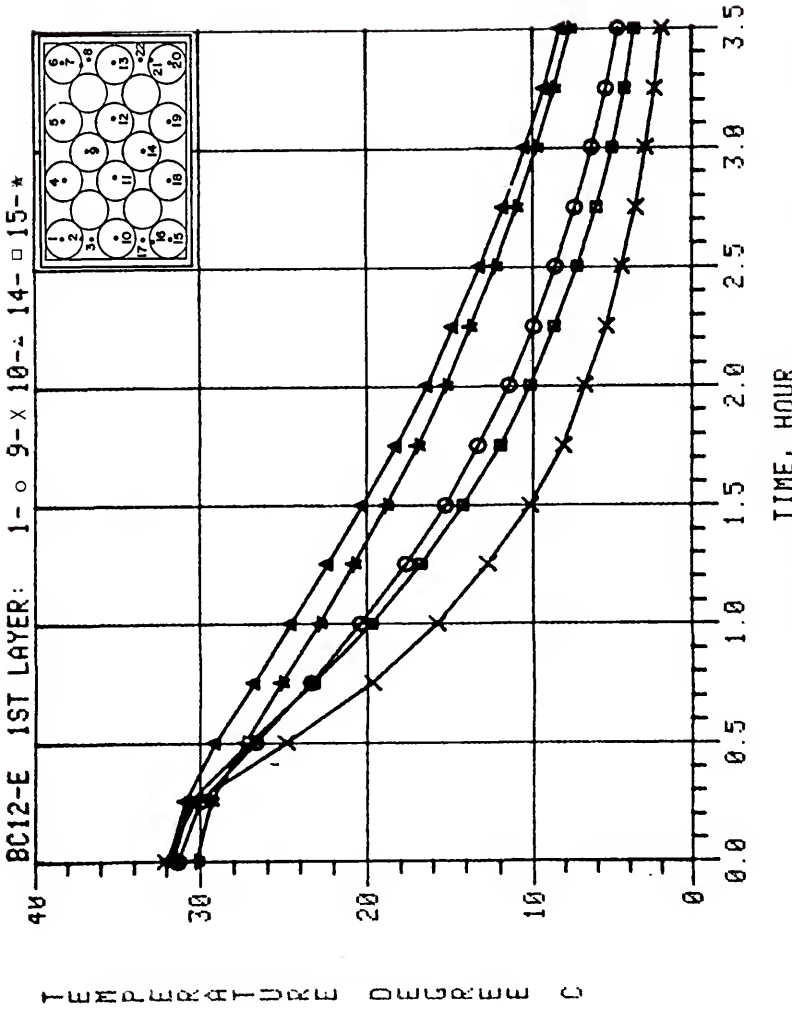


Figure E-3. Experimental center temperature response of oranges in an experimental orange carton for forced-air cooling (Boundary Condition 1-2, 1st-layer thermocouple locations 1, 9, 10, 14, and 15).

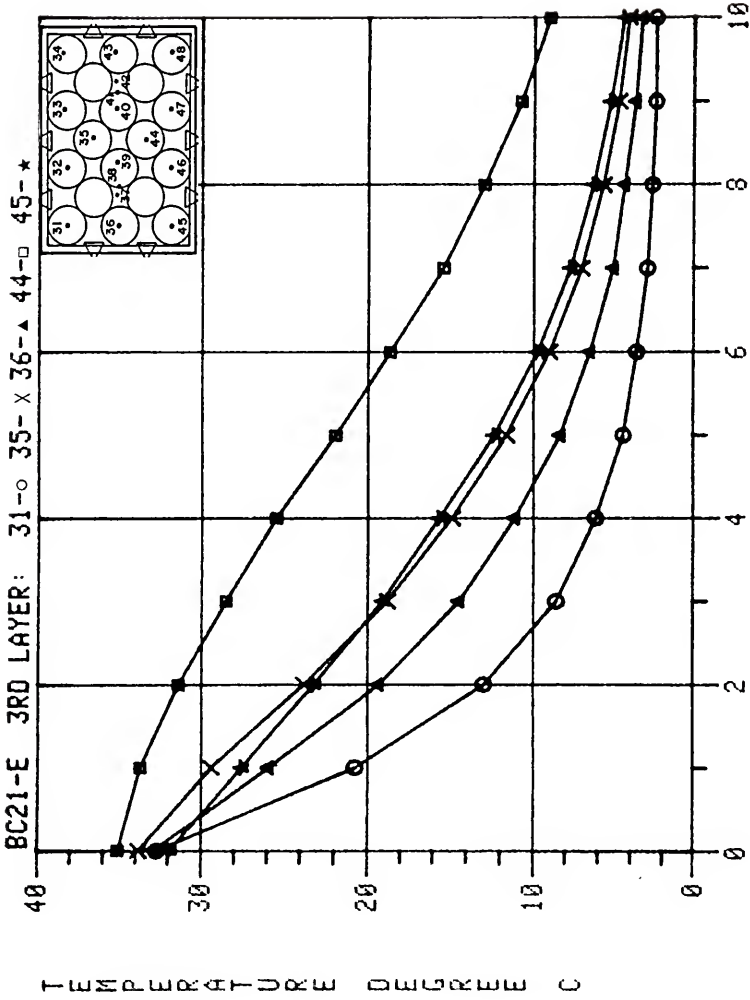


Figure E-4. Experimental center temperature response of oranges in an experimental orange carton for forced-air cooling (Boundary Condition 2-1, 3rd layer thermocouple locations 31, 35, 36, 44, and 45).

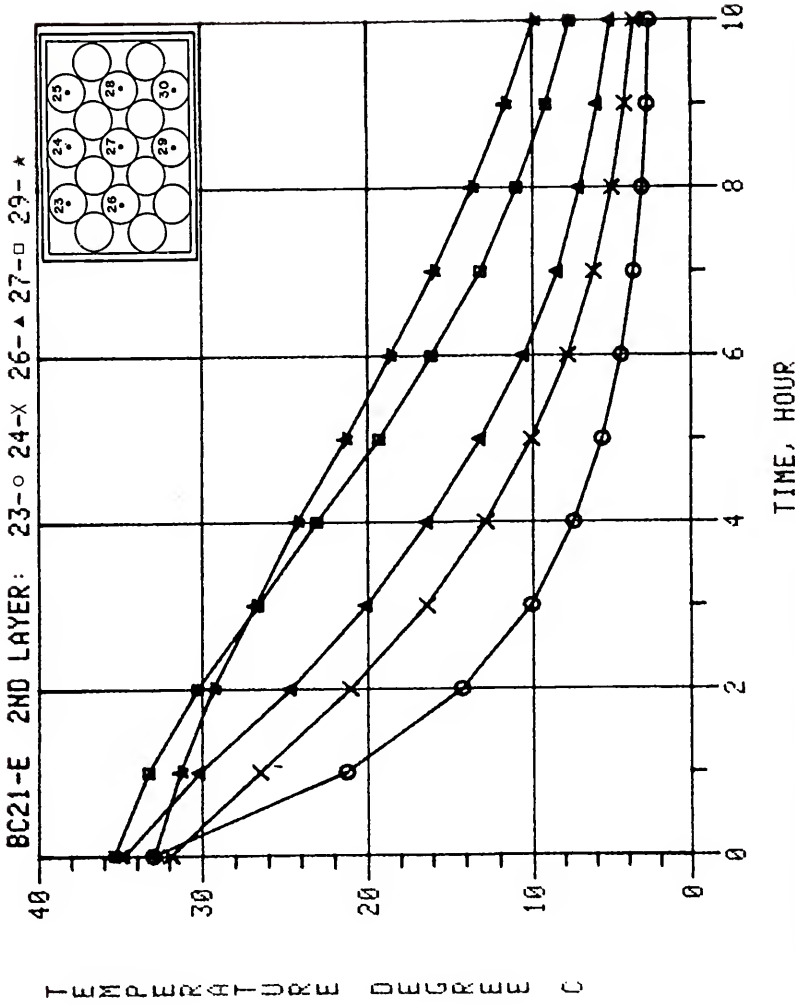


Figure E-5. Experimental center temperature response of oranges in an experimental orange carton for forced-air cooling (Boundary Condition 2-1, 2nd layer thermocouple locations 23, 24, 26, 27, and 29).

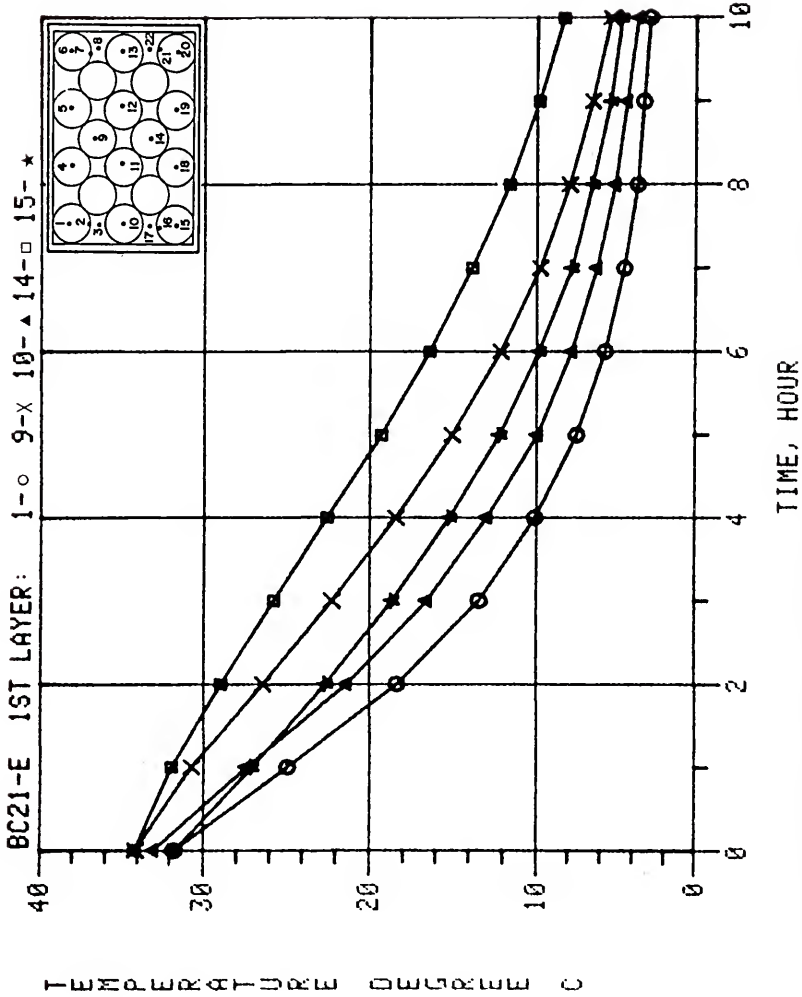


Figure E-6. Experimental center temperature response of oranges in an experimental orange carton for forced-air cooling (Boundary Condition 2-1, 1st layer thermocouple locations 1, 9, 10, 14, and 15).

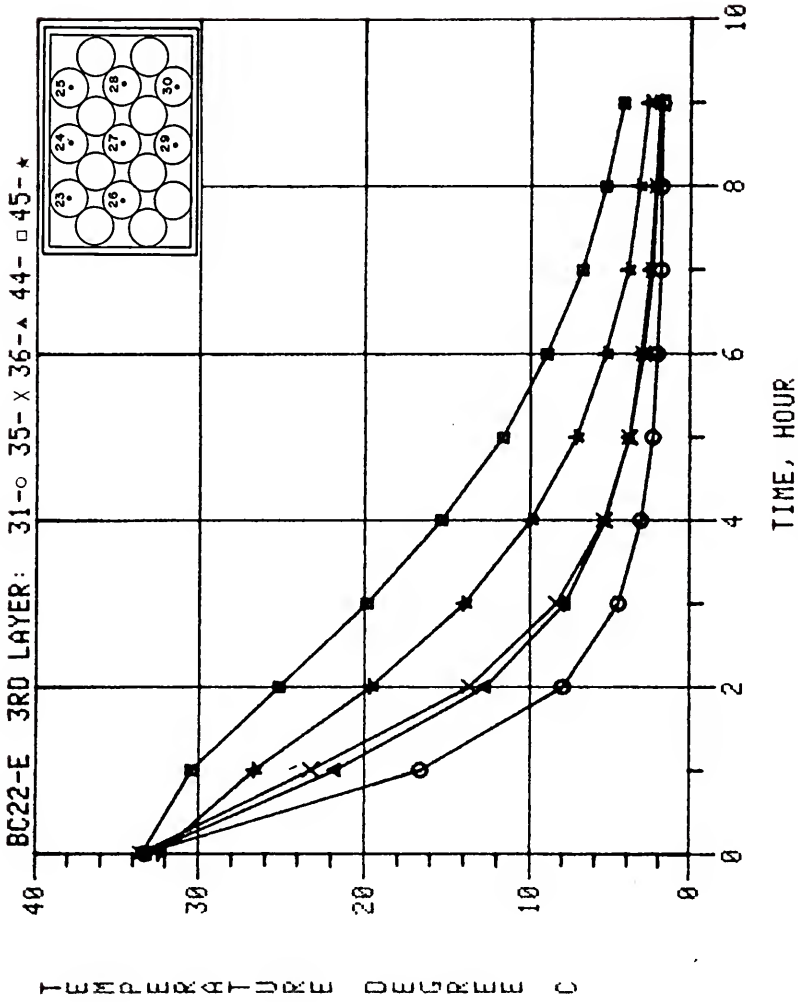


Figure E-7. Experimental center temperature response of oranges in an experimental orange carton for forced-air cooling (Boundary Condition 2-2, 3rd layer thermocouple locations 31, 35, 36, 44, and 45).

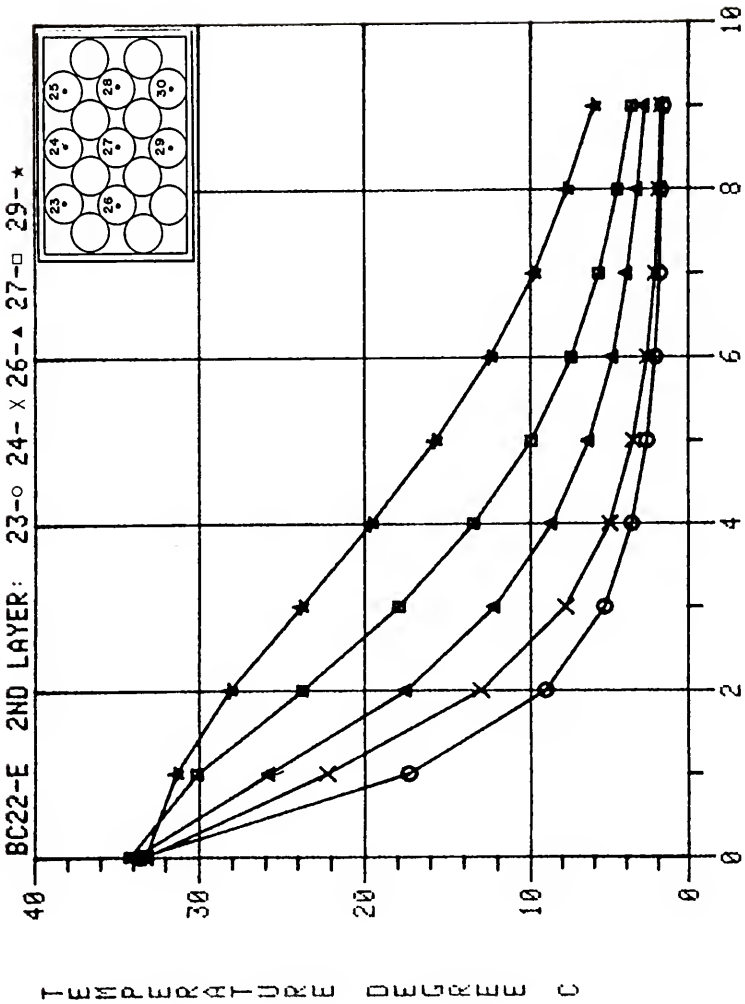


Figure E-8. Experimental center temperature response of oranges in an experimental orange carton for forced-air cooling (Boundary Condition 2-2, 2nd layer thermocouple locations 23, 24, 26, 27, and 29).

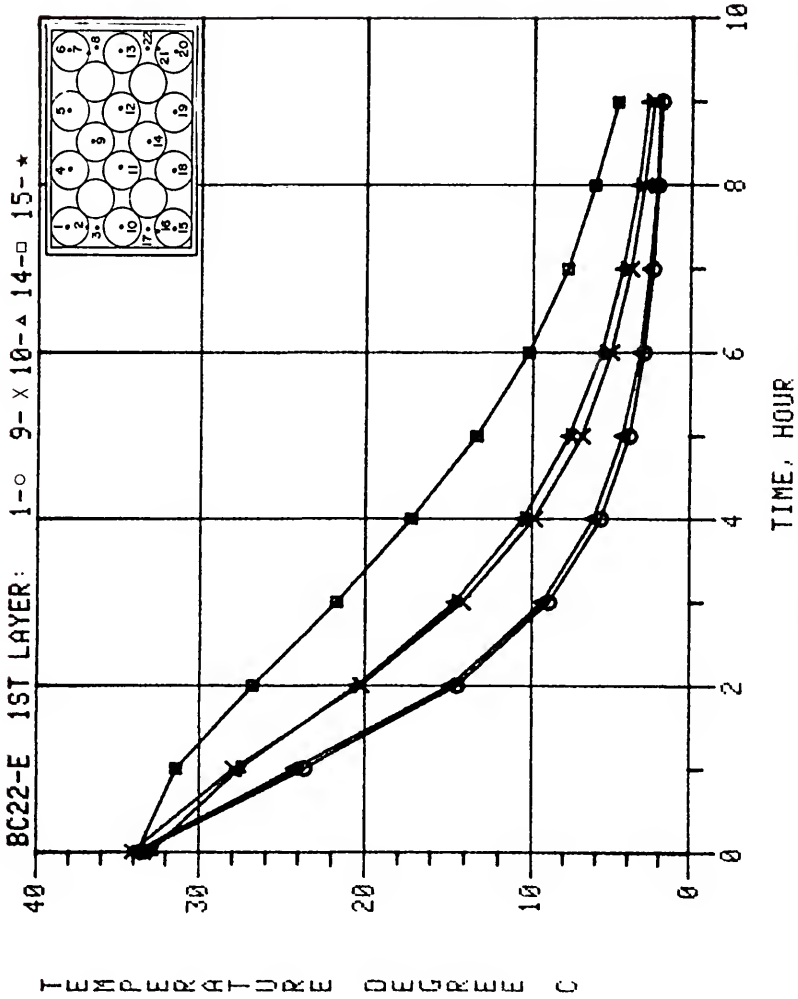


Figure E-9. Experimental center temperature response of oranges in an experimental orange carton for forced-air cooling (Boundary Condition 2-2, 1st layer thermocouple locations 1, 9, 10, 14, and 15).

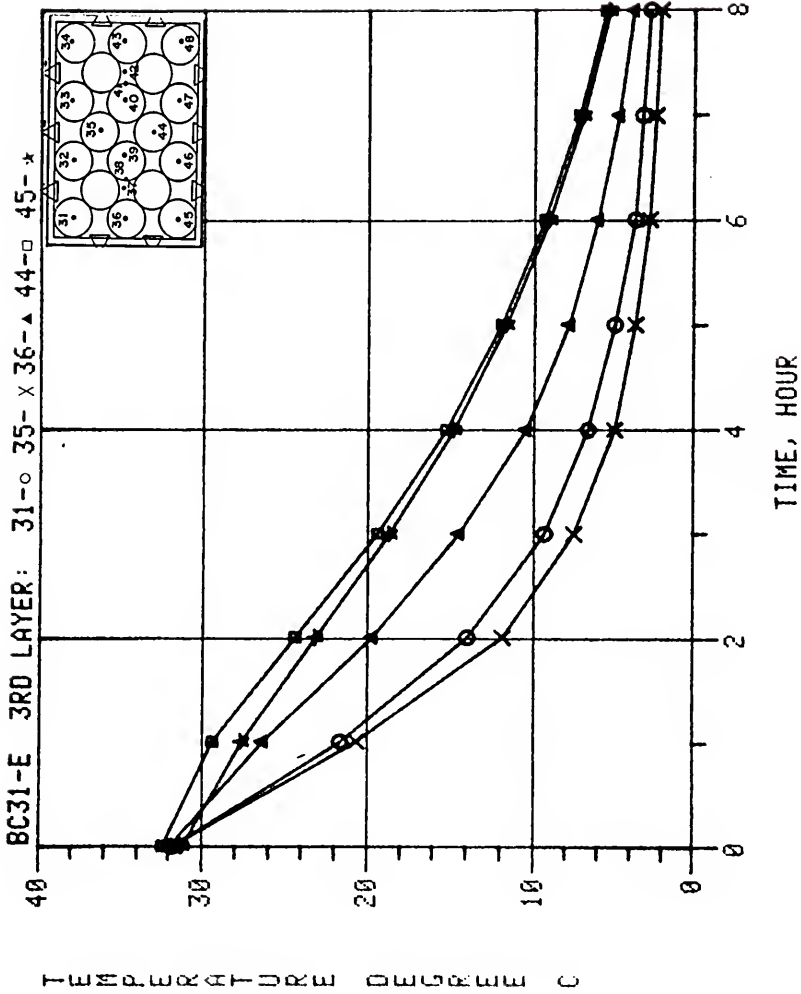


Figure E-10. Experimental center temperature response of oranges in an experimental orange carton for forced-air cooling (Boundary Condition 3-1, 3rd layer thermocouple locations 31, 35, 36, 44, and 45).

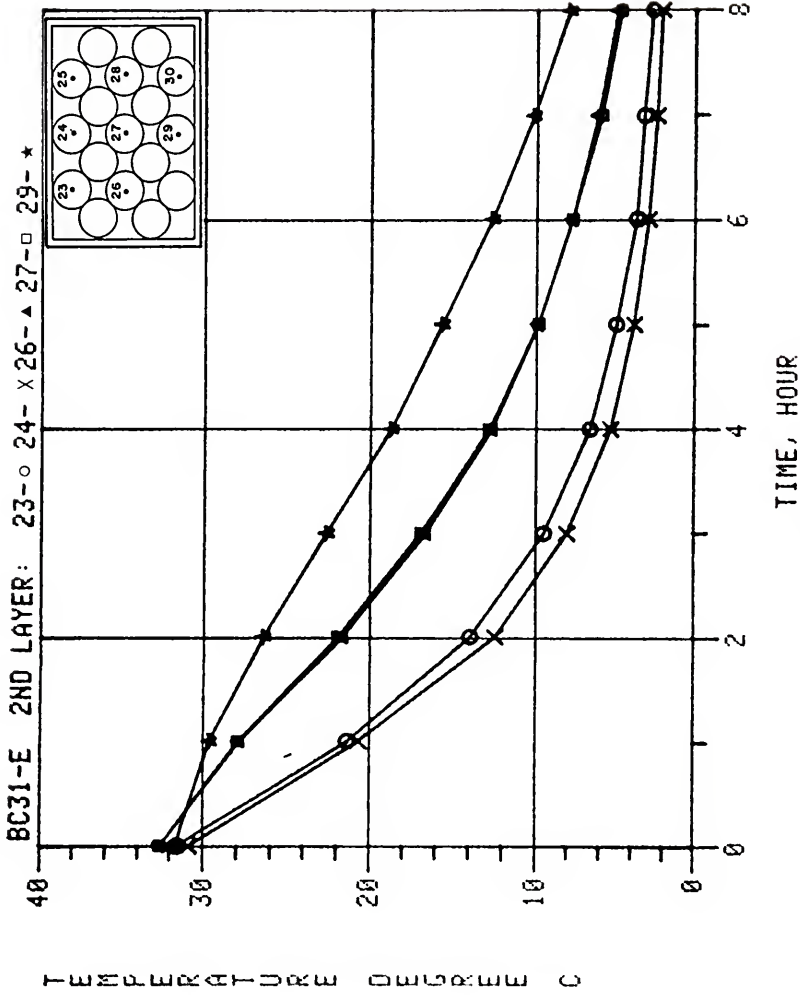


Figure E-11. Experimental center temperature response of oranges in an experimental orange carton for forced-air cooling (Boundary Condition 3-1, 2nd layer thermocouple locations 23, 24, 26, 27, and 29).

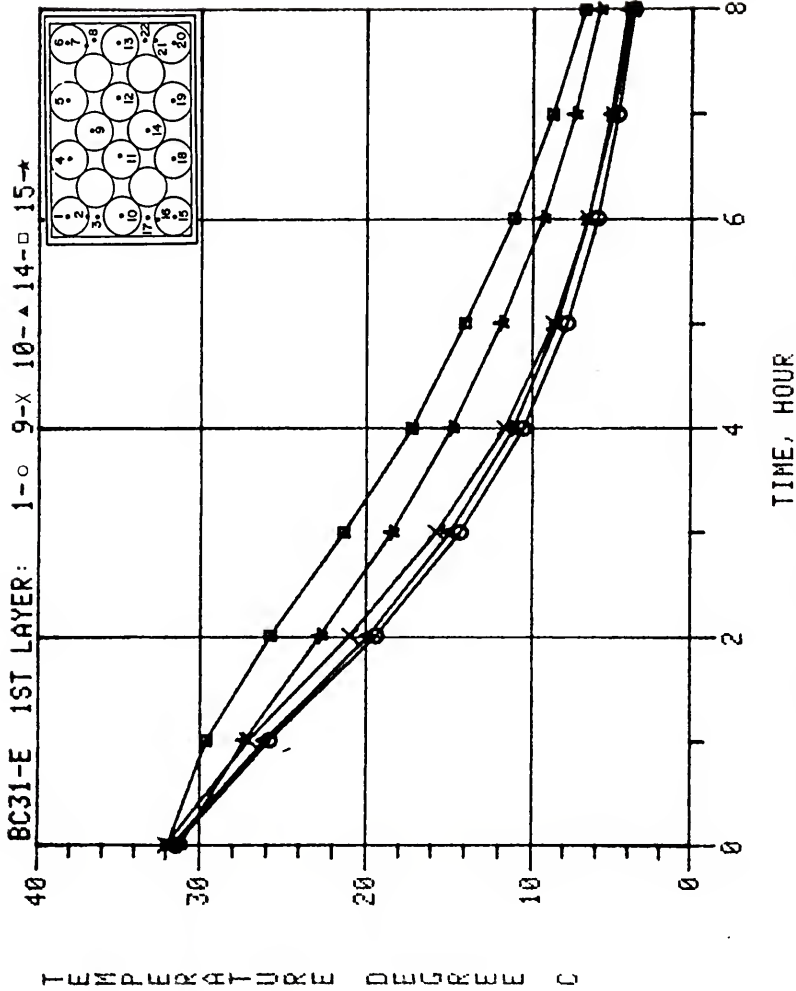


Figure E-12. Experimental center temperature response of oranges in an experimental orange carton for forced-air cooling (Boundary Condition 3-1, 1st layer thermocouple locations 1, 9, 10, 14, and 15).

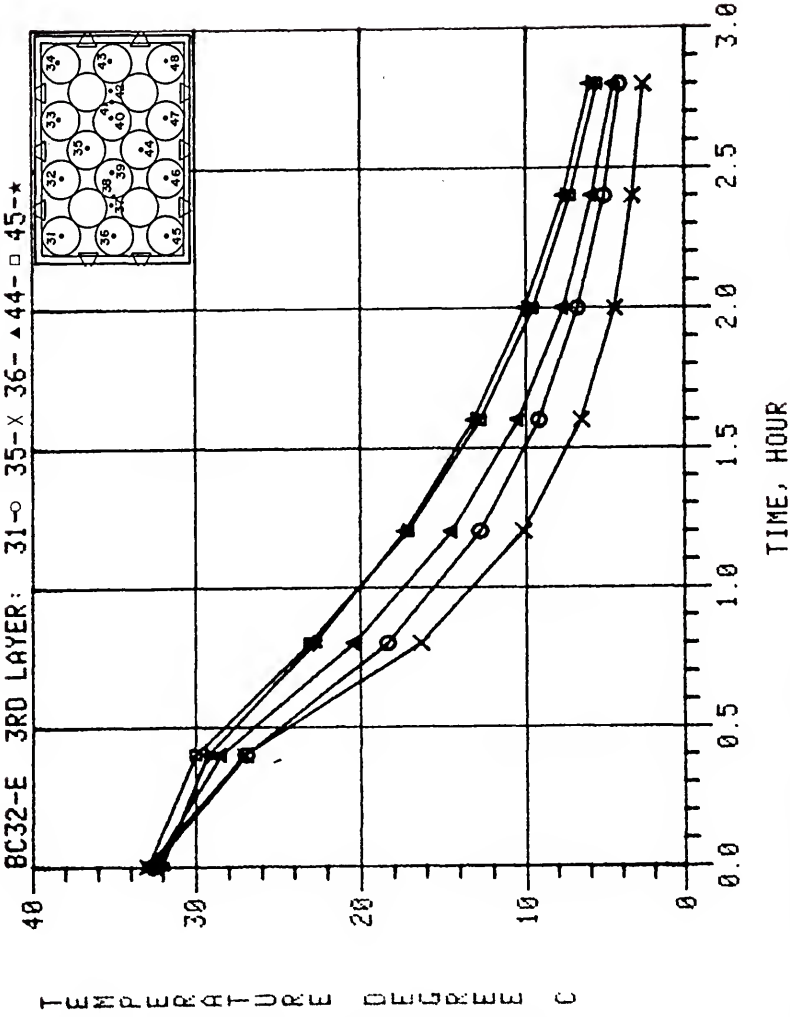


Figure E-13. Experimental center temperature response of oranges in an experimental orange carton for forced-air cooling (Boundary Condition 3-2, 3rd layer thermocouple locations 31, 35, 36, 44, and 45).

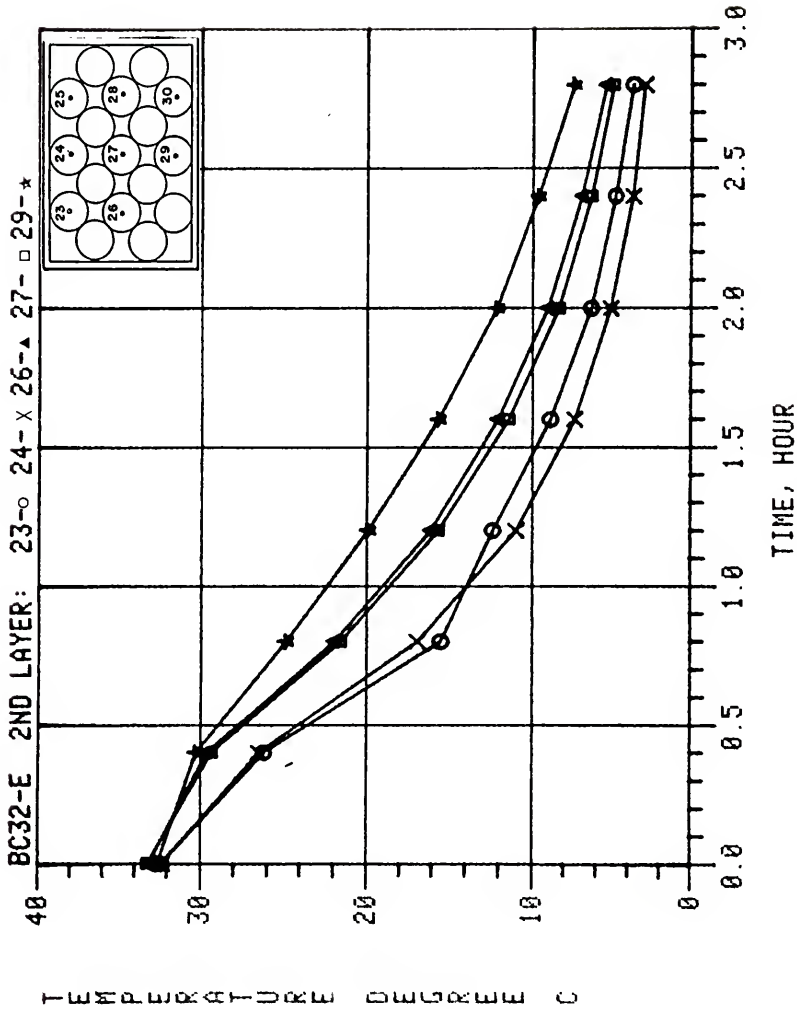


Figure E-14. Experimental center temperature response of oranges in an experimental orange carton for forced-air cooling (Boundary Condition 3-2, 2nd layer thermocouple locations 23, 24, 26, 27, and 29).

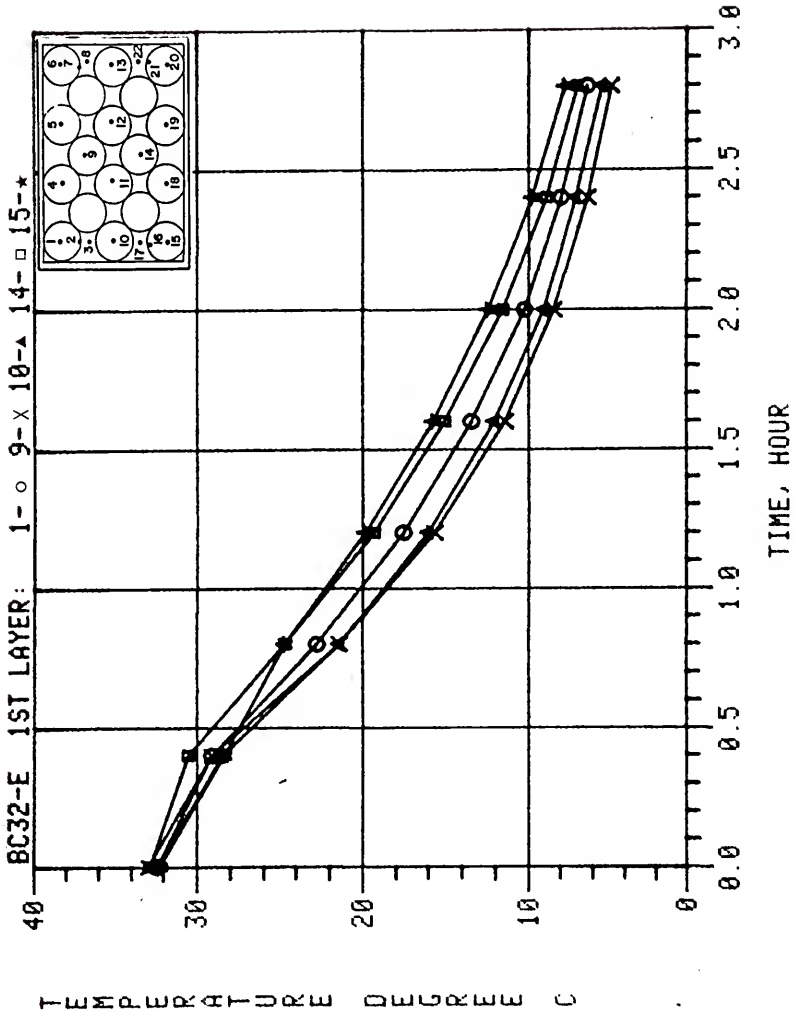


Figure E-15. Experimental center temperature response of oranges in an experimental orange carton for forced-air cooling (Boundary Condition 3-2, 1st layer thermocouple locations 1, 9, 10, 14, and 15).

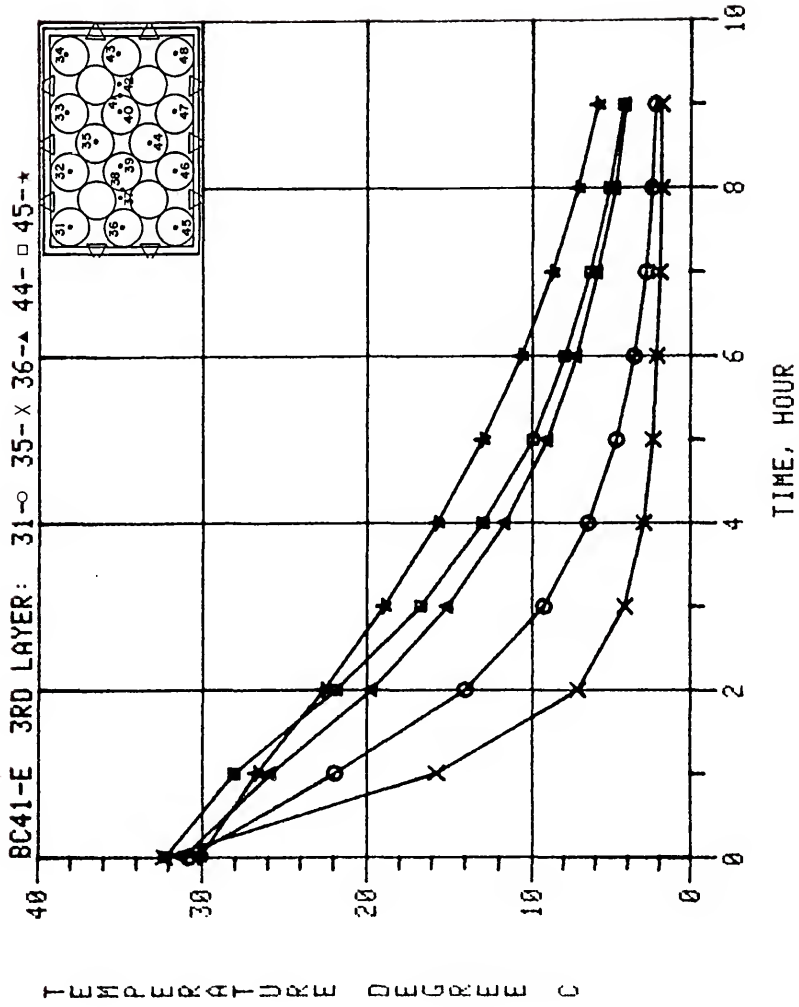


Figure E-16. Experimental center temperature response of oranges in an experimental orange carton for forced-air cooling (Boundary Condition 4-1, 3rd layer thermocouple locations 31, 35, 36, 44, and 45).

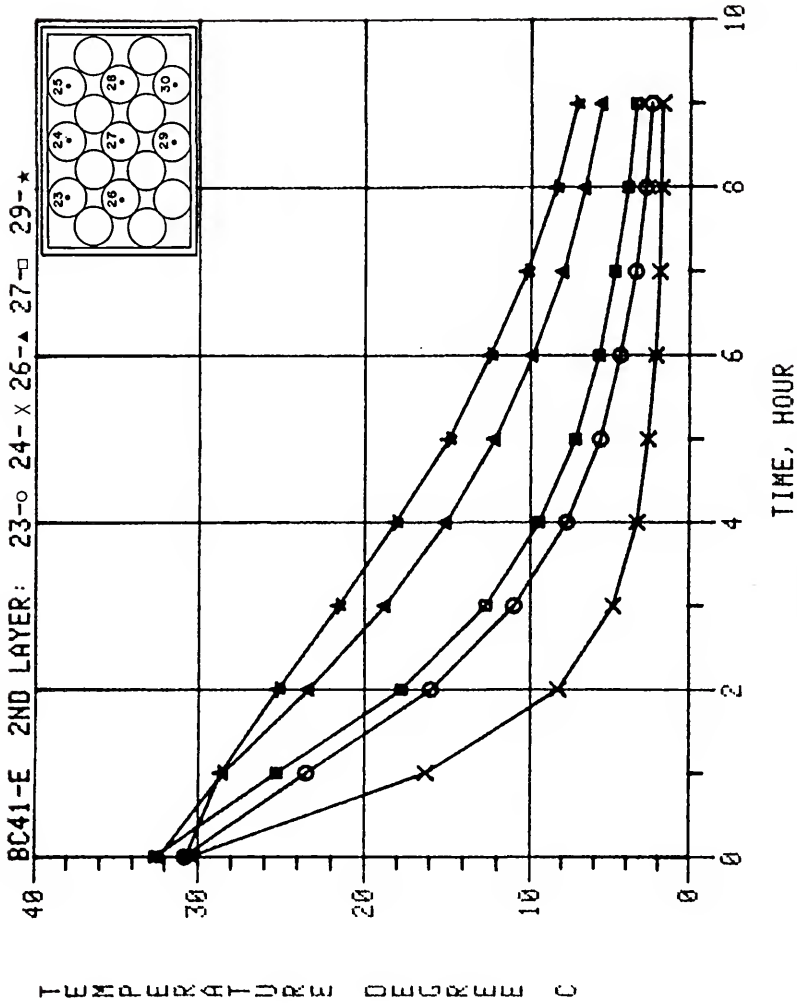


Figure E-17. Experimental center temperature response of oranges in an experimental orange carton for forced-air cooling (Boundary Condition 4-1, 2nd layer thermocouple locations 23, 24, 26, 27, and 29).

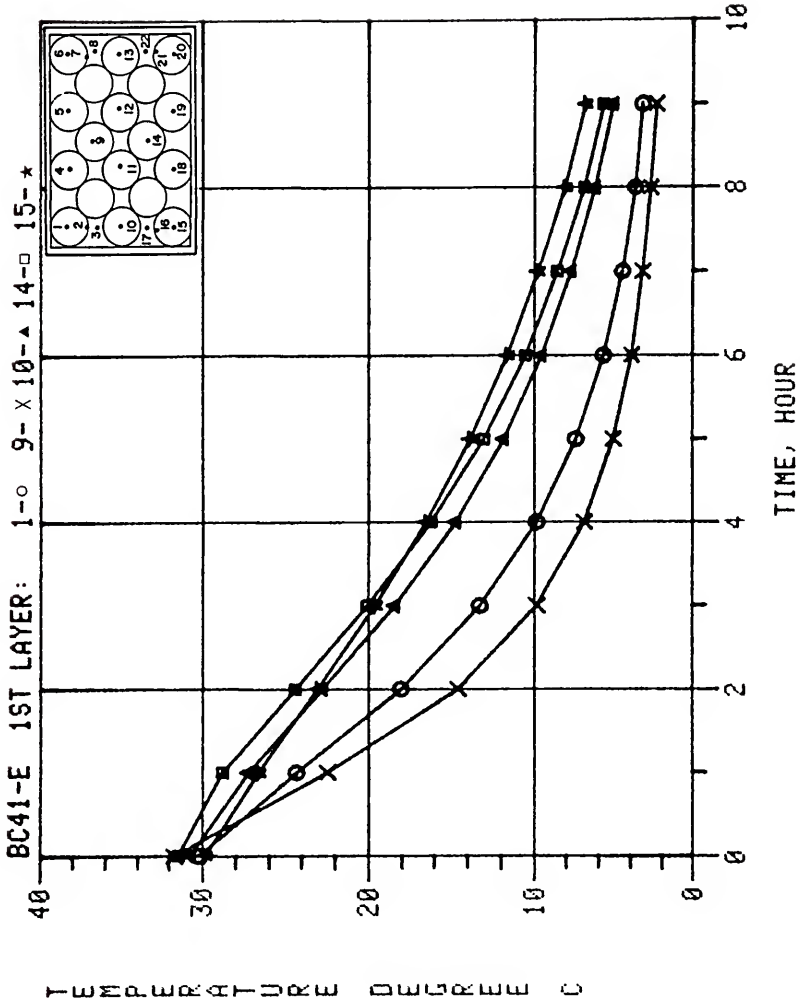


Figure E-18. Experimental center temperature response of oranges in an experimental orange carton for forced-air cooling (Boundary Condition 4-1, 1st layer thermocouple locations 1, 9, 10, 14, and 15).

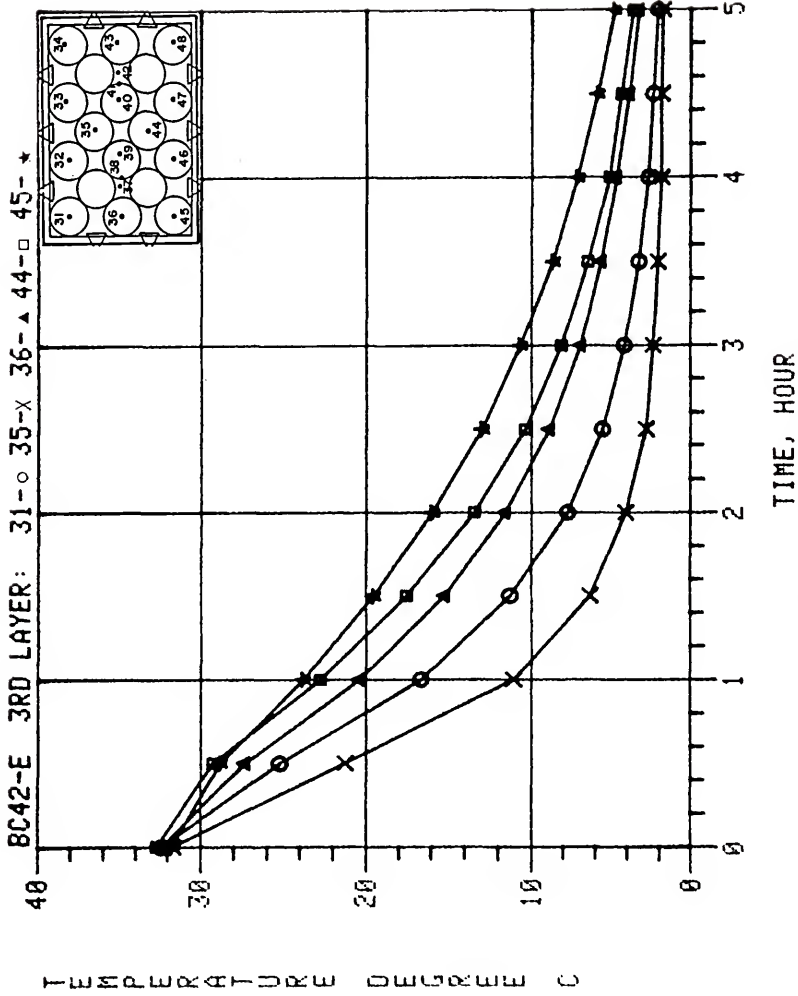


Figure E-19. Experimental center temperature response of oranges in an experimental orange carton for forced-air cooling (Boundary Condition 4-2, 3rd layer thermocouple locations 31, 35, 36, 44, and 45).

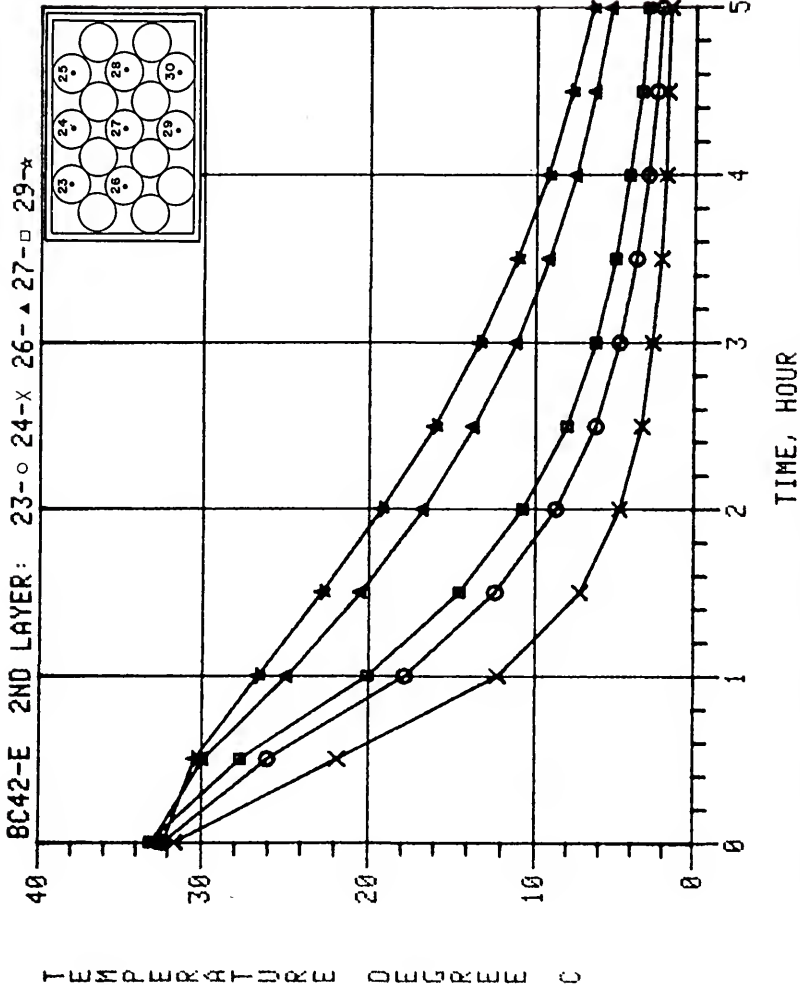


Figure E-20. Experimental center temperature response of oranges in an experimental orange carton for forced-air cooling (Boundary Condition 4-2, 2nd layer thermocouple locations 23, 24, 26, 27, and 29).

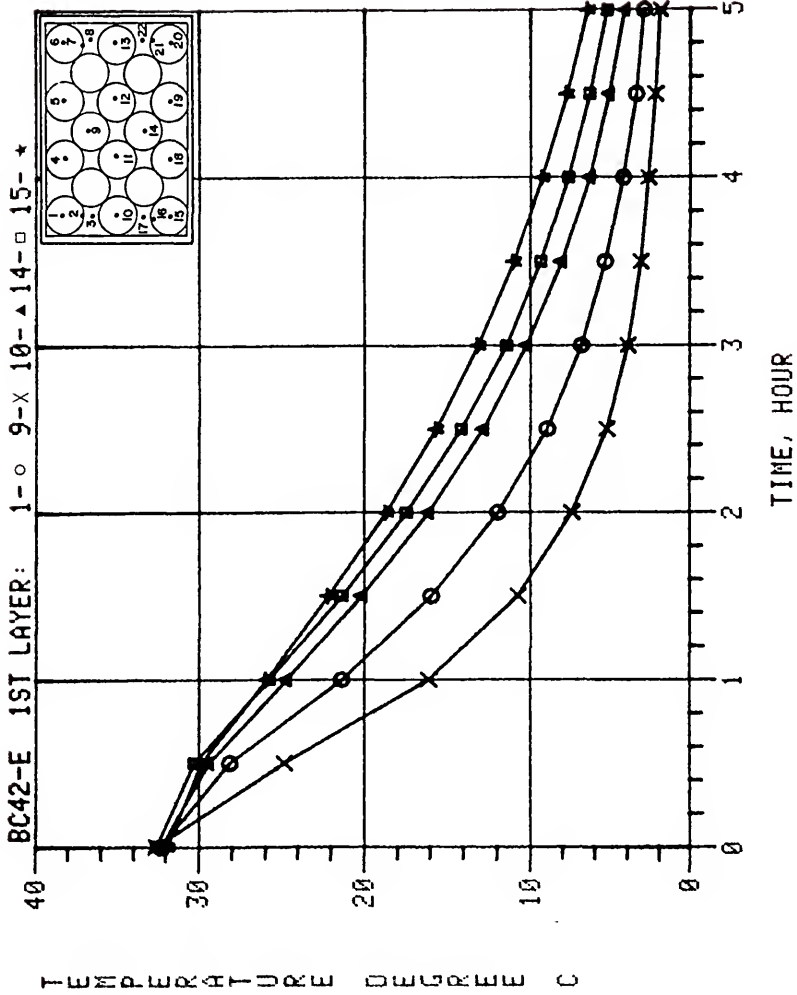


Figure E-21. Experimental center temperature response of oranges in an experimental orange carton for forced-air cooling (Boundary Condition 4-2, 1st layer thermocouple locations 1, 9, 10, 14, and 15).

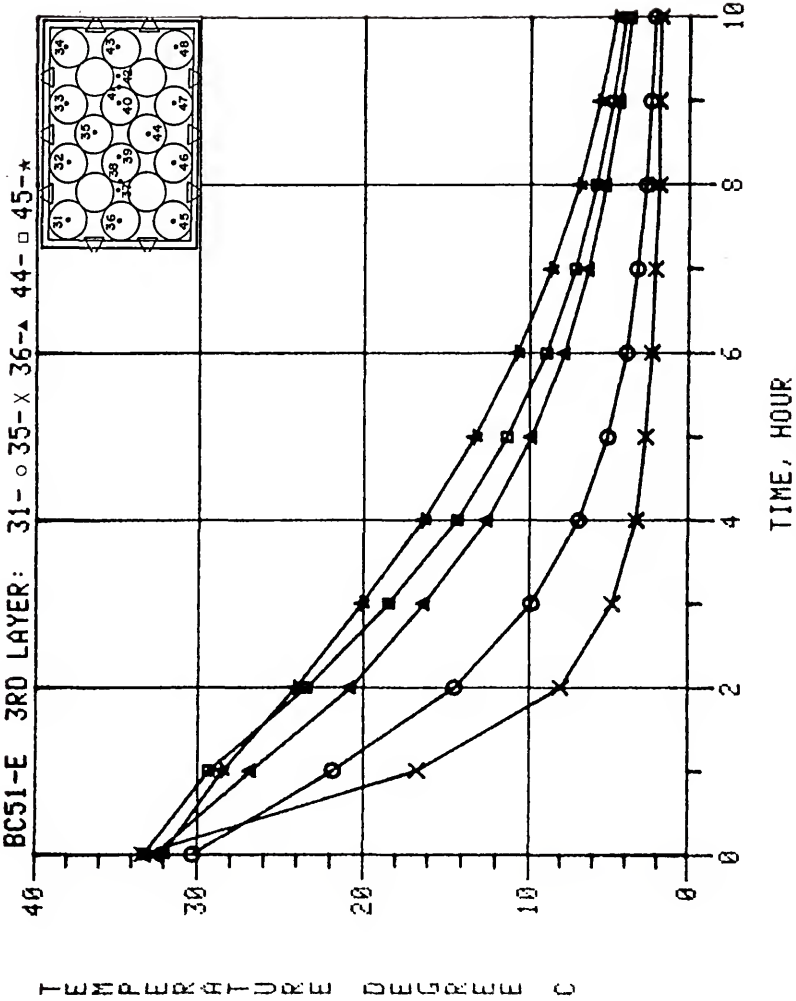


Figure E-22. Experimental center temperature response of oranges in an experimental orange carton for forced-air cooling (Boundary Condition 5-1, 3rd layer thermocouple locations 31, 35, 36, 44, and 45).

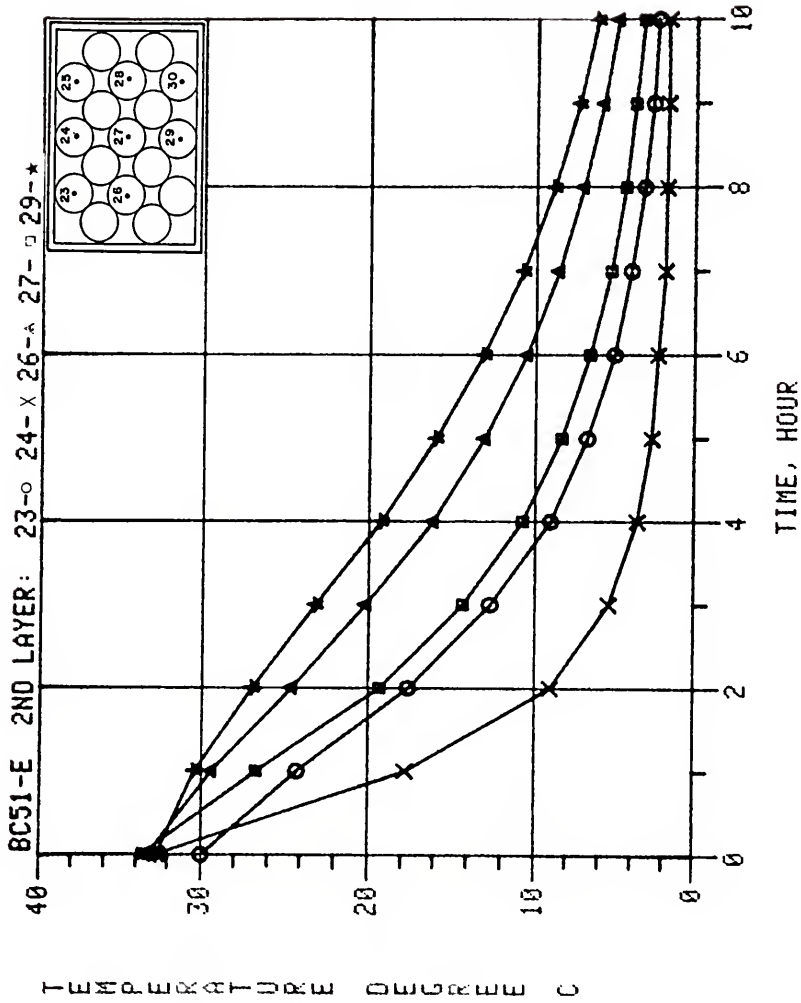


Figure E-23. Experimental center temperature response of oranges in an experimental orange carton for forced-air cooling (Boundary Condition 5-1, 2nd layer thermocouple locations 23, 24, 26, 27, and 29).

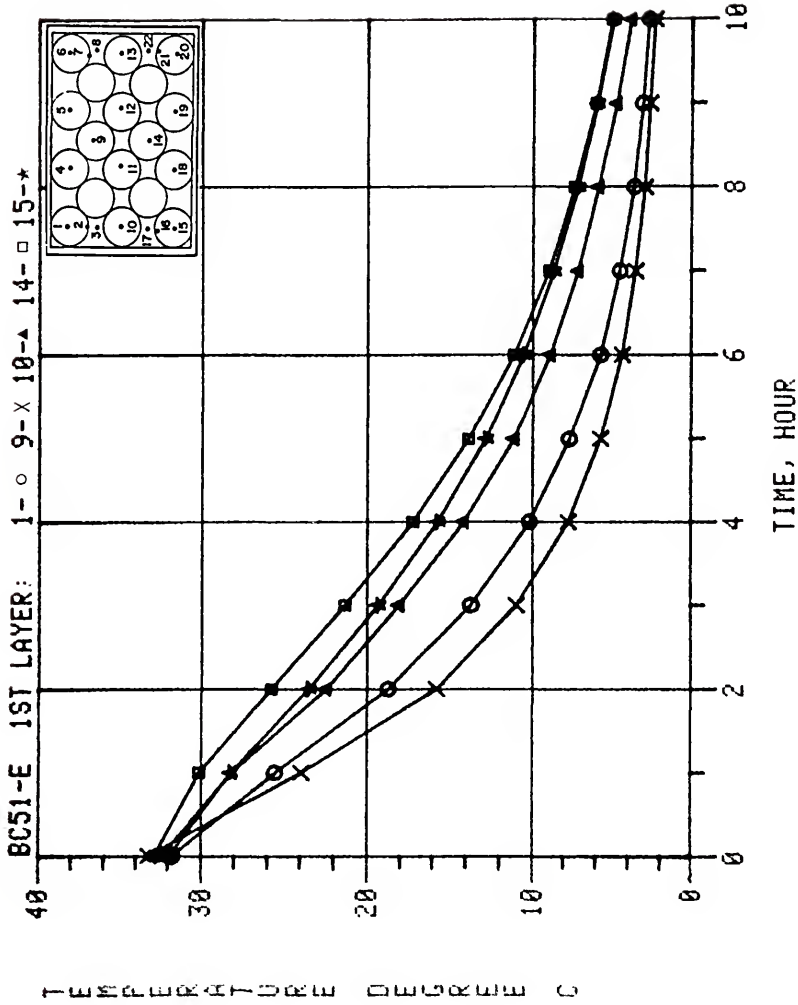


Figure E-24. Experimental center temperature response of oranges in an experimental orange carton for forced-air cooling (Boundary Condition 5-1, 1st layer thermocouple locations 1, 9, 10, 14, and 15).

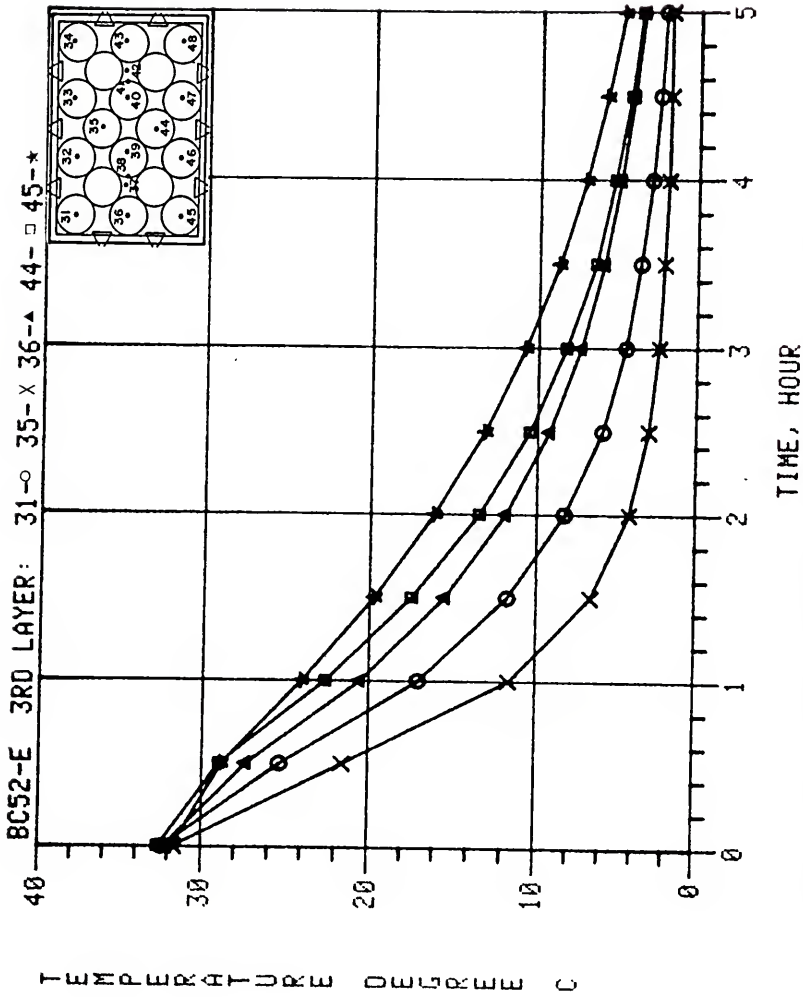


Figure E-25. Experimental center temperature response of oranges in an experimental orange carton for forced-air cooling (Boundary Condition 5-2, 3rd layer thermocouple locations 31, 35, 36, 44, and 45).

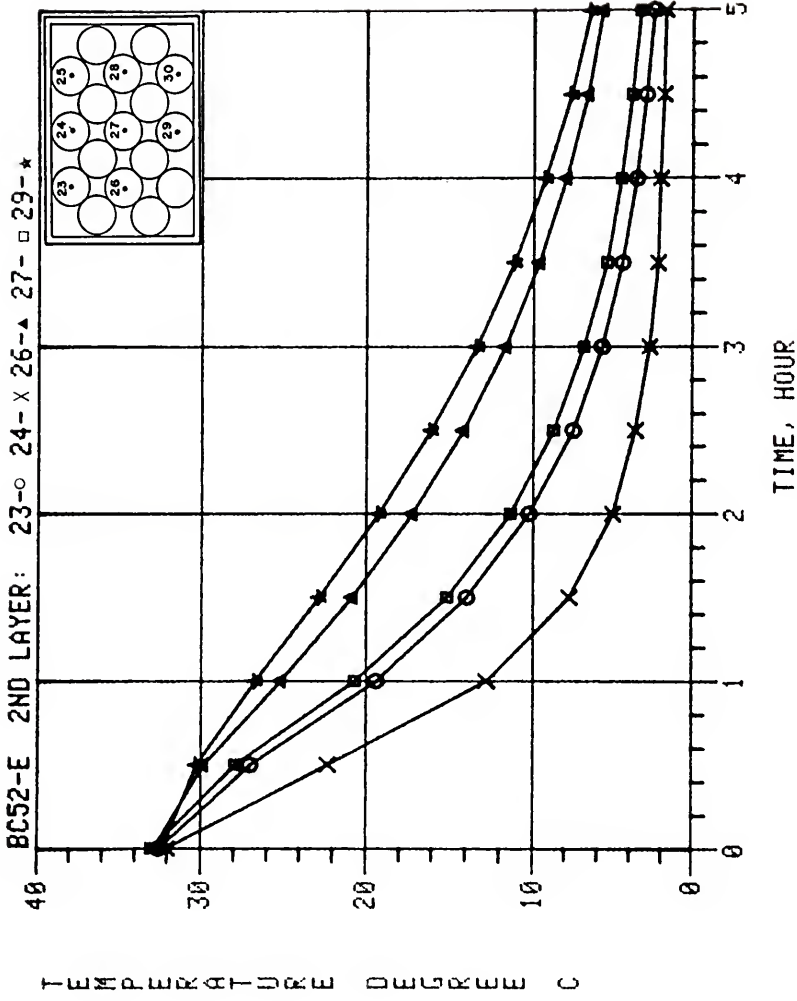


Figure E-26. Experimental center temperature response of oranges in an experimental orange carton for forced-air cooling (Boundary Condition 5-2, 2nd layer thermocouple locations 23, 24, 26, 27, and 29).

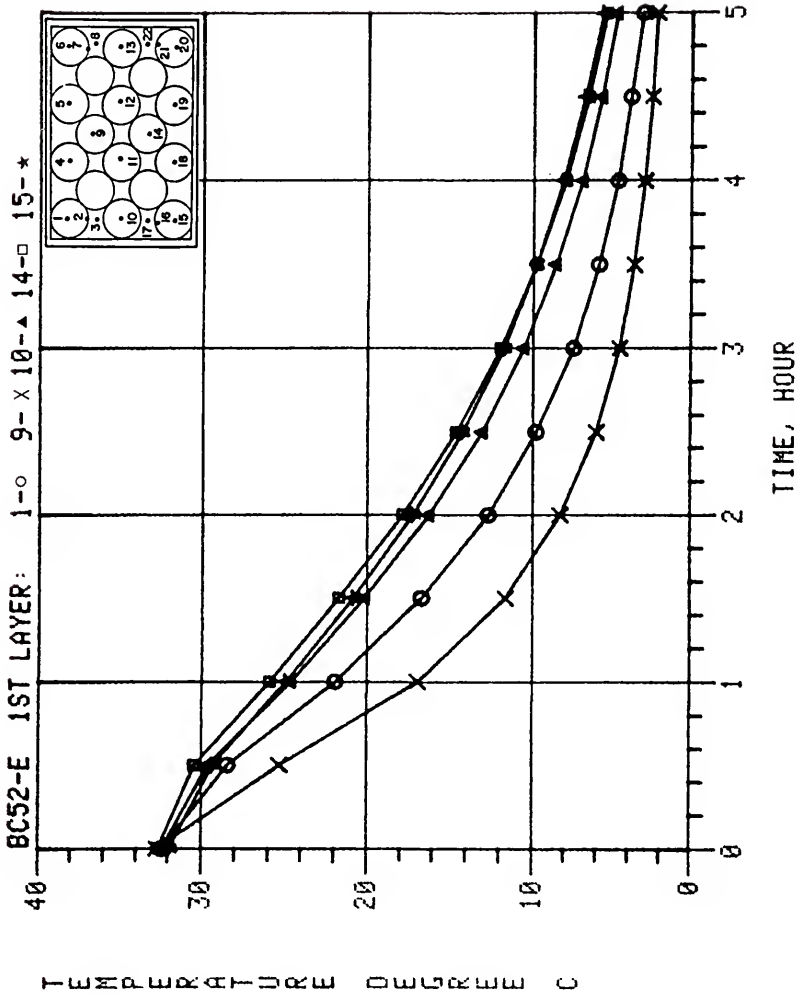


Figure E-27. Experimental center temperature response of oranges in an experimental orange carton for forced-air cooling (Boundary Condition 5-2, 1st layer thermocouple locations 1, 9, 10, 14, and 15).

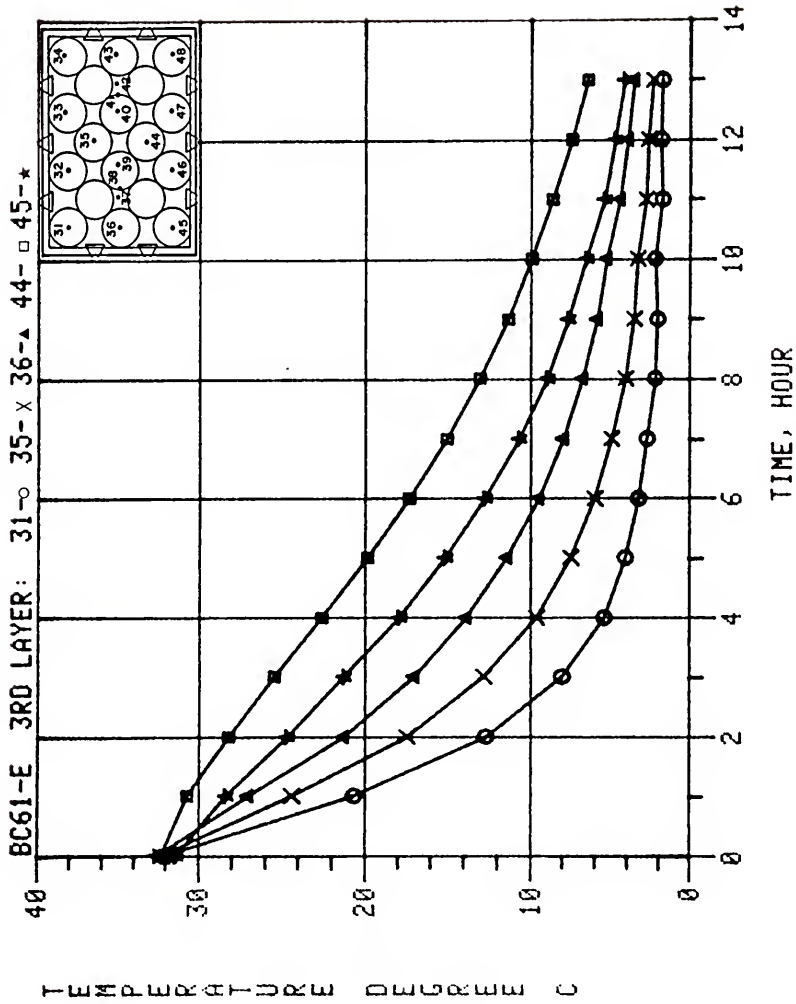


Figure E-28. Experimental center temperature response of oranges in an experimental orange carton for forced-air cooling (Boundary Condition 6-1, 3rd layer thermocouple locations 31, 35, 36, 44, and 45).

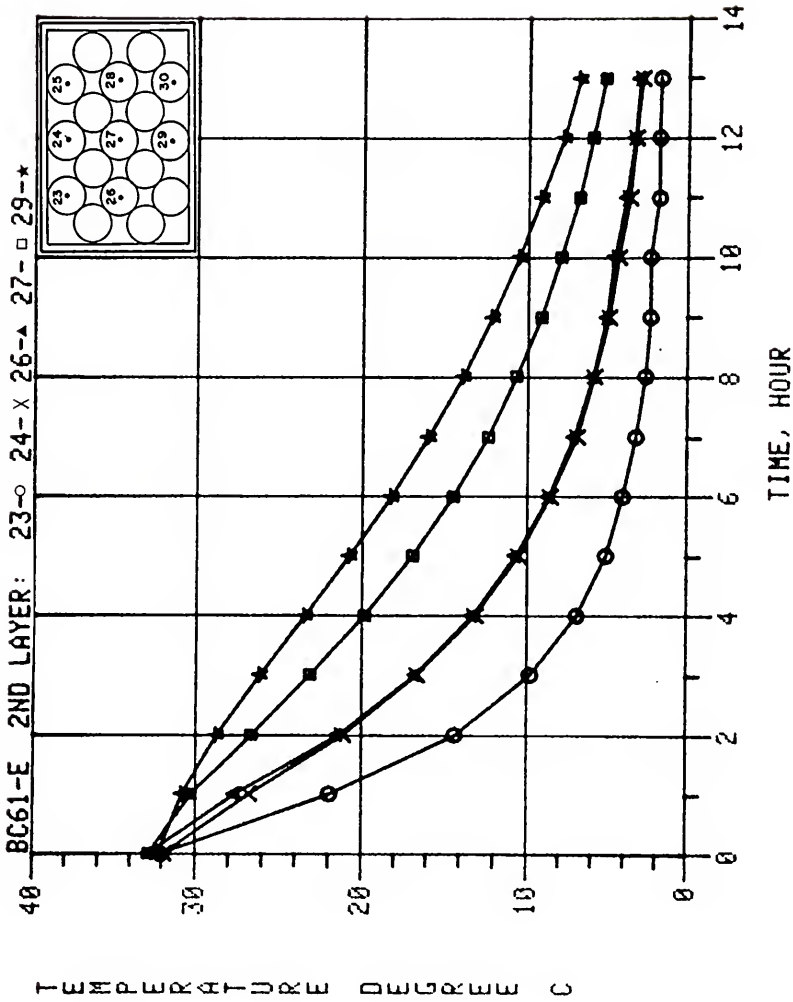


Figure E-29. Experimental center temperature response of oranges in an experimental orange carton for forced-air cooling (Boundary Condition 6-1, 2nd layer thermocouple locations 23, 24, 26, 27, and 29).

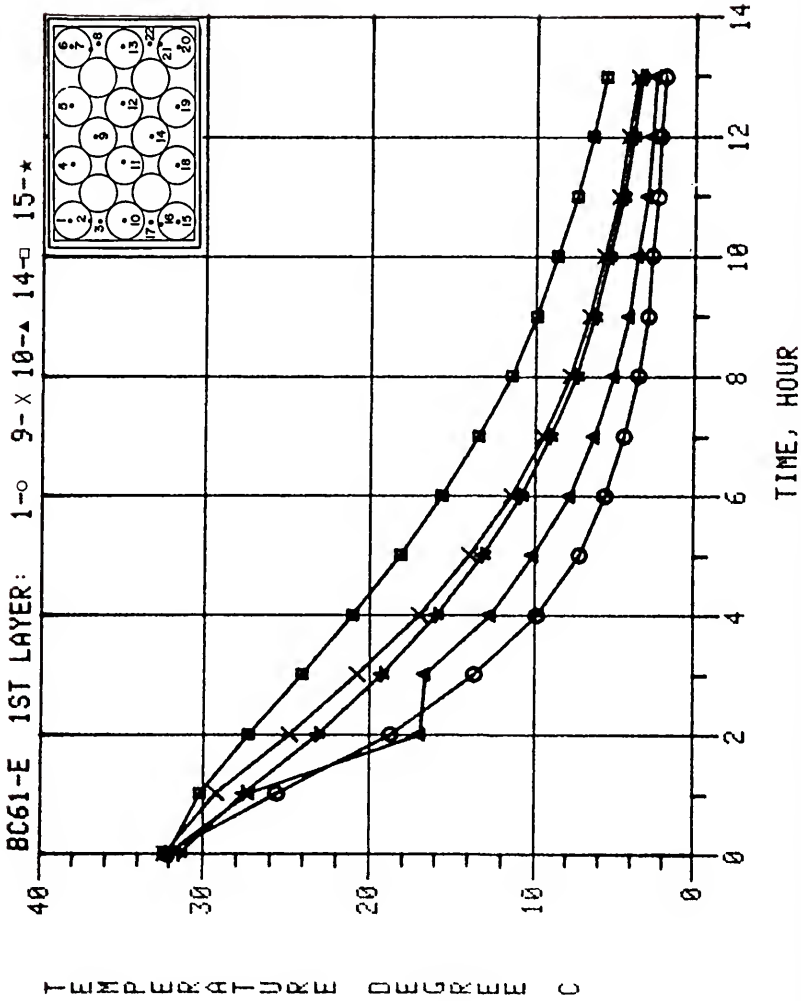


Figure E-30. Experimental center temperature response of oranges in an experimental orange carton for forced-air cooling (Boundary Condition 6-1, 1st layer thermocouple locations 1, 9, 10, 14, and 15).

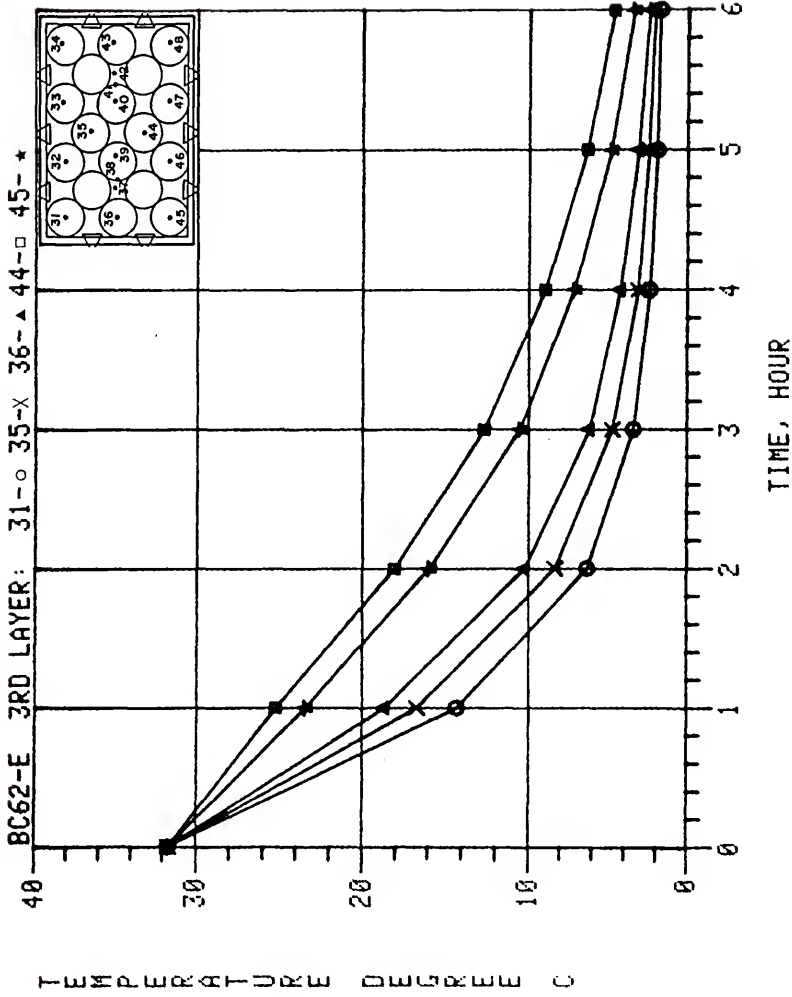


Figure E-31. Experimental center temperature response of oranges in an experimental orange carton for forced-air cooling (Boundary Condition 6-2, 3rd layer thermocouple locations 31, 35, 36, 44, and 45).

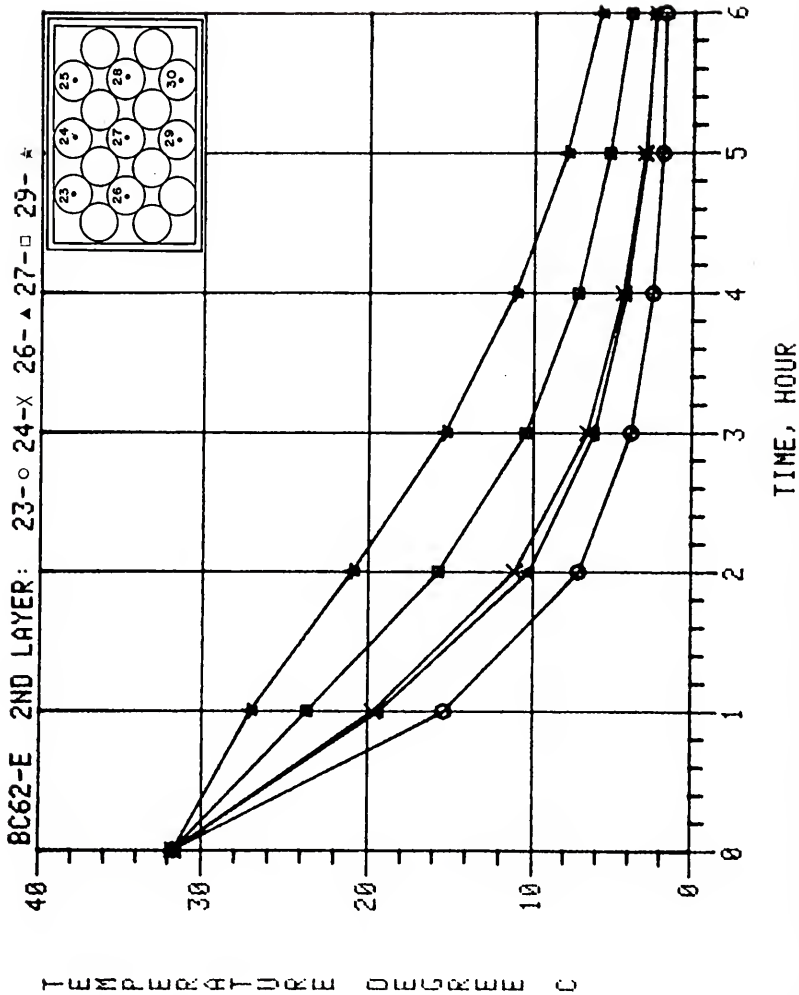


Figure E-32. Experimental center temperature response of oranges in an experimental orange carton for forced-air cooling (Boundary Condition 6-2, 2nd layer thermocouple locations 23, 24, 26, 27, and 29).

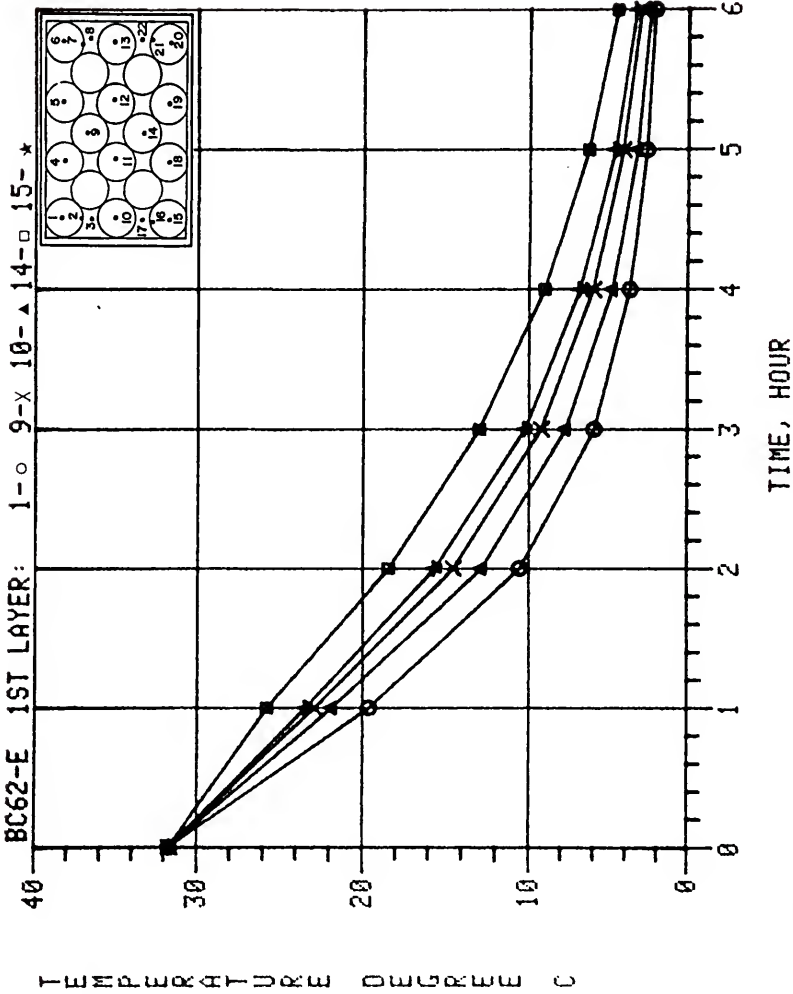


Figure E-33. Experimental center temperature response of oranges in an experimental orange carton for forced-air cooling (Boundary Condition 6-2, 1st layer thermocouple locations 1, 9, 10, 14, and 15).

APPENDIX F
ADDITIONAL PREDICTED TEMPERATURE RESPONSE

The predicted temperature response plots for the eleven boundary conditions not presented in the main text are included on the following pages. For each boundary condition, the temperature responses are presented in the same manner as Figures 49, 50, and 51, for Boundary Condition 1-1.

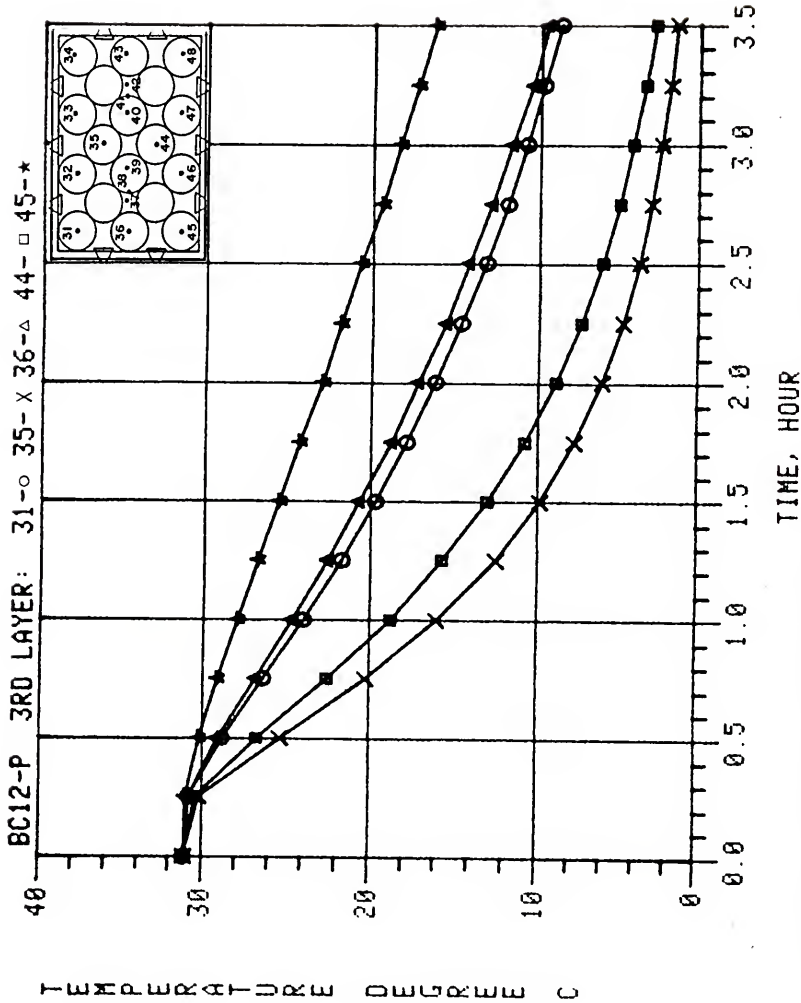


Figure F-1. Predicted center temperature response of oranges in an experimental orange carton for forced-air cooling (Boundary Condition 1-2, 3rd layer thermocouple locations 31, 35, 36, 44, and 45).

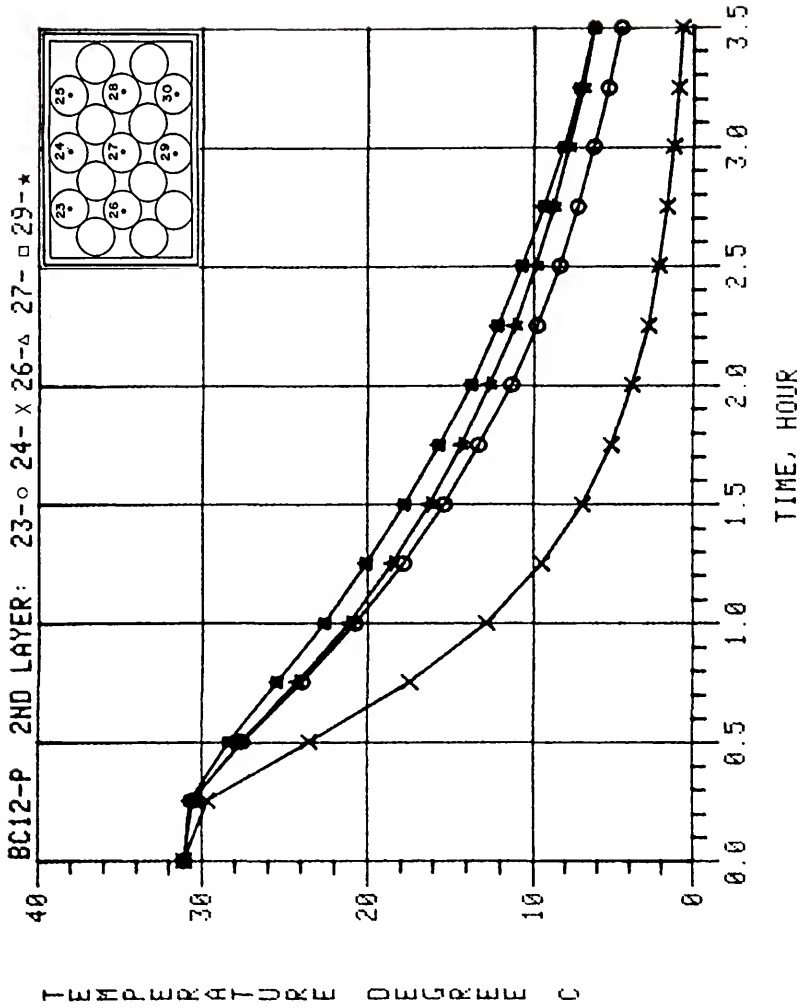


Figure F-2. Predicted center temperature response of oranges in an experimental orange carton for forced-air cooling (Boundary Condition 1-2, 2nd layer thermocouple locations 23, 24, 26, 27, and 29).

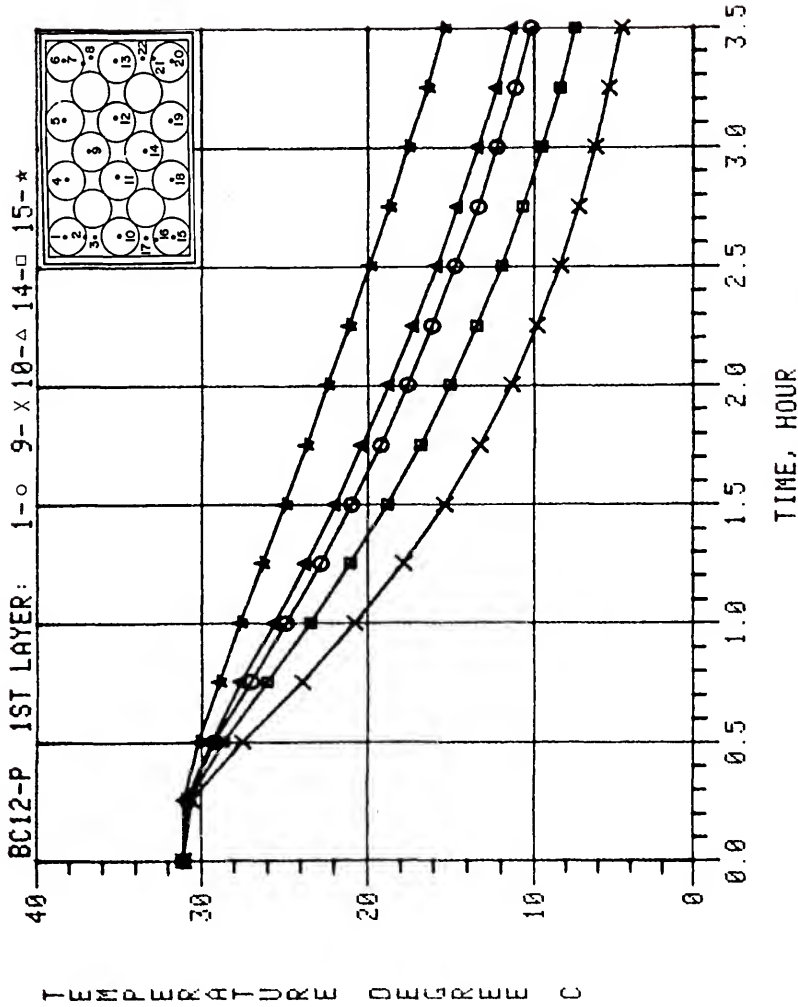


Figure F-3. Predicted center temperature response of oranges in an experimental orange carton for forced-air cooling (Boundary Condition 1-2, 1st layer thermocouple locations 1, 9, 10, 14, and 15).

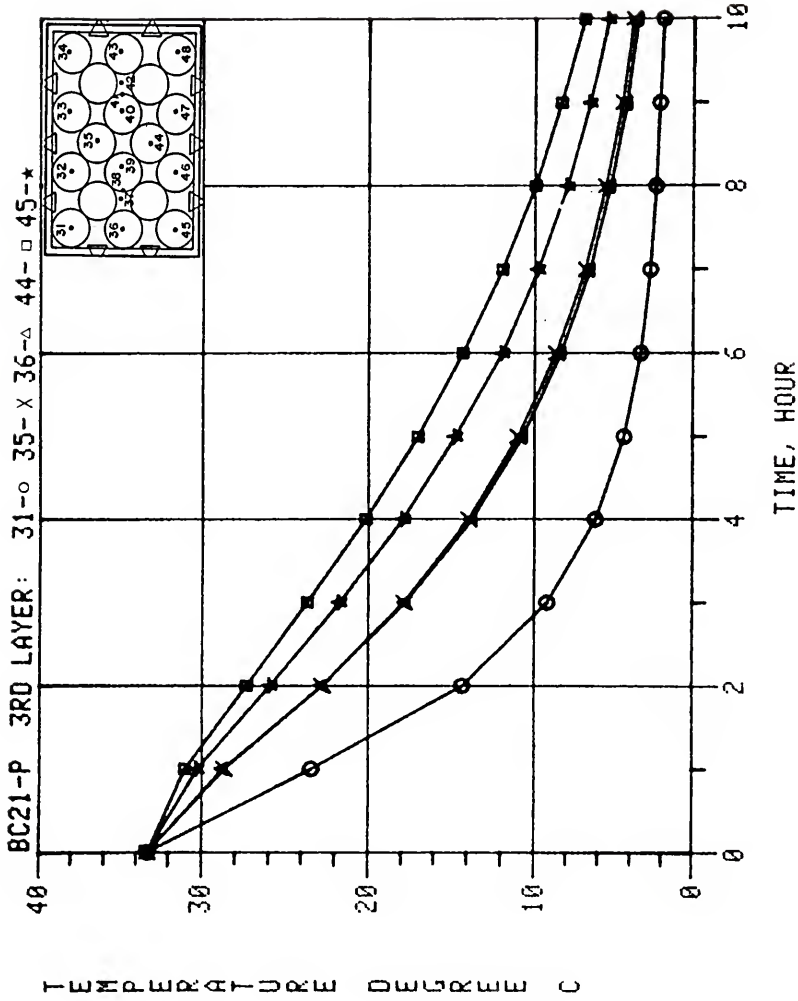


Figure F-4. Predicted center temperature response of oranges in an experimental orange carton for forced-air cooling (Boundary Condition 2-1, 3rd layer thermocouple locations 31, 35, 36, 44, and 45).

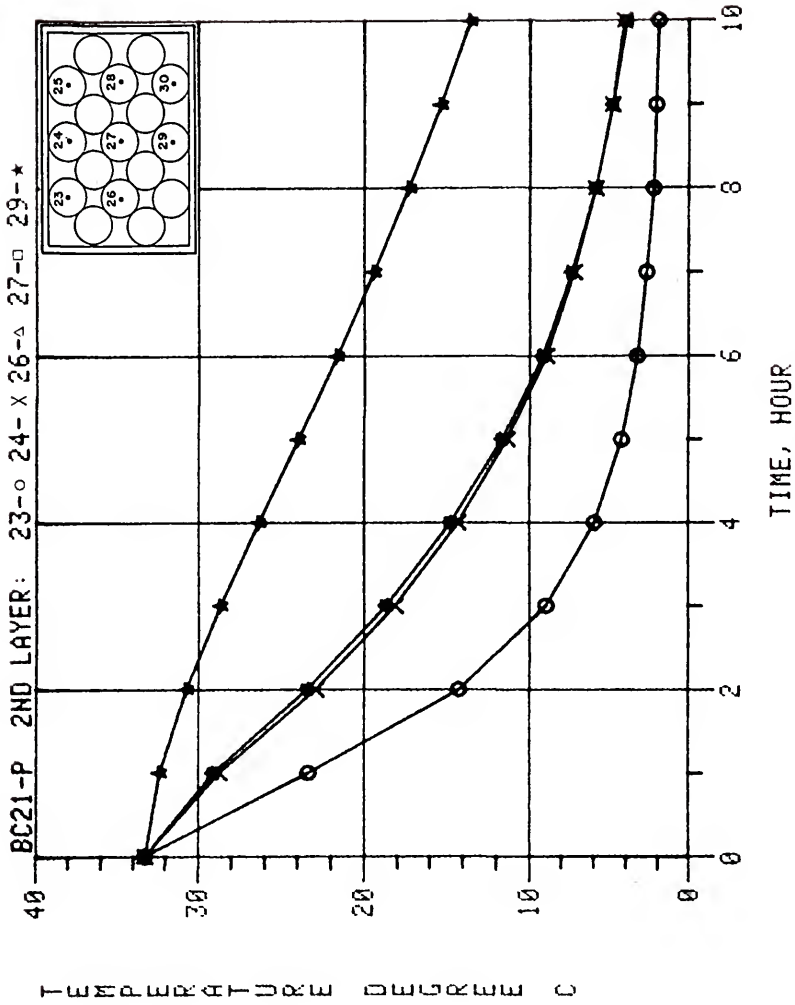


Figure F-5. Predicted center temperature response of oranges in an experimental orange carton for forced-air cooling (Boundary Condition 2-1, 2nd layer thermocouple locations 23, 24, 26, 27, and 29).

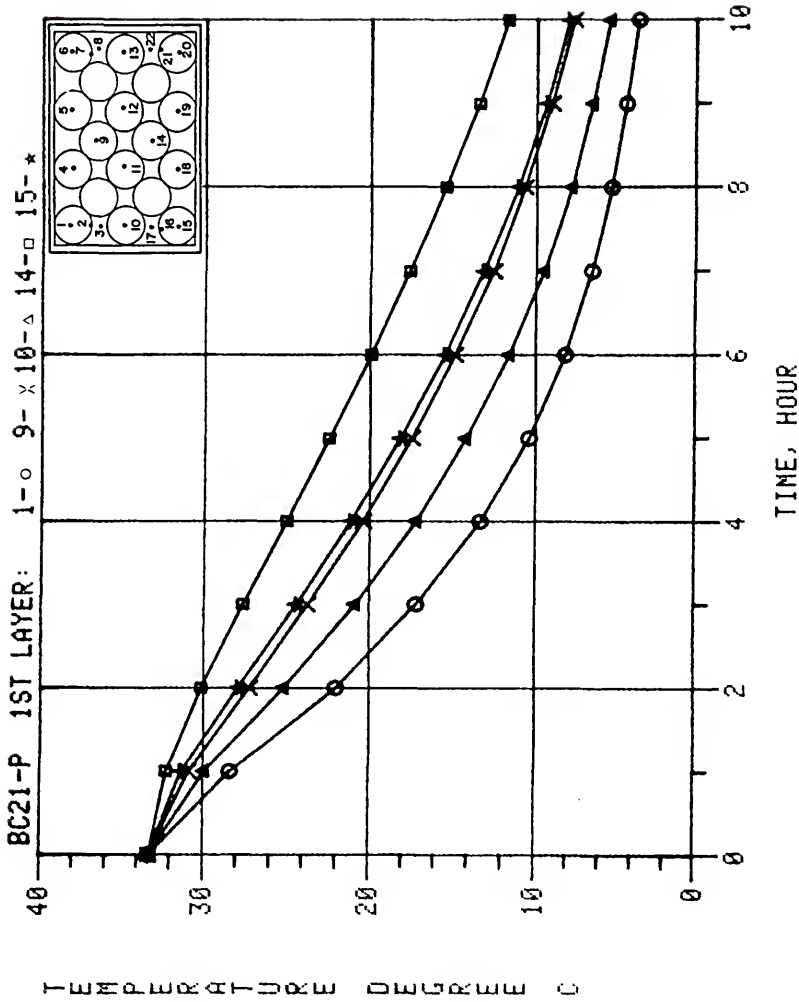


Figure F-6. Predicted center temperature response of oranges in an experimental orange carton for forced-air cooling (Boundary Condition 2-1, 1st layer thermocouple locations 1, 9, 10, 14, and 15).

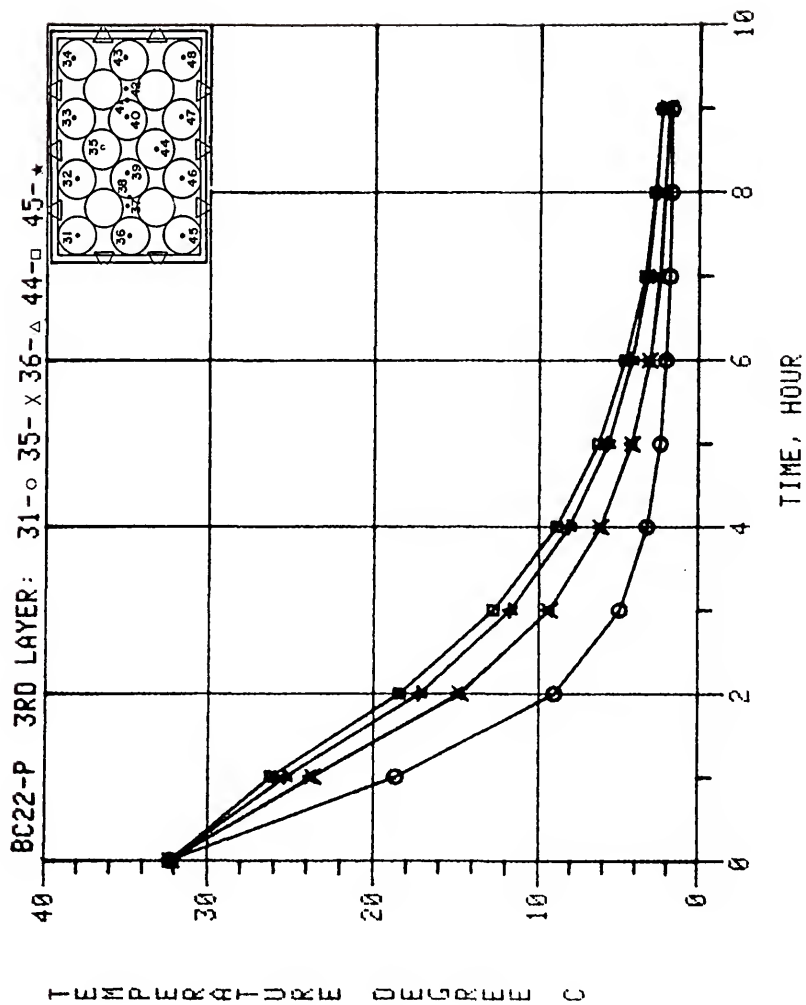


Figure F-7. Predicted center temperature response of oranges in an experimental orange carton for forced-air cooling (Boundary Condition 2-2, 3rd layer thermocouple locations 31, 35, 36, 44, and 45).

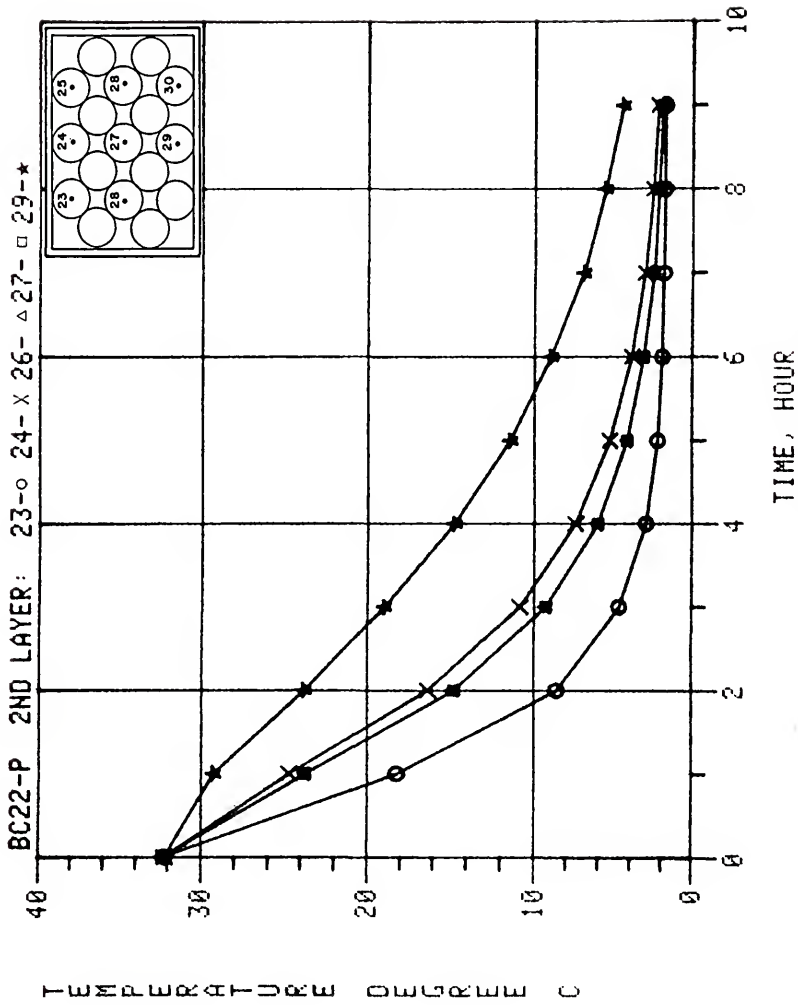


Figure F-8. Predicted center temperature response of oranges in an experimental orange carton for forced-air cooling (Boundary Condition 2-2, 2nd layer thermocouple locations 23, 24, 26, 27, and 29).

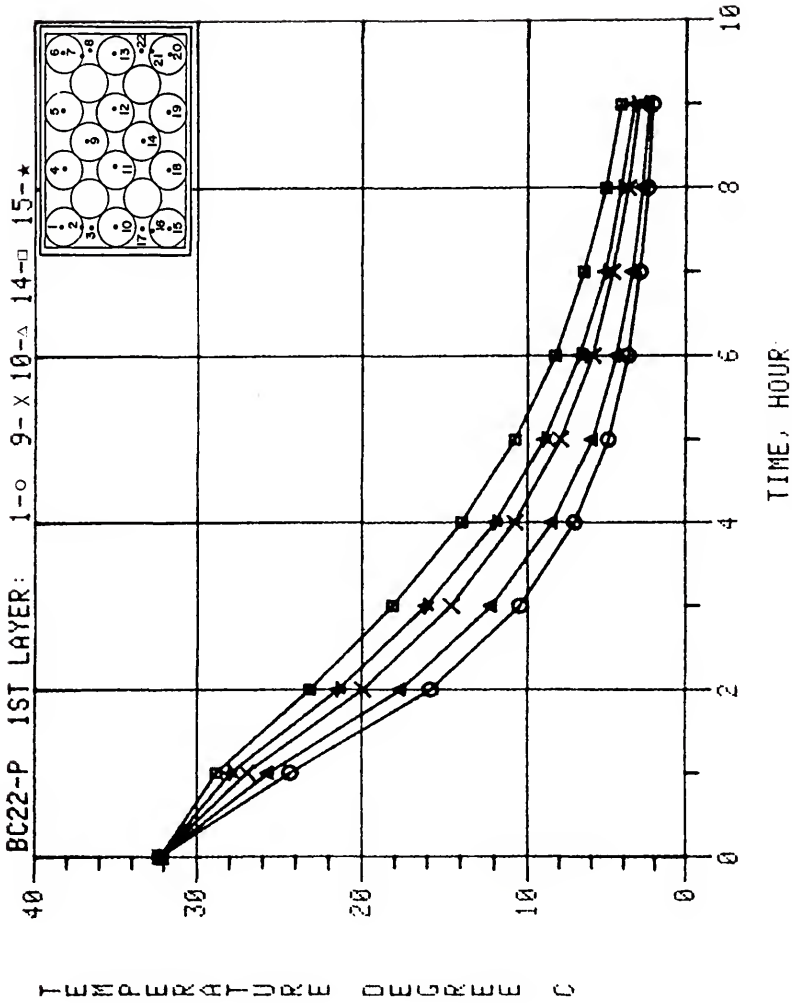


Figure F-9. Predicted center temperature response of oranges in an experimental orange carton for forced-air cooling (Boundary Condition 2-2, 1st layer thermocouple locations 1, 9, 10, 14, and 15).

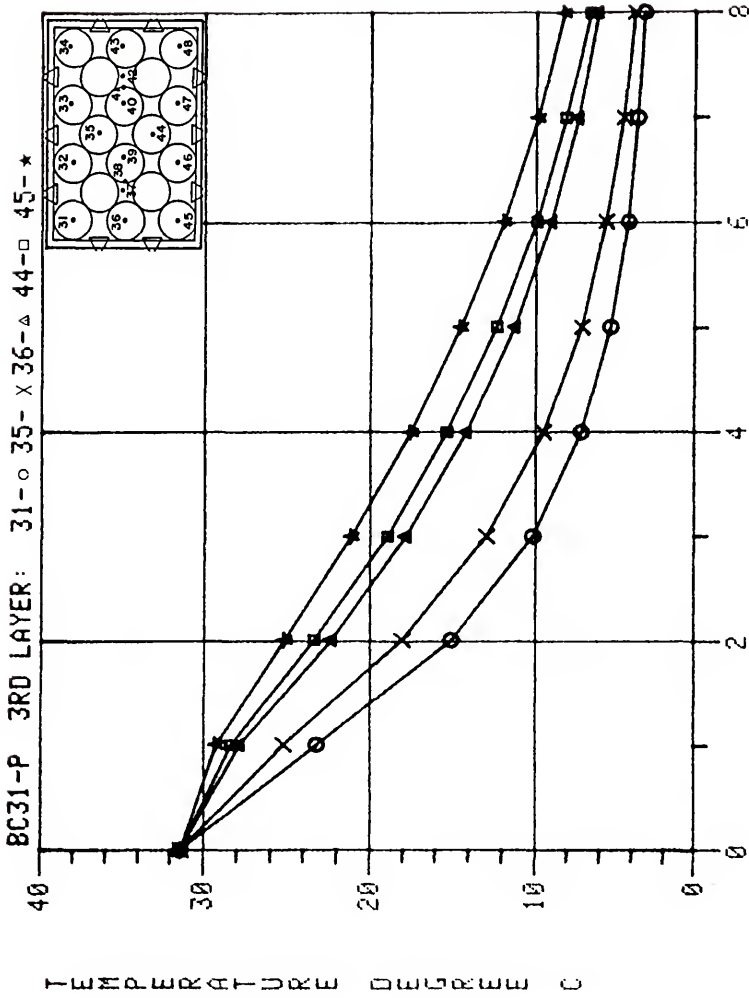


Figure F-10. Predicted center temperature response of oranges in an experimental orange carton for forced-air cooling (Boundary Condition 3-1, 3rd layer thermocouple locations 31, 35, 36, 44, and 45).

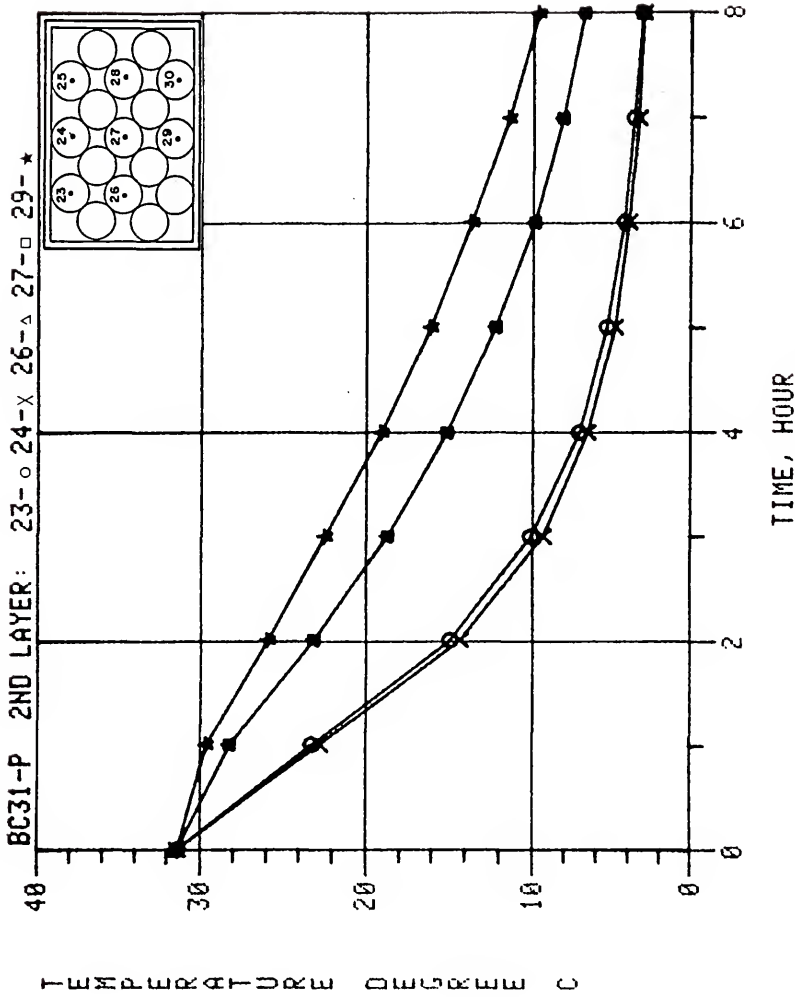


Figure F-11. Predicted center temperature response of oranges in an experimental orange carton for forced-air cooling (Boundary Condition 3-1, 2nd layer thermocouple locations 23, 24, 26, 27, and 29).

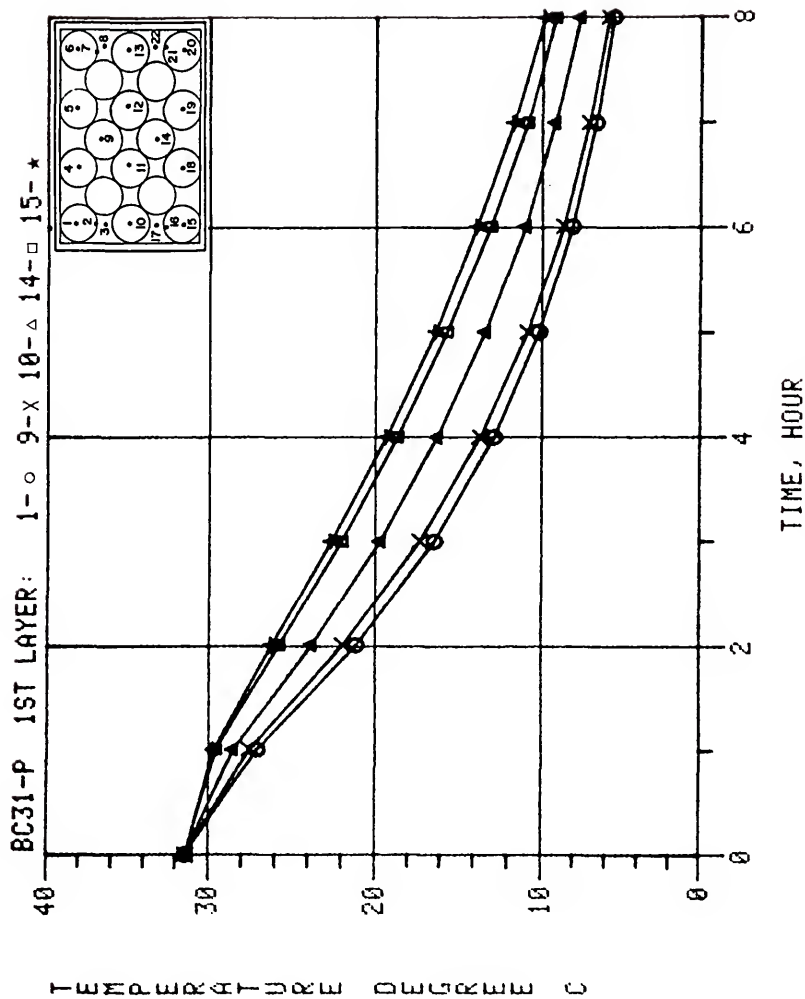


Figure F-12. Predicted center temperature response of oranges in an experimental orange carton for forced-air cooling (Boundary Condition 3-1, 1st layer thermocouple locations 1, 9, 10, 14, and 15).

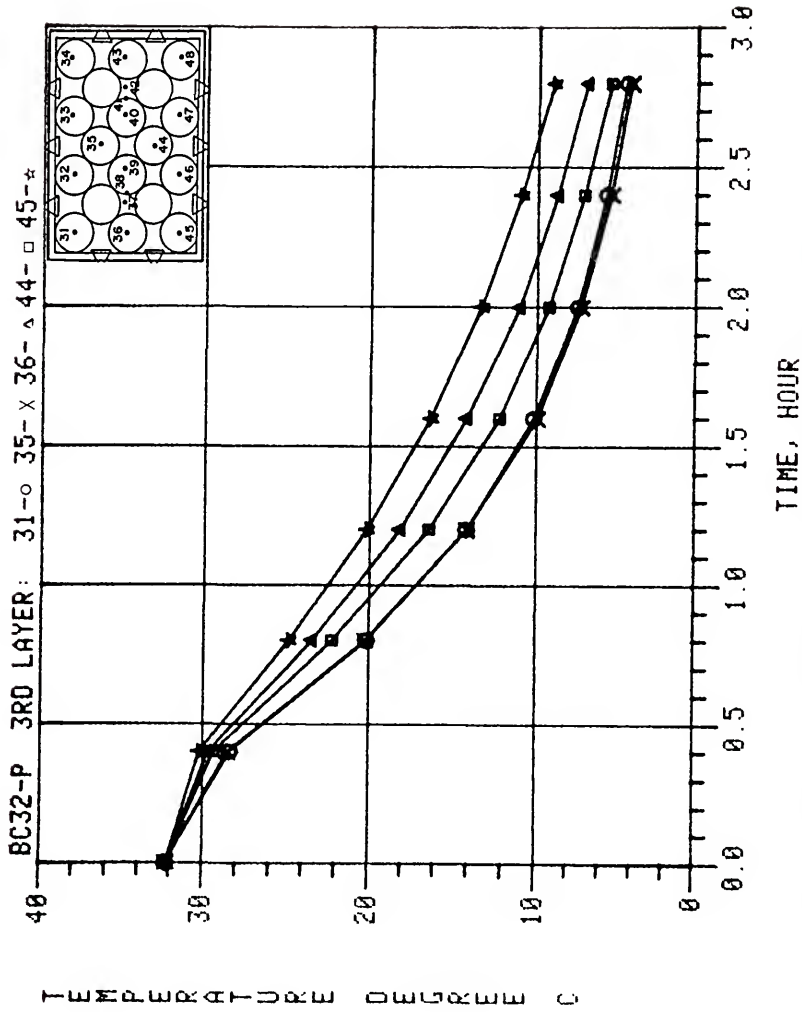


Figure F-13. Predicted center temperature response of oranges in an experimental orange carton for forced-air cooling (Boundary Condition 3-2, 3rd layer thermocouple locations 31, 35, 36, 44, and 45).

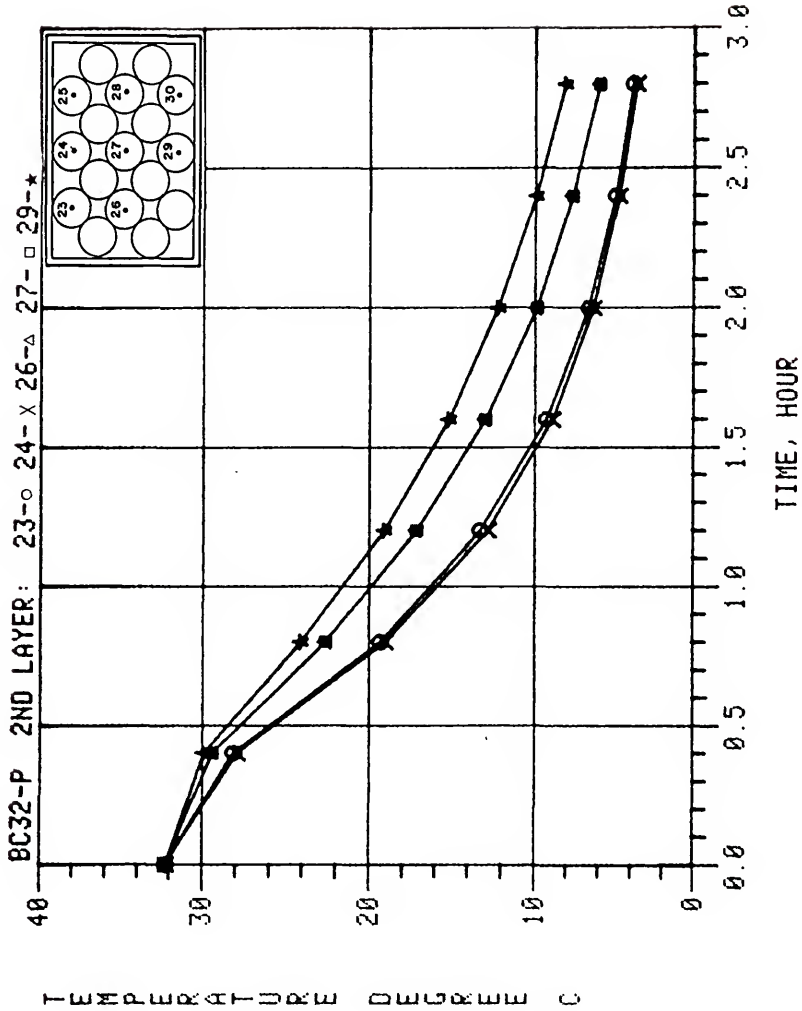


Figure F-14. Predicted center temperature response of oranges in an experimental orange carton for forced-air cooling (Boundary Condition 3-2, 2nd layer thermocouple locations 23, 24, 26, 27, and 29).

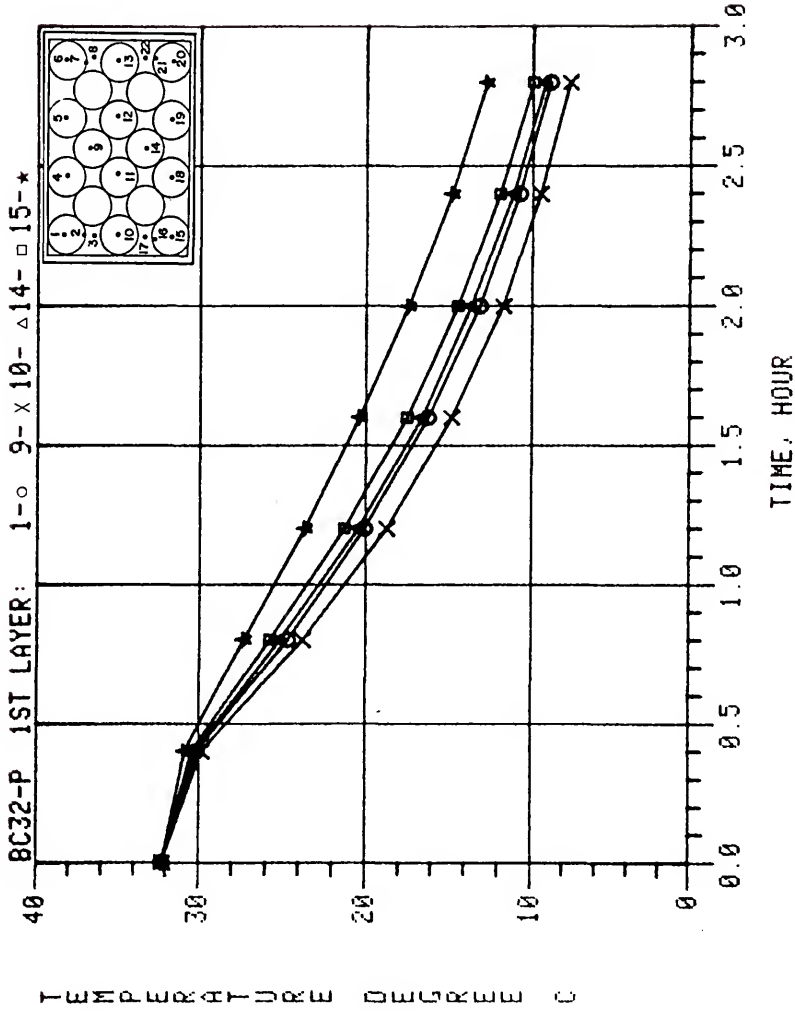


Figure F-15. Predicted center temperature response of oranges in an experimental orange carton for forced-air cooling (Boundary Condition 3-2, 1st layer thermocouple locations 1, 9, 10, 14, and 15).

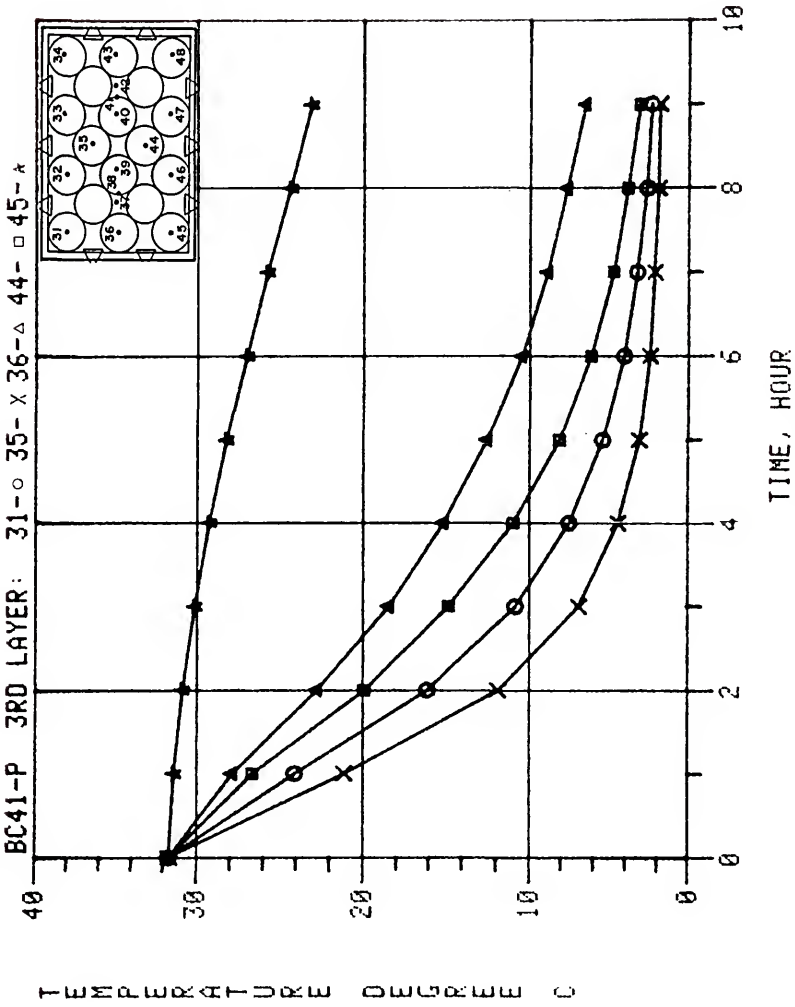


Figure F-16. Predicted center temperature response of oranges in an experimental orange carton for forced-air cooling (Boundary Condition 4-1, 3rd layer thermocouple locations 31, 35, 36, 44, and 45).

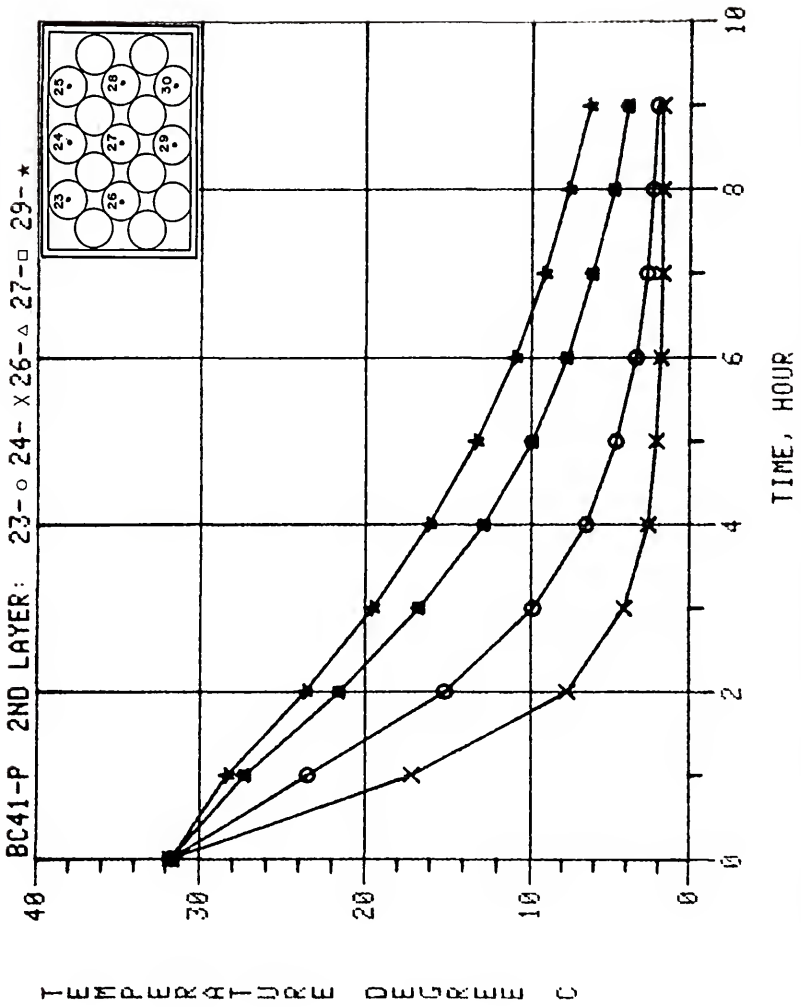


Figure F-17. Predicted center temperature response of oranges in an experimental orange carton for forced-air cooling (Boundary Condition 4-1, 2nd layer thermocouple locations 23, 24, 26, 27, and 29).

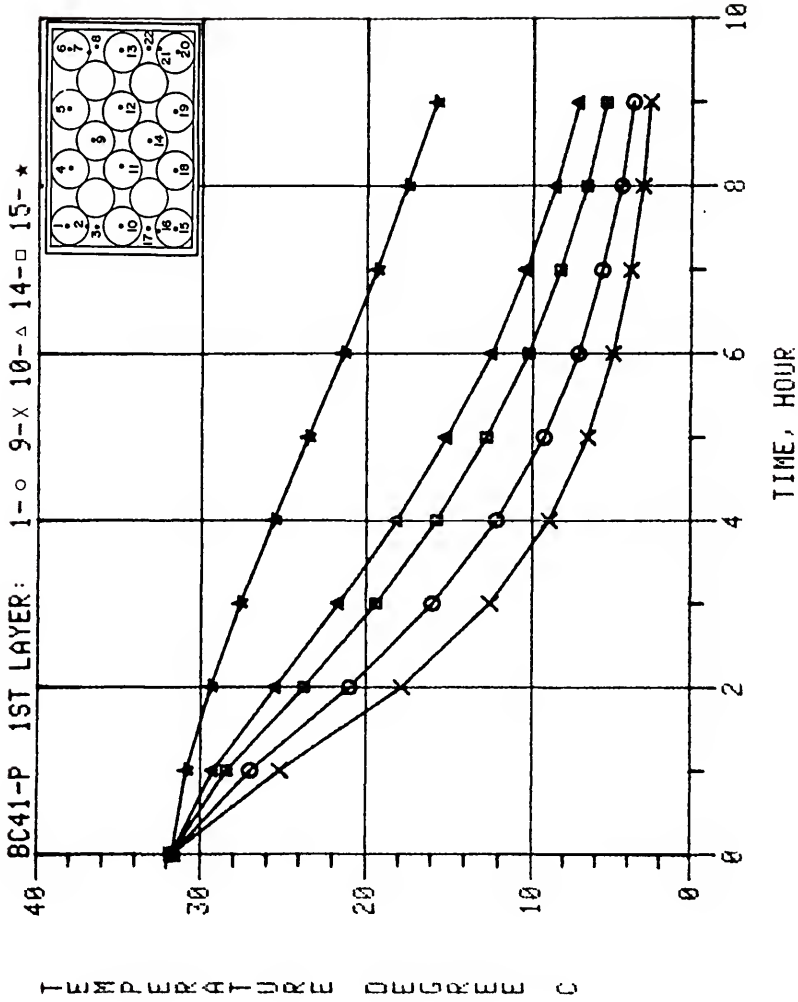


Figure F-18. Predicted center temperature response of oranges in an experimental orange carton for forced-air cooling (Boundary Condition 4-1, 1st layer thermocouple locations 1, 9, 10, 14, and 15).

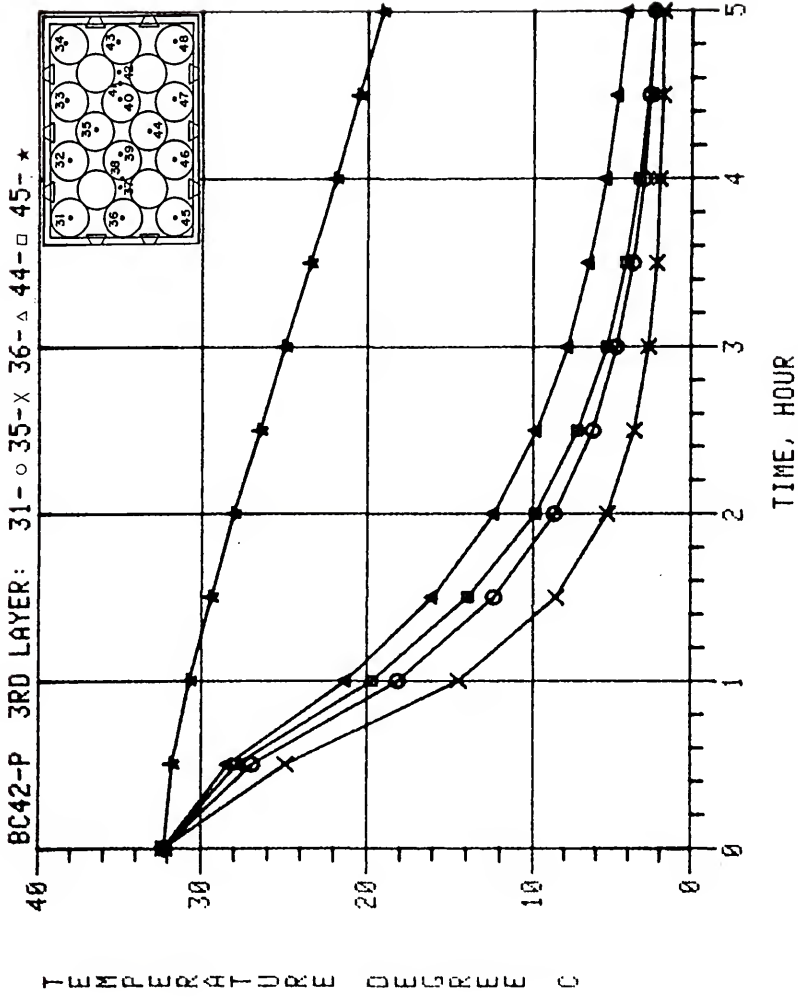


Figure F-19. Predicted center temperature response of oranges in an experimental orange carton for forced-air cooling (Boundary Condition 4-2, 3rd layer thermocouple locations 31, 35, 36, 44, and 45).

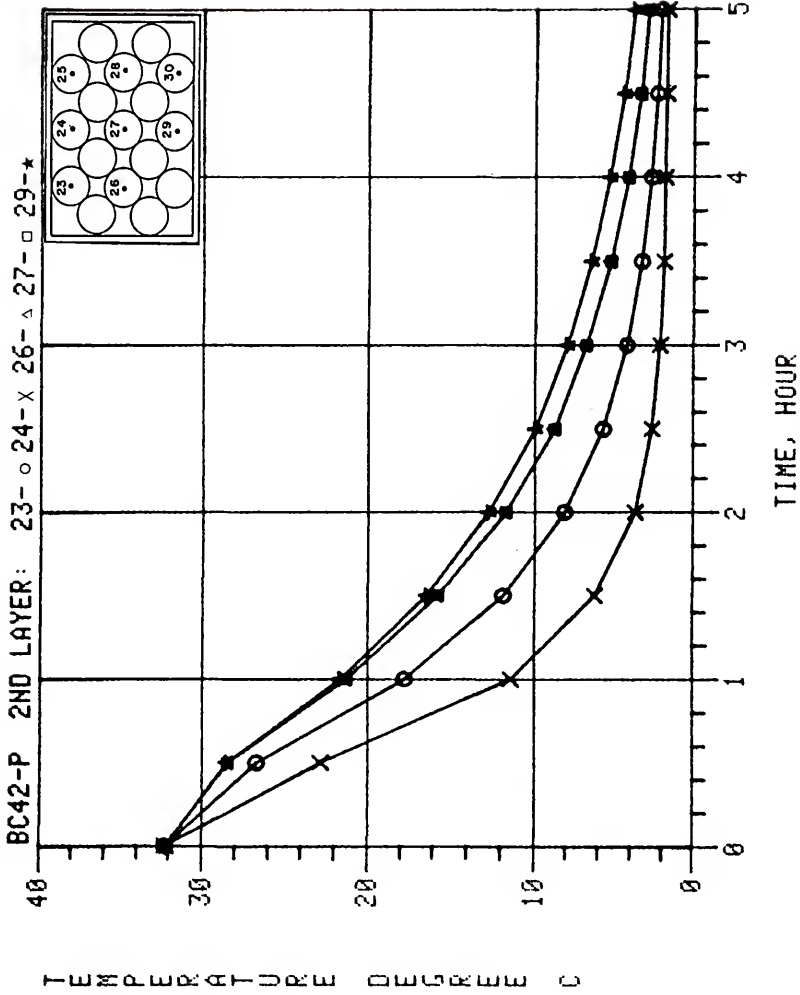


Figure F-20. Predicted center temperature response of oranges in an experimental orange carton for forced-air cooling (Boundary Condition 4-2, 2nd layer thermocouple locations 23, 24, 26, 27, and 29).

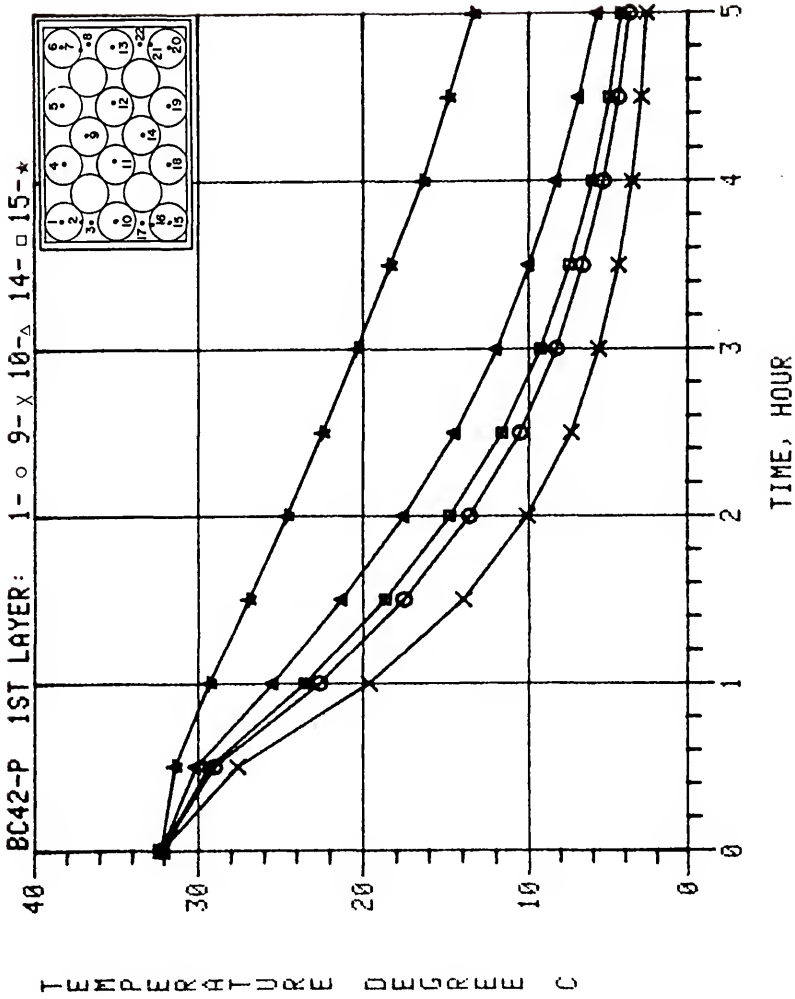


Figure F-21. Predicted center temperature response of oranges in an experimental orange carton for forced-air cooling (Boundary Condition 4-2, 1st layer thermocouple locations 1, 9, 10, 14, and 15).

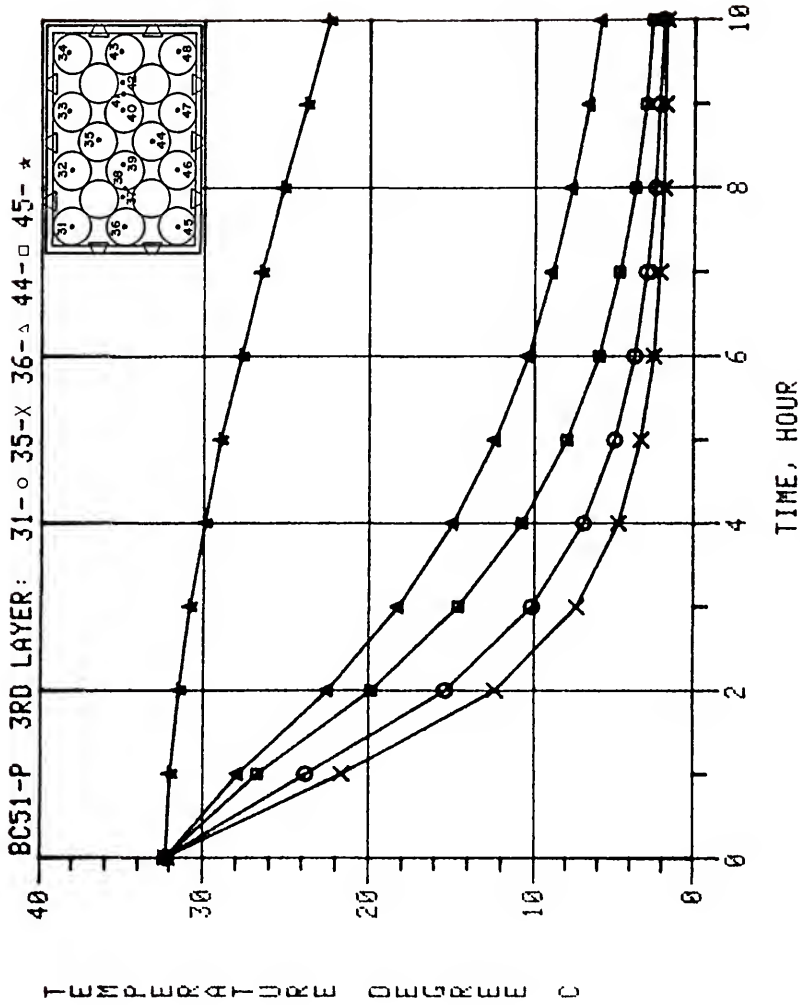


Figure F-22. Predicted center temperature response of oranges in an experimental orange carton for forced-air cooling (Boundary Condition 5-1, 3rd layer thermocouple locations 31, 35, 36, 44, and 45).

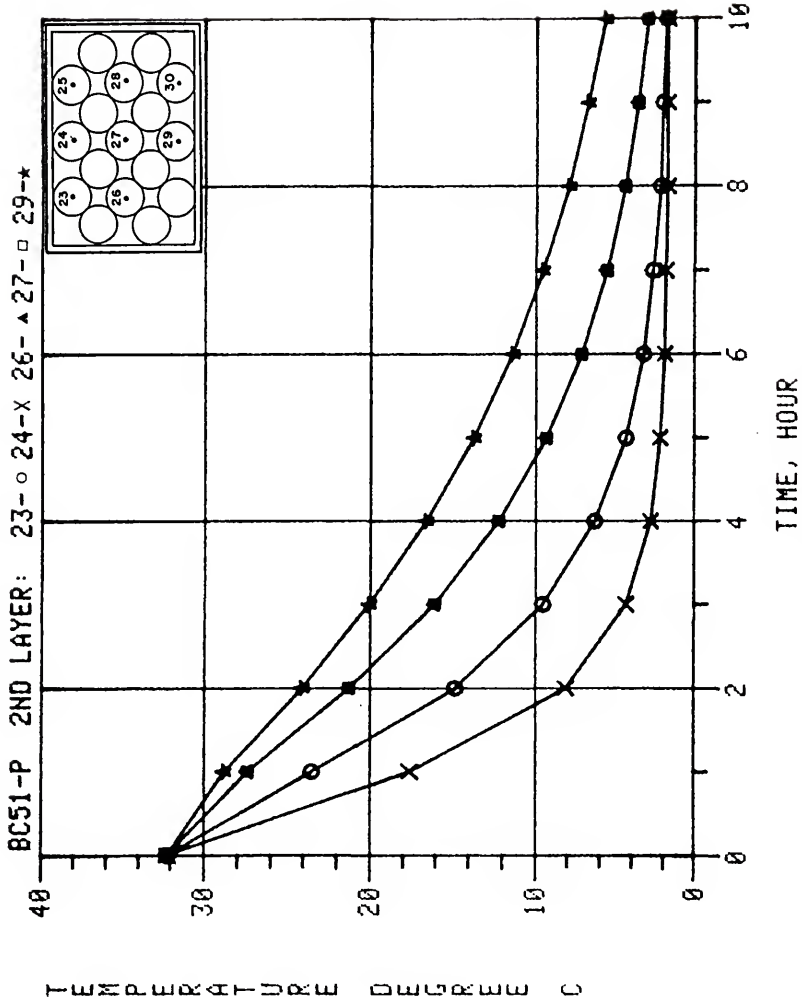


Figure F-23. Predicted center temperature response of oranges in an experimental orange carton for forced-air cooling (Boundary Condition 5-1, 2nd layer thermocouple locations 23, 24, 26, 27, and 29).

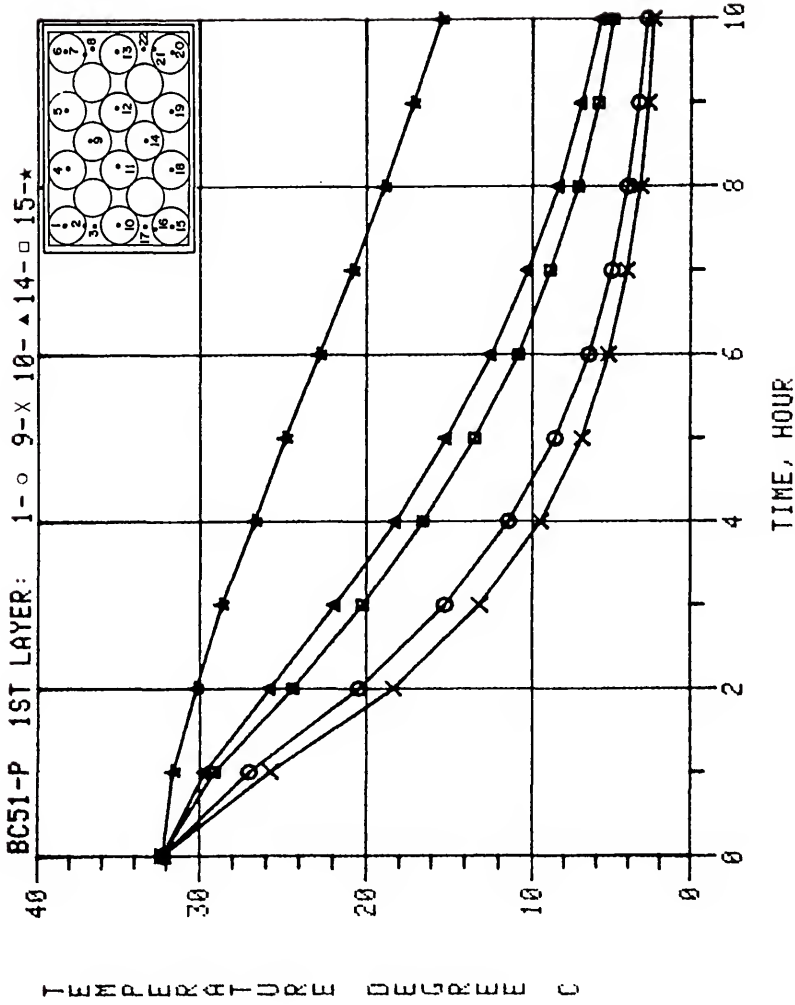


Figure F-24. Predicted center temperature response of oranges in an experimental orange carton for forced-air cooling (Boundary Condition 5-1, 1st layer thermocouple locations 1, 9, 10, 14, and 15).

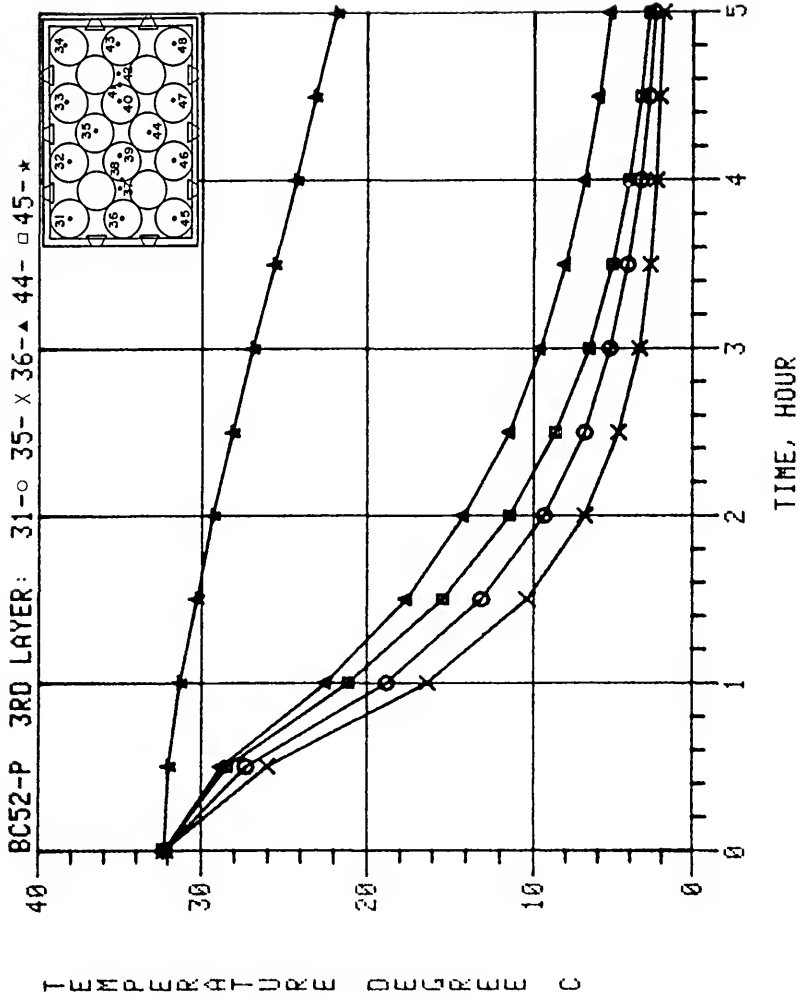


Figure F-25. Predicted center temperature response of oranges in an experimental orange carton for forced-air cooling (Boundary Condition 5-2, 3rd layer thermocouple locations 31, 35, 36, 44, and 45).

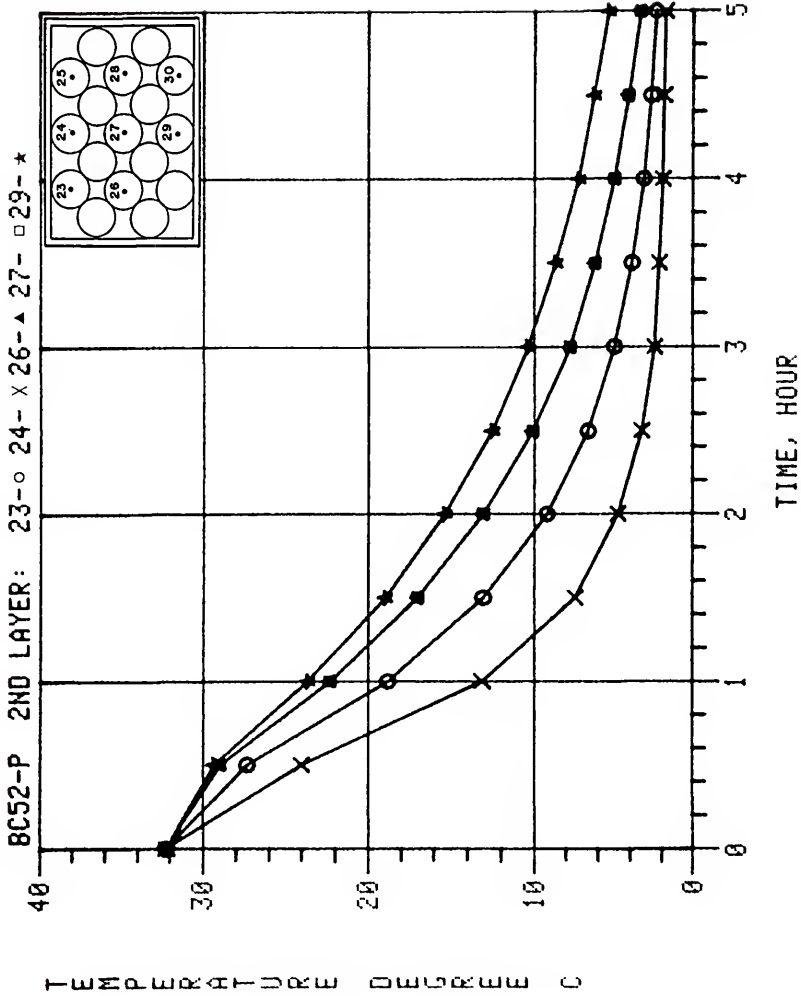


Figure F-26. Predicted center temperature response of oranges in an experimental orange carton for forced-air cooling (Boundary Condition 5-2, 2nd layer thermocouple locations 23, 24, 26, 27, and 29).

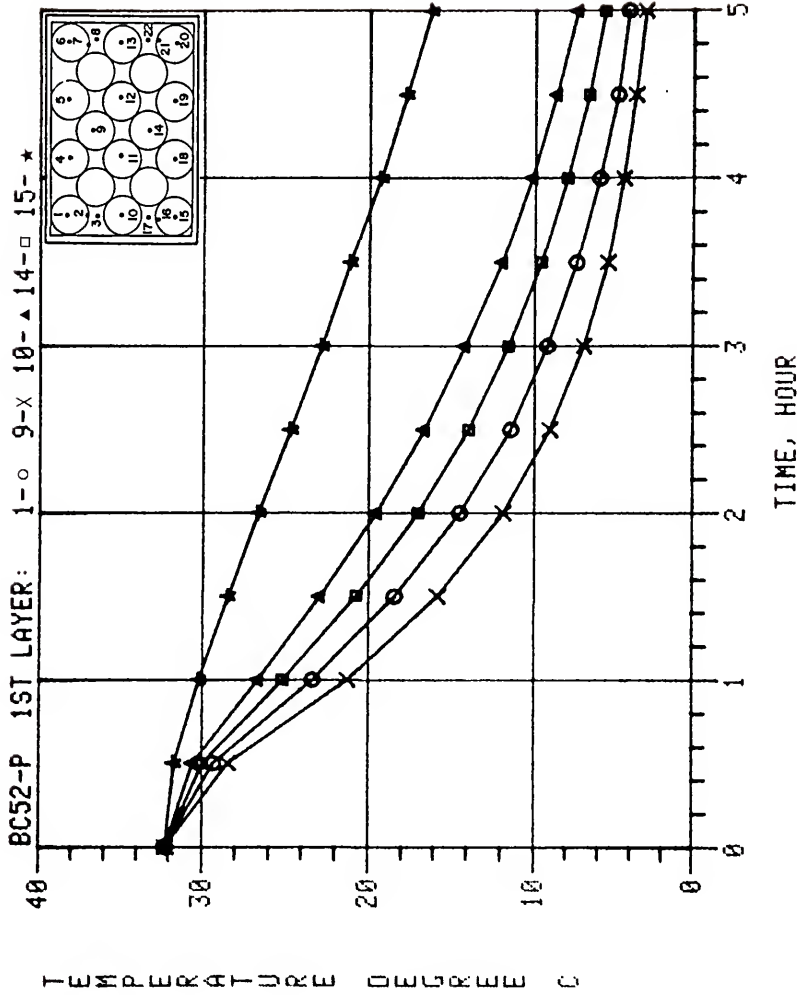


Figure F-27. Predicted center temperature response of oranges in an experimental orange carton for forced-air cooling (Boundary Condition 5-2, 1st layer thermocouple locations 1, 9, 10, 14, and 15).

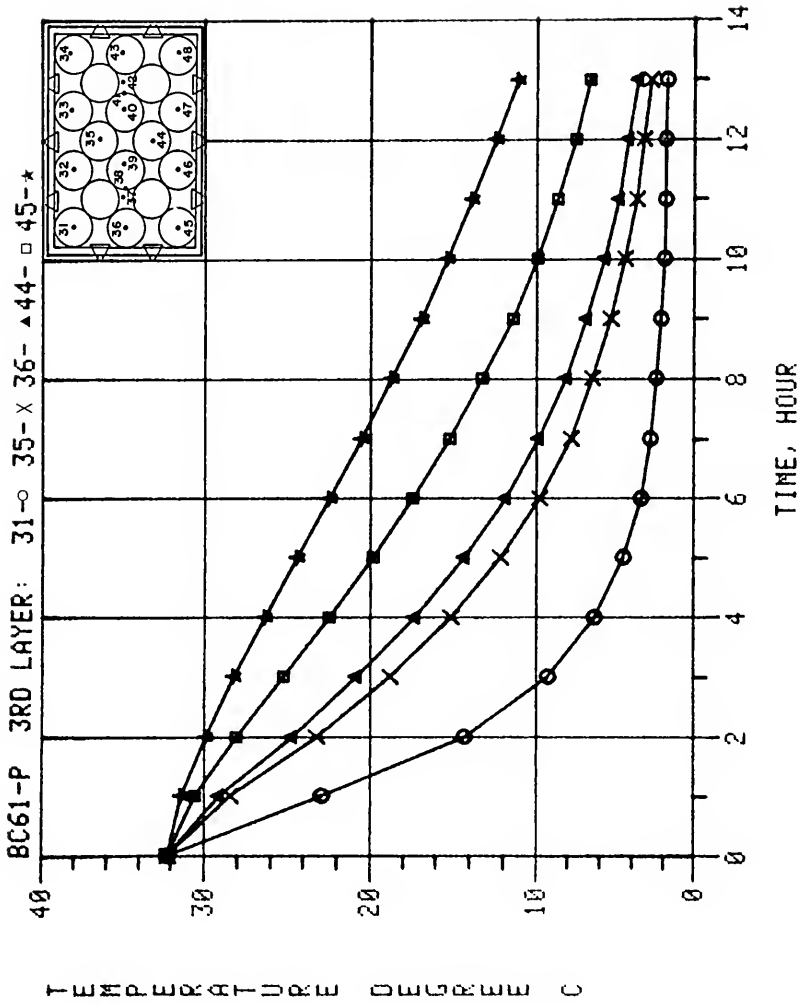


Figure F-28. Predicted center temperature response of oranges in an experimental orange carton for forced-air cooling (Boundary Condition 6-1, 3rd layer thermocouple locations 31, 35, 36, 44, and 45).

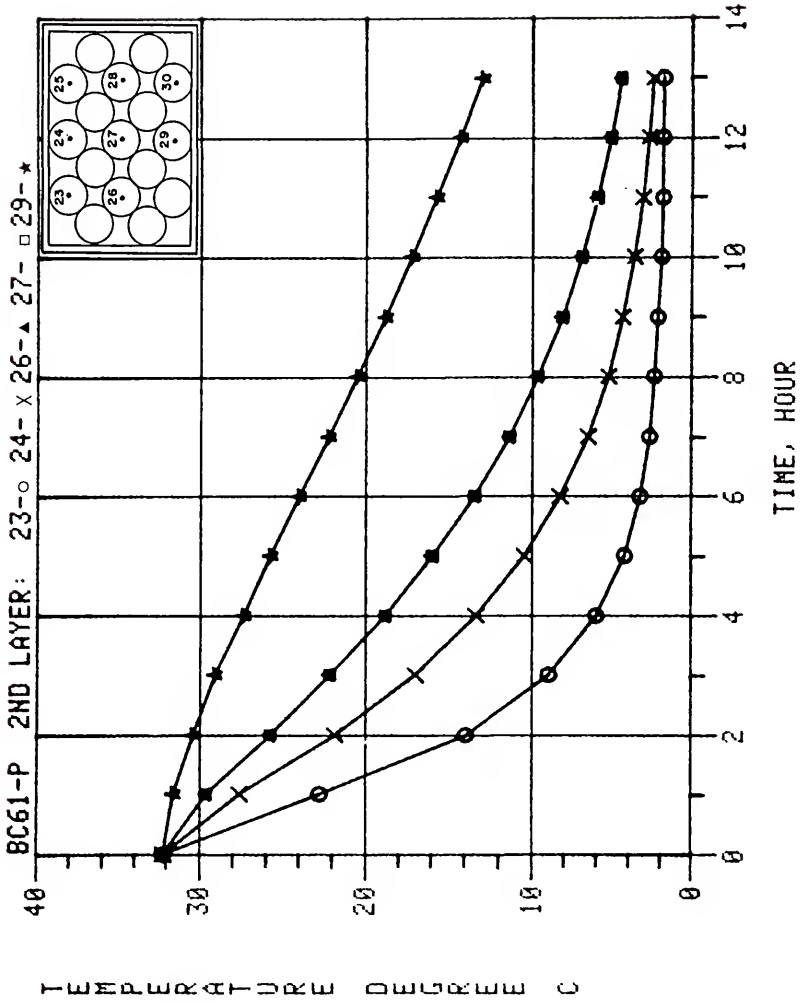


Figure F-29. Predicted center temperature response of oranges in an experimental orange carton for forced-air cooling (Boundary Condition 6-1, 2nd layer thermocouple locations 23, 24, 26, 27, and 29).

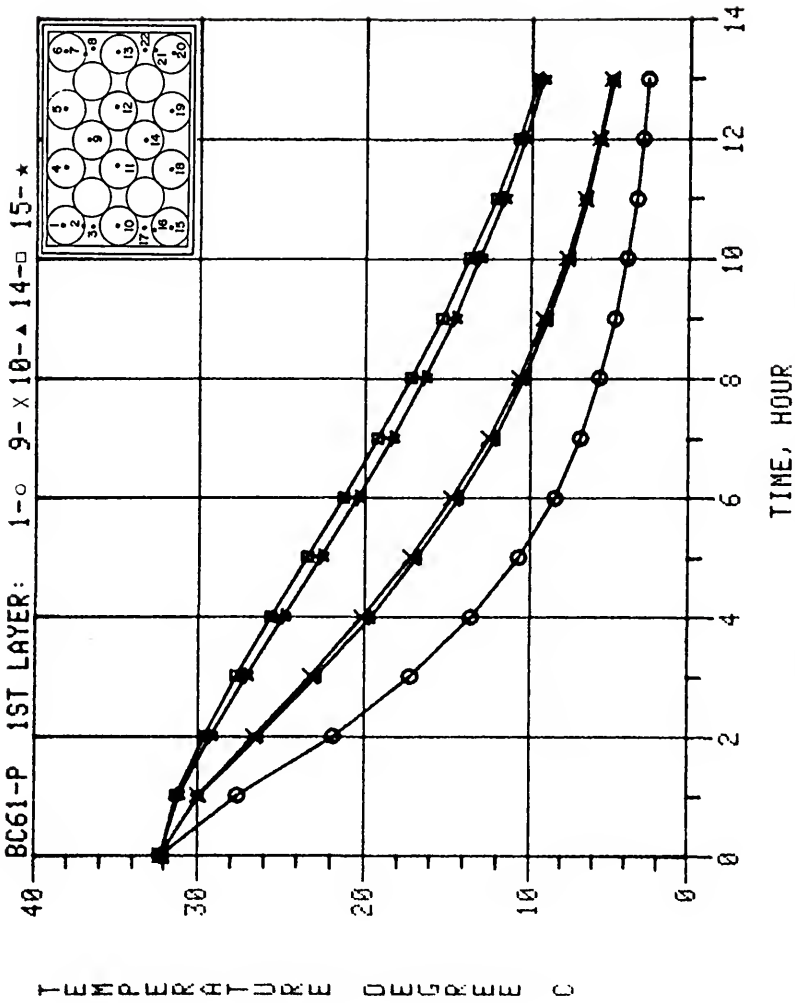


Figure F-30. Predicted center temperature response of oranges in an experimental orange carton for forced-air cooling (Boundary Condition 6-1, 1st layer thermocouple locations 1, 9, 10, 14, and 15).

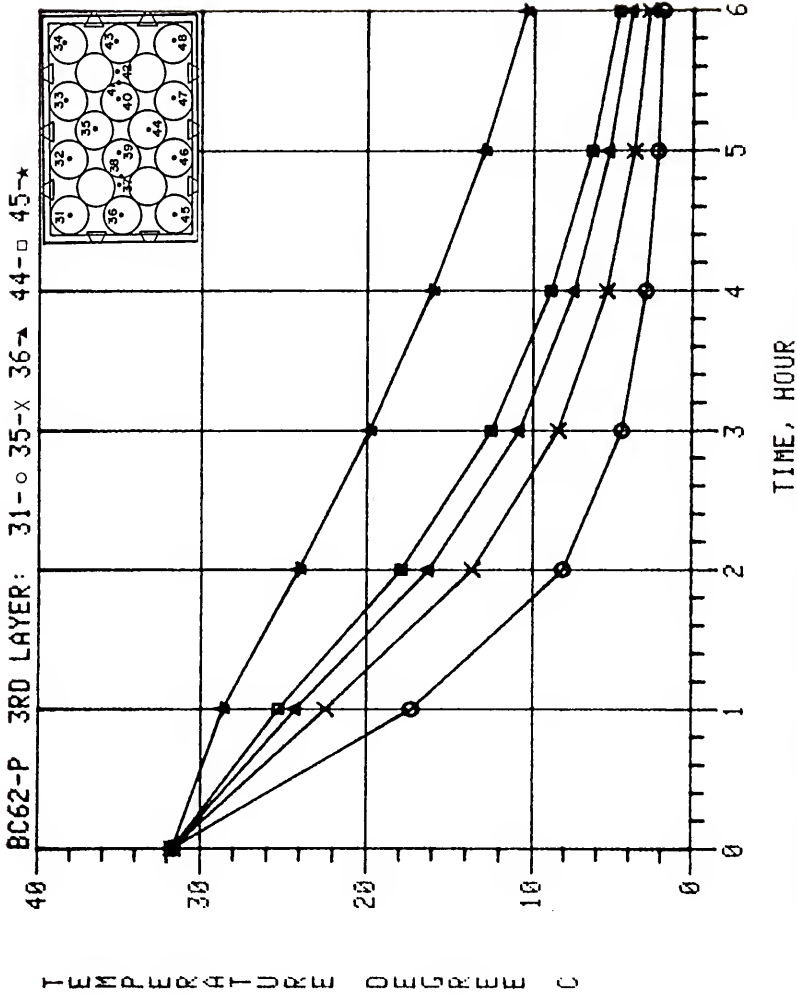


Figure F-31. Predicted center temperature response of oranges in an experimental orange carton for forced-air cooling (Boundary Condition 6-2, 3rd layer thermocouple locations 31, 35, 36, 44, and 45).

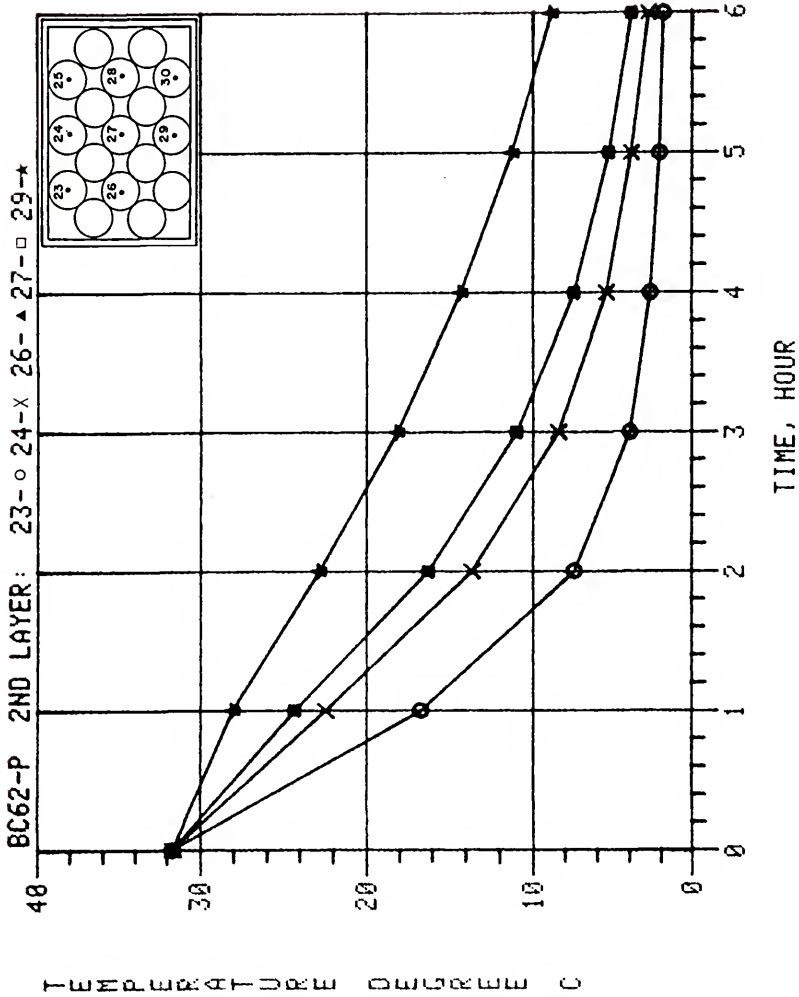


Figure F-32. Predicted center temperature response of oranges in an experimental orange carton for forced-air cooling (Boundary Condition 6-2, 2nd layer thermocouple locations 23, 24, 26, 27, and 29).

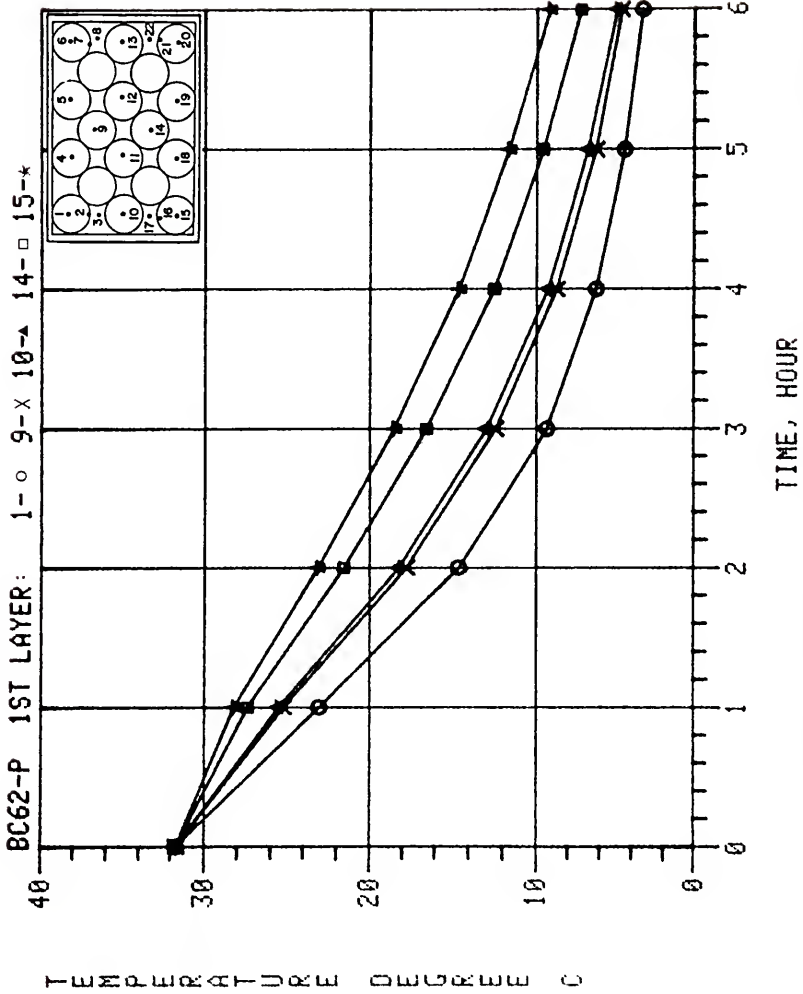


Figure F-33. Predicted center temperature response of oranges in an experimental orange carton for forced-air cooling (Boundary Condition 6-2, 1st layer thermocouple locations 1, 9, 10, 14, and 15).

APPENDIX G
ADDITIONAL PREDICTED VERSUS EXPERIMENTAL
TEMPERATURE RESPONSE GRAPHS

The predicted versus experimental temperature response plots for the eleven boundary conditions not presented in the main text are included on the following pages. For each boundary condition, the temperature responses are presented in the same manner as Figures 52, 53, 54, 55, 56, and 57, for Boundary Condition 1-1.

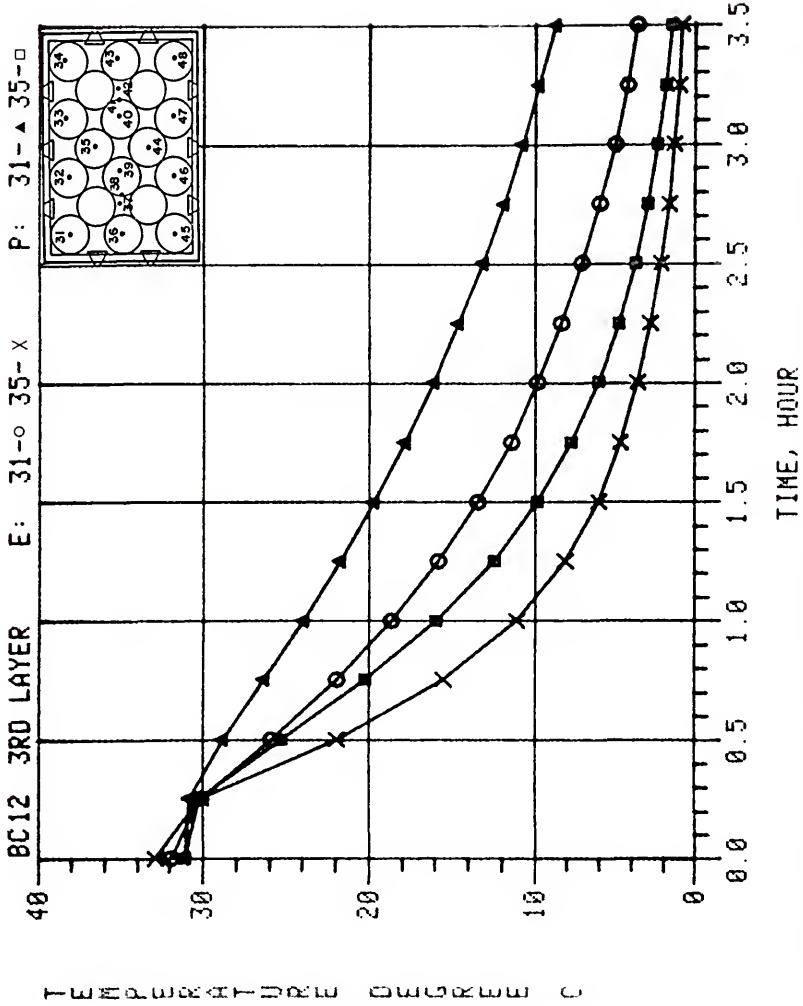


Figure G-1. Predicted versus experimental data for Boundary Condition 1-2, 3rd layer thermocouples 31 and 35.

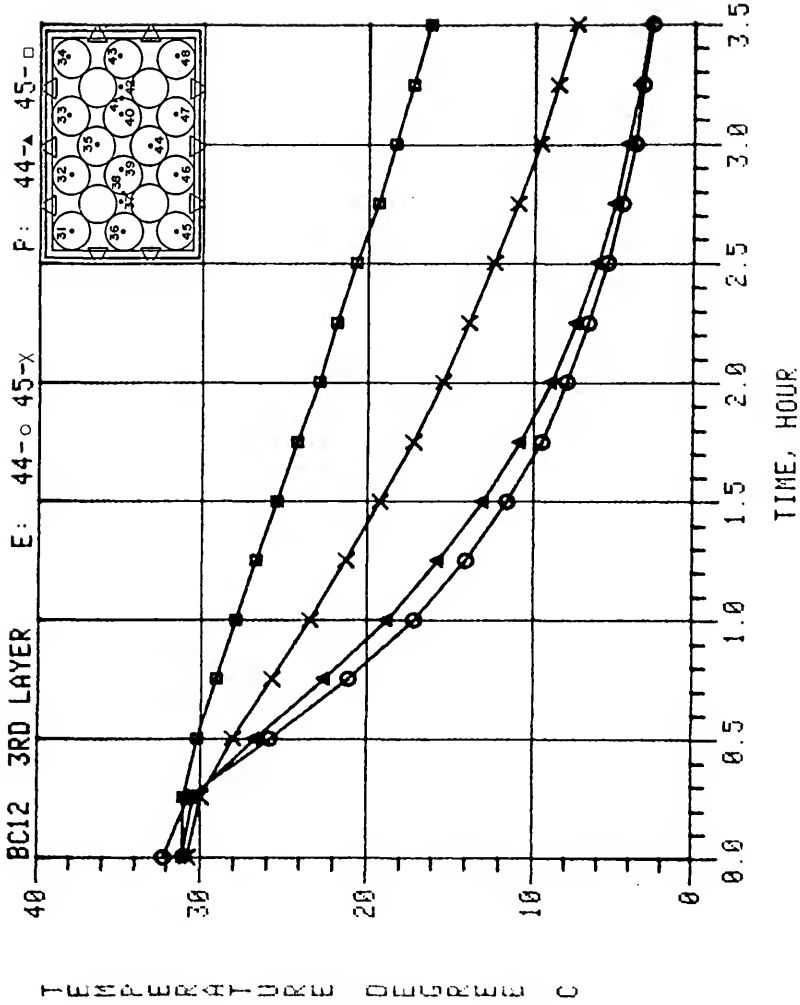


Figure G-2. Predicted versus experimental data for Boundary Condition 1-2, 3rd layer thermocouples 44 and 45.

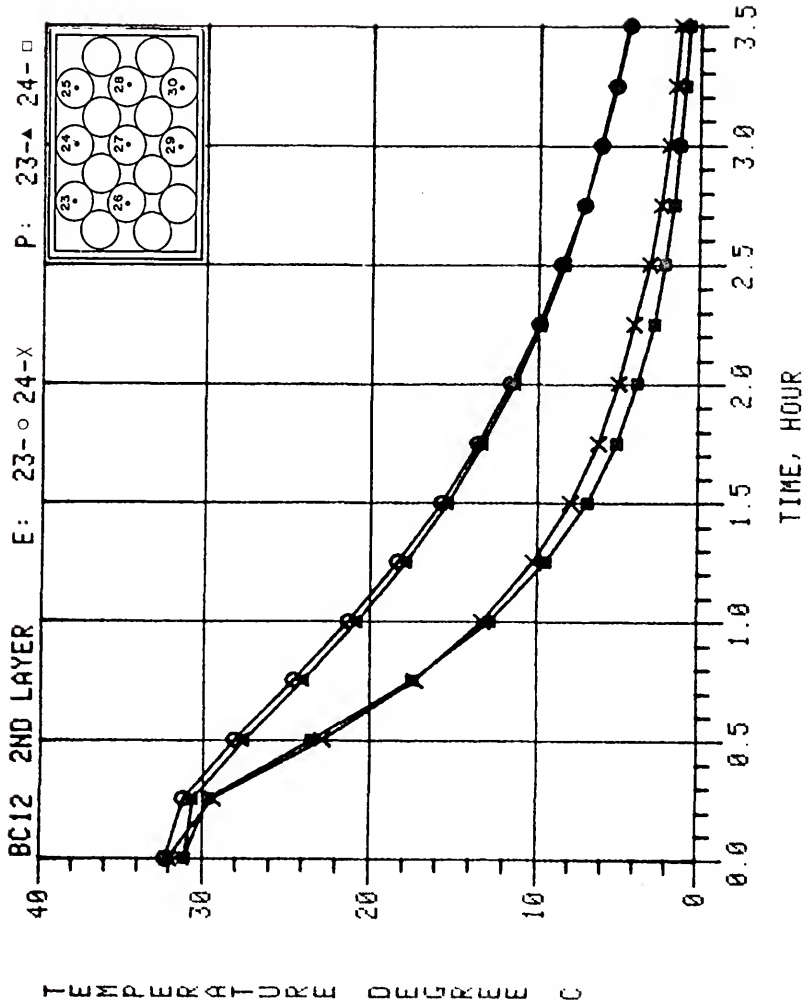


Figure G-3. Predicted versus experimental data for Boundary Condition 1-2, 2nd layer thermocouples 23 and 24.

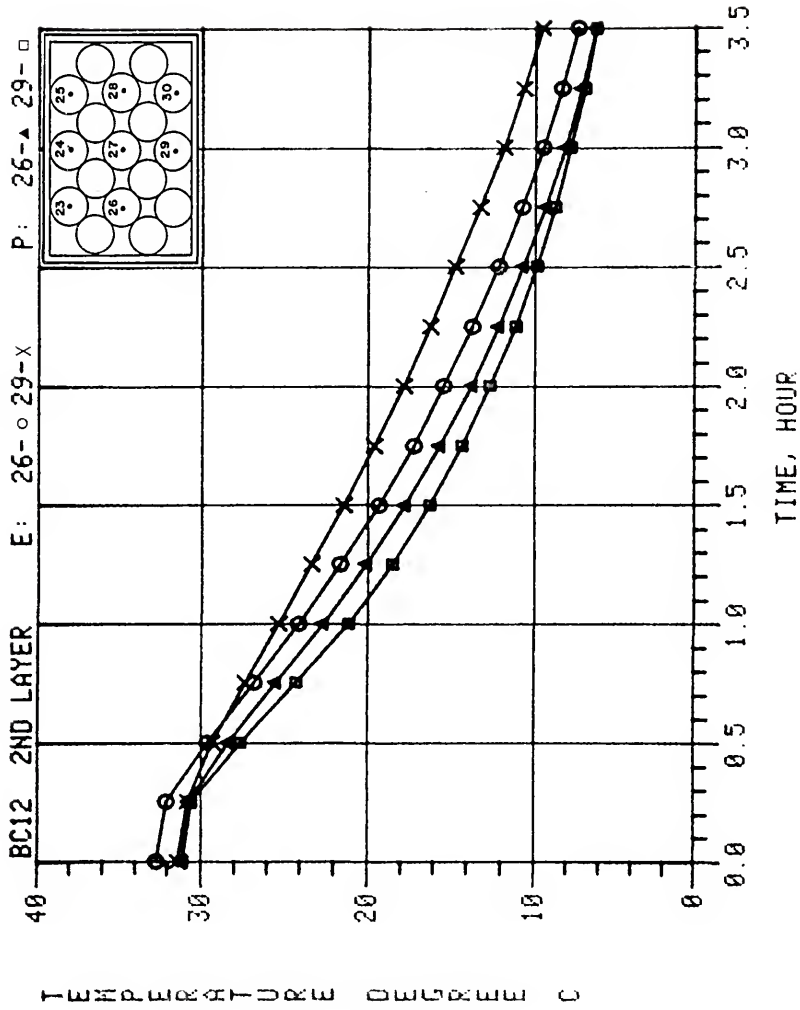


Figure G-4. Predicted versus experimental data for Boundary Condition 1-2, 2nd layer thermocouples 26 and 29.

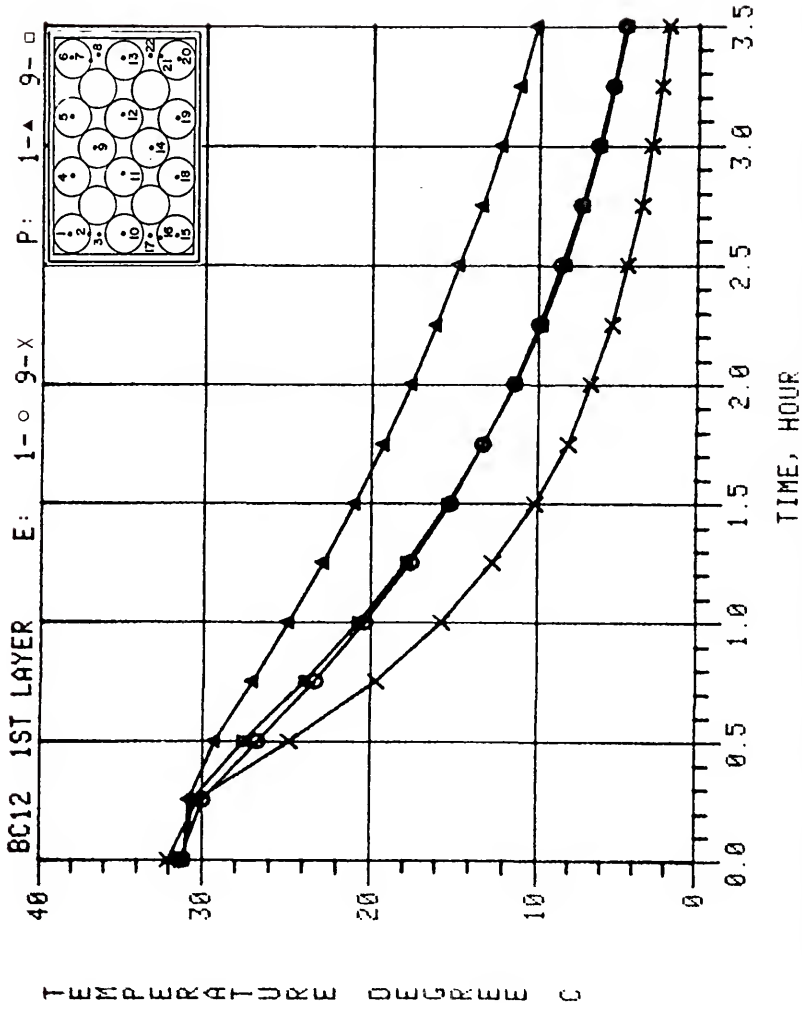


Figure G-5. Predicted versus experimental data for Boundary Condition 1-2, 1st layer thermocouples 1 and 9.

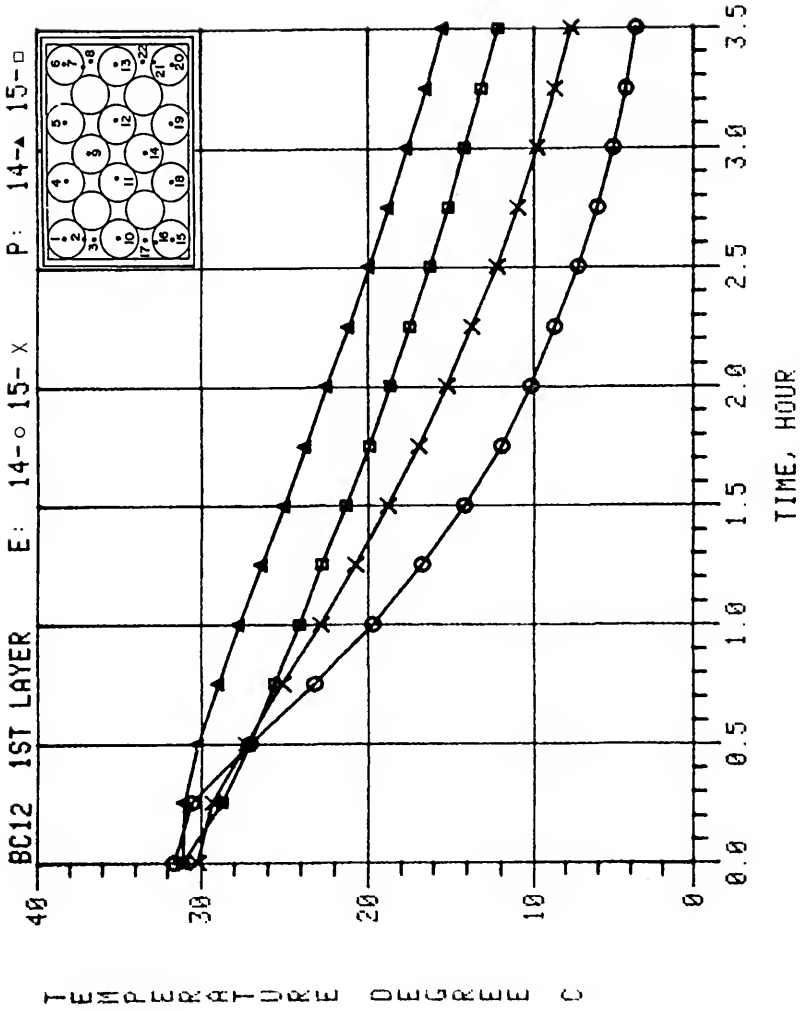


Figure G-6. Predicted versus experimental data for Boundary Condition 1-2, 1st layer thermocouples 14 and 15.

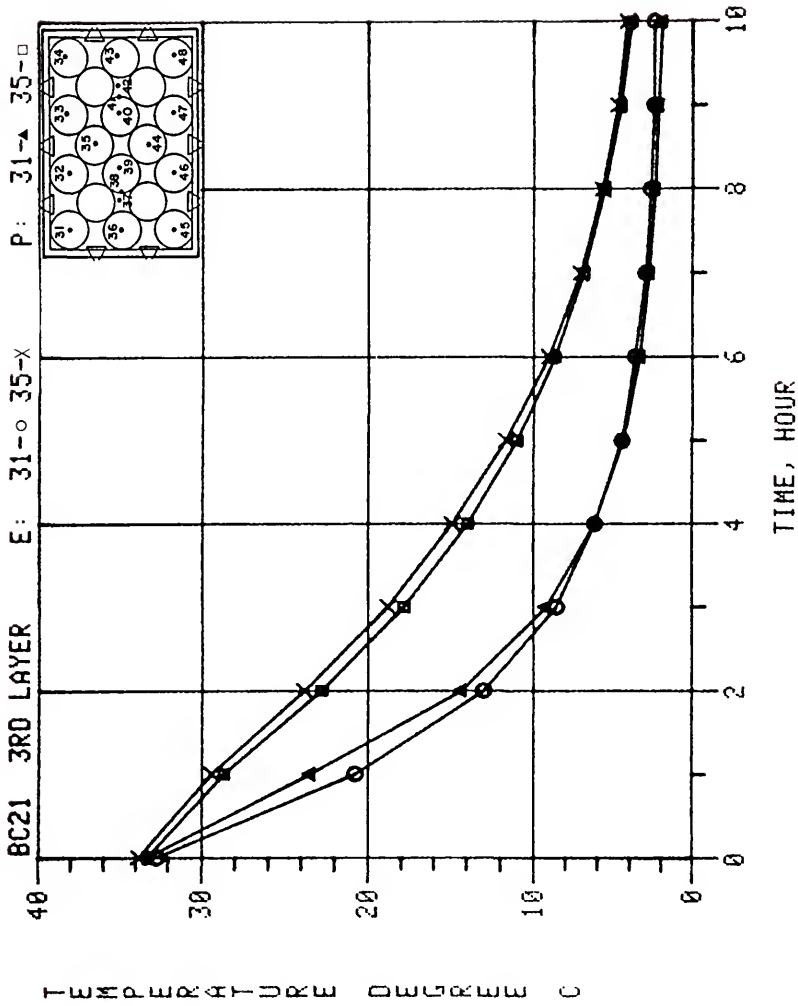


Figure G-7. Predicted versus experimental data for Boundary Condition 2-1, 3rd layer thermocouples 31 and 35.

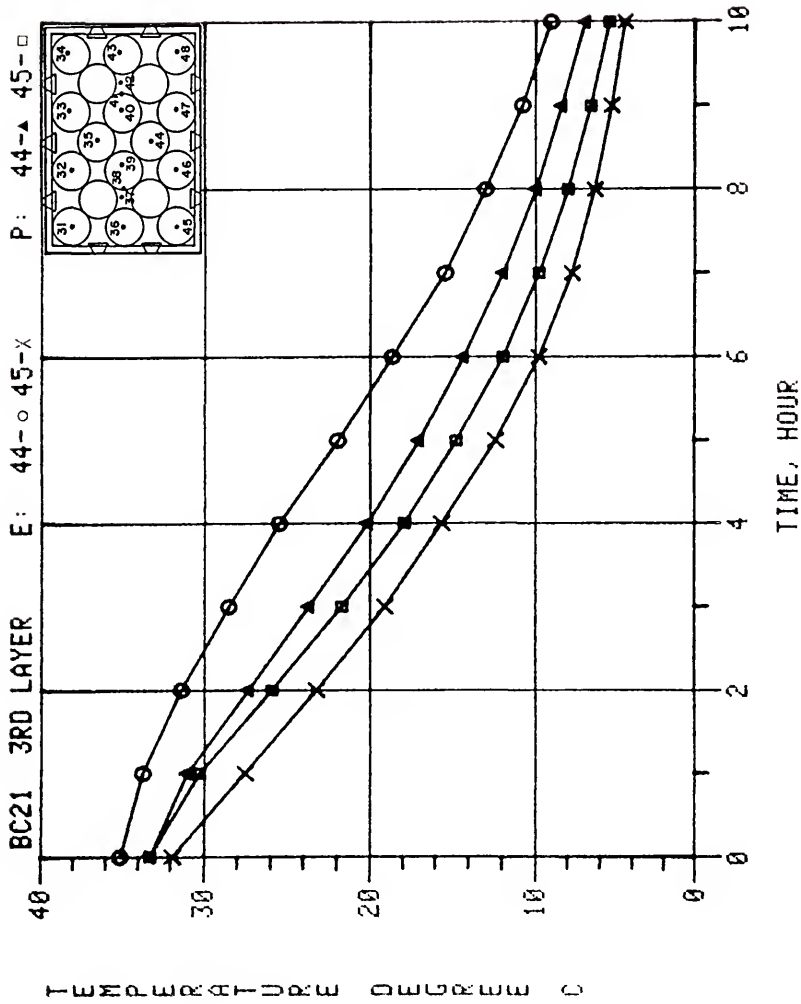


Figure G-8. Predicted versus experimental data for Boundary Condition 2-1, 3rd layer thermocouples 44 and 45.

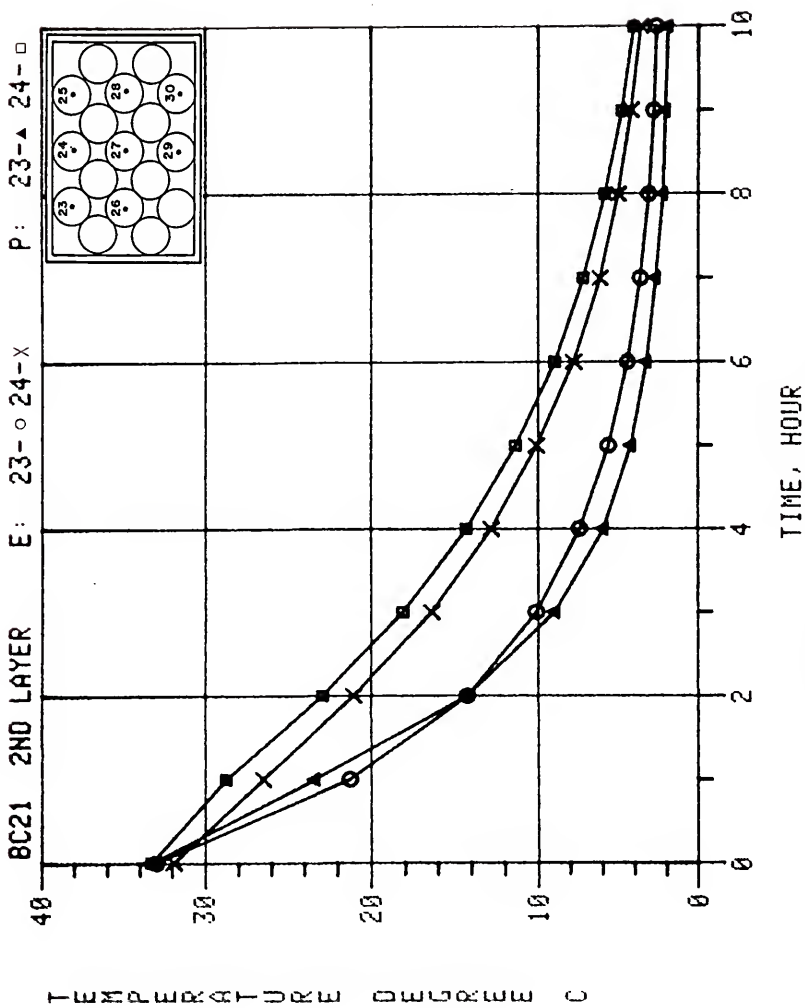


Figure G-9. Predicted versus experimental data for Boundary Condition 2-1, 2nd layer thermocouples 23 and 24.

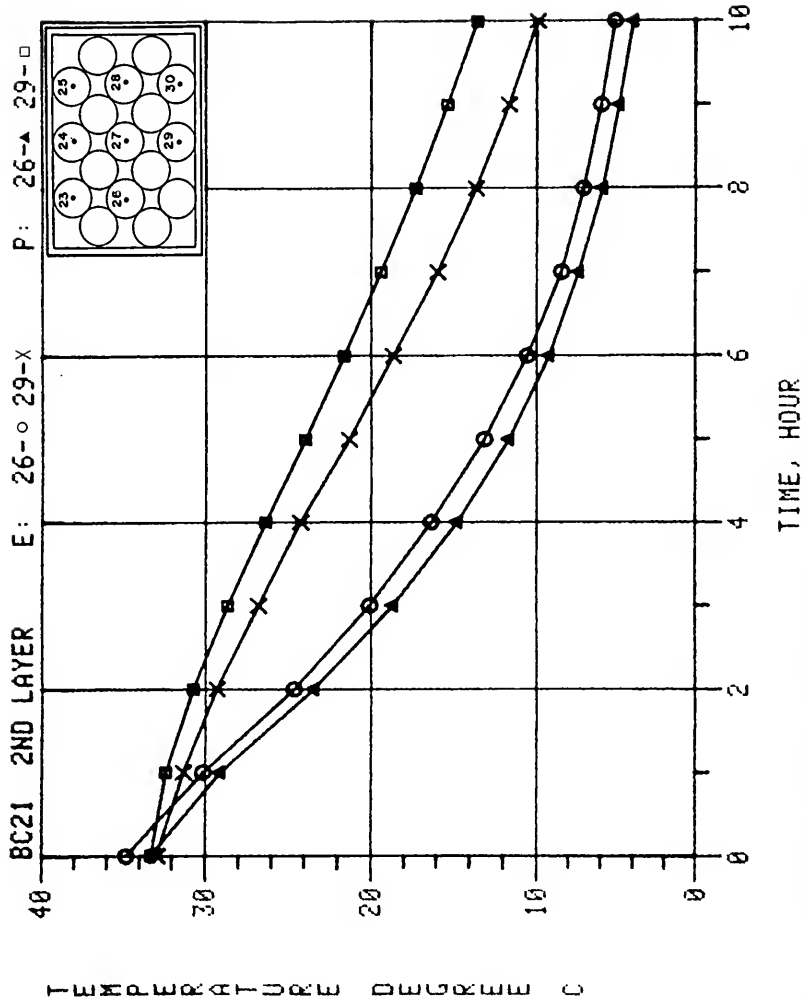


Figure G-10. Predicted versus experimental data for Boundary Condition 2-1, 2nd layer thermocouples 26 and 29.

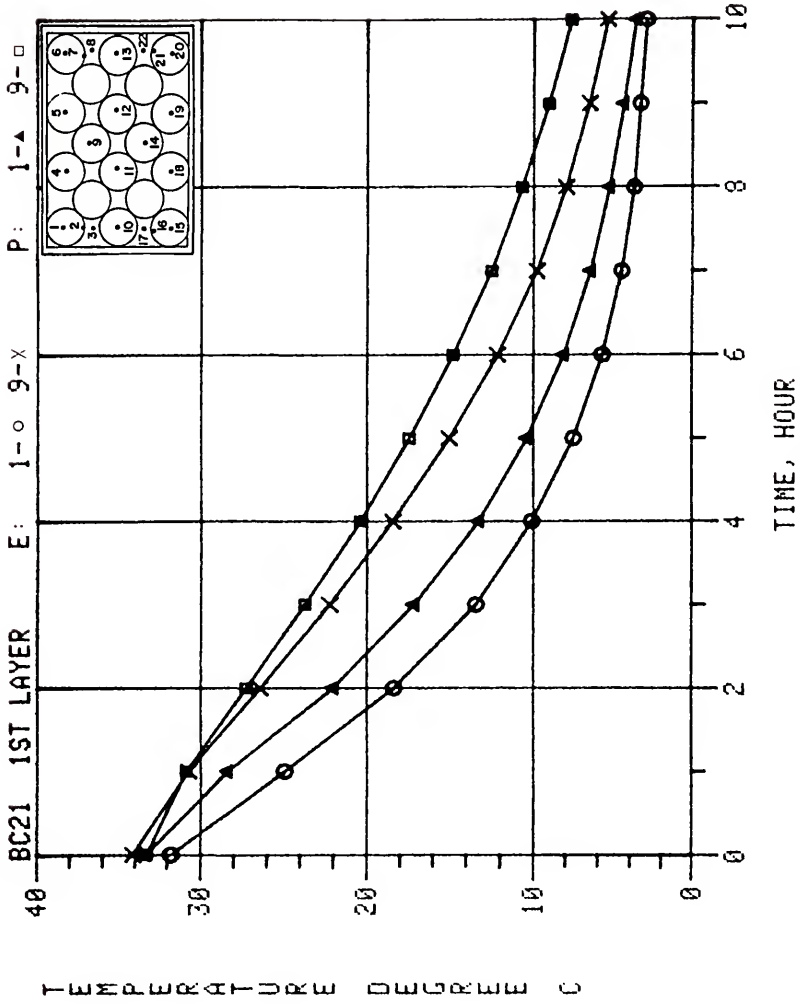


Figure G-11. Predicted versus experimental data for Boundary Condition 2-1, 1st layer thermocouples 1 and 9.

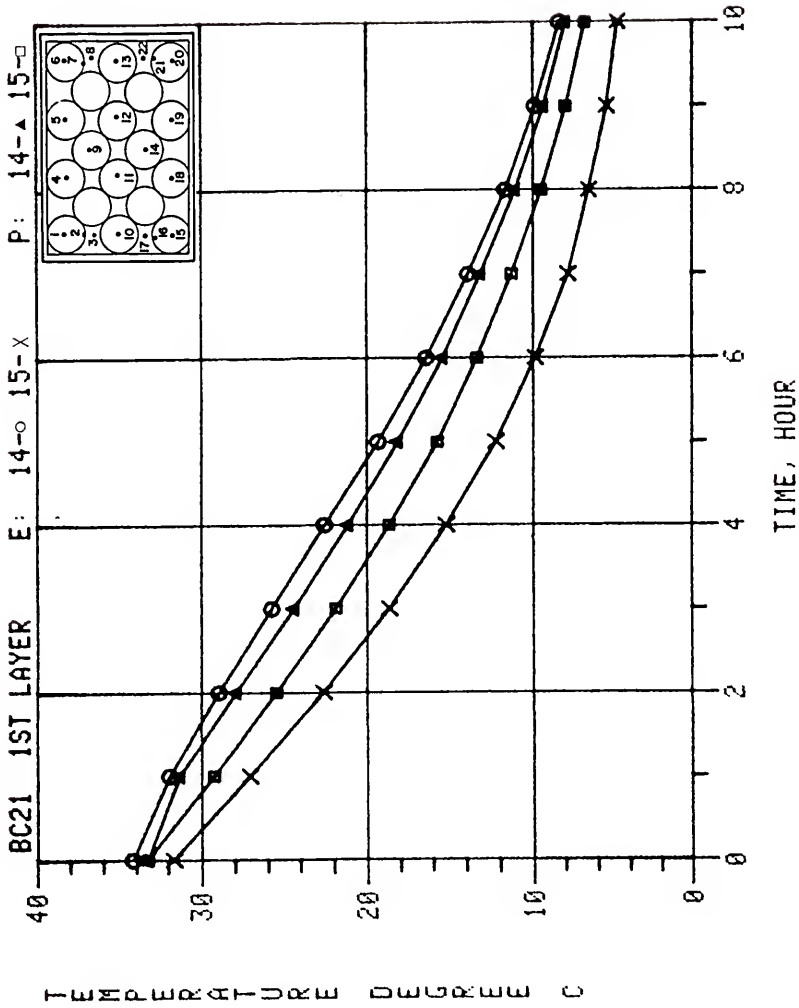


Figure G-12. Predicted versus experimental data for Boundary Condition 2-1, 1st layer thermocouples 14 and 15.

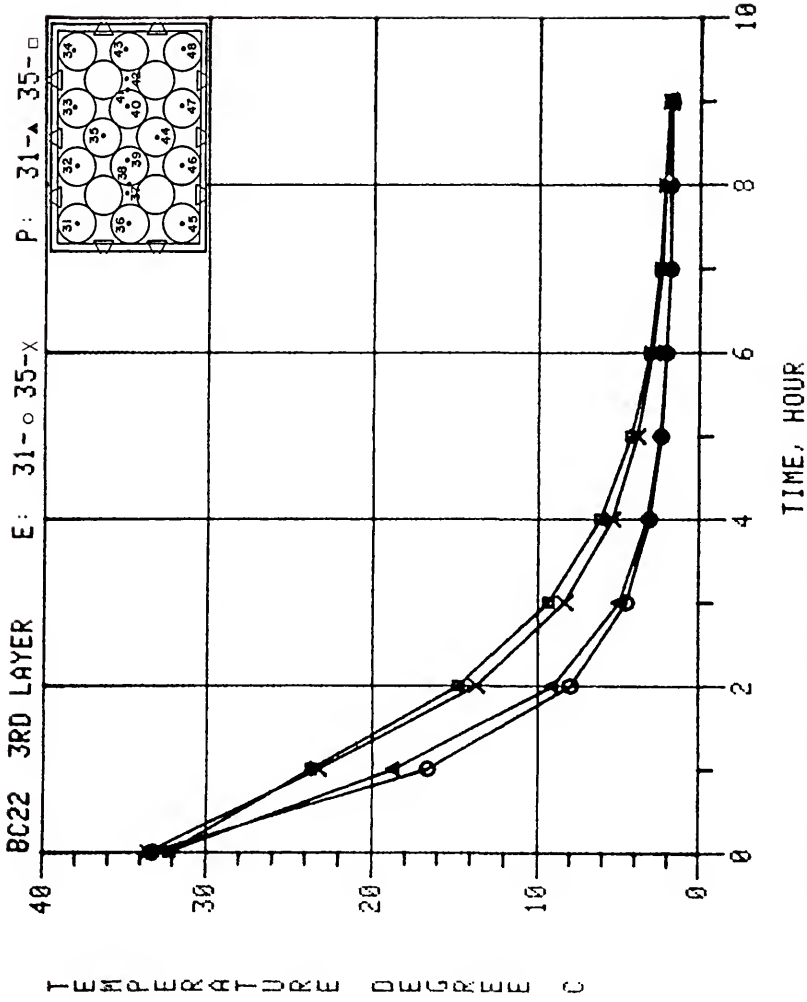


Figure G-13. Predicted versus experimental data for Boundary Condition 2-2, 3rd layer thermocouples 31 and 35.

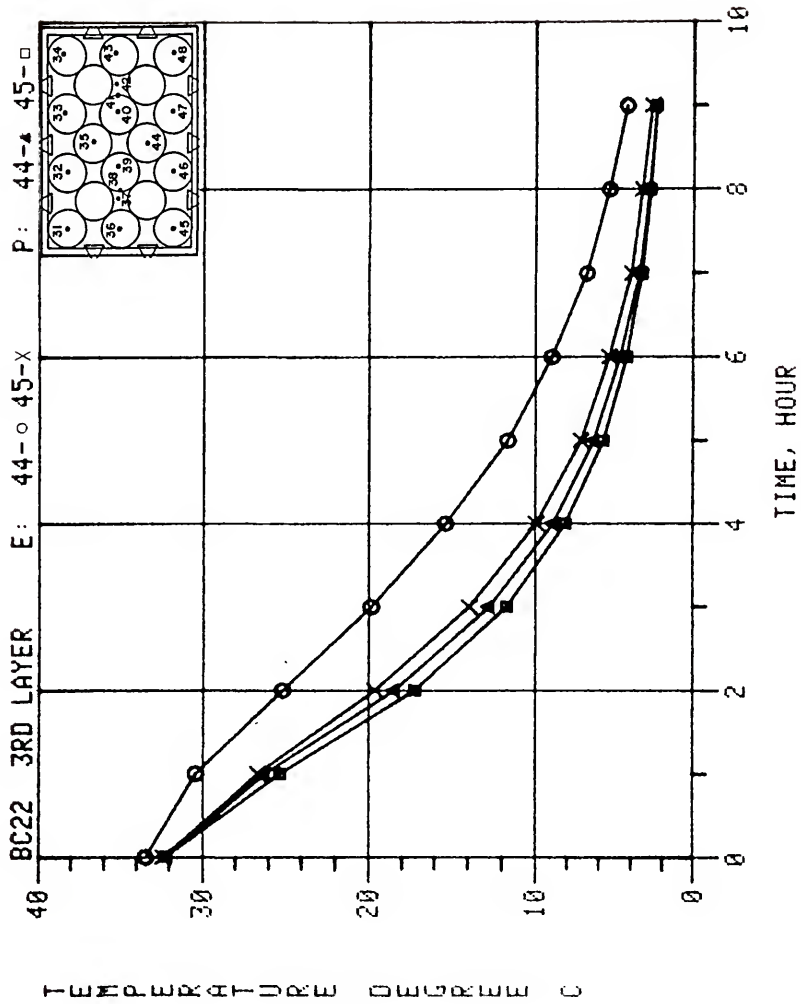


Figure G-14. Predicted versus experimental data for Boundary Condition 2-2, 3rd layer thermocouples 44 and 45.

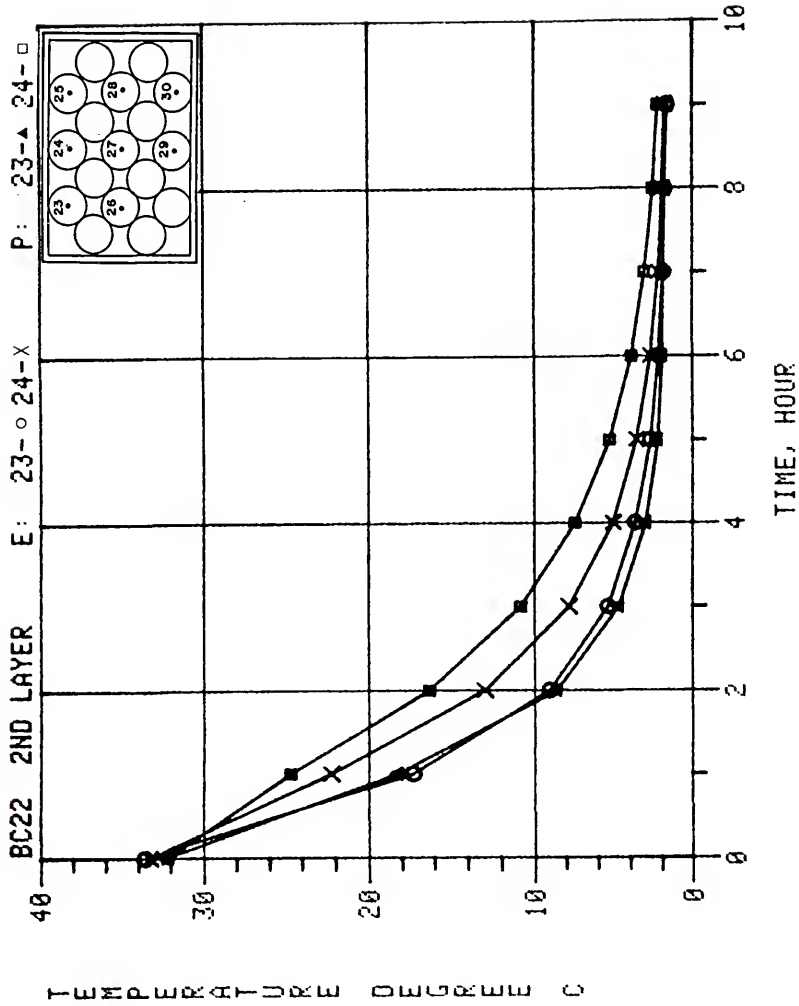


Figure G-15. Predicted versus experimental data for Boundary Condition 2-2, 2nd layer thermocouples 23 and 24.

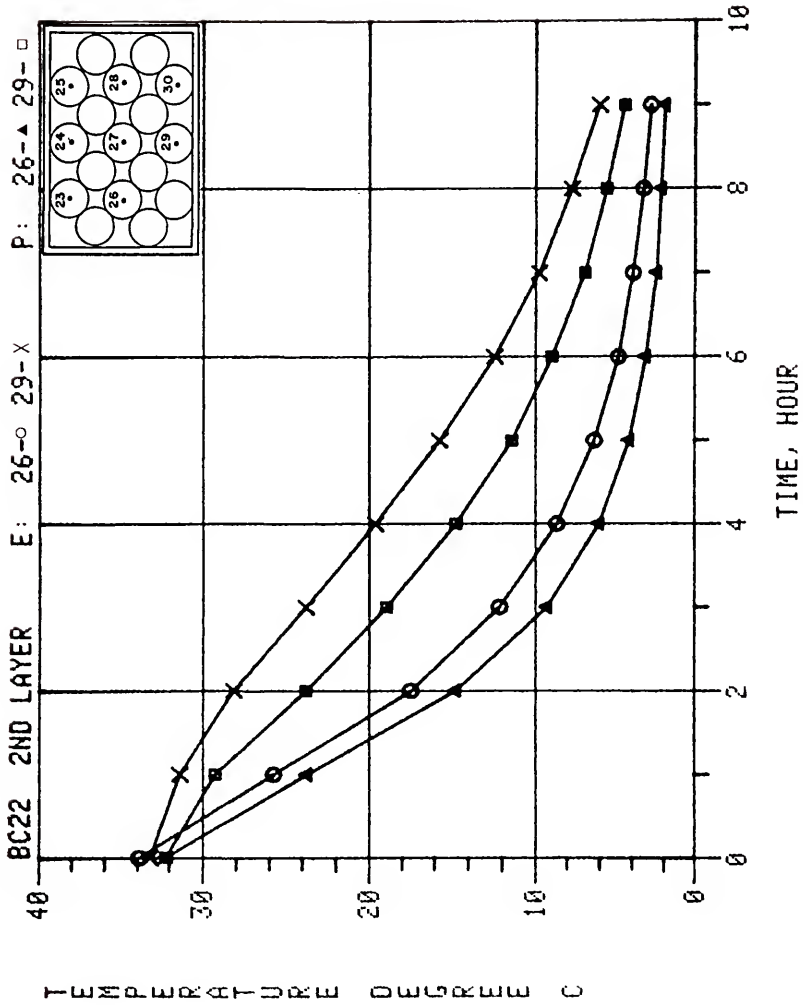


Figure G-16. Predicted versus experimental data for Boundary Condition 2-2, 2nd layer thermocouples 26 and 29.

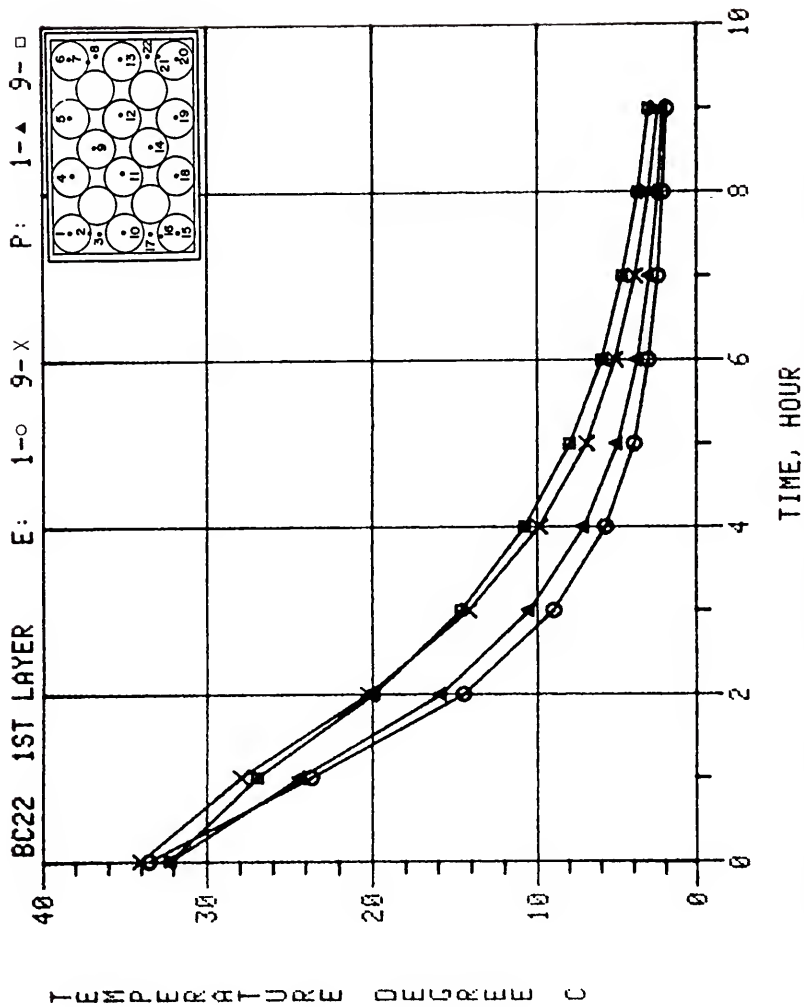


Figure G-17. Predicted versus experimental data for Boundary Condition 2-2, 1st layer thermocouples 1 and 9.

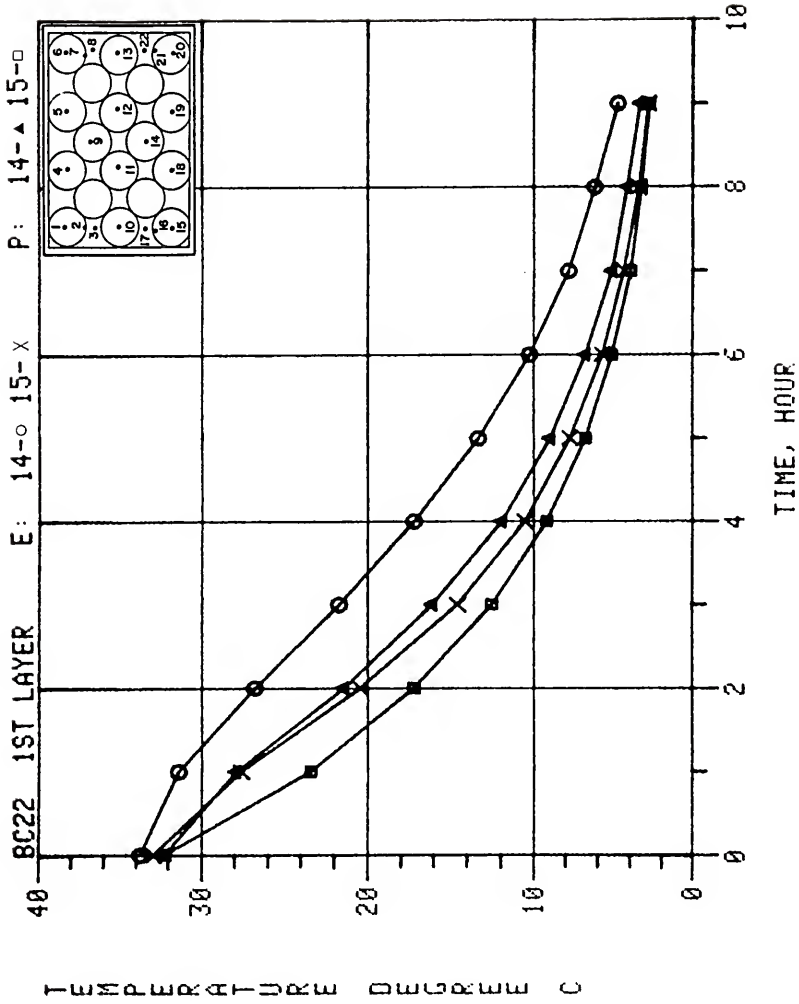


Figure G-18. Predicted versus experimental data for Boundary Condition 2-2, 1st layer thermocouples 14 and 15.

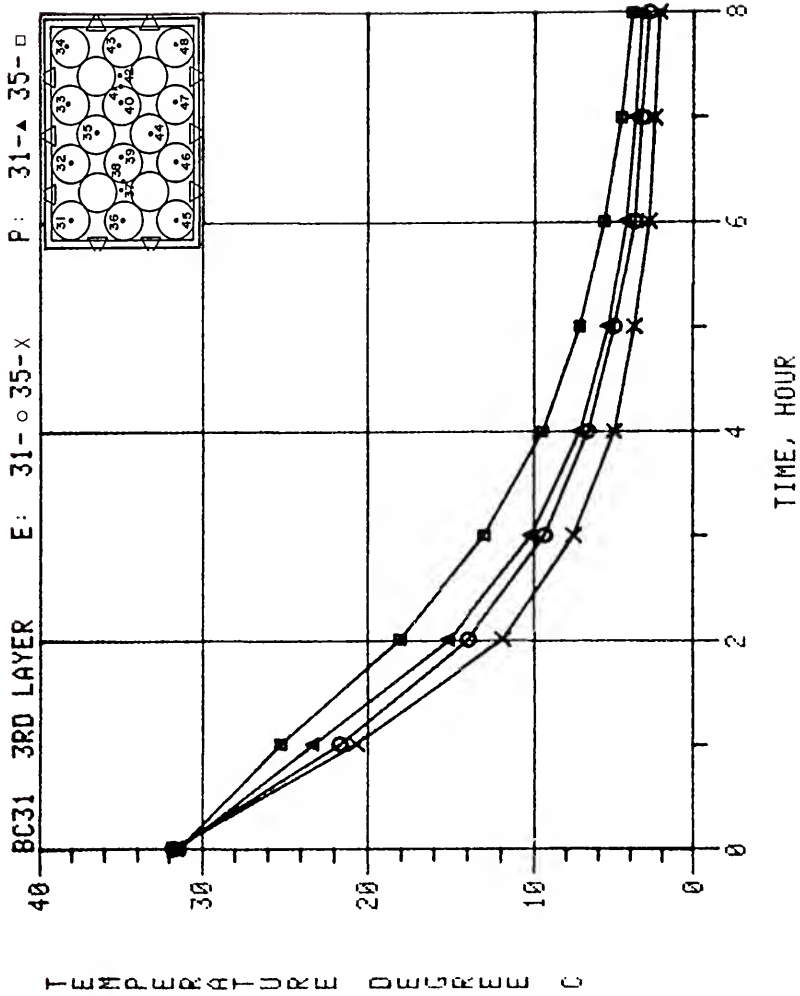


Figure G-19. Predicted versus experimental data for Boundary Condition 3-1, 3rd layer thermocouples 31 and 35.

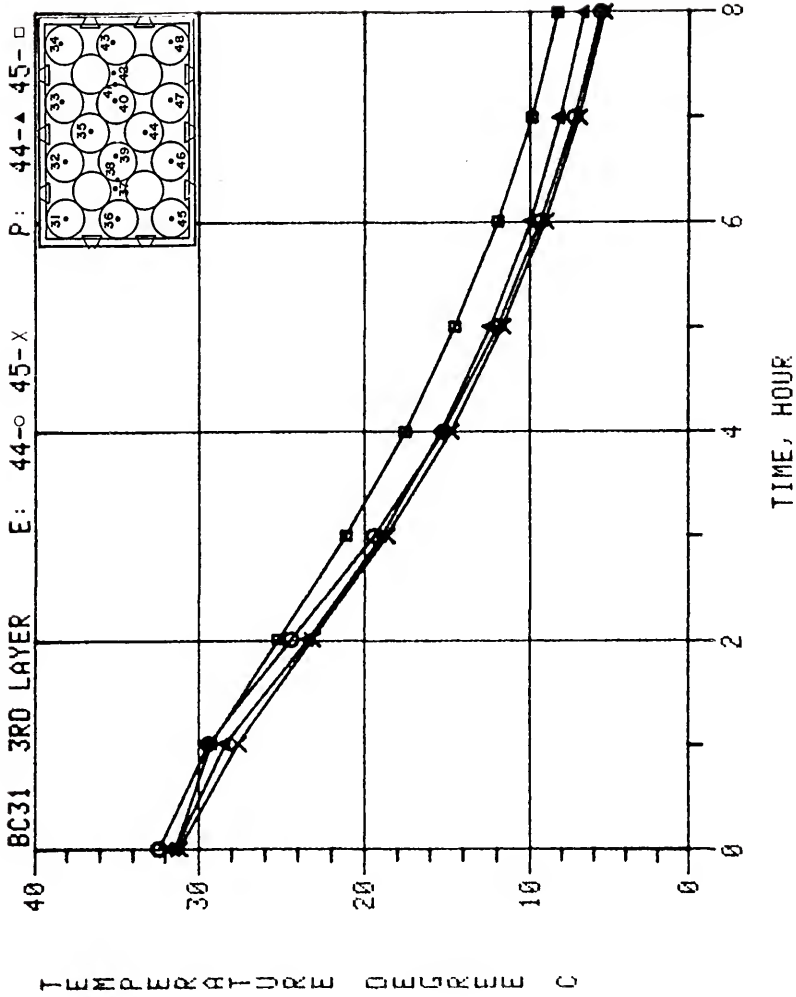


Figure G-20. Predicted versus experimental data for Boundary Condition 3-1, 3rd layer thermocouples 44 and 45.

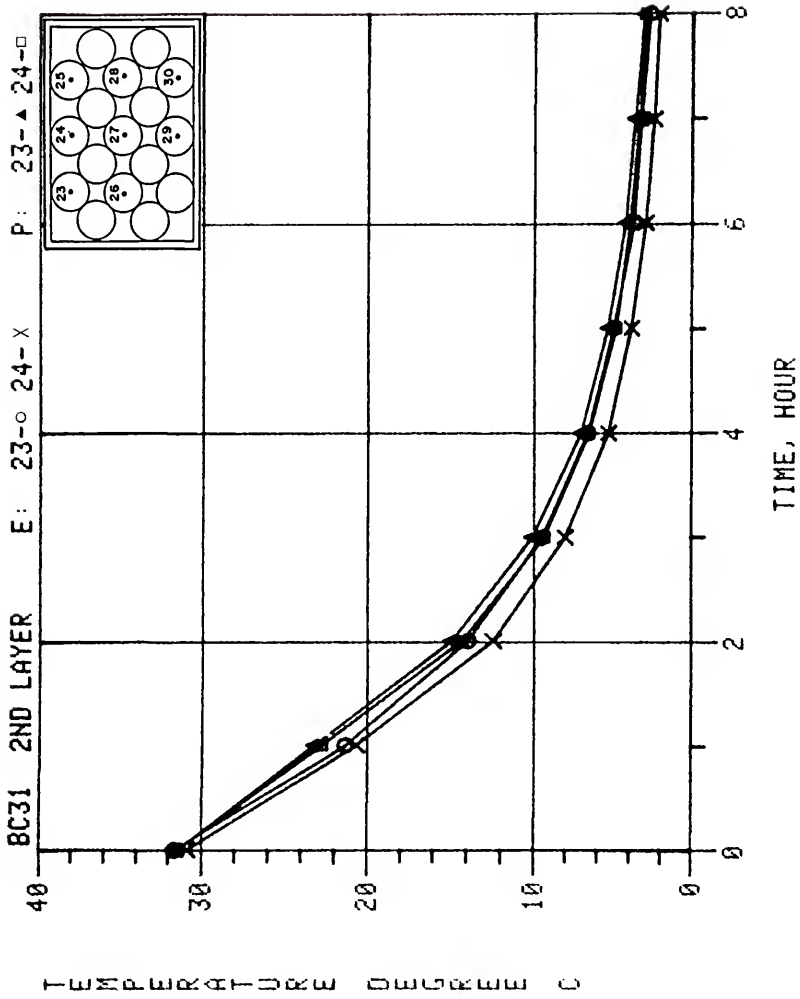


Figure G-21. Predicted versus experimental data for Boundary Condition 3-1, 2nd layer thermocouples 23 and 24.

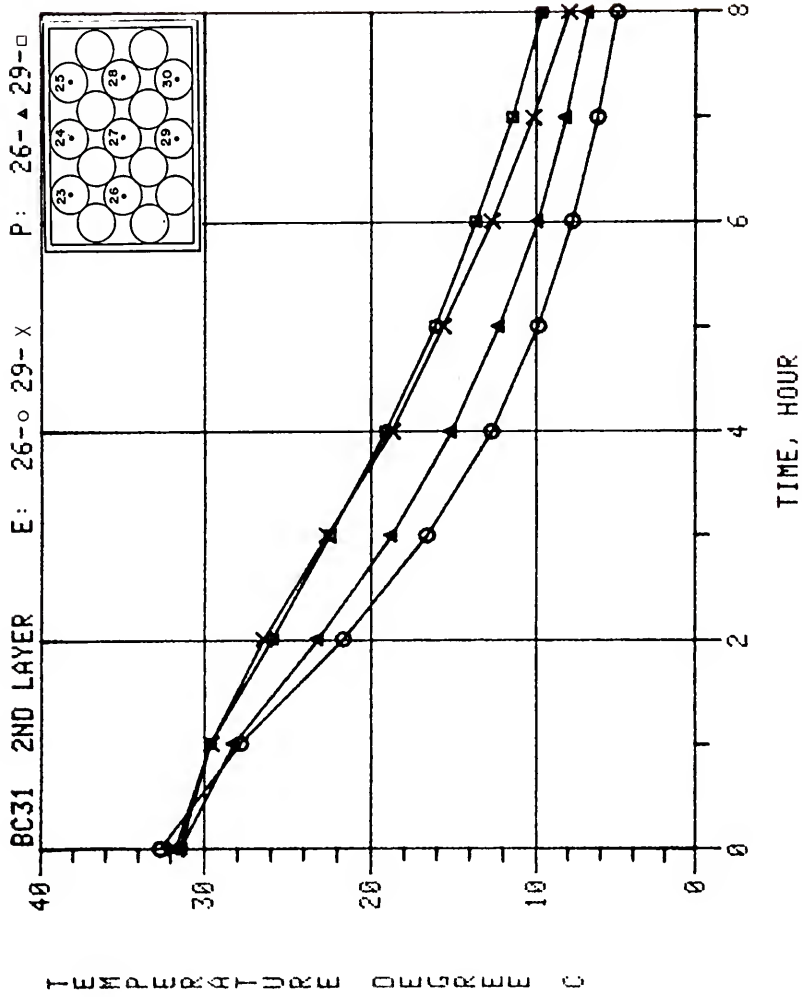


Figure G-22. Predicted versus experimental data for Boundary Condition 3-1, 2nd layer thermocouples 26 and 29.

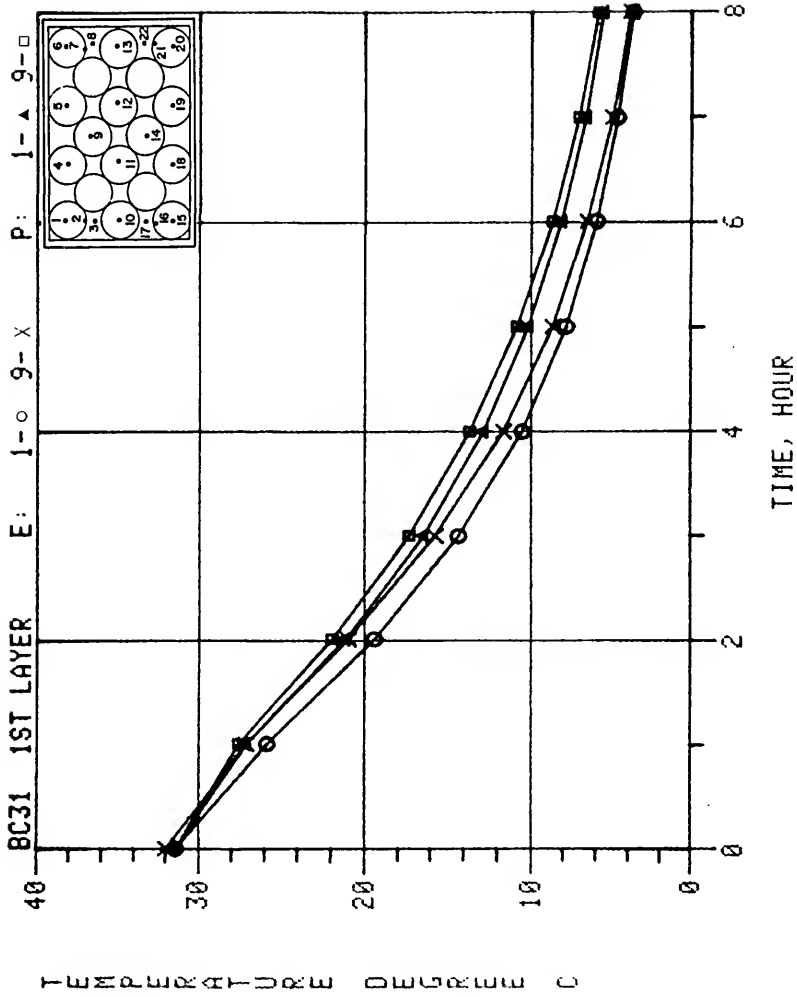


Figure G-23. Predicted versus experimental data for Boundary Condition 3-1, 1st layer thermocouples 1 and 9.

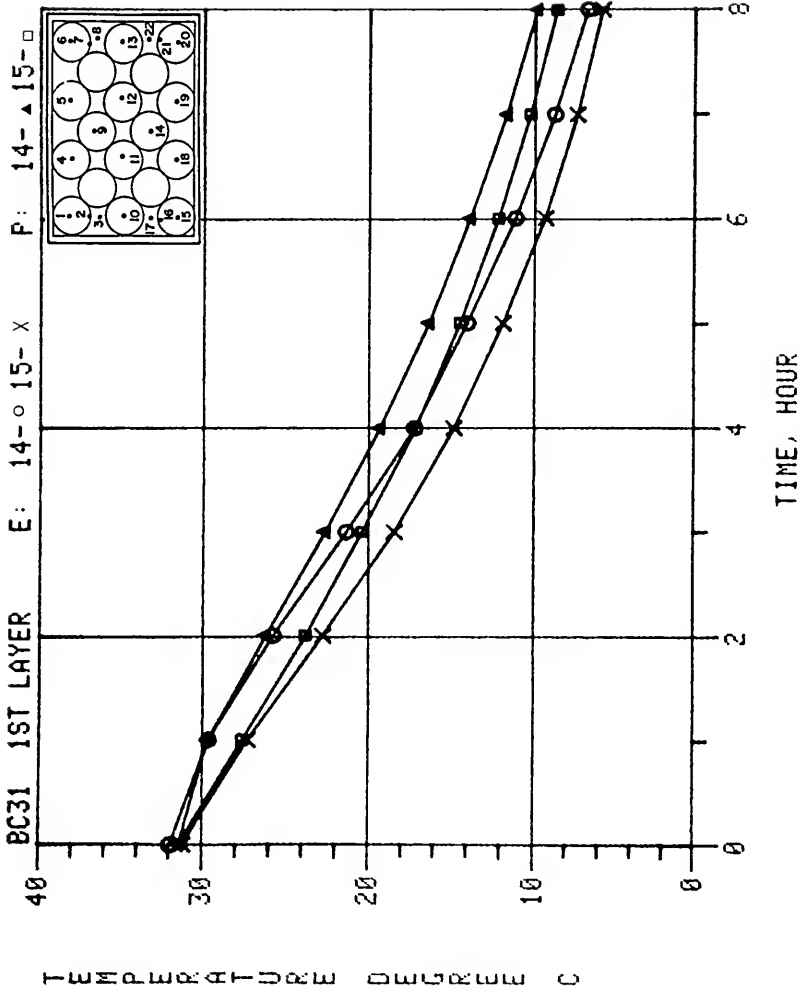


Figure G-24. Predicted versus experimental data for Boundary Condition 3-1, 1st layer thermocouples 14 and 15.

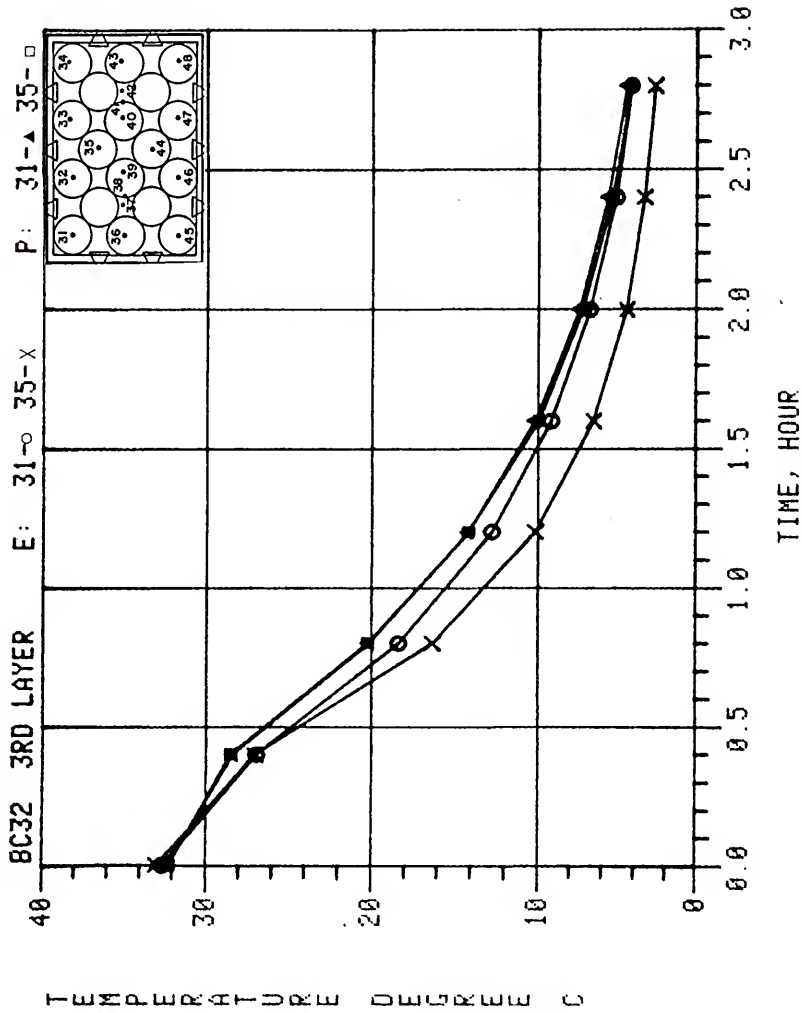


Figure G-25. Predicted versus experimental data for Boundary Condition 3-2, 3rd layer thermocouples 31 and 35.

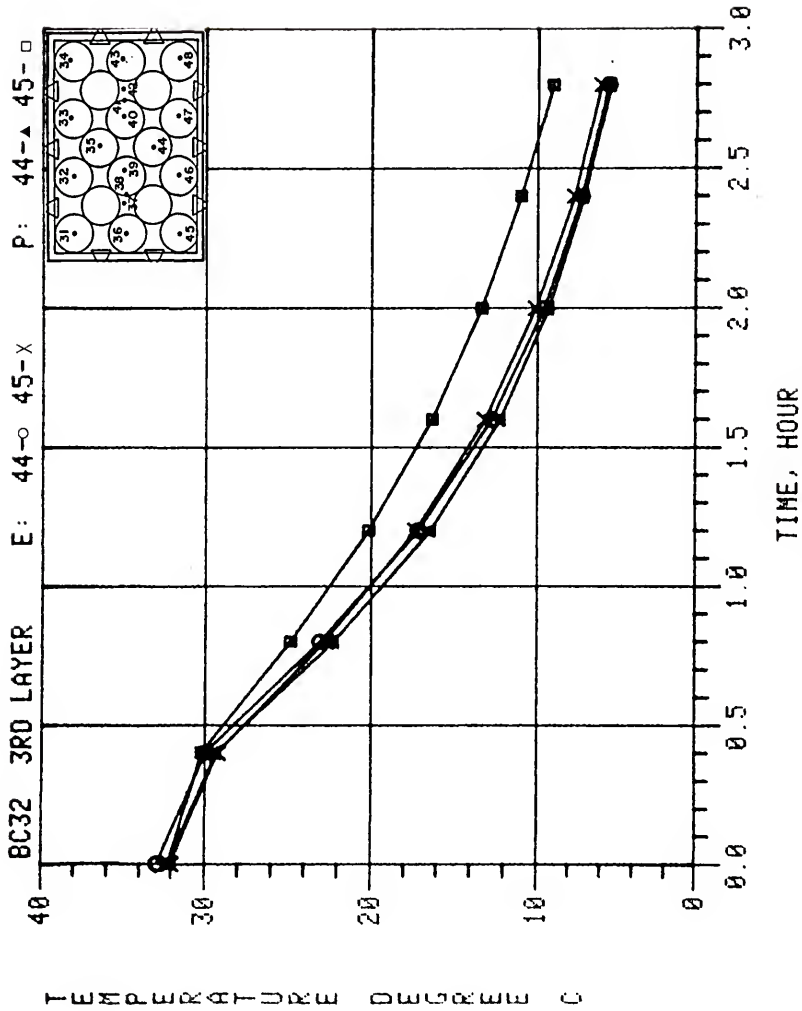


Figure G-26. Predicted versus experimental data for Boundary Condition 3-2, 3rd layer thermocouples 44 and 45.

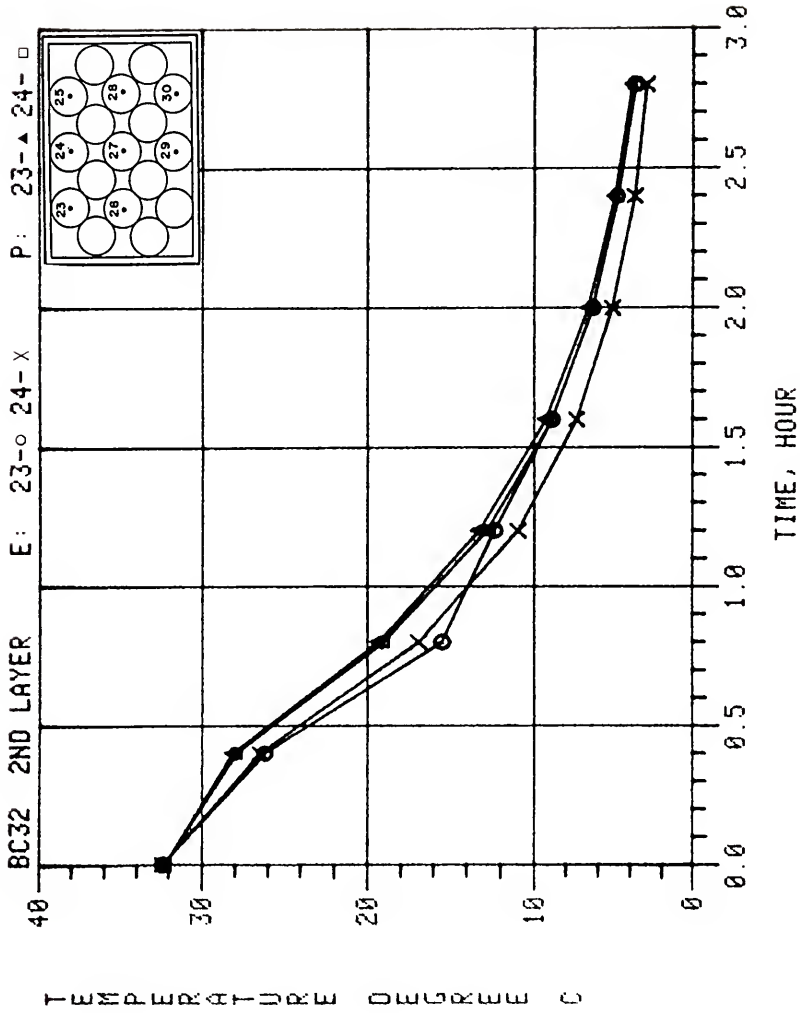


Figure G-27. Predicted versus experimental data for Boundary Condition 3-2, 2nd layer thermocouples 23 and 24.

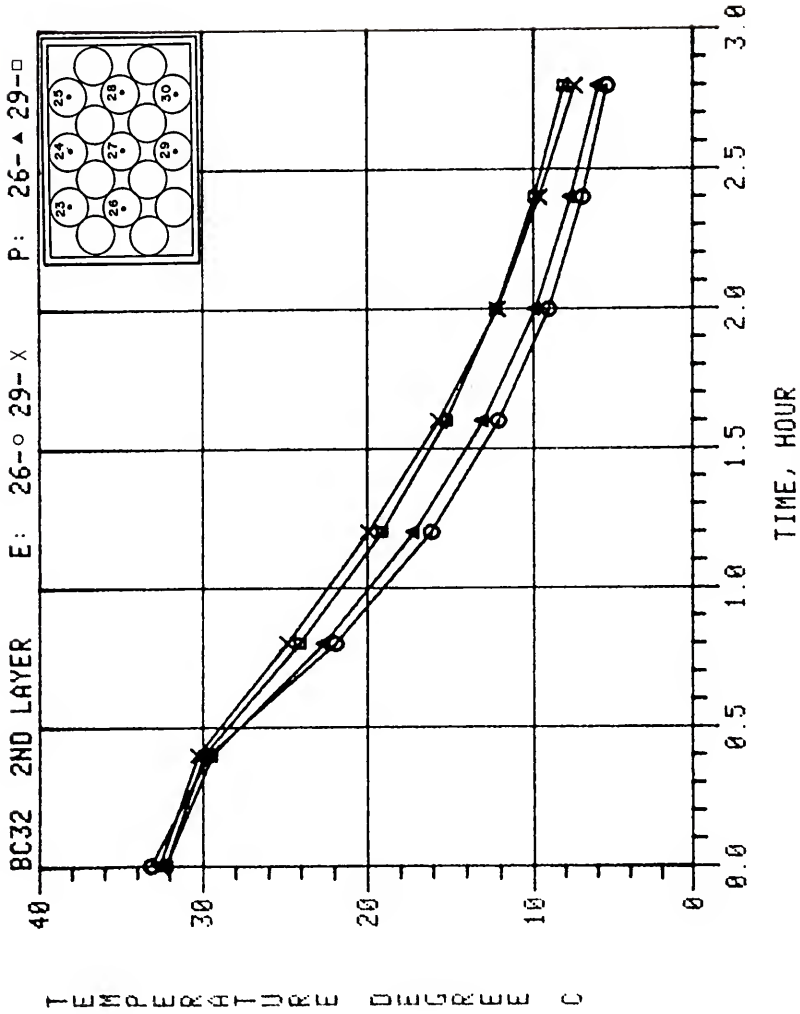


Figure G-28. Predicted versus experimental data for Boundary Condition 3-2, 2nd layer thermocouples 26 and 29.

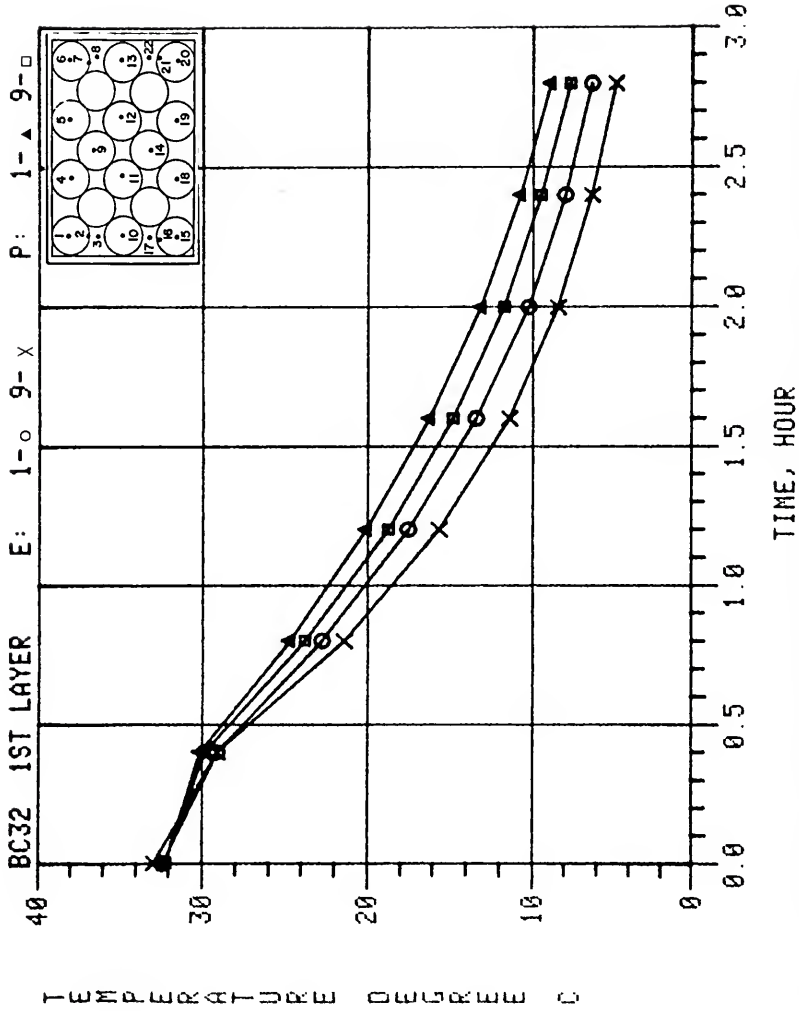


Figure G-29. Predicted versus experimental data for Boundary Condition 3-2, 1st layer thermocouples 1 and 9.

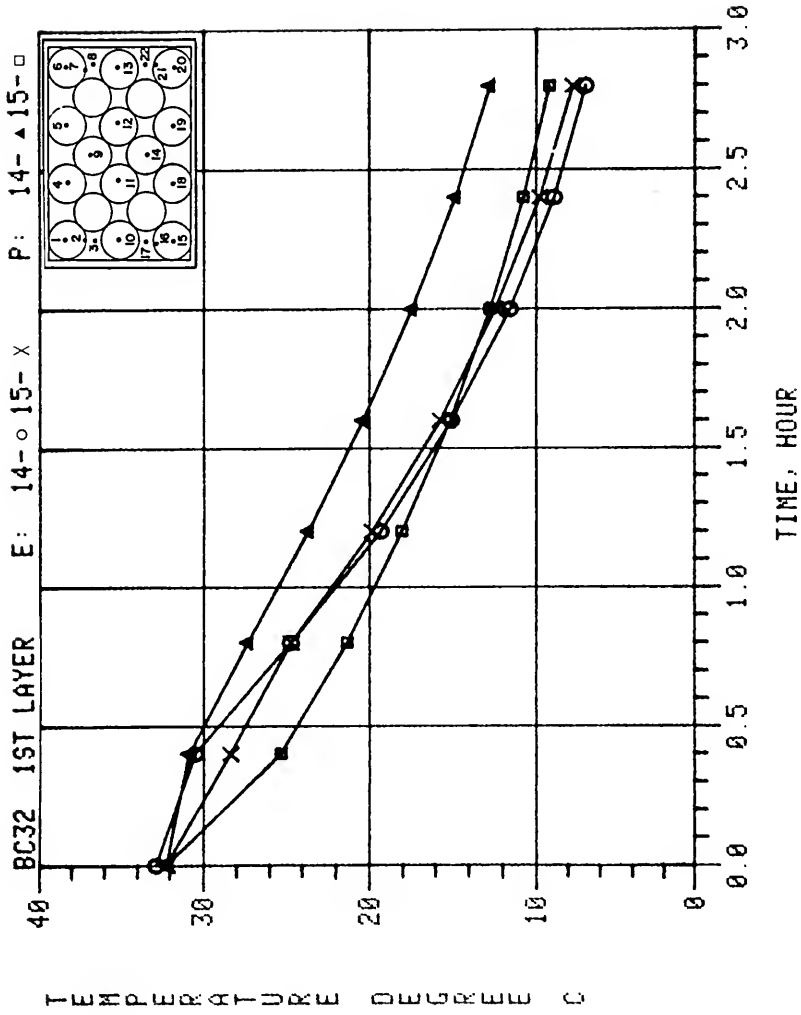


Figure G-30. Predicted versus experimental data for Boundary Condition 3-2, 1st layer thermocouples 14 and 15.

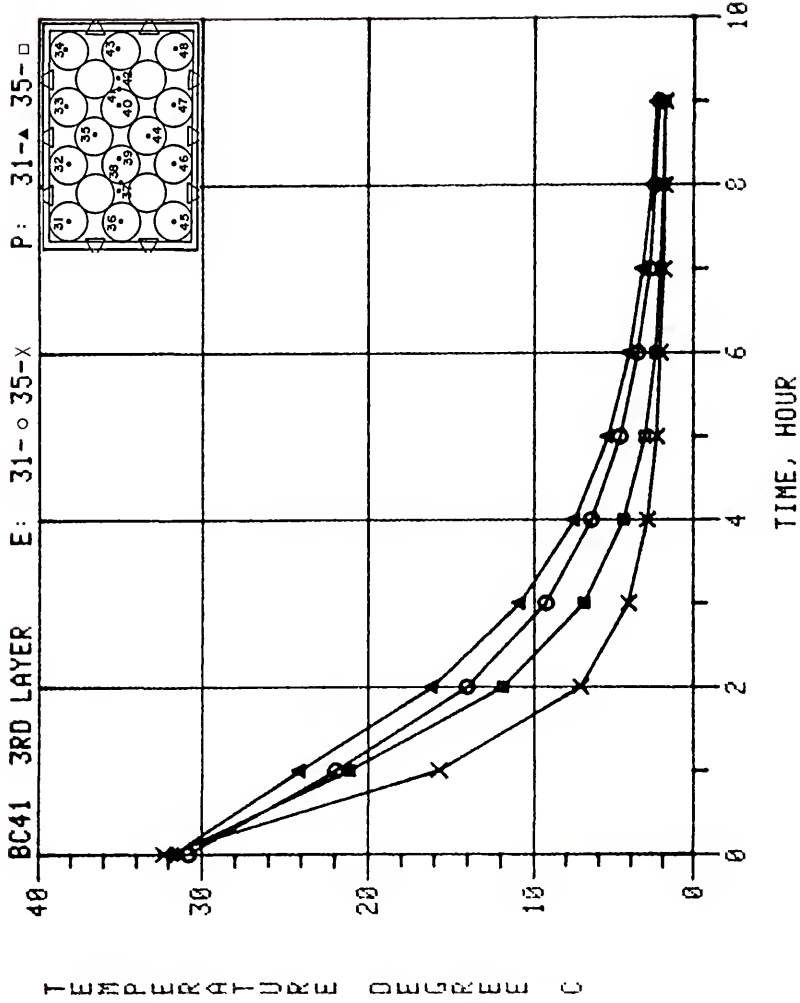


Figure G-31. Predicted versus experimental data for Boundary Condition 4-1, 3rd layer thermocouples 31 and 35.

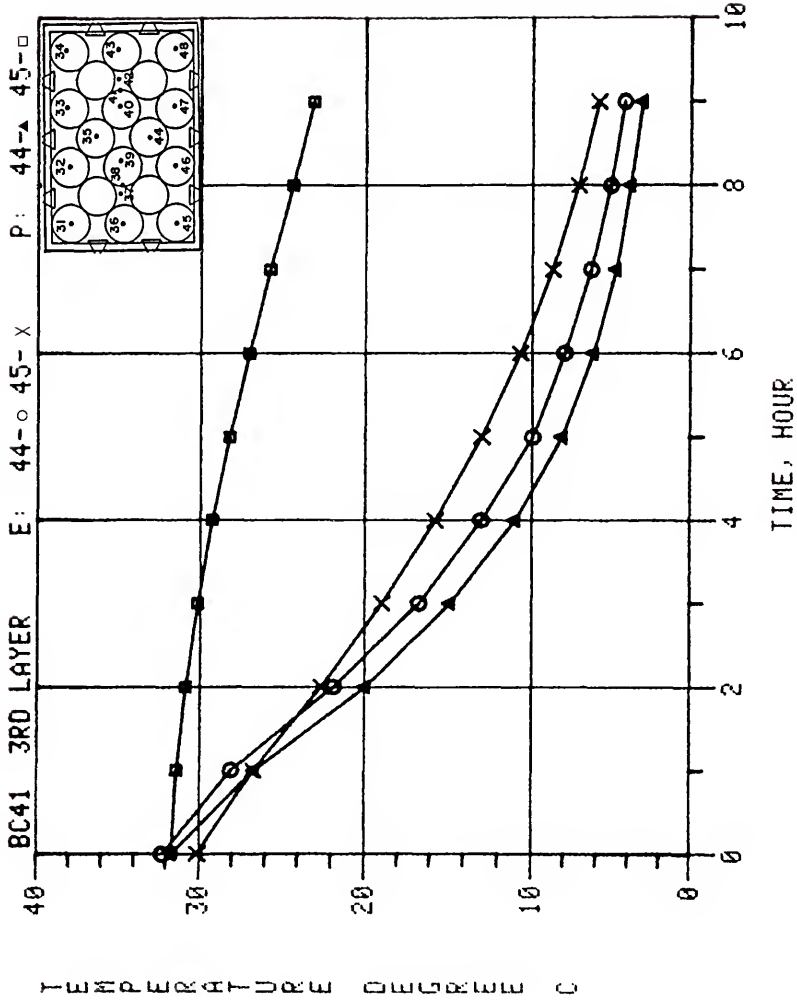


Figure G-32. Predicted versus experimental data for Boundary Condition 4-1, 3rd layer thermocouples 44 and 45.

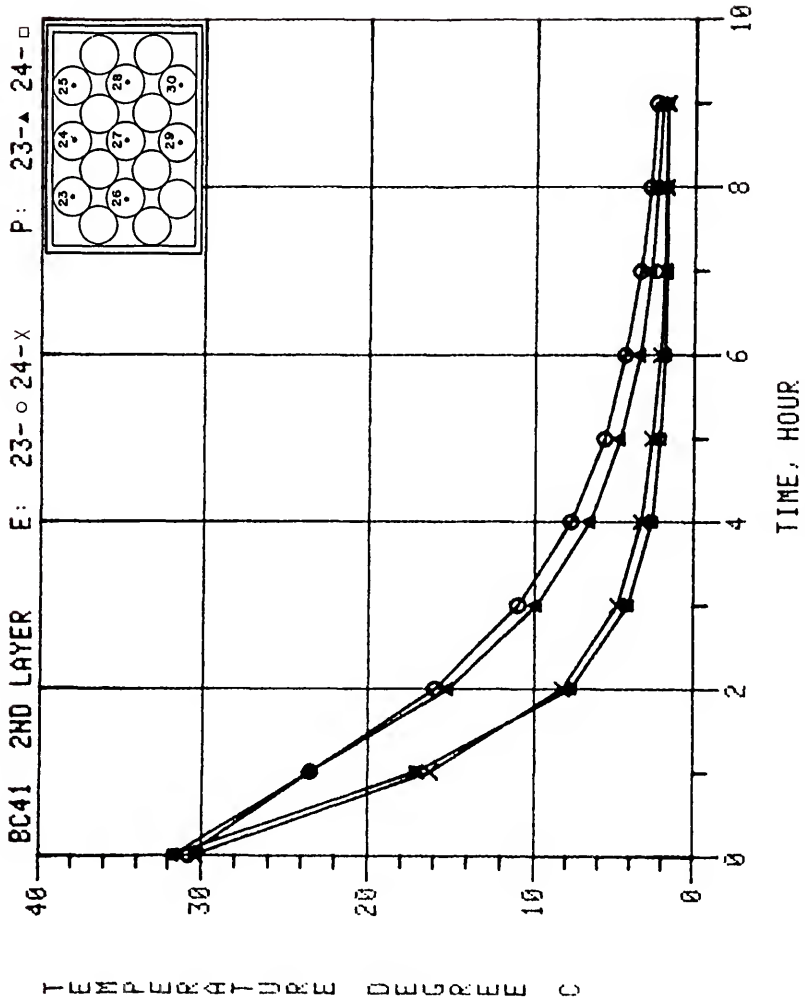


Figure G-33. Predicted versus experimental data for Boundary Condition 4-1, 2nd layer thermocouples 23 and 24.

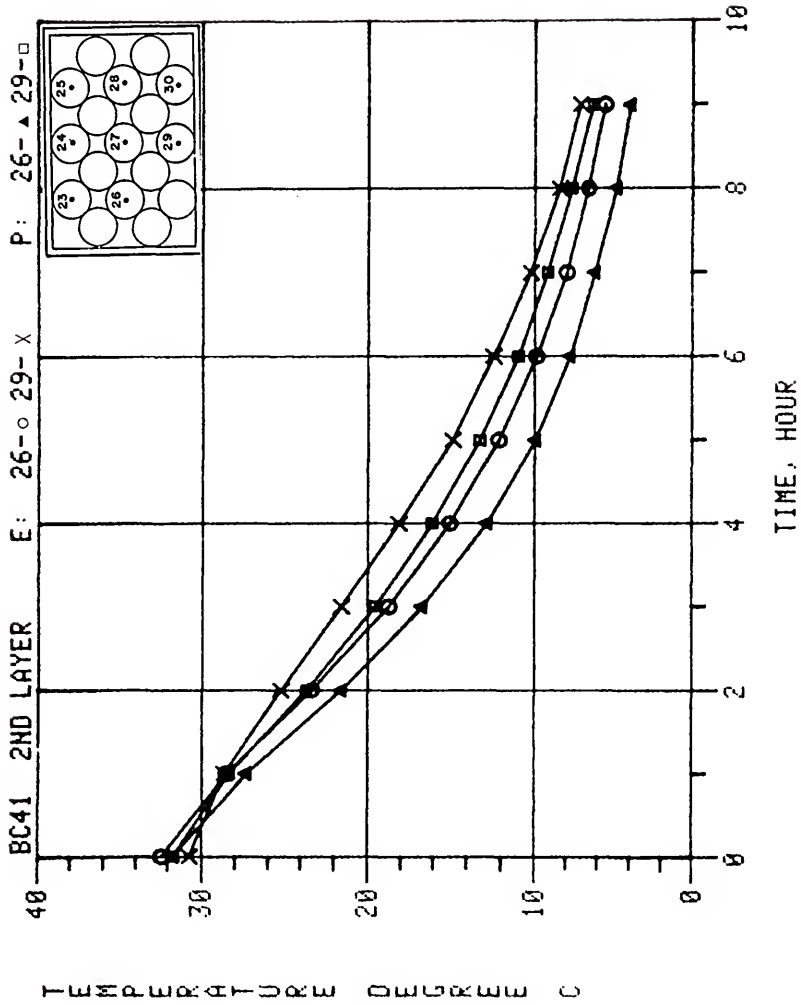


Figure G-34. Predicted versus experimental data for Boundary Condition 4-1, 2nd layer thermocouples 26 and 29.

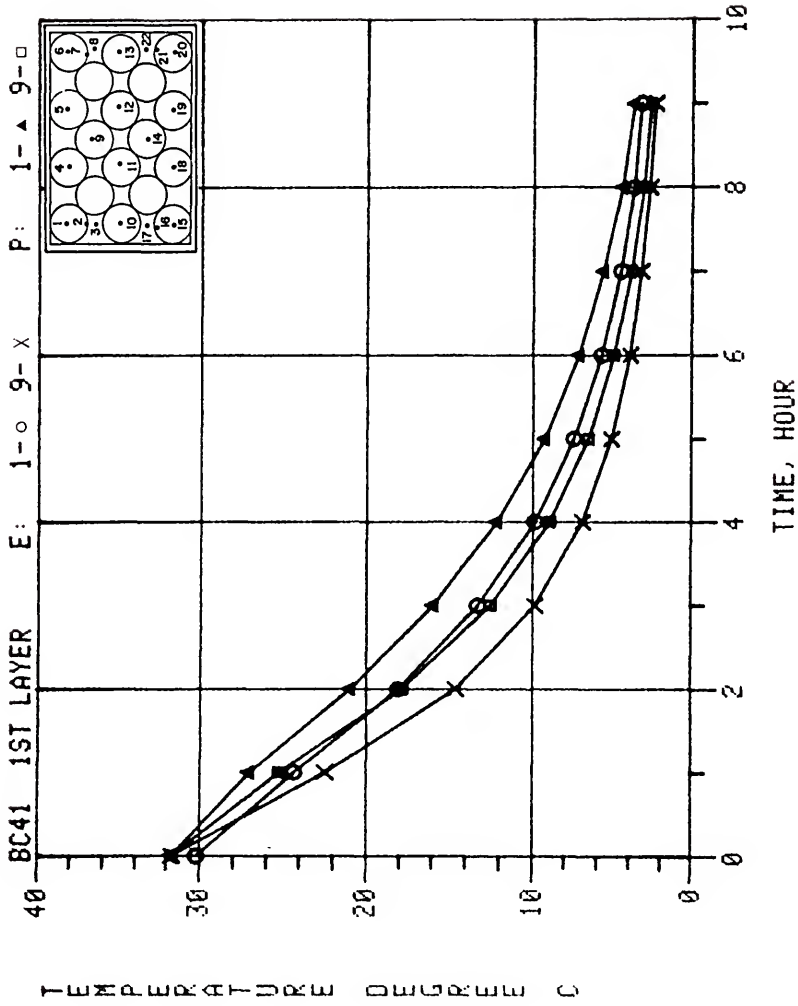


Figure G-35. Predicted versus experimental data for Boundary Condition 4-1, 1st layer thermocouples 1 and 9.

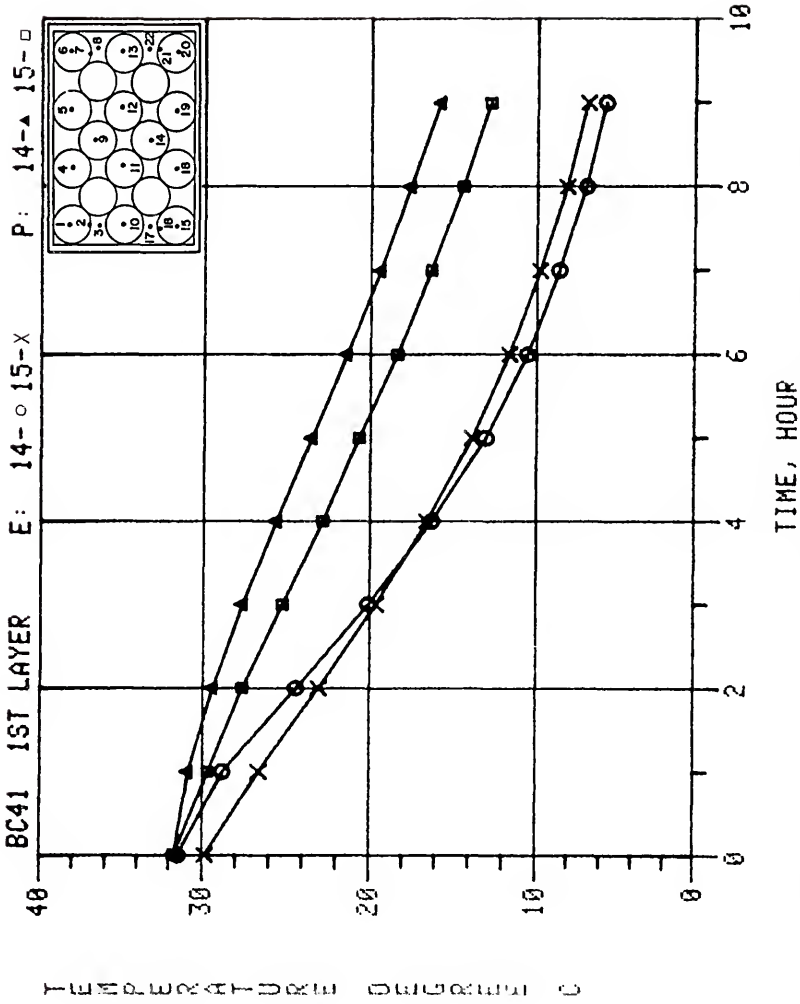


Figure G-36. Predicted versus experimental data for Boundary Condition 4-1, 1st layer thermocouples 14 and 15.

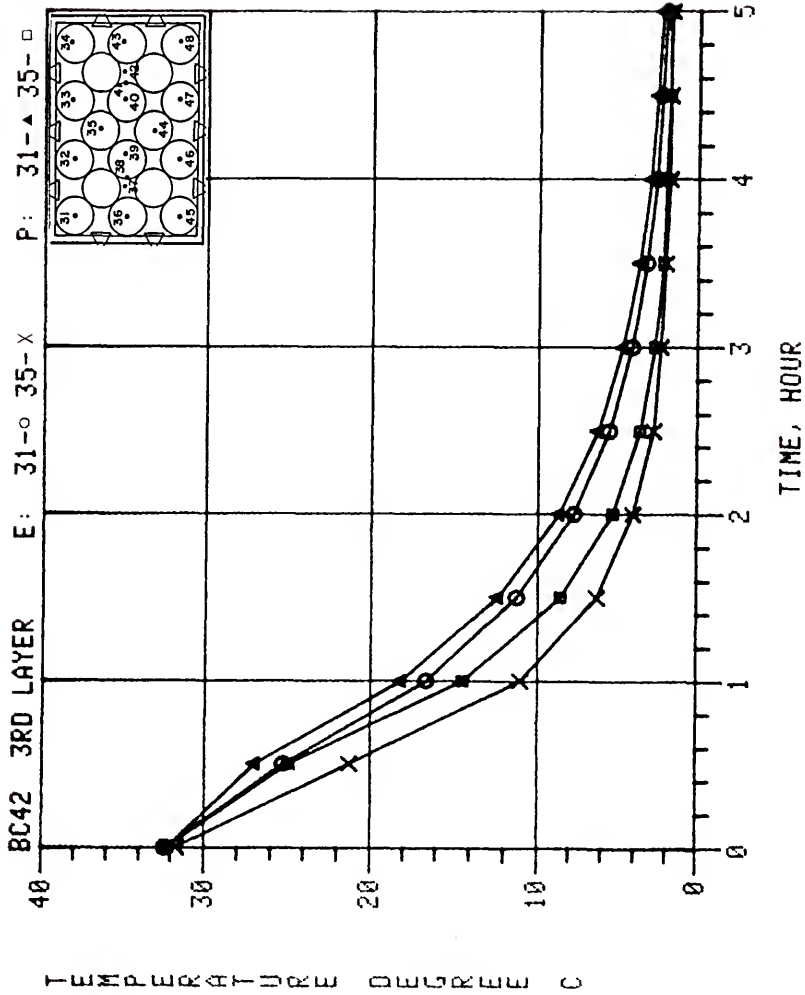


Figure G-37. Predicted versus experimental data for Boundary Condition 4-2, 3rd layer thermocouples 31 and 35.

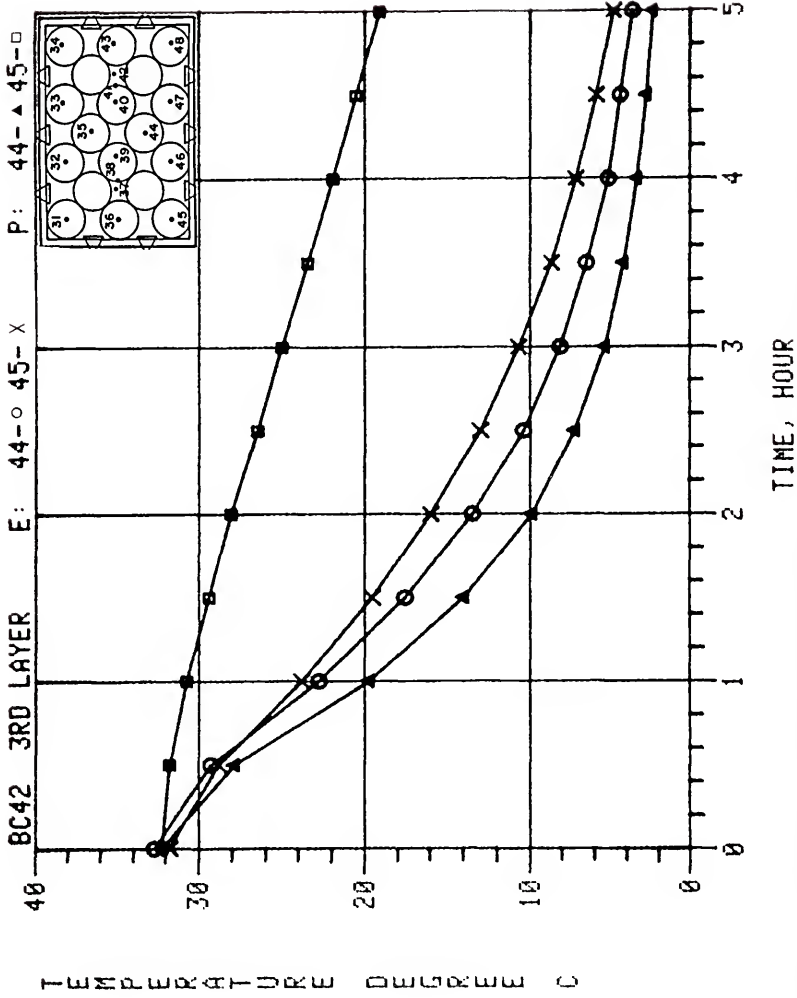


Figure G-38. Predicted versus experimental data for Boundary Condition 4-2, 3rd layer thermocouples 44 and 45.

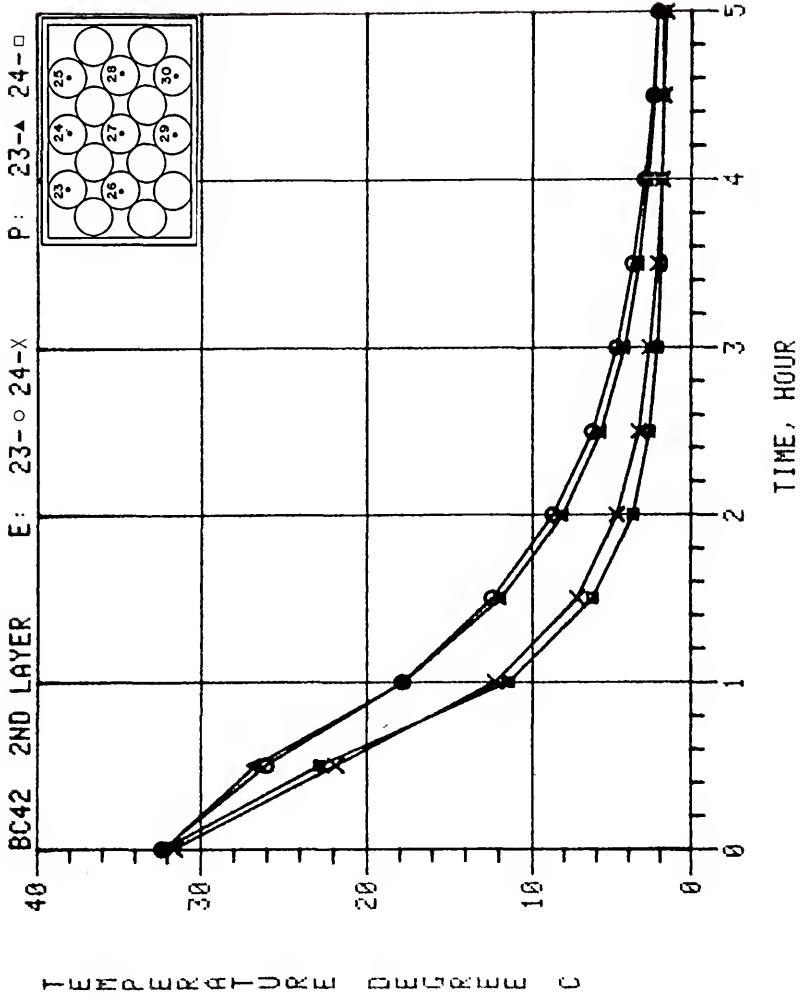


Figure G-39. Predicted versus experimental data for Boundary Condition 4-2, 2nd layer thermocouples 23 and 24.

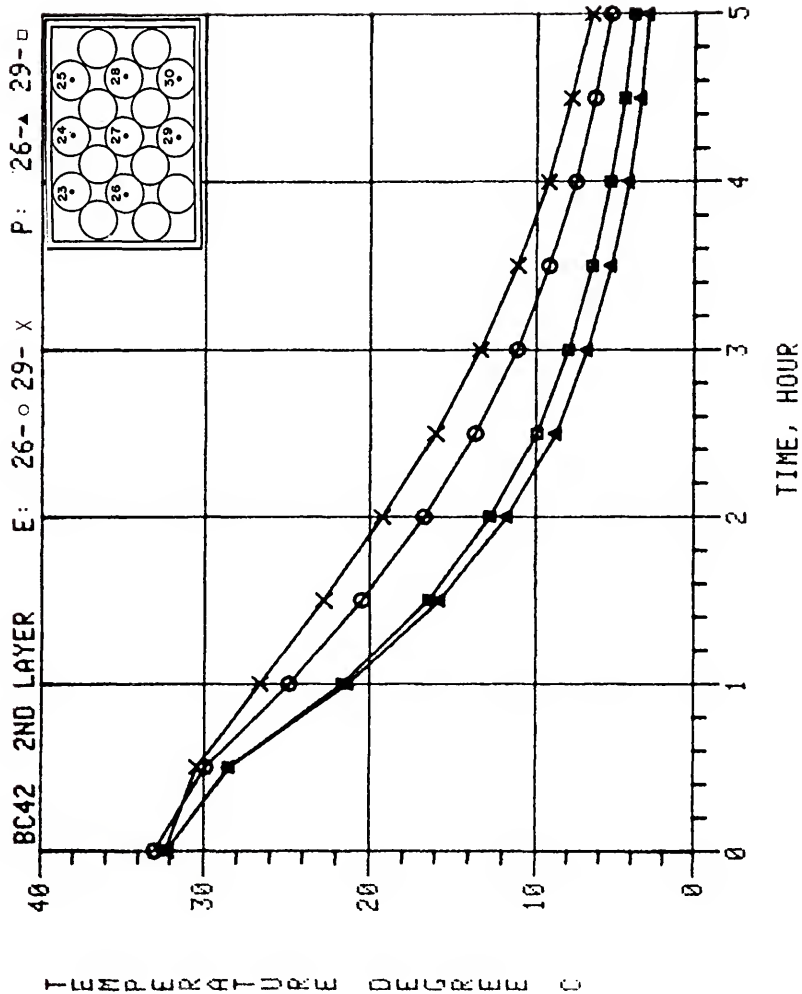


Figure G-40. Predicted versus experimental data for Boundary Condition 4-2, 2nd layer thermocouples 26 and 29.

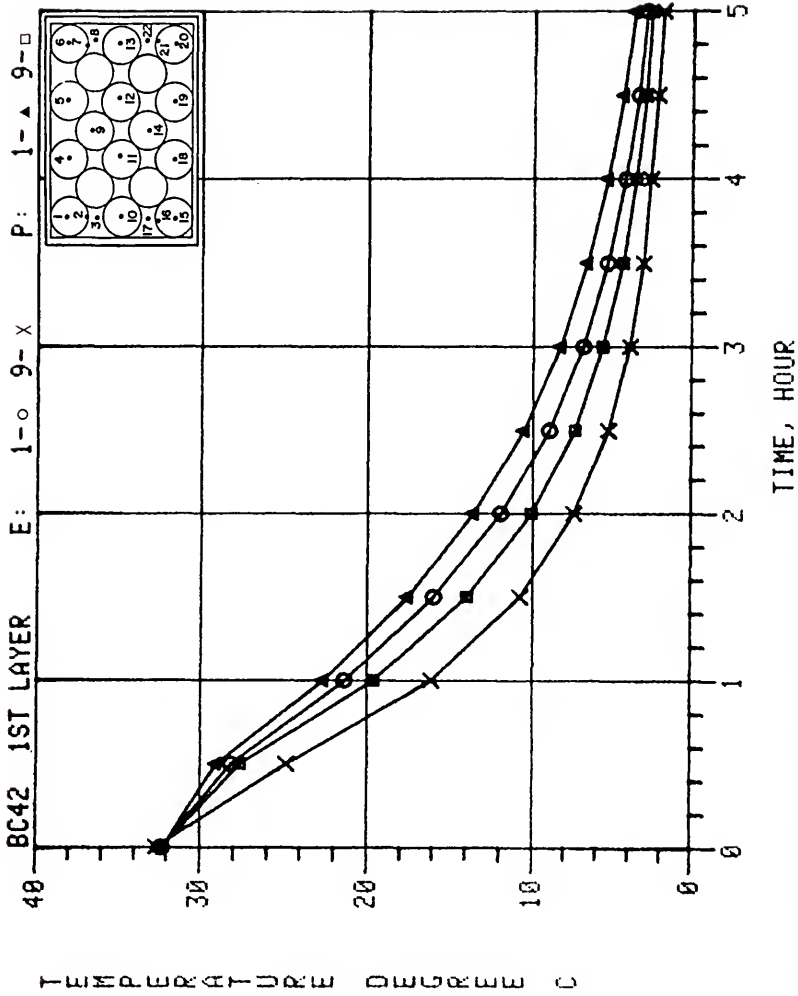


Figure G-41. Predicted versus experimental data for Boundary Condition 4-2, 1st layer thermocouples 1 and 9.

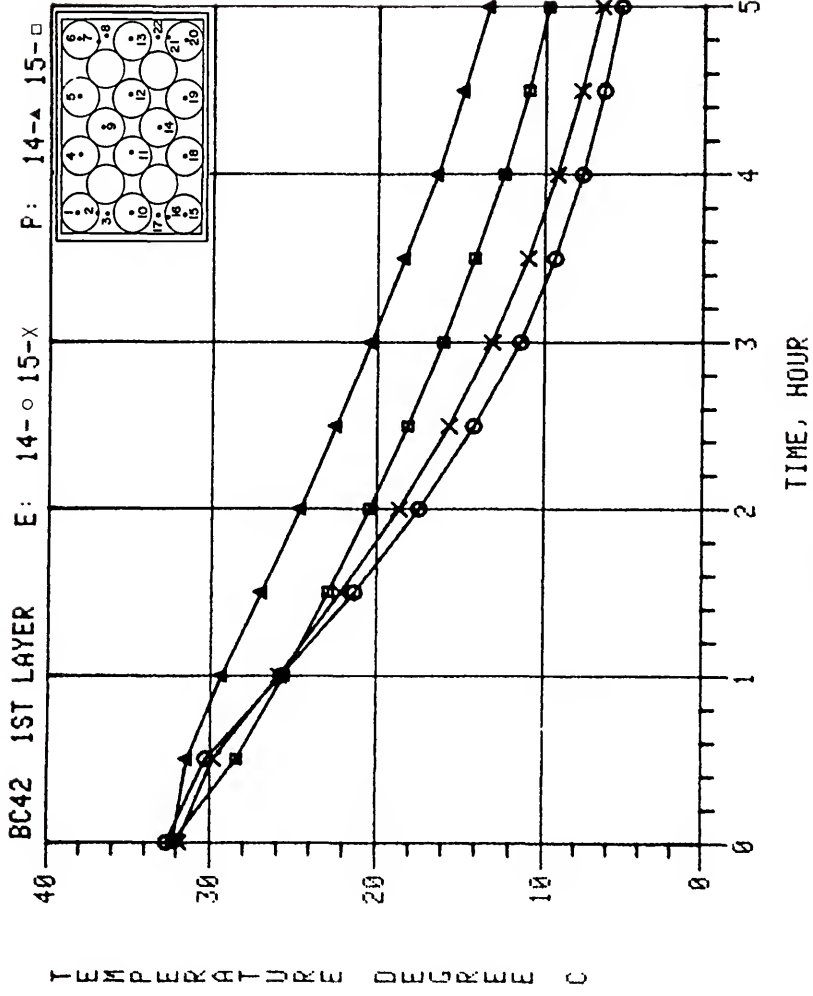


Figure G-42. Predicted versus experimental data for Boundary Condition 4-2, 1st layer thermocouples 14 and 15.

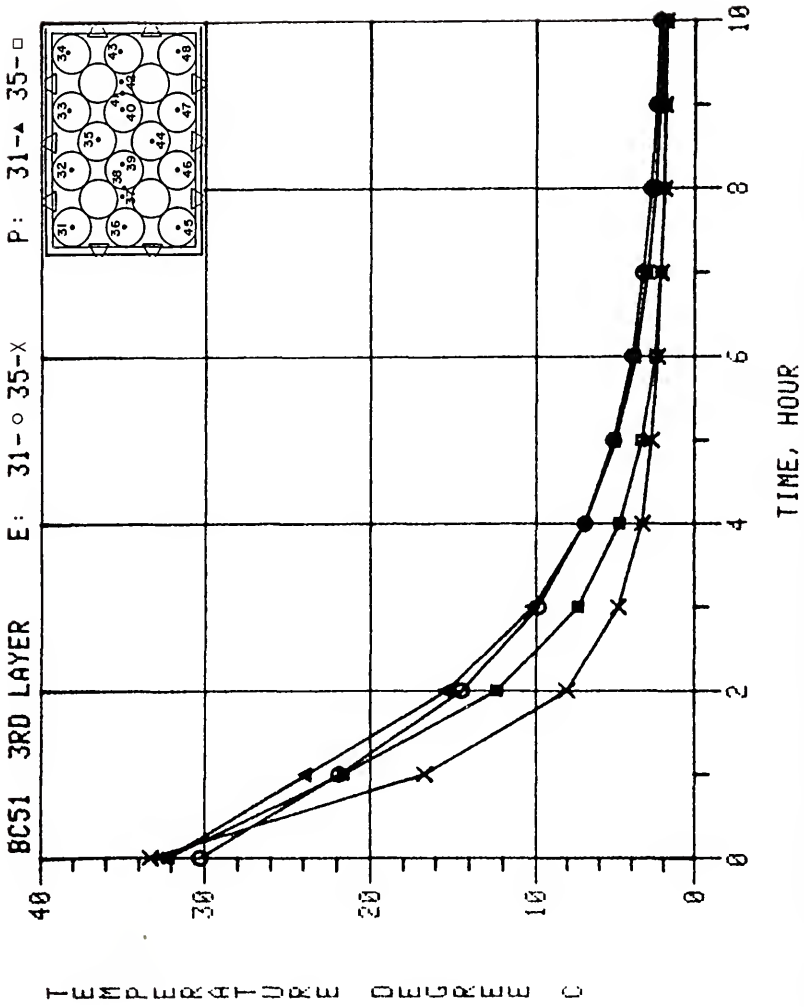


Figure G-43. Predicted versus experimental data for Boundary Condition 5-1, 3rd layer thermocouples 31 and 35.

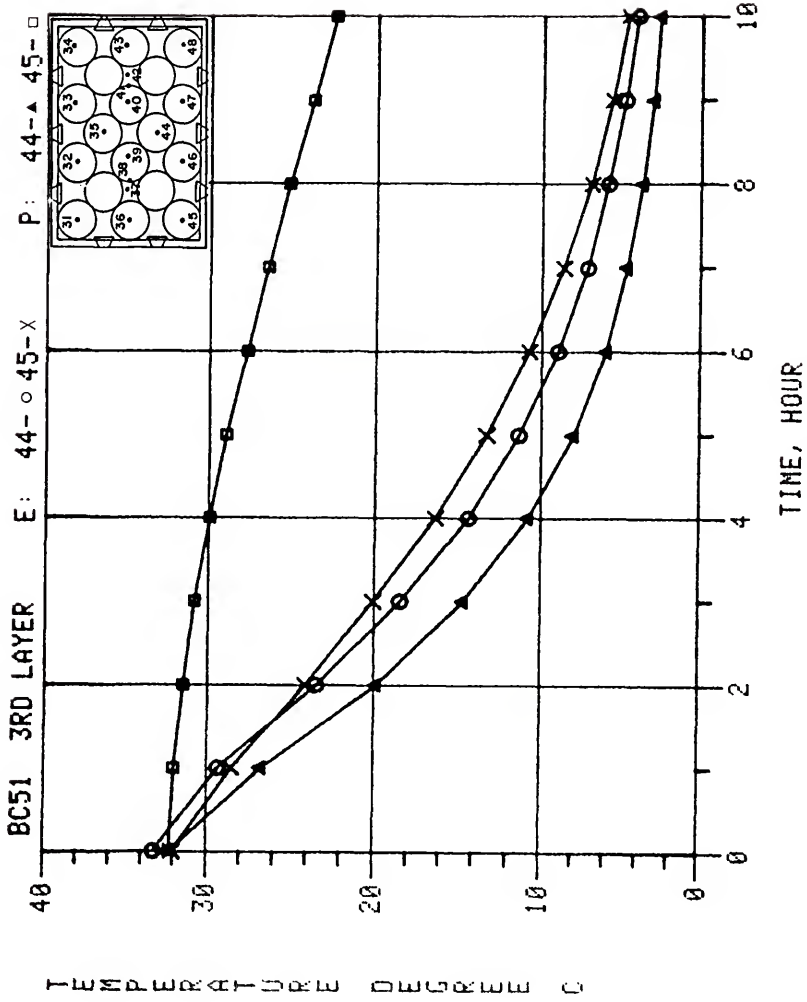


Figure G-44. Predicted versus experimental data for Boundary Condition 5-1, 3rd layer thermocouples 44 and 45.

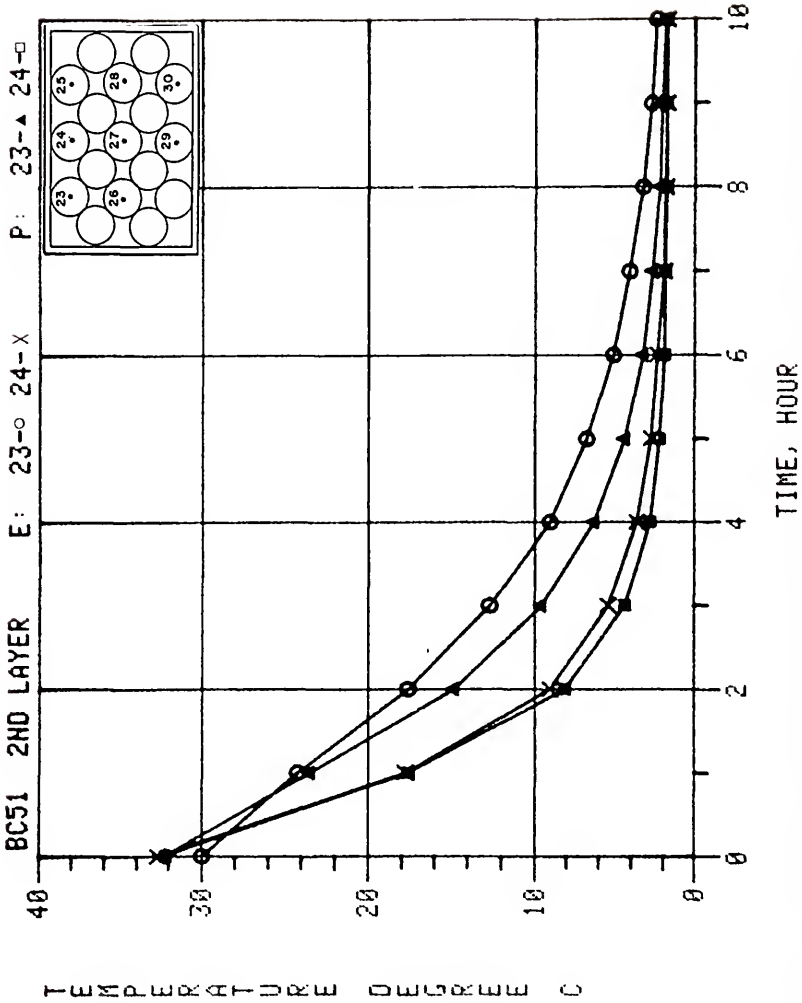


Figure G-45. Predicted versus experimental data for Boundary Condition 5-1, 2nd layer thermocouples 23 and 24.

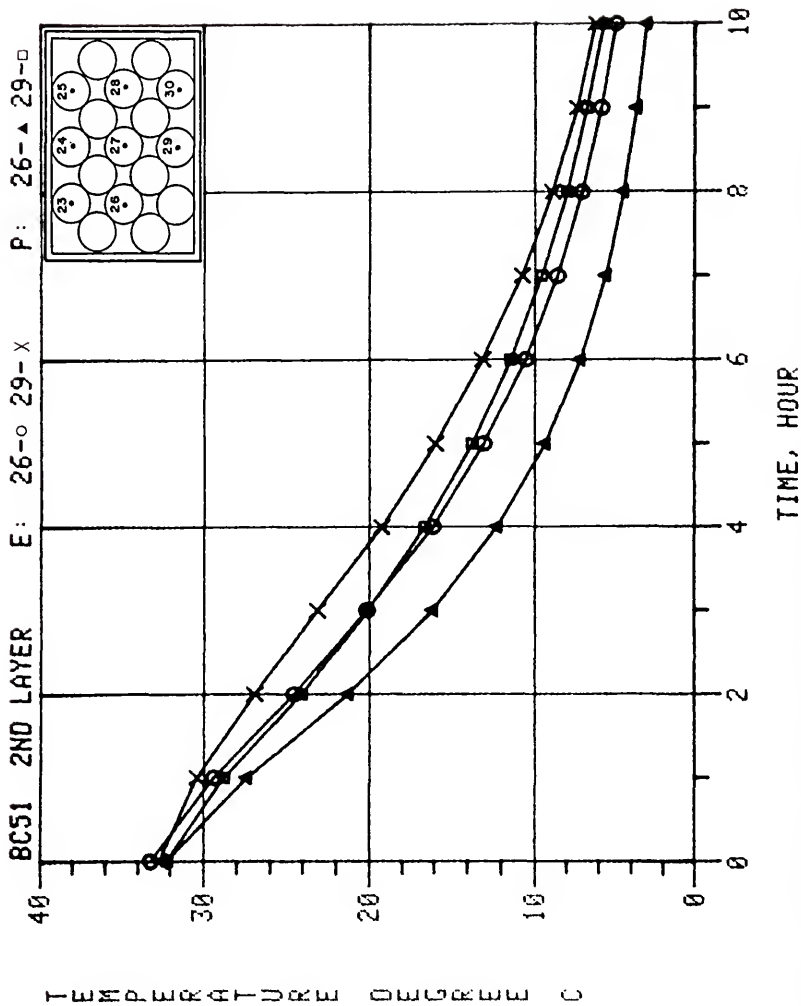


Figure G-46. Predicted versus experimental data for Boundary Condition 5-1, 2nd layer thermocouples 26 and 29.

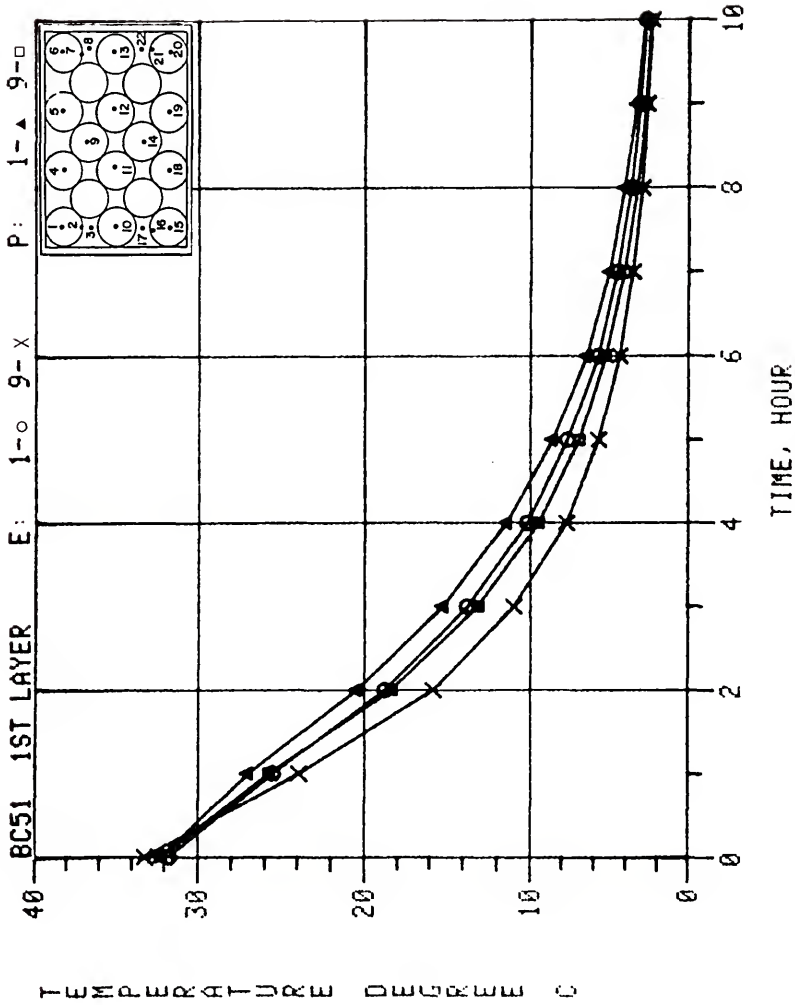


Figure G-47. Predicted versus experimental data for Boundary Condition 5-1, 1st layer thermocouples 1 and 9.

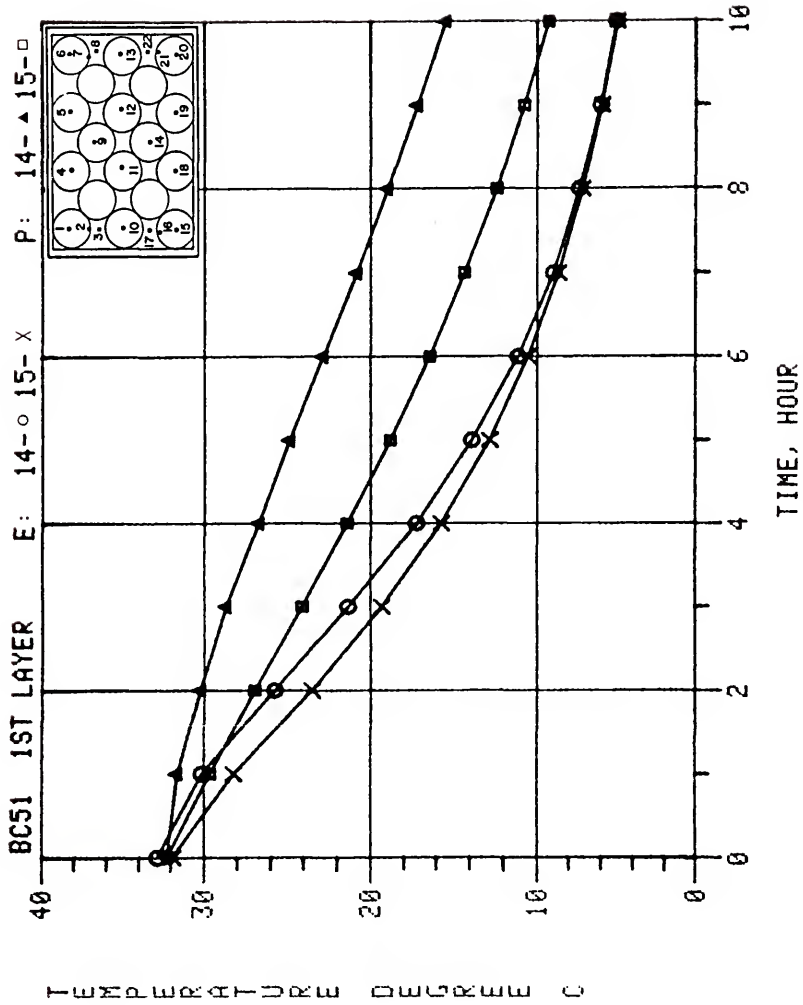


Figure G-48. Predicted versus experimental data for Boundary Condition 5-1, 1st layer thermocouples 14 and 15.

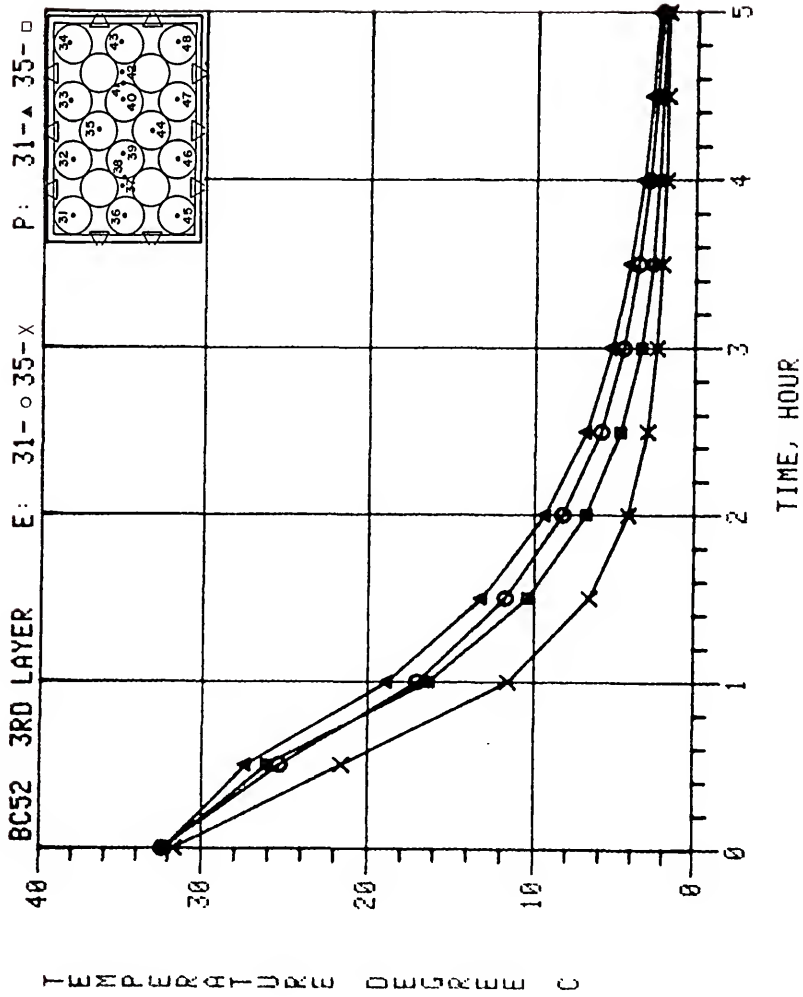


Figure G-49. Predicted versus experimental data for Boundary Condition 5-2, 3rd layer thermocouples 31 and 35.

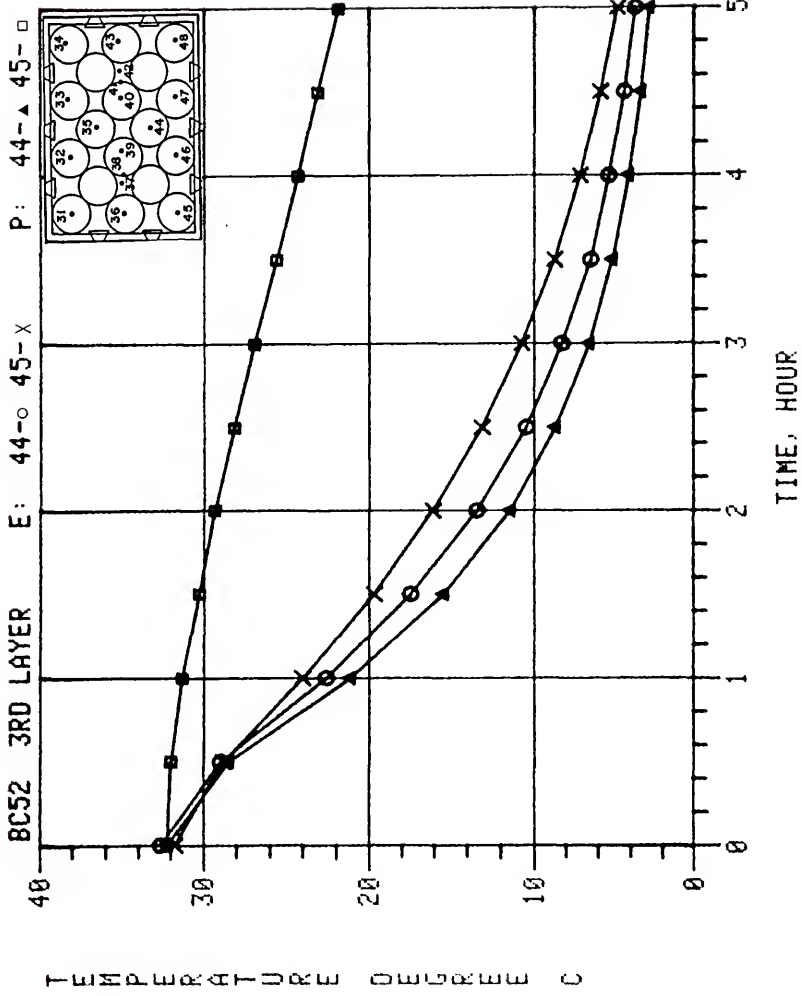


Figure G-50. Predicted versus experimental data for Boundary Condition 5-2, 3rd layer thermocouples 44 and 45.

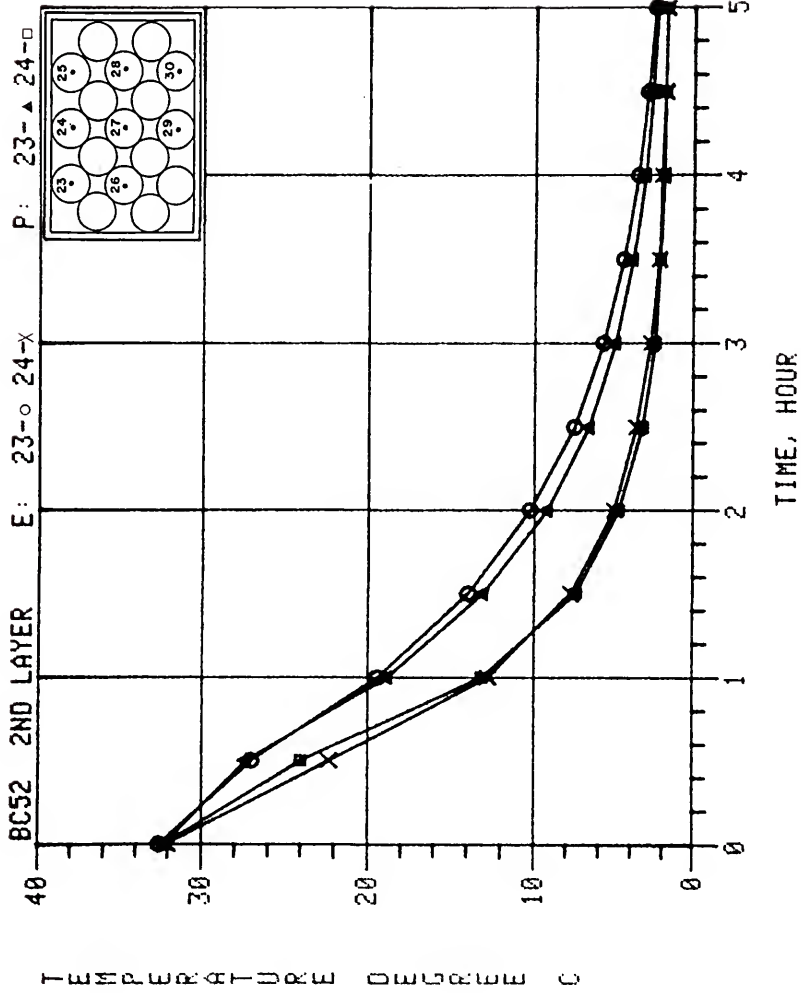


Figure G-51. Predicted versus experimental data for Boundary Condition 5-2, 2nd layer thermocouples 23 and 24.

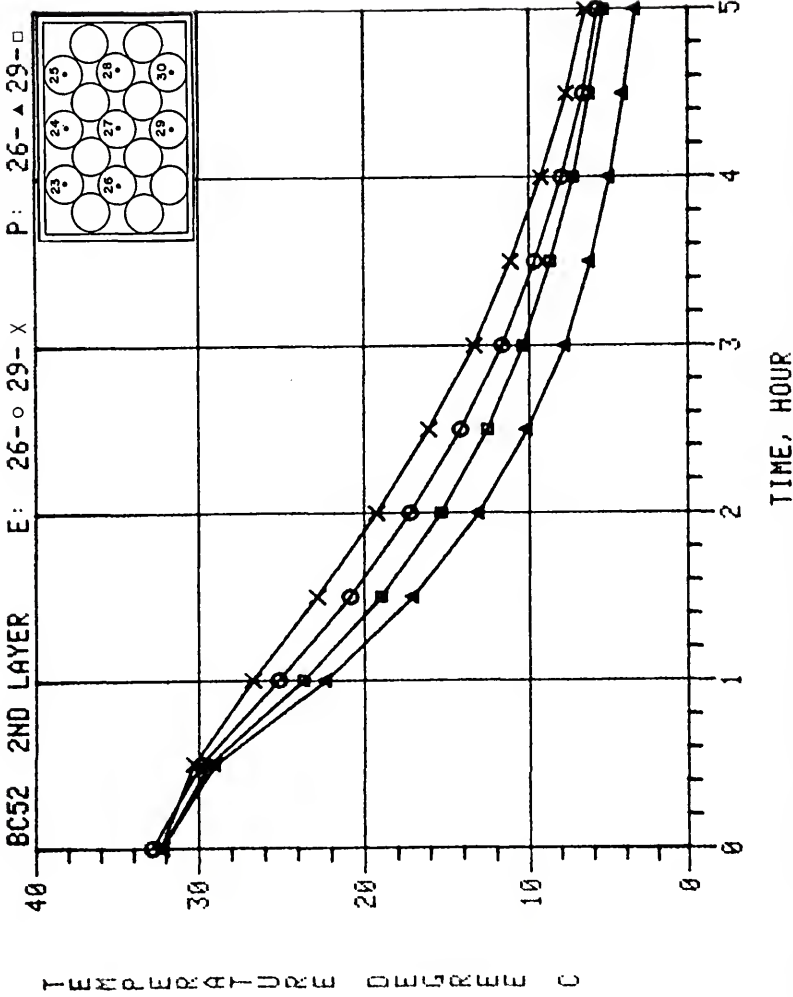


Figure G-52. Predicted versus experimental data for Boundary Condition 5-2, 2nd layer thermocouples 26 and 29.

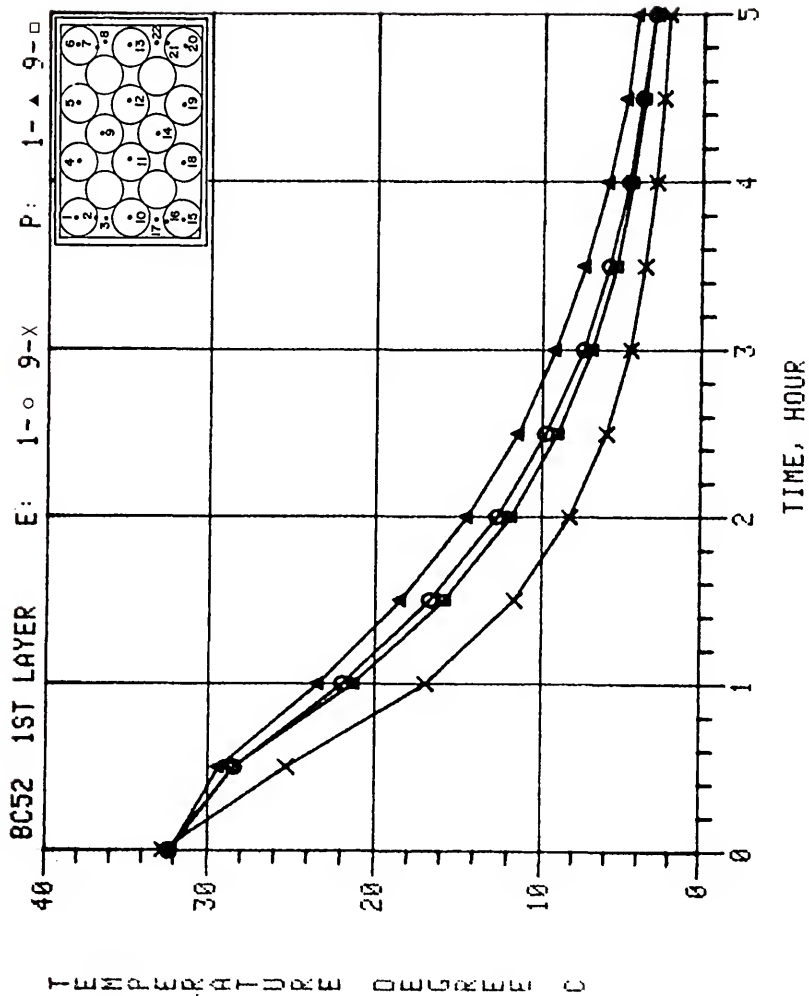


Figure G-53. Predicted versus experimental data for Boundary Condition 5-2, 1st layer thermocouples 1 and 9.

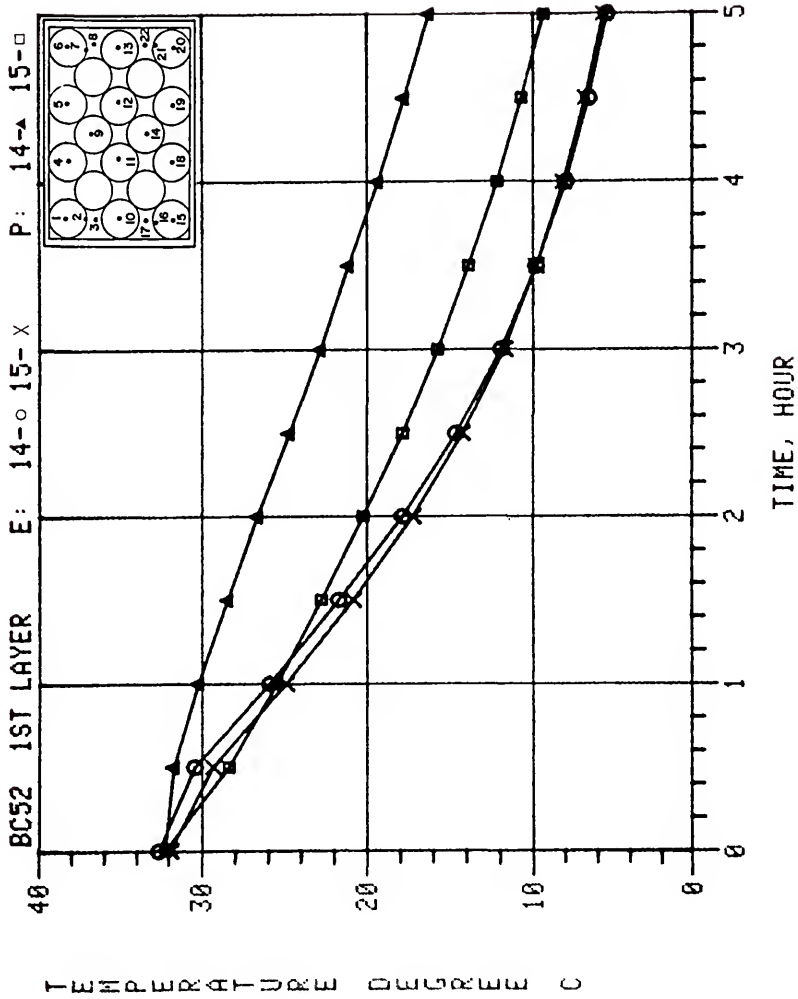


Figure G-54. Predicted versus experimental data for Boundary Condition 5-2, 1st layer thermocouples 14 and 15.

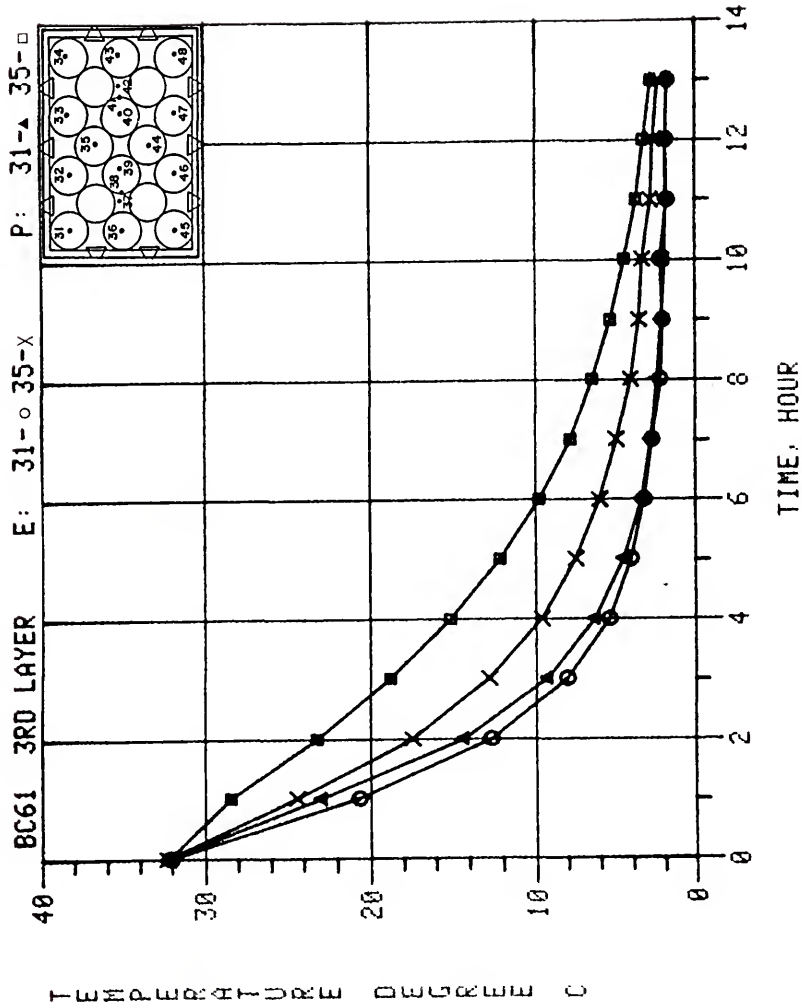


Figure G-55. Predicted versus experimental data for Boundary Condition 6-1, 3rd layer thermocouples 31 and 35.

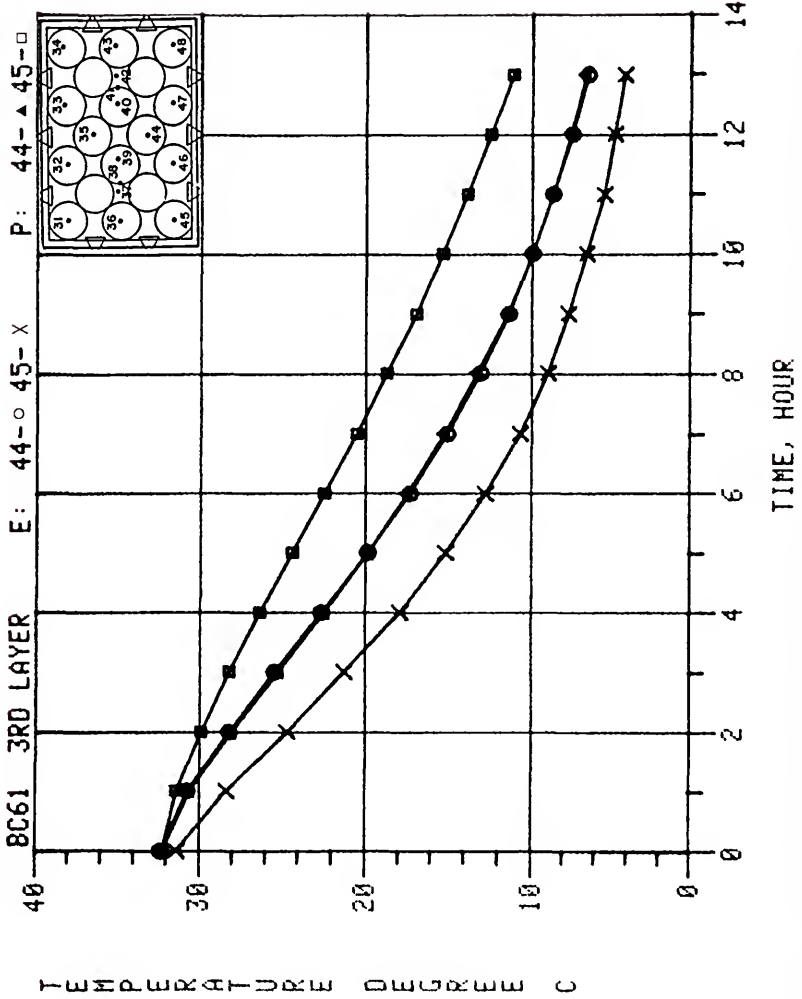


Figure G-56. Predicted versus experimental data for Boundary Condition 6-1, 3rd layer thermocouples 44 and 45.

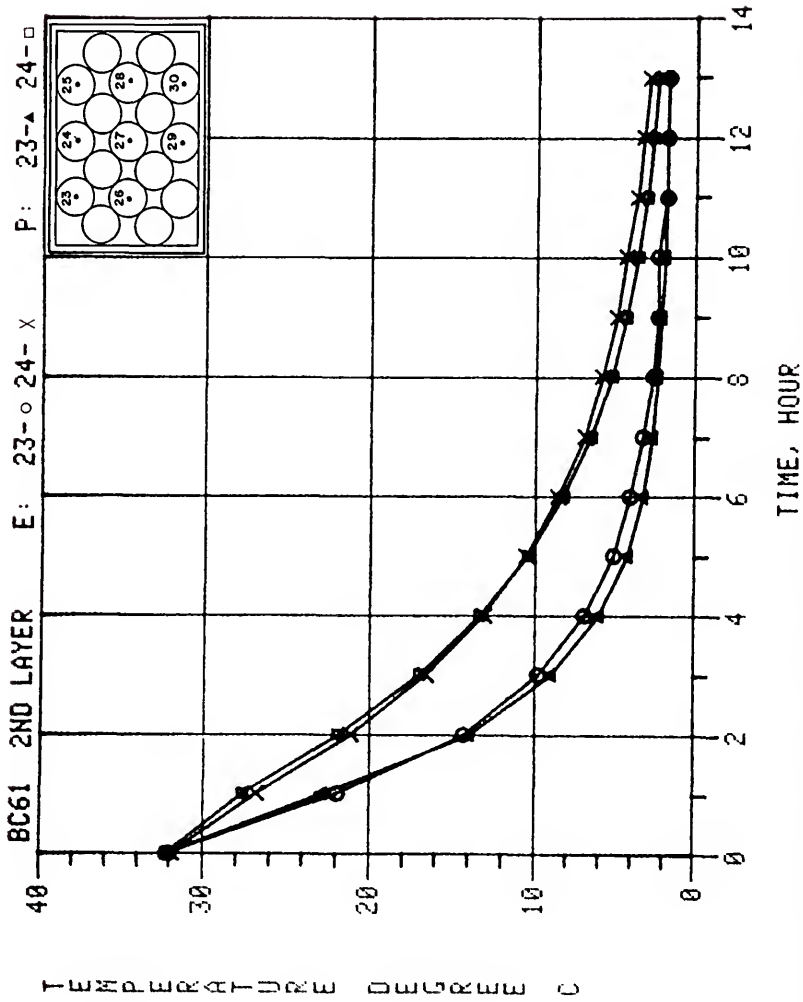


Figure G-57. Predicted versus experimental data for Boundary Condition 6-1, 2nd layer thermocouples 23 and 24.

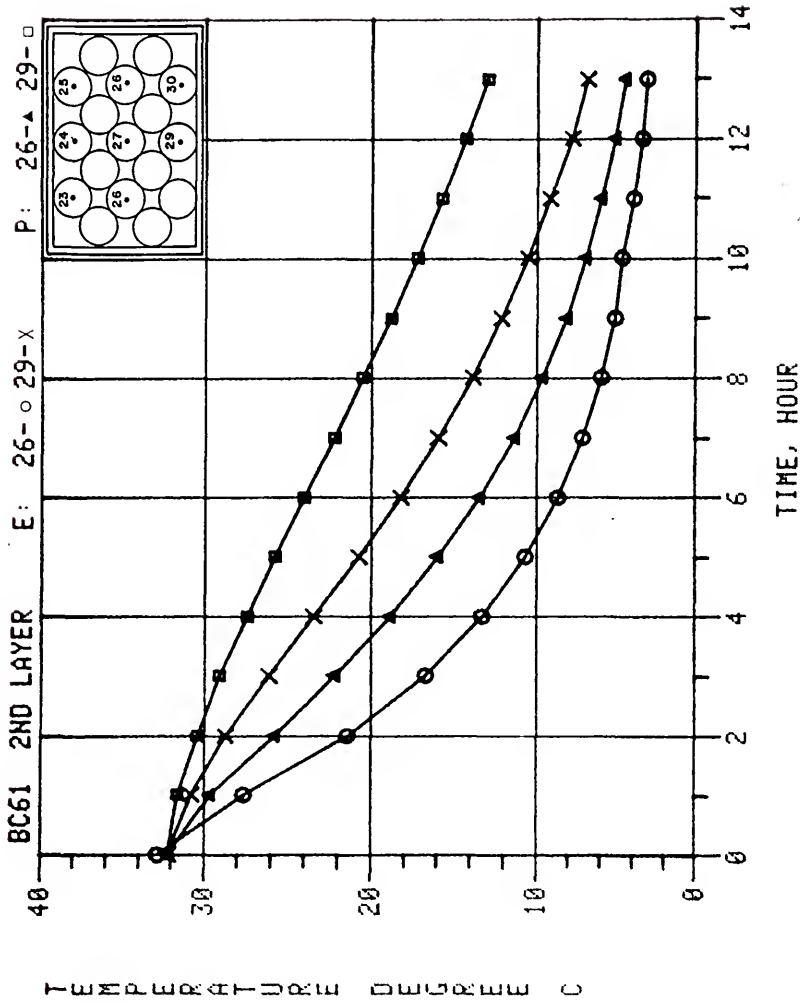


Figure G-58. Predicted versus experimental data for Boundary Condition 6-1, 2nd layer thermocouples 26 and 29.

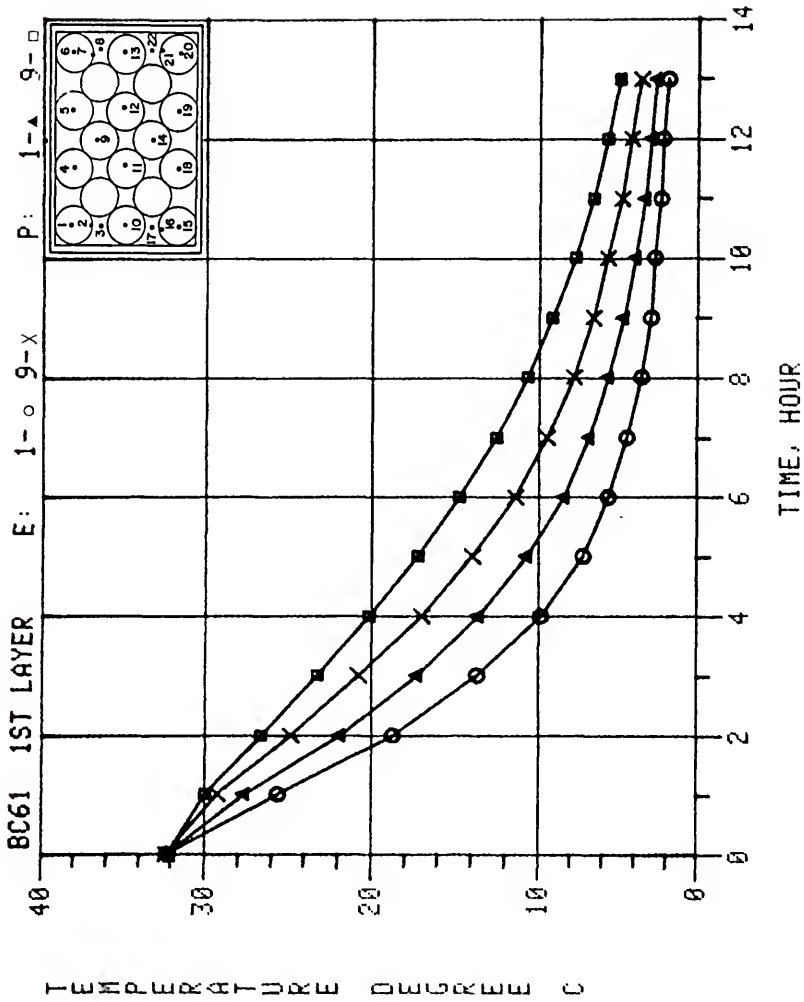


Figure G-59. Predicted versus experimental data for Boundary Condition 6-1, 1st layer thermocouples 1 and 9.

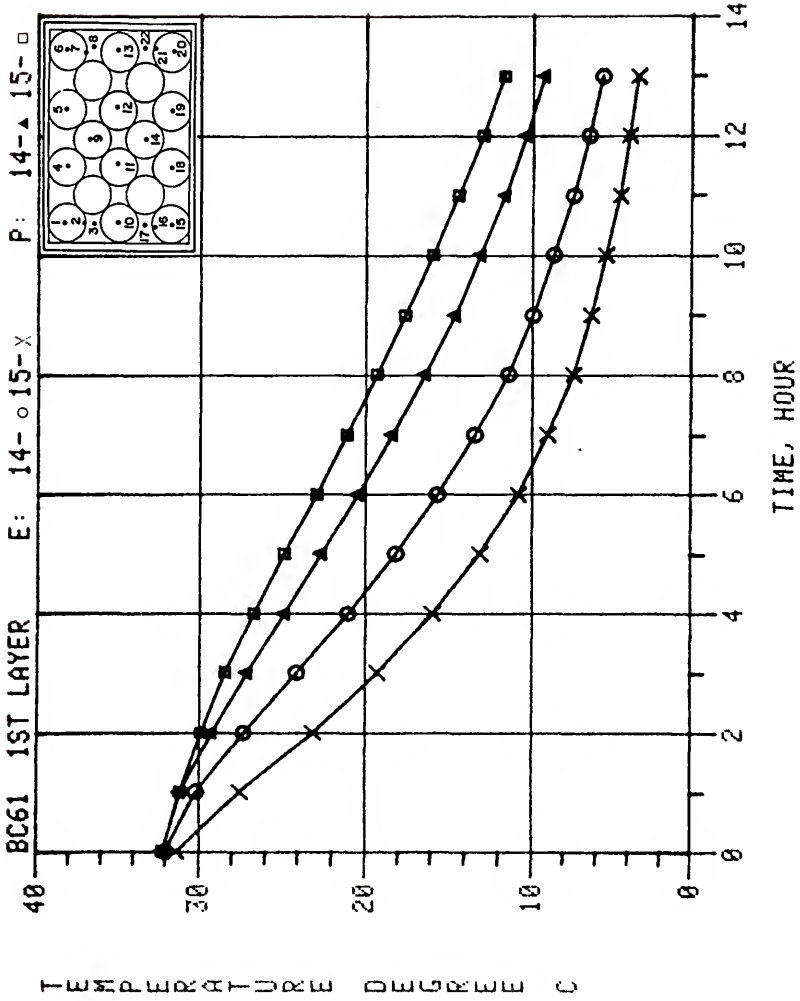


Figure G-60. Predicted versus experimental data for Boundary Condition 6-1, 1st layer thermocouples 14 and 15.

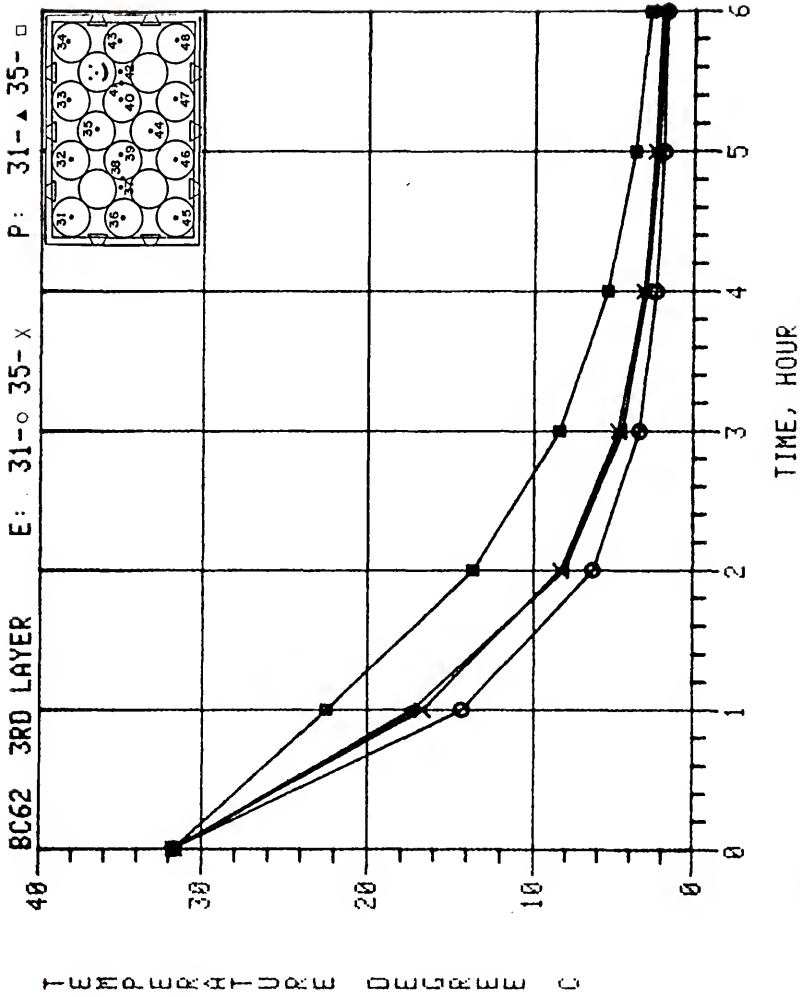


Figure G-61. Predicted versus experimental data for Boundary Condition 6-2, 3rd layer thermocouples 31 and 35.

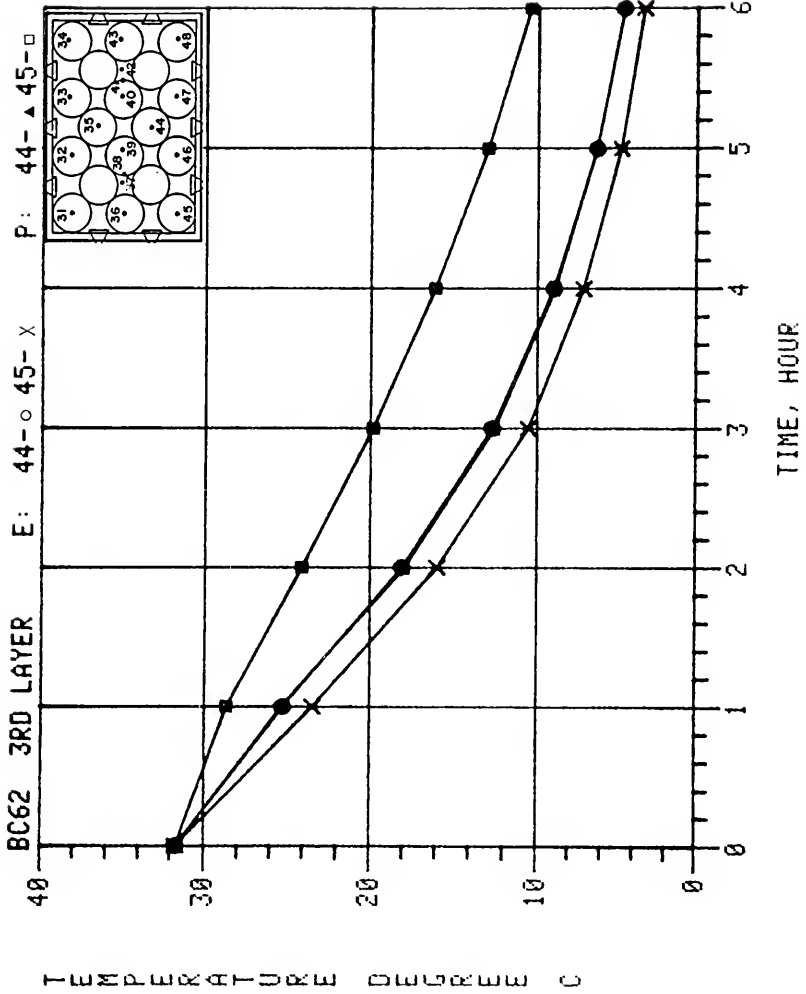


Figure G-62. Predicted versus experimental data for Boundary Condition 6-2, 3rd layer thermocouples 44 and 45.

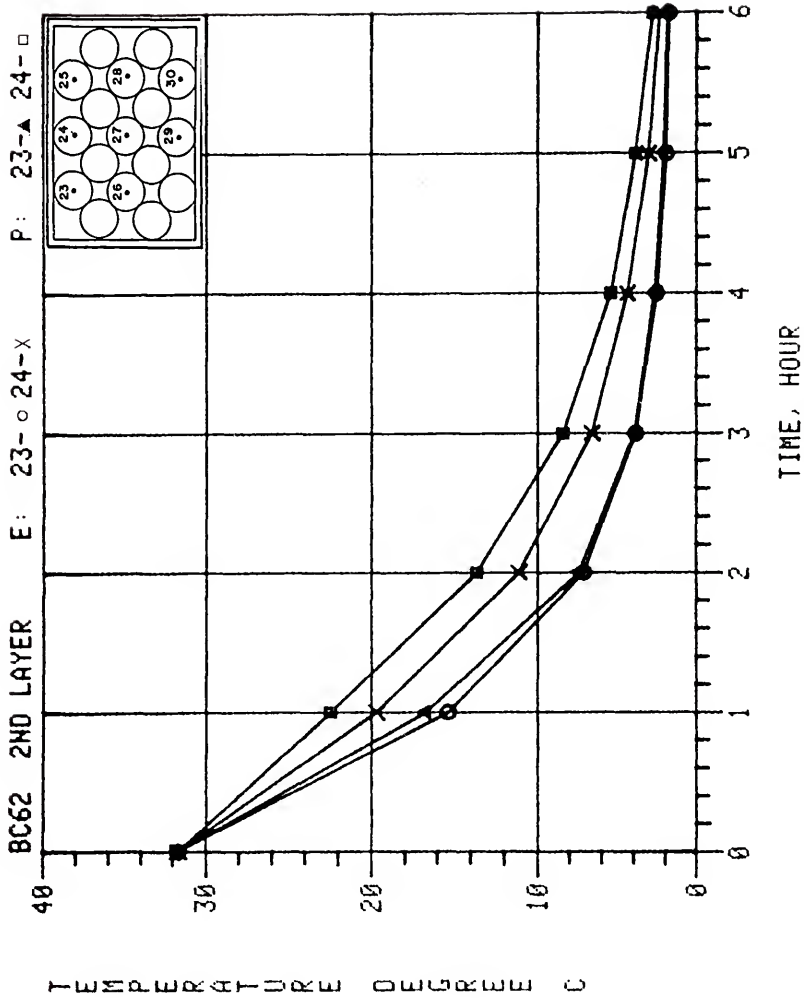


Figure G-63. Predicted versus experimental data for Boundary Condition 6-2, 2nd layer thermocouples 23 and 24.

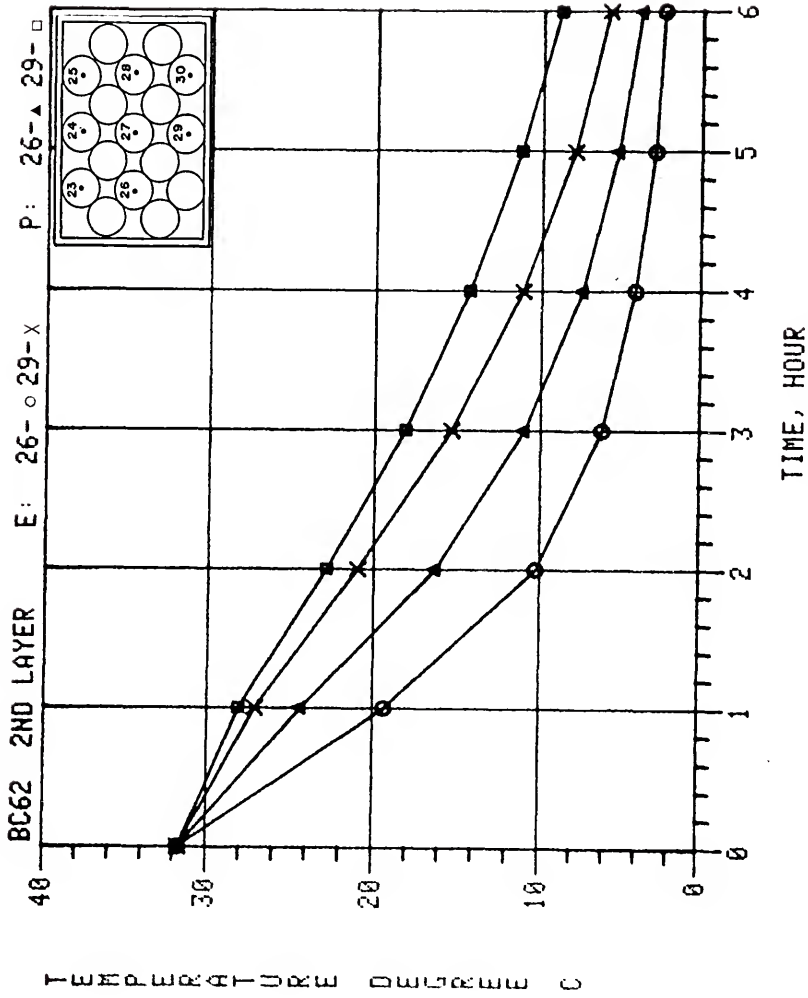


Figure G-64. Predicted versus experimental data for Boundary Condition 6-2, 2nd layer thermocouples 26 and 29.

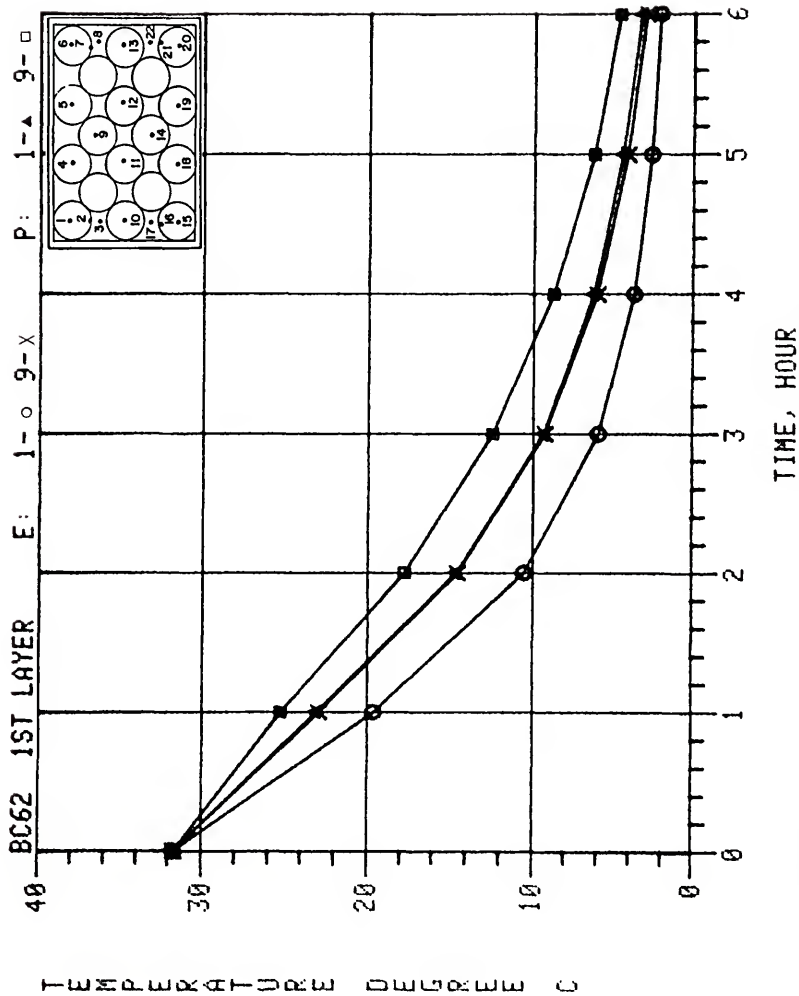


Figure G-65. Predicted versus experimental data for Boundary Condition 6-2, 1st layer thermocouples 1 and 9.

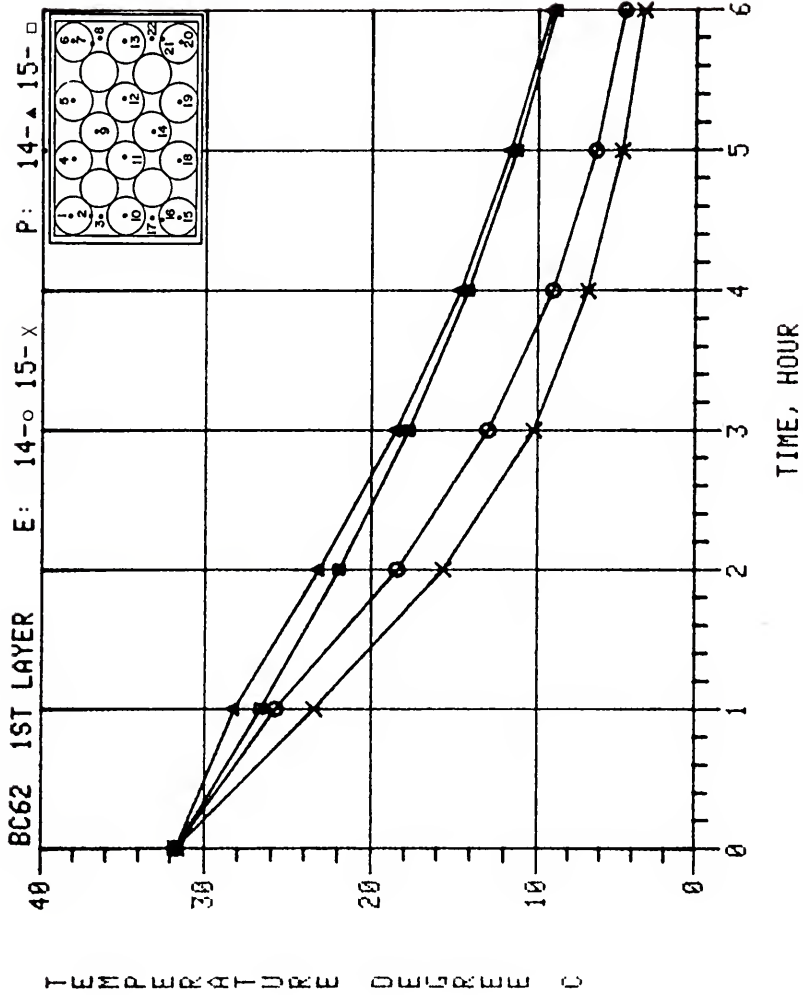


Figure G-66. Predicted versus experimental data for Boundary Condition 6-2, 1st layer thermocouples 14 and 15.

APPENDIX H
ADDITIONAL PREDICTED VERSUS EXPERIMENTAL
TEMPERATURE REGRESSION GRAPHS

The predicted versus experimental temperature regression plots for the eleven boundary conditions not presented in the main text are included on the following pages. For each boundary condition, the temperature regression graph is presented in the same manner as Figure 58 for Boundary Condition 1-1.

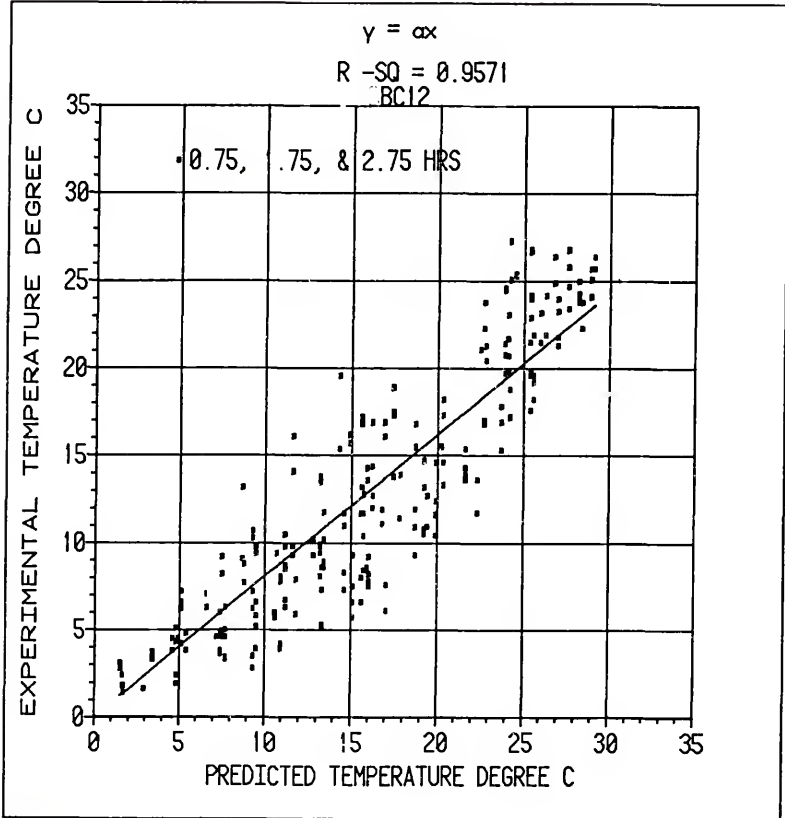


Figure H-1. Regression plot of the predicted temperature versus the experimental temperature for Boundary Condition 1-2 and test times of 0.75, 1.75, and 2.75 hours.

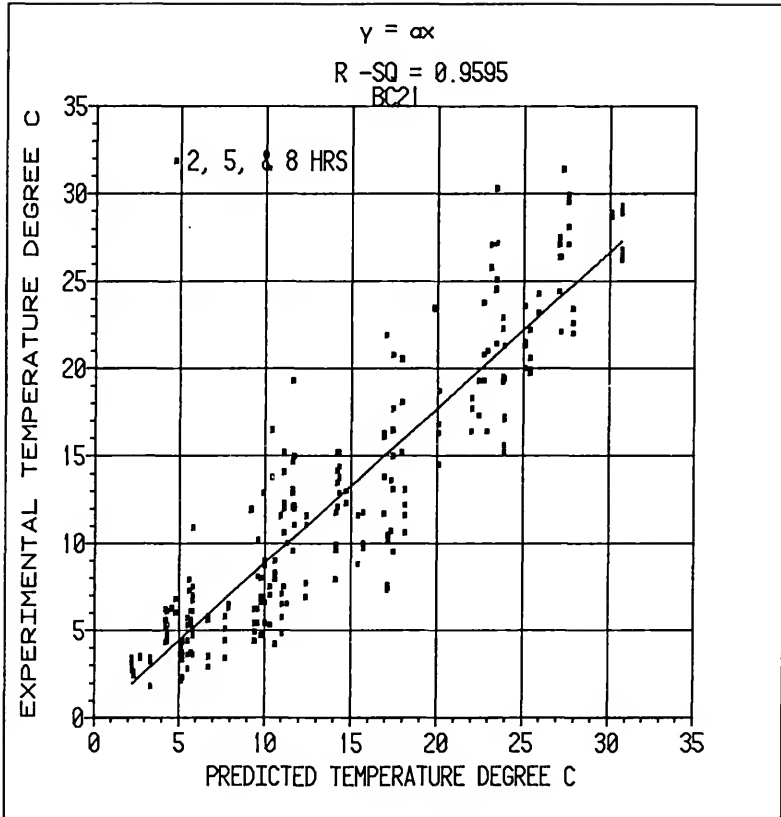


Figure H-2. Regression plot of the predicted temperature versus the experimental temperature for Boundary Condition 2-1 and test times of 2, 5, and 8 hours.

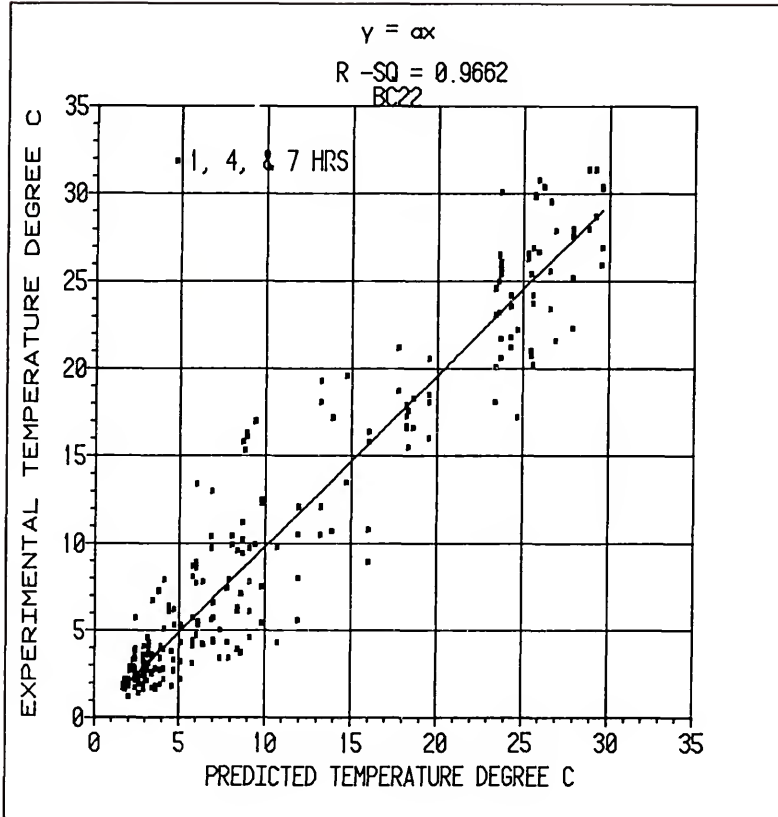


Figure H-3. Regression plot of the predicted temperature versus the experimental temperature for Boundary Condition 2-2 and test times of 1, 4, and 7 hours.

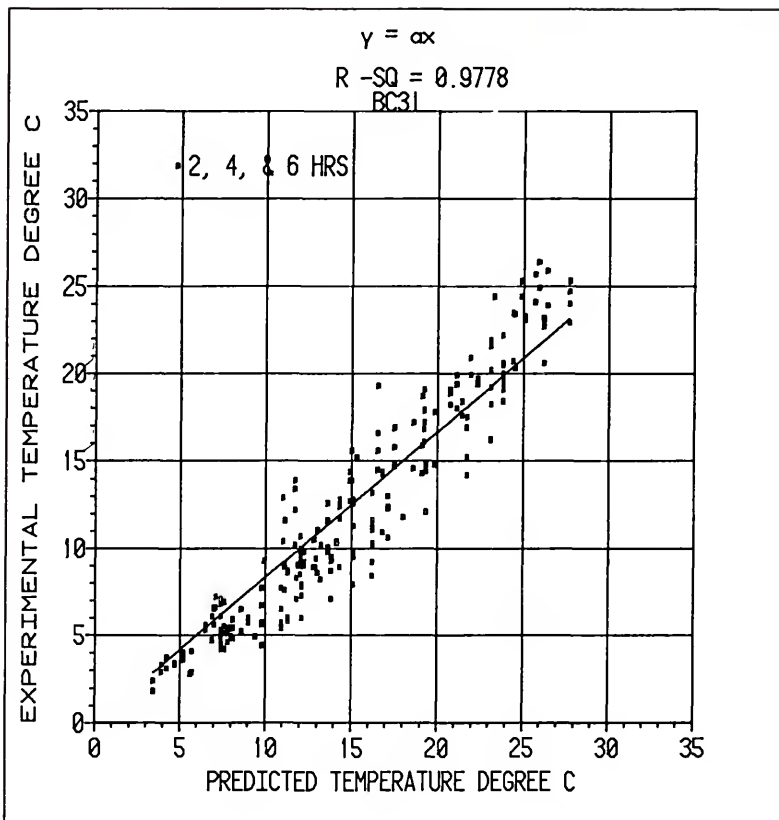


Figure H-4. Regression plot of the predicted temperature versus the experimental temperature for Boundary Condition 3-1 and test times of 2, 4, and 6 hours.

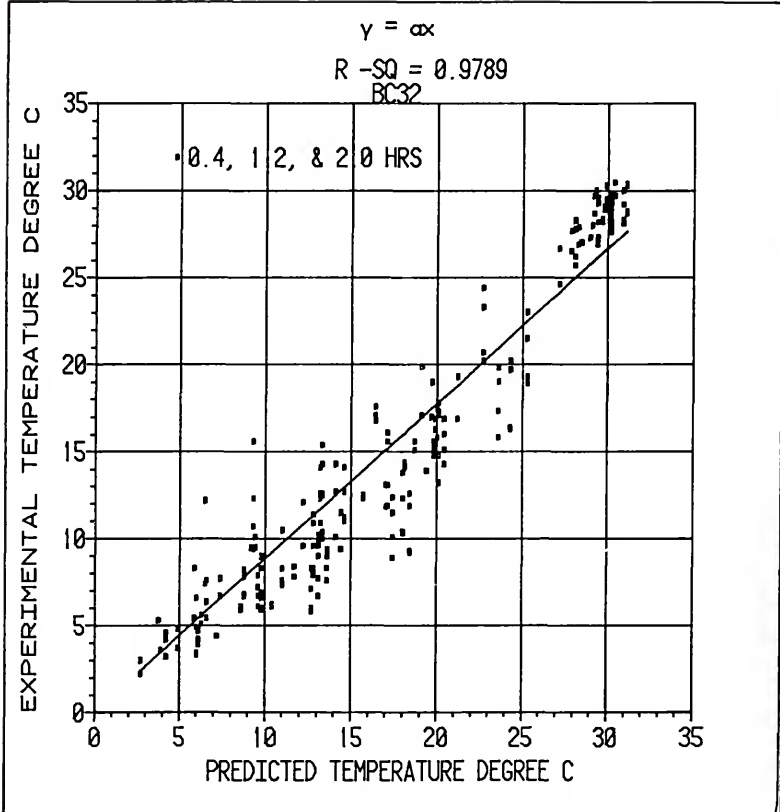


Figure H-5. Regression plot of the predicted temperature versus the experimental temperature for Boundary Condition 3-2 and test times of 0.4, 1.2, and 2.0 hours.

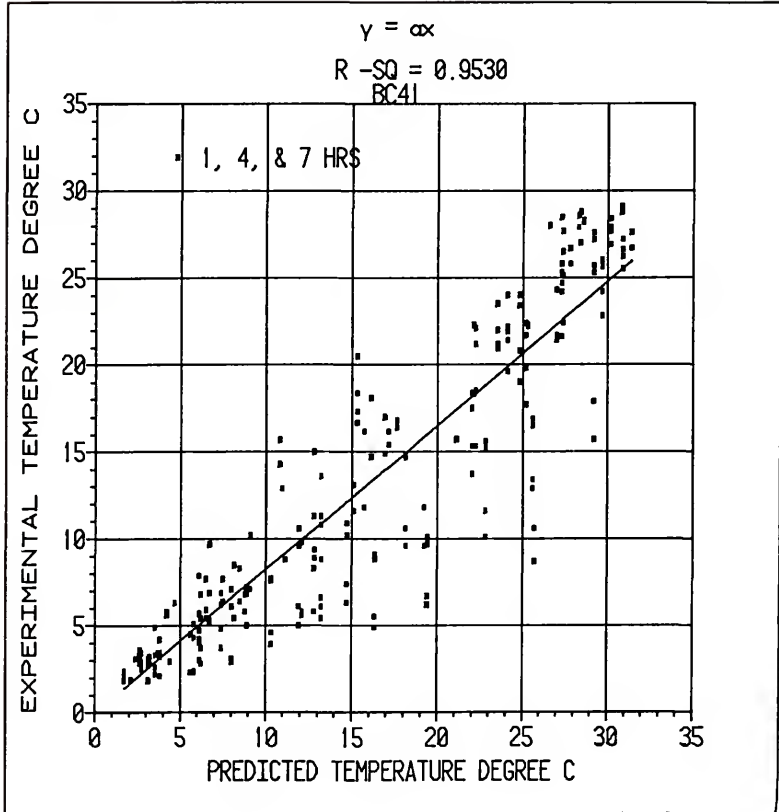


Figure H-6. Regression plot of the predicted temperature versus the experimental temperature for Boundary Condition 4-1 and test times of 1, 4, and 7 hours.

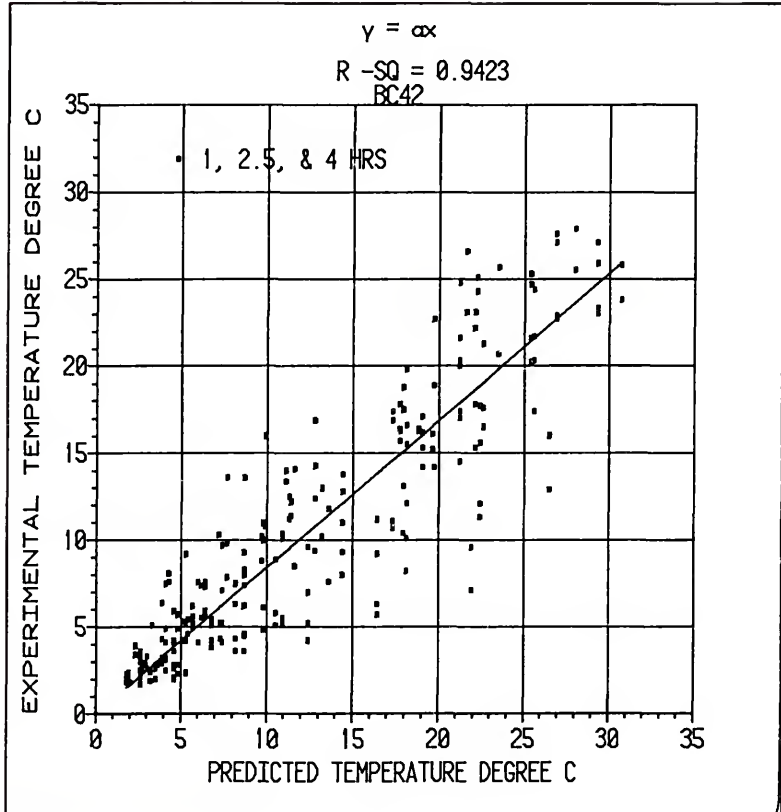


Figure H-7. Regression plot of the predicted temperature versus the experimental temperature for Boundary Condition 4-2 and test times of 1, 2.5, and 4 hours.

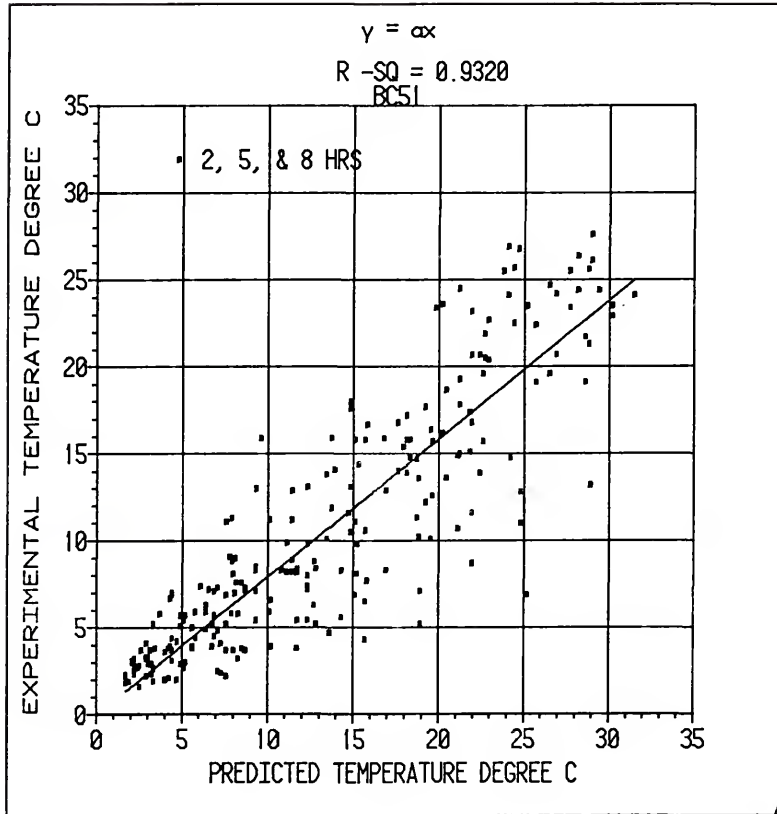


Figure H-8. Regression plot of the predicted temperature versus the experimental temperature for Boundary Condition 5-1 and test times of 2, 5, and 8 hours.

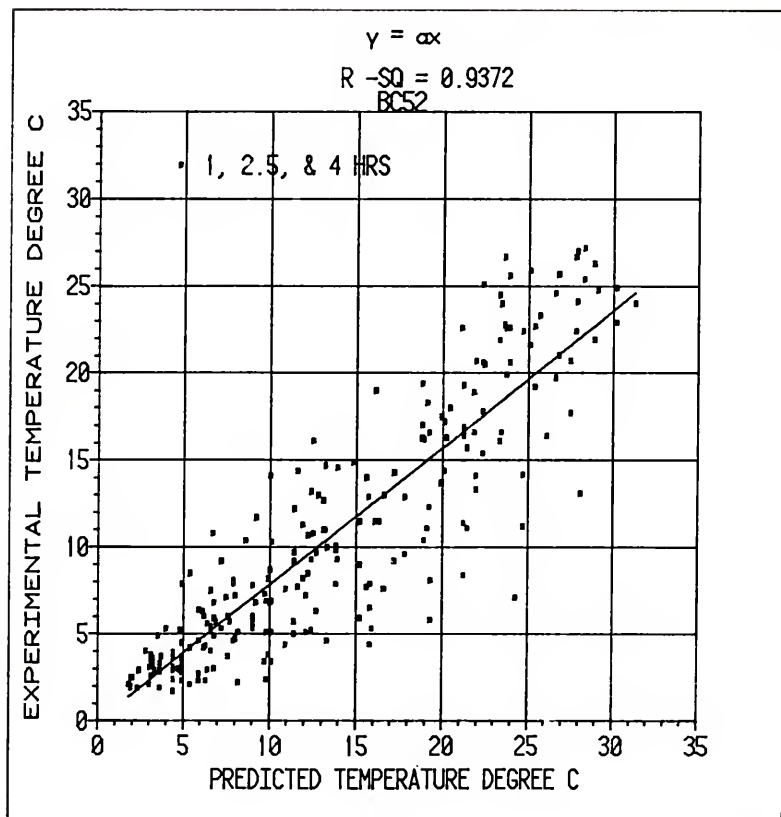


Figure H-9. Regression plot of the predicted temperature versus the experimental temperature for Boundary Condition 5-2 and test times of 1, 2.5, and 4 hours.

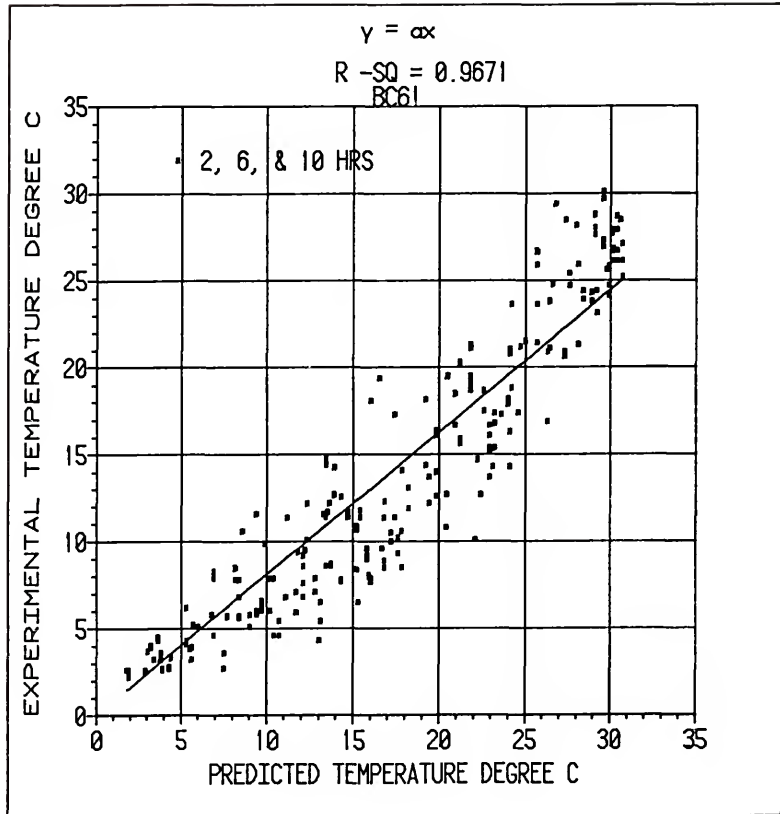


Figure H-10. Regression plot of the predicted temperature versus the experimental temperature for Boundary Condition 6-1 and test times of 2, 6, 10 hours.

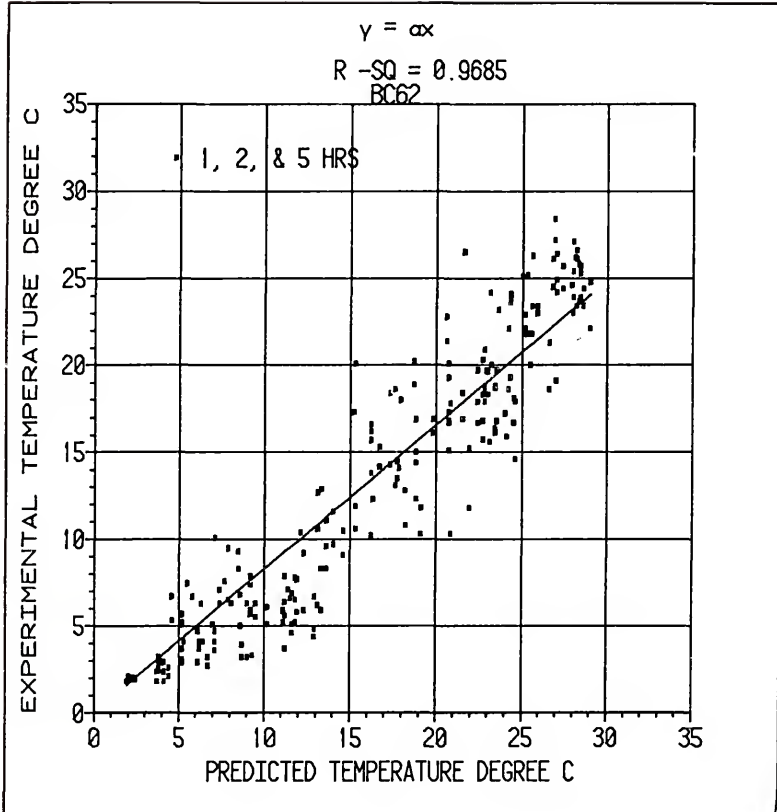


Figure H-11. Regression plot of the predicted temperature versus the experimental temperature for Boundary Condition 6-2 and test times of 1, 2, and 5 hours.

BIBLIOGRAPHY

Abrams, C. F. Jr. and J. D. Fish, Jr. 1978. Resistance of sweet potatoes to air flow. ASAE Paper 78-4523.

Akritidis, C.B. and A. J. Siatras. 1979. Resistance of pumpkin seeds to air flow. Transactions ASAE 2(6): 1414-1417.

Alyamovski, I.G. 1974. Heat exchange during cooling fruit and/or vegetables in stacks or in bulk. I.I.R. Bul. Annexe 3:75-81.

Andales, S.C. 1979. Two-dimensional cooling of bulk stored sugarbeets. Ph.D. Dissertatation, Washington State University. University Microfilms, Ann Arbor, Michigan.

Andales, S.C., C.A. Pellibone, and D.C. Davis. 1979. Two-dimensional cooling of bulk stored sugarbeets. ASAE Paper 79-4534.

Anderson, L.E.B. 1963. Pressure drop through packed beds. Transactions Royal Institute Technology, Stockholm, No. 201.

Anthony, Jr., J.P. 1969. Development of stacking patterns for handling and transporting unitized shipments of Florida citrus. USDA-ARS 52-42.

Baird, C.D. and J.J. Gaffney. 1974a. A numerical method for predicting heat transfer in a deep bed of fruits and vegetables. ASAE Paper 74-6018.

Baird, C.D. and J.J. Gaffney. 1974b. Temperature response of grapefruit during forced-air cooling. ASAE Paper 74-6523.

Baird, C.D. and J.J. Gaffney. 1976. A numerical procedure for calculating heat transfer in bulk loads of fruits and vegetables. ASHRAE Transactions 82(2):525-540.

Baird, C.D., J.J. Gaffney, and D. T. Kinard. 1975. Research facility for forced-air precooling of fruits and vegetables. Transactions ASAE 18(2):376-379.

Bakker-Arkema, F.W. and W.G. Bickert. 1966. A deep-bed computational cooling procedure for biological products. Transactions ASAE 9(6):834-836,845.

Bakker-Arkema, F.S., W.G. Bickert, and R.J. Patterson. 1967. Simultaneous heat and mass transfer during the cooling of a deep bed of biological products under varying inlet air conditions. J. Agr. Engng. Res. 12(4):297-307.

Bakker-Arkema, F.W., R.J. Patterson and W.G. Bickert. 1969. Static pressure--air flow relationships in packed beds of granular biological materials such as cherry pits. Transactions ASAE 12(1):134-136,140.

Bakker-Arkema, F.W., J.R. Rosenau, and W.H. Clifford. 1971. The effect of grain surface area on the heat and mass transfer rates in fixed and moving beds of biological products. Transactions ASAE 14(5):864-867.

Banks, P.J. 1970. Combined heat and moisture transfer in air flow through porous beds--prediction by analogy with heat transfer. I.I.R. Bul. Annexe 1970-3:39-46.

Barker, J.J. 1965. Heat transfer in packed beds. Ind. and Engng. Chem. 57(4):43-51.

Bauer, R. and E.U. Schlunder. 1978a. Effective radial thermal conductivity of packings in gas flow. Part I. Convective transport coefficient. Int. Chem. Engng. 18(2):181-188.

Bauer, R. and E.U. Schlunder. 1978b. Effective radial thermal conductivity of packing in gas flow. Part II. Thermal conductivity of the packing fraction without gas flow. Int. Chem. Engng. 18(2):189-204.

Beek, G.V. 1974. Heat transfer through layers of agricultural products of near spherical shape. I.I.R. Bul. Annexe 174-3:183-188.

Biales, A., W.F. Goddard, Jr., and T. Moffitt. 1973. Waterproof marine ventilation system for dry freight van containers. USDA Marketing Research Report No. 988. 23 p.

Bird, R.B., W.E. Stewart and E.N. Lightfoot. 1960. Transport phenomena. John Wiley and Sons, Inc., New York.

Borrowman, R. and D.S. Boyce. 1966. Air distribution from lateral ducts in barley. J. Agric. Engrg. Res. 11:243-247.

Breakiron, P.L. 1974. A definitive approach to engineering improved refrigerated trailer vans and containers. Transactions ASAE 17(1):38-41,45.

Brooker, D.B. 1958. Lateral duct airflow patterns in grain drying bins. *Agr. Engng.* 39:348-351.

Brooker, D.B. 1961. Pressure patterns in grain-drying systems established by numerical methods. *Transactions ASAE* 4(1):72-74,77.

Brooker, D.B. 1969. Computing air pressure and velocity distribution when air flows through a porous medium and non-linear velocity-pressure relationships exist. *Transactions ASAE* 12(1):118-120.

Bunn, J.M. and W.V. Hukill. 1963. Pressure pattern predictions for nonlinear air flow through porous media. *Transactions ASAE* 6(1):32-36.

Camp, T.H. 1979. Evaluation of a refrigerated barge-on-ship-system and loading patterns for postharvest quality of exported Texas grapefruit. *J. Amer. Soc. Hort. Sci.* 104(5):678-681.

Cargonell, R.G. 1979. Effect of pore distribution and flow segregation on dispersion in porous media. *Chem. Engng. Science* 34:1031-1039.

Carson, W.M. 1971. Approximate solution of the Navier Stokes equation for flow through a rectangularly packed bed of spheres. Ph.D. Dissertation, University of Idaho. University Microfilms, Ann Arbor, Michigan.

Carson, W.M. and G.L. Bloomsburg. 1972. Oseen approximation for packed bed flow--velocity profiles and friction factors. *Transactions ASAE* 15(3):543-547.

Carson, W.M., K.C. Watts and F. Desir. 1980. Design Data for air flow in plastic corrugated drainage pipes. *Transactions ASAE* 23(2):490-413.

Chalutz, E., M. Schiffman-Nadel, J. Waks, and F.S. Lattar. 1974. Precooling of citrus fruits prior to simulated transport in ventilated ships. *J. Amer. Soc. Hort. Sci.* 99(4):368-370.

Chau, K.V. 1980. Some new empirical equations for properties of moist air. *Transactions ASAE* 23(5):1267-1271,1280.

Chau, K.V., J.J. Gaffney, C.D. Baird, and G.A. Church III. 1983. Resistance to air flow of oranges in bulk and in cartons. *ASAE Paper* 83-6007.

Chau, K.V., J.J. Gaffney and S. Bellagha. 1984. Simulation of heat and mass transfer in products with internal heat generation and transpiration. ASAE Paper 84-6513.

Collins, R. E. 1961. Flow of fluids through porous materials. Reinhold Publishing Corp., New York.

Cunningham, M.E. and K.L. Peddicord. 1981. Heat convection in spheres packed in an infinite regular cubical array. IJHMT 24(7):1081-1088.

DeSalvo, G.J. 1982. ANSYS engineering analysis system verification manual. Swanson Analysis Systems, Inc. Houston, PA.

DeSalvo, G.J. and J.A. Swanson. 1983. ANSYS engineering analysis system user's manual. Swanson Analysis Systems, Inc. Houston, PA.

Eshleman, W.D., C.D. Baird and J.J. Gaffney. 1976. A numerical simulation of transient heat flow in irregular shaped foods. ASAE Paper 76-6504.

Ergun, S. 1952. Fluid flow through packed columns. Chem. Engng. Progress 48:89-94.

Felsenstein, G. and J. Zafrir. 1975. New methods for loading refrigerated containers for transporting fruit to Europe. Scientific Activities 1971-1974, Ministry of Agr. Institute of Agr. Engng., Bet Dagan, Israel. p. 67-72.

Fircozabadi, A. and D.L. Katz. 1979. An analysis of high-velocity gas flow through porous media. J. Petro. Tech. (Feb 1979):211-216.

Fountain, J.B. and R.M. Hovey. 1970. Feasibility of shipping golden delicious apples in tray-packed boxes. USDA Marketing Research Report No. 873. 11 p.

Gaffney, J. J. 1977. Engineering principles related to design of systems for air cooling of fruits and vegetables in shipping containers. Proc. 29th Int. Conf. Handling Perishable Agr. Commodities, Michigan State Univ. p. 151-164.

Gaffney, J.J. and C.D. Baird. 1977. Forced air cooling of bell peppers in bulk. Transactions ASAE 20(6):1174-1179.

Gaffney, J.J. and C.D. Baird. 1980. Physical and thermal properties of Florida Valencia oranges and Marsh grapefruit as related to heat transfer. ASAE Paper 80-6011.

Gaffney, J.J., C.D. Baird and W. D. Eshleman. 1980. Review and analysis of the transient method for determining thermal diffusivity of fruits and vegetables. ASHRAE Transactions 86(2):261-280.

Gaffney, J.J., C.D. Baird and K.V. Chau. 1985a. Influence of airflow rate, respiration, evaporative cooling, and other factors affecting weight loss calculations for fruits and vegetables. ASHRAE Transactions 91(1):200-216.

Gaffney, J.J., C.D. Baird and K.V. Chau. 1985b. Methods for calculating heat and mass transfer in fruits and vegetables. ASHRAE Transactions 91(28):333-352.

Galloway, L.R., W. Komarnicky and N. Epstein. 1957. Effect of packing configuration on mass and heat transfer in beds of stacked spheres. Canadian J. Chem. Engng. p. 139-150.

Geertsma, J. 1974. Estimating the coefficient of inertial resistance in fluid flow through porous media. Soc. Petro. Eng. J. (Oct 74):445-450.

Gentry, J.P. and K.E. Nelson. 1964. Conduction cooling of table grapes. Amer. J. Enology and Viticulture 15(1):41-46.

Goddard, W.F. 1972. Air distribution--the common denominator. ASHRAE Symposium Bul. No. 72-7:5-9.

Gottschlich, C.F. 1963. Axial dispersion in a packed bed. AIChE Journal 9(1):88-92.

Grierson, W., A.H. Bennett, and E.K. Bowman. 1970. Forced-air precooling of citrus fruit on a moving conveyor. USDA-ARS 52-40. 17 p.

Grierson, W. 1975. Vertical air distribution for cooling fruit in cartons. Proc. Fla. State Hort. Soc. 88:329-332.

Guillou, R. 1960. Coolers for fruits and vegetables. Calif. Agr. Exper. Sta. Bul. 773. 66 p.

Gupta, A.S. and G. Thodos. 1962. Mass and heat transfer through fixed and fluidized beds. Chem. Engng. Progress 58(7):58-62.

Haas, E. and G. Felsenstein. 1975. Operation and improvement of a commercial precooler for citrus fruit. Scientific Activities 1971-74. Ministry of Agr. Institute of Agr. Engng., Bet Dagan, Israel. p. 60-66.

Haas, E., G. Felsenstein, A. Shitzer, and G. Manor. 1976. Factors affecting resistance to air flow through packed fresh fruit. ASHRAE Transactions 82(2):548-554.

Hague, E., D.S. Chung and G.H. Foster. 1980. Pressure and velocity field in airflow through packed bed of corn mixed with fines under non-Darcy conditions. ASAE Paper 80-3016.

Hague, E., G.H. Foster, D.S. Chung, and F.S. Lai. 1978. Static pressure drop across a bed of corn mixed with fines. Transactions ASAE 31(5):997-1000.

Hale, P.W., L.A. Risse, and J.E. Jacobs. 1969. Feasibility of shipping temple oranges in plastic-cell tray-pack fiberboard boxes. USDA-ARS 52-35. 14 p.

Hale, P.W., R.H. Hinds, Jr., and T. Moffitt. 1973. Fiberboard cartons for exporting grapefruit. USDA-ARS-S-21. 7 p.

Hale, P.W. and L.A. Risse. 1974. Exporting grapefruit in tray pack cartons. Citrus and Vegetable Magazine. 37(12):12-13.

Happel, J. and N. Epstein. 1954. Cubical assemblages of uniform spheres. Ind. and Engng. Chem. 46(6):1187-1194.

Harris, C.M. and J.M. Harvey. 1976. Quality maintenance of California strawberries exported to far eastern markets. USDA Marketing Research Report No. 1053. 6 p.

Harris, C.M., F.M. Porter, and J.M. Harvey. 1969. Market quality and precooling rates of strawberries packed in various containers. USDA Marketing Research Report No. 851. 5 p.

Hicks, E.W. Sept. 1955. Precooling of fruit and vegetables--some theoretical considerations. Proc. IX Int. Congress of Refrigeration 078-085.

Hinds, Jr., R.H. and J.K. Robertson. 1965. A Better loading pattern for trailer shipments of citrus fruit. USDA Marketing Research Report No. 715. 8 p.

Hinsch, R.T., R.H. Hines, Jr., and W.F. Goddard, Jr. 1978. Lettuce temperatures in a van container with a reverse airflow circulation system. USDA Marketing Report No. 1082. 4 p.

Jindal, V.K. and T.L. Thompson. 1972. Air pressure patterns and flow paths in two-dimensional triangular-shaped piles of sorghum using forced convection. Transactions ASAE 15(4):737-741.

Kaminski, D.A. Ed. 1986a. General electric fluid flow data book. General Electric Company Corporate Research and Development, Schenectady, NY.

Kaminski, D.A. Ed. 1986b. General electric heat transfer data book. General Electric Company Corporate Research and Development, Schenectady, NY.

Kasmire, R.F. 1977. Carton venting is key to bell pepper cooling. Western Grower and Shipper, June. p 18.

Khompis, V. 1983. Three-dimensional finite element analysis of the flow field in cylindrical grain storages. Ph.D. Dissertation, Michigan State University. University Microfilms, Ann Arbor, Michigan.

Khompis, V., L.J. Segerlind, and R.C. Brook. 1984. Pressure patterns in cylindrical grain storages. ASAE Paper 84-3011.

Kindya, W.G. and A. Bongers. 1979. Results of test shipments of agricultural products cooled by outside air. Proc. XV Int. Congress of Refrigeration D2-21.

Kohnkle, P.C. 1982. ANSYS engineering analysis system theoretical manual. Swanson Analysis Systems, Inc. Houston, PA.

Kushman, L.J. and W.E. Ballinger. 1962. Forced-air cooling of blueberries. J. Amer. Soc. Hort. Science 81:281-287.

Lai, F.S. 1980. Three-dimensional flow of air through nonuniform grain beds. Transactions ASAE 23(3):729-734.

Lai, F.S. and E. Hague. 1976. Three-dimensional flow of air through nonuniform grain beds. ASAE Paper 76-3529.

Leggett, J.T. and G.E. Sutton. 1951. Precooling of citrus fruits. Univ. of Fla. College of Engineering. Bul. Series No. 43. 28 p.

Lindsay, R.T., M.A. Neale, and G.R. Westgate. 1976. Air cooling vegetables in small and large containers. NIAE No. DN/FB/423/3040.

Macdonald, I.F., M.S. El-Sayed, K. Mow, and F.A.L. Dullien. 1979. Flow through porous media--the Ergun equation revisited. Ind. and Engng. Chem. Fund. 18(3):199-208.

Marchant, J.A. 1976a. Prediction of fan pressure requirements in the drying of large hay bales. J. Agric. Engng. Res. 21:333-346.

Marchant, J.A. 1976b. Prediction of airflows in crop drying systems by finite elements method. J. Agr. Engng. Res. 21:417-429.

Marchant, J.A. and M.E. Nellist. 1977. Air pressure and flow in ducted crop drying systems. 1. single ducts. J. Agr. Engng. Res. 22:303-310.

Matthies, H.J. and H. Petersen. 1974. New data for calculating the resistance to airflow of stored granular materials. Transactions ASAE 17:1144-1149.

McDonald, R.E. and T.H. Camp. 1973. Effectiveness of three types of ventilation openings in full telescopic corrugated citrus cartons. USDA-ARS-S-25. 6 p.

McDonald, R.E., T.H. Camp, and W.F. Goddard, Jr. 1979. A modified fiberboard citrus box for conventional refrigerated trailers and USDA experimental van container. USDA Marketing Research Report No. 1100.

Meffert, H.F.T., J.W. Rudolphij and J.E. Rooda. 1973. Heat transfer during the cooling process of heat generating produce. Proc. XIII Int. Congress of Refrigeration 2:379-388.

Meffert, H.F.T. and G. Van Beek. 1975. Temperature development on product stacks of different size and geometry. I.I.R. Bul. Annexe 1974-3:69-74.

Meffert, H.F.T. and P. Van Vliet. 1971. Experimental methods for the evaluation of air circulation in containers. Proc. XIII Int. Congress of Refrigeration Sect. 7.11.

Meffert, H.F.T., P. Van Vliet, and G.R. Scrine. 1971. Temperatures of refrigerated cargoes in insulated vehicles. Proc. XIII Int. Congress of Refrigeration Sect. 7.12.

Mitchell, F.G., R. Guillou, and R.A. Parsons. 1972. Commercial cooling of fruits and vegetables. Univ. of Calif., Div. Agr. Sciences, Manual 43. 44p.

Mitchell, F.G., G. Mayer, and C.H. Campbell, Jr. 1968. Solid/spaced--A new carloading pattern for tight-fill packed fruit. Calif. Agr. 22(12):3-5.

Muskat, M. 1946. The flow of homogeneous fluids through porous media. J. W. Edwards, Inc. Ann Arbor, Michigan.

Neale, M.A. and H.J. M. Messer. 1976. Resistance of root and bulb vegetables to air flow. J. Agr. Res. 21:221-231.

Neale, M.A. and H.J. M. Messer. 1978. Resistance of leafy vegetables and inflorescences to air flow. J. Agr. Res. 23:67-75.

Olsen, K.L., G.O. Patchen, and H.A. Schomer. 1960. Cooling rates of apples packed in fiberboard boxes as influenced by vents, perforated trays, and stacking pattern. Wash. State Hort. Assoc. Proc. 56:214-220.

Pall R. and N.N. Mohsenin. 1977. Permeability of porous media as a function of porosity and particle size distribution. ASAE Paper 77-3061.

Parsons, R.A., F.G. Mitchell and G. Mayer. 1970. Forced-air cooling of palletized fresh fruit. ASAE Paper 70-875.

Parsons, R.A., F.G. Mitchell and G. Mayer. 1972. Forced air cooling of palletized fresh fruit. Transactions ASAE 15(4):729-731.

Patchen, G.L. 1969. Effects of vent holes on strength of fiberboard boxes and fruit cooling rate. USDA-ARS 52-34.

Patchen, G.O. and H.A. Schomer. 1971. Cooling and shipping sweet cherry gift packages. USDA-ARS 52-66. 7 p.

Patterson, R.J. 1969. Airflow-pressure drop characteristics of packed beds of biological particles. M.S., Michigan State University. University Microfilms, Ann Arbor, Michigan.

Patterson, R.J., F.W. Bakker-Arkema and W.G. Bicket. 1971. Static pressure-airflow relationships in packed beds of granular biological materials such as grain. II. Transactions ASAE 14(1):172-174,178.

Pentzer, W.T., C.E. Asbury, and W.R. Barger. 1945. Precooling California grapes and their refrigeration in transit. USDA Tech. Bul. No. 899. 64 p.

Perry, J.S., A.H. Bennett, and T.V. Minh. 1971. Experiments with a prototype commercial forced-air precooler on peaches, potatoes, apples and strawberries. Univ. Ga. Research Bul. 91. 19 p.

Pierce, R.O. and T. L. Thompson. 1974. Airflow patterns in conical shaped piles of grain. ASAE Paper 74-3015.

Pillai, K.K. 1977. Voldage variation at the wall of a packed bed of spheres. Chem. Engng. Science 32:59-61.

Ramaker, T.J. 1974. Thermal resistance of corrugated fiberboard. T.A.P.P.I. Journal 57(6):69-72.

Redit, W.H. and A.A. Hamer. 1959. Precooling and shipping Louisiana strawberries. USDA Marketing Research Report No. 358. 39 p.

Richardson, H.B., K.E. Nelson, and D. Meridith. 1955. Cooling tests of palletized units of table grapes using a portable and versatile research facility. Proc. XIII Int. Congress Refrigeration Sect. 4.54.

Ridgway, K. and K.J. Tarbuck. 1968. Voidage fluctuations in randomly-packed beds of spheres adjacent to a containing wall. Chem. Engng. Science 23:1147-1155.

Rij, R. E. 1977. Performance of 35-pound fiberboard boxes jumble-packed with peaches and nectarines. USDA Marketing Research Report No. 1077. 7 p.

Rosenau, J. 1970. Heat and mass transfer in onions. Ph.D. Dissertation, Michigan State University. University Microfilms, Ann Arbor, Michigan.

Rumsey, T. 1981. Pressure drop equations for fixed bed walnut dryers. ASAE Paper 81-3556.

Ryall, A.L. and W.T. Pentzer. 1967. The relation of air movement, container type, and load arrangement to the cooling rate of fruits and vegetables. Proc. XII Int. Congress of Refrigeration 3:87-92.

Sainsbury, G.F. 1951. Improved fruit cooling methods. Refrigerating Engng. 59(5):1-8.

Sainsbury, G.F. 1961. Cooling apples and pears in storage rooms. USDA Marketing Research Report No. 474. 55 p.

Sainsbury, G.F. and H.A. Schomer. 1967. Influence of carton stacking patterns on pear cooling rates. USDA Marketing Research Report No. 171 10 p.

Scheidegger, A.E., 1960. The physics of flow through porous media. University of Toronto Press, Toronto.

Schwartz, C.E. and J.M. Smith. 1953. Flow distribution in packed beds. Ind. and Engng. Chem. 45(6):1209-1218.

Segerlind, L.J. 1976. Applied finite element analysis. John Wiley and Sons, New York.

Segerlind, L.J., 1982. Solving the nonlinear airflow equation. ASAE Paper 82-3017.

Shedd, C.K. 1953. Resistance of grains and seed to air flow. Agr. Engng. 34:616-618.

- Shove, G.C. and W. V. Hukill. 1963. Predicting pressure gradients in perforated grain ventilation ducts. Transactions ASAE 6:115-122.
- Smith, E.A. 1982. Three-dimensional analysis of air velocity and pressure in beds of grain and hay. J. Agr. Engng. Res. 27(2):101-117.
- Soule, J., G.E. Youst, and A.H. Bennett. 1969. Experimental forced-air precooling of Florida citrus fruit. USDA Marketing Research Report No. 845. 27 p.
- Stanek, V. and E. Eckert. 1979. A study of the area porosity profiles in a bed of equal-diameter spheres confined by a plane. Chem. Engng. Science 34:933-940.
- Stanek, V. and J. Szekely. 1972. The effect of nonuniform porosity in causing flow maldistributions in isothermal packed beds. Canadian J. Chem. Engng. 50:9-14.
- Stanek, V. and J. Szekely. 1973. Flow maldistribution in two dimensional packed beds. Part V: The behavior of nonisothermal systems. Canadian J. Chem. Engng. 51:22-30.
- Stanek, V. and J. Szekely. 1974. Three-dimensional flow of fluids through nonuniform packed beds. AIChE Journal 20:974-980.
- Steele, J. L. 1974. Resistance of peanuts to air flow. Transactions ASAE 17(3):573-577.
- Stewart, J.K. 1977. Factors influencing temperatures of produce during transport. Proc. 29th Int. Conf. Handling Perishable Agr. Commodities. Michigan State Univ. pp 139-150.
- Thorpe, G.R. and A.J. Hunter. 1977. Expressions for pressure and velocity distributions in non-uniformly aerated grain bulks. J. Agr. Engng. Res. 22:27-35.
- Van Beek, G. 1975. Heat transfer through layers of agricultural products of near spherical shape. I.I.R. Bul. Annexe 1974-3:183-188.
- Wang, C.Y., T.R. Rumsey and R.P. Singh. 1979. Convective heat transfer coefficient in a packed bed of rice. ASAE Paper 79-3010.
- Wang, J.K. and K. Tunpun. 1969. Forced air precooling of tomatoes in cartons. Transactions ASAE 12(6):804-806.

Wentz, C.A. and G. Thodos. 1963a. Pressure drops in the flow of gases through packed and distended beds of spherical particles. *AIChE Journal* 9(1):81-84.

Wentz, C.A. and G. Thodos. 1963b. Total and form drag friction factors for the turbulent flow of air through packed and distended beds of spheres. *AIChE Journal* 9(3):359-361.

Whitaker, S. 1966. The equations of motion in porous media. *Chem. Engng. Science* 21:291-300.

Whitaker, S. 1969. Advances in theory of fluid motion in porous media. *Ind. and Engng. Chem.* 61(12):14-28.

Wilhelm, L.R., D.W. Jones, and C.A. Mullins. 1978. Air flow resistance of snap beans. *ASAE Paper* 78-3058.

Wilhelm, L.R., F.D. Tompkins, and C.A. Mullins. 1981. Air flow resistance of lima beans and southern peas. *ASAE Paper* 81-3034.

Winston, J.R, R.H. Cubbedge, and J. Kaufman. 1959. Shipping Florida citrus fruit in wirebound crates and cartons--A comparison of commercial practices. *USDA-AMS-342*.

Zienkiewicz, O.C. 1977. The finite element method (3rd ed.). McGraw-Hill, London.

BIOGRAPHICAL SKETCH

Michael Thomas Talbot was born December 29, 1948, in Florala, Alabama. He received his secondary education in Crestview, Florida. Upon graduation from Crestview High School he enrolled in Okaloosa-Walton Junior College, Valparaiso, Florida. He received his Associate of Arts degree in August, 1968. He enrolled as a junior in the College of Engineering of the University of Florida in September of 1968 and received a Bachelor of Science (with high honors) in agricultural engineering in June 1971. He enrolled in the Graduate School of the University of Florida in September of 1971 and received his Master of Engineering (thesis) in agricultural engineering in December 1973.

He was commissioned as a Second Lieutenant in the U.S. Army in June of 1972, after completing Advanced ROTC at the University of Florida. He began active duty as a Regular Army Engineer Officer in December 1973. After leaving active duty in June 1980, he accepted a position as Extension Agricultural Engineer in the Agricultural Engineering Department, where he is currently employed, and pursued the degree of Doctor of Philosophy in mechanical engineering on a part-time program until the present time.

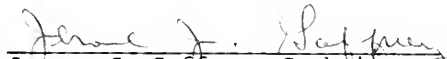
Michael T. Talbot was married to the former Anita Marie Hodge in June 1971, and they have one son, Michael.

I certify that I have read this study and that in my opinion it conforms to acceptable standards of scholarly presentation and is fully adequate, in scope and quality, as a dissertation for the degree of Doctor of Philosophy.



Calvin C. Oliver, Chairman
Professor of Mechanical
Engineering

I certify that I have read this study and that in my opinion it conforms to acceptable standards of scholarly presentation and is fully adequate, in scope and quality, as a dissertation for the degree of Doctor of Philosophy.



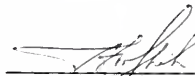
Jerome J. Gaffney, Cochairman
Associate Professor of
Agricultural Engineering

I certify that I have read this study and that in my opinion it conforms to acceptable standards of scholarly presentation and is fully adequate, in scope and quality, as a dissertation for the degree of Doctor of Philosophy.



Herbert A. Ingley, III
Associate Professor of
Mechanical Engineering

I certify that I have read this study and that in my opinion it conforms to acceptable standards of scholarly presentation and is fully adequate, in scope and quality, as a dissertation for the degree of Doctor of Philosophy.



Tom I. Shih
Assistant Professor of
Mechanical Engineering

I certify that I have read this study and that in my opinion it conforms to acceptable standards of scholarly presentation and is fully adequate, in scope and quality, as a dissertation for the degree of Doctor of Philosophy.

Richard F. Matthews

Richard F. Matthews
Professor of Food Science and
Human Nutrition

This dissertation was submitted to the Graduate Faculty of the College of Engineering and to the Graduate School and was accepted as partial fulfillment of the requirements for the degree of Doctor of Philosophy.

AUGUST 1987

Hubert A. Bewi

Dean, College of Engineering

Madelyn Gackhart

Dean, Graduate School

UNIVERSITY OF FLORIDA



3 1262 08666 254 0